



**HAL**  
open science

# High Temperature Durability of DS200+Hf Alloy

Lorena Mataveli Suave

► **To cite this version:**

Lorena Mataveli Suave. High Temperature Durability of DS200+Hf Alloy. Other. ISAE-ENSMA Ecole Nationale Supérieure de Mécanique et d'Aérotechnique - Poitiers, 2017. English. NNT : 2017ESMA0032 . tel-01735231

**HAL Id: tel-01735231**

**<https://theses.hal.science/tel-01735231v1>**

Submitted on 15 Mar 2018

**HAL** is a multi-disciplinary open access archive for the deposit and dissemination of scientific research documents, whether they are published or not. The documents may come from teaching and research institutions in France or abroad, or from public or private research centers.

L'archive ouverte pluridisciplinaire **HAL**, est destinée au dépôt et à la diffusion de documents scientifiques de niveau recherche, publiés ou non, émanant des établissements d'enseignement et de recherche français ou étrangers, des laboratoires publics ou privés.

# THESE

Pour l'obtention du Grade de  
DOCTEUR DE L'ECOLE NATIONALE SUPERIEURE DE MECANIQUE ET  
D'AEROTECHNIQUE  
(Diplôme National – Arrêté du 25 mai 2016)

Ecole Doctorale :  
Sciences et Ingénierie en Matériaux, Mécanique, Energétique et Aéronautique

Secteur de Recherche : Mécanique des Solides, des Matériaux, des Structures et des Surfaces

Présentée par :

Lorena MATAVELI SUAVE

\*\*\*\*\*

HIGH TEMPERATURE DURABILITY OF DS200+Hf ALLOY

\*\*\*\*\*

Directeur de thèse : Patrick Villechaise

Co-encadrants : Jonathan Cormier et Denis Bertheau

\*\*\*\*\*

Soutenue le 4 Décembre 2017

devant la Commission d'Examen

\*\*\*\*\*

## JURY

Rapporteurs :

Eric Andrieu

Catherine M.F. Rae

Professeur, ENSIACET, CIRIMAT, Toulouse

Professeur, Université de Cambridge, Cambridge

Membres du jury :

Rémy Chieragatti

Georges Cailletaud

Lionel Marcin

Jonathan Cormier

Patrick Villechaise

Professeur associé, ISAE-SUPAERO, Toulouse

Professeur, MINES ParisTech, Centre de Matériaux, Paris

Ingénieur Safran Tech, Magny Les Hameaux

Maitre de Conférences, ISAE-ENSMA, Institut Pprime, Poitiers

Directeur de Recherche CNRS, Institut Pprime, Poitiers



## Acknowledgments

Ce travail de thèse a été réalisé au sein du Département "Physique et Mécanique des Matériaux" de l'institut PPrime sur la direction de M. Dr. Patrick Villechaise, directeur de recherche CNRS, et l'encadrement de M. Dr. Jonathan Cormier, maître de conférences à l'ISAE-ENSMA, et de M. Dr. Denis Bertheau, ingénieur de recherche CNRS. Merci à vous par l'encadrement pendant ce projet.

I'd like to thank Mrs. Dr. Catherine Rae, professor of Cambridge University, for accepting to be the president of my PhD thesis jury and for reporting my PhD thesis manuscript. Thank you for your comments on my work and also for being patient about the English mistakes!

J'aimerais remercier M. Dr. Rémy Chieragatti, professeur associé à l'ISAE-SUPAERO, d'avoir accepté juger mon travail et partager de ses connaissances sur ce vieux alliage.

Merci à M. Dr. Éric Andrieu, professeur à l'ENSIACET, d'avoir accepté être rapporteur de ma thèse et de lire avec soin toutes ces pages remplies d'échantillons pleins de beaux oxydes...

Merci à M. Dr. Georges Cailletaud, professeur à l'École de Mines de Paris, et à M. Dr. Lionel Marcin, ingénieur à Safran, d'avoir participé au jury de thèse et à mon manuscrit.

Patrick et Denis, merci d'avoir partagé tant de connaissances, d'avoir toujours été si patients et constructifs! Je vous dois beaucoup de ce que je sais aujourd'hui. Je suis enchantée d'avoir pu partager toutes ces cartographies EBSD et ces essais mécaniques avec vous! J'aurais aimé avoir toujours eu des personnes aussi humbles et compétentes que vous dans mon parcours académique et professionnel.

Jonathan, le maître du fluage et des superalliages, mais pas que. Tu es source d'inspiration, de génialité et de générosité. Je dois te remercier d'avoir partagé de ton savoir. Ce que je sais aujourd'hui sur les superalliages n'est qu'un petit échantillon de tout ce que tu as dans ta tête mais m'est déjà une belle arme pour affronter les défis liés à mon travail sur ces cubes mis (ou non) en radeaux.

Georges, même si loin géographiquement tu as été présent pour apporter ta touche mécanique! Merci pour tout. Je regrette n'avoir pas consacré plus de temps sur les modèles mécaniques à ton côté, j'espère pouvoir rattraper un peu du retard dans mon avenir professionnel.

Lionel, merci d'avoir suivi ma thèse côté Safran. Tu m'as toujours appuyé et m'as aidé à acquérir plein d'expériences et connaissances au sein du groupe.

Merci à tous mes collègues Safran qu'on a suivis et participé à ma thèse. Vous avez été si participatifs et nombreux pendant ce temps que serait fou de ma part d'essayer de faire une liste de noms. Savoir que mon travail était exploité et me sentir utile pour le groupe m'ont poussé à faire mon mieux et m'ont donné de l'énergie pour continuer.

Merci à mes collègues de l'ENSMA et de PPRIME. Tout le personnel a été adorable et prêt pour me donner un coup de main à tout moment nécessaire. Avancer avec cette équipe était tellement plaisant et facile! J'ai vu tout au long de mon passage par le laboratoire beaucoup de professionnels passionnés mais aussi d'être humains prêts à partager. Je vous dois beaucoup de ce que j'ai pu faire. Merci aux doctorants, étudiants et stagiaires. J'ai eu l'opportunité de connaître plein de personnes géniales avant, pendant et après ma période de thèse et je garde en mémoire plein de bonnes choses sur les moments que j'ai pu passer avec vous.

Merci à mes amis « français » et « non français ». Dans ce pays j'ai pu connaître des personnes merveilleuses venues de tous les coins de ce monde. Quelle richesse humaine et culturelle votre amitié

a pu m'apporter ! Merci d'avoir été présents et avoir fait partie de cette étape de mon histoire. J'espère pouvoir partager encore beaucoup avec vous.

Primeiramente queria dizer que sem Ele nada disso teria sido possível. Muito obrigada meu Deus de ter me dado as armas necessárias pra conquistar o que eu tenho hoje.

Queria agradecer a todos aqueles que mesmo do outro lado do oceano tiveram todo esse tempo aqui dentro do meu coração e que me deram as bases e as forças pra continuar meu caminho por aqui.

Minha família: mamãe, papai e Belinha. Vocês são tudo na minha vida e sem vocês eu não seria nada e todo o resto não faria sentido. Muito obrigada por serem como vocês são e pela força que vocês me dão. A cada passo que eu dou aqui eu carrego vocês três comigo sempre.

Meu namorado e companheiro, você aparece em português também, afinal meu coração fala essa língua e é aqui dentro que você está! Você foi essencial para a realização desse projeto. Nenhuma palavra escrita é suficiente, simplesmente: obrigada!

Meus amigos brasileiros, vocês foram fundamentais em todos os momentos da minha vida e mesmo longe vocês colaboraram muito pra conquista de mais essa etapa. Muito obrigada por estarem sempre presentes.

Os professores que eu tive nesse país que amo tanto, se eu conquistei esse diploma hoje foi também com a educação e o conhecimento que vocês me transmitiram desde criança.

Famílias Mataveli e Suave, a carga genética não é fácil a canalizar mas vocês sabem que todos os meus passos são guiados por esses genes italianos difíceis e que sem vocês eu não teria chegado aqui!

# General Introduction

## General Introduction

Directionally solidified (DS) Ni-based superalloys are widely used for the manufacturing of blades and vanes in aero-engines and industrial gas turbines [1-3]. Despite the rather old character of the DS200+Hf (also known as PWA 1422 [4]), developed more than 45 years ago [5], it is still used for the design of modern aero-engines components such as cooled or un-cooled low pressure turbine (LPT) blades (Figure 1). One of the main reasons is related to its very good castability, allowing the design of sophisticated blade profile shapes and very thin trailing edges. This kind of material consists of nearly  $\langle 001 \rangle$  columnar grains oriented along the solidification direction and with random secondary orientations (see Figure 1).

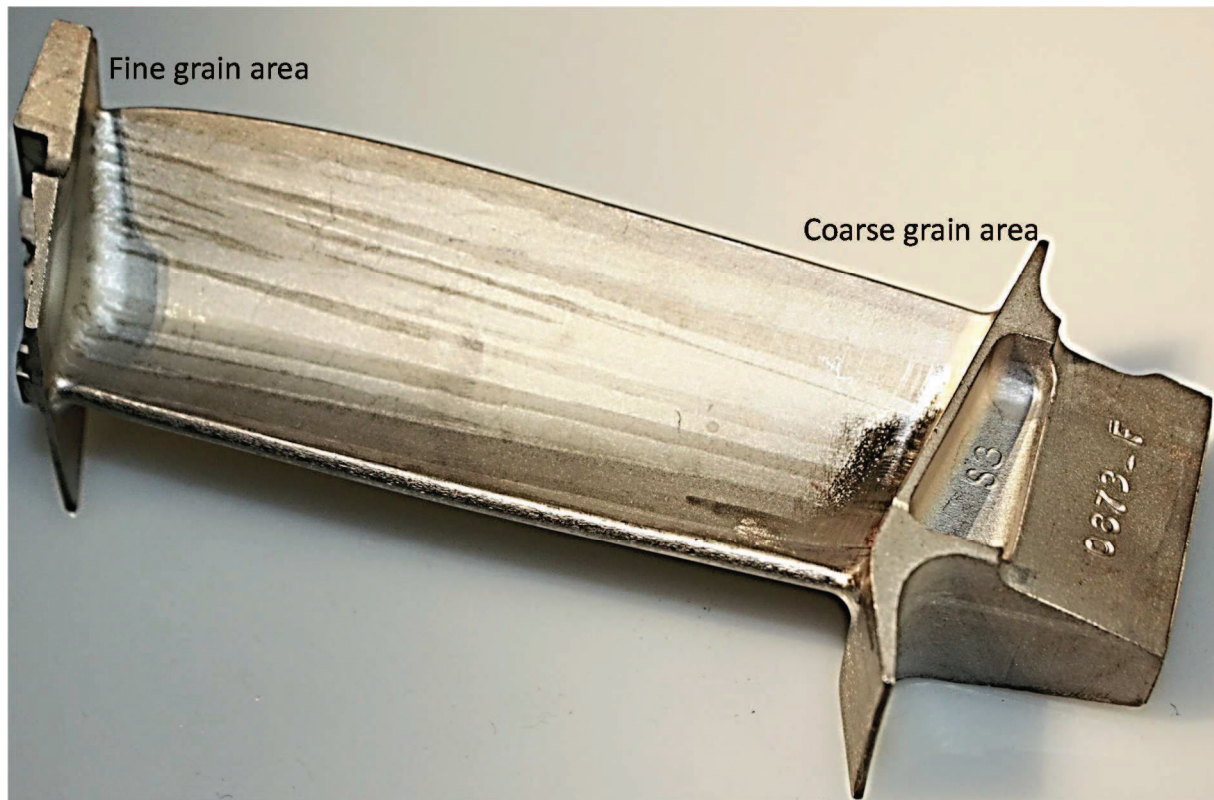


*Figure 1 - Example of a DS200+Hf low-pressure turbine blade used in a SAFRAN engine showing grain size differences between the top and the root (scale bar not added for confidential reasons).*

The alloy studied during this PhD thesis has been used at SAFRAN Aircraft Engines for nearly 40 years, since its pioneering application in the Olympus Engine used for the Concorde supersonic civil aircraft (DS200+Hf was used in this engine for the manufacturing of internally cooled high pressure turbine blades). From this application, a high hafnium content version of this alloy ( $\sim 1.5$  and  $1.8$  wt. pct) has been chosen to avoid grain boundary hot tearing issues during the solidification of large castings, and also to achieve a better grain boundary strength at high temperature [1-6], to improve the durability during service operations [2]. DS200+Hf has since that period been widely used for the manufacturing of airfoils used in several LPT stages of CFM 56\* engines used to power Airbus A319/A320/A321 and Boeing 737 civil aircrafts and also in SAFRAN military engines. More recently, this alloy has been introduced for the manufacturing of LPT blades in the new generation LEAP\* civil turbofans (part 8 in Figure 2) with increased efficiency and reduced specific consumption (compared to former CFM 56 engines). These newly developed engines are/will be used to power Airbus A320 Néo/A321 Néo, Boeing 737 MAX and Comac C919 newly developed medium range civil aircrafts. To achieve such

\* CFM 56 and LEAP engines are produced by the CFM international company which is a joint venture between General Electric (50%) and SAFRAN (50%).

increased efficiency and specific consumption in LEAP engines, higher operating temperatures are expected on LPT blades, leading to more demanding thermo-mechanical operating conditions that deserve to be characterized in a better way.

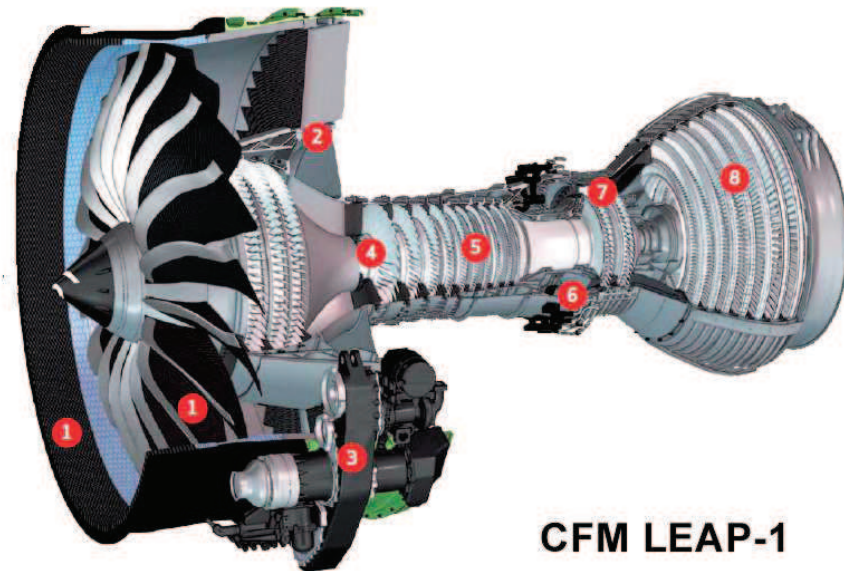


Figure 2 - Cut-out view of a LEAP – 1 turbofan, showing the different stages of the low-pressure turbine (8).

Moreover, during operations, due to the complex blade geometries with platforms, shrouds, internal cooling systems and possible profile twisting, the main mechanical loading direction does not only results from the centrifugal stresses along the solidification direction, as schematically illustrated in Figure 3. For example, the profile is mainly exposed to centrifugal forces along the  $\langle 001 \rangle$  solidification direction. However, shrouds are very critical parts because they are exposed to transverse and compressive loads at very high temperatures. Moreover, the presence of several stress concentrators (e.g. cooling holes for some cases of LPT blades), in addition to thermal gradients across the thickness, may locally lead to loading directions almost perpendicular to the solidification direction.

If the mechanical properties along the solidification direction are well characterized for these alloys [1, 2, 5, 7-10], very limited transverse mechanical properties are available in the open literature (in creep and fatigue). In addition, transverse mechanical properties have never been rationalized taking into account the grain size variation that can be observed at a component scale (see, e.g., Figure 1). The large scatter in mechanical properties observed could be due to this missing consideration [11-14]. **Then the characterization and understanding of the anisotropy in mechanical properties, in addition to the effect of grain size on transverse mechanical properties, will be two main objectives of this study.**

DS200+Hf is also known to have a rather poor environmental resistance compared to other DS or conventionally cast superalloys since this alloy does not form a continuous and dense alumina layer in the oxidation regime [2, 15]. This poor environmental resistance can be an issue for applications considering thin-walled uncoated components. Even if some studies about the influence of oxidation on creep properties of similar Ni-based single crystalline superalloys were published recently [16, 17], almost no study has been done on the characterization of the debit in mechanical properties induced by oxidation in DS Ni-based superalloys, and how the anisotropy in mechanical properties is affected



by oxidation. Hence, a special focus will be paid to the impact of oxidation on creep and low-cycle fatigue (LCF) properties by performing creep and LCF tests in air and in high vacuum or by reducing the specimen thickness in air. These characterizations will be used as inputs for the development of a creep-oxidation-damage coupled model to predict the impact of oxidation on the minimum strain rate and time to failure in creep.

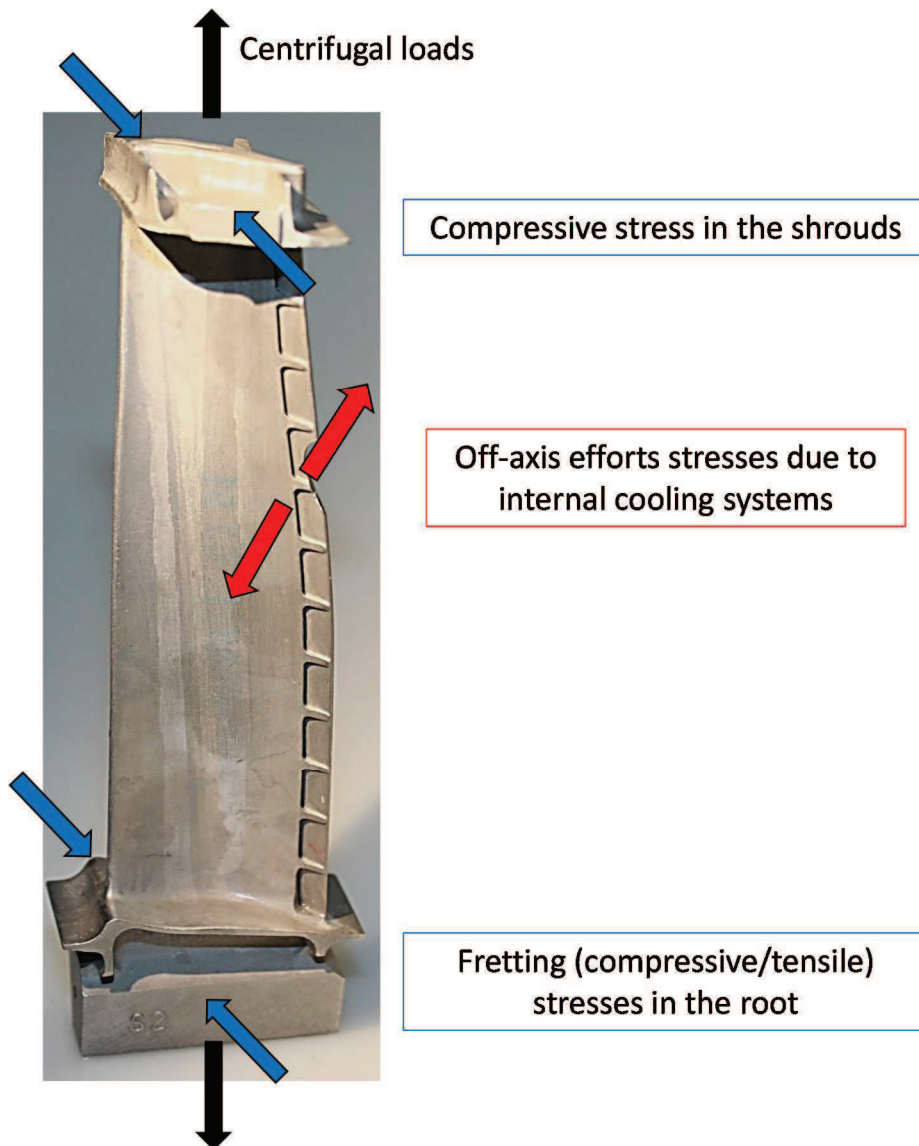


Figure 3 – DS200+Hf LPT blade main mechanical solicitations (without scale bar for confidentiality reasons).

Then, the main objective of this work is to investigate the damage mechanisms in creep, low cycle fatigue and dwell-fatigue of DS200+Hf alloy in a wide temperature range (650°C-1100°C), isolating, if possible, the contributions of oxidation and crystallography in the crack nucleation and subsequent propagation mechanisms. For this, this manuscript will fall into four main chapters:

1. Chapter 1 will be devoted to a literature review, focused on the fabrication processes and microstructure at different scales of DS nickel-based superalloys, on the mechanical properties of DS and Ni-based single crystal superalloys and on their environmental resistance.
2. In chapter 2, a presentation of the castings used for this study will be proposed, in addition to all the experimental procedures used for mechanical characterization in creep, low cycle

fatigue, dwell-fatigue, crack propagation and tension tests. Microstructural investigation procedures will also be presented.

3. Chapter 3 will present all mechanical results in tension, creep, LCF and dwell-fatigue, with a special focus on the stress-strain or strain rate-stress relationships and on the anisotropy in mechanical properties and durability.
4. Chapter 4, in which the most original results of this PhD thesis are presented, will especially be focused on the damage mechanisms, with a special focus on the role of oxidation, of grain boundaries and on the crystallography. Very unique experiments involving in situ strain measurements at the grain scale, complemented by EBSD characterizations will be presented in this chapter.

This PhD thesis has been conducted in the framework of a joint program involving SAFRAN companies (SAFRAN Tech, SAFRAN Aircraft Engines and SAFRAN Helicopter Engines), the Insitut Pprime at ISAE-ENSMA in Poitiers and the Centre des Matériaux, at Mines ParisTech in Paris. In addition to the present PhD thesis, a second PhD thesis recently defended by Florent Coudon [18] has been conducted at Mines Paristech. The aim of this second PhD was the identification of mechanical constitutive equations at the grain scale based on the results contained in the present manuscript. Then, the final objective was to propose a scale transition allowing the computation of the stress-strain state distributions in real components under different operating conditions, without any requirement of the exact crystallographic orientations of each grain within the component, neither the real morphology of grain boundaries.

## References of the Introduction

1. M.J. Donachie and S.J. Donachie, *Superalloys: a technical guide*. 2002: ASM international.
2. M. Gell, D.N. Duhl, and A.F. Giamei. *The development of single crystal superalloy turbine blades*. in *Superalloys 1980*. 1980. Seven Springs, PA, USA: TMS. p. 205-214.
3. R.C. Reed, *The Superalloys - Fundamentals and Applications*. 2006, Cambridge, UK: Cambridge University Press.
4. A.D. Cetel and D.N. Duhl. *Second generation columnar grain nickel-base superalloy*. in *Superalloys 1992*. 1992. Seven Springs, Champion, PA, USA: TMS. p. 287-296.
5. F.L. Versnyder and M.E. Shank, *The development of columnar grain and single crystal high temperature materials through directional solidification*. *Materials Science and Engineering*, 1970. **6**: p. 213-247.
6. D.N. Duhl and C.P. Sullivan, *Some effects of hafnium additions on the mechanical properties of a columnar-grained nickel-base superalloy*. *Journal of Metals*, 1971. **23**(7): p. 38-40.
7. M.-S. Chiou, S.-R. Jian, A.-C. Yeh, C.-M. Kuo, and J.-Y. Juang, *High temperature creep properties of directionally solidified CM-247LC Ni-based superalloy*. *Materials Science and Engineering: A*, 2016. **655**: p. 237-243.
8. K. Harris, G. Erickson, and R. Schwer, *Directionally solidified and single-crystal superalloys*. ASM International, *Metals Handbook*. Tenth Edition., 1990. **1**: p. 995-1006.
9. J.J. Jackson, M.J. Donachie, R.J. Henricks, and M. Gell, *The effects of volume percent of fine  $\gamma$  on creep in DS Mar-M200 + Hf*. *Metallurgical Transactions*, 1977. **8A**(October): p. 1615-1620.
10. Z. Yunrong, W. Yuping, X. Jizhou, P. Caron, and T. Khan. *Effect of chemistry modifications and heat treatments on the mechanical properties of DS MAR-M200 superalloy*. in *Superalloys 1988*. 1988. Seven Springs, Champion, PA, USA: TMS. p. 335-344.
11. X. He, Y. Zhang, H. Shi, J. Gu, C. Li, K. Kadau, and O. Luesebrink, *Influence of orientation and temperature on the fatigue crack growth of a nickel-based directionally solidified superalloy*. *Materials Science and Engineering: A*, 2014. **618**: p. 153-160.
12. J. Huang, D. Shi, and X. Yang, *A modern and robust methodology for modeling anisotropic creep characteristics of Ni-based DS and SC superalloys*. *Science China Technological Sciences*, 2014. **57**(9): p. 1802-1815.
13. M. Shenoy, D. McDowell, and R. Neu, *Transversely isotropic viscoplasticity model for a directionally solidified Ni-base superalloy*. *International journal of plasticity*, 2006. **22**(12): p. 2301-2326.
14. P.K. Wright and A.F. Anderson. *The influence of orientation on the fatigue of directionally solidified superalloys*. in *Superalloys 1980*. 1980. Seven Springs, Champion, PA, USA: TMS. p. 689-698.
15. K. Harris, G. Erickson, and R. Schwer. *CMSX single crystal, CM DS & integral wheel alloys properties & performance*. in *Cost Conference "High temperature alloys for gas turbines and other applications"*. 1986. Liège, Belgium. p. 6-9.
16. M. Brunner, M. Bensch, R. Völkl, E. Affeldt, and U. Glatzel, *Thickness influence on creep properties for Ni-based superalloy M247LC SX*. *Materials Science and Engineering: A*, 2012. **550**: p. 254-262.
17. A. Srivastava, S. Gopagoni, A. Needleman, V. Seetharaman, A. Staroselsky, and R. Banerjee, *Effect of specimen thickness on the creep response of a Ni-based single-crystal superalloy*. *Acta Materialia*, 2012. **60**(16): p. 5697-5711.
18. F. Coudon, *Comportement mécanique à haute température d'un superalliage à solidification dirigée DS200+Hf*, PhD Thesis. 2017, Mines ParisTech, Centre des Matériaux.

# Chapter 1 - Literature Review

## Chapitre 1 Etat de l'art

Le premier chapitre de ce manuscrit de thèse est dédié à la revue bibliographique des problématiques étudiées dans ces travaux de thèse. Il sera divisé en 4 axes principaux qui sont fondamentaux pour une bonne compréhension de cette étude:

- Développements, chimie, procédé de solidification (plus particulièrement, solidification dirigée), microstructure et défauts dans les superalliages base nickel (Ni), et plus spécifiquement du DS200;
- Changements microstructuraux et leur(s) impact(s) sur les modes de déformation, les propriétés mécaniques et la durabilité en fatigue et fluage;
- Anisotropie des propriétés mécaniques et de durabilité des alliages DS (solidification dirigée);
- Impact de l'environnement sur la durabilité des alliages DS.

Ce chapitre reprend le développement des superalliages base-nickel à partir de 1941, et plus spécifiquement, celui des alliages à solidification dirigée, les prédécesseurs des alliages monogranulaires (plus communément appelés monocristaux). Ensuite, il aborde la microstructure de ces superalliages à différentes échelles, plus spécifiquement celle du DS200 qui présente, au-delà de la matrice  $\gamma$  et des précipités  $\gamma'$ , un grand nombre de carbures ainsi que des pores résultant du procédé de solidification.

La chimie est un aspect mis en valeur, avec un bref descriptif des différentes compositions chimiques des générations successives de superalliages base Ni, en portant une attention particulière aux enjeux de la solidification et à la composition chimique de l'alliage DS200 utilisée dans ces travaux, surtout en ce qui concerne son haut taux d'hafnium.

Dans la présente étude, les défauts de fonderie joueront un rôle critique dans les mécanismes d'endommagement du DS200. Pour cela, ce chapitre de revue bibliographique détaille les principaux défauts rencontrés, les carbures de différents types et compositions ((HfC, TiC, NbC ...)) et les pores, ainsi que leur distribution.

La section dédiée aux modes de déformation et aux changements microstructuraux aborde le rôle du désaccord paramétrique de maille  $\gamma$ - $\gamma'$  sur la mobilité des dislocations, les différents modes de déformation selon les conditions de chargement appliquées (cisaillement des précipités favorisé à basse température, déformation dans la matrice aux plus hautes températures), ainsi que le phénomène de mise en radeaux. Ces évolutions microstructurales et modes de déformation sont, lorsque cela est possible, mis en relation directe avec les propriétés mécaniques et la durabilité.

Finalement, et ceci constitue la partie principale de cette revue de littérature, les propriétés mécaniques typiques des alliages à solidification dirigée en fluage, fatigue oligocyclique et traction sont présentées et positionnées par rapport aux alliages polycristallins coulés équiaxes et aux alliages monogranulaires. L'anisotropie de ces propriétés mécanique et de la durabilité selon les conditions testées est ensuite analysée. La contribution de l'environnement, notamment au travers de l'oxydation, sur cette anisotropie est ensuite établie.

L'originalité et la motivation de ces travaux de thèse est montrée sur la base de cette revue bibliographique. Même si le développement des superalliages à solidification dirigée a été l'un des premiers sauts technologiques concernant l'industrialisation des superalliages base Ni, les propriétés mécaniques de ces alliages restent relativement méconnues. En effet, leurs modes d'endommagement doivent être mieux rationalisés en prenant en compte notamment l'impact de la taille des grains (pour des sollicitations transverses), de l'environnement, de la microstructure, des modes de

déformation et des défauts métallurgiques (pores, carbures). Des études récentes ont été menées pour tenter combler ce manque d'informations, vu que ces alliages sont encore très utilisés pour la fabrication d'aubages de nouvelles turbines développées récemment, notamment du fait de leur bonne coulabilité. Cette thèse aura donc pour principal objectif de caractériser les propriétés mécaniques et la durabilité de DS200+Hf, en développant une meilleure compréhension des processus d'endommagement en fatigue, fluage et fatigue avec temps de maintien, via l'emploi d'essais sous vide ou fortement instrumentés.

## Table of contents (Chapter 1)

1. Literature Review .....	11
1.1 Introduction.....	11
1.2 Development of Ni-base superalloys for turbine blades applications .....	11
1.3 Microstructure of DS and SX Ni-based superalloys.....	14
1.4 Chemistry of Ni-based cast superalloys .....	15
1.5 MAR-M200 solidification processing conditions, chemical composition and Hf addition....	17
1.6 Casting defects .....	18
1.6.1 Porosity.....	18
1.6.2 Carbides: characterization, composition and distribution in MAR-M200.....	19
1.7 Microstructure evolutions in relation with the deformation mechanism and mechanical properties.....	20
1.7.1 $\gamma$ - $\gamma'$ lattice misfit – its relation with microstructure evolution and mechanical behavior .....	20
1.7.2 Deformation mechanisms of Ni-based superalloys at low, intermediate and high temperatures.....	22
1.7.3 Change in morphology, size and volume fraction of the $\gamma'$ precipitates due to temperature exposure and/or applied stress ( $\gamma'$ directional coarsening) .....	25
1.8 Mechanical behavior and durability anisotropy of directionally solidified superalloys.....	28
1.8.1 Tensile properties.....	28
1.8.2 Creep properties.....	31
1.8.3 Fatigue properties .....	39
1.8.4 Crack propagation behavior .....	48
1.9 Effect of environment on durability of cast Ni-based superalloys.....	51
1.9.1 Impact on creep properties.....	51
1.9.2 Impact on fatigue properties.....	54
1.10 Summary of the research motivations and objectives.....	58

## Figures and tables (Chapter 1)

Figure 1.1 - From the left to the right: polycrystalline (a), directionally solidified (b) and single-crystalline (c) turbine blades [2]. .....	11
Figure 1.2 - Schematical illustration of a furnace used for the production of SX turbine blades where the selection of the single grain takes place in elliptical crystal selector after [10] (a) and diagram of induction heated mold used to produce columnar structure after [6] (b). .....	13
Figure 1.3 - Comparative creep properties of MAR-M200 at 982°C and 206 MPa in A) polycrystalline, B) directionally solidified and C) single crystalline form (from [13]). .....	14
Figure 1.4 - Evolution of the high-temperature performance of Ni-based superalloys since their emergence in the 1940s (adapted from [2]). .....	14
Figure 1.5- Scanning electron microscope (SEM) observation of a 2 <sup>nd</sup> generation Ni-based SX superalloy in the fully heat-treated condition where the cuboidal $\gamma'$ precipitates (dark phase) are embedded in the $\gamma$ matrix (bright phase) (adapted from [8]). .....	15
Figure 1.6 - Stress to achieve 1% creep strain in 100h vs. temperature in $\sim \langle 001 \rangle$ oriented PWA 1480 SX and DS MAR-M200+Hf along longitudinal direction, showing benefits in operating temperature obtained from the use of commercial Ni-based single crystalline superalloys (adapted from [18]). ...	17
Figure 1.7 – Evolution of the creep life at 982°C/221 MPa as a function of the volume fraction of fine $\gamma'$ precipitates for coarse grain DS200 + Hf alloy (originally from [26]). .....	18
Figure 1.8 - Deformation pores in CMSX-4 after 292 h creep at 1100°C/120 MPa (a) and increase of porosity at high temperatures determined by density measurement (b)(adapted from [32]). .....	19
Figure 1.9 - Schematics of the formation and evolution of different types of dislocation networks on the $\{100\} \gamma/\gamma'$ interfaces of Ni-based superalloys during thermal exposure: (a) $\langle 110 \rangle$ diamond shaped dislocation network; (b) intermediate polygonal dislocation network; (c) $\langle 100 \rangle$ square dislocation network (after [53]). .....	21
<i>Figure 1.10 – Evolution of the minimum creep rate at 1100°C/137 MPa as a function of the <math>\gamma/\gamma'</math> interfacial dislocation density (i.e. the magnitude of the <math>\gamma/\gamma'</math> lattice mismatch) (after [59]). .....</i>	<i>22</i>
Figure 1.11 - TEM bright-field images showing the formation of dislocations pairs in the slightly deformed specimens of DS M4706 Ni-based superalloy at low temperatures: (a) and (d), RT, 0.23% plastic strain; (b) and (e), 400°C, 0.26% plastic strain; (c) and (f) 650°C, 0.24% plastic strain (after [64]). .....	23
Figure 1.12 - TEM BF images showing the typical microstructures of the specimens after a low magnitude plastic deformation at 950 and 980°C: (a) and (b), 950°C, 0.25% plastic strain; (c) and (d), 980°C, 0.21% plastic strain (after [64]). .....	25
Figure 1.13 - Microstructure evolutions in Udimet-700 which is an alloy with a positive lattice misfit: as-heat-treated state (a); stress-free high temperature exposure resulting in $\gamma'$ coarsening (b); tensile creep exposure resulting in P-rafts (c) and compressive creep exposure resulting in N-rafts (d) (after [88]). .....	26
Figure 1.14 - As-received (a) and type-N rafted (b) microstructures of MC2 alloy ( $\gamma'$ -phase in dark) (after [93]). N-type rafting in (b) has been obtained after 24 hours in tension creep at 1050°C/120 MPa. ...	27
Figure 1.15 - $\gamma'$ morphology in DZ411 alloy as heat treated (a), after 5,000 hours (b), 9,000 hours (c), 15,000 hours (d), 20,000 hours (e) and 24,000 hours (f) of thermal exposure at 900°C (after [78]). ...	28
Figure 1.16 – Impact of long-term thermal exposure on the creep properties at 980°C/220 MPa of DZ411 (adapted from [78]). .....	28



Figure 1.17 - Typical dynamic elastic moduli (Young's modulus) for MAR-M200 superalloy, under the polycrystalline cast form (a), along transverse direction (b) and along longitudinal direction (c) in a coarse grain DS casting (after [20]).	29
Figure 1.18 - Typical tensile properties of MAR-M200 superalloy for polycrystalline cast and DS coarse grain along longitudinal direction. Note that UTS is the ultimate tensile strength and YS is the yield strength (after [20]).	30
Figure 1.19 – Evolution of tensile properties as a function of temperature for DZ951 alloy (after [62]).	30
Figure 1.20 - Typical stress for 100 h rupture life of coarse grain DS MAR-M200 superalloy along longitudinal direction and polycrystalline MAR-M200 and Udimet™ 700 cast alloys (after [20]).	32
Figure 1.21 - Creep behavior at 982°C/207 MPa of polycrystalline MAR-M200 (PC) compared with single crystalline MAR-M200 along the <001> orientation (SCDS) and DS MAR-M200 along longitudinal direction (CGDS) (after [20]).	33
Figure 1.22 - Orientation dependence of the creep behavior of single crystalline MAR-M200 at 760°C/689.5 MPa (100 ksi), 871°C/345 MPa (50 ksi) and 962°C/207 MPa (30 ksi) (adapted from [20]).	35
Figure 1.23 - Creep behavior of MAR-M200 single crystalline specimens with loading axis close to the [001], [011] and [111] directions. Creep testing at 760°C/689.5 MPa (after [20]).	36
Figure 1.24 - Stress rupture lives as a function of orientation for MAR-M200 single crystals at 760°C and 689 MPa (after [13]) (a) and Larson-Miller diagram showing the anisotropy in creep life of MAR-M200 and MAR-M247 (after [95]) (b).	36
Figure 1.25 - Creep life evolution as a function of the applied stress of for DZ125 alloy at 760°C (a), 850°C (b), 900°C (c) and 980°C (d) (after [97]). Note that L-direction and T-direction correspond to the longitudinal and the transverse direction, respectively.	37
Figure 1.26 - Evolution of the high temperature creep life as a function of the $\gamma$ volume fraction under different conditions for TMS 75 and Inconel 713C alloys (adapted from [113]).	38
Figure 1.27 - Evolution of the number of thermal cycles up to failure as a function of the $\gamma$ area fraction measured in the gage section of each sample 1 mm far from the fracture surface (after [112]).	38
Figure 1.28 - Comparative thermal fatigue resistance of equiaxed and DS superalloys (adapted from [114]).	39
Figure 1.29 - Comparison of the thermo-mechanical fatigue lives of single crystal, polycrystalline and directional solidified cast nickel-based superalloys (longitudinal loading) (after [20]).	40
Figure 1.30 – LCF life anisotropy of DS René 120 alloy (after [114]). Note that the 0° orientation corresponds to a loading direction aligned with the solidification direction (i.e. orientation of the columnar grains) while 90° corresponds to perfect transverse loading direction.	41
Figure 1.31 – Effect of Young's modulus variation on peak stresses during strain-controlled LCF tests (after [114]).	41
Figure 1.32 – Crack initiation site at a sub-surface casting pore in a MAR-M200 [213] oriented SX specimen tested at 650°C (after [115]).	42
Figure 1.33 - Typical LCF crack initiation sites at 750°C in AM1 Ni-based SX alloy casted using different techniques leading to different pore sizes. Cracks initiated at internal and/or sub-surface casting pores (after [31]).	42
Figure 1.34 - Comparison of fatigue strength of <001> MAR-M200 SX alloy with (curve A) and without carbides (curve B) (after [18]). Surface observations of the specimens' gage length presented in this	

figure highlight a more homogeneous slip activity without carbides and almost no stress concentration like in the version of the alloy containing carbides.....	43
Figure 1.35 - Variation in the surface crack length as a function of the number of cycles for a short-life ~ [001] SX MAR-M200 specimen tested in LCF at 650°C (after [115]).	43
Figure 1.36 - Dislocation structure in MAR-M200 (a) and in MAR-M200+1.78 wt. pct Hf (b) tested in LCF 760°C/ $R_e = -1/f = 0.33\text{Hz}/\Delta\varepsilon_t = 1.2\%$ (after [24]).	44
Figure 1.37 - Effect of a 20 minutes strain hold on at mean stress maximum temperature out-of-phase on TMF behavior of DS CM247LC alloy/ $T=100\text{-}850^\circ\text{C}$ tested along longitudinal direction (after [89]).	45
Figure 1.38 - Effect of the prior $\gamma/\gamma'$ degradation in tension creep on LCF life of CMSX-4 at 700°C, $\Delta\varepsilon_t=1.25\%$ , $\varepsilon =6\%/min$ , $R_e=-1$ (after [32]).	46
Figure 1.39 - Crack propagation along $\gamma/\gamma'$ interfaces in LCF at 700°C, $\Delta\varepsilon_t=1.25\%$ , $\varepsilon =6\%/min$ , $R_e=-1$ in N-type pre-rafted CMSX-4 SX alloy (after [32]).	46
Figure 1.40 - Crack propagation through an oxidation spike penetrating into an interdendritic region within the P-type rafted microstructure in out-of-phase thermo-mechanical fatigue ( $\Delta T = 100\text{-}950^\circ\text{C}/\Delta\varepsilon_{mech} = 0.8\%$ ) (after [89]).	47
Figure 1.41 - Debonded carbide in the N-type rafted microstructure serving as a crack initiation site in in-phase thermo-mechanical fatigue ( $\Delta T = 100\text{-}850^\circ\text{C}/\Delta\varepsilon_{mech} = 1.1\%$ ) (after [89]).	47
Figure 1.42 – Illustration of the grain rotation close to the main crack at different fractions of the creep life of the MGA 1400 DS alloy loaded at 880°C/294 Mpa (Creep life $t_f = 156.8$ h): $t_i/t_f=0$ (a); $t_i/t_f=0.45$ (b); $t_i/t_f=0.73$ (c); $t_i/t_f=0.99$ (d); Inverse Pole Figure map at $t_i/t_f=0.99$ (e) (after [126]).	48
Figure 1.43 - Schematic illustration of misorientation development until accelerated creep region in creep (a), in creep–fatigue (b) and pure fatigue (c) (after [126]).	49
Figure 1.44 - Fatigue crack growth curves of TL (a), LT (b), and D (c) specimens at different temperatures (see schematic illustrations showing the solidification direction for each specimen) (Adapted from [131]).	50
Figure 1.45 - Crack deflection and branching during fatigue crack propagation at room temperature observed in MAR-M200 single crystalline specimens with the stress axis aligned along the [110] orientation (a) and along the [111] orientation (b) (adapted from [129]).	50
Figure 1.46 – Typical creep life debit as a function of the specimen’s thickness for polycrystalline, columnar grain and single-crystal nickel-based superalloys (trend expected for MAR-M200 and B1900 alloys). The creep lives have normalized by the results obtained for 3.8 mm thick specimens (after [20]).	51
Figure 1.47 – Creep properties of <001> SX MAR-M247LC at 980°C/150 MPa for different initial thicknesses in air without coating (a, b), in high vacuum (c, d) and coated in air (e, f) (after [135]).	52
Figure 1.48 – Transverse section of crept specimens at 980°C/150 MPa in air up to failure with a thickness of 1.0 mm (Creep life = 74 h) (a) and 0.3 mm (Creep life = 63 h) (b) (after [135]).	53
Figure 1.49 – Crack initiation assisted by oxidation in LCF at 950°C/ $R_\sigma = -1/f = 0.5\text{ Hz}/\sigma_{max} = 300\text{ MPa}$ in air using AM1 Ni-based SX superalloy solidified using Bridgman and Liquid Metal Cooling (LMC) processes (after [31]).	54
Figure 1.50 – S-N diagram at 950°C/ $R_\sigma = -1/f = 0.5\text{ Hz}$ in air and in high vacuum using AM1 Ni-based SX superalloy (after [31]).	55
Figure 1.51 - LCF crack in an argon environment at 975°C in DS MAR-M200+Hf alloy (after [138]).	56

Figure 1.52 - Microstructures and chemical compositions of the different layers beneath the crack surface after LCF in an Ar + 20% O<sub>2</sub> environment at 975°C using DS MAR-M200+Hf alloy (after [138]).  
 ..... 56

Figure 1.53 - Schematic diagram showing Laird model of crack growth by successive blunting and resharpening (a) to (d) in vacuum, (e) and (f) in air (after [139])..... 57

Table 1.1 - Compositions of common Ni-based SX superalloys (1<sup>st</sup>, 2<sup>nd</sup> and 3<sup>rd</sup> generation alloys in the upper, mid and lower part of the table, respectively) [2, 18]..... 16

Table 1.2 - Tensile properties of DS200 and DS200+Hf (with 1.78 wt. pct of hafnium) alloys (adapted from [24]). ..... 31

Table 1.3 - Creep properties at 760°C/690 MPa, 871°C/345 MPa and 982°C/207 MPa of polycrystalline MAR-M200 alloy compared to its <001> single crystalline and longitudinal DS counterparts (after [20]).  
 ..... 32

Table 1.4 - Creep properties of DS200 alloy and DS200+Hf (1.78 wt. pct of hafnium) alloy (adapted from [24]). ..... 34

Table 1.5 - Strain-controlled LCF results at 760°C/R<sub>ε</sub> = -1/f = 0.33Hz/Δε<sub>t</sub> = 1.4% [24] ..... 44

# 1. Literature Review

## 1.1 Introduction

This literature review covers different aspects related to single-crystal (SX) and directionally solidified (DS) Ni-based superalloys developments related to their chemistry, their processing and resulting mechanical behavior relevant to the scope of the PhD thesis. Available literature for DS alloys is, in general, limited and not recent compared to SX one. Because of this, SX advancements/knowledge will be used as a basis for discussion and understanding of many topics tackled in the present work. A special focus will be paid to the durability and damage mechanisms of DS alloys under various loading conditions in terms of temperature and mechanical loading profile. Moreover, the mechanical behavior anisotropy of these classes of alloys and the contribution of oxidation to the durability will be of special interest. In this chapter, paragraphs written in bold letters will highlight areas of research that still open based on the open literature and/or topics that will be investigated in deeper details in this PhD work.

## 1.2 Development of Ni-base superalloys for turbine blades applications

According to [1, 2] a gas turbine converts thermal energy resulting from the combustion of fuel into mechanical energy. Gas turbines are today widely used for power generation (e.g. large land-based gas turbine or Auxiliary Power Units –APU- for electricity production) or for aircraft/helicopter propulsion.

After combustion, the exhaust gas temperatures usually range from 920°C to 1600°C. The first rows of turbine blades next to the combustion chamber must hence withstand severe combinations of high temperature, stress and environment [1, 2]. Ni-based SX superalloys are first choice materials for this first line turbine blades due to their excellent mechanical strength and environmental resistance at high temperature. However, for low pressure turbine blades (metal temperature ranging from 650°C to 1100°C), DS Ni-based superalloys (Figure 1.1) are still used especially due to economic reasons and thanks to their very good castability.

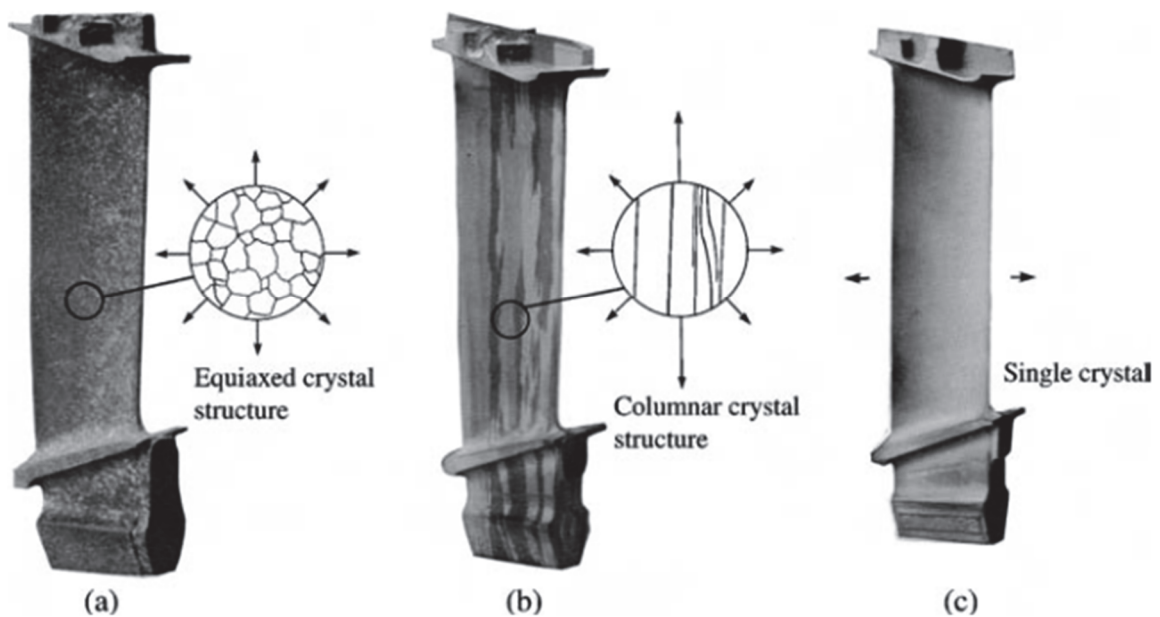


Figure 1.1 - From the left to the right: polycrystalline (a), directionally solidified (b) and single-crystalline (c) turbine blades [2].

The development of Ni-based superalloys began with the development of the first commercial Ni-based alloy Nimonic 80 in 1941 [3] and discovery of the hardening effect of the  $\gamma'$  phase in 1957 [4], as well as the induced increase of the creep properties of Ni-Cr alloys [5]. From Nimonic 80 development, Vacuum Induction Melting (VIM) and Vacuum Arc Remelting (VAR) were introduced in the 1950s, allowing the next major development in the production of superalloys for turbine blades applications, namely, the directional solidification technique in 1966 [6]. Indeed, for conventionally cast components (i.e. with an equiaxed grain structure), the intergranular cavitation and formation of voids at grain boundaries normal to the main blade axis was identified as a major deterioration of the mechanical properties, especially for creep [6]. This problem could be solved by the development of unidirectional solidification.

Unidirectionally (also directionally) solidified turbine blades can be successfully cast if the following two conditions are satisfied [7]: grain nucleation must be prevented in the melt ahead from the solidification front and the heat flow must be unidirectional, so that the liquid-solid interface moves along only one direction during the solidification, i.e. parallel to the thermal gradient [8].

For this, during solidification, spurious nucleation in the molten alloy is inhibited by superheating the molten charge 85°C to 165°C above the liquidus [9]. Unidirectional heat flow is obtained by the introduction of a water-cooled chill plate at the bottom of the casting mold (see Figure 1.2), while the temperature of the upper part is maintained well-above the liquidus. Transverse thermal gradients are prevented by a good insulation of the mold which is heated above the temperature of the molten alloy [8], and/or by the use of a baffle controlling lateral thermal gradients.

By withdrawing the mold containing the molten alloy in a controlled way, grain growth takes place parallel to the thermal gradient along the blade axis, resulting in a columnar grain structure (see Figure 1.1.b). To produce SX components (Figure 1.1c), a single grain is selected once the solidification starts by passing through a grain selector composed of chicanes (the so-called “pig tail”) or a helix as illustrated in Figure 1.2a. A typical furnace used for SX blade casting is schematically represented in Figure 1.2 [10]. Another option to achieve a SX crystalline structure is to use a seed having the desired crystallographic orientation instead of, or in addition to the chicane. During solidification, chemical fluctuations at the solidification front lead to localized variations of the solidus temperature of the molten charge and dendritic growth solidification occurs. Fortunately, dendritic growth occurs along the preferred low elastic modulus [001] direction, which was proved to give the best combination of mechanical properties when compared with [011] and [111] grown SX blades [11, 12].

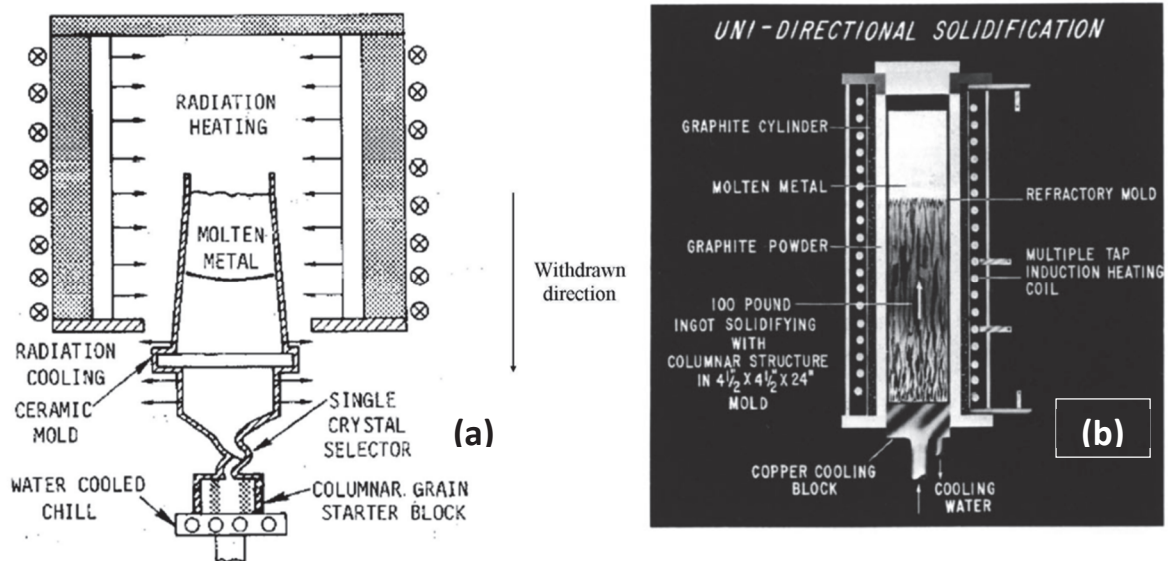


Figure 1.2 - Schematic illustration of a furnace used for the production of SX turbine blades where the selection of the single grain takes place in elliptical crystal selector after [10] (a) and diagram of induction heated mold used to produce columnar structure after [6] (b).

As shown previously in Figure 1.1.b, directionally solidified (DS) turbine blades exhibit a columnar structure with grains oriented parallel to the blade axis. They present superior creep properties compared to conventional polycrystalline alloys as shown in Figure 1.3, especially due to a higher creep ductility. Therefore, improvements in the casting procedure and the chemical composition of these DS alloys constitute a good candidate for aircraft applications, especially for intermediate and low pressure turbine blades.

The optimization of the DS casting procedure led the production of SX turbine blades, by suppressing completely grain boundaries. The result is a substantial improvement of the creep properties. This is also illustrated in Figure 1.3 where the creep properties at 982°C/206 MPa of the polycrystalline, DS and single-crystal version of the same alloy (MAR-M200 alloy) are compared [13].

The technological improvements mentioned above have allowed the development of many different Ni-based SX and DS superalloys up to the present day, resulting in a gain of nearly 350°C over the maximum metal temperature tolerated by the turbine blades in service. The processing development and the composition optimization are both concerned [14]. This is illustrated in Figure 1.4, where the evolution of the temperature to reach a 1000 h creep life at 137 MPa is plotted for various Ni-based superalloys from 1940 until now [2].

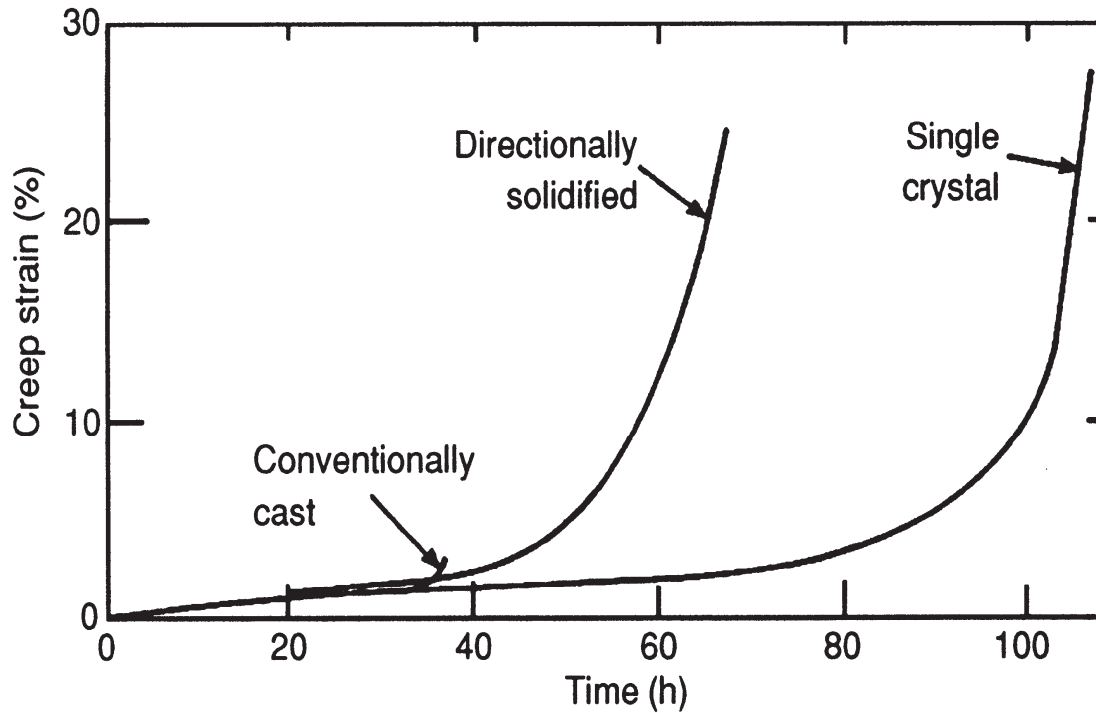


Figure 1.3 - Comparative creep properties of MAR-M200 at 982°C and 206 MPa in A) polycrystalline, B) directionally solidified and C) single crystalline form (from [13]).

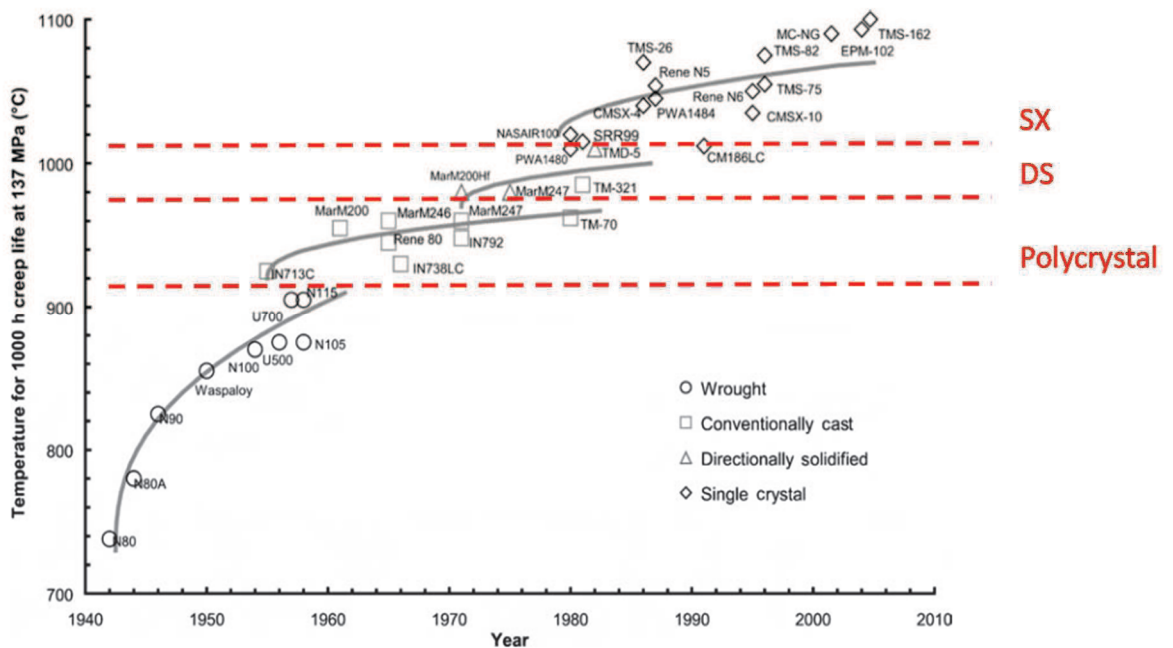


Figure 1.4 - Evolution of the high-temperature performance of Ni-based superalloys since their emergence in the 1940s (adapted from [2]).

### 1.3 Microstructure of DS and SX Ni-based superalloys

The microstructure of a typical cast Ni-based superalloy consists of different phases [15]:

- **The gamma phase, denoted  $\gamma$** , appearing as the white phase in Figure 1.5. This is a FCC disordered structure and, in nearly all cases, it forms a continuous matrix phase in which the other phases reside. It contains significant concentrations of elements such as cobalt, chromium, molybdenum, ruthenium and rhenium, when they are present in the chemical composition of the alloy;
- **The gamma prime phase, denoted  $\gamma'$**  and appearing as the dark phase in (Figure 1.5). It forms as a precipitate phase, with an ordered L1<sub>2</sub> structure which is, in most of the alloys, semi-coherent or coherent with the  $\gamma$  matrix. The  $\gamma'$  phase is rich in elements such as aluminum, titanium and tantalum;
- **Carbides and borides.** Carbon, often present at concentrations up to 0.2 wt. %, combines with reactive elements such as titanium, tantalum, niobium and hafnium to form MC carbides. During processing or service, these carbides can decompose to other species, such as M<sub>23</sub>C<sub>6</sub> and M<sub>6</sub>C, which preferentially appear at grain boundaries, and which are rich in chromium, molybdenum and tungsten. Boron can combine with elements such as chromium or molybdenum to form borides which also mainly form at grain boundaries.

Other phases can be found in some superalloys, particularly in the service-aged condition, for example, the topologically close-packed (TCP) phases  $\mu$ ,  $\sigma$ , Laves, etc. However, the compositions of the superalloys are today chosen to avoid, rather than to promote, the formation of these intermetallic compounds [2] since they are known to be detrimental to the mechanical properties [16].

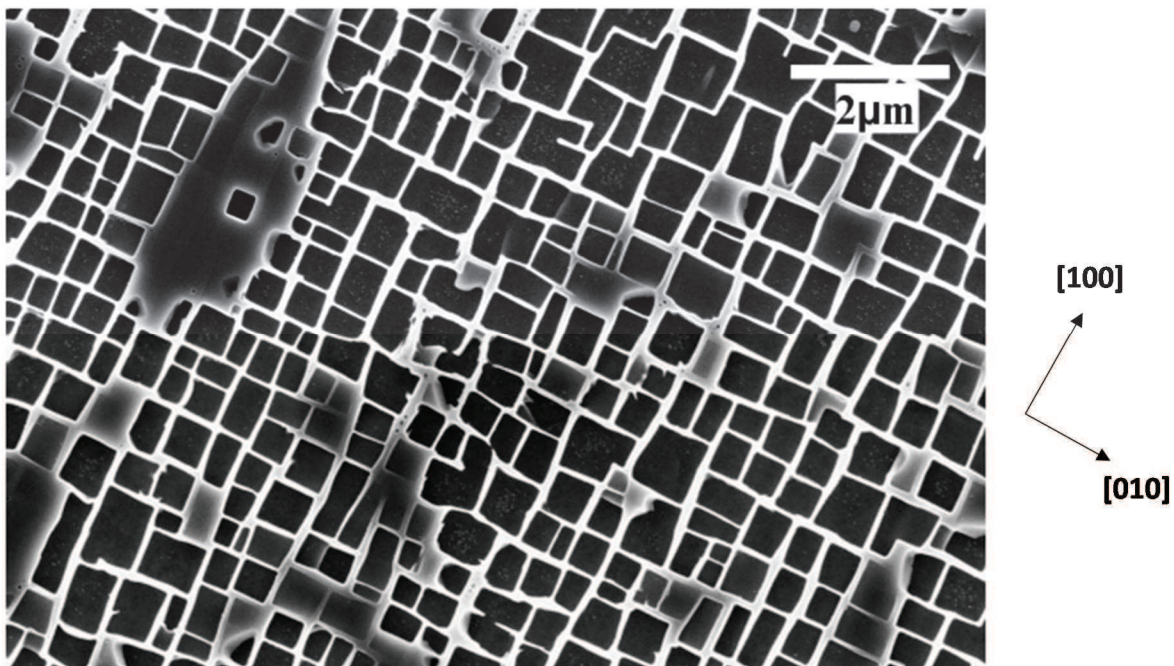


Figure 1.5- Scanning electron microscope (SEM) observation of a 2<sup>nd</sup> generation Ni-based SX superalloy in the fully heat-treated condition where the cuboidal  $\gamma'$  precipitates (dark phase) are embedded in the  $\gamma$  matrix (bright phase) (adapted from [8]).

#### 1.4 Chemistry of Ni-based cast superalloys

The strength of nickel-base superalloys depends essentially on the precipitation of the  $\gamma'$  (Ni<sub>3</sub>Al) phase, which typically presents a volume fraction in the order of 60-70 vol. % or more. Increasing the volume fraction and the solvus of the  $\gamma'$  phase constitutes a natural way to improve the mechanical properties. This solution is often obtained by a reduction in chromium content for the range 6-10 wt. % [6] and even lower considering the very last generations of Ni-based SX alloys (e.g. ~ 3 wt. Cr in TMS-138A [2]).



However, it can be very detrimental to the environmental resistance and to the durability of thermal barrier coating systems [2].

Table 1.1 lists the compositions of common commercial Ni-based SX superalloys. One can see that as many as 14 different alloying elements are added. The so-called first-generation single crystal superalloys, such as PWA1480, Rene N4 and SRR99, contain substantial quantities of the  $\gamma'$  hardening elements Al, Ti and Ta and grain-boundary-strengthening elements C and B. The last ones were added routinely to the earlier conventionally cast and DS superalloys and are no longer present since useless and since they decrease the incipient melting temperature of the alloys, hence increasing the difficulty of solution heat treatment schedule. Second-generation alloys, such as PWA1484, CMSX-4 and René N5, are characterized by the addition of a 3 wt. % concentration of rhenium, which is increased to about 6 wt. % for the third-generation alloys such as CMSX-10 and René N6. Generally speaking, last generation alloys are characterized by significantly lower concentrations of Cr and higher concentrations of Al and Re. Concentrations of Ti and Mo are now at very modest levels. The period since 2000 has seen the emergence of the fourth-generation (and even fifth and sixth-generation) single-crystal superalloys, such as MC-NG, EPM-102, TMS-162, TMS-196 TMS-238, PWA1497, which are characterized by additions of ruthenium and a lower rhenium content [2, 17].

Alloy	Cr	Co	Mo	W	Al	Ti	Ta	Nb	V	Hf	Ni	Density (g/cm <sup>3</sup> )
Nasair 100	9	—	1	10.5	5.75	1.2	3.3	—	—	—	Bal	8.54
CMSX-2	8	4.6	0.6	8	5.6	1	6	—	—	—	Bal	8.60
CMSX-6	9.8	5	3	—	4.8	4.7	2	—	—	0.1	Bal	7.98
PWA1480	10	5	—	4	5	1.5	12	—	—	—	Bal	8.70
SRR99	8	5	—	10	5.5	2.2	3	—	—	—	Bal	8.56
RR2000	10	15	3	—	5.5	4	—	—	1	—	Bal	7.87
Rene N4	9	8	2	6	3.7	4.2	4	0.5	—	—	Bal	8.56
AM1	7.8	6.5	2	5.7	5.2	1.1	7.9	—	—	—	Bal	8.60
AM3	8	5.5	2.25	5	6	2	3.5	—	—	—	Bal	8.25
TMS-6	9.2	—	—	8.7	5.3	—	10.4	—	—	—	Bal	8.90
TMS-12	6.6	—	—	12.8	5.2	—	7.7	—	—	—	Bal	9.07

Alloy	Cr	Co	Mo	Re	W	Al	Ti	Ta	Nb	Hf	Ni	Density (g/cm <sup>3</sup> )
CMSX-4	6.5	9	0.6	3	6	5.6	1	6.5	—	0.1	Bal	8.70
PWA1484	5	10	2	3	6	5.6	—	8.7	—	0.1	Bal	8.95
Rene N5	7	8	2	3	5	6.2	—	7	—	0.2	Bal	8.70
MC2	8	5	2	—	8	5	1.5	6	—	—	Bal	8.63
TMS-82+	4.9	7.8	1.9	2.4	8.7	5.3	0.5	6	—	0.1	Bal	8.93

Alloy	Cr	Co	Mo	Re	W	Al	Ti	Ta	Nb	Hf	Others	Ni	Density (g/cm <sup>3</sup> )
CMSX-10	2	3	0.4	6	5	5.7	0.2	8	0.1	0.03	—	Bal	9.05
Rene N6	4.2	12.5	1.4	5.4	6	5.75	—	7.2	—	0.15	0.05C 0.004B 0.01Y	Bal	8.97
TMS-75	3	12	2	5	6	6	—	6	—	0.1	—	Bal	8.89

Table 1.1 - Compositions of common Ni-based SX superalloys (1<sup>st</sup>, 2<sup>nd</sup> and 3<sup>rd</sup> generation alloys in the upper, mid and lower part of the table, respectively) [2, 18].

The compositions of 1<sup>st</sup> generation Ni-based SX superalloys were initially derived from that of DS alloys with the suppression of grain boundary strengthening elements (C, B, Hf, Zr). It resulted in a significant increase of the incipient melting temperature of the alloy: a nearly total dissolution of remaining  $\gamma/\gamma'$  eutectics pools could thus be obtained by increasing the solution heat treatment temperature after casting. A very strong improvement in the mechanical properties, especially for the stress-rupture lifetime, was reported [19, 20]. This can be observed in Figure 1.6, which shows an improvement in creep resistance of PWA 1480 SX compared to DS MAR-M200. Further improvements of the

mechanical properties (especially creep) of Ni-based SX superalloys were reported after substitution of W and Mo by Re, which led to the 2<sup>nd</sup> (up to 3.0 wt% Re) and 3<sup>rd</sup> (up to 6.0 wt. % Re) generation of SX superalloys [2].

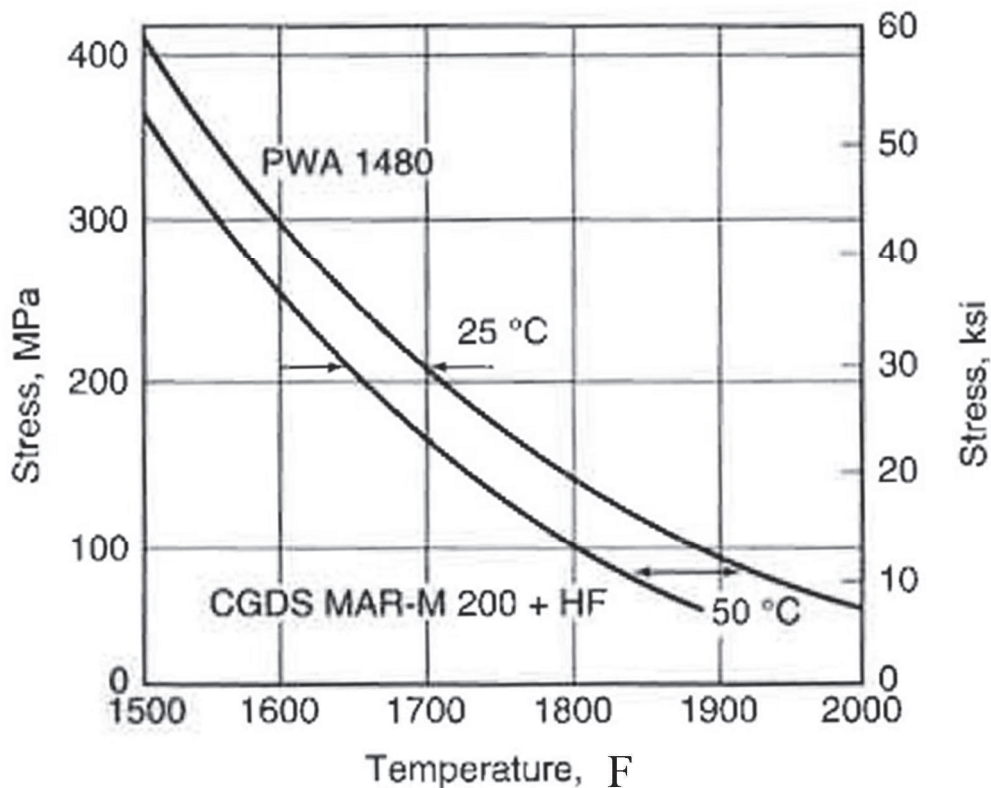


Figure 1.6 - Stress to achieve 1% creep strain in 100h vs. temperature in  $\sim \langle 001 \rangle$  oriented PWA 1480 SX and DS MAR-M200+Hf along longitudinal direction, showing benefits in operating temperature obtained from the use of commercial Ni-based single crystalline superalloys (adapted from [18])

#### 1.5 MAR-M200 solidification processing conditions, chemical composition and Hf addition

One of the standard chemical composition of MAR-M200 alloy found in the literature [6, 21, 22] is, in wt. %, 0.15 C, 9.0 Cr, 10.0 Co, 5.0 Al, 2.0 Ti, 12.5 W, 1.0 Nb, 0.015 B, 0.05 Zr, Bal. Ni. In the present study, MAR-M200 with an addition of Hafnium of about 1.6 wt. % has been used. Such a modified composition improves grain boundary strength at high temperature [2, 6, 10, 20, 21, 23], facilitates blades solidification and allows us to obtain very thin trailing-edges, even if these phenomena remain not fully understood. Final hafnium specifications represented a compromise between casting quality (inclusions, etc.), solidification cracking (i.e. hot tearing issues) and transverse ductility in creep [20]. In fact, according to Yunrong & al. [24], adding hafnium to MAR-M200 chemical composition is the best solution to achieve a good compromise between having a sufficient ductility at intermediate temperatures (i.e. in the 600-800°C temperature range) and limiting processing issues.

A pre-treatment of 3 hours at 1130°C has been determined to limit the occurrence of incipient melting during subsequent solution treatment, by partially removing chemical segregations across the dendritic structure [6, 24, 25]. This makes it possible to use a higher solution treatment temperature. According to Jackson & al. [26], the volume fraction of fine (efficient)  $\gamma'$  particles developed in DS MAR M200 + Hf increases significantly with solution temperature in the range of 1198°C to approximately

1210°C. The increase of the solution temperature and of the resulting fine  $\gamma'$  particles formed upon cooling has been shown to improve the creep-rupture life at 982°C/221 MPa in coarse grain DS200+Hf alloy, as shown in Figure 1.7 [26].

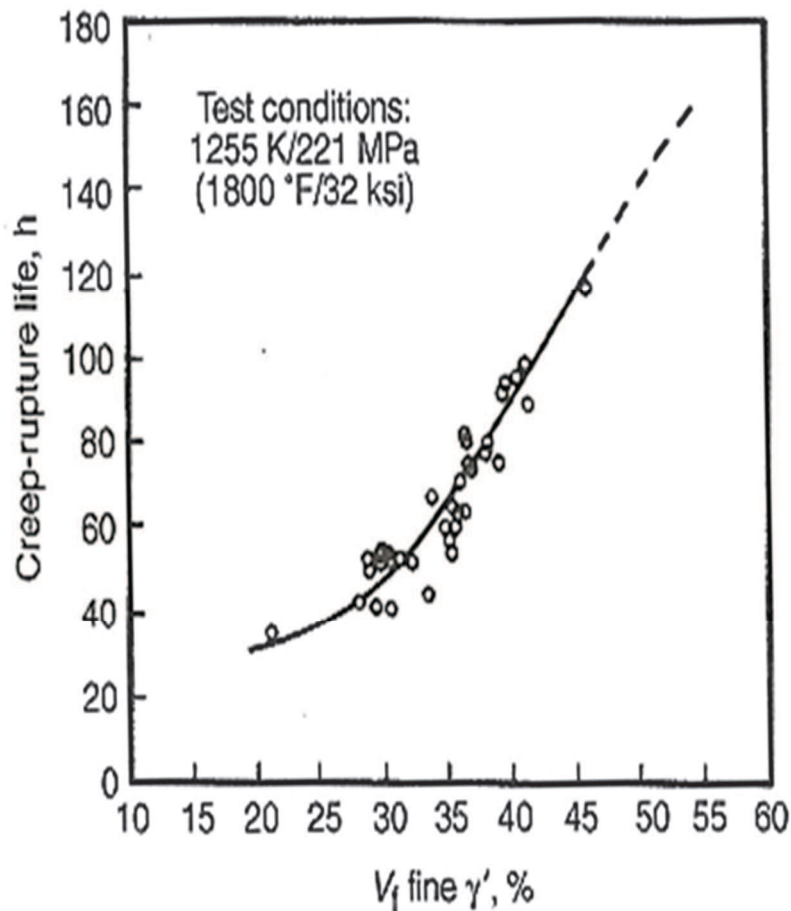


Figure 1.7 – Evolution of the creep life at 982°C/221 MPa as a function of the volume fraction of fine  $\gamma'$  precipitates for coarse grain DS200 + Hf alloy (originally from [26]).

## 1.6 Casting defects

### 1.6.1 Porosity

Microporosity, caused by gas or shrinkage, is a common defect in castings. The presence of pores in cast turbine blades is undesirable because it increases the scatter of creep rupture properties [25] as well as in fatigue. Microporosity formation in Ni-base superalloys depends on the casting parameters and on the chemical composition of the melt [27, 28]. It can be related to other microstructural constituents such as secondary dendrite arm spacing (SDAS) and carbides, as shown in [25]. This study also indicates that the reduction of porosity size follows the refinements of the SDAS and that increasing the carbide particle density reduces the porosity content of the alloy. Casting pores (also called solidification pores [29, 30]) have been shown recently to be the most critical pores controlling the fatigue life at low temperature ( $T < 800^\circ\text{C}$ ) of a first generation Ni-based superalloy, without any impact on the creep properties [31]. A second population of pores is formed during the solution heat treatment, due to cross-diffusion of elements across the dendritic structures [29, 30]. Finally, during high temperature creep, a third class of pore called deformation pores is likely to form.

Figure 1.8 shows deformation pores due to creep straining at 1100°C/120 MPa in CMSX-4 Ni-based SX alloy [32]. The porosity evolution is observed during high temperature long term creep tests (typically over 950°C in most of Ni-based DS and SX alloys), when vacancy diffusion is fast and plays an important role in the deformation processes. The creep deformation induces pore growth by vacancy condensation, specifically along sub-grain boundaries in the interdendritic regions. Figure 1.8b shows that the kinetics of porosity growth in CMSX-4 SX alloy is fast during the primary creep stage and it slows down during secondary creep stage, accelerating again during the tertiary creep stage. The entire porosity increase is related to the enlargement of pre-existing solidification and homogenization pores and to the nucleation of new deformation (creep) induced pores. This mechanism was already explained by Epishin and co-authors in [33]. Under applied load, most of the dislocations move non-conservatively along the  $\gamma/\gamma'$ -interfaces perpendicularly to the load axis, generating vacancies. The longitudinal dislocation movement, which absorbs vacancies, is much less active because it is not driven by the applied load and suppressed by the formation of  $\gamma'$ -rafts. This results in a supersaturation of vacancies, which condense on pores increasing their size or form new pores. Therefore, porosity increases rapidly during primary and tertiary creep, when interfacial dislocations movement is active, and in a slower way during the secondary creep stage, when dislocations mobility is lower.

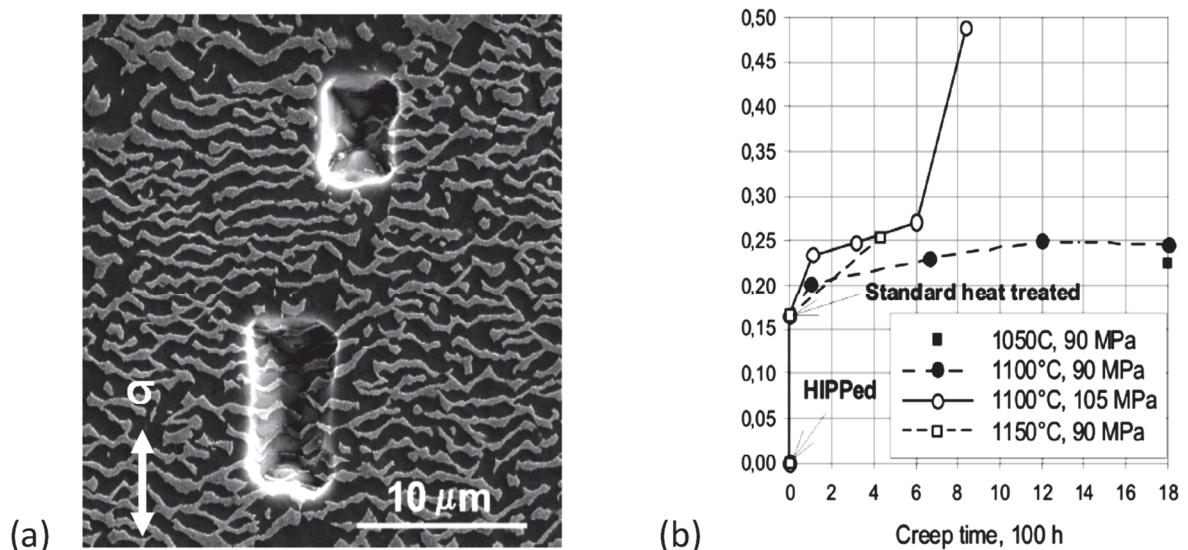


Figure 1.8 - Deformation pores in CMSX-4 after 292 h creep at 1100°C/120 MPa (a) and increase of porosity at high temperatures determined by density measurement (b)(adapted from [32]).

#### 1.6.2 Carbides: characterization, composition and distribution in MAR-M200

In polycrystalline Ni-based superalloys, carbide formation is required to stabilize the microstructure against high-temperature creep deformation, especially to limit diffusion creep at grain boundaries. This could be accomplished by the formation of carbide networks at the grain boundaries. These networks inhibit grain-boundary motion, thus increasing creep resistance and stress-rupture properties [34]. This strengthening mechanism is expected to be more efficient at elevated temperatures ( $T > 0.5 T_m$  where  $T_m$  is the melting point in absolute scale) where grain-boundary sliding becomes significant [35, 36]. Carbides may also induce an "unpinning" or "unstrengthening" mechanism if they are present as a continuous film which creates an easy path for crack propagation [25]. In general, optimum high-temperature mechanical properties are obtained when  $M_{23}C_6$  type carbides are present as discrete, uniformly distributed particles along grain boundaries [25].

The effect of carbides on high temperature mechanical properties is dependent on their chemical composition, morphology (shape, size), stability, location, casting parameters and heat treatments

[25]. However, the real effect (harmful or beneficial) of it is still open to debate [37], **and the identification of the role of carbides on creep and fatigue properties will be one of the main contributions of the present work.**

According to [6, 24, 25], in the as-cast MAR-M200 alloy, there are MC carbides having an ordered NaCl-type FCC structure, ( $\gamma+\gamma'$ ) eutectics, and minor  $M_3B_2$  and  $M_2SC$  phases. The primary MC carbides are TiC, ZrC, HfC, VC, NbC and TaC. These six compounds are isometric, they crystallize in the FCC NaCl-type structure and they have exceptional hardness, high melting point and low thermal conductivity [38]. In addition to these phases, there are also  $MC_2$  and  $Ni_5M$  in the Hf containing version of the alloy. Hafnium can change the script like morphology of MC carbides into blocky ones, but it cannot influence the amount of MC carbides independently. The solution heat treatment, which partially removes segregation, gives additional partially coherent  $M_{23}C_6$  secondary carbides. An effect produced by grain-boundary  $M_{23}C_6$  carbide precipitation is the occasional formation of areas depleted in  $\gamma'$  precipitates (precipitate-free zones PFZ), that may have significant effects on rupture life of these alloys. Should such zones become wide or much weaker than the matrix, deformation would concentrate there, resulting in premature failure [20].

When nickel-base superalloys are solution treated, some of the MC carbides present in the structure may dissolve and the carbon coming from this dissolution process is retained in super-saturation, upon rapid cooling down to room temperature. The most efficient way that so much carbide can form is perpendicular to a grain boundary and the extra boundary area produced by the carbide precipitation is detrimental to the stress-rupture life. If carbides precipitate as a continuous grain-boundary film, mechanical properties also can be severely degraded due to the associated drop of ductility at in high temperature, hence limiting the creep life [20]. This drop of mechanical properties could also be directly linked to carbide oxidation. However, to the author's best knowledge, past literature did not study this phenomena and its consequences on creep and fatigue properties in detail.

## 1.7 Microstructure evolutions in relation with the deformation mechanism and mechanical properties

### 1.7.1 $\gamma-\gamma'$ lattice misfit – its relation with microstructure evolution and mechanical behavior

Strengthening of nickel-based SX superalloys is mainly obtained by coherent precipitation of a large amount of  $\gamma'$  phase in a  $\gamma$  matrix [39]. Both cubic phases present a small lattice mismatch, which is usually expressed by the unconstrained misfit  $\delta = 2(a_{0\gamma'} - a_{0\gamma}) / (a_{0\gamma'} + a_{0\gamma})$ , where  $a_{0\gamma}$  and  $a_{0\gamma'}$  are the lattice parameters of the unconstrained  $\gamma$  and  $\gamma'$  phases, respectively. With this definition of what one may also call the natural  $\gamma/\gamma'$  lattice mismatch,  $\delta$  depends only on the composition of both phases and on temperature. For a given alloy, it can change with temperature, due to the variation of phase equilibrium and the difference in coefficients of thermal expansion [40, 41]. Coherency between  $\gamma$  and  $\gamma'$  phases at their interface leads to elastic deformation of their lattices. Therefore, a similar constrained misfit can be considered with the lattice parameters corresponding to the elastically deformed material (i.e. when a macroscopic applied stress is superimposed). This constrained misfit is more difficult to define since it actually depends on the microstructure (shape, volume fraction, arrangement, size distribution of precipitates, and type of  $\gamma/\gamma'$  interface), which results from the whole thermal history of the alloy [42]. Moreover, the constrained lattice parameters change from place to place in the microstructure with the cubic symmetry often being no more respected.

The lattice mismatch associated with interface coherency has a strong influence on mechanical properties of Ni-based alloys, since elastic distortion strongly contributes to their reinforcement. Conversely, it also controls the microstructure morphology [42]. Indeed, coherency stresses are

responsible for the arrangement of  $\gamma'$  precipitates into periodic arrays of nearly perfect cuboids during ageing [43-48], and for the high stability of this self-stabilized structure against dissolution [44, 45]. They also explain the so-called  $\gamma'$  rafting phenomenon occurring during deformation at high temperature and under low unidirectional stress [39, 47, 48].

Concerning creep loading at high temperatures, dislocations movement plays a major role in the plastic deformation and the eventual creep failure [49]. Slowing down or even stopping mobile dislocations helps increase the creep life. The high volume fraction and large number of  $\gamma'$ -phase cuboids in superalloys prevent dislocation movements in the  $\gamma$ -phase matrix [50], resulting in the formation of dislocation networks along the  $\gamma/\gamma'$  interfaces. Different morphologies of the dislocation networks in Ni-based single-crystal superalloys after creep testing at high temperatures have been observed [51, 52]. Figure 1.9 schematically illustrates these morphologies and their evolution. The first  $\langle 110 \rangle$  diamond shaped morphology, as illustrated in Figure 1.9(a) [53], consists of dislocations along the  $\langle 110 \rangle$  directions on the  $\{001\}$   $\gamma/\gamma'$  interfaces [52, 53]. This type of dislocation network is commonly observed during the early stages of creep deformation, especially during the primary creep stage [54]. During subsequent creep deformation, dislocation networks are densifying and evolve into intermediate polygonal shapes (e.g., hexagonal and octagonal) as depicted in Figure 1.9(b) [53].

Figure 1.9 shows that the cell size of the new  $\langle 100 \rangle$  network is smaller than the original  $\langle 110 \rangle$  network. The  $\langle 100 \rangle$  network is more compact and has a higher dislocation density. In this regard, the  $\langle 100 \rangle$  dislocation network is formed only during the later stages of creep deformation and is expected to have a stronger effect in hindering creep, as observed by Zhang et al. [55]. Indeed, the same authors have shown that increasing the magnitude of the  $\gamma/\gamma'$  lattice mismatch (i.e. having a more negative lattice misfit) leads to a higher dislocation density in interfacial networks, hence protecting in a much more efficient way from  $\gamma'$  shearing during creep at high temperature/low stress [54, 55]. This is illustrated in Fig. 1.11, where a lower minimum creep rate is observed at 1100°C/137 MPa when the  $\gamma/\gamma'$  interfacial dislocation density is high.

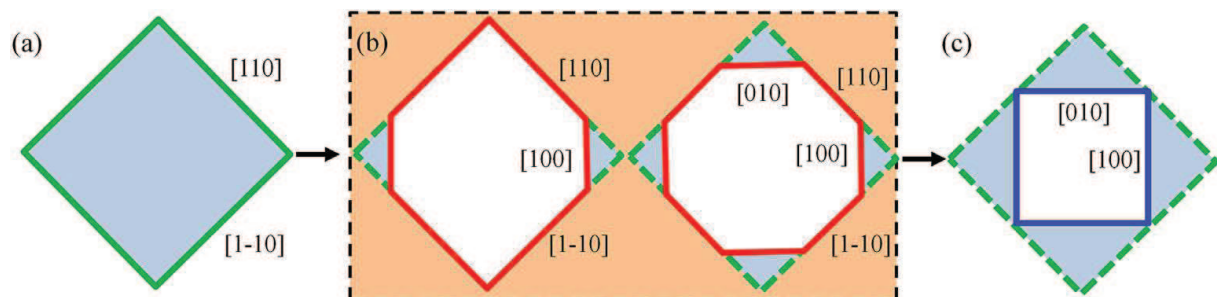


Figure 1.9 - Schematics of the formation and evolution of different types of dislocation networks on the  $\{100\}$   $\gamma/\gamma'$  interfaces of Ni-based superalloys during thermal exposure: (a)  $\langle 110 \rangle$  diamond shaped dislocation network; (b) intermediate polygonal dislocation network; (c)  $\langle 100 \rangle$  square dislocation network (after [53]).

Dislocation networks are formed under the influence of an applied load during creep testing [56, 57], but also in the absence of any applied stress under pure thermal aging conditions at high temperatures ( $T > 950^\circ\text{C}$ ) [51, 58]. This is to relax the internal stresses resulting from the coherency of both phases, meaning that local plastic activity occurs, even in the absence of a macroscopic applied stress. This means that for  $\gamma'$  high volume fraction Ni-based superalloys, strong internal stresses exist at the  $\gamma/\gamma'$  scale because of the lattice misfit between both phases.

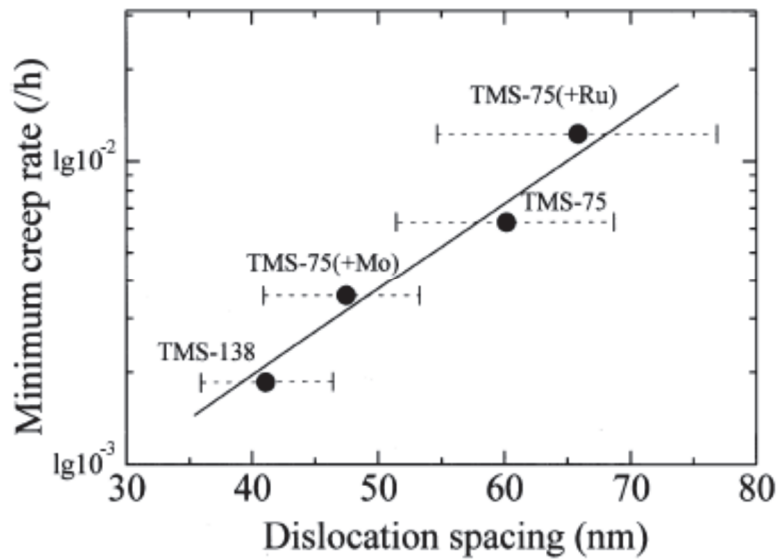


Figure 1.10 – Evolution of the minimum creep rate at 1100°C/137 MPa as a function of the  $\gamma/\gamma'$  interfacial dislocation density (i.e. the magnitude of the  $\gamma/\gamma'$  lattice mismatch) (after [59]).

#### 1.7.2 Deformation mechanisms of Ni-based superalloys at low, intermediate and high temperatures.

Previous work [60] on the Ni-base single crystal superalloy PWA 1480 revealed that the deformation dislocations substructures can be divided into three regimes. At low temperatures (below 700 °C), the deformation is dominated by  $\gamma'$  shearing by dislocations pairs. At high temperatures (above ~ 800-850 °C), plastic deformation is dominated by a  $\gamma'$  by-passing mechanism. Intermediate temperatures exhibit a transitional behavior. Subsequently, such behavior was also observed by Sajjadi et al. [61] in GTD-111 and by Chu et al. [62] in the DS Ni-base superalloy DZ951. Furthermore, Tian et al. [63] investigated the influence of temperature on the operative tensile deformation mechanism in a Co-rich Ni-based polycrystalline superalloy and showed that, when temperature increases from room temperature (RT) to 725 °C, the dominant deformation mechanism changes from APB (Anti-Phase Boundary) shearing to stacking fault shearing, and then to microtwinning [64].

Figure 1.11 [64] shows the typical microstructures of the specimens after a small tensile strain (about 0.2% plastic strain) at room temperature, 400°C and 650°C in the DS Ni-based superalloy M4706. Although the testing temperatures are different, all specimens exhibit similar deformation patterns. As illustrated in Figure 1.11(a) and (c), many pairs of dislocations can be seen in the matrix channels within the slip bands [60, 61, 65] and a high density of stacking faults is also observed, (Figure 1.11(a) to (f)). This contradicts the results reported in [66, 67], where the authors showed that stacking fault shearing rarely occurs at low temperatures. The formation processes of these faults have been discussed in great detail in [68], explaining that it strongly depends on the stacking fault energy required for  $\gamma'$  shearing (i.e. to the exact chemistry of the  $\gamma'$  phase).

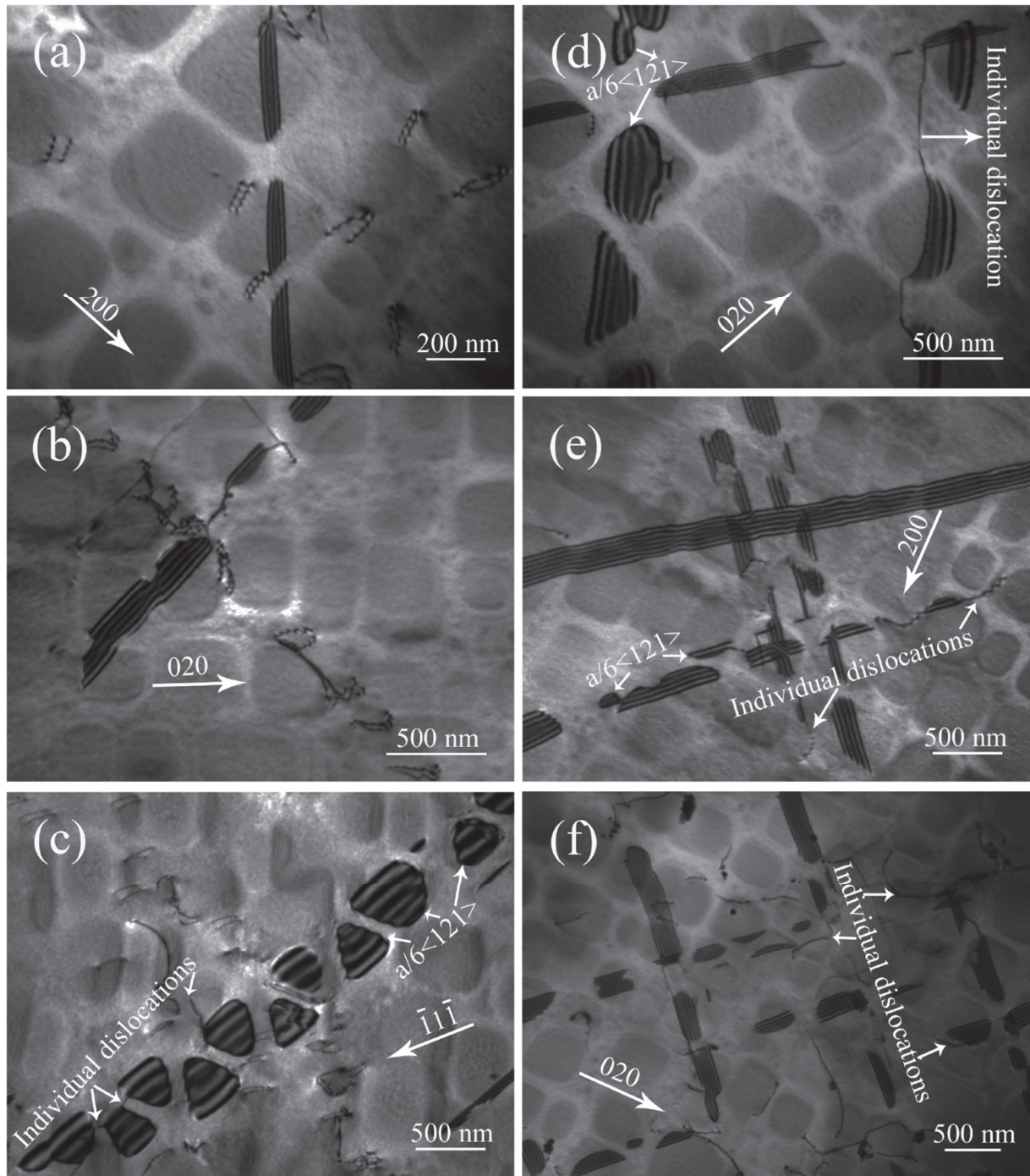


Figure 1.11 - TEM bright-field images showing the formation of dislocations pairs in the slightly deformed specimens of DS M4706 Ni-based superalloy at low temperatures: (a) and (d), RT, 0.23% plastic strain; (b) and (e), 400°C, 0.26% plastic strain; (c) and (f) 650°C, 0.24% plastic strain (after [64]).

Concerning the cyclic behavior, for temperatures below 750°C, the cyclic deformation of Ni-based superalloys is dominated by inhomogeneous slip and shearing of the precipitates on {111} slip planes. Due to this shearing mechanism, the behavior of Ni-based superalloys is absolutely strain rate independent at temperatures where the alloys strength derives from the matrix phase, which is generally the case below 750°C. At low temperatures, Ni-base superalloys deformation is restricted to slip along the {111} planes due to the limited amount of cross slip. A characteristic of low temperature fatigue is the formation of slip bands, which accommodates the plastic deformation, the ultimate spacing of which is an indication of the heterogeneity of the plastic deformation. However, increased



plastic strain leads to more homogeneous deformation, a decreased slip band spacing and an increase of the number of active slip systems [69, 70].

Deformation patterns observed at 700 and 750°C are almost identical to those observed at low temperatures and stacking fault shearing also operates actively [64]. Many of the dislocation pairs are strongly curved and surround the  $\gamma'$  precipitates (Figure 1.11(c) and (f)), more curved than at lower temperature (Figure 1.11(a)). This configuration was also evidenced in the experiments of Benyoucef et al. [71] and Grant et al. [72]. These observations suggest that the ordered  $\gamma'$  precipitate possesses a higher deformation resistance against shearing by dislocations when increasing the temperature from room temperature to  $\sim 700$ -750°C, compared to the softer matrix (a result already widely known, see [73]).

At temperatures in the 750-900°C range, thermally-assisted processes begin to become possible, so that cross-slip of dislocations is feasible. Further, for superalloys tested at low strain ranges under thermo-mechanical fatigue conditions, especially in out-of-phase mode, localized recrystallization along slip bands developed at low temperature in a heavily deformed material can be observed. This recrystallization process may lead to a non-crystallographic fracture of superalloys [74-76].

The formation mechanism of stacking faults created at high temperatures ( $T > 850^\circ\text{C}$ ) is similar to that of the faults produced at low and intermediate temperatures. However, dislocations pairs and  $\gamma'$  precipitates sheared by stacking faults are rarely visible within the matrix channels. Instead, individual bowed dislocations and zigzag dislocations are more frequent at temperatures greater than 850°C, as shown in Figure 1.12 [64]. These dislocation structures were also observed in DZ951 after tensile deformation at 1000°C [62] and in the superalloy TMS-75 after creep deformation at 1100°C [55]. In these references, authors pointed out that these configurations result from combined activation of glide and climb of dislocations, as shown in Figure 1.12: apart from a few straight dislocations, numerous strongly curved dislocations and wavy dislocations are visible. Furthermore, with respect to the dislocation structures, the distribution of matrix dislocations is more homogeneous as compared to those at low and intermediate temperatures (Figure 1.11). This is consistent with the results reported by Takeuchi and Argon [77].

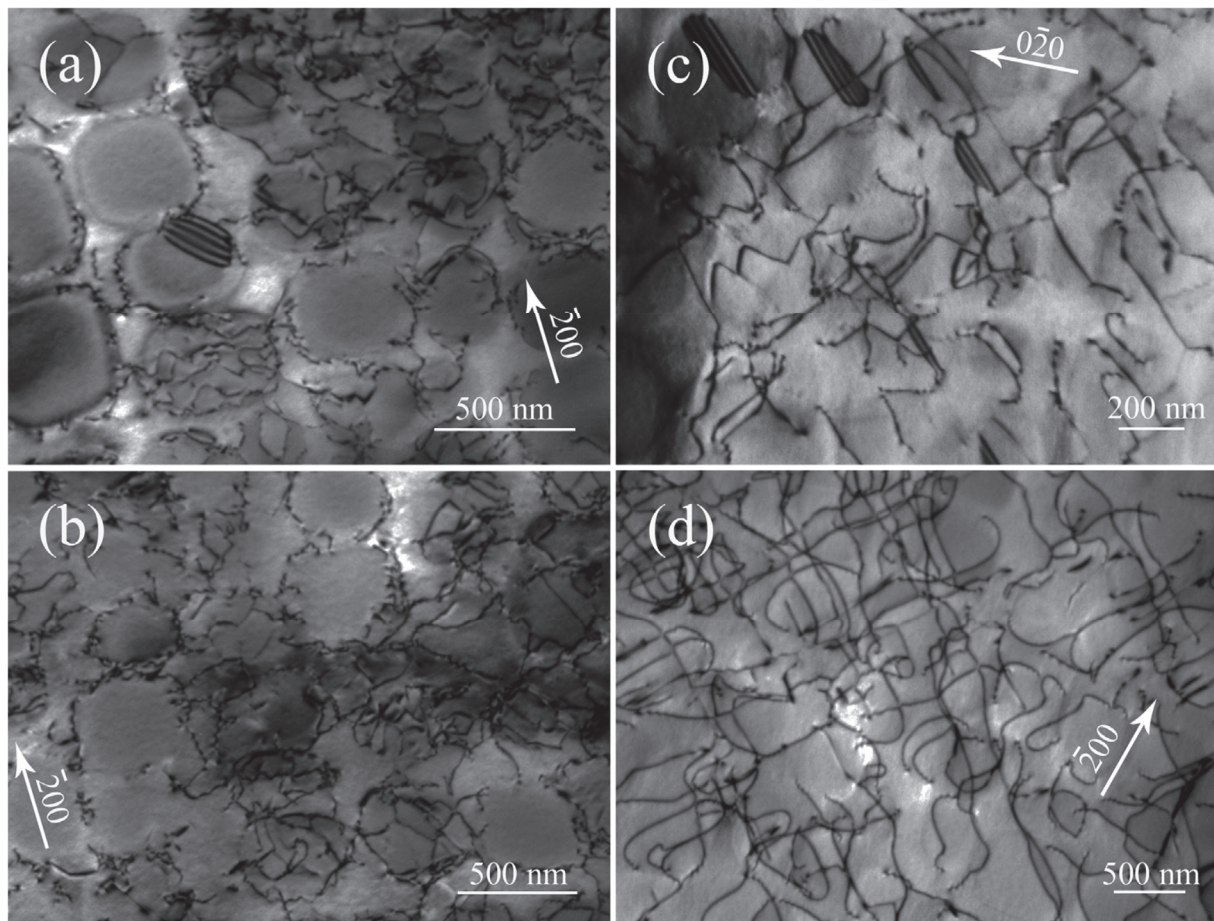


Figure 1.12 - TEM BF images showing the typical microstructures of the specimens after a low magnitude plastic deformation at 950 and 980°C: (a) and (b), 950°C, 0.25% plastic strain; (c) and (d), 980°C, 0.21% plastic strain (after [64]).

### 1.7.3 Change in morphology, size and volume fraction of the $\gamma'$ precipitates due to temperature exposure and/or applied stress ( $\gamma'$ directional coarsening)

Temperature or applied stress can affect significantly the microstructure of Ni-based DS and SX alloys, changing morphology, size, and volume fraction of  $\gamma'$  precipitates [78]. One example is  $\gamma'$  directional coarsening (the so-called  $\gamma'$ -rafting) phenomenon, i.e. a modification of the microstructure of Ni-based SX and DS superalloys observed under applied stress, above typically 850°C. It is characterized by a change of the  $\gamma'$  precipitate morphology from their initial cuboidal shape into “rafts”.

$\gamma'$  rafting was first studied by Tien and Copley in Udimet 700 alloy (see Figure 1.13) [79]. It was then observed several times in many commercial Ni-based SX alloys after creep deformation at temperatures and stresses relevant to service conditions of turbine blades [80-85]. Figure 1.14 illustrates the microstructure observed before and after a 24 h creep test at 1050°C/120 MPa on the first generation MC2 alloy.

Some theoretical and experimental studies have shown that the lattice parameter misfit between  $\gamma$  and  $\gamma'$  phases and the sign of the applied stress are the two main parameters influencing the morphological evolution of the  $\gamma'$  precipitates [87]. For a superalloy with negative misfit (the majority of commercial Ni-based SX and DS superalloys), “type N” is the  $\gamma'$  rafting leading to a directional coarsening perpendicular to loading direction during tension creep along the  $\langle 001 \rangle$  crystallographic

orientation, while “type P” corresponds to rafting parallel to the loading direction (observed during compression creep). An example of an alloy with positive lattice misfit is illustrated in Figure 1.13.

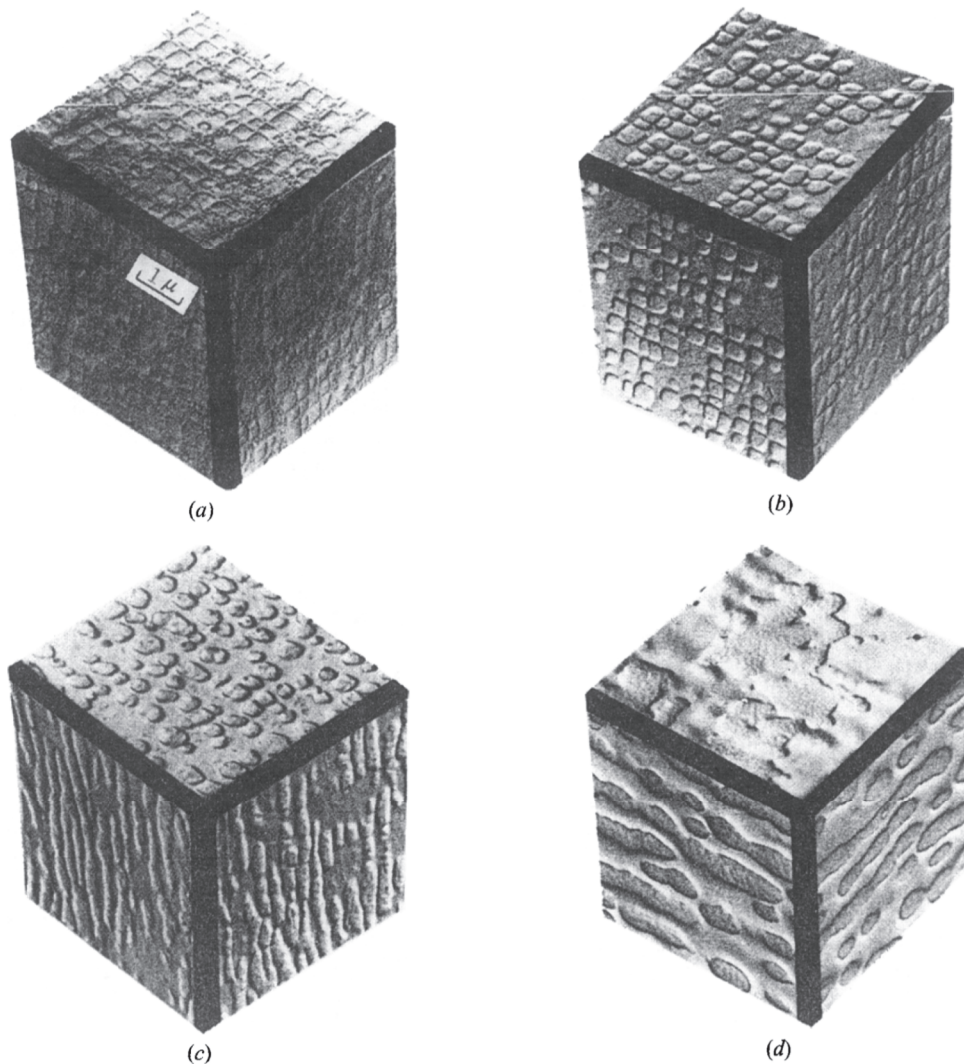


*Figure 1.13 - Microstructure evolutions in Udimet-700 which is an alloy with a positive lattice misfit: as-heat-treated state (a); stress-free high temperature exposure resulting in  $\gamma'$  coarsening (b); tensile creep exposure resulting in P-rafts (c) and compressive creep exposure resulting in N-rafts (d) (after [88]).*

M. Kirka has recently shown that with the application of a compressive creep stress, the widening rate of the  $\gamma$  channels is reduced in comparison to tensile creep conditions for the same stress level in DS CM247LC alloy [89]. This reduction can be attributed to the fact that the movement of dislocations through the vertical channels occurs at a reduced rate compared to the horizontal channels [90, 91]. Kirka also investigated the effect of P-type or N-type  $\gamma'$  rafting on the cyclic behavior as well as on the LCF resistance of DS CM247LC along longitudinal direction at room temperature [89, 92]. More details about these results are going to be presented in 1.8.

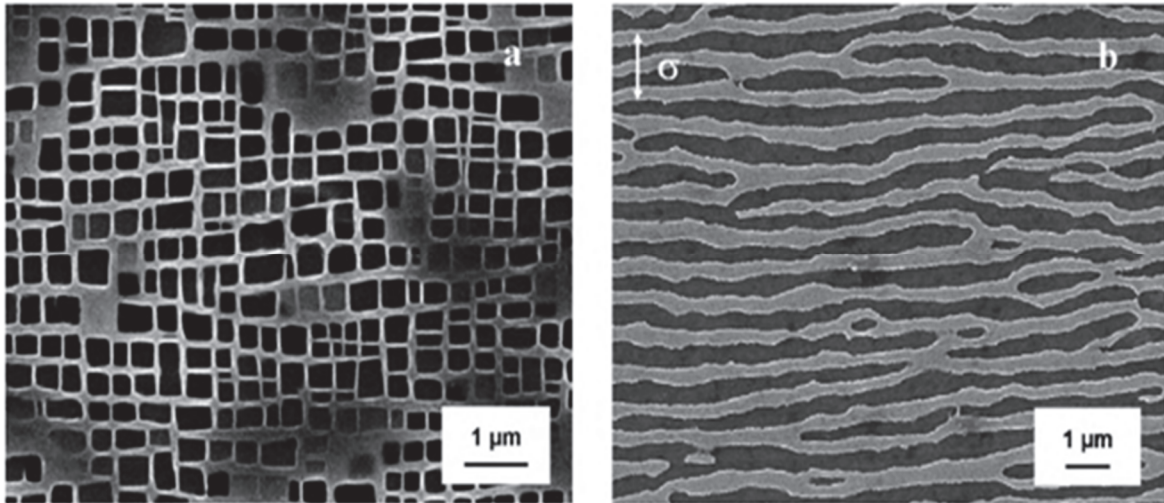


Figure 1.14 - As-received (a) and type-N rafted (b) microstructures of MC2 alloy ( $\gamma$ -phase in dark) (after [93]). N-type rafting in (b) has been obtained after 24 hours in tension creep at 1050°C/120 MPa.

Another significant evolution in morphology, size, and volume fraction of  $\gamma$  precipitates is observed after a long-term exposure at high temperature without applied load (e.g. 900°C in Figure 1.15 for a DS alloy), involving a coarsening of the  $\gamma$  precipitation. In the specimen exposed for 5,000 hours, tertiary  $\gamma$  precipitates dissolved and the secondary  $\gamma$  particles became larger and degenerated with rounded corners, and wider matrix channels. The coarsening process of the secondary  $\gamma$  precipitation and coalescence of smaller  $\gamma$  precipitates continues when thermal exposure was extended to 15,000 hours, increasing gradually up to 24,000 hours of thermal exposure.

As for the  $\gamma$  rafting phenomena, this change of morphology affects mechanical properties [78]. Creep life at 980°C/200 MPa of the thermally exposed specimens is indeed remarkably reduced with the extended thermal exposure. The elongation increased from 16 to 31% within 5,000 hours exposure, and then decreased to 23% up to 24,000 hours, as illustrated in Figure 1.16. This is due to both coarsening of the  $\gamma$  phase and precipitation of a continuous  $M_{23}C_6$  grain boundary layer. This causes grain boundary embrittlement that becomes notch sensitive and prone to cracking.

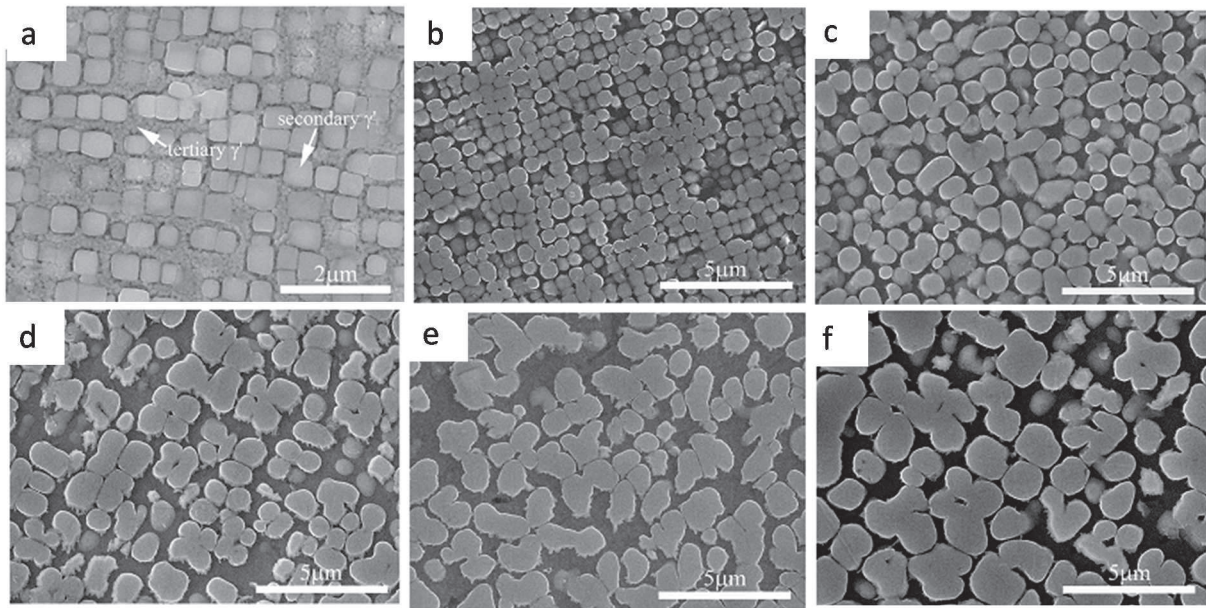


Figure 1.15 -  $\gamma$  morphology in DZ411 alloy as heat treated (a), after 5,000 hours (b), 9,000 hours (c), 15,000 hours (d), 20,000 hours (e) and 24,000 hours (f) of thermal exposure at 900°C (after [78]).

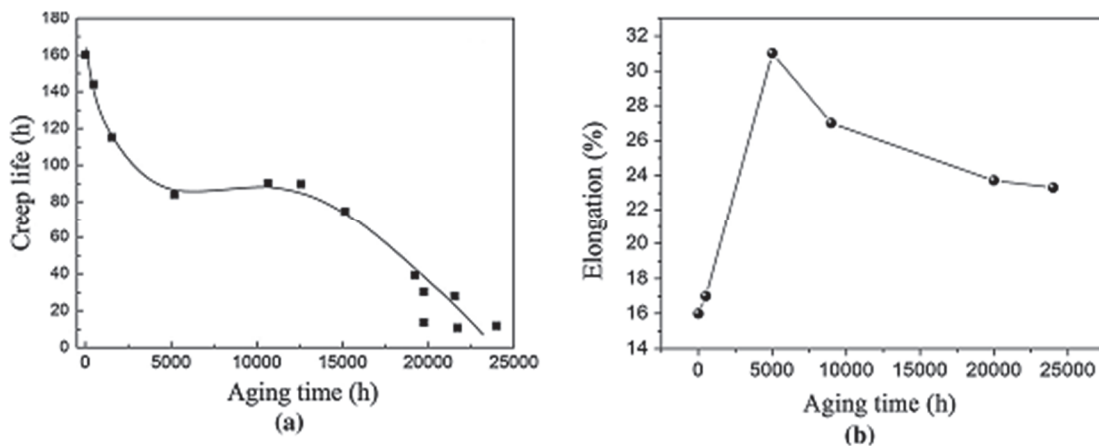


Figure 1.16 – Impact of long-term thermal exposure on the creep properties at 980°C/220 MPa of DZ411 (adapted from [78]).

## 1.8 Mechanical behavior and durability anisotropy of directionally solidified superalloys

### 1.8.1 Tensile properties

Ni-based SX and DS alloys are highly anisotropic materials, especially considering their elastic properties. Figure 1.17 shows that the dynamic Young's modulus for coarse grain DS MAR-M200 superalloy is greater for the polycrystalline cast alloy (a index in Figure 1.17), followed by the modulus of the DS alloy along transverse direction (i.e. in a plane perpendicular to the solidification direction) and the one along longitudinal direction (i.e. parallel to the solidification direction). Such differences result from the almost isotropic transverse character of the elastic properties if one considers a perfect  $\langle 001 \rangle$  orientation for each columnar grain and an infinite number of secondary orientations. However, if the order between these curves appears logical, the lack of precise information concerning the sample of polycrystalline material does not permit us to understand easily the high level of Young's modulus (curve a in Figure 1.17). One should considered the specimen's size used for these elastic

constant measurement relatively to the grain size as well as a possible crystalline texture than are missing in reference [20].

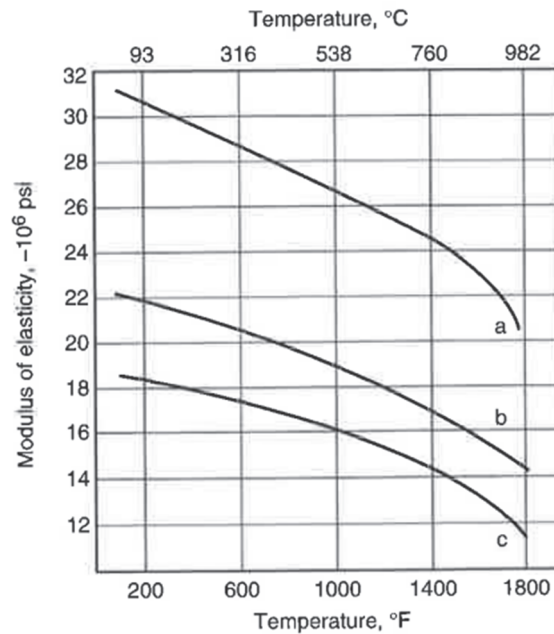


Figure 1.17 - Typical dynamic elastic moduli (Young's modulus) for MAR-M200 superalloy, under the polycrystalline cast form (a), along transverse direction (b) and along longitudinal direction (c) in a coarse grain DS casting (after [20]).

Regarding the inelastic tensile properties, it is observed in Figure 1.18 that DS MAR-M200 performs better along longitudinal direction compared to polycrystalline cast MAR-M200 in terms of ultimate tensile stress (UTS), yield stress (YS) and elongation at failure in all the temperature range. The higher elongation at low temperature also contributes to the higher UTS observed for DS MAR-M200 along the longitudinal direction. Figure 1.18 shows also that tensile properties decrease rapidly beyond about 815°C for all type of castings of this alloy. Alloy DZ951, which is also a DS Ni-based alloy, presents a similar tensile behavior, as mentioned in Figure 1.19. UTS and YS are strongly decreasing for temperatures greater than 800°C, while the elongation increases in parallel to the loss of mechanical resistance. This drop in tensile properties above 800-850°C results from the progressive dissolution of the strengthening  $\gamma'$  phase. Microstructural changes affect directly mechanical properties as UTS and YS and such a trend is not specific to DS alloys, but is observed for most Ni-based alloys strengthened by a high volume fraction of  $\gamma'$  particles.

As previously discussed in 1.7.3, M. Kirka [89, 92, 94] investigated the  $\gamma'$  rafting consequences on mechanical properties. Concerning tensile yielding along longitudinal orientation, a reduction of about 150 MPa was observed in yield stress at 0.2% plastic strain in the range room temperature - 800°C after a prior N-type rafting, showing that a microstructure coarsening is detrimental to tensile properties involving  $\gamma'$  particles shearing. Indeed, when tensile properties at 950°C are considered, no more difference in yielding is observed between rafted and virgin microstructures since deformation mechanisms are mainly restricted to the  $\gamma$  matrix at this temperature.

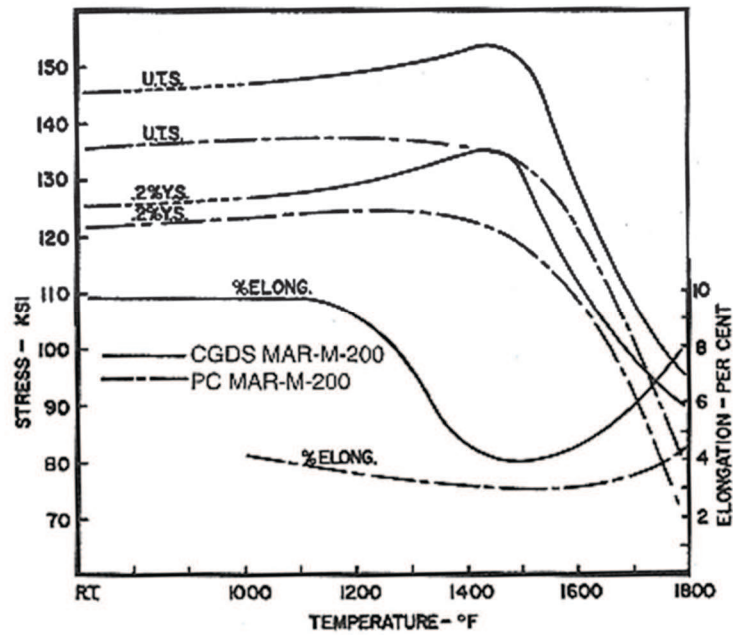


Figure 1.18 - Typical tensile properties of MAR-M200 superalloy for polycrystalline cast and DS coarse grain along longitudinal direction. Note that UTS is the ultimate tensile strength and YS is the yield strength (after [20]).

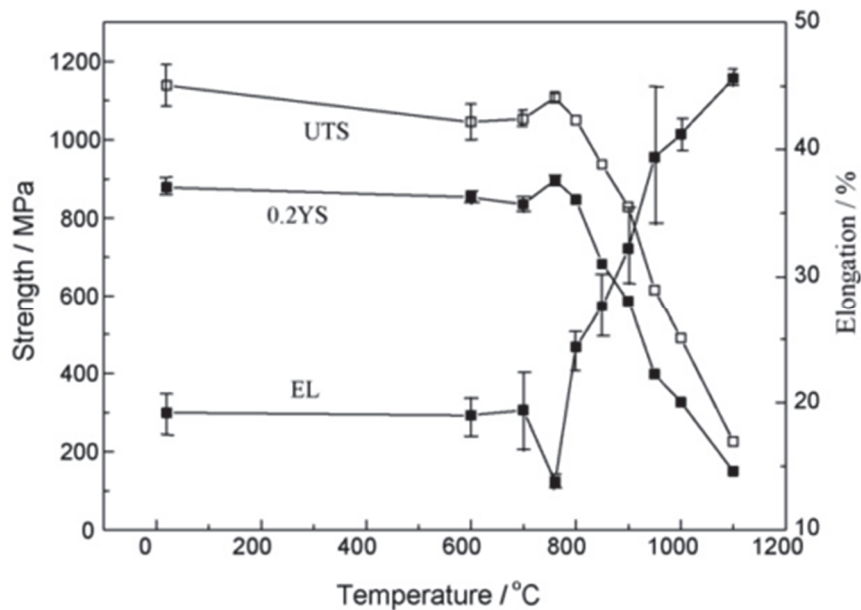


Figure 1.19 – Evolution of tensile properties as a function of temperature for DZ951 alloy (after [62]).

UTS and YS properties along longitudinal direction have also been evaluated as a function of the hafnium content in DS MAR-M200 alloy, as shown in Table 1.2 [24]. Hafnium addition presents a positive effect on these properties, increasing the mechanical resistance of this alloy at temperatures of interest for this study (650°C up to 950°C). However, this effect is not always positive, taking in consideration the strain at failure ( $\delta$  in Table 1.2), because hafnium-rich carbides oxidize at grain boundaries, causing premature crack initiation and a possible loss of high temperature ductility. It is

then necessary to optimize hafnium content to achieve the desired mechanical properties for a given application. **The exact role of hafnium in mechanical durability of DS MAR-M200 will be one of the specific issues investigated in this PhD work. A special attention will be paid to the environmental resistance of the alloy and how hafnium-rich carbides oxidize.**

Temperature °C	D. S. Condition	Hf-free alloy					Hf-containing alloy				
		H. T.	0.2%Y.S. (MPa)	U.T.S (MPa)	$\delta$ (%)	$\psi$ (%)	H. T.	0.2%Y.S. (MPa)	U.T.S (MPa)	$\delta$ (%)	$\psi$ (%)
R. T.	BIAM	11	1007	1115	5.85		111	1024	1217	5.63	
		1	1001	1197			1	1091	1284		
		1	989	1238	10.8	13.5	1	1106	1256	8.4	9.6
650	BIAM	11	927	1119	11.1		111	977	1173	8.7	
760	BIAM	11	1030	1109	6.5		111	1078	1121	11.2	
		1	967	1205	8.8	14.0	1	1091	1317	7.0	10.0
		1	990	1227	9.2	14.5	1	1106	1332	7.2	10.6
	ONERA	1	886	1107	6.2	7.0	1	920	1118	4.7	8.7
950	BIAM	11	437	559	16.1		111	555	641	22.5	

Table 1.2 - Tensile properties of DS200 and DS200+Hf (with 1.78 wt. pct of hafnium) alloys (adapted from [24]).

1.8.2 Creep properties

Creep behavior of DS MAR-M200 alloy was investigated in previous studies, and compared to the polycrystalline version of the alloy (Figure 1.20, Figure 1.21 and Table 1.3). Longitudinally oriented coarse grain specimens have a better creep resistance than polycrystalline ones (ratio in creep life of around 2), and this behavior is even improved when the alloy is solution heat treated. However, according to Figure 1.21, the single crystalline version of the alloy presents a better creep life when compared to DS specimen loaded along longitudinal direction, with an improvement of nearly 20%. The creep strength improvement concerning DS or SX version of MAR-M200 mainly results from the spectacular improvement in creep ductility compared to the polycrystalline version of the alloy (a factor of nearly 5 in creep strain at failure between SX/DS castings and the conventionally cast alloy (Figure 1.21). However, in this creep condition, the early stages of creep are not significantly affected by the casting type (i.e. all curves are nearly superimposed during the first 20 hours of creep straining in Figure 1.21), the minimum creep rate reported in Table 1.3 confirms this point. According to this Table, it seems that casting type mainly affect the low temperature/high stress minimum creep rate.



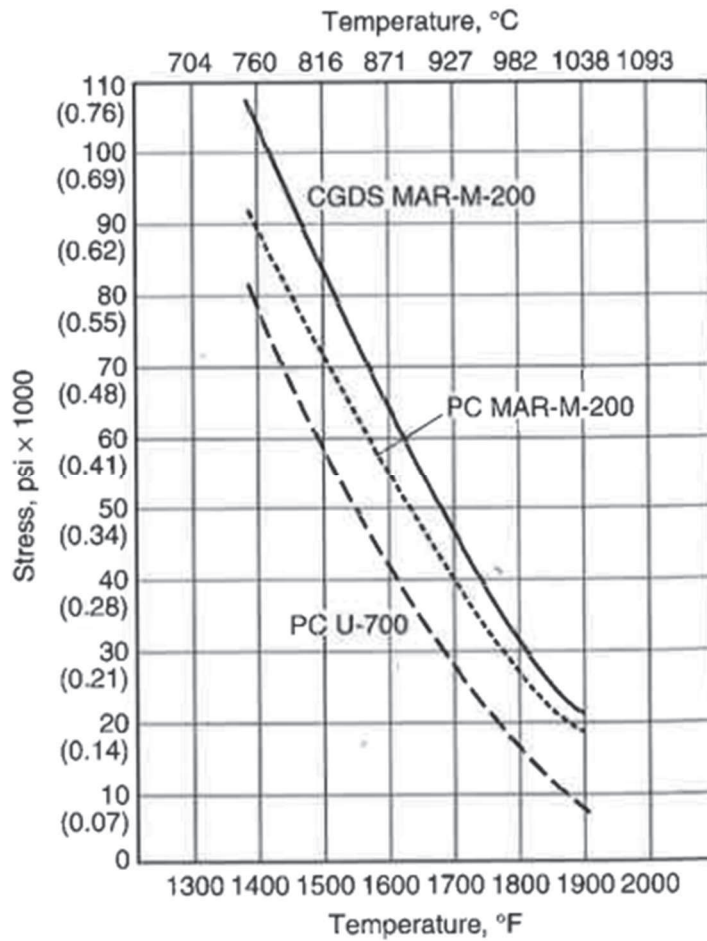


Figure 1.20 - Typical stress for 100 h rupture life of coarse grain DS MAR-M200 superalloy along longitudinal direction and polycrystalline MAR-M200 and Udimet™ 700 cast alloys (after [20]).

	1400 °F/100 ksi			1600 °F/50 ksi			1800 °F/30 ksi		
	Rupture life, h	Elongation, %	Min creep rate, in./in./h	Rupture life, h	Elongation, %	Min creep rate, in./in./h	Rupture life, h	Elongation, %	Min creep rate, in./in./h
Polycrystalline	4.9	0.45	$70.0 \times 10^{-5}$	245.9	2.2	$3.4 \times 10^{-5}$	35.6	2.6	$23.8 \times 10^{-5}$
Columnar grain	366.0	12.6	$14.5 \times 10^{-5}$	280.0	35.8	$7.7 \times 10^{-5}$	67.0	23.6	$25.6 \times 10^{-5}$
Single crystal	1914.0	14.5	$2.2 \times 10^{-5}$	848.0	18.1	$1.4 \times 10^{-5}$	107.0	23.6	$16.1 \times 10^{-5}$

Table 1.3 - Creep properties at 760°C/690 MPa, 871°C/345 MPa and 982°C/207 MPa of polycrystalline MAR-M200 alloy compared to its <001> single crystalline and longitudinal DS counterparts (after [20]).

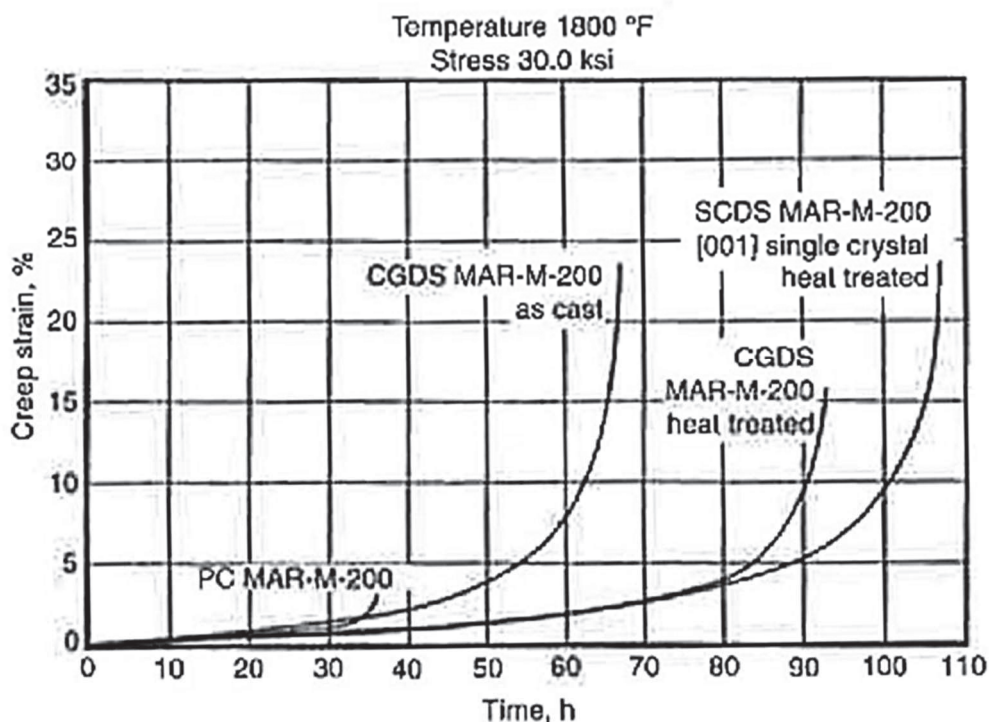


Figure 1.21 - Creep behavior at 982°C/207 MPa of polycrystalline MAR-M200 (PC) compared with single crystalline MAR-M200 along the <001> orientation (SCDS) and DS MAR-M200 along longitudinal direction (CGDS) (after [20]).

As for tensile properties, creep properties of MAR-M200 with and without addition of hafnium were investigated and some results are presented in Table 1.4. Creep life is increased by a factor of almost 5 at 760°C adding nearly 1.8 wt. % hafnium. This spectacular increase in creep life during longitudinal creep testing of DS MAR-M200 + Hf alloy mainly results from a better resistance of grain boundaries due to hafnium additions [21], an effect that still remains to be fully understood. The difference in creep life with and without hafnium is, however, less pronounced at higher temperatures (factor of only 1.7 at 1050°C). This difference in creep resistance when increasing the temperature results from changes in the creep damage mechanisms controlling time to failure. **A special focus will be paid in chapter 4 to creep damage mechanisms, by developing specific experimental procedures to track creep crack initiation and the first stages of propagation.**

Very few studies investigated the mechanical properties of DS alloys along transverse directions and the effect of the grain size on these properties. However, several investigations have been performed on the creep anisotropy of SX Ni-based superalloys, as shown in Figure 1.22 and Figure 1.23. This is indeed useful to understand the creep behavior along transverse direction of DS alloys, since this type of casting can be seen as a collection of vertical nearly <001> grains, with random secondary orientations. Hence, when characterizing transverse creep properties of DS alloys, orientations ranging from <100> up to a <110> can be met along the loading direction, considering an almost perfect <001> texture for these columnar grains.

According to Figure 1.22 and Figure 1.23 showing the creep behavior at 760°C/689.5 MPa (100 ksi), 871°C/345 MPa (50 ksi) and 962°C/207 MPa (30 ksi), SX specimens oriented close to [001] direction present a better creep strength, followed by specimens oriented close to [111] crystallographic

orientation. Samples oriented close to [011] orientation have a poor creep life for all tested conditions, allowing to conclude that transversally loaded DS MAR-M200 may also present a poor mechanical behavior since <110> oriented grains come into play in test along transverse directions.

Test Conditions			Hf-free alloy			Hf-containing alloy			
Temperature °C	Stress (MPa)	H.T.	Time for 1% creep (h)	Rupture life (h)	Elongation (%)	H.T.	Time for 1% creep (h)	Rupture life (h)	Elongation (%)
760	750	II	13	351	8.6	III	5	1300	--
850	450	II	45	197	19.6	III	162	323	24.7
950	200	II	125	251	6.8	III	228	625	26.5
1050	100	II	104	173	13.6	III	156	254	21.2

Table 1.4 - Creep properties of DS200 alloy and DS200+Hf (1.78 wt. pct of hafnium) alloy (adapted from [24]).

This effect is clear in Figure 1.23, which compares the creep behavior of several MAR-M200 SX specimens at 760°C/689.5 MPa. Sample 18, oriented close to [011], presents only about 5 hours of creep life, compared to 1050 and 1950 hours for samples 16 and 4 respectively. This poor creep resistance results from the absence of strain hardening in creep (i.e. no transition from primary to a secondary creep stage is observed in the creep curve of specimen 18 in Figure 1.23).

Similar results were obtained by Kear and Pearcey using MAR-M200 alloy [13], however, at 982°C, the crystallographic orientations exerted much less influence on the stress rupture life. These results are summarized in Figure 1.24. This study demonstrated that at lower stress levels and higher testing temperatures, the dependence on orientation is less pronounced because multiple slips occurs typically for temperatures higher than 850°C (see sub-section 1.7.2).

Rebecca MacKay and co-workers have analyzed the anisotropy in creep resistance over a wide temperature range using MAR-M247 single crystals (see Figure 1.24(b)) [95], and they have compared their results with data extracted from Kear and Pearcey [13] for MAR-M200. In a Larson-Miller plot, it is observed that the best creep properties are obtained along the  $[\bar{1}11]$  while the [001] orientation has an intermediate creep life under all tested conditions. This result is in contradiction with the creep behavior shown in the previous figures (i.e. Figure 1.22 and Figure 1.23), where [001] oriented specimens were the most resistant, whatever the creep condition. As a striking result from Figure 1.24 (b), it is observed that creep life anisotropy increases as temperature decreases. Such a result has been widely observed for several Ni-based SX superalloys [68, 96].

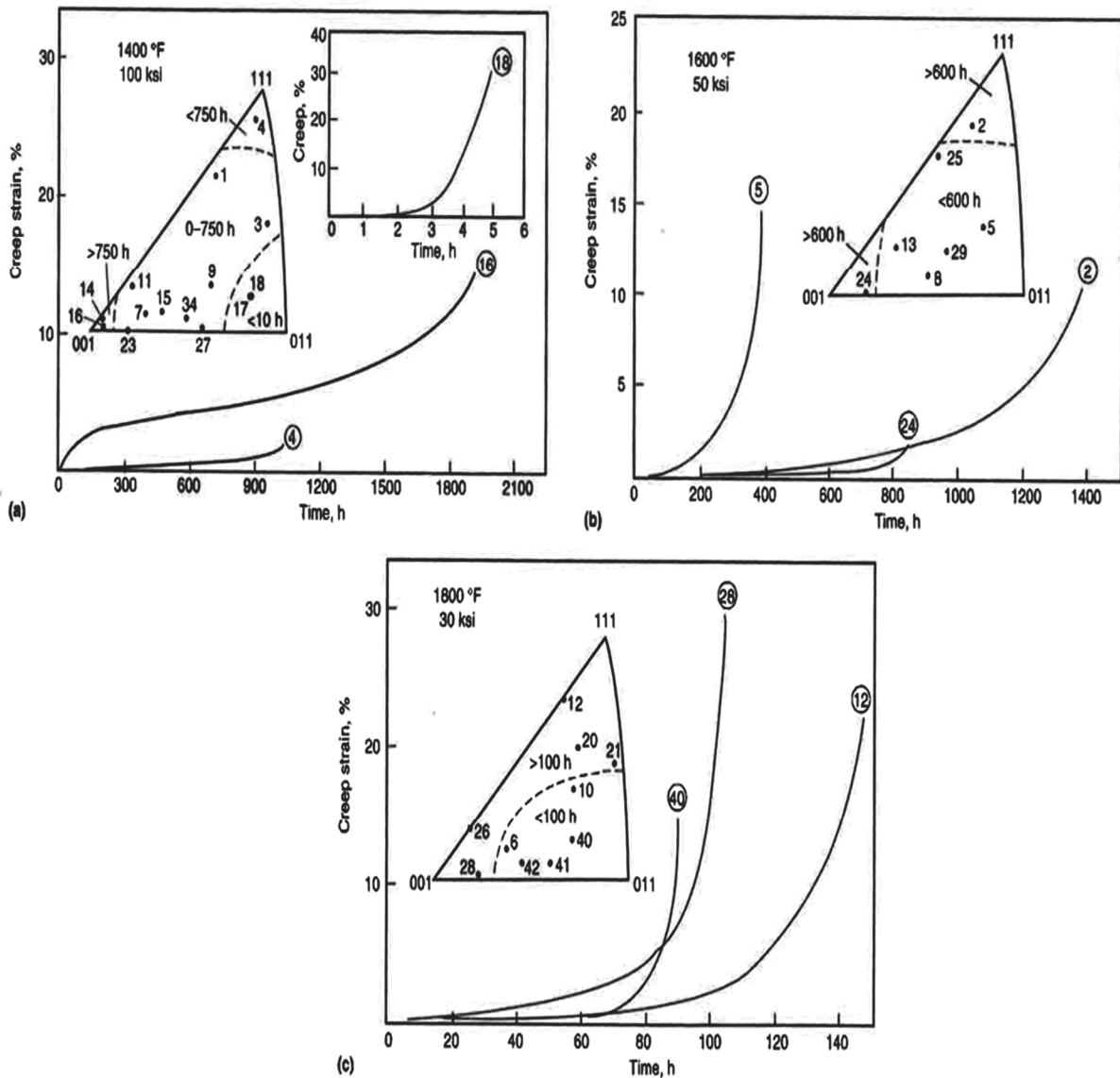


Figure 1.22 - Orientation dependence of the creep behavior of single crystalline MAR-M200 at 760°C/689.5 MPa (100 ksi), 871°C/345 MPa (50 ksi) and 962°C/207 MPa (30 ksi) (adapted from [20]).

As mentioned previously, very little information on transverse creep properties is available for DS alloys. Figure 1.25 shows a comparison between transverse and longitudinal creep lives of DZ125 (a Chinese DS alloy whose chemical composition is very close to René 125 at different temperatures) [97]. For this alloy, the variation of rupture life according to orientation is less marked when temperature increases, in good agreement with single crystalline specimens.

For DS alloys, microstructural changes inside crystals have to be taken account when mechanical properties are evaluated, such as the  $\gamma'$ -rafting and volume fraction of  $\gamma'$  precipitates. It is widely known [2, 98] that increasing the  $\gamma'$  content improves the high temperature isothermal creep properties.  $\gamma'$  rafting generally results in a decrease of the mechanical properties, such as the reduction of yield stress at low temperatures [99], as discussed above (1.7.3 and 1.8.1). However the impact of  $\gamma'$  rafting on the creep properties remains a controversial issue [100].

Some authors assumed that  $\gamma'$  rafting is beneficial to the isothermal creep properties at high temperature/low stress by building very efficient obstacles to dislocation motion in the  $\gamma$  matrix [101-

103]. It is also reported that in these testing conditions, the steady-state creep rate is controlled mainly by dynamic recovery of the matrix dislocations involving  $\gamma'$ -rafts pairwise cutting by a combined glide/climb process [104-107]. More precisely, the steady state creep rate was reported to be limited by the viscous motion of the climbing dislocations.

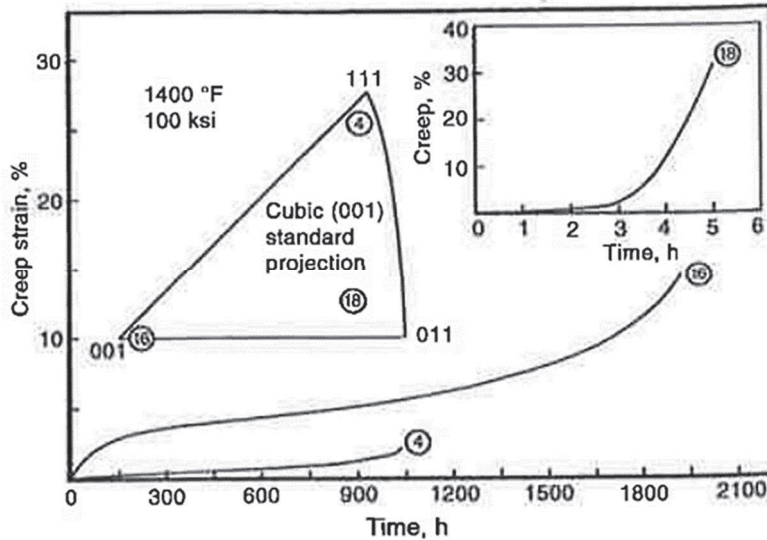


Figure 1.23 - Creep behavior of MAR-M200 single crystalline specimens with loading axis close to the [001], [011] and [111] directions. Creep testing at 760°C/689.5 MPa (after [20]).

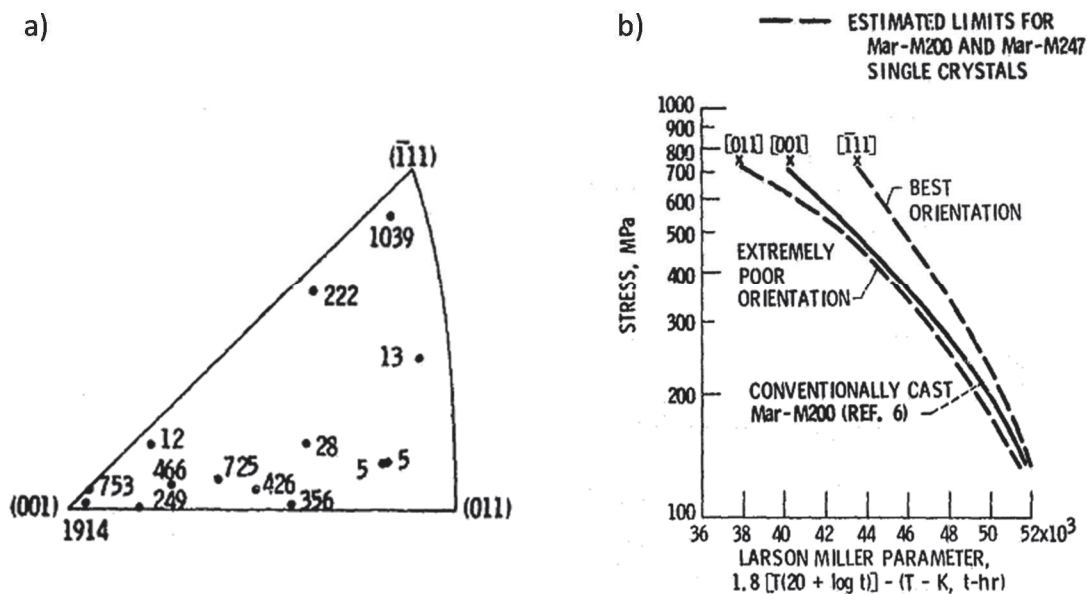


Figure 1.24 - Stress rupture lives as a function of orientation for MAR-M200 single crystals at 760°C and 689 MPa (after [13]) (a) and Larson-Miller diagram showing the anisotropy in creep life of MAR-M200 and MAR-M247 (after [95]) (b).

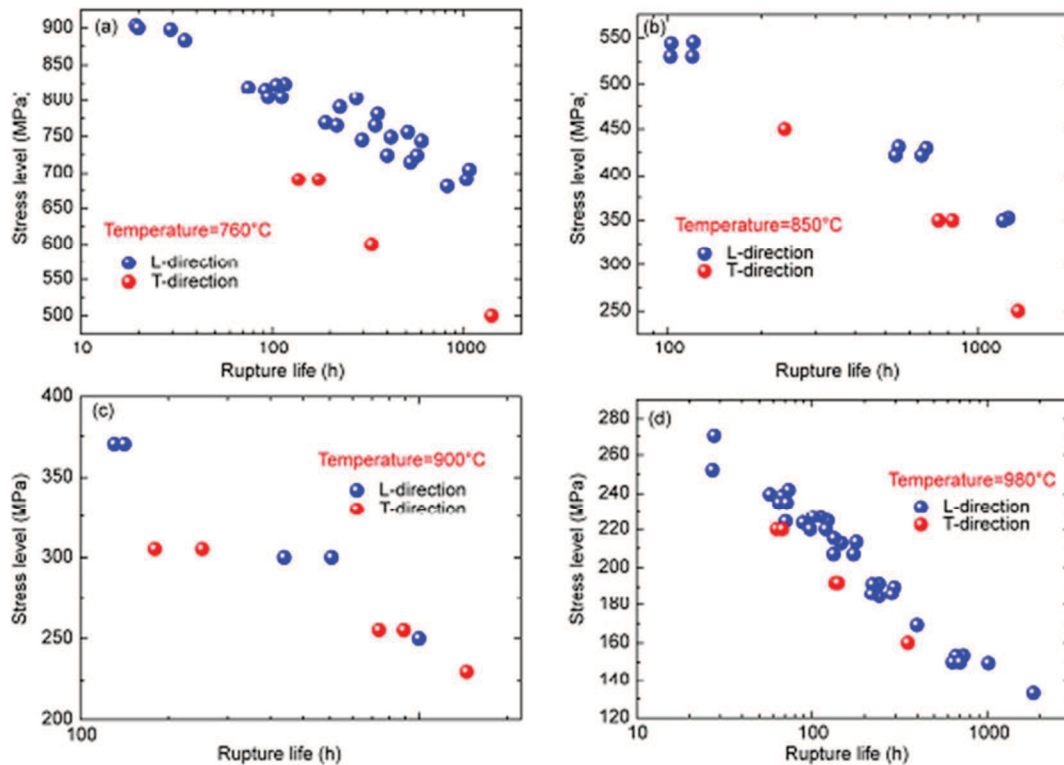


Figure 1.25 - Creep life evolution as a function of the applied stress of for DZ125 alloy at 760°C (a), 850°C (b), 900°C (c) and 980°C (d) (after [97]). Note that L-direction and T-direction correspond to the longitudinal and the transverse direction, respectively.

However, some recent studies have proved that at high temperatures,  $\gamma'$  rafting is detrimental to non-isothermal creep properties [108-110]. Milhet et al [109] have indeed shown that the minimum creep rate, known to be related to matrix dislocations recovery by  $\gamma'$ -cutting, seems to be very dependent on the backstress due to dislocations deposited at the  $\gamma/\gamma'$  interfaces in the course of the deformation process.

Another group has shown that  $\gamma'$  rafting could be beneficial to isothermal creep properties in a DS Ni-based superalloy [111]. The results indicated that a higher cooling rate during the solution heat treatment led to finer  $\gamma'$  precipitates and improved high-temperature creep life. The microstructural analyses using both scanning electron microscopy and transmission electron microscopy revealed that finer  $\gamma'$  precipitates and narrower  $\gamma$  channel width could result in a denser rafting structure, which might have hindered the climb of dislocations across the precipitate rafts. A similar interpretation was also proposed recently by Steuer et al. regarding high temperature isothermal and thermal cycling creep properties [110].

Regarding the effect of the  $\gamma'$  volume fraction, improvement of the high temperature isothermal creep properties by increasing the  $\gamma'$  content is clearly observed in Figure 1.27, where the creep life is peaking for a  $\gamma'$  fraction of nearly 60-70% in different alloys (either SX or polycrystalline Ni-based alloys). A similar result is also obtained under closer-to-reality conditions (flight conditions of thermomechanical fatigue). Indeed, according to J. Cormier [112], an improved durability has been observed during high temperature thermal cyclic creep with large  $\gamma'$  contents (see Figure 1.27). The average number of cycles to failure is just 2 for a  $\gamma'$  content of  $\sim 15\%$  at 1160°C (the case of MAR-M200+Hf SX alloy), while it reaches 319 for a remaining  $\gamma'$  content of  $\sim 56\%$  at 1160°C (case of CMSX-10K alloy). The increase in creep resistance is especially effective for  $\gamma'$  volume fractions greater than 45-50% at 1160°C.

All these results [112] are in good agreement with past papers where microstructural factors contributing to the very high ( $T > 1100^{\circ}\text{C}$ ) temperature creep resistance of Ni-based single crystal superalloys are analysed. They show that, under such conditions, the remaining  $\gamma'$  fraction is the main parameter controlling creep life [98, 103, 113]. Indeed, a high  $\gamma'$  content at high temperature effectively prevents the dislocation motion to occur by increasing both Orowan stress [87, 110] and the number of  $\gamma/\gamma'$  interfaces, hence lowering the dislocation climb velocity [100].

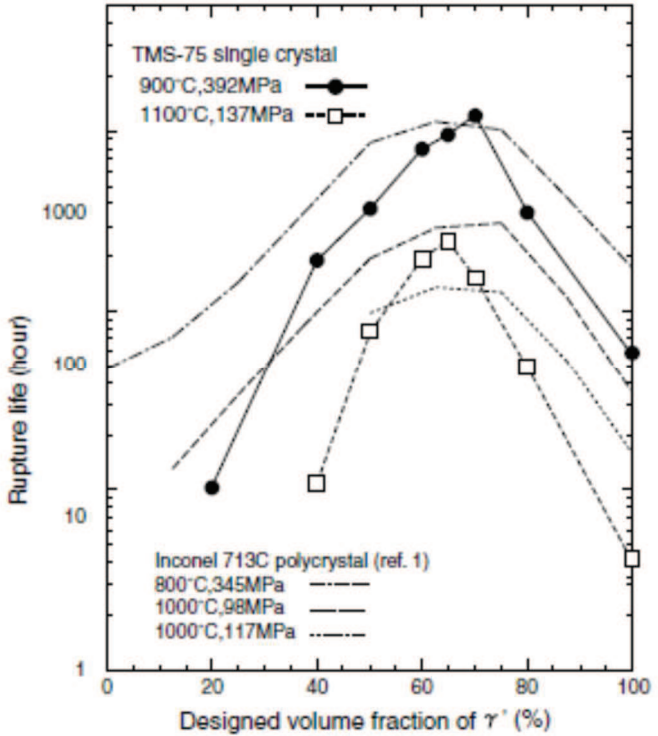


Figure 1.26 - Evolution of the high temperature creep life as a function of the  $\gamma'$  volume fraction under different conditions for TMS 75 and Inconel 713C alloys (adapted from [113])

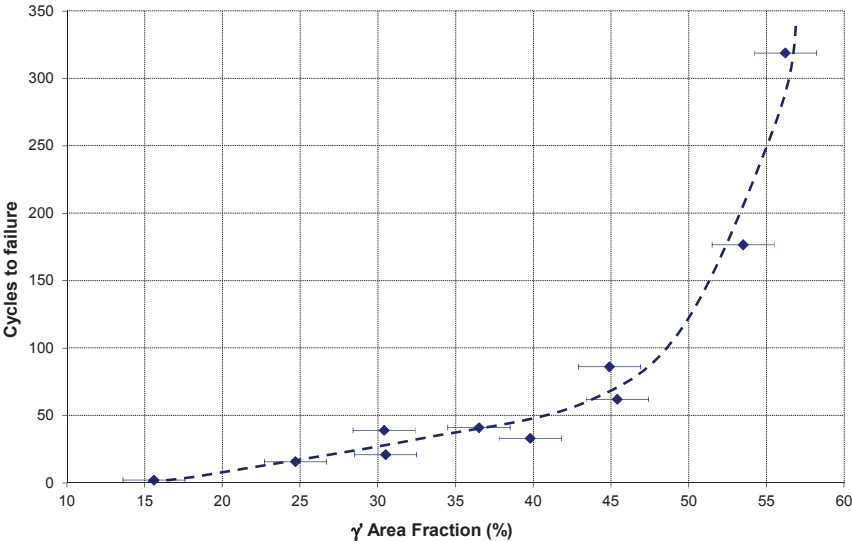


Figure 1.27 - Evolution of the number of thermal cycles up to failure as a function of the  $\gamma'$  area fraction measured in the gage section of each sample 1 mm far from the fracture surface (after [112]).

In summary, the [001] crystallographic direction for SX castings or the longitudinal direction for DS castings always presents a better rupture life in creep compared to other directions, whatever the temperature range. The decrease in creep (and tensile) anisotropy at high temperature results from the fast degradation of the well-organized cuboidal  $\gamma/\gamma'$  microstructure for both types of castings, a microstructure specifically developed during heat treatments (solution and aging heat treatments) to optimize mechanical properties at low temperatures [11]. The  $\gamma'$  directional coarsening (see section 1.7.3) induces wider  $\gamma$  channels and easier plastic flow within the matrix and allows a much more homogeneous plastic deformation in the volume and then, a decrease of the creep life anisotropy for DS and SX Ni-based superalloys. **However, oxidation may also affect crack initiation and subsequent propagation stages, a process that could also contribute, at least partly, to the creep life anisotropy. We will then try to elucidate oxidation contribution to the creep life anisotropy.**

### 1.8.3 Fatigue properties

The development of DS alloys was not only motivated by the improvement of the creep resistance as seen in the previous section, but also by the need to obtain a better fatigue resistance by means of the crystallographic texture and grain boundary orientation. An example of thermal fatigue life improvement with DS alloys is shown in Figure 1.28 for René 80 and René 150 [114].

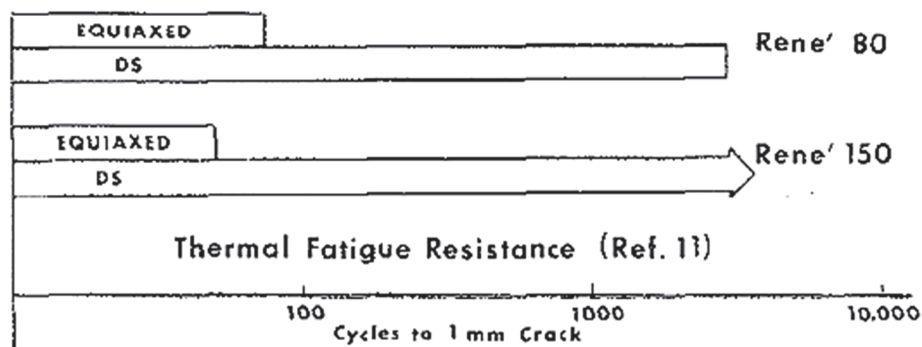


Figure 1.28 - Comparative thermal fatigue resistance of equiaxed and DS superalloys (adapted from [114]).

Similarly to creep properties, DS Ni-based superalloys also exhibit an intermediate LCF and thermo-mechanical fatigue resistance between these of their equivalent polycrystalline and single crystalline alloys, as shown in Figure 1.29.

Regarding the anisotropy in fatigue properties of DS alloys, an extensive study has been performed by Wright and Anderson [114]. They have investigated the effect of the loading direction during strain-controlled LCF of DS René 120 at 650°C and 982°C (Figure 1.30). Most of the data for the various orientations fall into one master curve at each temperature if the maximum tensile stress met after cyclic stabilization is plotted as a function of the number of cycles to failure. A detailed analysis of such data indicates a link between LCF anisotropy and the variation in Young's modulus, as shown in Figure 1.31.

Indeed, during strain-controlled LCF tests, a higher Young's modulus (i.e. a deviation of the loading axis from the main solidification direction) leads to a higher maximum tensile stress and hence, to faster crack initiation from internal defects or from the surface. The only exception to this trend was for



982°C, where the 90° (i.e. transverse loading) data fall significantly below the 0° to 45° oriented specimen data band. Fractographic analyses clarified this result.

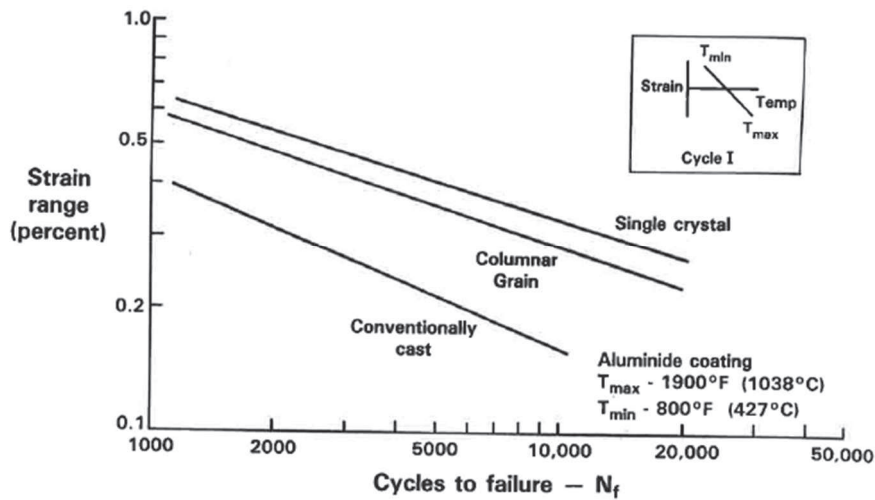


Figure 1.29 - Comparison of the thermo-mechanical fatigue lives of single crystal, polycrystalline and directional solidified cast nickel-based superalloys (longitudinal loading) (after [20]).

Indeed, at 650°C, cracks initiate from defects such as casting pores or carbides clusters (also observed in another study by Chieragatti and Rémy [115], see Figure 1.32). Surface crack initiation is then observed, due to the contribution of oxidation. The rupture mode at this temperature is transgranular for 0° to 45° orientations and intergranular for specimens oriented at 90° of the loading direction. The intergranular cracking mode, induced and/or favored by oxidation, was also observed for equiaxed specimens of the same chemical composition as DS René 120. Hence, as shown in Figure 1.30, equiaxed and DS specimens loaded along transverse direction exhibit the same fatigue resistance at 982°C.

All these LCF results for DS René 120 are in good agreement with recent ones obtained for the AM1 first generation SX alloy by Steuer et al. [31]. Indeed, fractographic observations revealed that cracks initiate from defects (i.e. casting pores in that case) at low temperature (750°C), whatever their size, while surface crack initiation from oxidized layers was observed at higher temperature (950°C). Typical crack initiation sites in broken AM1 LCF specimens at 750°C are shown in Figure 1.33. From the previous figures, it is hence clearly illustrated that at low temperature, in the absence of a huge contribution of oxidation, crack initiation is mainly controlled by the size and position of casting defects, i.e., by the solidification process parameters. In the case of MAR-M200 SX alloy, it can also be controlled by the chemistry of the alloy, since carbides have been shown to be detrimental to the LCF properties at 650°C.

Figure 1.34 indeed shows that a carbide free version of MAR-M200 SX alloy presents a better LCF life at room temperature compared to a version containing carbides. This results from a much more homogeneous distribution of plastic activity within the gage length of the specimens, resulting in a decrease in the number of stress concentrators.

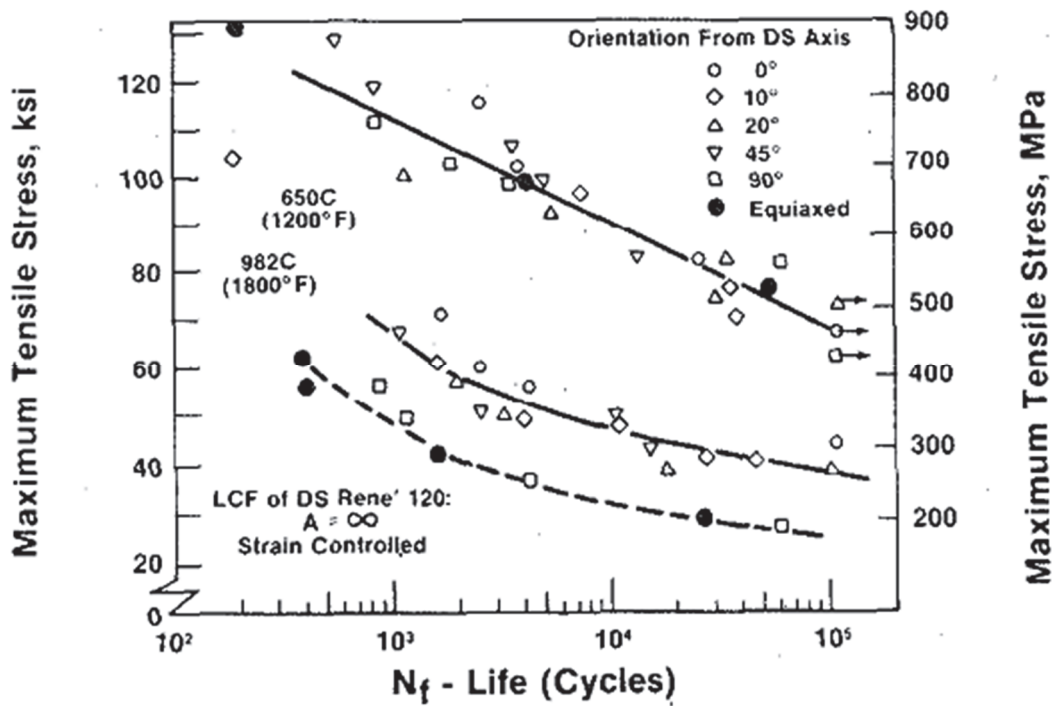


Figure 1.30 – LCF life anisotropy of DS René 120 alloy (after [114]). Note that the  $0^\circ$  orientation corresponds to a loading direction aligned with the solidification direction (i.e. orientation of the columnar grains) while  $90^\circ$  corresponds to perfect transverse loading direction.

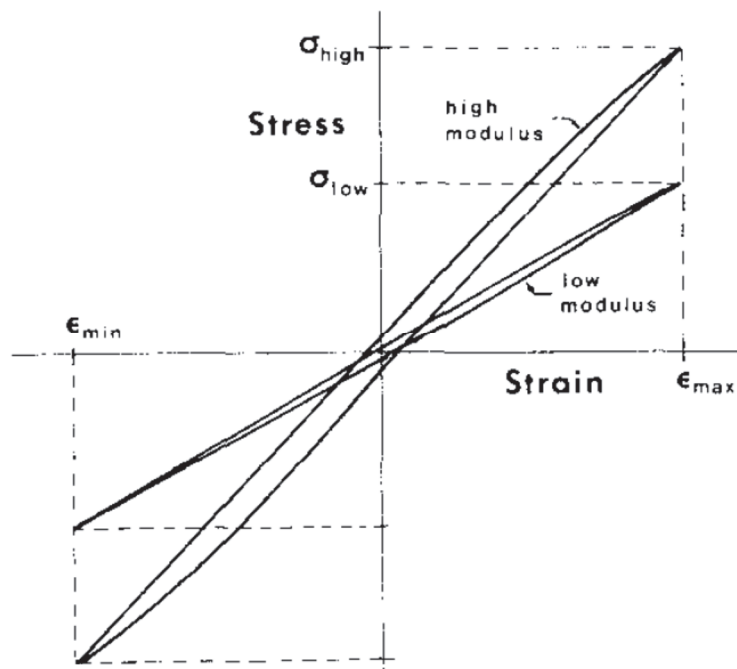


Figure 1.31 – Effect of Young's modulus variation on peak stresses during strain-controlled LCF tests (after [114]).

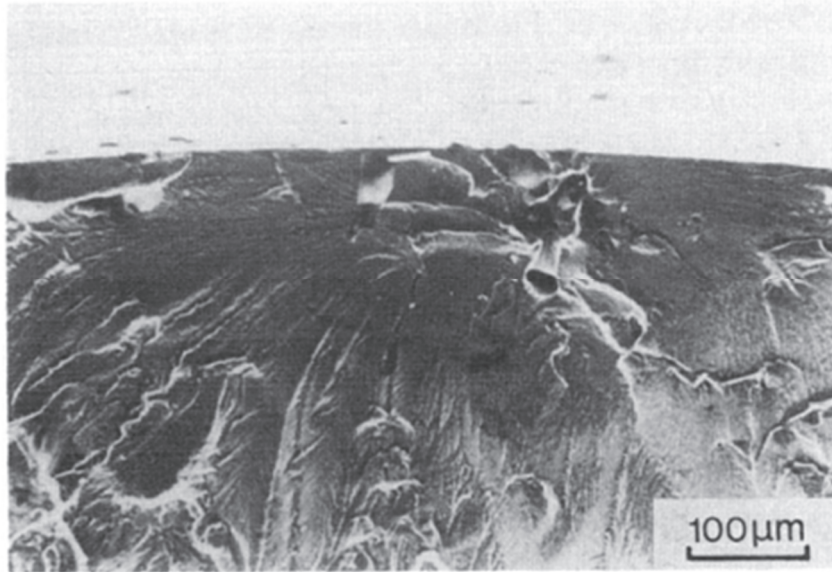


Figure 1.32 – Crack initiation site at a sub-surface casting pore in a MAR-M200 [213] oriented SX specimen tested at 650°C (after [115]).

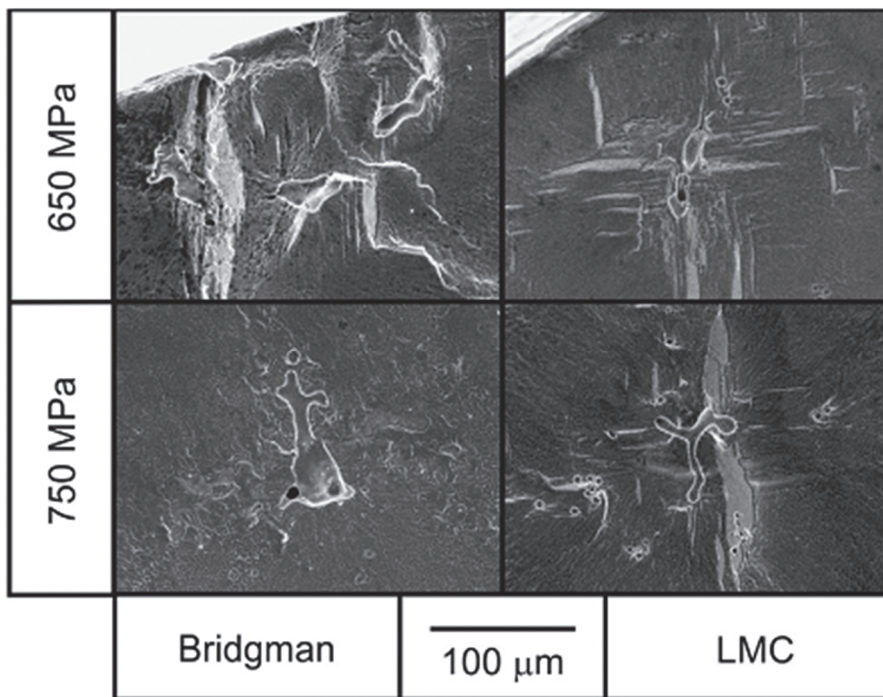


Figure 1.33 - Typical LCF crack initiation sites at 750°C in AM1 Ni-based SX alloy casted using different techniques leading to different pore sizes. Cracks initiated at internal and/or sub-surface casting pores (after [31]).

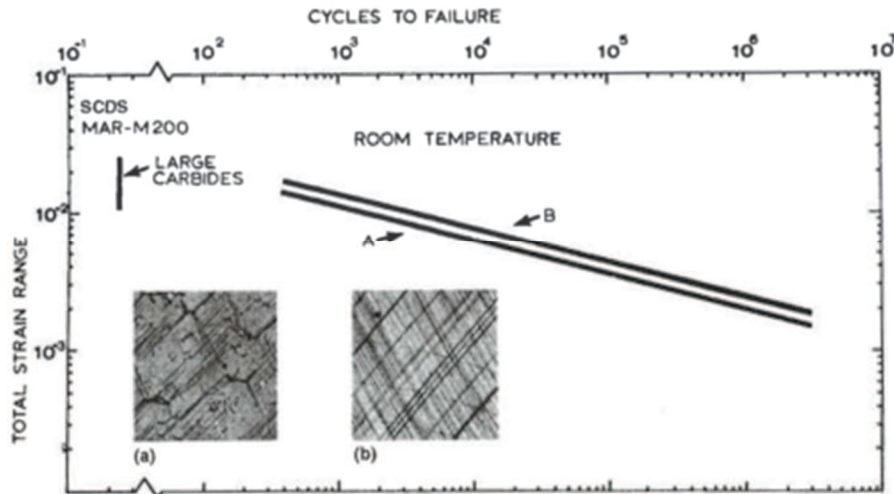


Figure 1.34 - Comparison of fatigue strength of  $\langle 001 \rangle$  MAR-M200 SX alloy with (curve A) and without carbides (curve B) (after [18]). Surface observations of the specimens' gage length presented in this figure highlight a more homogeneous slip activity without carbides and almost no stress concentration like in the version of the alloy containing carbides.

Another study from Chieragatti and Rémy concerned consistent results for MAR-M200 SX alloy tested along the  $[001]$  crystallographic direction at  $650^\circ\text{C}$  [115]. It shows that, for large plastic strain ranges, crack nucleation occurs almost immediately and small cracks are visible on the gage surface of the specimens within the first cycles of the expected life. In their case, cracks have been observed to nucleate from primary MC carbides or from casting pores. The typical evolution of the surface crack length as a function of the number of cycles is shown in Figure 1.35 for a  $[001]$  specimen, demonstrating that the total life is mainly controlled by the crack propagation rate.

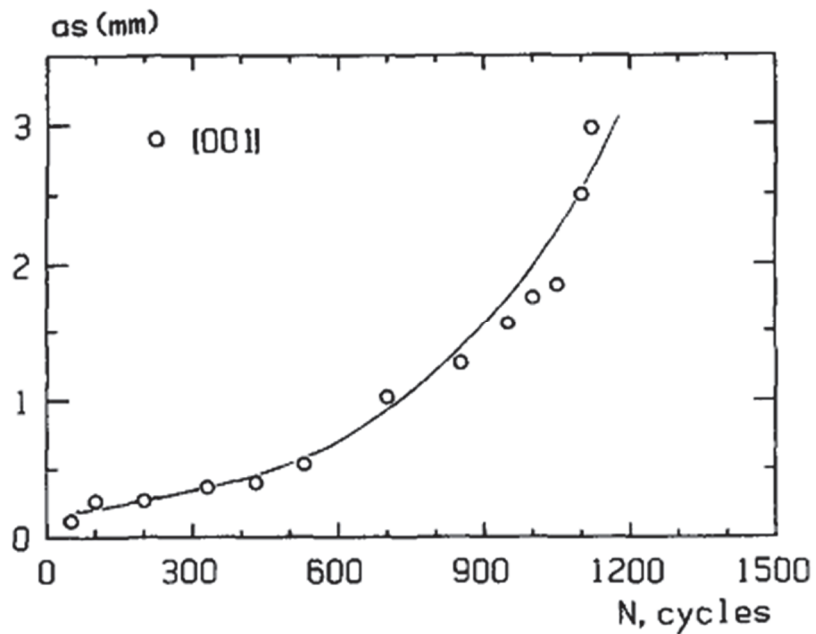


Figure 1.35 - Variation in the surface crack length as a function of the number of cycles for a short-life  $\sim [001]$  SX MAR-M200 specimen tested in LCF at  $650^\circ\text{C}$  (after [115]).

In agreement with Chieragatti and Rémy [115], Gell and Leverant have shown that the main damage mechanism during isothermal LCF of a carbon containing MAR-M200 single crystal superalloy in the 20-800°C temperature range is the linking of cracks emanating from debonded carbides [116, 117]. In comparison, for a low carbon content version of the same alloy, the LCF life is controlled by a single crack initiation site from a casting pores, for frequencies ranging from 0.033 Hz up to nearly 1 kHz [118]. The more detrimental impact of MC carbides compared to casting pores, as already shown in Figure 1.34, results from the expected thermal strain mismatch between the bulk  $\gamma/\gamma'$  superalloy and the MC/M<sub>23</sub>C<sub>6</sub> carbides at low temperature after solidification and further heat treatments. It is indeed estimated to be about 0.5%-1.0% at room temperature, so that large compressive strains develop in the material surrounding the carbides [119, 120], thus favoring crack initiation.

The effect of hafnium on the DS version of MAR-M200 has also been investigated in LCF. It improves significantly the strain-controlled LCF resistance at 760°C/R<sub>ε</sub> = -1/f = 0.33 Hz [24]. The addition of 1.78 wt. % hafnium leads to an LCF improvement of nearly one order of magnitude. According to Yunrong et al. [24], this results from a more uniform deformation pattern with hafnium addition (see Figure 1.36), that decreases cracks density (Table 1.5). The reasons behind this more uniform dislocations activity has not been clearly identified by the authors. It may results either from a more homogeneous distribution of stress concentrators (i.e. primary MC carbides) and/or, from an impact of the hafnium element on  $\gamma$  solid solution strengthening and/or  $\gamma'$  stacking fault energy.

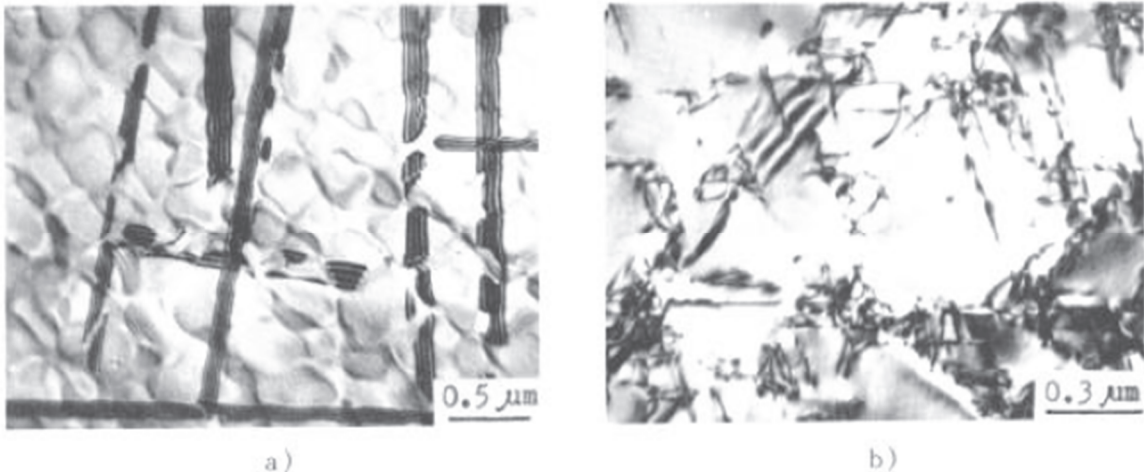


Figure 1.36 - Dislocation structure in MAR-M200 (a) and in MAR-M200+1.78 wt. pct Hf (b) tested in LCF 760°C/R<sub>ε</sub> = -1/f = 0.33Hz/Δε<sub>t</sub> = 1.2% (after [24]).

Alloy	Specimen No.	Cycle Nf	Result	Density of Cracks N/mm <sup>2</sup>	Length of Cracks L(mm/mm <sup>2</sup> )	Average Length $\bar{L}$ (mm)
Mar-M 200	4T	21	unruptured	2.30	0.12	0.0534
	6B	57	ruptured	3.89	0.22	0.0561
Mar-M 200+Hf	3T	203	unruptured	0	0	0
	3B	315	ruptured	0.07	0.0064	0.0875

Table 1.5 - Strain-controlled LCF results at 760°C/R<sub>ε</sub> = -1/f = 0.33Hz/Δε<sub>t</sub> = 1.4% [24]

During high temperature fatigue testing (T > 850°C) of Ni-based DS and SX alloys at low frequencies, one has to consider the contribution of creep to the bulk  $\gamma/\gamma'$  microstructure degradation and overall

fatigue life. No specific attention will be paid here to the effect of oxidation to the fatigue life since a specific sub-section devoted to the role of oxidation on the crack initiation and crack propagation mechanisms will be introduced later in this chapter.

M. Kirka [89] studied the effect of a strain hold at peak temperature on the thermo-mechanical cyclic behavior of DS CM247-LC Ni-based alloy. For this purpose, he introduced a 20 minutes strain hold at 850°C. A comparison of the TMF cyclic behavior with and without dwell is shown in Figure 1.37. The introduction of a dwell period resulted in a twice (or greater) reduction in fatigue life. This life reduction has been attributed to the rapid debonding of carbides and fatigue crack nucleation in the surrounding matrix due to the accumulation of voids. Moreover, a faster degradation of the  $\gamma/\gamma'$  microstructure, under the form of P-type rafting, has been observed.

It is known that rafting perpendicular to the load axis significantly reduces LCF life [32, 121]. Ott and Mughabi [121] found that the degradation in tension creep of CMSX-4 and CMSX-6 alloys at 1050°C and 1100°C reduces their LCF life at 950°C and 1050°C by a factor of about 2. In another study, Epishin et al. performed LCF tests using specimens degraded in tension creep at 1100°C and 1050°C under 90 MPa for different times, and then tested in LCF at 700°C,  $\Delta\epsilon=1.25\%$ ,  $\dot{\epsilon}=6\%/min$ ,  $R_e=-1$  [32] (Figure 1.38). Just after N-type rafting, the LCF life at 700°C decreases by a factor of nearly 8 due to the fast propagation of fatigue cracks along the extended incoherent  $\gamma/\gamma'$ -interfaces of the  $\gamma'$  rafts, as shown in Figure 1.39. It has indeed been shown by Mughrabi et al. that, since crack propagation dominated, the LCF life at high temperature ( $T > 850^\circ\text{C}$ ) after N-type pre-rafting is greatly reduced in comparison to a virgin cuboidal microstructure [121-124]. Under these LCF conditions, P-type rafting is observed to increase the LCF life, by favoring a multiple-deviated crack path.

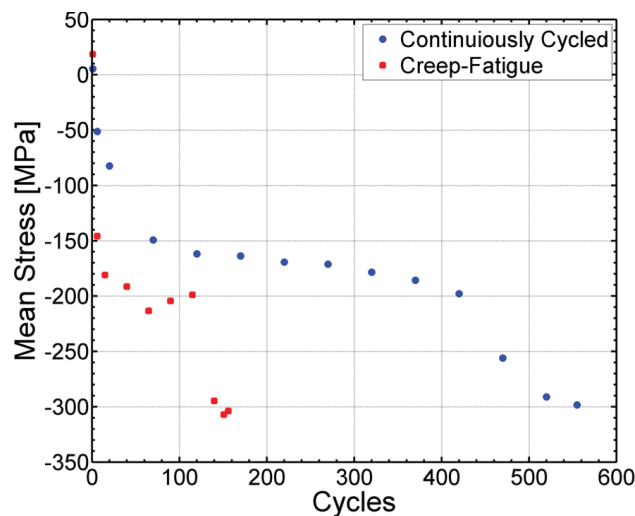


Figure 1.37 - Effect of a 20 minutes strain hold on at mean stress maximum temperature out-of-phase on TMF behavior of DS CM247LC alloy/  $T=100-850^\circ\text{C}$  tested along longitudinal direction (after [89]).

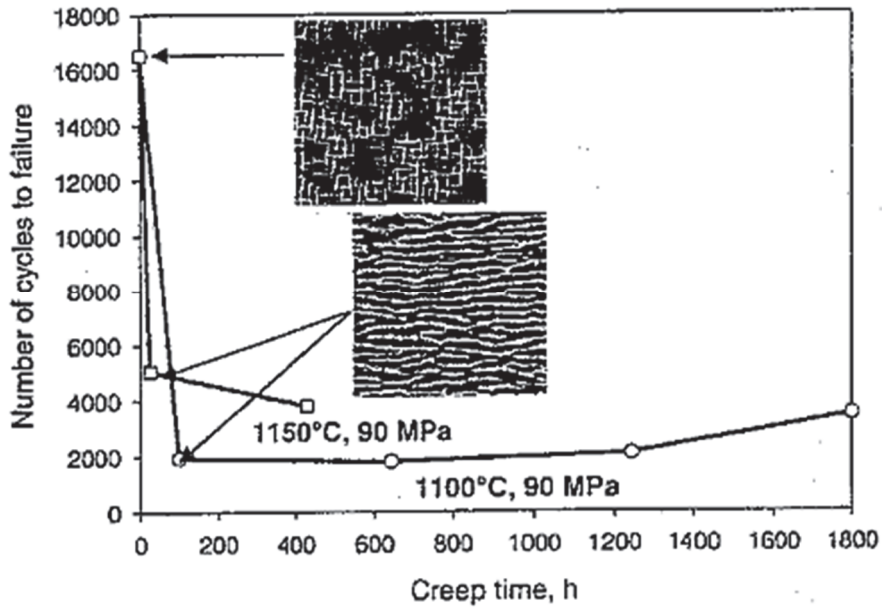


Figure 1.38 - Effect of the prior  $\gamma/\gamma'$  degradation in tension creep on LCF life of CMSX-4 at 700°C,  $\Delta\epsilon_t=1.25\%$ ,  $\dot{\epsilon}=6\%/min$ ,  $R_\epsilon=-1$  (after [32]).

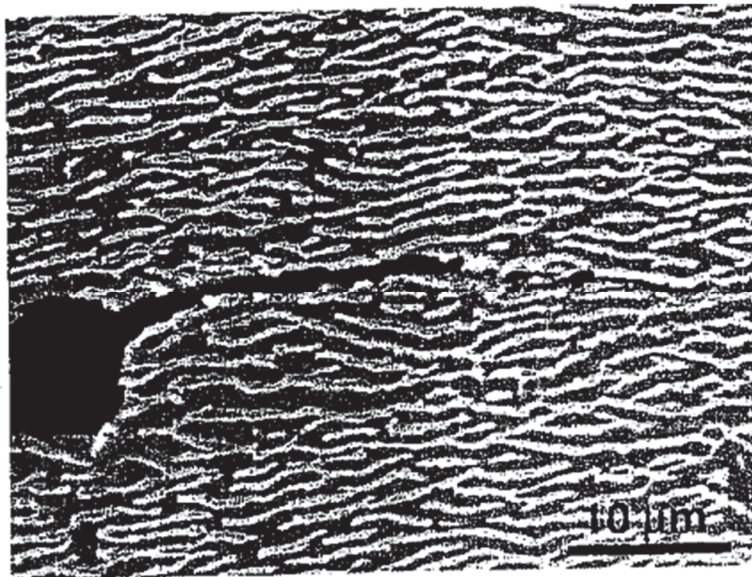


Figure 1.39 - Crack propagation along  $\gamma/\gamma'$  interfaces in LCF at 700°C,  $\Delta\epsilon_t=1.25\%$ ,  $\dot{\epsilon}=6\%/min$ ,  $R_\epsilon=-1$  in N-type pre-rafted CMSX-4 SX alloy (after [32]).

A similar trend has been observed by M. Kirka [89]. He concluded that the N-rafted microstructure exhibit a 50% reduction in fatigue life compared to the virgin microstructure under cyclic conditions at 850 and 950°C. These life reductions are consistent with reported results for other Ni-base superalloys with tensile pre-creep treatments.

In this same work [89], thermo-mechanical fatigue ( $T = 100-950^\circ\text{C}$ ) results indicate that primary failure of the P-rafted material is indeed associated with a single fatal fatigue crack originating from an oxidation spike along the interdendritic-dendritic boundary similar to the one shown in Figure 1.40. For N-type rafted microstructures, crack propagation can be decomposed into two main stages for a DS superalloy: crack initiation from a debonded carbide under LCF conditions (Figure 1.41), eventually

controlled/accelerated by oxidation; and then, a rapid fatigue crack propagation along the high dislocation density channels perpendicular to the applied load, leading generally to a very flat fracture. Similar findings have been reported in GTD-111 and CMSX-4 amongst other Ni-base superalloys [32, 94, 125].

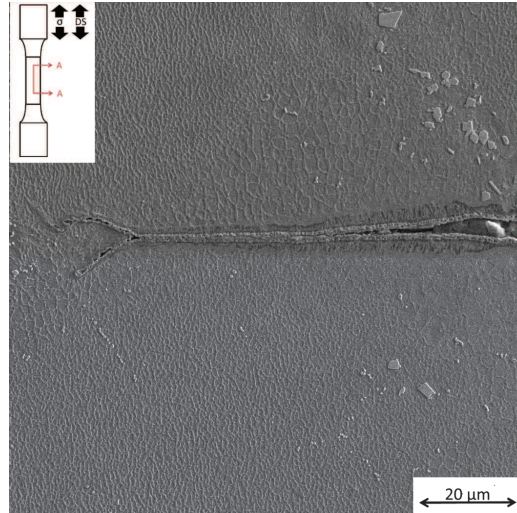


Figure 1.40 - Crack propagation through an oxidation spike penetrating into an interdendritic region within the P-type rafted microstructure in out-of-phase thermo-mechanical fatigue ( $\Delta T = 100\text{-}950^\circ\text{C}/\Delta\varepsilon_{\text{mech}} = 0.8\%$ ) (after [89]).

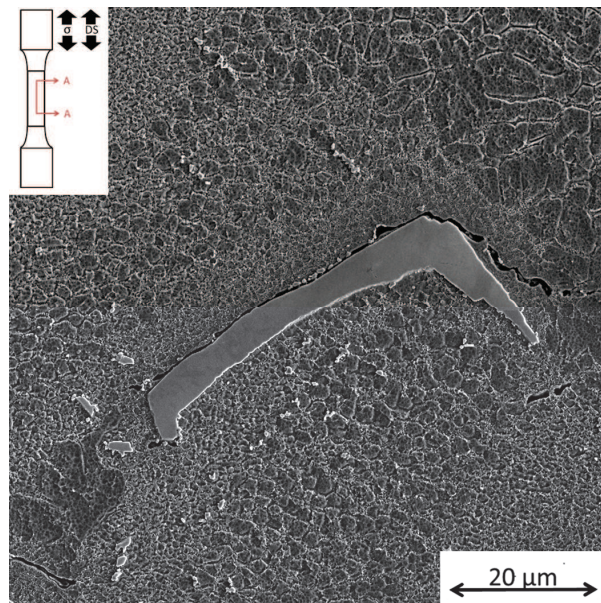


Figure 1.41 - Debonded carbide in the N-type rafted microstructure serving as a crack initiation site in in-phase thermo-mechanical fatigue ( $\Delta T = 100\text{-}850^\circ\text{C}/\Delta\varepsilon_{\text{mech}} = 1.1\%$ ) (after [89]).

Since most of the fatigue tests in the present PhD work will be performed under load control mode, it will be investigated in greater details if crack initiation at low temperature is still controlled by the defect size and position, since no effect of the Young's modulus will deserve to be considered. Moreover, the contribution of oxidation at high temperature (i.e.  $900^\circ\text{C}$ ) will be of special focus to understand the failure mode along different orientations. Special attention will be paid to evaluate the contributions of crack initiation and crack propagation to the total LCF life. Finally, due to the very limited number of such tests in the literature, creep-fatigue interaction will be investigated by



**performing dwell-fatigue tests under load control at 900°C (or cyclic creep tests) with various dwell-time at maximum load.**

#### 1.8.4 Crack propagation behavior

In order to characterize creep-fatigue crack growth in a Ni-based DS superalloy, D. Kobayashi and co-workers [126] have carried out an investigation combining creep, fatigue and dwell-fatigue tests using notched specimens and electron backscattered diffraction (EBSD) characterizations. This study shows that the local average misorientation (compared to the initial undeformed state) in the vicinity of notches increases linearly with creep strain up to the initiation of cracks under pure creep or creep-fatigue conditions (see Figure 1.42).

However, in pure fatigue, cracks are growing without any indication of lattice rotation in the vicinity of the crack tip (Figure 1.43). The hold time at maximum applied stress clearly influences the behavior of creep and creep-fatigue cracks and the appearance of misorientation development. However, these authors have shown that the relationship between the average misorientation and the relative notch opening displacement was independent of the testing conditions such as temperature, stress and stress waveform. This study clearly suggests that the crack initiation mechanism under viscoplastic conditions results from local lattice rotation.

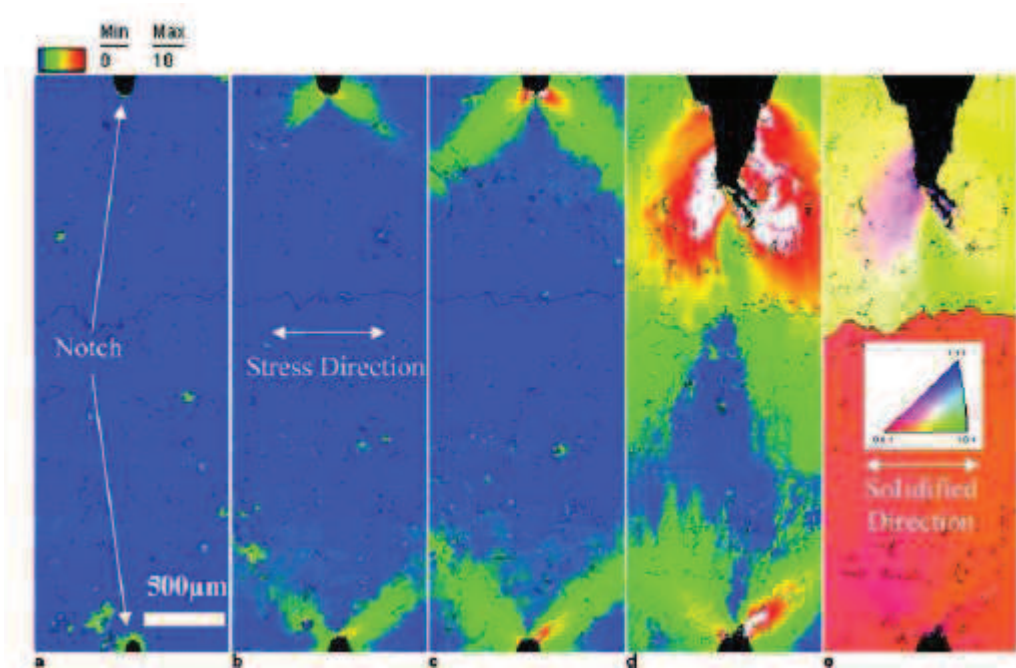


Figure 1.42 – Illustration of the grain rotation close to the main crack at different fractions of the creep life of the MGA 1400 DS alloy loaded at 880°C/294 Mpa (Creep life  $t_f = 156.8$  h):  $t_i/t_f=0$  (a);  $t_i/t_f=0.45$  (b);  $t_i/t_f=0.73$  (c);  $t_i/t_f=0.99$  (d); Inverse Pole Figure map at  $t_i/t_f=0.99$  (e) (after [126]).

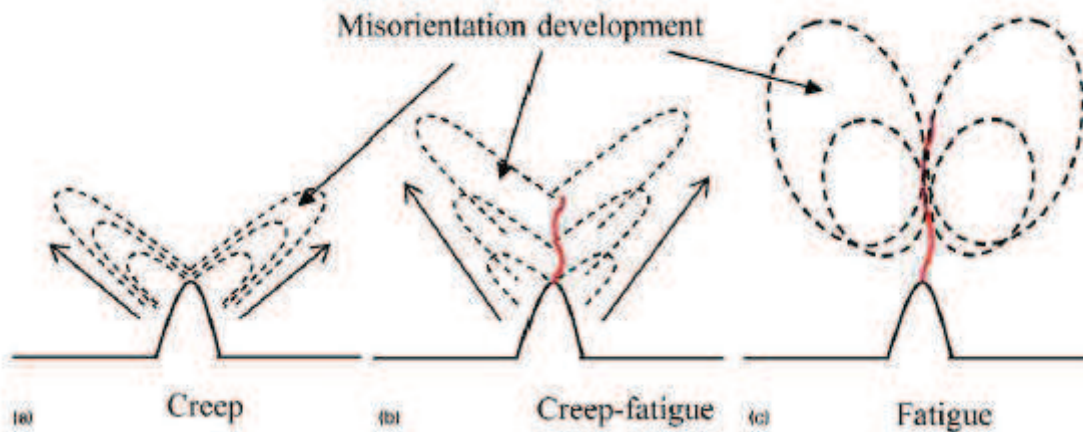


Figure 1.43 - Schematic illustration of misorientation development until accelerated creep region in creep (a), in creep-fatigue (b) and pure fatigue (c) (after [126]).

The influence of temperature on fatigue crack growth (FCG) in DS superalloys has been investigated since the end of the 70s, especially at NASA concerning MAR-M200 DS alloy [118]. The material presents crystallographic fracture at low temperature and high frequency and, mode I fracture at high temperature and low frequency. The same failure modes at different temperatures have been sequentially observed by other researchers [127-129].

J. S. Crompton also shows that the dependence on crystallography of the crack growth increases for MAR-M200 single crystalline specimens when temperature decreases [130]. At room temperature, crack advance takes place by shear associated with the  $\{111\}$  slip planes. At elevated temperature (650°C and 850°C), however, crack growth occurs on  $\{100\}$  type planes. A detailed analysis has shown that plastic deformation is confined in the matrix, and crack propagation within the matrix is associated with striations. Due to the increased strength of the  $\gamma'$  precipitates for high temperature, the crack is forced to remain in the matrix thus propagate on  $\{100\}$  planes between the cuboidal  $\gamma'$  precipitates. More recently, Gordon [123] attributed this change in crack propagation to the microstructural change at the precipitate scale ( $\gamma'$  coarsening) and the induced degradation of the mechanical properties. It is also worth mentioning that the crack propagation at high temperature is largely affected by oxidation, both in terms of crack propagation rate and propagation type. This will be examined in greater details in a subsequent section devoted to the environmental impact on mechanical properties.

A recent study from He and co-workers attempted to investigate the anisotropy in crack propagation rate in a DS Ni-based superalloy, by machining CT (i.e. Compact Tension) specimens with different directions of pre-notches (see Figure 1.34) with respect to the solidification direction of the alloy [131]. These authors have shown that cracks in all three orientations exhibit a similar propagating behavior, while the temperature shows a significant effect on the crack propagation regardless of the influence of orientation, especially close to the stress intensity factor threshold. A higher temperature leads to a faster fatigue crack growth (FCG) rate in the initial stage due to the cyclic response of materials. However, the FCG rates at low temperatures increase rapidly and exceed those observed at high temperature in the following stage. This is attributed to the crack closure effect induced by oxidation at higher temperature.

Up to now, there is still no general agreement about the orientation dependence of the crack growth properties for Ni-based superalloys. In fact, crystallography dependence is proven for some temperature ranges. K. Chan et al. show that the FCG rate of MAR-M200 single crystals at 982°C is independent of the crystallographic orientation [129]. Another study about the FCG response of SRR99

Ni-based SX alloy found that it depends on the frequency, temperature and crystallographic orientation of the specimen at 650 and 850°C [132]. Orientations that do not contain slip directions normal to the crack front and/or slip planes passing through the crack front did not necessarily form ridges, due to shear accommodation on “cuboidal” cross-slip systems. At 650°C, those orientations accommodate crack tip shear by slip on primary (octahedral) slip planes that are nearly parallel to the crack front, providing the best FCG resistance, whilst at 850°C, the best FCG response was found for the orientations that have developed large scale ridges as a result of out-of-plane cuboidal slip activity.

**In this work, a few crack propagation tests will be performed, to better characterize the crack initiation fatigue life, after having characterized the total LCF life.**

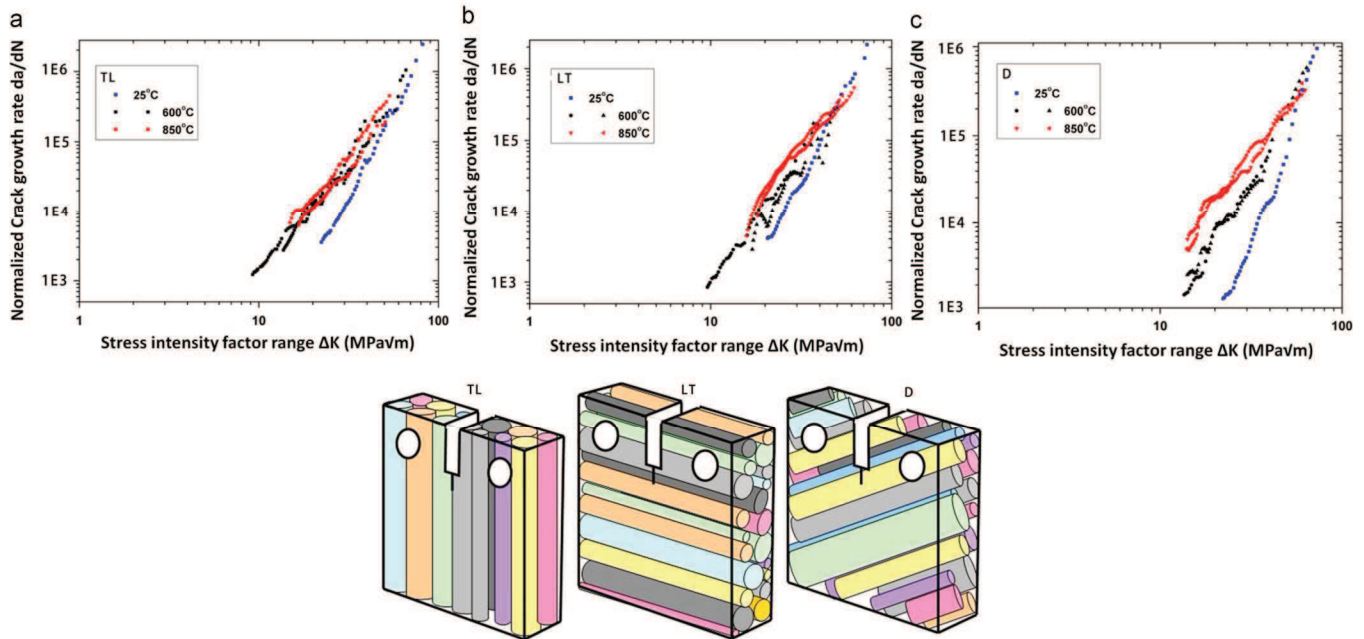


Figure 1.44 - Fatigue crack growth curves of TL (a), LT (b), and D (c) specimens at different temperatures (see schematic illustrations showing the solidification direction for each specimen) (Adapted from [131]).

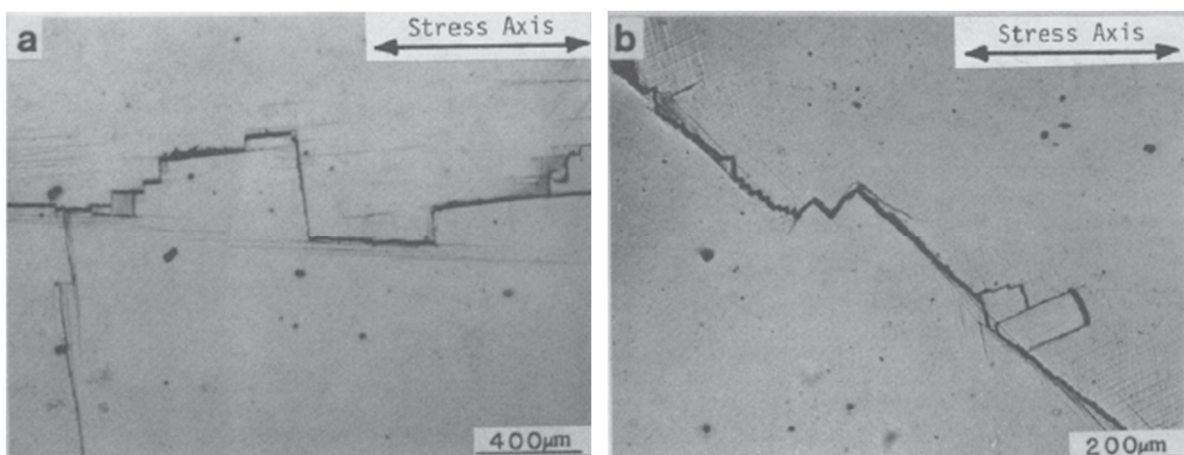


Figure 1.45 - Crack deflection and branching during fatigue crack propagation at room temperature observed in MAR-M200 single crystalline specimens with the stress axis aligned along the [110] orientation (a) and along the [111] orientation (b) (adapted from [129]).

## 1.9 Effect of environment on durability of cast Ni-based superalloys

### 1.9.1 Impact on creep properties

Columnar grain superalloys are more sensitive to oxidation effects, compared to single crystalline alloys, due to the presence of grain boundaries. Moreover, it is known in MAR-M200 that carbides concentrated at grain boundaries are highly sensitive to oxidation, as observed recently by Kontis et al. in Inconel 792 polycrystalline superalloy [133].

The effect of oxidation on creep durability are enhanced when specimens present a small thickness, since the surface exposed to oxidation is large relatively to the load bearing section. This effect is schematically demonstrated in Figure 1.46 at 982°C, for a <001> oriented SX alloy, a DS alloy loaded along its longitudinal direction, and a polycrystalline alloy, all having exactly the same chemistry. In this figure, the creep life is normalized by the creep life of massive specimens for which the impact of oxidation is negligible. It is observed that the thinner the specimen is, the greater the debit in creep life, especially for polycrystalline alloys [134, 135]. This is generally accompanied by a loss of creep ductility. It is also observed that the drop in creep life due to specimen thickness reduction can be up to a factor of five for a conventionally cast alloy, a result that could also be expected for creep testing along transverse direction for a DS alloy.

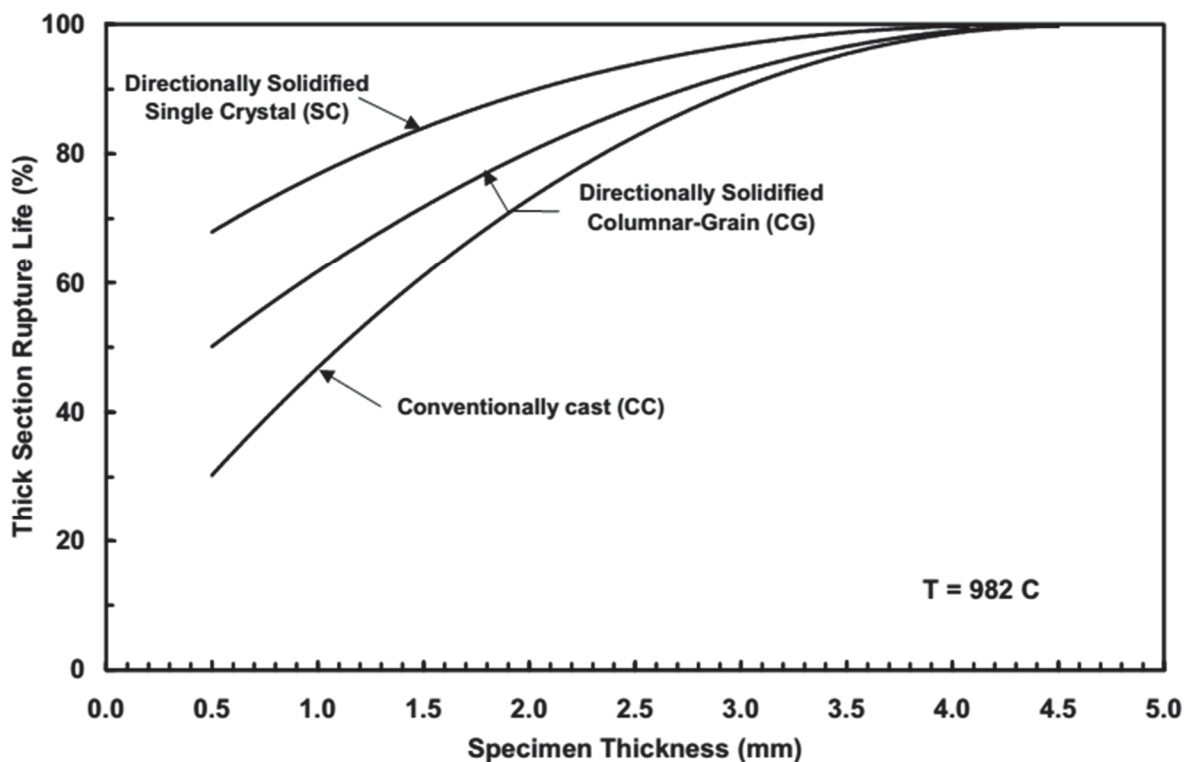


Figure 1.46 – Typical creep life debit as a function of the specimen's thickness for polycrystalline, columnar grain and single-crystal nickel-based superalloys (trend expected for MAR-M200 and B1900 alloys). The creep lives have normalized by the results obtained for 3.8 mm thick specimens (after [20]).

Some studies about the influence of oxidation on creep properties were published recently for SX specimens [134, 135]. Depending on the alloy chemistry and metallurgical inclusions, oxidation may affect creep life considerably. An illustration for that affirmation is shown in Figure 1.47: the experiments performed using the MAR-M247LC SX alloy show that the thickness reduction decreases the creep strength in air at 980°C/150 MPa. However, creep life presents a large scatter under these conditions for 0.3 mm thick specimens (see Figure 1.47(a)), probably due to the fact that they have

been machined from bars, leading to different spatial distribution of defects (pores and carbides) with respect to the free surface). This thickness effect is also observed for creep tests performed in high vacuum, i.e. in the absence of oxidation, hence highlighting that the thin wall debit in creep may not only result from oxidation, as proposed by Baldan [136]. Moreover, creep lives in air and under high vacuum are very similar for this alloy under these creep testing conditions.

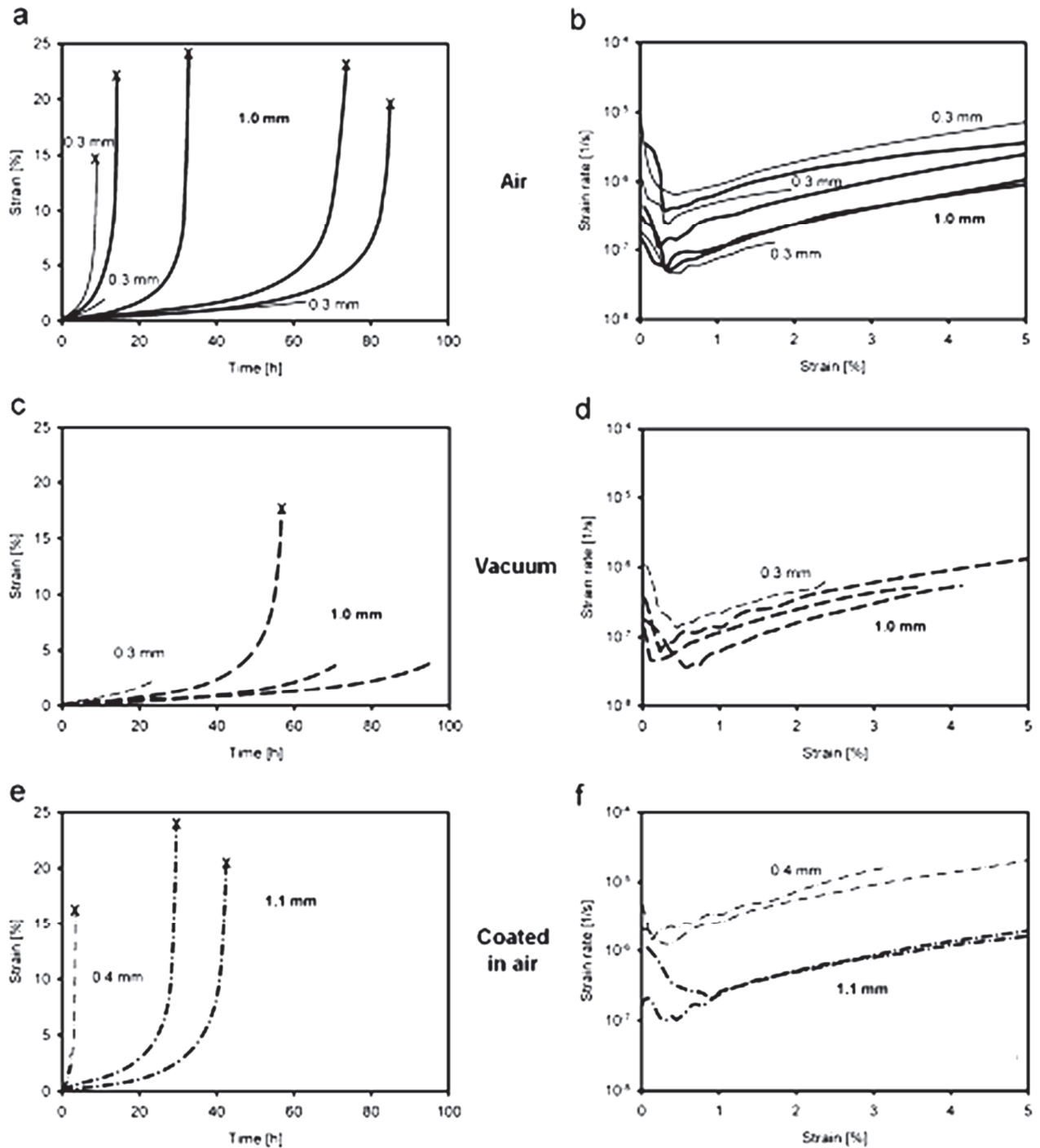


Figure 1.47 – Creep properties of  $\langle 001 \rangle$  SX MAR-M247LC at  $980^{\circ}\text{C}/150\text{ MPa}$  for different initial thicknesses in air without coating (a, b), in high vacuum (c, d) and coated in air (e, f) (after [135]).

Figure 1.47(e) shows, however, that an alumina forming coating decreases the creep strength in air, due to loss of load bearing capacity of the specimens associated to the interdiffusion layer between

the coating and the substrate. Microstructure observations of MAR-M247LC specimens tested in creep up to failure are shown in Figure 1.48. Porous oxides (i.e. not protective) form at the surface of the specimens. In addition, the  $\gamma$  depleted layer below the oxide layer may also affects the overall creep properties. A similar creep condition was tested for PWA 1484 (982°C/248 MPa), comparing specimens thickness (h) of 0.51 mm and 3.18 mm [134]. It was shown that the minimum creep rate increases by decreasing the specimens' thickness and that the time to rupture for the thinnest specimens was 25% less. However, there was little or even no systematic dependence of the strain to rupture to the specimen's thickness.

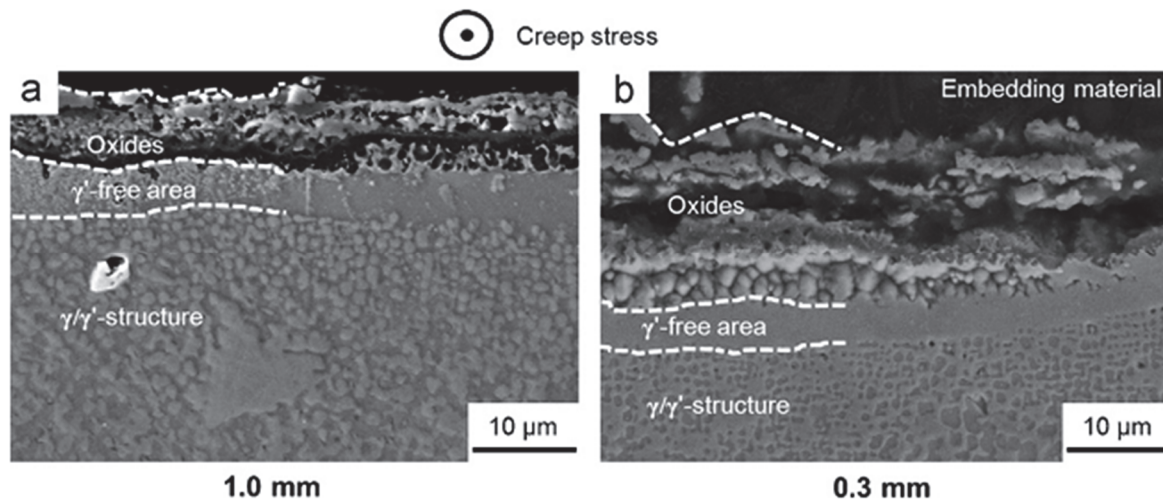


Figure 1.48 – Transverse section of crept specimens at 980°C/150 MPa in air up to failure with a thickness of 1.0 mm (Creep life = 74 h) (a) and 0.3 mm (Creep life = 63 h) (b) (after [135]).

One should also mention that a pronounced thin-wall debit in creep has been observed in PWA 1484 second generation superalloy at low temperature and high applied stress (760°C/758 MPa) [137]. Contrary to the moderated thickness debit observed at 982°C/248 MPa in this alloy, which is directly related to the contribution of oxidation, the spectacular creep life drop at 760°C/758 MPa results from the fact that casting pores, acting as crack initiation sites, occupy a larger fraction of the load bearing section when decreasing the specimens' thickness. A similar trend was observed by Baldan in SX MAR-M002 alloy [136]. They are hence much more critical from a mechanical point of view, especially considering the induced stress field in their vicinity. However, this large creep debit observed on specimens machined from “large” (~ 14 to 16 mm in diameter) SX bars may not be so pronounced in thin-walled components, since the maximum pore size may then be smaller due to local faster solidification, and spatially distributed in a different way (especially close to the surface) compared to machined specimens [137].

Variations in material microstructure such as carbides and pores at the surface, differences between dendritic and interdendritic regions, depletion of aluminum and therefore a creation of  $\gamma$ -reduced and  $\gamma$ -free zones are key parameters in controlling mechanical properties of thin specimens due to the high surface to volume ratio [135]. This was claimed by Srivastava et al [134]. Therefore, the debit in creep at high temperatures ( $T > 900^\circ\text{C}$ ), where oxidation is active, mainly results from a decrease of the load bearing capacity of the alloys close to their external surfaces and is highly dependent on the alloy chemistry. The situation however still remains unclear at lower temperatures ( $T < 850^\circ\text{C}$ ) and requires further analyzes [134]. **Moreover, to the author's best knowledge, the physical mechanisms responsible for the thin-wall debit in creep of DS alloys have never been investigated. According to the literature review that has been performed during this PhD thesis, one should admit that, despite**

the schematic illustration shown in Figure 1.46, no clear experimental data are available in the open literature regarding this point for DS Ni-based superalloys. Hence, in the last chapter of the manuscript, the thin wall debit in creep of MAR-M200+Hf alloy will be investigated at 900°C, to better understand the contribution of oxidation to creep life, and with the aim to develop an oxidation sensitive creep life approach. Isothermal creep results at 900°C/350 MPa and 900°C/400 MPa along both longitudinal and transverse loading directions of DS200+Hf will be presented and compared to those obtained with SX specimens loaded along the [001] direction.

### 1.9.2 Impact on fatigue properties

As already presented earlier in the literature review, Wright and Anderson have investigated the effect of the loading direction during strain-controlled LCF of DS René 120 alloy at 650°C and 982°C [114]. Their main results have been presented in Figure 1.30. Without discussing again the results established at 650°C, at 982°C crack initiation is controlled by oxidation, since most of the crack initiation sites are located at the surface, within or in the vicinity of the oxide layer (also shown in other studies [115], see fractographic observations in Figure 1.32). The rupture mode at 982°C is transgranular for specimens machined from 0° to 45° orientation with respect to the solidification direction and intergranular for specimen machined along transverse direction. The intergranular cracking mode was also observed in equiaxed grained samples, due to the activity of oxidation at grain boundaries.

At temperatures higher than ~ 850°C, the contribution of oxidation to crack initiation mechanisms in LCF is really prominent for Ni-based DS and SX superalloys. Indeed, as shown unambiguously by Steuer et al. for the AM1 first generation SX alloy [31], the LCF life in air at 950°C is totally controlled by oxidation, whatever the size of casting pores (see Figure 1.49 and Figure 1.50). However, when experiments are performed in high vacuum, crack initiation occurs from surface/sub-surface pores and the LCF life depends on pore size, as observed in LCF at lower temperature ( $T < 850^\circ\text{C}$ ). Indeed, LCF loadings in high vacuum leads to longer lives than in air, and they become again dependent on pore size (see Figure 1.50).

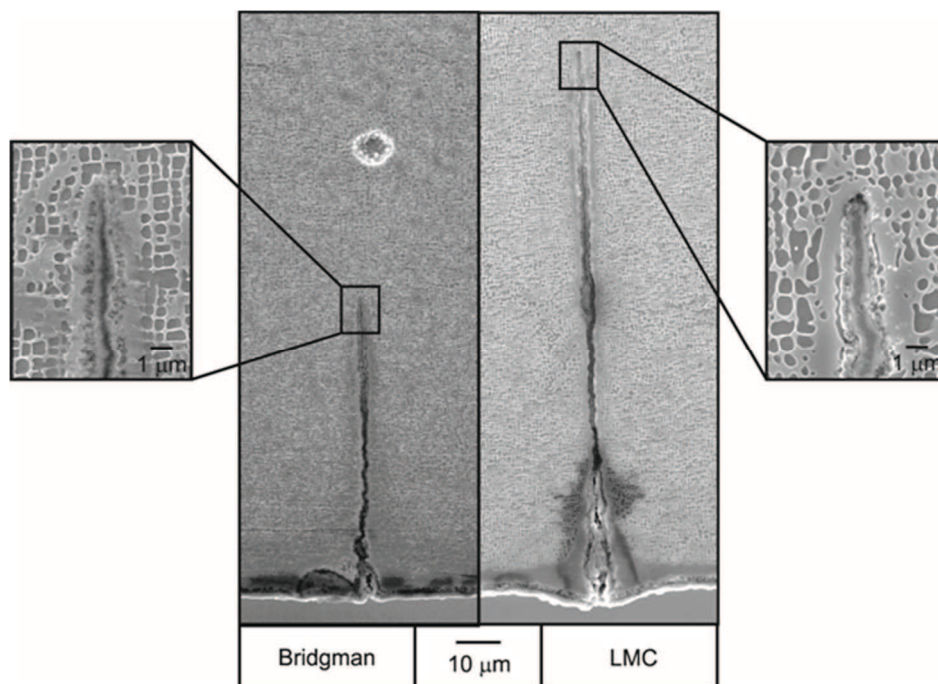


Figure 1.49 – Crack initiation assisted by oxidation in LCF at 950°C/ $R_\sigma = -1/f = 0.5 \text{ Hz}$ / $\sigma_{max} = 300 \text{ MPa}$  in air using AM1 Ni-based SX superalloy solidified using Bridgman and Liquid Metal Cooling (LMC) processes (after [31]).

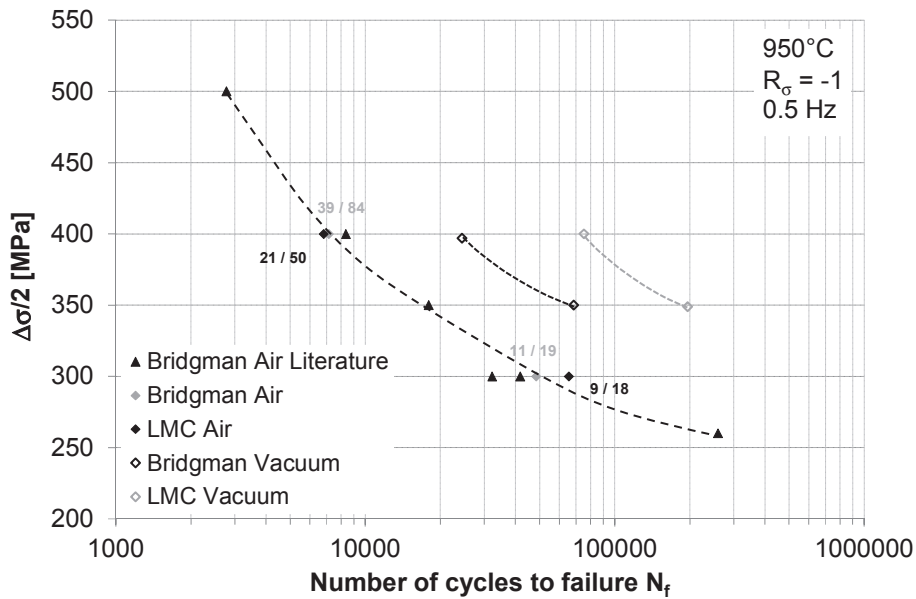


Figure 1.50 – S-N diagram at 950°C/  $R_{\sigma} = -1/f = 0.5$  Hz in air and in high vacuum using AM1 Ni-based SX superalloy (after [31]).

A study of the environmental influences on LCF failure of DS MAR-M200+Hf at 975°C has contributed to a better understanding of grain boundary oxidation and its effect on the fatigue damage development [138]. For this purpose, tests were performed in air and in an inert gas (argon) atmosphere. The cyclic load was constant and included both creep tension and plastic compression.

Under an inert argon atmosphere, a pure transgranular fracture, free of environmental influences, was obtained (see Figure 1.51). Indeed, no  $\gamma'$  depletion could have been identified along the crack path. In synthetic Air + 20% O<sub>2</sub> atmosphere, the fracture was intergranular following a path through the interdendritic microsegregated zones. In the area close to the propagating crack tip, a single  $\gamma$  phase layer was detected, resulting from a process of internal oxidation which developed a preferred oxide-type bonding with the main elements contributions to the principle  $\gamma'$  precipitating phase, namely titanium and aluminum (Figure 1.52). The internal oxidation led to changes in the boundary layer between the matrix and  $\gamma'$  phase, so that the original coherence between them was lost.

In order to reduce the surface energy between the precipitate and the matrix, a process of growth and coarsening of  $\gamma'$  phase took place in these conditions. The internal oxidation and the formation of the  $\gamma$  uniphased layer increased the brittleness over a comparatively wide area adjacent to the crack tip. As a result, crack branching and blunting took place during propagation in the oxygen-containing atmosphere. The combination of these phenomena increased the crack propagation life compared with that in the inert atmosphere, due to crack closure effect. Hence, the addition of 20% oxygen to the inert argon atmosphere leads to an increase in the service life of the alloy [138]. From these results, it appears that all phenomena and changes at the edge of the crack and in the area adjacent to its tip originate from chemical and mechanical relaxation processes of the material system arising in reaction to the stress concentration and the presence of the atmosphere.



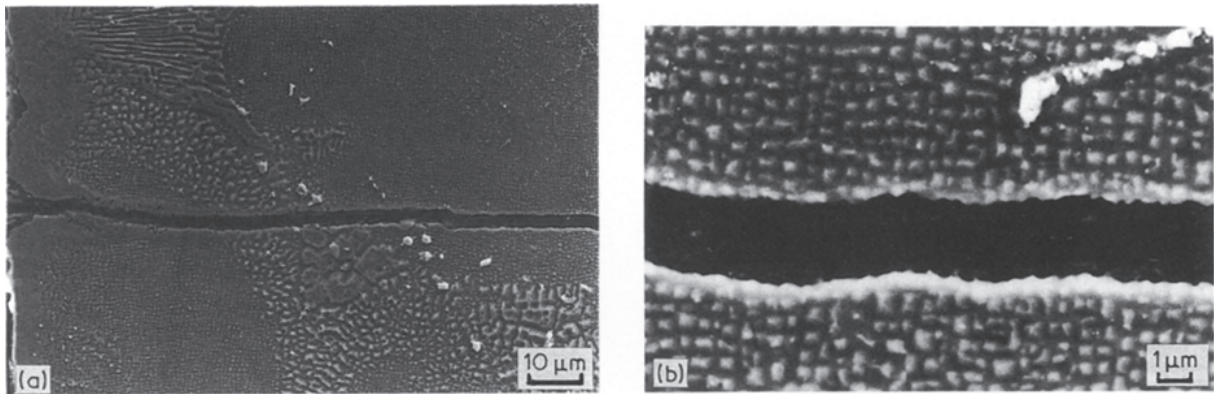


Figure 1.51 - LCF crack in an argon environment at 975°C in DS MAR-M200+Hf alloy (after [138]).

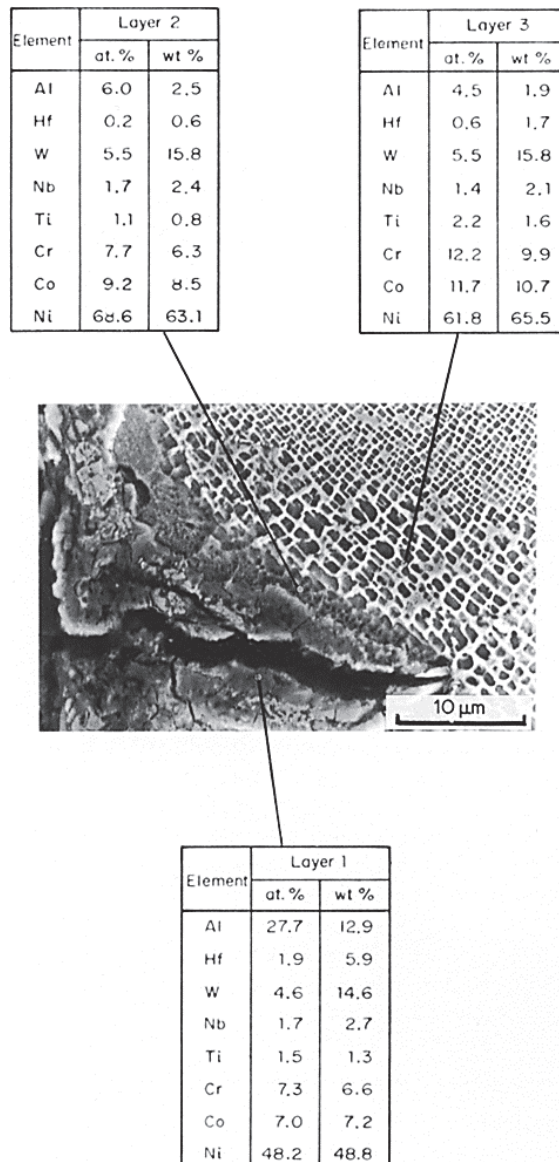


Figure 1.52 - Microstructures and chemical compositions of the different layers beneath the crack surface after LCF in an Ar + 20% O<sub>2</sub> environment at 975°C using DS MAR-M200+Hf alloy (after [138]).

Another study tried to compare the contribution of crack initiation and crack propagation to the total fatigue life of the MAR-M200 SX superalloy [139]. As already presented and discussed before, below

760°C, the fatigue life of nickel-base SX superalloys is (almost) unaffected by the environment. Fatigue cracks in both air and vacuum tests are initiated in “vacuum” (i.e. most of the crack initiation sites are internal in air, from casting pores or inclusions) and, since the initiation stage is the major part of the fatigue life, it is suggested that the rates of internal Stage I crack initiation in air and surface initiation in vacuum are about the same.

Internal fatigue crack initiation in air is attributed to a reduction in the surface slip intensity due to dynamic oxidation of newly emerging slip steps, thus preventing surface crack initiation from occurring. At 920°C, the fatigue lives of MAR-M200 nickel-base superalloy single crystals are greater in air than in vacuum. At this temperature, bulk oxidation fills surface cracks and reduces crack growth rates by interfering with the plastic blunting mechanism of Stage II fatigue crack growth at the surface, thus causing internal crack initiation and growth. It is suggested that delayed internal Stage II crack initiation in air compared to surface initiation in vacuum accounts for the greater fatigue life in air (see Figure 1.53 for a schematic illustration of the crack propagation mechanisms).

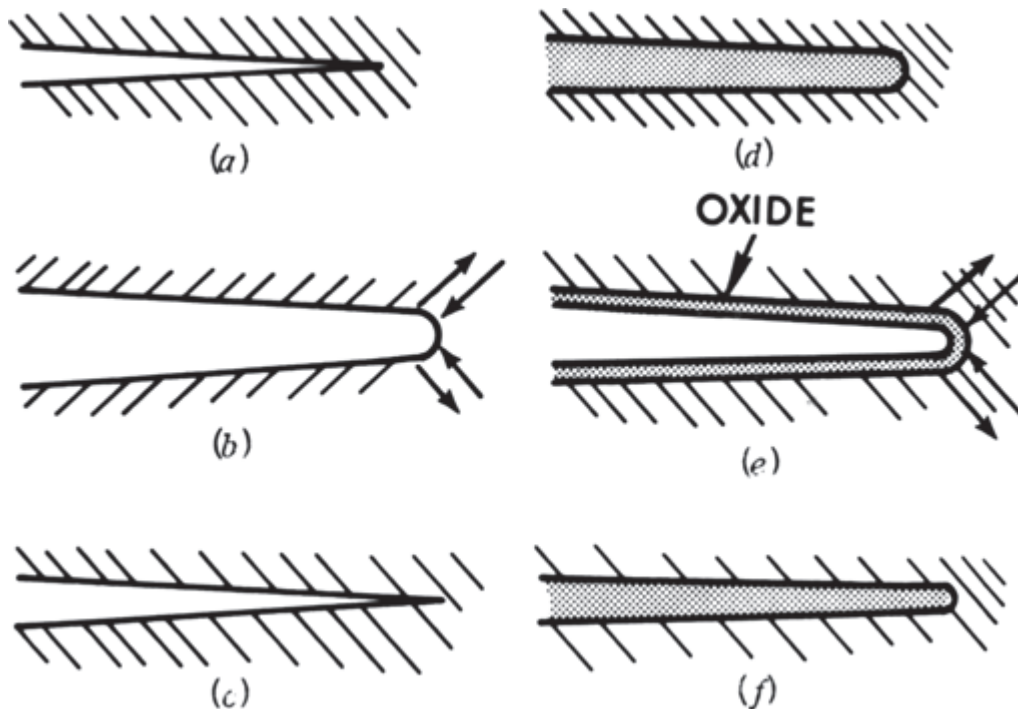


Figure 1.53 - Schematic diagram showing Laird model of crack growth by successive blunting and resharpening (a) to (d) in vacuum, (e) and (f) in air (after [139]).

According to the previous LCF results, it is seen that the LCF life at high temperature ( $T > 850^{\circ}\text{C}$ ) is very sensitive to oxidation, and hence, to the alloy's chemistry. Indeed, an alloy developing a stable, dense and continuous oxide layer (preferentially of  $\alpha\text{-Al}_2\text{O}_3$  type) at a given temperature will be much more LCF resistant, especially in terms of crack initiation mechanisms. **In the present work, a special focus will be paid to the role of oxidation on both crack initiation and crack propagation stages, trying to evaluate, at least qualitatively, the role of carbides.**

### 1.10 Summary of the research motivations and objectives

This literature review shows that DS Ni-based superalloys are widely used for the manufacturing of blades and vanes in aero-engines and industrial gas turbines [2, 10, 20]. Despite DS200+Hf (also known as PWA 1422 [23]) being an old alloy, developed more than 40 years ago [5], it is still used for the design of modern aero-engines components such as low pressure turbine blades, especially thanks to its very good castability, allowing sophisticated blade profile shapes and very thin trailing edges to be made. This kind of materials consists of nearly  $\langle 001 \rangle$  columnar grains oriented along the solidification direction and with random secondary orientations. The alloy studied here, DS200+Hf, has a high hafnium content of about 1.6%, which has been chosen to achieve a better grain boundary strength at high temperature [2, 6, 10, 20, 21, 23], improving the durability during service operations [10]. However, due to the complex blade geometries with platforms, shrouds and possible profile twisting, in addition to the thermal in service gradients, the main loading direction is not always the common crystallographic direction (i.e. the solidification direction). Moreover, due to the casting process, there are significant grain size differences from the root to the tip of the components that may influence the mechanical properties at high temperature, especially along transverse directions. Some grains may also present a misorientation from the perfect  $\langle 001 \rangle$  crystallographic orientation (up to 10 degrees).

The mechanical properties are not well documented for DS alloys and very limited transverse mechanical properties are available in the open literature (especially in creep and fatigue). Even if there are more studies concerning DS loaded along the solidification direction [6, 10, 20, 24, 26, 111, 140], the present literature review has taken advantage of the advanced literature focused on SX alloys to better understand the anisotropy in mechanical properties, if any. In addition, transverse mechanical properties have never been rationalized taking into account the grain size and a large scatter in mechanical properties was observed, probably due to this missing consideration [97, 114, 131, 141]. Finally, DS200+Hf is known to present a rather poor environmental resistance compared to other DS or conventionally cast superalloys since this alloy does not form a continuous and dense alumina scale in the oxidation regime [10, 142].

**There is a lack of information in the literature about the relation between grain size, loading orientation and grain boundary oxidation for DS alloys, especially for DS200+Hf alloy. Which kind of fracture mode is observed for transverse loading? Is it different when grain size is variable? Is this related to grain boundary oxidation? What is the role of carbides on DS alloys damage? Which condition (grain size, loading, temperature range) present better durability? All these questions are not well assessed according to the past literature and are going to be the focus of this work, in addition to all the other points highlighted previously in this literature review.**

Within this context, the main objective of this work is to investigate the anisotropy in mechanical properties of DS200+Hf alloy in the RT-1100°C temperature range, with a special emphasis on durability. A special attention will be paid to the contributions of oxidation and crystallography to damage mechanisms. It is also recalled here that several data from this PhD thesis also serve as inputs for the PhD thesis of Florent Coudon [143] for the identification of mechanical behavior constitutive equations. Despite the present thesis is mainly focused on the mechanical behavior and damage processes from an experimental point of view, constitutive modeling approaches, especially for damage, will also be proposed in the last chapter of the manuscript.

## References of Chapter 1

1. M.P. Boyce, *Gas turbine engineering handbook*. 2011: Elsevier.
2. R.C. Reed, *The Superalloys - Fundamentals and Applications*. 2006, Cambridge, UK: Cambridge University Press.
3. L. Pfeil, N. Allen, and C. Conway. *Nickel-Chromium-Titanium Alloys of the Nimonic 80 Type*. in *Symposium on High-Temperature Steels and Alloys for Gas Turbines, Special Report*. 1951. p. 37-45.
4. W. Betteridge and A. Franklin, *The effect of heat treatment and structure on the creep and stress-rupture properties of Nimonic-80A*. *Journal of the Institute of Metals*, 1957. **85**(11): p. 473-&.
5. N. Allen. *A Survey of the Development of Creep-Resisting Alloys*. in *Symposium on High Temperature Steels and Alloys for Gas Turbines, London: The Iron and Steel Institute*. 1952. p. 1-10.
6. F.L. Versnyder and M.E. Shank, *The development of columnar grain and single crystal high temperature materials through directional solidification*. *Materials Science and Engineering*, 1970. **6**: p. 213-247.
7. G. Cole and R. Cremisio, *Solidification and structure control in superalloys*. Michigan and Materials Technology associates. New York, 1972: p. 479-508.
8. S. Pierret, *Microstructure of single crystal Ni-based superalloys during blade manufacturing process and creep deformation*, PhD Thesis. 2012, EPFL: Lausanne, Switzerland.
9. W.R. Freeman-Junior, C.T. Sims, N.S. Stoloff, and W.C. Hagel, *Investment casting*, in *Superalloys II*. 1987, John Wiley & Sons: New York. p. 411–439.
10. M. Gell, D.N. Duhl, and A.F. Giamei. *The development of single crystal superalloy turbine blades*. in *Superalloys 1980*. 1980. Seven Springs, PA, USA: TMS. p. 205-214.
11. P. Caron, P.J. Henderson, T. Khan, and M. McLean, *On the effects of heat treatments on the creep behaviour of a single crystal superalloy*. *Scripta Metallurgica*, 1986. **20**(6): p. 875-880.
12. V. Sass, W. Schneider, and H. Mughrabi, *On the orientation dependence of the intermediate-temperature creep behaviour of a monocrystalline nickel-base superalloy*. *Scripta metallurgica et materialia*, 1994. **31**(7): p. 885-890.
13. B.H. Kear and B.J. PEARCEY, *Tensile and creep properties of single crystals of the nickel-base superalloy Mar-M 200(Nickel-base single crystal superalloy tensile and creep properties, comparing single and multiple slip orientations)*. *AIME Transactions*, 1967. **239**: p. 1209-1215.
14. M. Durand-Charre, *The microstructure of superalloys, translated by Davidson*. JH, Gordon and Breach Science Publishers, 1997.
15. B.B. Seth. *Superalloys-the utility gas turbine perspective*. in *Superalloy 2000*. 2000. Seven Springs, PA, USA: TMS. p. 3-16.
16. M. Simonetti and P. Caron, *Role and behaviour of  $\mu$  phase during deformation of a nickel-based single crystal superalloy*. *Materials Science and Engineering: A*, 1998. **254**(1): p. 1-12.
17. K. Kawagishi, A.-C. Yeh, T. Yokokawa, T. Kobayashi, Y. Koizumi, and H. Harada. *Development of an oxidation-resistant high-strength sixth-generation single-crystal superalloy TMS-238*. in *Superalloys 2012*. 2012. Seven Springs, PA, USA: TMS. p. 189-195.
18. P. Caron and T. Khan, *Evolution of Ni-based superalloys for single crystal gas turbine blade applications*. *Aerospace Science and Technology*, 1999. **3**(8): p. 513-523.
19. T. Strangman, G. Hoppin, C. Phipps, K. Harris, and R. Schwer. *Development of Exothermically Cast Single Crystal MAR M 247 and Derivative Alloys*. in *Superalloys 1980*. 1980. Seven Springs, PA, USA: TMS. p. 215-224.
20. M.J. Donachie and S.J. Donachie, *Superalloys: a Technical Guide*. 2002: ASM international.
21. D.N. Duhl and C.P. Sullivan, *Some effects of hafnium additions on the mechanical properties of a columnar-grained nickel-base superalloy*. *Journal of Metals*, 1971. **23**(7): p. 38-40.
22. B. Pearcey and F. VerSnyder, *A new development in gas turbine materials-The properties and characteristics of PWA 664*. *Journal of Aircraft*, 1966. **3**(5): p. 390-397.

23. A.D. Cetel and D.N. Duhl. *Second generation columnar grain nickel-base superalloy*. in *Superalloys 1992*. 1992. Seven Springs, PA, USA: TMS. p. 287-296.
24. Z. Yunrong, W. Yuping, X. Jizhou, P. Caron, and T. Khan. *Effect of chemistry modifications and heat treatments on the mechanical properties of DS MAR-M200 superalloy*. in *Superalloys 1988*. 1988. Seven Springs, Champion, PA, USA: TMS. p. 335-344.
25. A. Baldan, *Effects of growth rate on carbides and microporosity in DS200+ Hf superalloy*. *Journal of materials science*, 1991. **26**(14): p. 3879-3890.
26. J.J. Jackson, M.J. Donachie, R.J. Henricks, and M. Gell, *The effects of volume percent of fine  $\gamma$  on creep in DS Mar-M200 + Hf*. *Metallurgical Transactions*, 1977. **8A**(October): p. 1615-1620.
27. K.C. Antony and J.F. Radovich. *Solute effects of boron and zirconium on microporosity*. in *3rd International Symposium on Superalloys*. 1976. Seven Springs, PA, USA: TMS. p. 137-146.
28. R. Cook and A. Guthrie, *Factors affecting foundry characteristics of nickel-rich alloys for high-temperature applications*. *FOUNDRY TRADE J*, 1966. **120**(2580): p. 686-689.
29. J.-B. le Graverend, J. Adrien, and J. Cormier, *Ex-situ X-ray tomography characterization of porosity during high-temperature creep in a Ni-based single-crystal superalloy: Toward understanding what is damage*. *Materials Science and Engineering: A*, 2017. **695**: p. 367-378.
30. T. Link, S. Zabler, A. Epishin, A. Haibel, M. Bansal, and X. Thibault, *Synchrotron tomography of porosity in single-crystal nickel-base superalloys*. *Materials Science and Engineering: A*, 2006. **425**(1): p. 47-54.
31. S. Steuer, P. Villechaise, T. Pollock, and J. Cormier, *Benefits of high gradient solidification for creep and low cycle fatigue of AM1 single crystal superalloy*. *Materials Science and Engineering: A*, 2015. **645**: p. 109-115.
32. A. Epishin, T. Link, H. Klingelhofer, P. Portella, and B. Fedelich, *Creep damage of single-crystal superalloys: mechanisms and effect on low cycle fatigue*. *Materials At High Temperature*, 2010. **23**(1): p. 53-59.
33. A. Epishin and T. Link, *Mechanisms of high-temperature creep of nickel-based superalloys under low applied stresses*. *Philosophical Magazine*, 2004. **84**(19): p. 1979-2000.
34. C.T. Sims, *A contemporary view of nickel-base superalloys(Nickel-base superalloy technology, stressing structural stability and hot corrosion resistance)*. *Journal of Metals*, 1966. **18**: p. 1119-1130.
35. B. Harris and A.R. Bonsell, *Structure and Properties of Engineering Materials*. Longman, 1977: p. 296.
36. A. Wisniewski and J. Beddoes, *Influence of grain boundary morphology on creep on a wrought Ni-base superalloy*. *Materials Science and Engineering A*, 2009. **510-511**: p. 266-272.
37. P. Berthod and E. Conrath, *Creep and oxidation kinetics at 1100 C of nickel-base alloys reinforced by hafnium carbides*. *Materials & Design*, 2016. **104**: p. 27-36.
38. W.S. Williams, *Physics of transition metal carbides*. *Materials Science and Engineering: A*, 1988. **105**: p. 1-10.
39. G. Brunetti, A. Settefrati, A. Hazotte, S. Denis, J.-J. Fundenberger, A. Tidu, and E. Bouzy, *Determination of  $\gamma$ - $\gamma'$  lattice misfit in a single-crystal nickel-based superalloy using convergent beam electron diffraction aided by finite element calculations*. *Micron*, 2012. **43**(2): p. 396-406.
40. D. Grose and G. Ansell, *The influence of coherency strain on the elevated temperature tensile behavior of Ni-15Cr-Al-Ti-Mo alloys*. *Metallurgical Transactions A*, 1981. **12**(9): p. 1631-1645.
41. L. Müller, T. Link, and M. Feller-Kniepmeier, *Temperature dependence of the thermal lattice mismatch in a single crystal nickel-base superalloy measured by neutron diffraction*. *Scripta metallurgica et materialia*, 1992. **26**(8): p. 1297-1302.
42. A. Hazotte, *Transformations et contraintes de cohérence dans les superalliages et les intermétalliques de base TiAl*. *Matériaux & Techniques*, 2009. **97**: p. 23-31.
43. P. Footner and B. Richards, *Long-term growth of superalloy  $\gamma'$  particles*. *Journal of Materials Science*, 1982. **17**(7): p. 2141-2153.
44. T. Grosdidier, A. Hazotte, and A. Simon, *On the dissolution mechanisms of  $\gamma'$  precipitates in nickel-based superalloys*. *Scripta metallurgica et materialia*, 1994. **30**(10): p. 1257-1262.

45. T. Grosdidier, A. Hazotte, and A. Simon, *Precipitation and dissolution processes in  $\gamma/\gamma'$  single crystal nickel-based superalloys*. *Materials Science and Engineering: A*, 1998. **256**(1): p. 183-196.
46. A. Hazotte, T. Grosdidier, and S. Denis,  *$\gamma'$  Precipitate splitting in Nickel-based superalloys: A 3-D finite element analysis*. *Scripta materialia*, 1996. **34**(4): p. 601-608.
47. A. Pineau, *Influence of uniaxial stress on the morphology of coherent precipitates during coarsening—elastic energy considerations*. *Acta metallurgica*, 1976. **24**(6): p. 559-564.
48. S. Socrate and D. Parks, *Numerical determination of the elastic driving force for directional coarsening in Ni-superalloys*. *Acta Metallurgica et Materialia*, 1993. **41**(7): p. 2185-2209.
49. W.F. Hosford, *Mechanical behavior of materials*. 2010: Cambridge University Press.
50. J. Zhang, T. Murakumo, Y. Koizumi, T. Kobayashi, and H. Harada, *Slip geometry of dislocations related to cutting of the  $\gamma'$  phase in a new generation single-crystal superalloy*. *Acta materialia*, 2003. **51**(17): p. 5073-5081.
51. L. Carroll, Q. Feng, and T. Pollock, *Interfacial dislocation networks and creep in directional coarsened Ru-containing nickel-base single-crystal superalloys*. *Metallurgical and Materials Transactions A*, 2008. **39**(6): p. 1290-1307.
52. M. Hantcherli, F. Pettinari-Sturmel, B. Viguier, J. Douin, and A. Coujou, *Evolution of interfacial dislocation network during anisothermal high-temperature creep of a nickel-based superalloy*. *Scripta Materialia*, 2012. **66**(3): p. 143-146.
53. H. Long, H. Wei, Y. Liu, S. Mao, J. Zhang, S. Xiang, Y. Chen, W. Gui, Q. Li, and Z. Zhang, *Effect of lattice misfit on the evolution of the dislocation structure in Ni-based single crystal superalloys during thermal exposure*. *Acta Materialia*, 2016. **120**: p. 95-107.
54. J. Zhang, H. Harada, Y. Koizumi, and T. Kobayashi, *Dislocation motion in the early stages of high-temperature low-stress creep in a single-crystal superalloy with a small lattice misfit*. *Journal of materials science*, 2010. **45**(2): p. 523.
55. J. Zhang, J. Wang, H. Harada, and Y. Koizumi, *The effect of lattice misfit on the dislocation motion in superalloys during high-temperature low-stress creep*. *Acta Materialia*, 2005. **53**(17): p. 4623-4633.
56. M. Kolbe, A. Dlouhy, and G. Eggeler, *Dislocation reactions at  $\gamma/\gamma'$ -interfaces during shear creep deformation in the macroscopic crystallographic shear system (001)[110] of CMSX6 superalloy single crystals at 1025° C*. *Materials Science and Engineering: A*, 1998. **246**(1): p. 133-142.
57. F. Louchet and M. Ignat, *Tem analysis of square-shaped dislocation configurations in the  $\gamma'$  phase of a Ni-based superalloy*. *Acta Metallurgica*, 1986. **34**(8): p. 1681-1685.
58. T. Link, A. Epishin, M. Paulisch, and T. May, *Topography of semicoherent  $\gamma/\gamma'$ -interfaces in superalloys: investigation of the formation mechanism*. *Materials Science and Engineering: A*, 2011. **528**(19): p. 6225-6234.
59. J.X. Zhang, T. Murakumo, Y. Koizumi, T. Kobayashi, H. Harada, and S. Masaki, *Interfacial Dislocation Networks Strengthening a fourth-generation single-crystal TMS-138 superalloy*. *Metallurgical and Materials Transactions A*, 2002. **33A**(December): p. 3741-3746.
60. W.W. Milligan and S.D. Antolovich, *Yielding and deformation behavior of the single crystal superalloy PWA 1480*. *Metallurgical Transactions A*, 1987. **18**(1): p. 85-95.
61. S.A. Sajjadi, S. Nategh, M. Isac, and S.M. Zebarjad, *Tensile deformation mechanisms at different temperatures in the Ni-base superalloy GTD-111*. *Journal of materials processing technology*, 2004. **155**: p. 1900-1904.
62. Z. Chu, J. Yu, X. Sun, H. Guan, and Z. Hu, *Tensile property and deformation behavior of a directionally solidified Ni-base superalloy*. *Materials Science and Engineering: A*, 2010. **527**(12): p. 3010-3014.
63. C. Tian, G. Han, C. Cui, and X. Sun, *Effects of Co content on tensile properties and deformation behaviors of Ni-based disk superalloys at different temperatures*. *Materials & Design*, 2015. **88**: p. 123-131.

64. P. Zhang, Y. Yuan, S. Shen, B. Li, R. Zhu, G. Yang, and X. Song, *Tensile deformation mechanisms at various temperatures in a new directionally solidified Ni-base superalloy*. Journal of Alloys and Compounds, 2017. **694**: p. 502-509.
65. M. Feller-Kniepmeier, T. Link, I. Poschmann, G. Scheunemann-Frerker, and C. Schulze, *Temperature dependence of deformation mechanisms in a single crystal nickel-base alloy with high volume fraction of  $\gamma'$  phase*. Acta materialia, 1996. **44**(6): p. 2397-2407.
66. W.W. Milligan and S.D. Antolovich, *On the mechanism of cross slip in Ni 3 Al*. Metallurgical and Materials Transactions A, 1989. **20**(12): p. 2811-2818.
67. Y. Yuan, Y. Gu, Z. Zhong, T. Yokokawa, and H. Harada, *Enhanced strength at intermediate temperatures in a Ni-base disk superalloy with high Co addition*. Materials Science and Engineering: A, 2012. **556**: p. 595-600.
68. P. Caron, Y. Ohta, Y.G. Nakagawa, and T. Khan. *Creep deformation anisotropy in single crystal superalloys*. in *Superalloys 1988*. 1988. Seven Springs, Champion, PA, USA: TMS. p. 215-224.
69. A. Shyam and W. Milligan, *Effects of deformation behavior on fatigue fracture surface morphology in a nickel-base superalloy*. Acta materialia, 2004. **52**(6): p. 1503-1513.
70. B. Larrouy, P. Villechaise, J. Cormier, and O. Berteaux, *Grain boundary - Slip bands interactions: impact on the fatigue crack initiation in a polycrystalline forged Ni-based superalloy*. Acta Materialia, 2015. **99**: p. 325-336.
71. M. Benyoucef, N. Clement, and A. Coujou, *TEM in situ straining of the MC2 superalloy at room temperature*. Philosophical Magazine A, 1995. **72**(4): p. 1043-1056.
72. B.M. Grant, E.M. Francis, J.Q. da Fonseca, M.R. Daymond, and M. Preuss, *Deformation behaviour of an advanced nickel-based superalloy studied by neutron diffraction and electron microscopy*. Acta Materialia, 2012. **60**(19): p. 6829-6841.
73. P. Beardmore, R.G. Davies, and T.L. Johnston, *On the temperature dependence of the flow stress of nickel-base alloys*. Trans. Met. Soc. of AIME, 1969. **245**(7): p. 1537-1545.
74. J.J. Moverare, S. Johansson, and R.C. Reed, *Deformation and damage mechanisms during thermal-mechanical fatigue of a single crystal superalloy*. Acta Materialia, 2009. **57**(7): p. 2266-2276.
75. J.J. Moverare, M. Segersäll, A. Sato, S. Johansson, and R.C. Reed. *Thermomechanical Fatigue of Single-Crystal Superalloys: Influence of Composition and Microstructure*. in *Proceedings of the International Symposium on Superalloys*. 2012. p. 369-377.
76. M. Segersäll, J.J. Moverare, K. Simonsson, and S. Johansson. *Deformation and damage mechanisms during thermomechanical fatigue of a single-crystal superalloy in the  $\langle 001 \rangle$  and  $\langle 011 \rangle$  directions*. in *Superalloys 2012*. 2012. Seven Springs, PA, USA: TMS. p. 215-223.
77. S. Takeuchi and A. Argon, *Steady-state creep of single-phase crystalline matter at high temperature*. Journal of materials science, 1976. **11**(8): p. 1542-1566.
78. X. Jiang, D. Wang, G. Xie, H. Li, L. Lou, and J. Zhang, *The Effect of Long-Term Thermal Exposure on the Microstructure and Stress Rupture Property of a Directionally Solidified Ni-Based Superalloy*. Metallurgical and Materials Transactions A, 2014. **45**(13): p. 6016-6026.
79. J. Tien and S. Copley, *The effect of orientation and sense of applied uniaxial stress on the morphology of coherent gamma prime precipitates in stress annealed nickel-base superalloy crystals*. Metallurgical Transactions, 1971. **2**(2): p. 543-553.
80. M. Nathal and L. Ebert, *Gamma prime shape changes during creep of a nickel-base superalloy*. Scripta metallurgica, 1983. **17**(9): p. 1151-1154.
81. P. Caron and T. Khan, *Improvement of creep strength in a nickel-base single crystal superalloy by heat treatment*. Materials Science and Engineering, 1983. **61**: p. 173-194.
82. M. Feller-Kniepmeier and T. Link, *Correlation of microstructure and creep stages in the  $\langle 100 \rangle$  oriented superalloy SRR 99 at 1253 K*. Metallurgical Transactions A, 1989. **20**(7): p. 1233-1238.
83. F. Diologent and P. Caron, *On the creep behavior at 1033K of new generation single-crystal superalloys*. Materials Science and Engineering: A, 2004. **385**(1): p. 245-257.

84. J. Cormier, M. Jouiad, F. Hamon, P. Villechaise, and X. Milhet, *Very high temperature creep behavior of a single crystal Ni-based superalloy under complex thermal cycling conditions*. Philosophical Magazine Letters, 2010. **90**(8): p. 611-620.
85. M. Zitara, A. Cetel, and A. Czyrska-Filemonowicz, *Microstructure stability of 4th generation single crystal superalloy, PWA 1497, during high temperature creep deformation*. Materials Transactions, 2011. **52**(3): p. 336-339.
86. T. Miyazaki, K. Nakamura, and H. Mori, *Experimental and theoretical investigations on morphological changes of  $\gamma'$  precipitates in Ni-Al single crystals during uniaxial stress-annealing*. Journal of Materials Science, 1979. **14**(8): p. 1827-1837.
87. T. Pollock and A. Argon, *Creep resistance of CMSX-3 nickel base superalloy single crystals*. Acta Metallurgica et Materialia, 1992. **40**(1): p. 1-30.
88. J. Tien and R. Gamble, *Effects of stress coarsening on coherent particle strengthening*. Metallurgical and Materials Transactions B, 1972. **3**(8): p. 2157-2162.
89. M. Kirka, *Thermomechanical behavior of a directionally solidified nickel-base superalloys in the aged state*, PhD Thesis. 2014, Georgia Institute of Technology.
90. C. Carry and J. Strudel, *Apparent and effective creep parameters in single crystals of a nickel base superalloy—II. Secondary creep*. Acta Metallurgica, 1978. **26**(5): p. 859-870.
91. C. Carry and J. Strudel, *Apparent and effective creep parameters in single crystals of a nickel base superalloy—I Incubation period*. Acta Metallurgica, 1977. **25**(7): p. 767-777.
92. M. Kirka, K. Brindley, R. Neu, S. Antolovich, S. Shinde, and P. Gravett, *Influence of coarsened and rafted microstructures on the thermomechanical fatigue of a Ni-base superalloy*. International Journal of Fatigue, 2015. **81**: p. 191-201.
93. J. Cormier and G. Cailletaud, *Constitutive modeling of the creep behavior of single crystal superalloys under non-isothermal conditions inducing phase transformations*. Materials Science and Engineering: A, 2010. **527**(23): p. 6300-6312.
94. M. Kirka, K. Brindley, R. Neu, S. Antolovich, S. Shinde, and P. Gravett, *Parameters influencing thermomechanical fatigue of a directionally-solidified Ni-base superalloy*. International Journal of Fatigue, 2015. **81**: p. 48-60.
95. R.A. MacKay, R.L. Dreshfield, and R.D. Maier. *Anisotropy of nickel-base superalloy single crystals*. in *Superalloys 1980*. 1980. Seven Springs, Champion, PA, USA: TMS, Warrendale, PA. p. 385-394.
96. G.M. Han, J.J. Yu, Y.L. Sun, X.F. Sun, and Z.Q. Hu, *Anisotropic stress rupture properties of the nickel-base single crystal superalloy SRR99*. Materials Science and Engineering, 2010. **A527**: p. 5383-5390.
97. J. Huang, D. Shi, and X. Yang, *A modern and robust methodology for modeling anisotropic creep characteristics of Ni-based DS and SC superalloys*. Science China Technological Sciences, 2014. **57**(9): p. 1802-1815.
98. P. Caron. *High  $\gamma'$  solvus new generation nickel-based superalloys for single crystal turbine blade applications*. in *Superalloys 2000*. 2000. Seven Springs, PA, USA: TMS. p. 737-746.
99. A. Epishin, Link, T., Nazmy, M., Staubli, M. and Nolze, G. , *Microstructural degradation of CMSX-4, kinetics and effect on mechanical properties*, in *Superalloys 2008*. 2008, TMS: Seven Springs, PA, USA. p. 725-731.
100. H. Mughrabi and U. Tetzlaff, *Microstructure and High-Temperature Strength of Monocrystalline Nickel-Base Superalloys*. Advanced Engineering Materials, 2000. **2**(6): p. 319-326.
101. D. MacLachlan and D. Knowles, *Creep-behavior modeling of the single-crystal superalloy CMSX-4*. Metallurgical and materials transactions A, 2000. **31**(5): p. 1401-1411.
102. H. Mughrabi, W. Schneider, V. Sass, and C. Lang, *The effect of raft formation on the high-temperature creep deformation behaviour of the monocrystalline nickel-base superalloy CMSX-4*. Strength of Materials. ICSMA 10, 1994: p. 705-708.
103. R. Reed, D. Cox, and C. Rae, *Damage accumulation during creep deformation of a single crystal superalloy at 1150 C*. Materials Science and Engineering: A, 2007. **448**(1): p. 88-96.



104. A. Kostka, G. Mälzer, G. Eggeler, A. Dlouhy, S. Reese, and T. Mack, *L12-phase cutting during high temperature and low stress creep of a Re-containing Ni-base single crystal superalloy*. Journal of materials science, 2007. **42**(11): p. 3951-3957.
105. G. Eggeler and A. Dlouhy, *On the formation of <math>\langle 010 \rangle</math>-dislocations in the  $\gamma'$ -phase of superalloy single crystals during high temperature low stress creep*. Acta materialia, 1997. **45**(10): p. 4251-4262.
106. R. Srinivasan, G. Eggeler, and M. Mills,  *$\gamma'$ -cutting as rate-controlling recovery process during high-temperature and low-stress creep of superalloy single crystals*. Acta materialia, 2000. **48**(20): p. 4867-4878.
107. J. Zhang, H. Harada, and Y. Koizumi, *New configuration of a [001] superdislocation formed during high-temperature creep in the  $\gamma'$  phase of a single-crystal superalloy TMS-138*. Journal of materials research, 2006. **21**(03): p. 647-654.
108. R. Giraud, J. Cormier, Z. Hervier, D. Bertheau, K. Harris, J. Wahl, X. Milhet, J. Mendez, and A. Organista, *Effect of the prior microstructure degradation on the high temperature/low stress non-isothermal creep behavior of CMSX-4@ Ni-based single crystal superalloy*. Reed RC, others, editors. Superalloys, 2012: p. 265-74.
109. X. Milhet, J. Cormier, and A. Organista, *On the role of the internal stress during non-isothermal creep life of a first generation nickel based single crystal superalloy*. Materials Science and Engineering: A, 2010. **527**(9): p. 2280-2288.
110. S. Steuer, Z. Hervier, S. Thabart, C. Castaing, T. Pollock, and J. Cormier, *Creep behavior under isothermal and non-isothermal conditions of AM3 single crystal superalloy for different solutioning cooling rates*. Materials Science and Engineering: A, 2014. **601**: p. 145-152.
111. M.-S. Chiou, S.-R. Jian, A.-C. Yeh, C.-M. Kuo, and J.-Y. Juang, *High temperature creep properties of directionally solidified CM-247LC Ni-based superalloy*. Materials Science and Engineering: A, 2016. **655**: p. 237-243.
112. J. Cormier. *Thermal Cycling Creep Resistance of Ni-Based Single Crystal Superalloys*. in *Superalloys 2016: Proceedings of the 13th International Symposium of Superalloys*. 2016. Seven Springs, PA, USA: Wiley Online Library. p. 383-394.
113. T. Murakumo, T. Kobayashi, Y. Koizumi, and H. Harada, *Creep behaviour of Ni-base single-crystal superalloys with various  $\gamma'$  volume fraction*. Acta Materialia, 2004. **52**(12): p. 3737-3744.
114. P.K. Wright and A.F. Anderson. *The influence of orientation on the fatigue of directionally solidified superalloys*. in *Superalloys 1980*. 1980. Seven Springs, Champion, PA, USA: TMS. p. 689-698.
115. R. Chieragatti and L. Remy, *Influence of orientation on the low cycle fatigue of MAR-M 200 single crystals at 650°C. I: Fatigue life behaviour*. Materials Science and Engineering: A, 1991. **141**(1): p. 1-9.
116. M. Gell and G. Leverant, *The fatigue of the nickel-base superalloy, Mar-M 200, in single-crystal and columnar-grained forms at room temperature (Ni based superalloy cyclic deformation and fracture and high and low cycle fatigue at room temperature, comparing single crystal and columnar grained forms)*. AIME, Transactions, 1968. **242**: p. 1869-1879.
117. G. Leverant and M. Gell, *The elevated temperature fatigue of a Nickel-base superalloy, MAR-M 200, in conventionally cast and directionally solidified forms*. Trans. Met. Soc. AIME, 1969. **245**(6): p. 1167-1173.
118. G. Leverant and M. Gell, *The influence of temperature and cyclic frequency on the fatigue fracture of cube oriented nickel-base superalloy single crystals*. Metallurgical Transactions A, 1975. **6**(2): p. 367-371.
119. P.S. Karamched and A.J. Wilkinson, *High resolution electron back-scatter diffraction analysis of thermally and mechanically induced strains near carbide inclusions in a superalloy*. Acta Materialia, 2011. **59**(1): p. 263-272.
120. S. McHugh, *Modelling the thermo-mechanical behavior of a carbide inclusion in a nickel superalloy including residual stress effects with a simple finite-element model*. Mathematical and Computer Modelling, 1990. **14**: p. 933-941.

121. M. Ott and H. Mughrabi, *Dependence of the high-temperature low-cycle fatigue behaviour of the monocrystalline nickel-base superalloys CMSX-4 and CMSX-6 on the  $\gamma/\gamma'$ -morphology*. Materials Science and Engineering: A, 1999. **272**(1): p. 24-30.
122. D. Arrell, M. Hasselqvist, C. Sommer, and J. Moverare. *On TMF damage, degradation effects, and the associated TMin influence on TMF test results in  $\gamma/\gamma'$  alloys*. in *Superalloys 2004*. 2004. Seven springs, PA, USA: The Minerals, Metals and Materials Society, TMS. p. 291-294.
123. A.P. Gordon, *Crack initiation modeling of a directionally-solidified nickel-base superalloy*, PhD Thesis. 2006, Georgia Institute of Technology: Atlanta, Georgia, USA.
124. F.C. Neuner, U. Tetzlaff, and H. Mughrabi, *Enhancement of thermomechanical fatigue resistance of a monocrystalline nickel-base superalloy by pre-rafting*, in *Thermomechanical Fatigue Behavior of Materials: 4th Volume*. 2003, ASTM International.
125. C. Engler-Pinto Jr, C. Nosedá, M. Nazmy, and F. Rezai-Aria, *Interaction between creep and thermo-mechanical fatigue of CM247LC-DS*. Super alloys, 1996: p. 319.
126. D. Kobayashi, M. Miyabe, M. Achiwa, R. Sugiura, and A. Yokobori, *Creep-fatigue crack growth behaviour based on EBSD observations for notched specimen made of directionally solidified Ni-base superalloy*. Materials at High Temperatures, 2014. **31**(4): p. 326-333.
127. J. Telesman and L.J. Ghosn. *Fatigue crack growth behavior of PWA 1484 single crystal superalloy at elevated temperatures*. in *ASME 1995 International Gas Turbine and Aeroengine Congress and Exposition*. 1995: American Society of Mechanical Engineers. p. V005T14A040-V005T14A040.
128. B.F. Antolovich, A. Saxena, and S.D. Antolovich, *Fatigue crack propagation in single-crystal CMSX-2 at elevated temperature*. Journal of Materials Engineering and Performance, 1993. **2**(4): p. 489-495.
129. K. Chan, J. Hack, and G. Leverant, *Fatigue crack growth in MAR-M200 single crystals*. Metallurgical and Materials Transactions A, 1987. **18**(4): p. 581-591.
130. J. Crompton and J. Martin, *Crack growth in a single crystal superalloy at elevated temperature*. Metallurgical Transactions A, 1984. **15**(9): p. 1711-1719.
131. X. He, Y. Zhang, H. Shi, J. Gu, C. Li, K. Kadau, and O. Luesebriink, *Influence of orientation and temperature on the fatigue crack growth of a nickel-based directionally solidified superalloy*. Materials Science and Engineering: A, 2014. **618**: p. 153-160.
132. M. Henderson and J. Martin, *The influence of crystal orientation on the high temperature fatigue crack growth of a Ni-based single crystal superalloy*. Acta Materialia, 1996. **44**(1): p. 111-126.
133. P. Kontis, D.M. Collins, S. Johansson, A.J. Wilkinson, J.J. Moverare, and R.C. Reed. *Crack Initiation and Propagation During Thermal-Mechanical Fatigue of IN792: Effects of Dwell Time*. in *Superalloys 2016: Proceedings of the 13th International Symposium of Super alloys*. 2016. Seven Springs, PA, USA: Wiley Online Library. p. 763-772.
134. A. Srivastava, S. Gopagoni, A. Needleman, V. Seetharaman, A. Staroselsky, and R. Banerjee, *Effect of specimen thickness on the creep response of a Ni-based single-crystal superalloy*. Acta Materialia, 2012. **60**(16): p. 5697-5711.
135. M. Brunner, M. Bensch, R. Völkl, E. Affeldt, and U. Glatzel, *Thickness influence on creep properties for Ni-based superalloy M247LC SX*. Materials Science and Engineering: A, 2012. **550**: p. 254-262.
136. A. Baldan, *On the thin-section size dependent creep strength of a single crystal nickel-base superalloy*. Journal of Materials Science, 1995. **30**: p. 6288-6298.
137. V. Seetharaman and A. Cetel. *Thickness debit in creep properties of PWA 1484*. in *Superalloys 2004*. 2004. Seven Springs, PA, USA: TMS. p. 207-214.
138. E. Aghion, M. Bamberger, and A. Berkovits, *High-temperature low-cycle fatigue of a nickel-based MAR-M200+ Hf alloy in AR and AR+ 20% O<sub>2</sub> environment*. Journal of materials science, 1991. **26**(7): p. 1873-1881.

139. D. Duquette and M. Gell, *The effects of environment on the elevated temperature fatigue behavior of nickel-base superalloy single crystals*. Metallurgical Transactions, 1972. **3**(7): p. 1899-1905.
140. K. Harris, G. Erickson, and R. Schwer, *Directionally solidified and single-crystal superalloys*. ASM International, Metals Handbook. Tenth Edition., 1990. **1**: p. 995-1006.
141. M. Shenoy, D. McDowell, and R. Neu, *Transversely isotropic viscoplasticity model for a directionally solidified Ni-base superalloy*. International journal of plasticity, 2006. **22**(12): p. 2301-2326.
142. K. Harris, G. Erickson, and R. Schwer. *CMSX single crystal, CM DS & integral wheel alloys properties & performance*. in *Cost Conference "High temperature alloys for gas turbines and other applications"*. 1986. Liège, Belgium. p. 6-9.
143. F. Coudon, *Comportement mécanique à haute température d'un superalliage à solidification dirigée DS200+Hf*, PhD Thesis. 2017, Mines ParisTech, Centre des Matériaux.

## Chapter 2 - Experimental Procedures

## Chapitre 2 Procédures expérimentales

Ce deuxième chapitre est dédié à la présentation des moyens d'essais, procédures, préparations et caractérisations expérimentales employés/menés au cours de ces travaux de thèse.

Le matériau utilisé (DS200+Hf) a été fourni sous forme de plaques ou barreaux coulés à Safran Aircraft Engines Gennevilliers. Différents types d'échantillons et d'éprouvettes utilisées pour les caractérisations microstructurales et pour les essais mécaniques ont été prélevés dans ces plaques et barreaux. Pour chaque type d'essai, des états de surface spécifiques à chaque type de sollicitation mécanique sont nécessaires et ces spécificités sont détaillées dans ce chapitre.

Cinq types d'essais mécaniques différents ont été mis en place : traction, fluage, fatigue oligocyclique, fatigue avec temps de maintien et fissuration. Les conditions appliquées pour chaque type d'essai, les réglages, les procédures d'essais et machines employées sont détaillés.

Concernant la caractérisation de l'impact environnemental, et plus particulièrement de l'oxydation, des essais d'ATG (analyse thermogravimétrique) avec des échantillons présentant différentes tailles de grain ont été mis en place. De plus, afin de renforcer la contribution de l'oxydation, des essais de fluage avec des éprouvettes à parois minces ont été mis en place, ce qui est l'une des grandes plus-values de ces travaux de thèse.

Un autre développement expérimental très innovant employé pour ces travaux consiste en l'analyse de la déformation en fluage in situ, à l'échelle des grains. Cela a été mise en place de deux manières. A l'Institut Pprime, des marqueurs céramiques ont été déposés en surface des échantillons afin de mesurer la déformation moyenne par grain par vidéo-extensométrie. Par ailleurs, des expériences de corrélation d'image in situ ont été mises en place avec l'Université de Californie – Santa Barbara pour avoir accès à des champs de déformations et pour caractériser plus particulièrement les processus de localisations aux joints des grains. Cela a été fondamental pour investiguer l'amorçage des fissures aux joints de grains.

Finalement, les caractérisations microstructurales sont détaillées, en mettant en valeur les moyens de microscopie utilisés (microscopie optique, microscopie électronique à balayage en mode électrons secondaires/rétro-diffusés, EDX). Des investigations par sonde tomographique atomique ont été réalisées en collaboration avec le Max-Planck-Institut de Düsseldorf. Ces caractérisations à haute valeur ajoutée, ont notamment permis de mieux comprendre la chimie des carbures et leur résistance à l'oxydation.



## Table of contents (Chapter 2)

2.	Experimental Procedures .....	69
2.1	Material .....	69
2.2	Specimen preparation .....	73
2.3	Tensile tests .....	74
2.4	Fatigue tests .....	75
2.5	Creep tests.....	75
2.6	Crack propagation tests.....	80
2.7	TGA measurements .....	81
2.8	Microstructural analyzes .....	82

## Figures and tables (Chapter 2)

Figure 2.1 - Typical DS200+Hf plate used to machine specimens used in this thesis. ....	70
Figure 2.2 - EBSD characterization in a plane perpendicular to the solidification direction (a) in the CG area and (b) in the FG area.....	71
Figure 2.3 - Microstructure at the dendritic scale with Hf/Ti/Nb-rich carbides and eutectics (a) and at the $\gamma/\gamma'$ precipitation scale in the primary dendrite arm (b) and in the interdendritic zones (c). ....	71
Figure 2.4 - (001) and (101) pole figures for DS-FG and DS-CG.....	71
Figure 2.5 - Pseudo-rocking curves around the $\langle 001 \rangle$ crystallographic direction in the CG area (a) and FG area (b).....	72
Figure 2.6 – Crystallographic orientations that can be encountered during transverse mechanical tests of DS200+Hf alloy in FG and CG areas.....	72
Figure 2.7 - Tensile and creep specimens. ....	74
Figure 2.8 - Tensile and fatigue Instron 8562 electromechanic machine.....	75
Figure 2.9 - LCF specimens.....	76
Figure 2.10 - Thin-walled creep specimens.....	76
Figure 2.11 - Creep frame equipped with a radiant furnace. ....	77
Figure 2.12 - In situ monitoring of creep strain heterogeneities testing procedure details: ceramics markers and grain boundaries revealed by chemical etching (a); example of picture taken during a creep test (b) and plot of creep curves in different grain of the specimen (c). ....	78
Figure 2.13 - Induction coil for heating system during creep test and experimental set-up for digital image correlation measurement during creep deformation at high temperature. ....	79
Figure 2.14 - Servohydraulic Instron 1271 testing system with a high vacuum chamber.....	80
Figure 2.15 - CT32 specimens used for crack propagation tests. ....	81
Figure 2.16 - Thermo-Gravimetric Analysis (TGA) experimental set-up. ....	82
Figure 2.17 – Determination of the $\gamma'$ volume fraction in DS200+Hf alloy by APT characterization. ....	83
Table 2.1 - Chemical composition of DS200+Hf used in this study (in wt. pct).....	69
Table 2.2 – MAR-M200+Hf SX bars used in this study and their respective orientations according to the FCC standard stereographic triangle.....	73
Table 2.3 - Specimens preparation.....	73
Table 2.4 – Chemical composition of $\gamma$ and $\gamma'$ phases (in at. pct) as determined by APT characterizations. ....	83



## 2. Experimental Procedures

In this chapter, all the details about castings and sample preparation will be presented first. The experimental procedures to perform microstructural analyzes and mechanical tests will be then detailed.

### 2.1 Material

The alloy studied here, DS200+Hf, has a high hafnium content, of about 1.6%, which has been chosen to achieve a better grain boundary strength at high temperature [1-6], improving the durability during service operations [2]. Chemical composition of the ingots re-melted to grow the castings used in this study is specified on Table 2.1.

Element	Ni	Cr	W	Co	Al	Ti	Nb	Hf	C	B	Zr	Fe
Wt. Pct	Bal.	8.6	11.8	9.5	4.90	1.87	0.86	1.58	0.13	0.015	0.01	0.02

Table 2.1 - Chemical composition of DS200+Hf used in this study (in wt. pct).

DS200+Hf samples were machined out from heat treated plates (dimensions are 110x65x15 mm<sup>3</sup> (Figure 2.1) by electron discharge machining (EDM) and subsequent turning. These plates were directionally solidified (DS) at SAFRAN Aircraft Engines-Gennevilliers, France. They were solution heat-treated at SAFRAN Aircraft Engines according to the following sequence: 1210°C/30 minutes + 1225°C/30 minutes + 1240°C/4 hours + cooling at or greater than 45°C/minute until 700°C and then air quenched (AQ). This solution treatment was used to dissolve as much as possible eutectics without reaching incipient melting close to carbides/borides and also, to reduce the dendritic segregation obtained after solidification. These plates were further heat treated at Pprime Institute in air for 5 hours at 1100°C/AQ + 16 hours at 870°C/AQ to optimize the  $\gamma'$  precipitate size and morphology, and hence, the resulting mechanical properties, specifically for creep [7].

As observed in Figure 2.2, showing an EBSD characterization in a plane perpendicular to the solidification direction, the grain size is  $\sim 181 \mu\text{m}$  in the fine grain zone (i.e. bottom of the plate in Figure 2.1), with equiaxed grains and about 2.5 mm in the coarse grain zone (i.e. top of the plate in Figure 2.1), with very serrated grain boundaries (Figure 2.2). Image analyzes were performed using Visilog<sup>®</sup> software to extract the distributions in carbides and  $\gamma'$  precipitates sizes in the full heat-treated state. The average sizes of Hf/Ti/Nb-riched carbides and  $\gamma'$  precipitates were about 5  $\mu\text{m}$  and between 350 and 400 nm, respectively (see Figure 2.3(a) and (b) for typical carbides and  $\gamma/\gamma'$  microstructures in the alloy). Besides the presence of huge carbides clusters, it is easy to find  $\gamma/\gamma'$  eutectics as shown in Figure 2.3(a) and (c). They were remaining after the solution heat treatment since it is impossible to fully solution them without reaching the incipient melting temperature in the interdendritic spacings due to the large amount of hafnium [8].

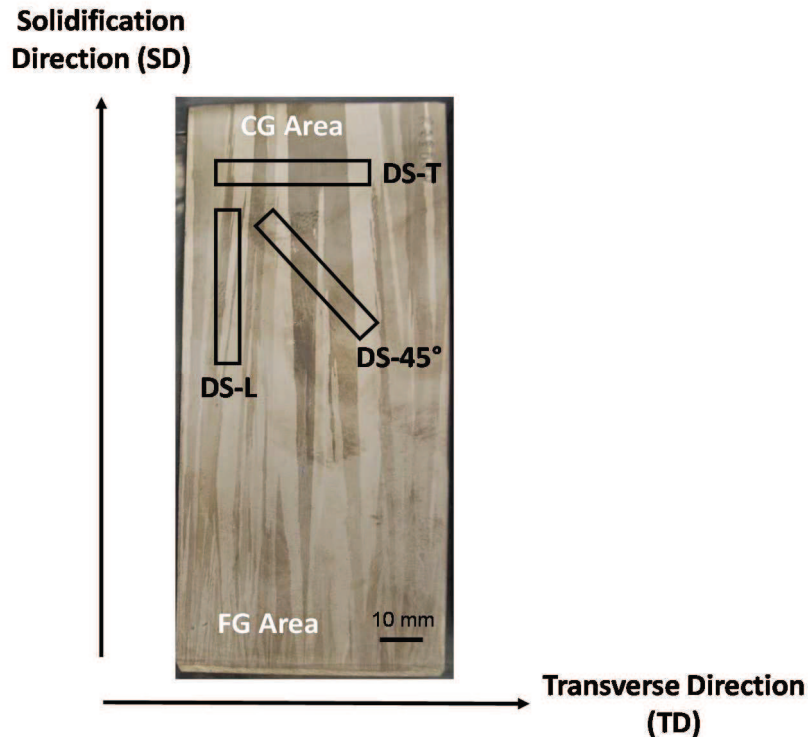


Figure 2.1 - Typical DS200+Hf plate used to machine specimens used in this thesis.

According to EBSD characterizations, the scatter around a  $\langle 001 \rangle$  crystallographic orientation was found to be more pronounced in the fine grained (FG) area of the plate compared to the coarse grains (CG) one ( $\langle 001 \rangle$  pole figures in Figure 2.4). Pseudo-rocking curves presented in Figure 2.5 clearly show that grains whose primary orientation is oriented up to 20 degrees away from the perfect  $\langle 001 \rangle$  crystallographic orientation can be found in the FG area (Figure 2.5(b)) while a maximum primary misorientation of up to 10 degrees from the  $\langle 001 \rangle$  direction is observed in the CG area (Figure 2.5(a)).  $\langle 101 \rangle$  pole figures for DS-FG and DS-CG (Figure 2.4) also show a very low lateral texture. According to Figure 2.4 and Figure 2.5, a large variety of crystallographic orientations for each individual grain can be encountered during transversal loading (i.e. oriented at  $90^\circ$  from the solidification direction), as shown by the dashed areas in the standard stereographic triangles of Figure 2.6.

To better understand the “grain effect” on damage mechanisms, MAR-M200+Hf single crystalline (SX) samples were machined from bars which were solidified at SAFRAN Aircraft Engine - Gennevilliers using a standard Bridgman process. These SX bars were mainly solidified along the  $\langle 001 \rangle$  crystallographic orientation but additional bars were solidified far away from this orientation, using a grain selector and seeds. The average primary dendrite arm spacing was measured to be in the 300-350  $\mu\text{m}$  range in these SX bars. These bars were further heat treated using the same above mentioned solution and aging heat treatments used for the DS plates. The exact orientations of all the SX bars tested are listed in Table 2.2. Table 2.1 - Chemical composition of DS200+Hf used in this study (in wt. pct). Due to a relatively low primary misorientation, most of the SX bars can be considered as close to a  $\langle 001 \rangle$  orientation, while two SX bars (X8205K and X8206B) were selected to be representative of possible grain orientations that can be met in creep testing along transverse direction of DS samples. The bar X8206B, with a  $\sim 46$  degrees primary misorientation and 20 degrees secondary misorientation, is near the farthest configuration away from the  $[001]$  direction that could be encountered in FG areas, according to Figure 2.6 – Crystallographic orientations that can be encountered during transverse mechanical tests of DS200+Hf alloy in FG and CG areas.. One has to notice that these bars and plates

were cast using ingots from the same master heat as the DS plates, whose chemical composition was already given in Table 2.1.

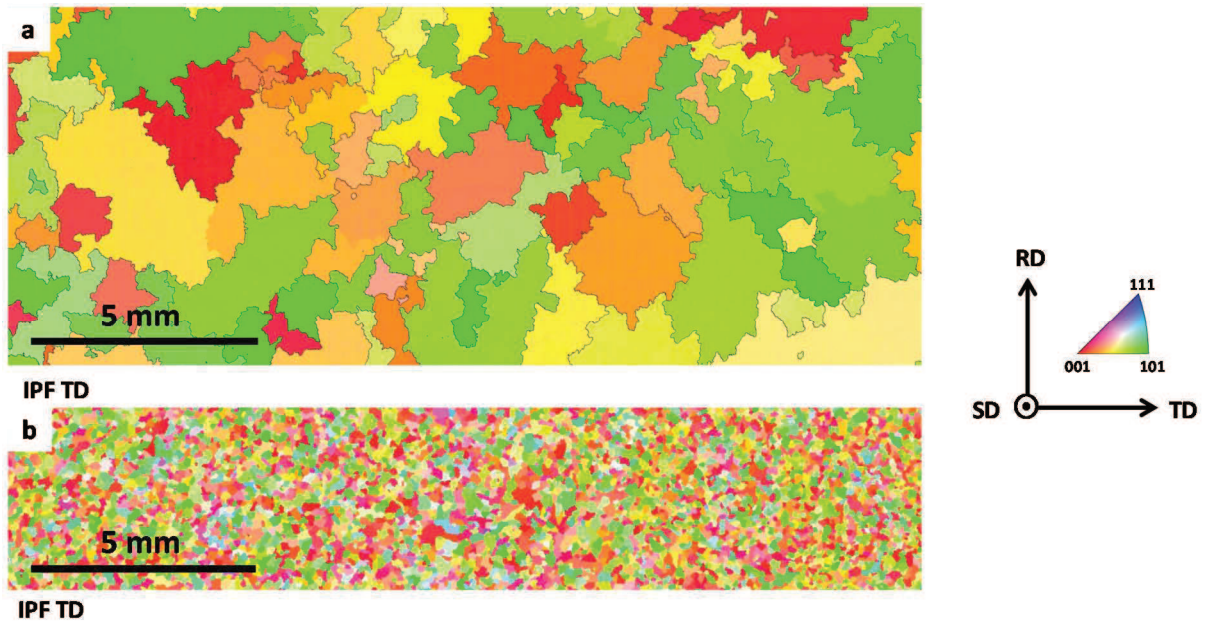


Figure 2.2 - EBSD characterization in a plane perpendicular to the solidification direction (a) in the CG area and (b) in the FG area.

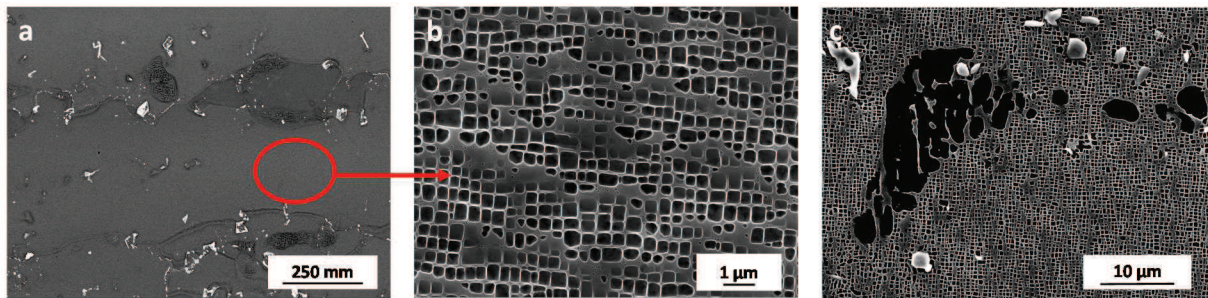


Figure 2.3 - Microstructure at the dendritic scale with Hf/Ti/Nb-rich carbides and eutectics (a) and at the  $\gamma/\gamma'$  precipitation scale in the primary dendrite arm (b) and in the interdentritic zones (c).

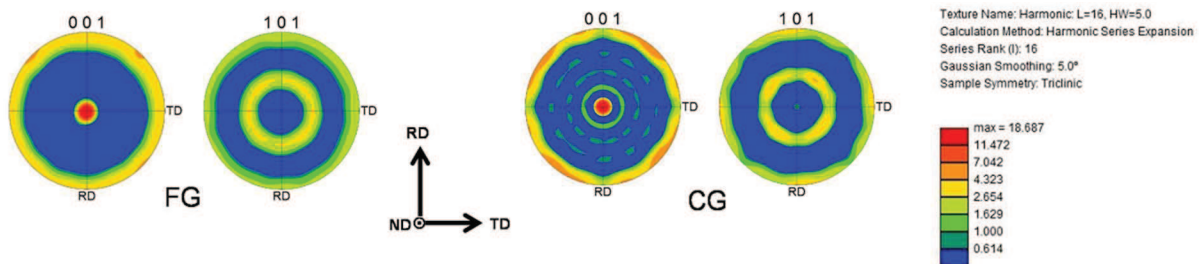


Figure 2.4 - (001) and (101) pole figures for DS-FG and DS-CG.

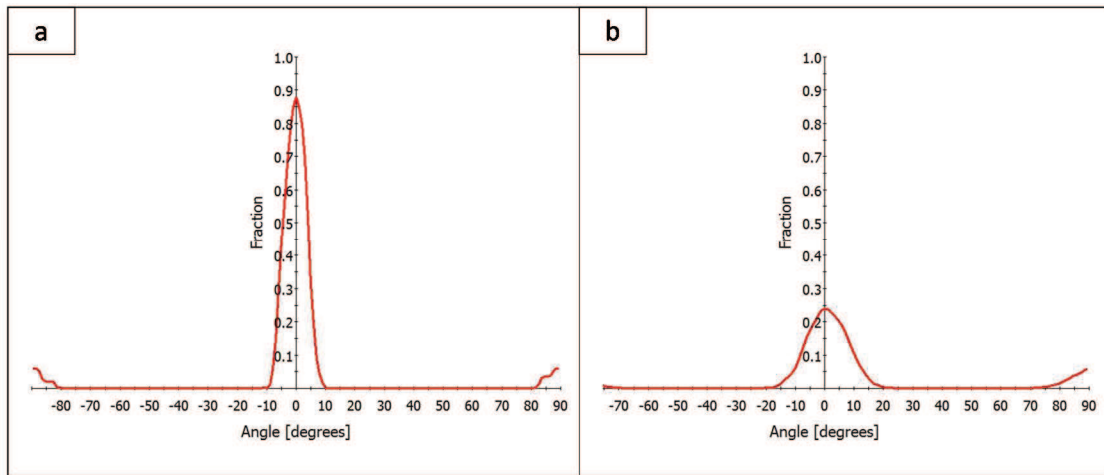


Figure 2.5 - Pseudo-rocking curves around the  $\langle 001 \rangle$  crystallographic direction in the CG area (a) and FG area (b).

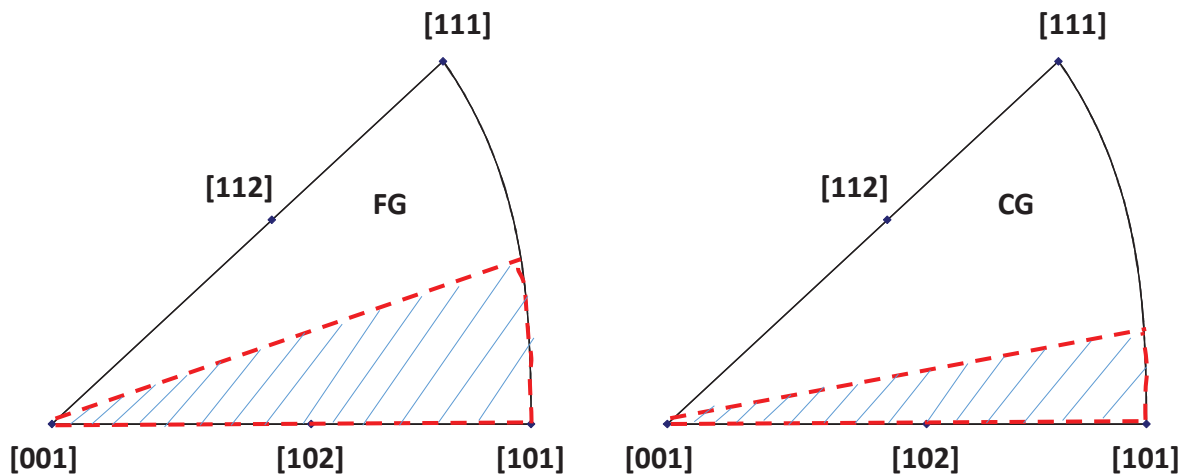


Figure 2.6 – Crystallographic orientations that can be encountered during transverse mechanical tests of DS200+Hf alloy in FG and CG areas.

However, since the orientation that has to be considered is the one of the gauge length, due to the geometry of the specimens employed (see subsequent sections), it was not possible to completely explore the influence of the loading direction for the finest grain size at the extremity of DS plates.

In summary, five types of specimens have been studied:

- FG DS200+Hf specimens (grain size in the 200-900  $\mu\text{m}$  range) longitudinally loaded (i.e. parallel to the solidification direction); these samples will be identified as “DS-L”;
- FG DS200+Hf specimens (grain size in the 200-600  $\mu\text{m}$  range) loaded at 45° of the solidification direction (see Figure 2.1 - Typical DS200+Hf plate used to machine specimens used in this thesis.); these samples will be identified as “DS-45°”;
- FG DS200+Hf (grain size of about 150-300  $\mu\text{m}$ ) transversally loaded, denoted as “DS-T-FG”;
- CG DS200+Hf (grain size of about 2.5 mm) transversally loaded, denoted as “DS-T-CG” in the following;

- MAR-M200+Hf single crystals, mainly loaded along a near  $\langle 001 \rangle$  crystallographic orientation, and denoted as “ $\langle 001 \rangle$ -SX”. SX bars oriented far away from the perfect  $\langle 001 \rangle$  crystallographic orientation will clearly be identified in the following of the manuscript.

Specimens studied under fatigue solicitations were taken into the plate along transverse or longitudinal directions without considering grain size differences due to their geometry (these specimen are not small enough to be taken into plate extremities, especially in FG areas).

Bars	Primary misorientation $\theta(^{\circ})$	secondary misorientation $\rho(^{\circ})$
X8204E	0.6	43.3
X8204H	3.1	12.3
X8204J	1.6	31.1
X8204K	0.8	27.2
X8204M	1.8	36.7
X8204N	1.6	18.2
X8204R	1.5	33.4
X8205A	7.8	34.8
X8205B	6.6	37.9
X8205E	5.9	4.8
X8205F	7.7	11.4
X8205K	24.4	8.5
X8205N	0.6	43.8
X8206B	45.8	20.0
X8206J	3.2	14.1
X8206P	2.3	2.4
X8206R	1.5	0.2
X8206S	3.6	11.9

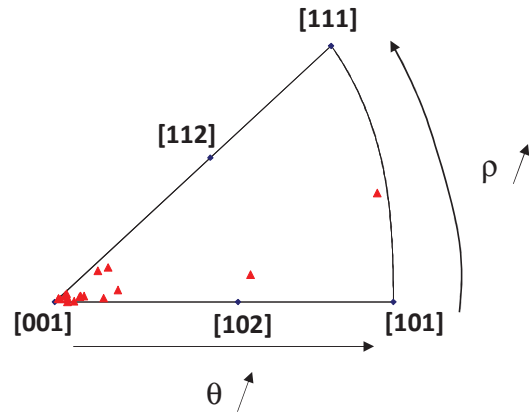


Table 2.2 – MAR-M200+Hf SX bars used in this study and their respective orientations according to the FCC standard stereographic triangle.

## 2.2 Specimen preparation

Before each mechanical test, specimens gauge length was polished up to a 4000 grade SiC paper for creep and tensile tests and up to a mirror finish using a 1  $\mu\text{m}$  diamond spray for fatigue tests (see details in Table 2.3) and crack propagation tests.

Step	Material	Time	Lubricant
1	320 grit SiC Abrasive Paper	Until smooth	Water
2	500 grit SiC Abrasive Paper	30 minutes	Water
3	1000 grit SiC Abrasive Paper	30 minutes	Water
4	2000 grit SiC Abrasive Paper	30 minutes	Water
5	4000 grit SiC Abrasive Paper	30 minutes	Water
6	Diamond spray 3 $\mu\text{m}$	20 minutes	Blue
7	Diamond spray 1 $\mu\text{m}$	20 minutes	Red

Table 2.3 - Specimens preparation.

To characterize the microstructure evolution of DS200+Hf after creep tests, samples were subsequently cut longitudinally, mechanically polished until step 7 of Table 2.3 and then, etched in a solution made of 1/3  $\text{HNO}_3$  and 2/3  $\text{HCl}$  (vol. pct.) for 10 s to reveal the  $\gamma$ - $\gamma'$  microstructure. This chemical attack selectively dissolves the  $\gamma'$ -phase. This preparation allows both the characterization of the grain structure and of the different classes of precipitates (carbides,  $\gamma'$  phase).

### 2.3 Tensile tests

Tensile specimens have a 42 mm total length, with a 14 mm gauge length and a 4 mm gauge diameter (Figure 2.7). Tensile tests were performed using an electromechanical Instron 8562 (Figure 2.8) testing system equipped with a high temperature extensometer positioned onto the specimen surface after temperature stabilization (30 minutes). Heating was ensured with a two zones regulated resistive furnace and monitored with S-type thermocouples attached to the specimen surface, with a +/- 2°C accuracy. The heating procedure is the following: heating rate of 15°C/min until T1 and 3°C/min until T2 (T1=645°C and T2=672°C for a 650°C target and T1=870°C and T2=910°C for a 900°C target). A tensile load of 0.1 kN is imposed all along the heating procedure to ensure its alignment within the furnace. Tensile test data have all been post-processed so that to plot the true stress " $\sigma$ " ( $\sigma = (F/S_0) \cdot (1+e)$ ) and true strain " $\epsilon$ " ( $\epsilon = \ln(1+e)$ ) knowing the evolution of the load F and of the conventional strain "e" ( $e = \text{elongation}/\text{initial gauge length}$ ) during the test, as well as the initial bearing section " $S_0$ ".

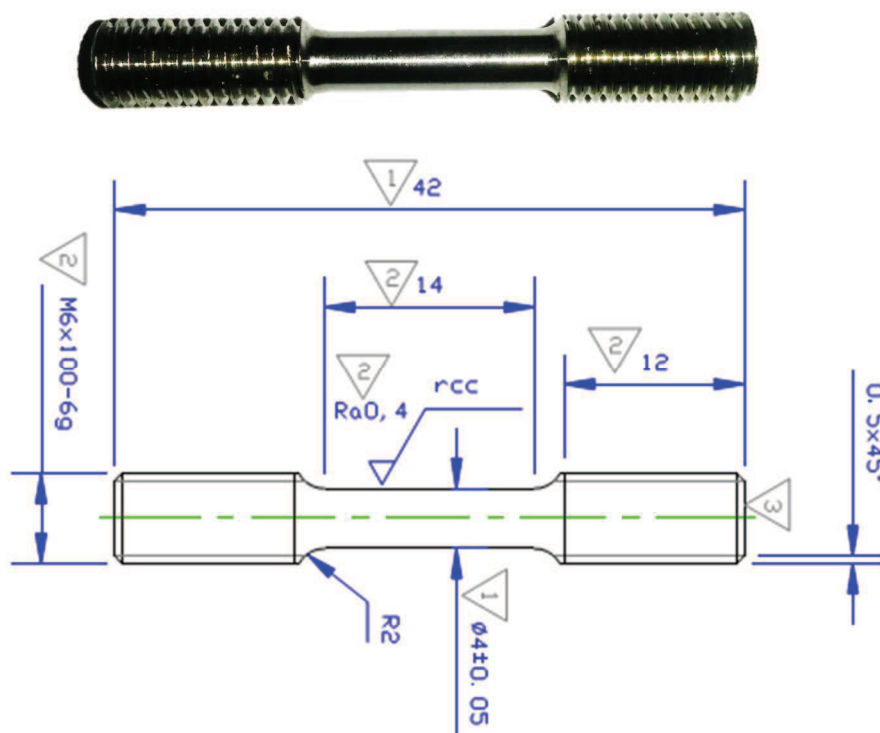


Figure 2.7 - Tensile and creep specimens.

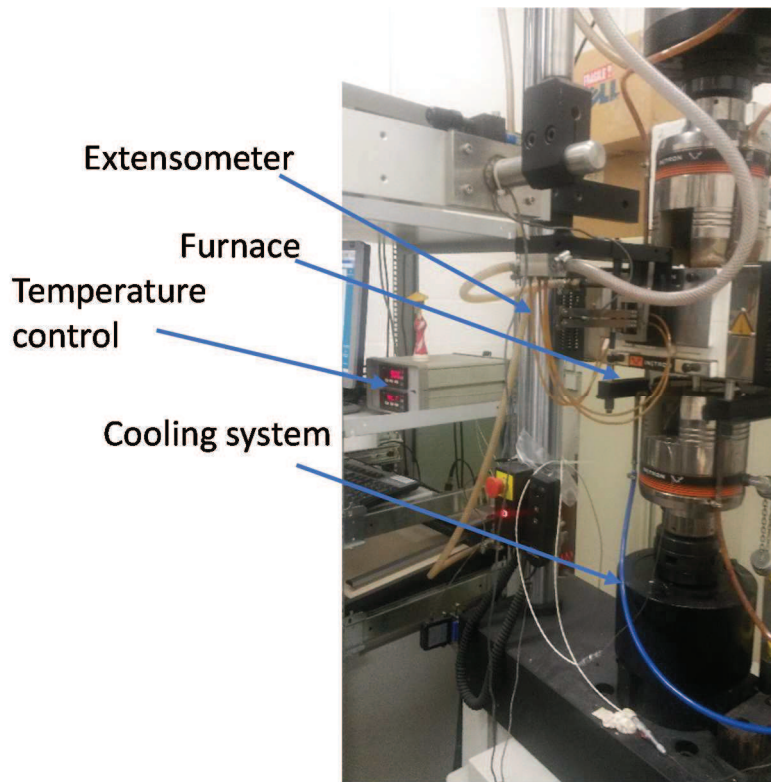


Figure 2.8 - Tensile and fatigue Instron 8562 electromechanic machine.

#### 2.4 Fatigue tests

LCF specimens have a 56 mm total length, a 13 mm gauge length and a 4.37 mm gauge diameter. (Figure 2.9). These tests were performed using exactly the same bench and procedures than tensile ones. A special attention is paid to avoid any kind of damage of the specimen surface when thermocouples and extensometer are placed.

LCF tests were performed under load control, at 650°C or 900°C, using stress ratios  $R\sigma=-1$  and  $R\sigma=0.05$  at 650°C and  $R\sigma=0.05$  at 900°C. A sinusoidal waveform has been used for these experiments and 0.5 Hz frequency. Moreover, load-controlled dwell fatigue tests have been conducted using a trapezoidal waveform, with a dwell time  $\Delta t$  at maximum load ranging from 1 to 300 seconds and loading and unloading periods of 1 second each.

#### 2.5 Creep tests

Massive creep specimens are identical to tensile ones (see Figure 2.7). Additional thin-walled creep samples were further machined from the cylindrical ones to either perform creep tests during which each grain elongation is followed by ceramic markers (by videoextensometry), or to investigate the thin-wall debit in creep. Two parallel flats extending all along the gauge length were machined by EDM to reach thicknesses of nearly 0.5 mm, 0.8 mm and 1.5 mm (Figure 2.10 shows a drawing for 1.5 mm thick specimens, the others being identical to this one, changing the thickness). Flat surfaces of the gauge sections have been machined close to a (100) or (010) plane for SX specimens.

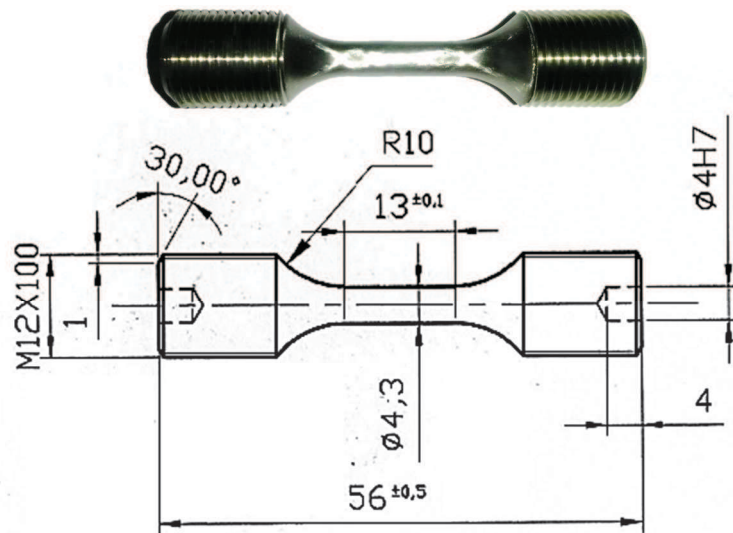


Figure 2.9 - LCF specimens.

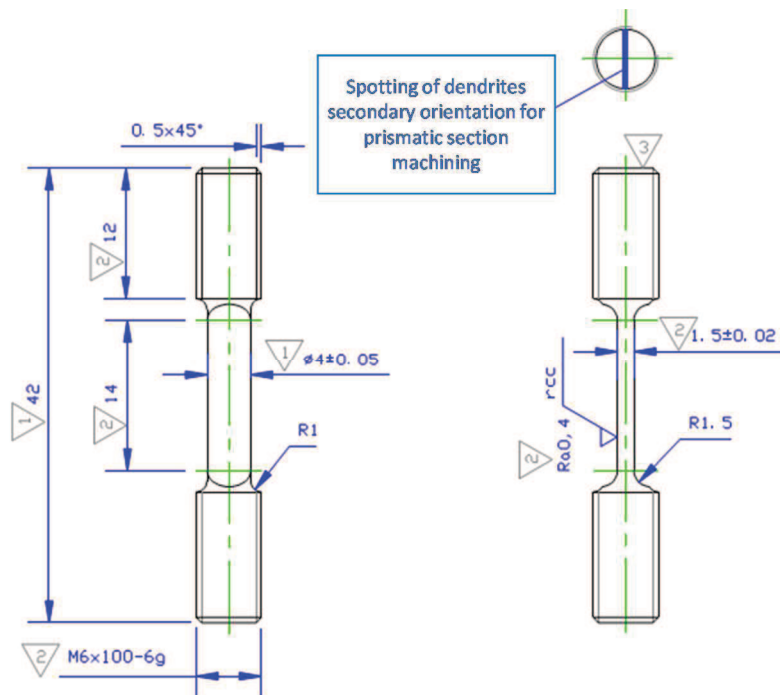


Figure 2.10 - Thin-walled creep specimens.

Most of the massive creep tests were performed in a creep machine equipped with a radiant furnace and with a laser extensometer (Figure 2.11). During these tests, a maximum 10°C temperature heterogeneity along the gauge length has been measured (i.e. for a creep test performed at 900°C, the temperature in the extremity of the filleted areas of the specimens is ~ 890°C, the temperature being almost constant on 4 mm in the center of the gauge length). During heating, the temperature increases in 20 seconds from room temperature up to 650°C and then a heating rate of 100°C/min was used to reach the target temperature. Before applying the constant mechanical load, a 15 minutes soak time was used before applying the mechanical load. During these tests, the temperature was controlled



using a S-type thermocouple attached to the specimen upper head with a +/- 2°C accuracy. Strain measurements were performed using an optical micrometer whose beam passes through the furnace through slots (Figure 2.11). The displacement accuracy of this equipment up to 1200°C is 5 µm in isothermal conditions.

The thin-wall debit in creep properties was investigated using a double-line creep frame equipped with a resistive furnace ensuring a minimum temperature heterogeneity along the gauge length of 1°C, far smaller than the one measured during creep tests using the test bench equipped with a radiant furnace. This is especially important considering that the reduction in specimen thickness strongly affects creep ductility. The thin-wall debit in creep properties has only been investigated at 900°C. The heating procedure was the following: heating from room temperature up to 850°C in 10 minutes, and then, heating from 850°C up to 900°C at 2.5 °C/min. A 3 hours soak time was systematically applied to the specimens to ensure a good temperature homogeneity in the grip lines as well as in the devices allowing the measurement of the creep elongation with LVDTs (Linear Variable Displacement Transducers).

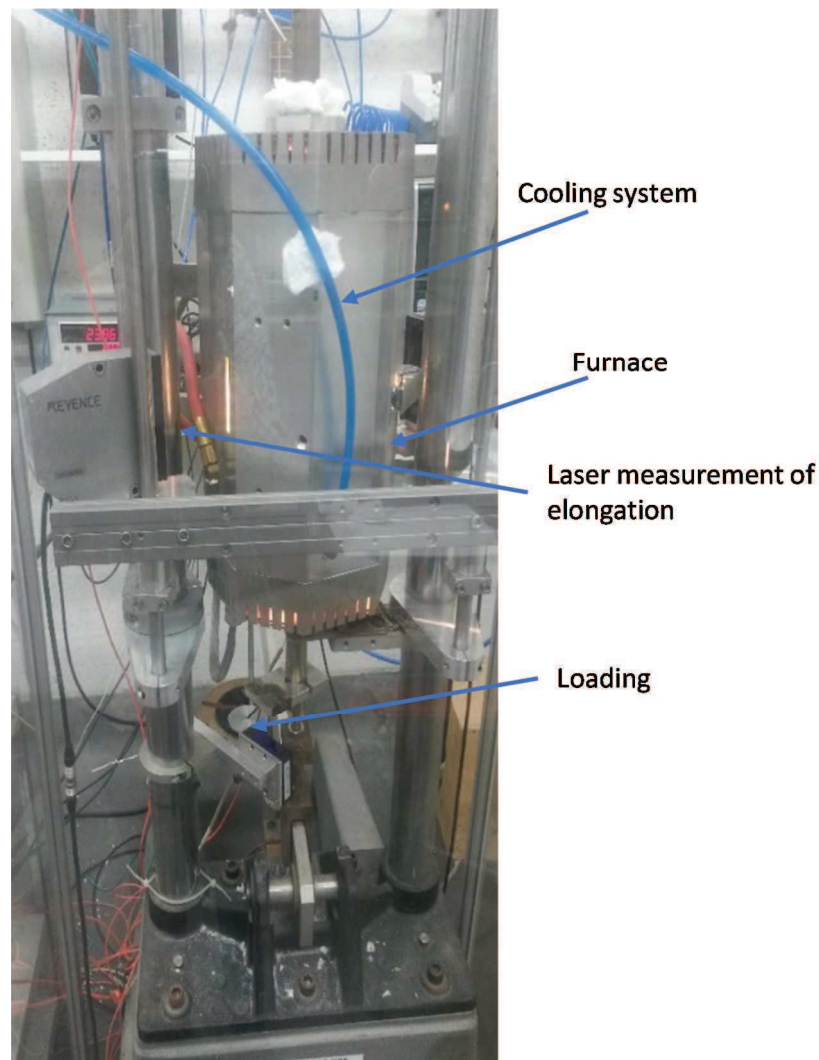


Figure 2.11 - Creep frame equipped with a radiant furnace.

In situ monitoring of creep strain heterogeneities at the grain scale was performed to better understand intergranular crack initiation during transverse creep testing. For these tests, 1.5 mm thick and a particular case of 0.5 mm thick specimens were machined from cylindrical DS-T-CG specimens

by EDM. After polishing until step 5 of Table 2.3 and subsequent chemical etching to reveal grain contrasts (i.e. sample preparation), ceramic markers were placed with special care in each different grain in order to measure local displacement by videoextensometry (see Figure 2.12(a)). Before placing these markers, in some particular cases, an EBSD map has been performed to be able to localize grain boundaries and to know the orientation of each grain before creep straining. S-type thermocouples used to control the temperature during the tests were spot welded according to standard TMF COP (Thermo-Mechanical Fatigue Code of Practice) on the rear face of the specimens (see Figure 2.12(b)). During creep tests, the barycenter of the markers was filmed with a high resolution camera (AVT Manta G-917B, CCD camera, 9Mpix and optical lentils Tamron 1A1HB, 75mm) through a slot machined in the radiant furnace used to heat the specimens. Pictures have been recorded with a frequency of 10 Hz. Pictures were then optically filtered using an in house-made software that supplies the evolution of the barycenter position of each marker using a contour detection algorithm. The data were then post-processed to obtain the strain evolution at the surface of each grain. Figure 2.12(c) shows the curves obtained from data extracted by this software, allowing to compare the strain of each grain in the whole specimen. Each point of the curve corresponds to an average value calculated from 120 pictures. After creep tests, if necessary, an EBSD map has been done to detect possible grain rotations during the tests and to analyze the crack initiation mechanisms.

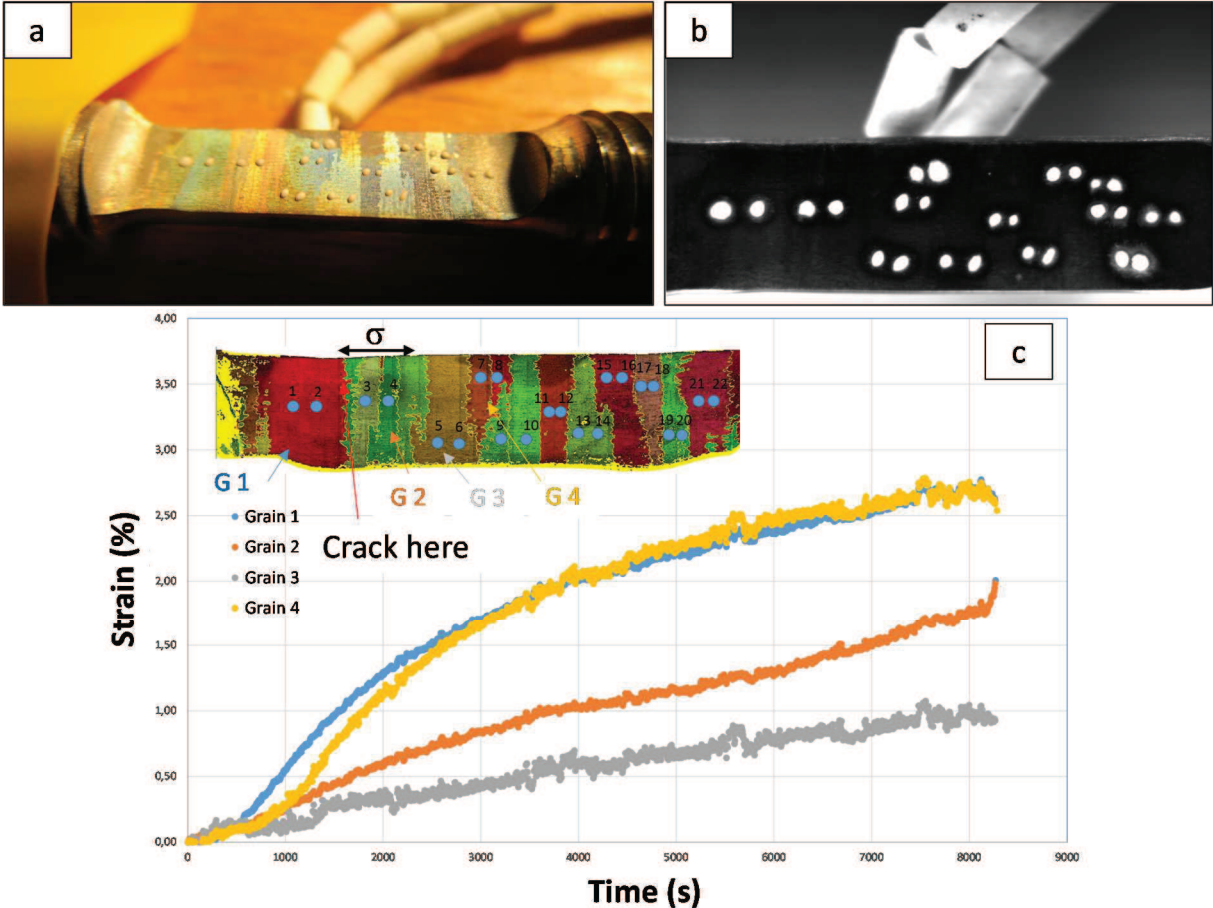


Figure 2.12 - In situ monitoring of creep strain heterogeneities testing procedure details: ceramics markers and grain boundaries revealed by chemical etching (a); example of picture taken during a creep test (b) and plot of creep curves in different grain of the specimen (c).

An additional monitoring of creep strain heterogeneities at the surface of a cylindrical specimen (3 mm in diameter) loaded along transverse direction has been performed using a digital image correlation

(DIC) technique and a special set-up. Creep tests were performed at the University of California – Santa Barbara (USA) using an Instron 5582 universal testing machine equipped with an Easyheat induction heating system, in collaboration with Dr. Jean-Charles Stinville. An in-house induction coil was used to minimize the temperature gradient across the creep specimen and to give a visual access to the entire surface of the specimen. The coil is shown in Figure 2.13. Such a coil induces temperature gradient of about 15°C (at 750°C) along the specimen gauge length. A two color pyrometer provides temperature measurements at the surface of the specimen as shown in Figure 2.13. Closed loop system between the pyrometer and induction heating system was performed to adjust the induction power to maintain constant temperature during creep test. The coil is maintained by high-temperature resistant fiber glass material in order to carefully position the coil in relation to the specimen.

The rig is composed of a Nikon D5300 digital camera with a CCD resolution of 6036×4020 pixels. AF-S DX Nikkor 18-55 mm f1:3.5 macro lens was used in these experiments. The magnification factor leads to a resolution of 80 pixels/mm. One pixel hence corresponds to 12.5 μm. A polarized lens filter was used to capture the surface of the specimen during creep test at high temperature.

Orientalmotor high resolution hollow rotary actuator allows rotating the camera around the gage length of the specimen as displayed in Figure 2.13. High resolution images before and during creep test are processed for each rotation step by digital image correlation using the VIC-2D 2009 software. Strain field is obtained at the surface of the specimen during creep test using a subset and step size of 21×21 pixels and 5 pixels respectively. A decay filter of 5×5 is used in the calculation of the strain field. Such procedure allows to obtain the in plane strain field along the loading direction for the entire gage length by doing a 360° rotation of the rig. A typical rotation step of 15° was used during the creep test. Typical rotation step occurred in a time lapse in the order of tens of minutes.

A sprayed speckle pattern suitable for strain measurement is applied at the surface of the specimen using an airbrush kit and high-temperature resistant paint. Typical circular particles with diameters in the order of 50 micrometers were obtained (see Figure 2.13)

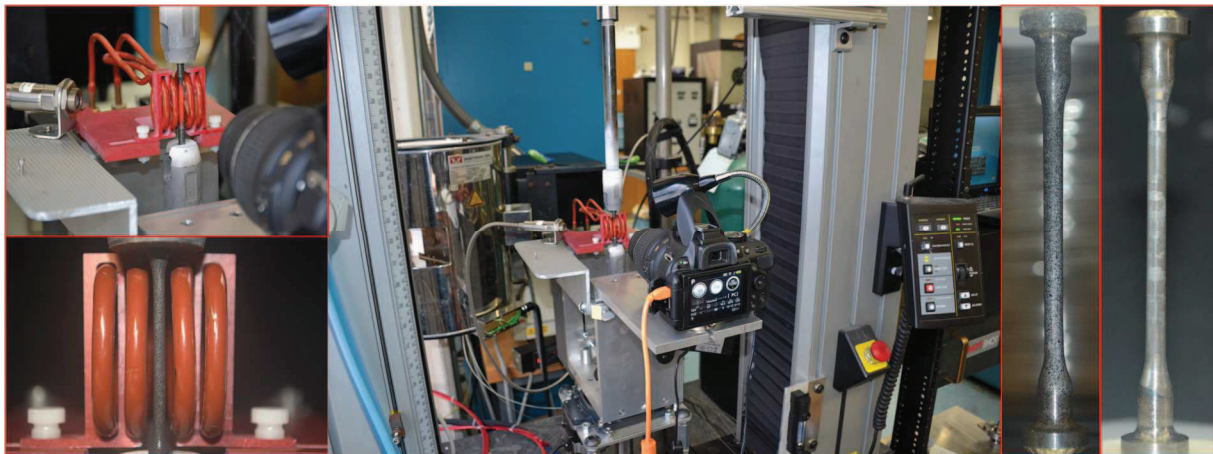


*Figure 2.13 - Induction coil for heating system during creep test and experimental set-up for digital image correlation measurement during creep deformation at high temperature.*

Creep tests in high vacuum (pressure below  $8.0 \cdot 10^{-6}$  mbar) were performed using a computer controlled servohydraulic Instron 1271 testing system (Figure 2.14). Experimental procedures are identical to tensile creep ones performed in air. This equipment has also been used to perform load – controlled LCF and dwell-fatigue tests, using the same waveform and parameters as the ones conducted in air.



Figure 2.14 - Servohydraulic Instron 1271 testing system with a high vacuum chamber.

## 2.6 Crack propagation tests

Figure 2.15 shows the specimens used for crack propagation tests. Two compact test (CT) specimens were machined out from the plates, in the upper and lower parts, in the solidification direction ( $\langle 001 \rangle$  direction) as shown in Figure 2.15. The tests were performed at 650°C and 900°C. Two different conditions were chosen: in air using a computer controlled servohydraulic 810 MTS material testing system and in high vacuum, with the same machine used for the creep tests (see Figure 2.14). For these tests, a pre-cracking at room-temperature at a stress intensity factor  $\Delta K$  of 11 MPa.m<sup>0.5</sup> has been performed to induce a first symmetric crack initiation, and lately crack length is followed by electrical potential drop method. Crack propagation tests have been performed at 650°C and 900°C in air and at 650°C under high vacuum with a crack closure measurement set-up, with a stress ratio  $R\sigma = 0.2$  and a frequency  $f=20$  Hz. During these experiments, the frequency was reduced to 0.5 Hz for 10 cycles each 10,000 cycles to be able to measure accurately and periodically the crack opening during the cycles. No crack closure measurements have been performed at 900°C in high vacuum since it was impossible to maintain the crack closure measurement device during the test. It is worth mentioning that crack propagation tests have been performed with a progressive increase of the applied load amplitude, starting from an initial  $\Delta K = 10$  MPa.m<sup>0.5</sup> and increasing progressively the  $\Delta K$  value up to achieving the first stages of crack propagation.

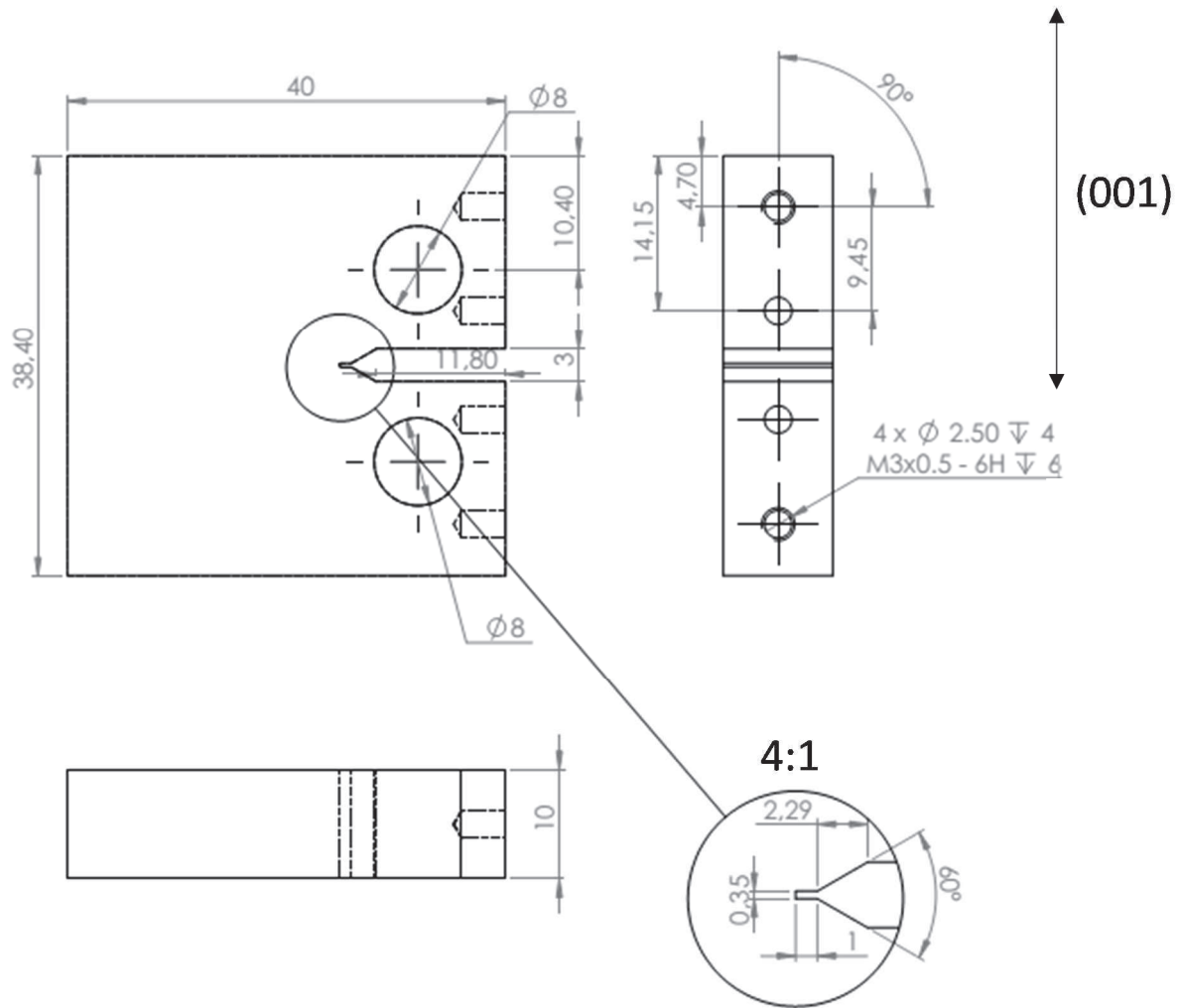


Figure 2.15 - CT32 specimens used for crack propagation tests.

## 2.7 TGA measurements

Thermogravimetric experiments have been performed to characterize the oxidation kinetics of the specimen and how grain boundary density affects these kinetics. Isothermal oxidation samples of 14 mm in diameter and 0.9 mm thick were machined by EDM in both CG and FG regions of DS plates, as well as in a  $\langle 001 \rangle$  oriented SX bar (normal to the specimen surface close to a  $[001]$  direction). These tests were performed using a SETARAM SETSYS Evolution 16/18 thermobalance (Figure 2.16). Thanks to its symmetrical furnace arrangement, this thermobalance offers an excellent accuracy (of  $\sim 0.002 \mu\text{g}$ ) with limited drift and buoyancy effects. Experiments were performed at  $900^\circ\text{C}$  with  $\pm 0.2^\circ\text{C}$  precision, in synthetic air (i.e. without humidity and other impurities).

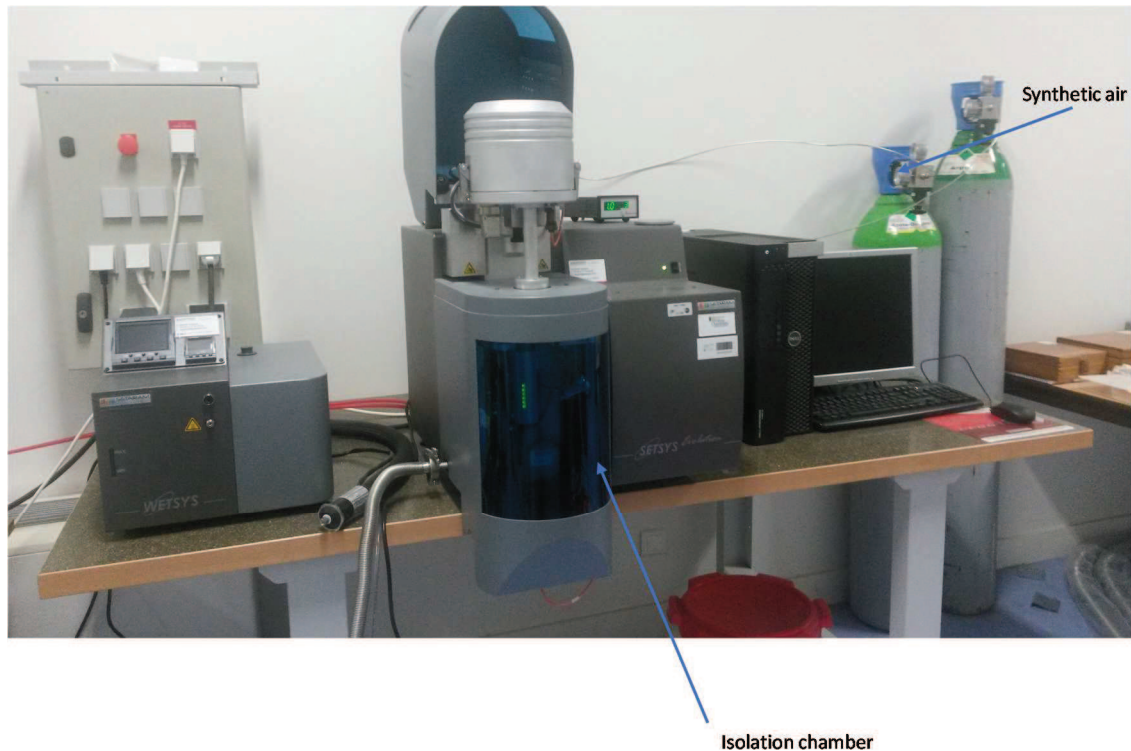


Figure 2.16 - Thermo-Gravimetric Analysis (TGA) experimental set-up.

## 2.8 Microstructural analyzes

$\gamma/\gamma'$  microstructure and fracture surface observations were performed using a JEOL JSM™ 7000F Field Emission Gun scanning electron microscope (SEM) and a JEOL JSM™ 6400 SEM respectively. Both secondary (SEI) and backscattered (BSE) electron imaging modes with a magnification range of 20 up to 50,000 were used. Observations were performed using an acceleration voltage of 25 kV.

After SEM observations, several  $\gamma/\gamma'$  stereological investigations have been performed using the Visilog software, or, alternatively, MATLAB algorithms developed at Institut Pprime by Dr. Vincenzo Caccuri. After a contrast inversion of the SEM pictures and subsequent application of a median filter to allow a better contour detection of the precipitates, a thresholding was applied to separate each precipitate from the matrix. Standard stereological parameters were then extracted, such as the precipitate area fraction, precipitates length/thickness distributions and matrix channel width, removing particles connected to the image boundaries to avoid any artifact in the size distributions. An illustration of the application of these algorithm using the Visilog software can be found in Vaunois et al. [9].

Electron Backscatter Diffraction (EBSD) analyzes were carried out using a JEOL JSM™ 6100 SEM equipped with an orientation imaging microscopy (OIM) system. EBSD measurements require a flat surface and also a high quality of final polishing. Electrolytic polishing was performed to reveal the microstructure and to obtain adequate electron back-scattering diffraction patterns, using a Struers A3 solution, at  $-4^{\circ}\text{C}$ , under 45 V for 8 seconds.

The orientation mapping of such a columnar grain material requires a compromise between the time consumed to map the area of interest and the spatial resolution of the scanning grid. EBSD measurements were performed with a scanning step between 0.25 and 3  $\mu\text{m}$  and an acceleration voltage of 25 kV. Due to the size of the specimens, several scan maps were performed with a step-wise displacement of the specimen and lately merged to constitute a line scan. All line scans assembly

constitute a complete scan map of the specimen. EBSD maps used in this work present dedicated scan lines of around 20,000 X 800  $\mu\text{m}^2$ .

Electron Dispersive Spectrometry X-rays (EDX) analyzes were carried out to investigate the oxidation mechanisms close to grain boundaries, close to carbides and for oxide types identification as well. It has also been used to identify the nature of the crack initiation sites in fatigue. For this, a JEOL JSM™ 6100 SEM equipped with a Bruker AXS Silicon Drift corrected detector was employed with an acceleration voltage of 20 KV, a working distance of 15 mm and low beam current conditions. Either line scan, element mapping or point scan characterizations were performed.

Atom probe tomography (APT) analyzes were finally carried out in collaboration with Dr. Paraskevas Kontis at Max-Planck-Institut für Eisenforschung GMBH, Düsseldorf, Germany. Specimens for APT were prepared from site specific lift-outs from grain boundary regions where the carbides under investigation were located, using a dual column SEM-FIB FEI Helios 600 following procedures described in [10]. Specimens were analysed on a Camera LEAP 3000 HR instrument operating in laser pulsing mode with a repetition rate of 250 kHz, laser pulse energy 0.6 nJ and at a base temperature of 70 K.

In addition, the compositions of  $\gamma$  matrix and  $\gamma'$  precipitates as collected from the APT analysis are given in Table 2.4. By plotting the nominal concentration for each element minus the solute content in the  $\gamma$  matrix ( $C_n - C_\gamma$ ) versus the difference in composition between  $\gamma'$  and  $\gamma$  ( $C_{\gamma'} - C_\gamma$ ), following the lever rule described in [11], it is possible to determine the volume fraction of  $\gamma'$  phase in the alloy. The slope of the best-fit line of the graph given in Figure 2.17 corresponds to the  $\gamma'$  volume fraction, which in this case is 63.7%. However, this  $\gamma'$  phase fraction is not the one of fine and efficient cuboidal  $\gamma'$  precipitates (as observed in Figure 2.3(b)) since part of  $\gamma'$  elements remain trapped with the  $\gamma/\gamma'$  eutectic pools. Hence, the volume fraction of efficient  $\gamma'$  particles is around 58-60%, removing the volume fraction of eutectic pools determined by image analyzes.

Element	Ni	Cr	Co	W	Al	Ti	Nb	Hf	Ta	Si	B	C	Zr
$\gamma$ phase	51.08	22.12	18.79	3.76	3.25	0.32	0.15	0.08	0.08	0.05	0.01	0.0	0.0
$\gamma'$ phase	67.59	2.59	6.18	2.34	16.48	3.56	0.52	0.60	0.01	0.04	0.03	0.0	0.0

Table 2.4 – Chemical composition of  $\gamma$  and  $\gamma'$  phases (in at. pct) as determined by APT characterizations.

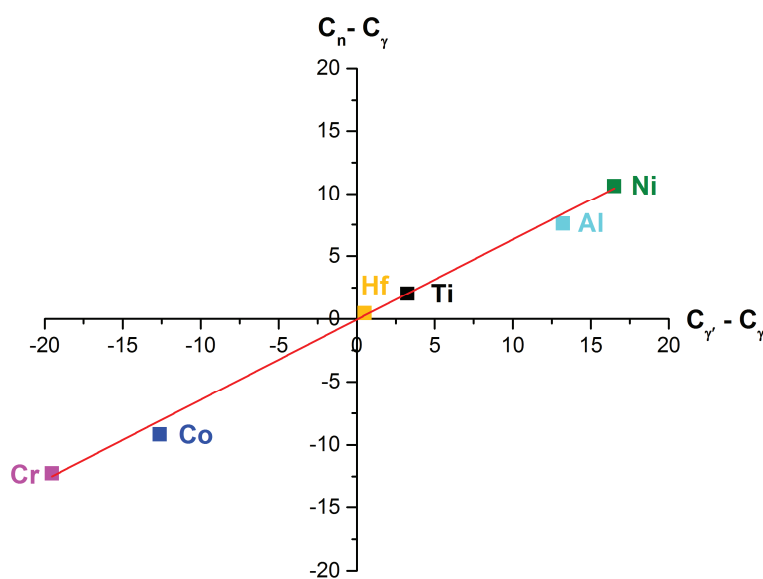


Figure 2.17 – Determination of the  $\gamma'$  volume fraction in DS200+Hf alloy by APT characterization.

## References of Chapter 2

1. M.J. Donachie and S.J. Donachie, *Superalloys: a Technical Guide*. 2002: ASM international.
2. M. Gell, D.N. Duhl, and A.F. Giamei. *The development of single crystal superalloy turbine blades*. in *Superalloys 1980*. 1980. Seven Springs, PA, USA: TMS. p. 205-214.
3. R.C. Reed, *The Superalloys - Fundamentals and Applications*. 2006, Cambridge, UK: Cambridge University Press.
4. A.D. Cetel and D.N. Duhl. *Second generation columnar grain nickel-base superalloy*. in *Superalloys 1992*. 1992. Seven Springs, PA, USA: TMS. p. 287-296.
5. F.L. Versnyder and M.E. Shank, *The development of columnar grain and single crystal high temperature materials through directional solidification*. *Materials Science and Engineering*, 1970. **6**: p. 213-247.
6. D.N. Duhl and C.P. Sullivan, *Some effects of hafnium additions on the mechanical properties of a columnar-grained nickel-base superalloy*. *Journal of Metals*, 1971. **23**(7): p. 38-40.
7. J.-B. le Graverend, et al., *Effect of fine  $\gamma'$  precipitation on non-isothermal creep and creep-fatigue behaviour of nickel base superalloy MC2*. *Materials Science and Engineering: A*, 2010. **527**(20): p. 5295-5302.
8. M. Hajjaji, *Solid solubility of hafnium in nickel*. *Journal of alloys and compounds*, 1998. **274**(1): p. 185-188.
9. J.R. Vaunois, J. Cormier, P. Villechaise, A. Devaux, and B. Flageolet. *Influence of both  $\gamma'$  distribution and grain size on the tensile properties of UDIMET 720Li at room temperature*. in *7<sup>th</sup> International Symposium on Superalloy 718 and Derivatives*. 2010. Pittsburgh, PA, USA: TMS. p. 199-213.
10. K. Thompson, D. Lawrence, D. Larson, J. Olson, T. Kelly, and B. Gorman, *In situ site-specific specimen preparation for atom probe tomography*. *Ultramicroscopy*, 2007. **107**(2): p. 131-139.
11. D. Blavette, P. Caron, and T. Khan. *An atom-probe study of some fine-scale microstructural features in Ni-based single crystal superalloys*. in *Superalloys 1988*. 1988. Seven Springs, PA, USA: TMS. p. 305-314.



## Chapter 3 – Mechanical Behavior

## Chapitre 3 Comportement mécanique

Ce chapitre est consacré à la présentation du comportement mécanique du DS200+Hf en traction, fluage, fatigue oligocyclique et fatigue avec temps de maintien (ou fluage cyclique). Ces essais mécaniques ont été réalisés à haute température (dans la gamme 650°C à 1100°C). Ces essais ont été menés dans le sens long, en sens transverse et à 45° de l'axe de solidification. En ce qui concerne l'orientation transverse, l'effet de la taille des grains a été pris en compte par le prélèvement d'échantillons dans les zones à gros grains et à petits grains de la plaque. Ces résultats ont été comparés de façon systématique à la version monocristalline de l'alliage, de même composition chimique (i.e. avec des carbures primaires HfC, NbC et TiC notamment). Le focus de ce chapitre a été porté sur les comportements mécaniques en traction, fluage, fatigue avec temps de maintien. La durée de vie en fluage, fatigue avec temps de maintien et fatigue, plus spécialement en ce qui concerne les mécanismes d'endommagement, seront au cœur du prochain chapitre.

Les propriétés en traction ont été caractérisées à 650°C et 900°C, en employant différentes vitesses de déformation, plus particulièrement à 900°C. Des investigations plus détaillées du comportement en fluage et de la durabilité ont été réalisées au travers d'essais à 750°C, 900°C et 1100°C, avec un plus fort effort expérimental sur la température intermédiaire. Des investigations des hétérogénéités de déformation en fluage à l'échelle des grains pour une sollicitation transverse ont montré la très forte hétérogénéité de déformation locale grain à grain, particulièrement à 750°C. Cette hétérogénéité de déformation tend à diminuer pour des essais à 900°C, notamment en raison de la dégradation progressive de la microstructure de précipitation  $\gamma'$  (i.e. mise en radeaux).

Les essais de fatigue oligocyclique ont été réalisés à 650°C et à 900°C en utilisant un signal sinusoïdal, sous une fréquence de 0,5 Hz et avec rapport de charge imposée de  $R\sigma=0,05$  pour les deux températures et également  $R\sigma=-1$  à 650°C. L'objectif principal a été d'investiguer le comportement cyclique à ces deux températures ainsi que l'anisotropie de comportement cyclique.

Finalement, les interactions entre fluage et fatigue à 900°C ont été présentées, avec l'analyse de l'effet du temps de maintien. Des temps de maintien de 1, 10 et 300 secondes ont été imposés avec deux contraintes maximales différentes appliquées. L'évolution microstructurale  $\gamma/\gamma'$  en fonction du temps de maintien et de la durée totale des essais a été analysée en fonction du temps de maintien et comparée avec celle observée en fluage pure.

L'anisotropie de comportement mécanique et de durabilité de l'alliage est présentée en fil conducteur de ce chapitre, principalement à 650°C et 900°C, avec des caractérisations additionnelles à 750°C et 1100°C. Le comportement mécanique de l'alliage suivant différentes orientations par rapport à la direction de solidification a été comparé avec celui des échantillons monocristallins ayant différentes orientations cristallographiques, mais exactement la même composition chimique.

Les principales conclusions suivantes ont pu être établies à l'issue de ce chapitre:

1. Le comportement en traction monotone est très anisotrope à 650°C pour tous les échantillons à solidification dirigée (DS) et monogranulaires (SX), principalement en considérant la limite d'élasticité et la résistance à la traction. Cela est principalement dû au nombre de systèmes de glissement activés. A 900°C, cette anisotropie est considérablement réduite mais l'alliage présente une sensibilité à la vitesse de déformation prononcée. Son comportement est donc très viscoplastique à cette température. Une ductilité très réduite a été observée pour les échantillons DS testés en sens travers.
2. L'anisotropie des propriétés/durabilité en fluage diminue avec l'augmentation de la température à la fois pour les échantillons DS et SX. Cela est corrélé à la mise en radeaux des

précipités, qui est déjà observée pour de courtes expositions (< 40h) en fluage à 900°C, et qui a comme conséquence une déformation en fluage plus homogène dans la matrice. La forme des courbes de fluage obtenues sont en accord avec celles obtenues d'après la littérature disponibles sur le comportement en fluage des superalliages base Nickel à forte fraction de phase durcissante  $\gamma'$ .

3. La ductilité en fluage est également réduite pour les échantillons DS sollicités en sens travers (typiquement inférieure à 5%). Cela résulte en des durées de vie réduites pour cette direction, indépendamment de la condition de fluage appliquée. Cet effet est encore plus prononcé avec la diminution de la taille de grain. Cette baisse de ductilité induit une rupture prématurée au cours du fluage primaire à basse température/forte contrainte.
4. Les évolutions de déformation en fluage à 750°C en sens traverse ont montré une grande hétérogénéité d'allongement à l'échelle du grain contrairement à celui qui a été observé à 900°C.
5. Le comportement en fatigue LCF à 650°C/ $R\sigma=0,05$  est caractérisé par un rochet cyclique pendant les vingt premiers cycles, puis un comportement macroscopiquement élastique pour le restant de la durée de vie est observé, pour tous les types d'échantillons. A 650°C/  $R\sigma=-1$ , un comportement élastique a été observé à l'exception des essais avec une forte amplitude de contrainte imposée, pour lesquels une forte ouverture plastique en compression a été observée. A 900°C/ $R\sigma=0,05$ , un rochet plastique continu jusqu'à rupture est observé.
6. Les monograins orientés suivant la direction <001> présentent une durée de vie comparable voire meilleure aux échantillons DS sollicités en sens long pour toutes les conditions de fatigue testées. Des sollicitations en sens travers conduisent systématiquement à des durées de vies inférieures, en partie à cause leur plus faible ductilité.
7. A 900°C, l'effet de l'environnement (essais sous air ou sous vide) semblent ne pas affecter la durée de vie en fatigue oligocyclique pour les échantillons DS et SX. Ce point sera ré-analysé plus en détails au chapitre 4.
8. Une lente mise en radeaux des précipités est observée pour tous les types d'échantillon testés en fatigue oligocyclique à 900°C/ $R\sigma=0,05$ .
9. Les essais de fatigue avec temps de maintien à 900°C/ $R\sigma=0,05$  ont montré pour tous les temps de maintien à charge maximale des durées de vie supérieures à leurs équivalents en fluage pur, mais inférieures à leurs références respectives en fatigue pure. Quand le temps de maintien augmente la durée de vie finale chute (à la fois en nombre de cycles et en durée cumulée à charge maximale).
10. L'augmentation du temps de maintien conduit à une vitesse de déformation plastique plus élevée et à une ductilité augmentée. Cela est dû à une mise en radeaux plus prononcée et notamment, à une plus forte augmentation de la largeur des couloirs  $\gamma$ , ce qui facilite l'écoulement viscoplastique de par la chute de la contrainte d'Orowan. Ainsi, la mise en radeaux des précipités  $\gamma'$  peut être vue comme un « endommagement » microstructural.
11. Même si les essais avec temps de maintien sont plus longs et donc restent plus longtemps à haute température, ceux avec un temps de maintien plus court exhibent une microstructure  $\gamma/\gamma'$  plus fine. Cela suggère que l'évolution des précipités  $\gamma'$  est très complexe et sensible à la fois au temps de maintien et au chargement cyclique.

Dans la suite de ce manuscrit, l'analyse du comportement mécanique sera complétée par des analyses à l'échelle de la microstructure, avec un focus sur le développement des fissures et leur propagation pendant les diverses sollicitations mécaniques appliquées. Une attention particulière sera portée sur le rôle de l'oxydation en termes d'amorçage et de propagation des fissures.

## Table of contents (Chapter 3)

3.	Mechanical behavior .....	88
3.1	Introduction.....	88
3.2	Tensile behavior .....	88
3.2.1	Anisotropy effect.....	88
3.2.2	Strain rate effect.....	91
3.3	Creep behavior .....	92
3.3.1	Creep behavior anisotropy.....	92
3.3.2	Microstructure evolutions during creep experiments .....	99
3.3.3	In situ monitoring of creep strain heterogeneities .....	101
3.4	Low-cycle fatigue behavior.....	104
3.5	Dwell-fatigue behavior .....	108
3.6	Conclusions.....	113

## Figures and tables (Chapter 3)

Figure 3.1 - Tensile behavior at $650^{\circ}\text{C}/10^{-3} \text{ s}^{-1}$ of DS200+Hf alloy tested along the longitudinal direction (DS-L), the transverse one (DS-T) for both fine grain (FG) and coarse grain (CG) material in this last case. Results are compared with the $\langle 001 \rangle$ single crystalline specimens of the alloy (SX- $\langle 001 \rangle$ ). .....	89
Figure 3.2 - Tensile behavior at $650^{\circ}\text{C}$ of single crystalline specimens made of MAR-M200+Hf alloy. Note the each specimen is described by its (primary misorientation/secondary misorientation) with respect to the perfect $[001]$ direction in the standard stereographic triangle. ....	90
Figure 3.3 - Tensile behavior at $900^{\circ}\text{C}/10^{-5} \text{ s}^{-1}$ of DS200+Hf alloy tested along the longitudinal direction (DS-L), the transverse one (DS-T) for both fine grain (FG) and coarse grain (CG) material in this last case, and at $45^{\circ}$ of the solidification direction (DS- $45^{\circ}$ ). Results are compared with the $\langle 001 \rangle$ single crystalline specimen of the alloy (SX- $\langle 001 \rangle$ ). ....	91
Figure 3.4 - Variation in tensile behavior at $900^{\circ}\text{C}$ as a function of the strain rate for $\langle 001 \rangle$ MAR-M200+Hf specimen (a) and for DS200+Hf alloy tested along longitudinal direction (b), along transverse direction with coarse grains (c) and along transverse direction with fine grains (d).....	92
Figure 3.5 – Larson-Miller diagrams comparing the creep strength of DS specimens with the $\langle 001 \rangle$ SX specimens (a) and the dependence of creep strength to the crystallographic orientation in SX specimens (b). ....	93
Figure 3.6 - Creep behavior at $750^{\circ}\text{C}/800 \text{ MPa}$ of DS200+Hf alloy tested along the longitudinal direction (DS-L), the transverse one (DS-T) for both fine grain (FG) and coarse grain (CG) material in this last case. Results are compared with the $\langle 001 \rangle$ , $\langle 102 \rangle$ and $\langle 212 \rangle$ single crystalline specimens (SX- $\langle 001 \rangle$ , SX- $\langle 102 \rangle$ and SX- $\langle 212 \rangle$ respectively).....	95
Figure 3.7 – Creep strain rate as a function of the creep strain at $750^{\circ}\text{C}/800 \text{ MPa}$ for DS-L specimen.	95
Figure 3.8 - Anisotropy in creep behavior of DS200+Hf alloy at $900^{\circ}\text{C}/350 \text{ MPa}$ in air/radiant furnace: (a) Creep strain versus time and (b) Creep strain rate versus creep strain. ....	96
Figure 3.9 – Evolution of the minimum creep rate at $900^{\circ}\text{C}$ as a function of the initial applied stress.	97
Figure 3.10 – Evolution of the creep strain to failure at $900^{\circ}\text{C}$ as a function of the initial applied stress. ....	98
Figure 3.11 - Creep behavior anisotropy of MAR-M200+Hf SX alloy at $900^{\circ}\text{C}/300 \text{ MPa}$ . ....	98
Figure 3.12 - Creep behavior at $1100^{\circ}\text{C}/70 \text{ MPa}$ of DS200+Hf alloy tested along the longitudinal direction (DS-L), the transverse one (DS-T) for both fine grain (FG) and coarse grain (CG) material in this last case. Results are compared with the $\langle 001 \rangle$ single crystalline specimen of the alloy (SX- $\langle 001 \rangle$ ). ....	99
Figure 3.13 - $\gamma/\gamma'$ microstructure after creep tests up to failure performed at (a) $750^{\circ}\text{C}/800 \text{ MPa}$ , (b) $900^{\circ}\text{C}/400 \text{ MPa}$ , (c) $900^{\circ}\text{C}/250 \text{ MPa}$ and (d) $1100^{\circ}\text{C}/70 \text{ MPa}$ (L type specimens). Arrows in the insert in (b) show remaining $\gamma$ matrix islands trapped in the $\gamma'$ precipitates.....	100
Figure 3.14 - Variation in $\gamma'$ directional coarsening according to each grain orientation after creep testing at $900^{\circ}\text{C}/350 \text{ MPa}$ for 86.4 hours in a coarse grain specimen, along transverse direction. ....	101
Figure 3.15 - Creep strain heterogeneity during transverse loading, at $750^{\circ}\text{C}/800 \text{ MPa}$ (a) and $900^{\circ}\text{C}/400 \text{ MPa}$ (b). Note that the color code used in the EBSD maps of the gauge surfaces presented in this figure refers to the loading axis. The grains in which creep strain evolutions are presented have been identified on each EBSD map (grains G1, G2, G3 and G4). The dotted circle in (a) highlights the creep acceleration once the main crack has been developed. ....	102
Figure 3.16 - Creep strain heterogeneity during transverse loading, at $750^{\circ}\text{C}/700 \text{ MPa}$ . Note that the color code used in the EBSD maps of the gauge surfaces presented in this figure refers to the loading axis. The grains in which creep strain evolutions are presented have been identified on each EBSD map (grains G1, G2 and G3). ....	103

Figure 3.17 – Cyclic behavior for a $\sim\langle 001 \rangle$ SX specimen tested at $650^\circ\text{C}/R\sigma=-1/\sigma_{\max}=-\sigma_{\min}=885$ MPa showing the 1 <sup>st</sup> cycle and the first fourth of the 2 <sup>nd</sup> one, as well as the 6 <sup>th</sup> one.....	104
Figure 3.18 – Typical cyclic behavior under $R\sigma=0.05/f=0.5\text{Hz}$ at $650^\circ\text{C}$ (a,b) and at $900^\circ\text{C}$ (c,d), whatever the specimen type. The tests presented in (a,b) and (c,d) have respectively been performed for a DS-L specimen at $\sigma_{\max}=1050$ MPa and for a $\langle 001 \rangle$ -SX specimen at $\sigma_{\max}=520$ MPa. ....	105
Figure 3.19 – Typical $\gamma/\gamma'$ microstructure within a primary dendrit arm after a LCF test at $900^\circ\text{C}/R\sigma=0.05/\sigma_{\max}=520$ MPa using a $\sim\langle 001 \rangle$ SX specimen ( $Nf=114,608$ cycles/Test duration $\sim 65$ hours).....	106
Figure 3.20 - LCF results at $650^\circ\text{C}/R\sigma=0.05$ and $R\sigma=-1/f=0.5$ Hz. ....	106
Figure 3.21 - LCF results at $650^\circ\text{C}/R\sigma=0.05/f=0.5$ Hz with a normalization of $\sigma_{\max}$ by the yield stress (YS) (a) or by the ultimate tensile stress (UTS) (b). ....	107
Figure 3.22 - LCF results at $900^\circ\text{C}/R\sigma=0.05/f=0.5$ Hz. ....	108
Figure 3.23 – Effect of the dwell time at maximum stress ( $\sigma_{\max}$ ) on the inelastic elongation during dwell-fatigue tests at $900^\circ\text{C}/\sigma_{\max}=400$ MPa/ $R\sigma=0.05$ for $\sim\langle 001 \rangle$ SX specimens (a), for DS specimens loaded along longitudinal (c) and transverse (d) directions and at $900^\circ\text{C}/\sigma_{\max}=520$ MPa/ $R\sigma=0.05$ for $\sim\langle 001 \rangle$ SX specimens (b). Results have been compared with the pure creep behavior reference at $900^\circ\text{C}/400$ MPa for each kind of specimen. Note the X-axis is the time spent at maximum applied stress $\sigma_{\max}$ . ....	109
Figure 3.24 - Comparison LCF and dwell-fatigue (DF) results for each type of specimens at $900^\circ\text{C}/R\sigma=0.05$ for different dwell times.....	110
Figure 3.25 - Typical $\gamma/\gamma'$ microstructure observed at the end of dwell-fatigue tests at $900^\circ\text{C}/R\sigma=0.05/\sigma_{\max}=400$ MPa for a $\sim\langle 001 \rangle$ SX specimen/ $\Delta t = 300$ s/ $Nf = 1,834$ cycles (a); a $\sim\langle 001 \rangle$ SX specimen/ $\Delta t = 10$ s/ $Nf = 59,139$ cycles (b); a DS-L specimen/ $\Delta t = 300$ s/ $Nf = 2,351$ cycles (c); a DS-L specimen/ $\Delta t = 10$ s/ $Nf = 71,038$ cycles (d); a DS-L specimen/ $\Delta t = 1$ s/ $Nf = 748,352$ cycles (e); a DS-T specimen/ $\Delta t = 300$ s/ $Nf = 1,292$ cycles (f); a DS-T specimen/ $\Delta t = 10$ s/ $Nf = 30,728$ cycles (g) and a DS-T specimen/ $\Delta t = 1$ s/ $Nf = 359,020$ cycles (h). ....	111
Figure 3.26 – Distributions of $\gamma$ channel width (a-d) and $\gamma'$ thickness (e-h) after dwell fatigue tests at $900^\circ\text{C}/\sigma_{\max} = 400$ MPa/ $R\sigma=0.05$ using DS specimens loaded along longitudinal direction. Note that the dwell time ( $\Delta t$ ) and total time at $\sigma_{\max}$ have been added on each plot to ease the reading and that pure creep tests are identified by a dwell time $\Delta t=\infty$ .....	112
Figure 3.27 - Comparison of mean $\gamma'$ thickness and mean $\gamma$ channel width at the end of dwell-fatigue tests at $900^\circ\text{C}/\sigma_{\max} = 400$ MPa/ $R\sigma=0.05$ using DS specimens loaded along longitudinal direction and $\sim\langle 001 \rangle$ SX specimens and compared to their respective counterparts at the end of creep tests. Note that their creep results have been artificially positionned at a dwell time $\Delta t = 2000$ s to ease the comparison. ....	113

## 3. Mechanical behavior

### 3.1 Introduction

This chapter is devoted to the mechanical behavior at high temperature of DS200+Hf alloy in tension, creep, low-cycle fatigue (LCF) and load-controlled dwell-fatigue (or cyclic creep). The tests were performed along the solidification direction, the transverse direction and, in some cases, at 45° of the solidification direction. Along transverse direction, the effect of the grain size has also been considered by machining specimens both in the fine grains (FG) and coarse grains (CG) areas of the plate (see Figure 2.1, chapter 2). The properties of DS specimens have been systematically compared to the ones of single crystalline (SX) specimens having the same chemical composition. The main objective of this chapter concerns the stress-strain relationships, as well as the creep, LCF and dwell-fatigue behavior.

Tensile properties have been characterized at 650°C and 900°C, using different strain rates, especially at 900°C. Deeper investigations of the creep behavior and durability were carried out using tests at 750°C, 900°C and 1100°C, with a special focus on the intermediate temperature. Investigations of the creep strain heterogeneities at the grain scale in a DS loaded along transverse directions were also carefully done to investigate the variation in local strain across grain boundaries.

LCF tests in air were performed at 650°C and 900°C, using a sinusoidal wave-form, with a 0.5 Hz frequency under load-controlled mode with  $R\sigma=0.05$  for both temperatures and also with  $R\sigma=-1$  at 650°C. The main aim of such tests was to investigate the cyclic behavior at both temperatures and to identify the main damage mechanisms that will be further considered in the next chapter.

Finally, creep-fatigue interactions will be presented by analyzing the dwell-fatigue behavior. The tests were performed at 900°C with dwell times of 1, 10 and 300 seconds. A special attention will be paid to both strain rate evolution and strain to failure as a function of dwell time at maximum load. Moreover, the morphological evolution of the  $\gamma/\gamma'$  microstructure as a function of dwell time will be analyzed and compared to the one observed under pure creep conditions.

### 3.2 Tensile behavior

#### 3.2.1 Anisotropy effect

All macroscopic tensile properties determined at 650°C and 900°C in terms of yield stress defined at 0.2% plastic elongation (YS 0.2%), ultimate tensile stress (UTS), strain at failure (A%) and reduction in load bearing section (Z%) are listed in Appendix 1. According to Figure 3.1, DS200+Hf alloy shows a strong tensile anisotropy at 650°C in terms of yield stress (YS) and ultimate tensile stress (UTS) when changing the loading direction with respect to the solidification direction. This difference in yield stress at 0.2% can be as large as  $\sim 200$  MPa comparing  $\langle 001 \rangle$  single crystalline properties to the properties along transverse direction. At this temperature, it is observed that the tensile ductility along transverse direction is slightly higher (between 6 and 8% of strain at failure) than the one obtained along longitudinal direction (between 3 and 6%) or for the  $\langle 001 \rangle$  single crystalline specimen ( $\sim 5\%$  of strain at failure).

This huge tensile anisotropy observed at 650°C is better understood by looking at the evolution of the tensile properties as a function of the crystal orientation for SX specimens. It is indeed observed in Figure 3.2 that the primary misorientation with respect to the perfect  $\langle 001 \rangle$  crystallographic orientation deeply affects tensile properties, especially for a misorientation greater than 20°.

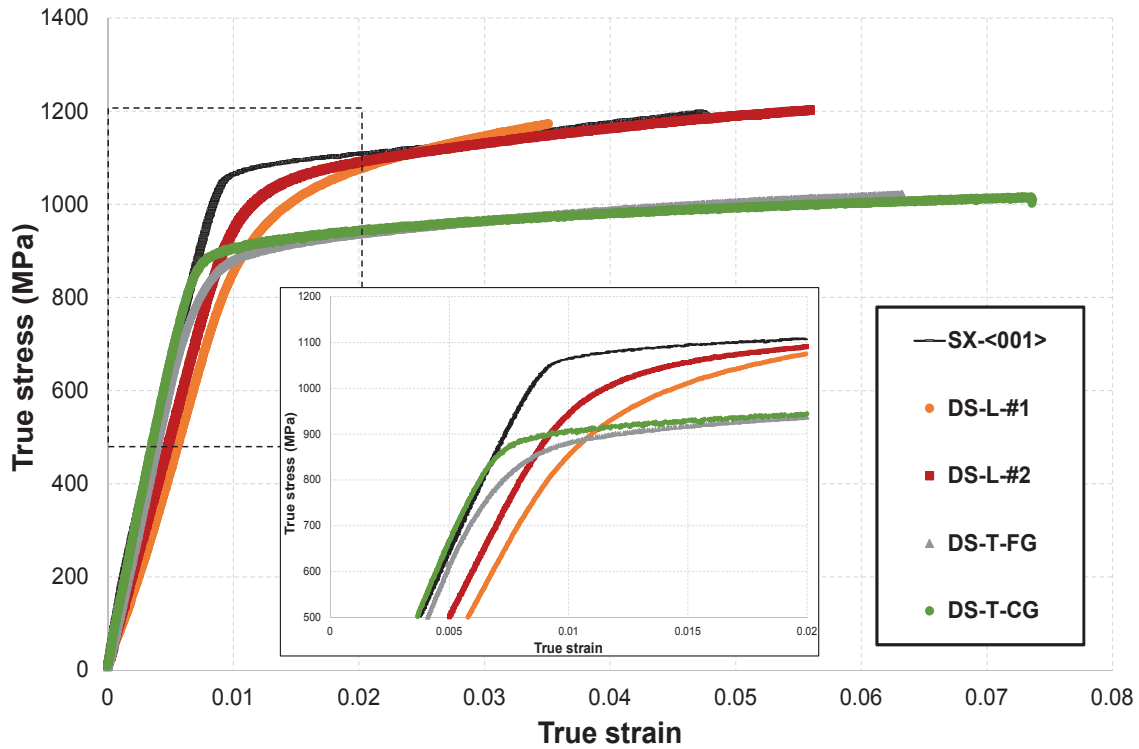


Figure 3.1 - Tensile behavior at  $650^{\circ}\text{C}/10^{-3} \text{ s}^{-1}$  of DS200+Hf alloy tested along the longitudinal direction (DS-L), the transverse one (DS-T) for both fine grain (FG) and coarse grain (CG) material in this last case. Results are compared with the  $\langle 001 \rangle$  single crystalline specimens of the alloy (SX- $\langle 001 \rangle$ ).

The tensile behavior is almost perfectly plastic for the SX specimen having a high primary misorientation (e.g. a primary misorientation of  $24.5^{\circ}$ , green curve in Figure 3.2) while a progressive strain hardening is observed for the other curves closer to a  $\langle 001 \rangle$  crystallographic orientation. The specimen with a  $24.5^{\circ}$  primary misorientation has, as expected, a high Young's modulus, but about 250 MPa drop in yield stress compared to the nearly perfect  $\langle 001 \rangle$  SX specimen. Such an almost perfect plastic behavior results from a single slip activity while the other specimens are oriented favorably for multiple slip activation that favors interactions between slip systems inducing strain hardening.

Then at  $650^{\circ}\text{C}$  (Figure 3.1 and Figure 3.2), the crystal orientation is predominant in controlling the yield stress and ultimate tensile strength magnitudes. Tensile properties at this temperature are mainly controlled by the number of active slip systems and by their respective Schmid factor, as suggested by Mackay et al. [1]. This factor is defined by the following expression:

$$\tau = \frac{F}{S_0} \cos \theta \cos \alpha$$

Where  $\cos \theta \sin \alpha$  is the Schmid factor,  $\tau$  is the resolved shear stress in the slip direction of the most heavily loaded  $\{111\}$  plane necessary to initiate slip in a grain,  $\frac{F}{S_0}$  is the magnitude of the applied tensile stress,  $\theta$  is the angle between the normal of the slip plane and the direction of the applied force, and  $\alpha$  is the angle between the slip direction and the direction of the applied force. Indeed, Ni-based single crystals with a high Schmid factor favorably oriented for single slip exhibit lower tensile strength and higher ductility. Contrarily, those corresponding to a multiple slip configuration with lower Schmid factors exhibit a higher tensile strength and a lower ductility, as presented previously in the literature review section. The evolution of the ductility at  $650^{\circ}\text{C}$  observed in Figure 3.1 and Figure 3.2 seems to be in good agreement with these previous characterizations.



It is worth noting that the elastoplastic transition for DS-L is smoothed compared with the single crystal behavior, whatever the orientation (Figure 3.1). Indeed, columnar grains are not oriented perfectly along the  $\langle 001 \rangle$  direction the way one individual grain plasticized may affect the surrounding one. This effect has been taken into account in the twin PhD study of Florent Coudon using a so-called “intergranular hardening” matrix [2]. In comparison, a very sharp elastoplastic transition is obtained for DS-T specimens (Figure 3.1). Along this loading direction, yielding first occurs in the grain most favorably oriented for slip, leading to a yielding behavior very similar to SX specimens (see Figure 3.2).

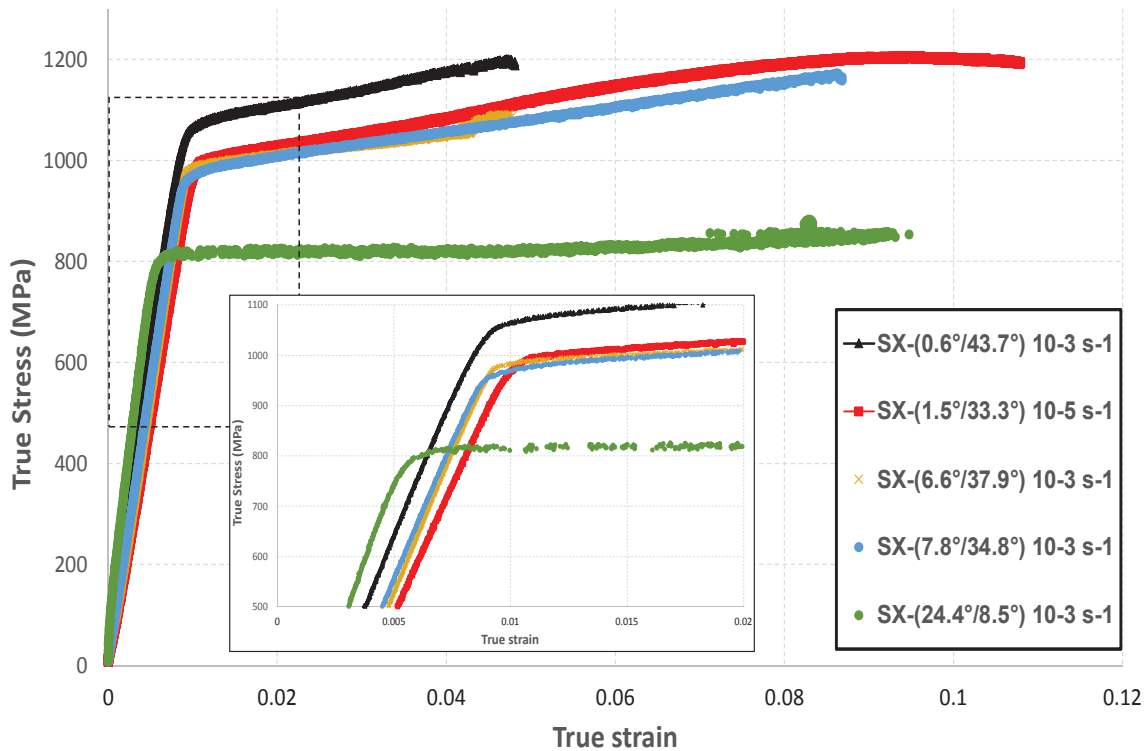


Figure 3.2 - Tensile behavior at 650°C of single crystalline specimens made of MAR-M200+Hf alloy. Note the each specimen is described by its (primary misorientation/secondary misorientation) with respect to the perfect  $[001]$  direction in the standard stereographic triangle.

Figure 3.3 presents the tensile behavior at 900°C with a slow tensile strain rate of  $10^{-5} \text{ s}^{-1}$ . The effect of the strain rate will be presented in the next sub-section. As a first observation, yielding at this temperature is more progressive than for tests performed at 650°C. The first strain hardening is systematically followed by a more or less progressive softening. This softening is associated to the viscoplastic activity of the alloy as well as to a progressive degradation of the  $\gamma/\gamma'$  microstructure (i.e.  $\gamma'$  coarsening and/or  $\gamma'$  rafting) according to Desmorat et al. [3].

Under these conditions, DS-L and  $\langle 001 \rangle$  SX specimens have almost the same tensile behavior (Figure 3.3) and a considerably reduced tensile anisotropy in terms of yield stress is also observed for DS-T, with a variation ranging from 549 MPa (transverse loading, fine grain alloy) to 596 MPa ( $\sim \langle 001 \rangle$  SX). Such a tensile behavior mainly results from a plastic activity within the  $\gamma$  matrix, with dislocations climb or dislocations precipitate by-passing as the main deformation mechanisms [4]. It is hence mainly dependent on the precipitate volume fraction and initial size, which is almost the same for each specimen.

Finally, the main tensile characteristic affected by the loading direction is the strain at failure. The strain at failure is above 20% along longitudinal direction and for SX specimens while it is around 4-5%

along transverse direction and around 14% at 45 degrees of the solidification direction. This huge anisotropy will be better understood in chapter 4 taking into account damage mechanisms. Finally, it is also worth mentioning that the ultimate tensile stress variations measured in these experiments will appear as a key parameter to rationalize the minimum creep strain rate anisotropy. This will also be better described in chapter 4.

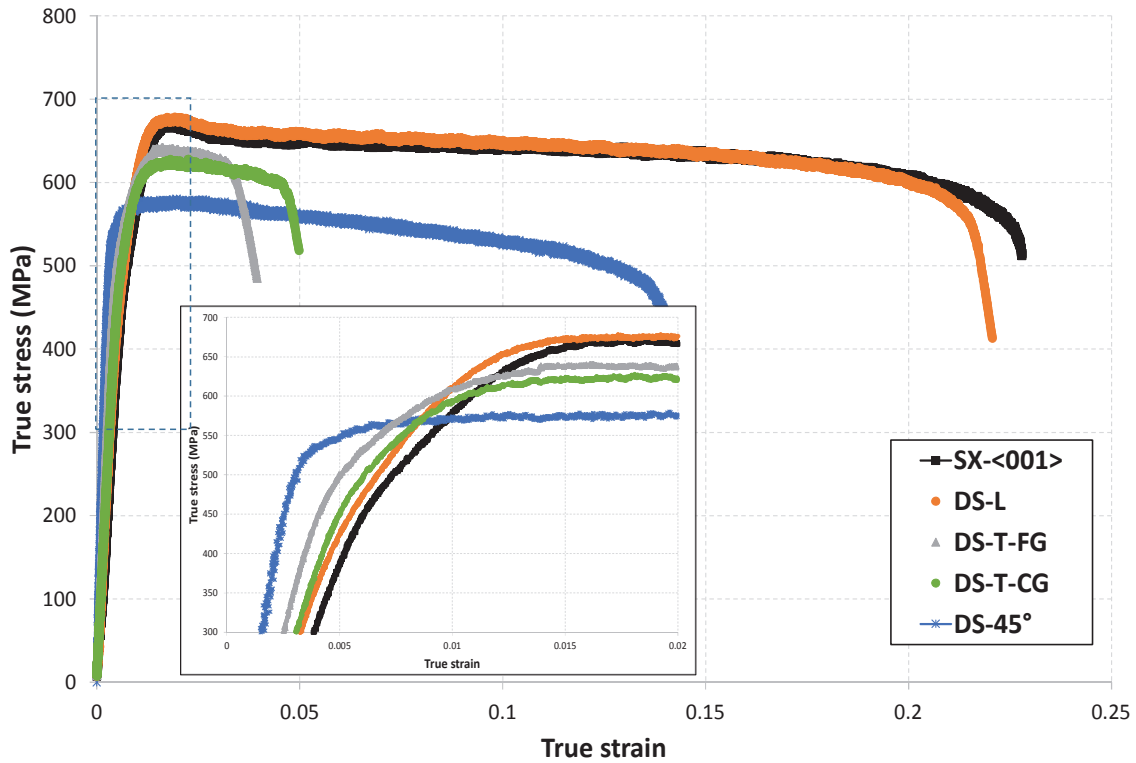


Figure 3.3 - Tensile behavior at  $900^{\circ}\text{C}/10^{-5}\text{ s}^{-1}$  of DS200+Hf alloy tested along the longitudinal direction (DS-L), the transverse one (DS-T) for both fine grain (FG) and coarse grain (CG) material in this last case, and at  $45^{\circ}$  of the solidification direction (DS- $45^{\circ}$ ). Results are compared with the  $\langle 001 \rangle$  single crystalline specimen of the alloy (SX- $\langle 001 \rangle$ ).

### 3.2.2 Strain rate effect

The effect of strain rate on the tensile behavior at  $650^{\circ}\text{C}$  has been investigated by performing tensile tests in the  $[10^{-3} - 10^{-5}\text{ s}^{-1}]$  range using a  $\langle 001 \rangle$  type SX specimen. Figure 3.2 shows a decrease in YS by nearly 75 MPa reducing the strain rate from  $10^{-3}\text{ s}^{-1}$  to  $10^{-5}\text{ s}^{-1}$  and the elastoplastic transition type does not change. This strain rate dependence of the tensile behavior is weak at this temperature in comparison to the effect of loading direction (see previous section). Hence, no further characterization of the tensile properties strain rate dependence has been undertaken at this temperature.

For tests performed at  $900^{\circ}\text{C}$ , Figure 3.4 shows when the strain rate decreases, yield and ultimate tensile stresses decrease for all specimen types, with almost the same proportions (note that the Y-scale is the same in all the plots of Figure 3.4). The YS decreases in the 200-250 MPa range by decreasing the tensile strain rate by 2 orders of magnitude. A similar variation is observed for the ultimate tensile stress. These YS and UTS evolutions are more marked than at  $650^{\circ}\text{C}$ . This is a clear indication of the viscoplastic behavior of the alloy at this temperature. To highlight this character, the following section will present the creep behavior anisotropy in deeper details at this specific temperature, in addition to the ones observed at  $750^{\circ}\text{C}$  and  $1100^{\circ}\text{C}$ .

A substantial increase of the ductility (strain at failure) appears with decreasing strain rate for  $\langle 001 \rangle$  SX specimens as well as for DS specimens loaded along longitudinal direction and along transverse

direction for a coarse grain structure. However, no clear correlation can be established between the tensile strain rate and the ductility along the transverse direction for fine grain DS specimen.

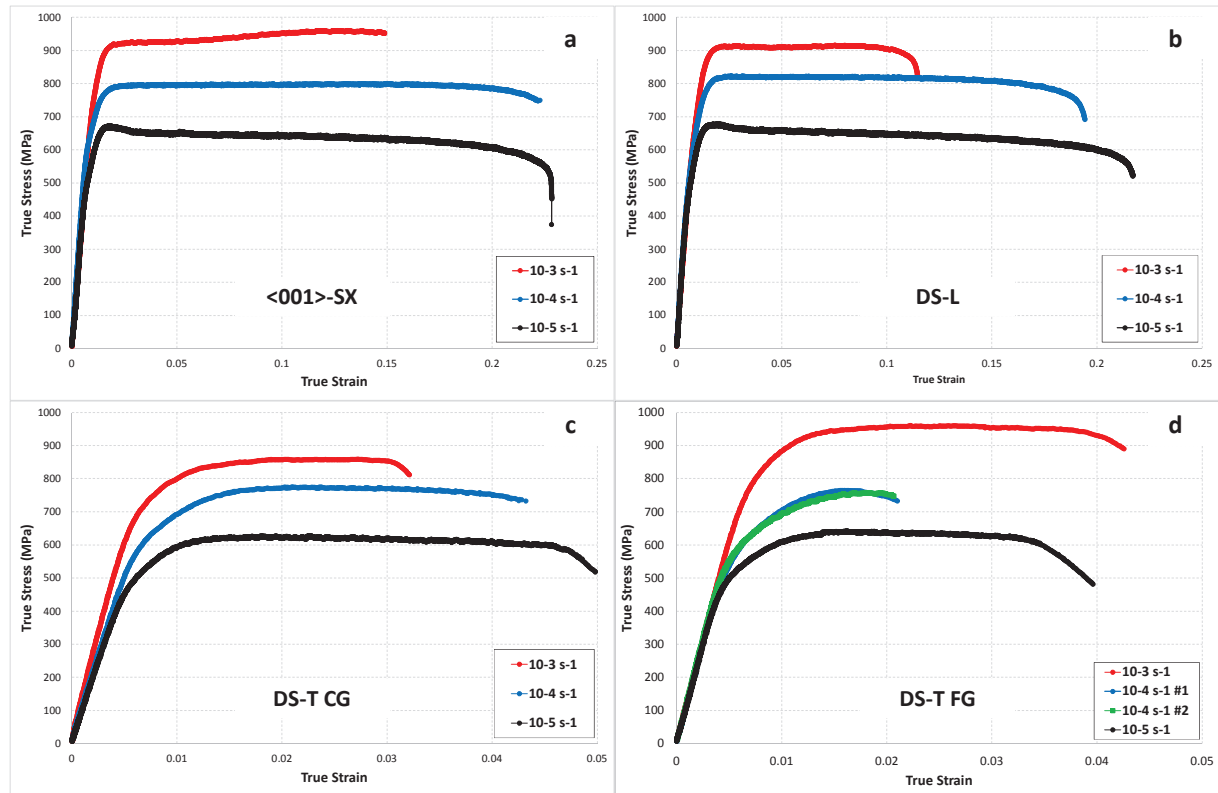


Figure 3.4 - Variation in tensile behavior at 900°C as a function of the strain rate for <001> MAR-M200+Hf specimen (a) and for DS200+Hf alloy tested along longitudinal direction (b), along transverse direction with coarse grains (c) and along transverse direction with fine grains (d)

### 3.3 Creep behavior

#### 3.3.1 Creep behavior anisotropy

Creep tests were performed at 900°C (250 MPa, 300 MPa, 350 MPa, 400 MPa and 520 MPa), 750°C (700 MPa, 750 MPa and 800 MPa) and 1100°C (70 MPa). A deeper attention has been paid to the creep conditions tests at 900°C as it can be analyzed looking at the huge database generated at this specific temperature (see Appendix 2 for creep results using massive specimens and Appendix 3 for creep results using thin-walled specimens). Figure 3.5 presents the Larson-Miller diagrams summarizing the relative creep strength along different orientations of DS specimens compared to the <001> SX specimens (Figure 3.5(a)) as well as the effect of the crystallographic orientation on the creep strength for SX specimens (Figure 3.5(b)). It is here worth mentioning that all creep results presented in these Larson-Miller diagrams were obtained using a creep rig equipped with a radiant furnace. In this figure, the Larson-Miller Parameter (LMP) is defined as:

$$LMP = (T[°C] + 273) \times (\text{Log}_{10}(\text{Creep life}[\text{Hours}]) + 20)$$

These diagrams hence compare the creep strength of each specimen in terms of time to failure, without any direct consideration of the creep strain rate.

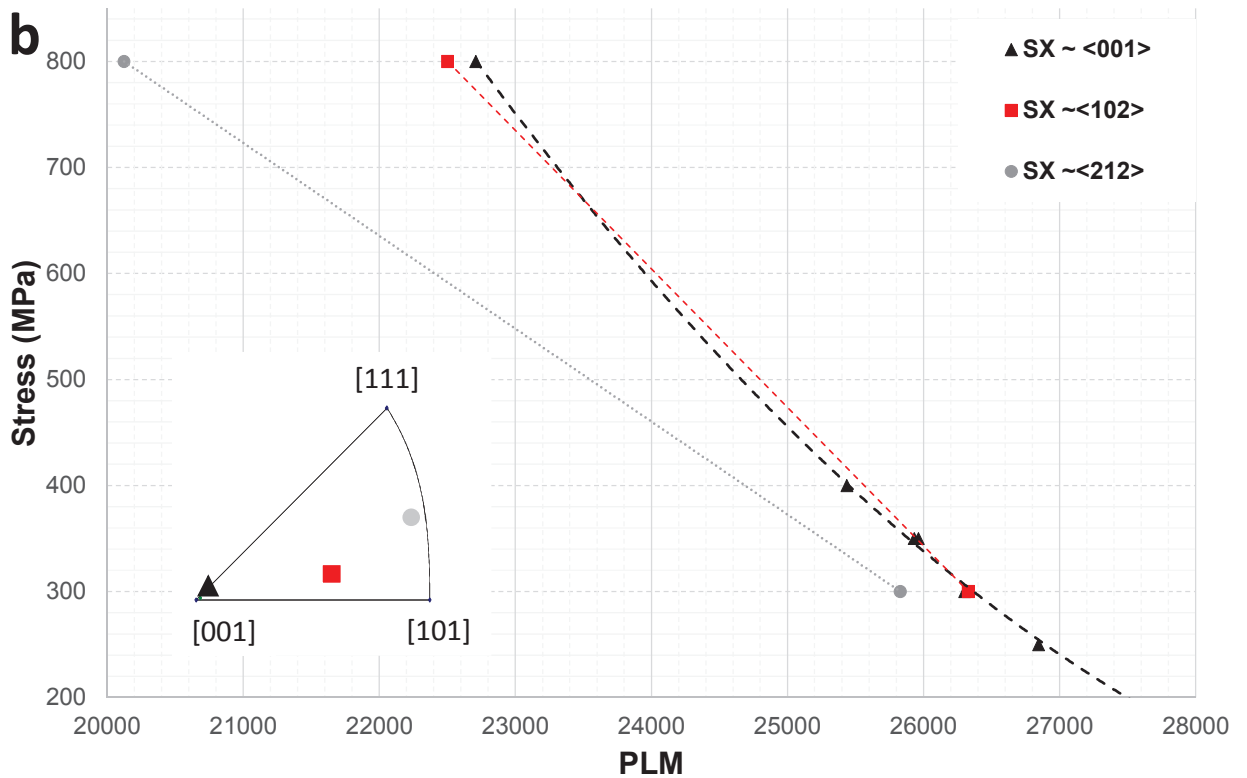
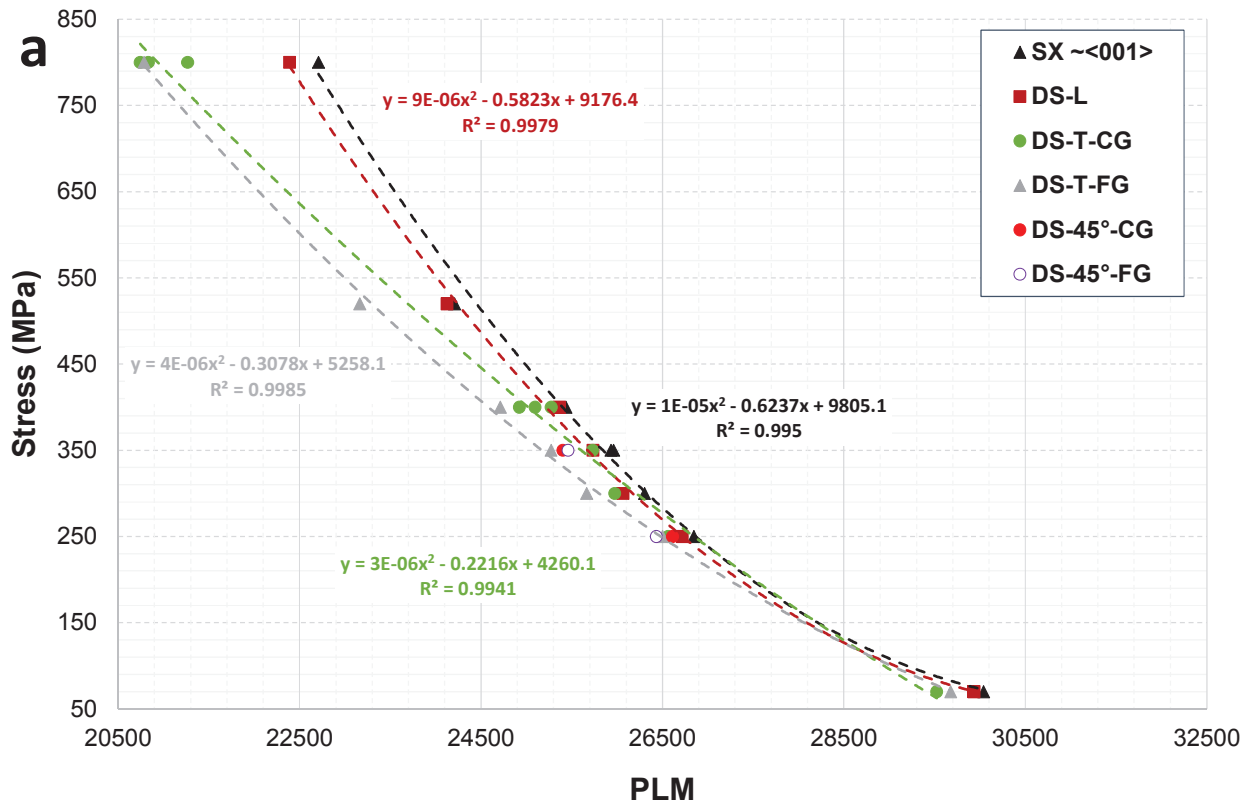


Figure 3.5 – Larson-Miller diagrams comparing the creep strength of DS specimens with the <001> SX specimens (a) and the dependence of creep strength to the crystallographic orientation in SX specimens (b).

The Larson-Miller plots (Figure 3.5) show that the creep life anisotropy of MAR-M200 alloy increases at lower temperatures (i.e. for high applied stresses) and is greatly reduced at very high temperature. This is in good agreement with past studies on single crystal alloys [5-7]. The creep testing conditions covers complex possible interactions between oxidation,  $\gamma/\gamma'$  microstructure degradation or anisotropy effects. The following sections attempt to separate these different contributions.

#### 3.3.1.1 Creep behavior at 750°C

Several creep experiments have been performed at 750°C/800 MPa (Figure 3.6). The creep curves at 750°C/800 MPa exhibit the classical three stages of creep deformation for DS-L, DS-T and <001> SX specimens. Under this low temperature/high stress creep condition, a large primary creep strain amplitude up to 4-5% appears along longitudinal direction or for the <001> SX specimens (see Figure 3.6). This behavior is typical for close-to-<001>-oriented Ni-based SX submitted to high applied stress conditions, typically greater than 500 MPa [8-10]. Such a kind of creep behavior results from the dissociation of matrix dislocations, resulting in the activity of  $\{111\}<112\}$  type slip systems, involving extended shearing of  $\gamma/\gamma'$  microstructure under the form of dislocation ribbons. This type of creep behavior has recently been revisited and termed as “double minimum creep rate” by X. Wu et al. [11] what could also be verified in our experiments, as shown in Figure 3.7 for DS-L specimen. Under this creep condition, DS specimens loaded along transverse direction fail during the primary creep stage without any evidence of tertiary creep (see insert in Figure 3.6). Their creep behavior and life are scattered, especially in the coarse grain areas of the plates. This very surprising creep behavior at the macroscopic scale is probably due to the intrinsic lack of high temperature ductility of DS specimen under transverse direction under such a creep condition [12]. This will be investigated in deeper details in chapter 4 to get a better understanding of the crack initiation mechanism. Specific experiments using local strain measurements (either strain markers within each grain or a DIC technique - EBSD analyzes). These experiments will also be introduced in a subsequent sub-section of the chapter with the aim to highlight the heterogeneity in creep deformation at the grain scale.

Figure 3.6 also shows the creep performances of MAR-M200+Hf SX specimens oriented far away from the perfect <001> crystallographic orientation. These specimens termed as <102> and <212> in Figure 3.6 have exactly the same orientation than specimens K and B (respectively) tested at 900°C/300 MPa (see further Figure 3.11). The crystallographic orientation has clearly a huge impact on the creep properties at 750°C/800 MPa. Indeed, the <212> SX specimen does not present any hardening and, after a short incubation period of nearly 2 minutes, it failed in less than 30 minutes (blue curve at the extreme left in Figure 3.6). Such a creep behavior is in good agreement with the well-known anisotropy in creep behavior and life at low temperature and high applied stress as seen in the literature review [5, 6, 13]. The <102> SX specimen performs well in terms of strain rate and creep life (see Figure 3.6 and Appendix 2). It is characterized by the absence of a marked primary creep, probably since its orientation leads to a low Schmid factor for the activation of any  $<112\>\{111\}$  slip and then favors  $<110\>\{111\}$  type matrix slip.

Considering all creep tests included in Figure 3.6, a creep life anisotropy factor higher than 300 is obtained between the strongest and the weakest specimens (i.e. <001> and <212> specimens respectively) and a factor of nearly 40 is obtained considering only DS specimens. Although oxidation favors grain boundary crack initiation and subsequent propagation (as it will be shown and discussed in the next chapter), it is observed that the largest variation in creep life is obtained at 750°C (see Figure 3.5(a)), where the impact of oxidation on the damage process can be ruled out. At this temperature, the anisotropy in creep life mainly results from the differences in creep behavior at the grain scale (differences in creep strain rate), as well as the differences in local stress field especially

close to grain boundaries and the ability for grain rotation, as proposed by Stinville et al. [14]. This will be presented in deeper details in a next sub-section (paragraph 3.3.3).

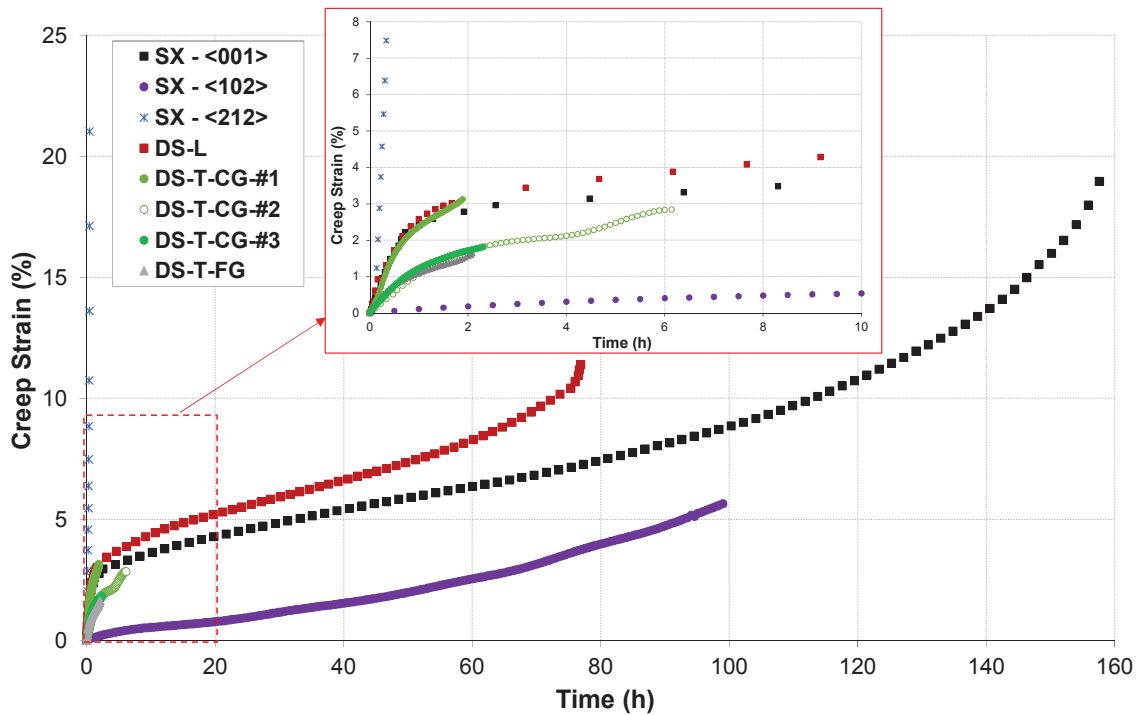


Figure 3.6 - Creep behavior at 750°C/800 MPa of DS200+Hf alloy tested along the longitudinal direction (DS-L), the transverse one (DS-T) for both fine grain (FG) and coarse grain (CG) material in this last case. Results are compared with the <001>, <102> and <212> single crystalline specimens (SX-<001>, SX-<102> and SX-<212> respectively).

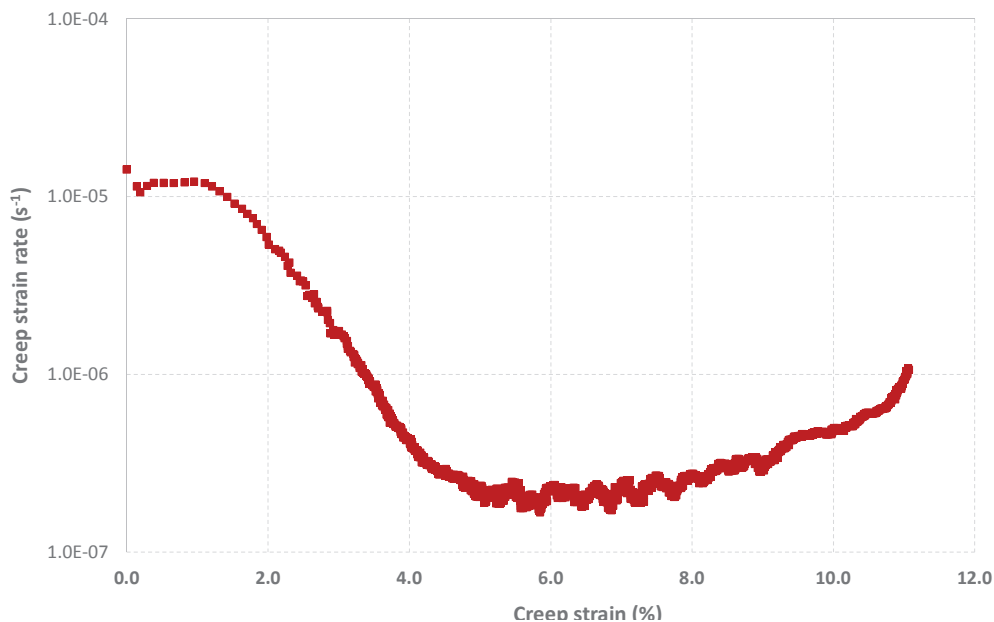


Figure 3.7 – Creep strain rate as a function of the creep strain at 750°C/800 MPa for DS-L specimen.

### 3.3.1.2 Creep behavior at 900°C

Most of the creep tests have been performed at 900°C, for industrial applications reasons. As observed in Figure 3.8, the creep curves at 900°C/350 MPa are characterized by a fast and limited primary creep stage ending for a creep strain between 0.5 and 1%. This short primary creep stage is more clearly

visible in Figure 3.8(b) where the creep strain rate is plotted as a function of the creep strain. Almost no secondary creep stage is present in these conditions and, at the end of the primary creep, a continuous increase of the creep strain rate is observed up to failure. This tertiary creep stage is better highlighted by the Figure 3.8(b). It occupies most of the creep time (nearly 90% of the creep time for DS-L and SX specimens).

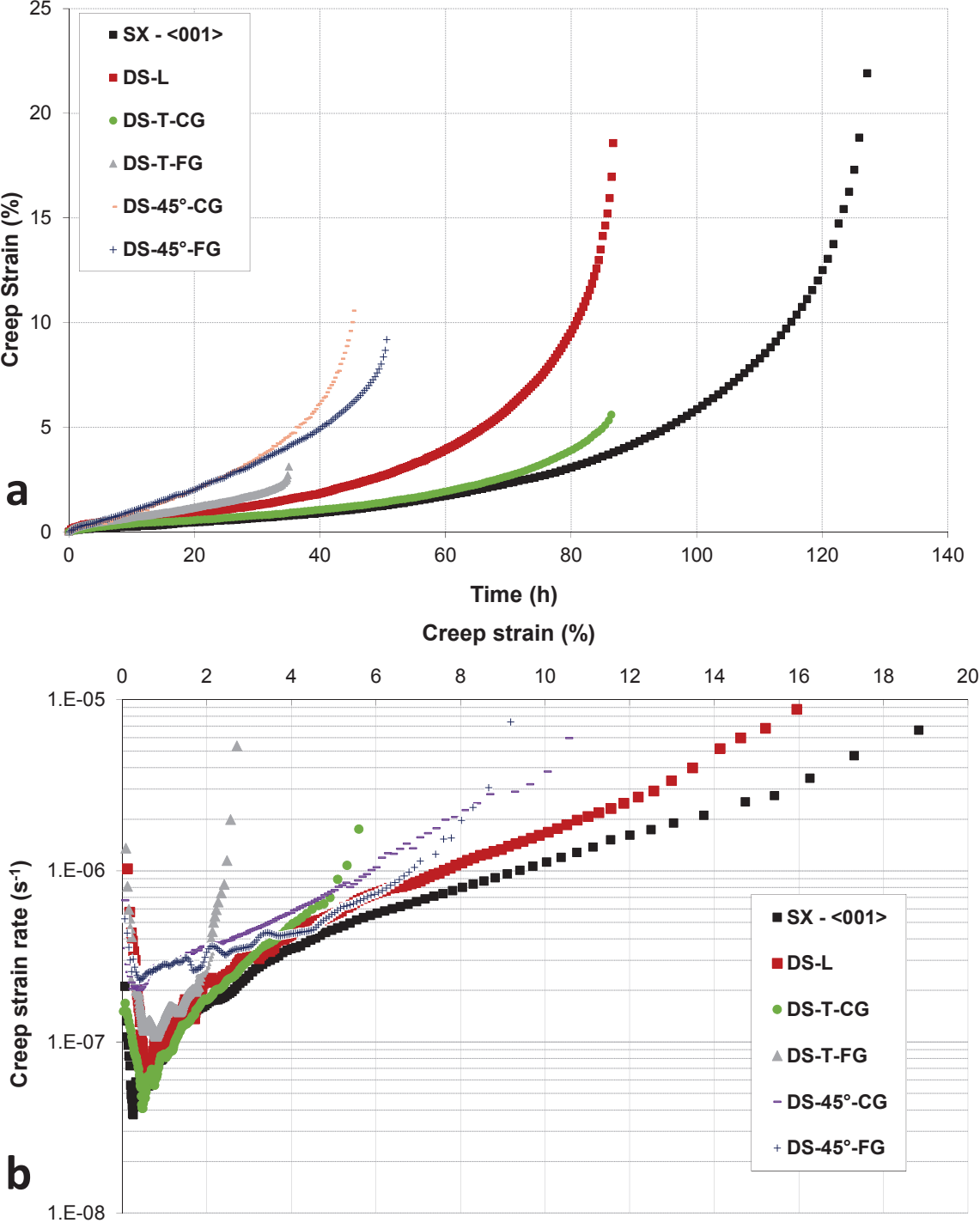


Figure 3.8 - Anisotropy in creep behavior of DS200+Hf alloy at 900°C/350 MPa in air/radiant furnace: (a) Creep strain versus time and (b) Creep strain rate versus creep strain.

This typical creep behavior has been established for all creep conditions at 900°C (i.e. for applied stresses of 250 MPa, 300 MPa, 350 MPa, 400 MPa and 520 MPa) and the effect of the applied stress magnitude is only characterized in terms of primary creep strain amplitude and minimum creep strain rate. Indeed, a higher primary creep strain is generally observed upon increasing the applied stress magnitude. According to Figure 3.9, the minimum creep rate obey to a power-law dependence to the initial applied stress in a very satisfying way according to the coefficients of correlation, whatever the specimen type. It hence means that a Norton's law approach will be a good candidate to model the creep behavior as confirmed in the next chapter. As a surprising result from the plot of Figure 3.9, there is a very weak dependence of the minimum strain rate to the specimen type, since all the results are almost stacked within one single trend. This kind of creep behavior is characterized by both a weak dependence of the minimum creep rate to the loading direction as well as no secondary creep and a very long tertiary creep stage (in which a continuous increase of the creep rate is observed). Such a behavior is present when a continuous degradation of the  $\gamma/\gamma'$  microstructure occurs during the creep deformation, under the form of a slow  $\gamma'$  rafting, followed by the so-called  $\gamma/\gamma'$  topological inversion [3, 15-17].

The main effect of the loading direction at this temperature, is a reduced ductility along transverse direction in comparison to DS-L and SX specimens (see Figure 3.8(a) and Figure 3.8(b)), especially for fine grain specimens having the lower creep lives. It has been verified for all creep conditions investigated at 900°C (see Figure 3.10). It will be shown in chapter 4 that the reason associated to the lower ductility along transverse direction is a change in fracture mode, from a purely ductile and transgranular mode for DS-L and SX specimens, to an intergranular mode for DS-T specimens. The ductility of specimens loaded at 45° of the solidification direction is in between DS-L and DS-T specimens, with a fracture mode also intergranular.

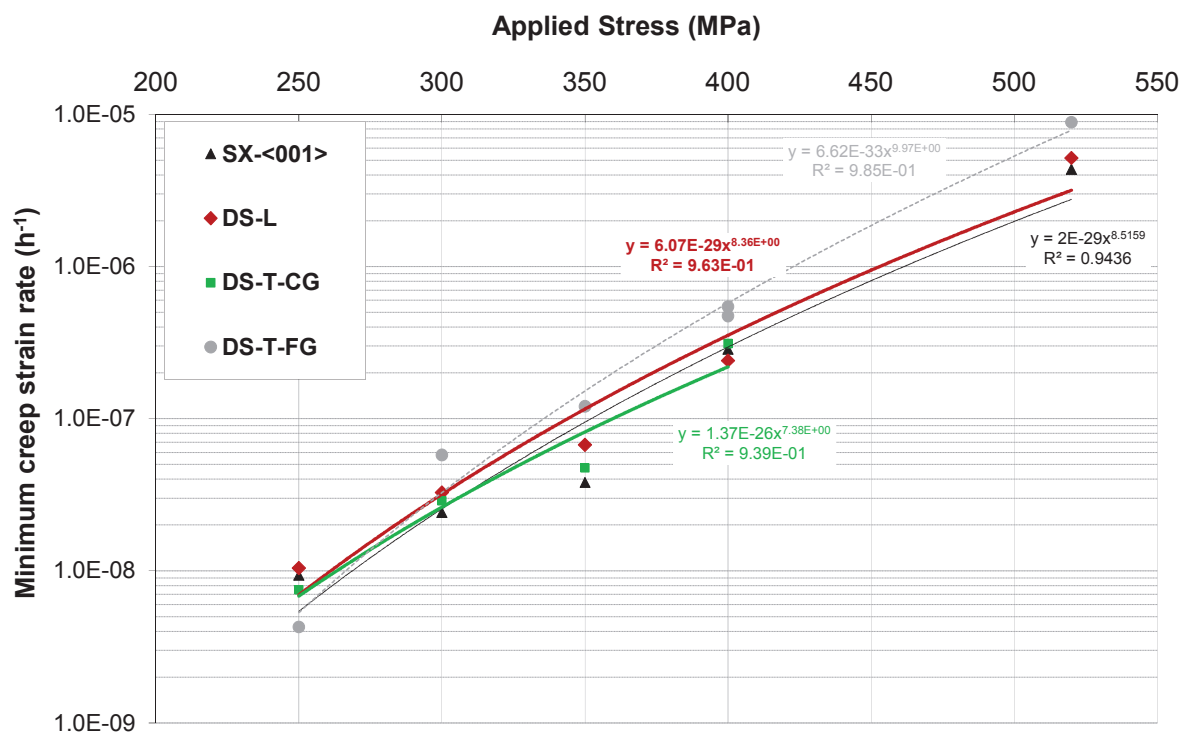


Figure 3.9 – Evolution of the minimum creep rate at 900°C as a function of the initial applied stress.



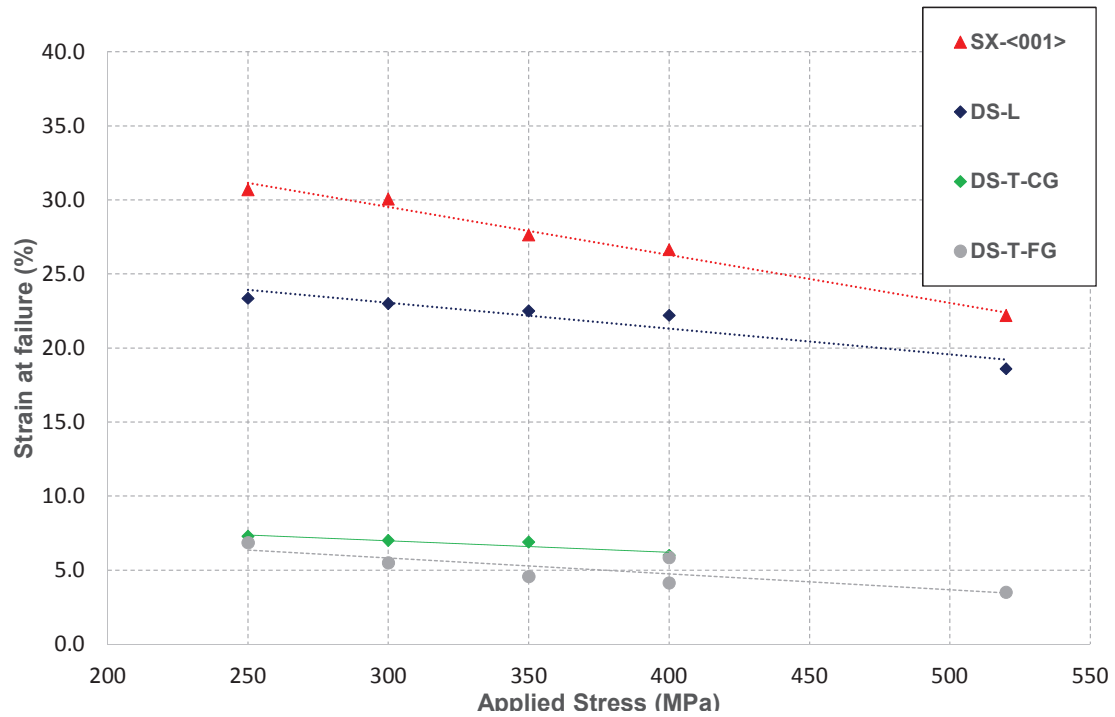


Figure 3.10 – Evolution of the creep strain to failure at 900°C as a function of the initial applied stress.

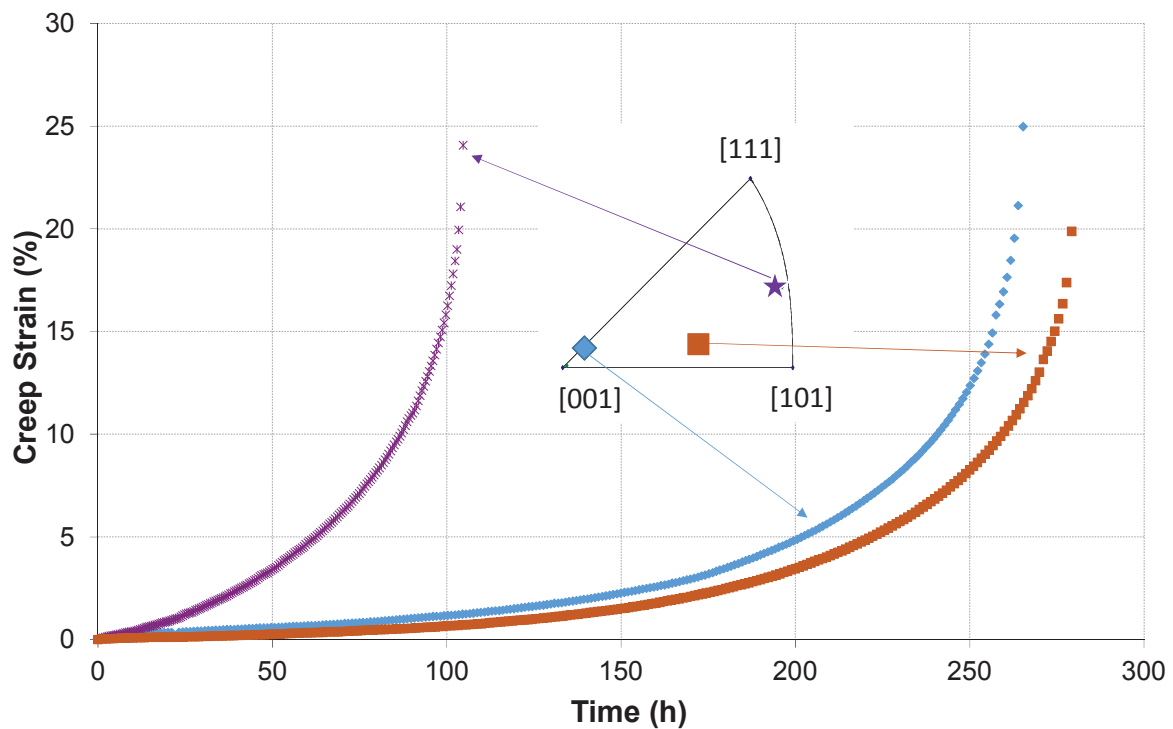


Figure 3.11 - Creep behavior anisotropy of MAR-M200+Hf SX alloy at 900°C/300 MPa.

In order to better characterize the DS200+Hf anisotropy of creep properties at 900°C, three experiments were also performed at 900°C/300 MPa using single crystalline specimens far away from the perfect <001> crystallographic orientation (Figure 3.11). If  $\sim$ <001> and  $\sim$ <102> specimens have almost the same creep resistance and creep behavior at 900°C/300 MPa (see blue and brown curves in Figure 3.11), a faster creep rate is observed for a  $\sim$ <212> specimen, especially during the tertiary creep stage (purple curve in Figure 3.11). Such an effect of the crystallographic orientation on the creep

properties at 900°C/300 MPa is linked to the kinetics of  $\gamma'$  rafting and to the morphology of  $\gamma'$  rafts once formed [18].

### 3.3.1.3 Creep behavior at 1100°C

At 1100°C/70 MPa (Figure 3.12), the creep behavior consists in a fast primary creep stage, followed by a slow and extended secondary creep stage and a steep tertiary creep stage. Such creep behavior is typical of the one obtained in the  $\gamma'$ -rafting regime, the end of the primary creep stage being linked to the kinetics of  $\gamma'$ -rafting completion and the stage II strain rate to the stability of the  $\gamma/\gamma'$  lamellar structure [19]. Under this creep condition, and very differently from the creep behavior at 900°C, the tertiary creep lasts for  $\sim 10$  to 15% of the total creep test duration.

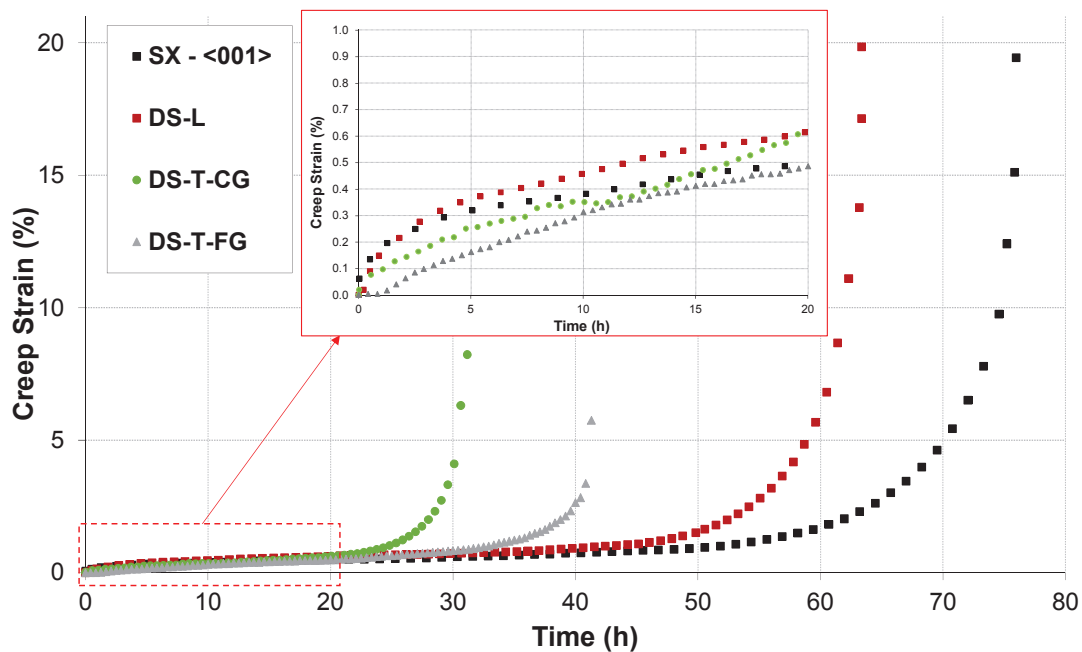


Figure 3.12 - Creep behavior at 1100°C/70 MPa of DS200+Hf alloy tested along the longitudinal direction (DS-L), the transverse one (DS-T) for both fine grain (FG) and coarse grain (CG) material in this last case. Results are compared with the <001> single crystalline specimen of the alloy (SX-<001>)

For this extreme creep condition for MAR-M200+Hf alloy (note that the  $\gamma'$ -solvus of MAR-M200+Hf is about 1200°C [20]), primary and secondary creep stages are strongly affected by the specimen type and the creep life varies within a factor of nearly 2, a reduced value compared to the creep results obtained at 900°C. Creep failure is still intergranular for creep tests along transverse direction and transgranular along longitudinal direction and for the SX specimen.

### 3.3.2 Microstructure evolutions during creep experiments

Previous studies [21, 22] have shown that Ni-based superalloys like DS200+Hf maintained at high temperatures (beyond nearly 800°C) under mechanical load present a microstructural evolution of  $\gamma'$  precipitates corresponding to directional coarsening, the so-called  $\gamma'$  rafting. This progressive microstructure transformation has already been presented in Chapter 1. It consists in an increase in  $\gamma$  channel width along one (or two) direction(s) and an elongation of the  $\gamma'$  precipitates due to the mechanical stress, even if this stress is not constant, as already shown in the literature [23, 24]. Once a small prior creep deformation is introduced at high temperature (e.g. 0.1% at 950°C) and then the applied stress is removed,  $\gamma'$  rafting continues and is dependent on the time spent at high temperature, even in absence of stress.

During creep tests performed at 900°C and 1100°C, the  $\gamma'$ -rafting phenomenon is observed, whatever the testing direction (see Figure 3.13 and Figure 3.14 showing the  $\gamma/\gamma'$  morphology at the end of creep tests for DS-L and DS-T specimens, respectively). The main difference in  $\gamma/\gamma'$  morphological evolution for tests under transverse direction is that the  $\gamma'$ -rafting process depends on the grain orientation, and not directly on the direction of the applied stress (see e.g. Figure 3.14). Such an observation is in good agreement with recent compression creep experiments performed using the polycrystalline Inconel 738LC alloy [25]. Figure 3.13(b) and Figure 3.13(c) show the difference in  $\gamma'$  directional coarsening at 900°C/250 MPa, and 900°C/400 MPa. A more developed  $\gamma'$  rafting is observed after failure at 900°C/250 MPa due to a longer time spent at high temperature. In Figure 3.13(b),  $\gamma'$ -rafting is clearly under progress, with some remaining  $\gamma$ -remaining zones trapped inside  $\gamma'$  precipitates (see arrows in the insert in Figure 3.13(b)), in agreement with Reed et al. [26]. Since  $\gamma'$ -rafting was already observed in the rhenium containing CMSX-4 alloy at temperatures greater than 850°C by Epishin et al. [27], this is not a surprise to observe this microstructure degeneration at this relatively low temperature. As this phenomenon is a function of temperature and exposure time, obviously specimens crept at 1100°C exhibited  $\gamma'$ -rafting even for shorter tests (see Figure 3.13(d)). It is also noted in Figure 3.13(d) the precipitation of a low amount (area fraction below 1%) of TCP phases under the form of needles, which are presumed to be  $\mu$ -type particles. At 750 °C/800MPa, no evidence of  $\gamma'$  morphological evolution has been noticed (see Figure 3.13(a)), despite large creep strains reached at failure for single crystalline and L-type DS specimens.

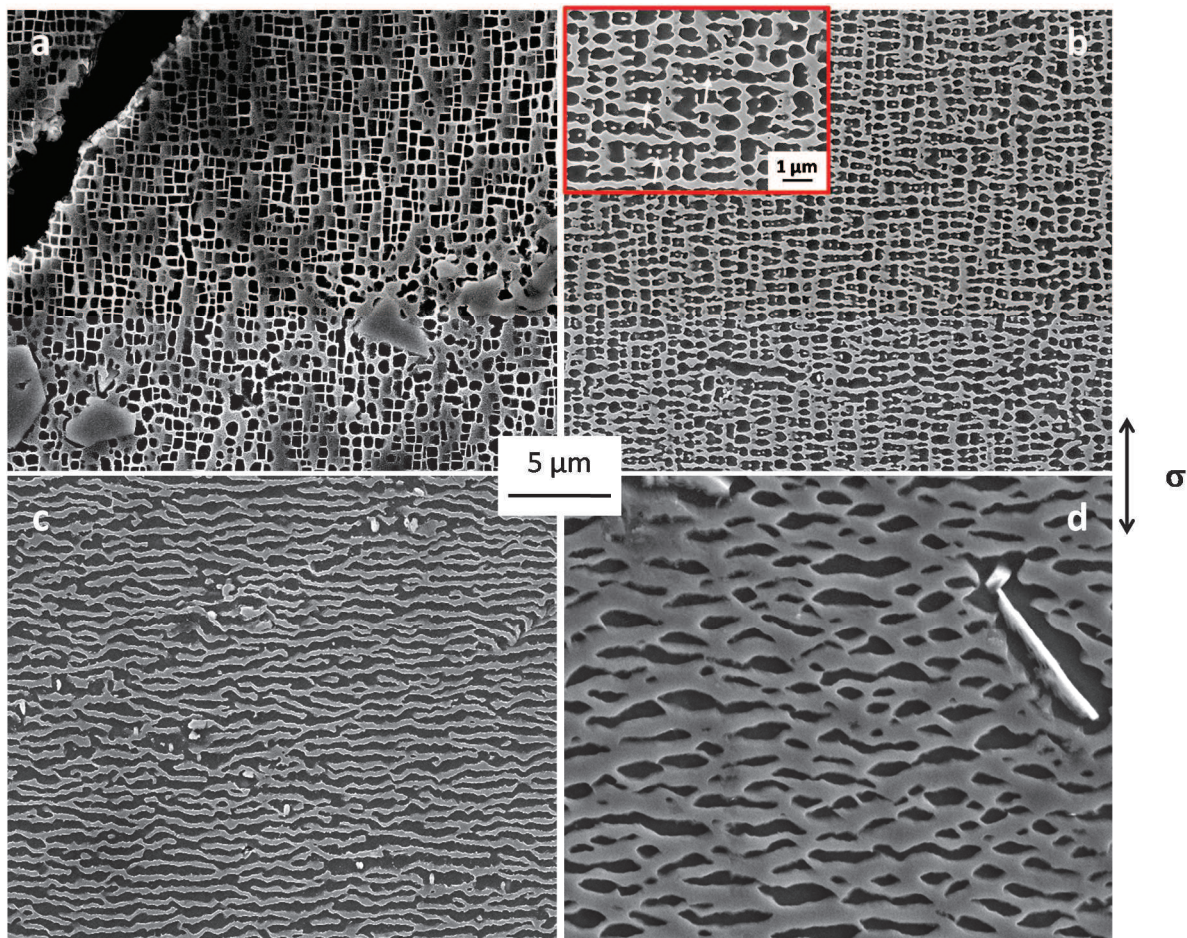


Figure 3.13 -  $\gamma/\gamma'$  microstructure after creep tests up to failure performed at (a) 750°C/800 MPa, (b) 900°C/400 MPa, (c) 900°C/250 MPa and (d) 1100°C/70 MPa (L type specimens). Arrows in the insert in (b) show remaining  $\gamma$  matrix islands trapped in the  $\gamma'$  precipitates.

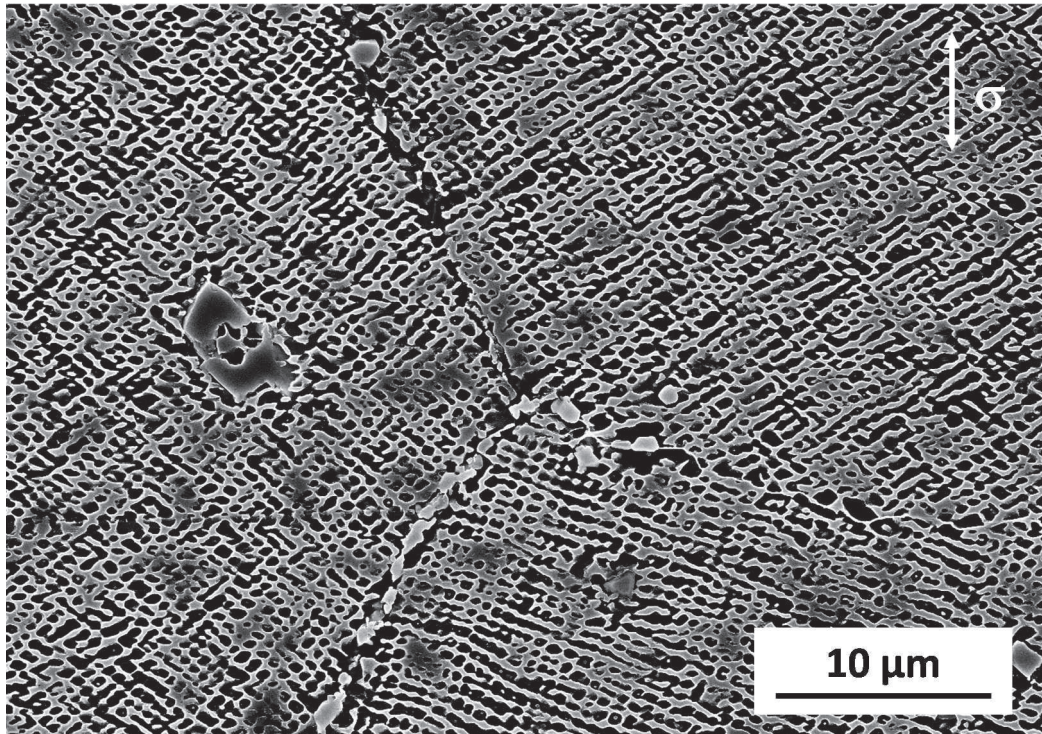


Figure 3.14 - Variation in  $\gamma'$  directional coarsening according to each grain orientation after creep testing at 900°C/350 MPa for 86.4 hours in a coarse grain specimen, along transverse direction.

### 3.3.3 In situ monitoring of creep strain heterogeneities

To better understand the creep behavior at the grain scale, as well as the ability for grain rotation, in situ monitoring of creep strain heterogeneities was performed at 750°C/800 MPa (Figure 3.15(a)), 750°C/700 MPa (Figure 3.16), 750°C/750 MPa and 900°C/400 MPa (Figure 3.15(b)). Before experiments, EBSD characterizations were performed on the gage surfaces and markers were positioned at the grain scale to allow local strain measurements. The solidification direction is vertical in the EBSD maps shown in Figure 3.15 and Figure 3.16 (i.e. perpendicular to the stress axis). The creep tests performed at 750°C have especially been chosen since no tertiary creep stage can be observed at this temperature during transverse creep testing. Moreover, a limited impact of oxidation on grain boundaries (GB) crack nucleation and no  $\gamma/\gamma'$  morphological evolution compared to the tests performed at 900°C are expected.

According to Figure 3.15, differences in creep elongation at the grain scale are observed for both conditions, especially at 750°C/800 MPa where a factor greater than 2.5 appears between the grains having undergone the largest creep strains (grains 1 and 4 in Figure 3.15(a)) and the grain with the lowest plastic deformation (grain 3 in Figure 3.15(a)). Moreover, it is observed that Grain 1 and Grain 4 are developing primary creep in this experiment while no clear primary creep is observed for the other grains. At the end of the creep test, it is observed either an increase (Grain 2) or a decrease (Grains 1, 3 and 4) of the measured strain at the grain scale, corresponding to the development of the main crack. This crack hence developed at the very end of the test and rapidly led to failure. Very similar trends have also been observed at 750°C/700 MPa (Figure 3.16). Slightly higher creep strains were reached at the grain scale and the main crack had developed close to grains having undergone large creep strains in comparison to other grains (creep curves have not been shown for all grains to limit figure overloading). For this specific experiment, it is observed that the main crack developed about 15 minutes before final failure. The crack initiation mechanism and the subsequent first stages

of crack propagation observed during these experiments will be analyzed in greater details in the next chapter.

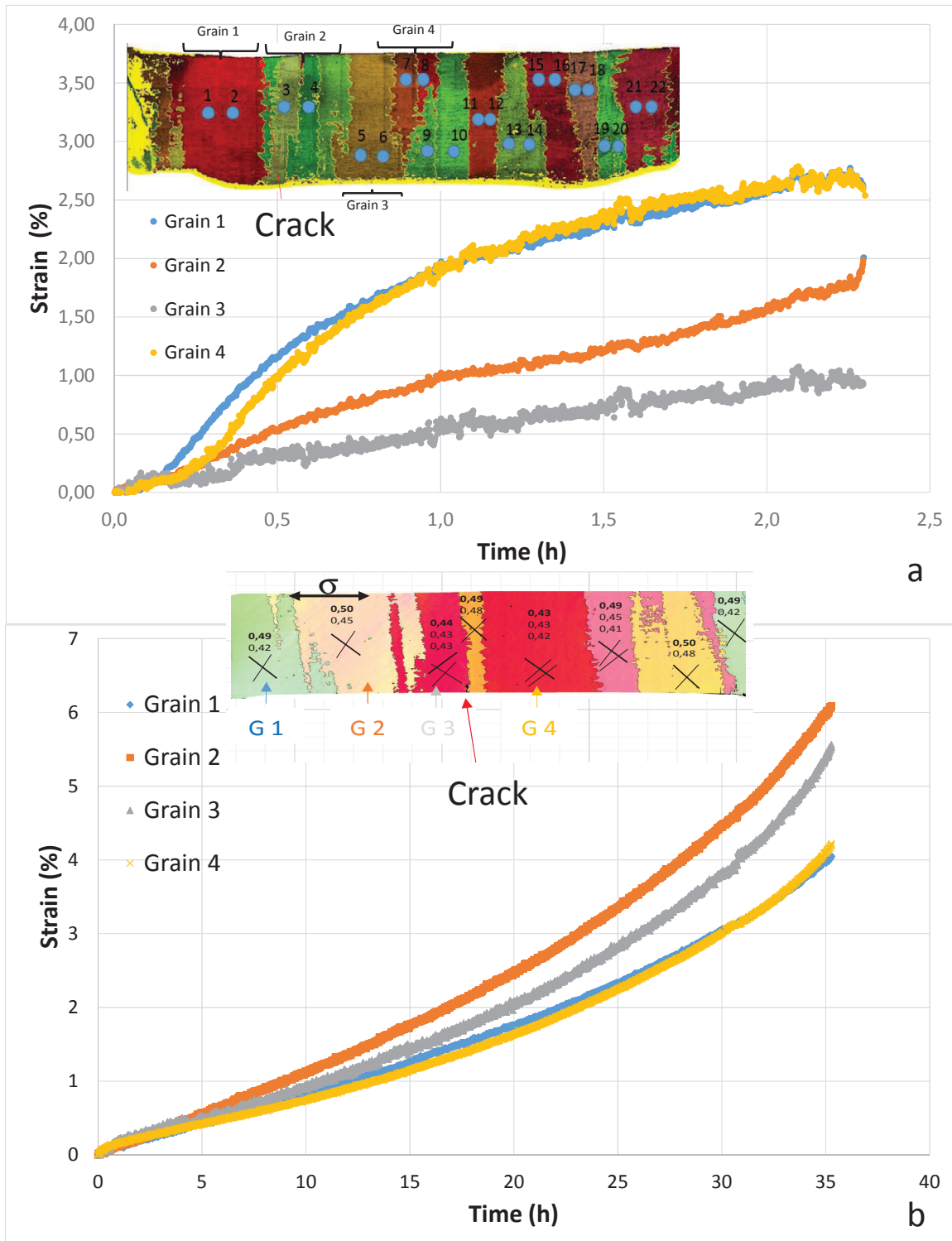


Figure 3.15 - Creep strain heterogeneity during transverse loading, at 750°C/800 MPa (a) and 900°C/400 MPa (b). Note that the color code used in the EBSD maps of the gauge surfaces presented in this figure refers to the loading axis. The grains in which creep strain evolutions are presented have been identified on each EBSD map (grains G1, G2, G3 and G4). The dotted circle in (a) highlights the creep acceleration once the main crack has been developed.

At 900°C (Figure 3.15(b)), a more homogeneous creep strain field is observed, with a contrast in creep strain at the grain scale lower than 1.5 at the end of the experiments (see arrows). All grains are developing a similar creep curve, having the same characteristics as the one previously presented at the macroscopic scale in Figure 3.8 (i.e. a very limited primary creep followed by an extended accelerating creep stage). The creep strain heterogeneity at 900°C/400 MPa develops specifically during the creep strain acceleration regime, when the  $\gamma'$  rafting has already taken place, leading to a more homogeneous creep deformation. For this case, there is no crack opening at the end of the test. It is hence presumed that crack nucleation and the first stages of crack propagation are occurring in a much more progressive manner compared to creep tests at 750°C. It should be mentioned that in both experiments, crack development occurred at grain boundaries (see arrows in Figure 3.15 and Figure 3.16).

During transverse creep testing (like experiments presented in Figure 3.15 and Figure 3.16, since crack nucleation is intergranular, the stress state at grain boundaries is critical in controlling crack initiation and this stress state is highly dependent on both the grain boundary morphology and on each grain elasticity. Increasing the temperature to 900°C and above leads to a more homogeneous creep deformation at the grain scale due to the degradation of the  $\gamma/\gamma'$  microstructure, as observed in Figure 3.15(b). However, despite being lower, the variation of creep life versus orientation is still pronounced at 900°C (see Figure 3.16) due to the impact of oxidation on the grain boundary crack initiation and propagation. The most critical grain boundary configurations and the contribution of oxidation in terms of crack initiation will be studied in the next chapter, by re-analyzing these results on the light of EBSD characterizations, as well as analyzing a transverse creep test equipped with in situ full field strain measurements using a DIC technique.

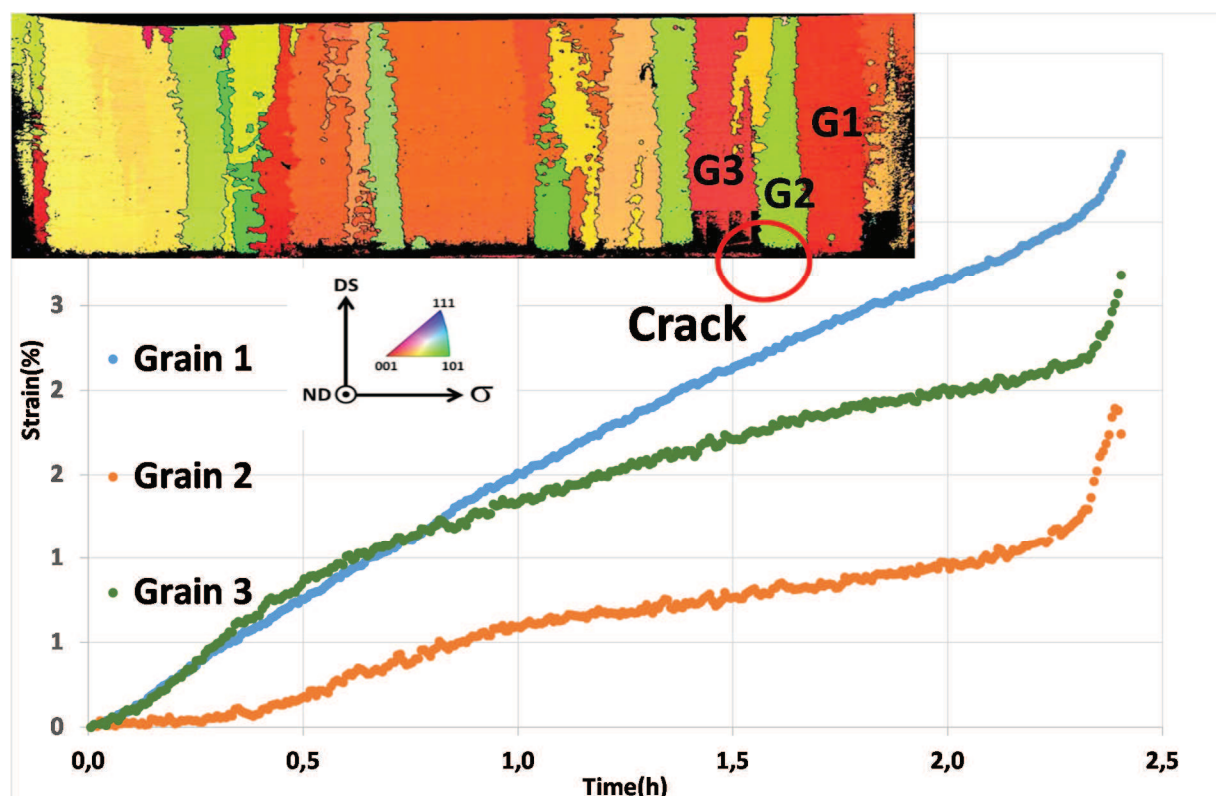


Figure 3.16 - Creep strain heterogeneity during transverse loading, at 750°C/700 MPa. Note that the color code used in the EBSD maps of the gauge surfaces presented in this figure refers to the loading axis. The grains in which creep strain evolutions are presented have been identified on each EBSD map (grains G1, G2 and G3).

### 3.4 Low-cycle fatigue behavior

LCF tests in air were performed at 650°C and 900°C with a sinusoidal wave-form and a frequency of 0.5 Hz. A stress ratio  $R\sigma=0.05$  has been applied at both temperatures while a second one of  $R\sigma=-1$  has also been applied at 650°C. For LCF tests at 650°C/ $R\sigma=-1$ , all the tests present fully elastic loops, except for the test using a  $\langle 001 \rangle$  SX specimen with  $\sigma_{\max} = 885$  MPa and the one using a DS specimen loaded along transverse direction,  $\sigma_{\max} = 785$  MPa. In both cases, a cyclic ratcheting toward the compression side is observed, especially for the SX specimen. This is clearly highlighted in Figure 3.17 where two selected loops have been plotted. This example exhibits a very spectacular loop opening, due to the absence of hardening in the compression branch, leading to an overall very low LCF life for this specimen ( $N_f=16$  cycles). The reason behind this cyclic ratcheting toward the compression side is a pronounced yield stress dissymmetry, as observed in Figure 3.17. This asymmetry in YS has already been observed in the past using PWA 1480 SX specimens [28] and results from the specific plastic behavior of the  $\gamma'$  phase in the 600°C-800°C temperature range [29].

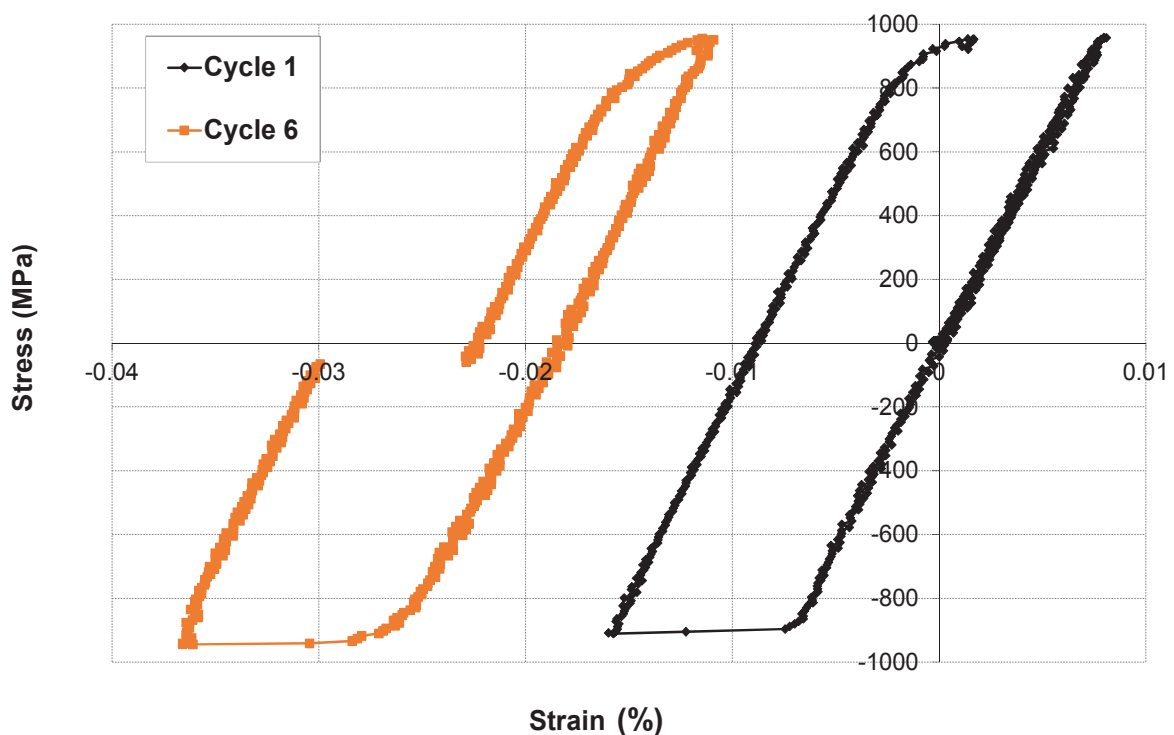


Figure 3.17 – Cyclic behavior for a  $\langle 001 \rangle$  SX specimen tested at 650°C/ $R\sigma=-1/\sigma_{\max}=-\sigma_{\min}=885$  MPa showing the 1<sup>st</sup> cycle and the first fourth of the 2<sup>nd</sup> one, as well as the 6<sup>th</sup> one.

At  $R\sigma=0.05$ , fatigue tests at 650°C present a cyclic ratcheting during the first 5-20 cycles and then, a stabilization of the cyclic behavior whatever the specimen type (see Figure 3.18(a) and Figure 3.18(b)). The number of cycles needed to reach an elastic loop is dependent to the maximum applied stress: the higher  $\sigma_{\max}$ , the higher the number of cycles needed to reach the elastic accommodation. In Figure 3.18(b) a very sudden increase of the maximum total strain (as measured at the end of each cycle) at the very end of the tests is exhibited, corresponding to the main crack initiation and development. Such behavior has systematically been observed under these conditions, whatever the specimen type, indicating that the overall fatigue life is probably mainly controlled by crack initiation. Regarding the microstructure at the precipitation scale, there is no marked change in  $\gamma/\gamma'$  microstructure, if compared to the as-received state.

At 900°C, a continuous cyclic ratcheting has been observed (see Figure 3.18(c) and Figure 3.18(d)). The fatigue loops were almost elastic (Figure 3.18(c)), with a plastic opening outside of the resolutions limits of the extensometer. It clearly suggests that the specimens are undergoing creep deformation at 900°C/ $R\sigma=0.05$  despite zero dwell-time at maximum load has been applied during these tests. This is related to the  $\gamma'$ -rafting phenomena already discussed in the previous creep section, that happens at 900°C, as observed in Figure 3.19. This microstructure degradation is known to induce cyclic softening during LCF tests at high temperature [30-32] hence leading to an increase of the macroscopic strain rate during LCF experiments with a positive stress ratio (i.e. faster cyclic ratcheting), as observed in Figure 3.18(d). Contrary to LCF test performed at 650°C/ $R\sigma=0.05$ , there is no increase of the maximum total strain measured at the end of each cycle (Figure 3.18(d)), suggesting that the main crack development is probably more progressive under these conditions. A better understanding of the damage development will be proposed in chapter 4, by analyzing LCF results performed under high vacuum, as well as crack propagation tests.

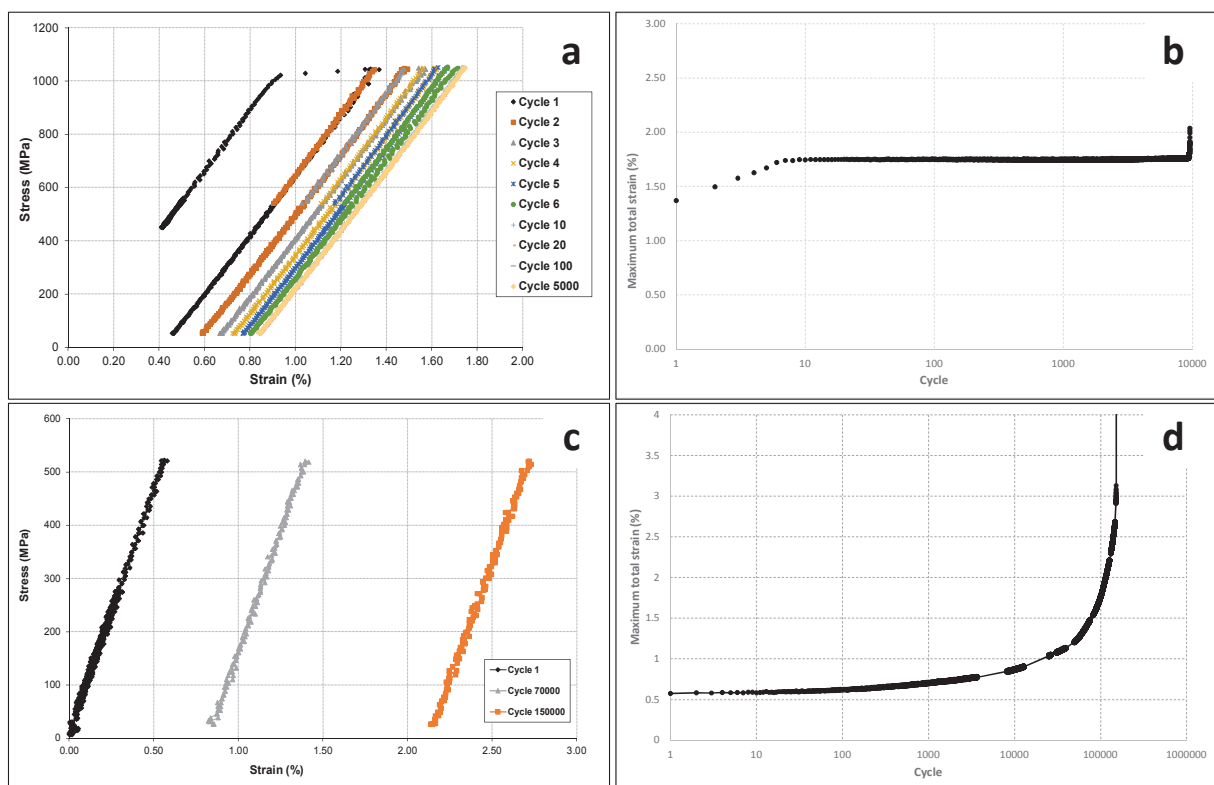


Figure 3.18 – Typical cyclic behavior under  $R\sigma=0.05/f=0.5\text{Hz}$  at 650°C (a,b) and at 900°C (c,d), whatever the specimen type. The tests presented in (a,b) and (c,d) have respectively been performed for a DS-L specimen at  $\sigma_{max}=1050\text{ MPa}$  and for a <001>-SX specimen at  $\sigma_{max}=520\text{ MPa}$ .

Fatigue tests at 650°C, both at  $R\sigma=0.05$  and  $R\sigma=-1$  are summarized in Figure 3.20, comparing the different loading conditions and specimen types. To better describe the low-cycle fatigue domain, tests with a stress ratio  $R\sigma=0.05$  were performed with a maximum stress equal or very close to the yield stress obtained from tensile tests (see. Figure 3.1 and Appendix 4). Figure 3.20 shows that the <001> oriented SX specimen presents a better fatigue resistance for positive stress ratio, followed by longitudinal and then transverse DS specimens. 45° oriented specimens seems to present a different curve slope which remains to be understood, but their fatigue resistance is very similar to DS specimens loaded along longitudinal directions. For a negative stress ratio, the ranking in LCF strength is similar, except that DS-L and SX specimens have almost the same LCF life. As for most of the metallic materials, a lower fatigue life is obtained at  $R\sigma=-1$  compared to  $R\sigma=0.05$  for tests with the same  $\sigma_{max}$ .



The variation of LCF performances versus specimen orientation is somehow different from the Wright and Anderson on René 120 DS specimens machined along different orientations with respect to the solidification direction [33]. They indeed observed no orientation dependence of their strain-controlled LCF results at 650°C, when plotting the maximum tensile stress as a function of the number of cycles to failure. According to them, this was due to the fact that crack initiation started from internal metallurgical defects such as pores which are, by nature, the same when specimens machined from the same castings.

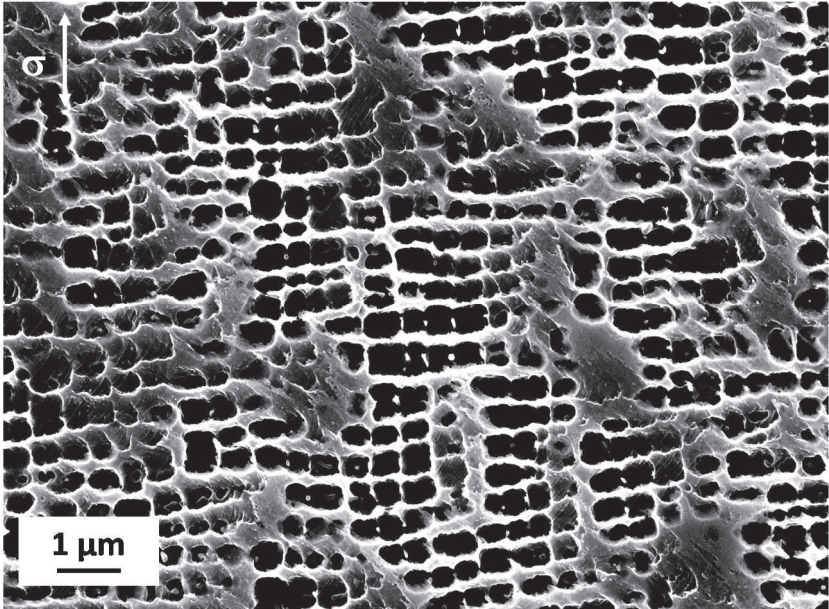


Figure 3.19 – Typical  $\gamma/\gamma'$  microstructure within a primary dendrit arm after a LCF test at 900°C/ $R\sigma=0.05/\sigma_{max}= 520$  MPa using a  $\sim \langle 001 \rangle$  SX specimen ( $N_f= 114,608$  cycles/Test duration  $\sim 65$  hours).

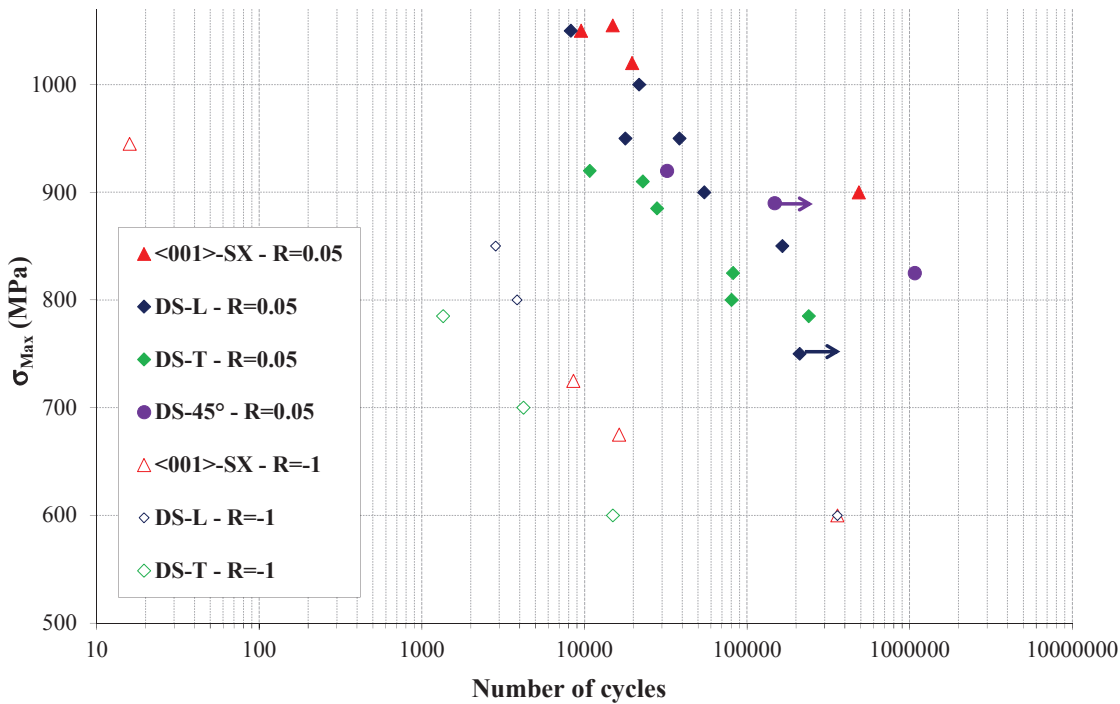


Figure 3.20 - LCF results at 650°C/ $R\sigma=0.05$  and  $R\sigma=-1/f=0.5$  Hz.

In our case, the LCF anisotropy mainly results from the differences in YS as determined from tensile tests, much more than from the difference in UTS (see Figure 3.1 and Appendix 1). Indeed, one single trend is observed in Figure 3.21(a) normalizing the maximum stress by the yield stress for LCF tests performed at  $R\sigma=0.05$  while such a trend is not so clear by normalizing by UTS (Figure 3.21(b)). The only results lying outside of this “master-curve” in this modified S-N diagram correspond to specimens machined at  $45^\circ$  of the solidification direction. Further investigations would be necessary to understand better why these specimens are lying outside the main trend.

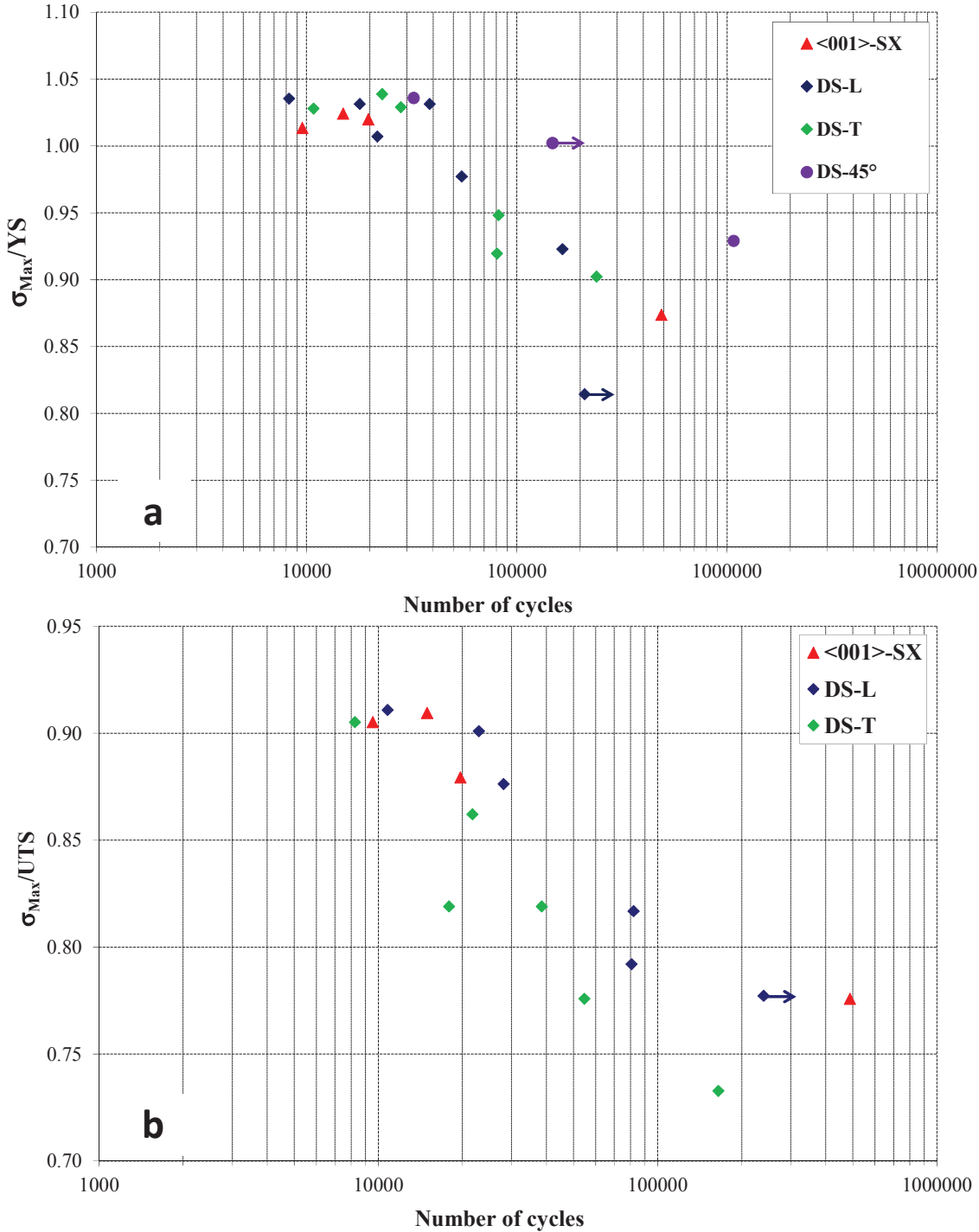


Figure 3.21 - LCF results at  $650^\circ\text{C}/R\sigma=0.05/f=0.5$  Hz with a normalization of  $\sigma_{max}$  by the yield stress (YS) (a) or by the ultimate tensile stress (UTS) (b).

Figure 3.22 below summarizes LCF lives obtained at 900°C. At this temperature, tests have been performed both in air and in high vacuum to check a possible effect of oxidation on the LCF durability. SX and DS-L specimens perform almost equally in low cycle fatigue under these conditions. They are performing better than specimens machined at 45° of the solidification direction, themselves performing better than specimens machined along transverse direction. Such an orientation dependent LCF resistance at 900°C meets the results obtained at 982°C by Wright and Anderson on René 120 DS specimens [33]. They indeed observed that DS specimens machined along transverse direction perform worse in comparison to all other orientations and almost similarly to the polycrystalline equiaxed version of René 120 alloy. The ranking obtained for the LCF strength at 900°C is also found in creep (see Figure 3.5 and Figure 3.8), which seems to be in good agreement with the cyclic behavior of the alloy at this temperature and under a stress ratio  $R\sigma=0.05$ , characterized by a continuous ratcheting (see Figure 3.18(d)). According to the LCF lives obtained in high vacuum conditions (see Figure 3.22), it seems that the oxidation has only a limited impact on the total fatigue durability at 900°C.

To better analyze these LCF results at 650°C and 900°C, typical fractographic observations of the specimens tested in air at both temperatures or in high vacuum at 900°C will be presented in the next chapter. A special attention will be paid to the crack initiation mechanisms as well as to the crack propagation behavior, establishing crack propagation curves in air and in high vacuum, close to the crack propagation threshold as well as in the Paris domain. The apparent absence of any oxidation effect in LCF tests at 900°C (as shown by Figure 3.22) will be analyzed in deeper details.

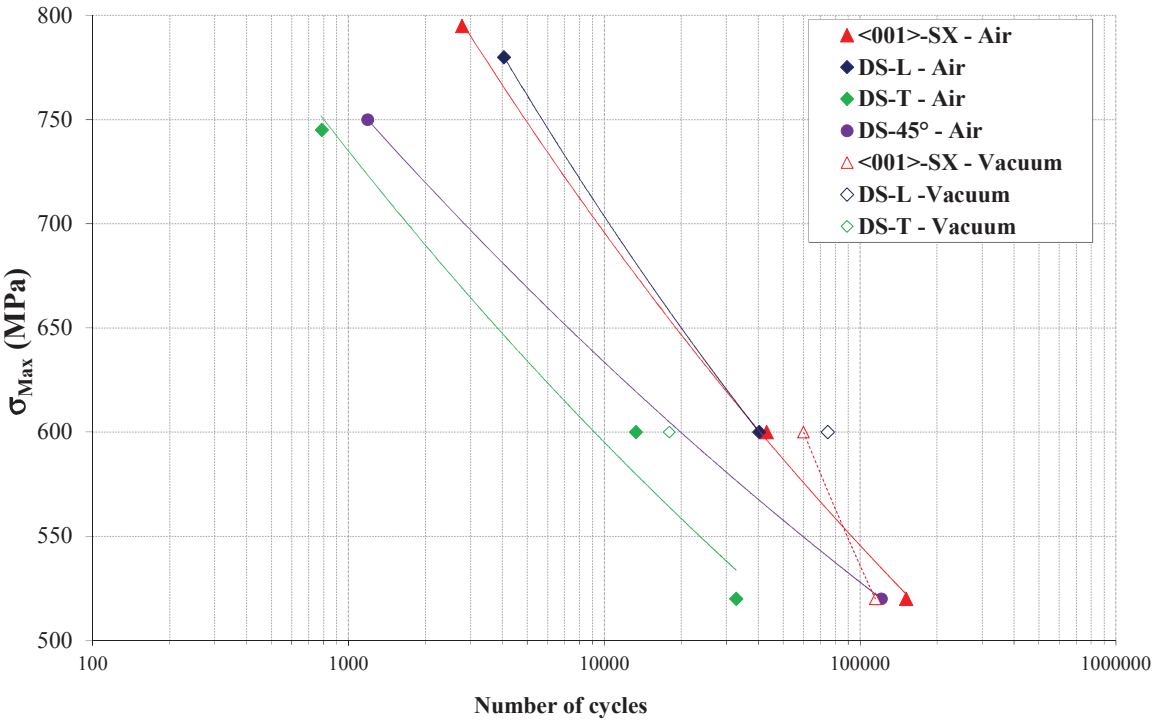


Figure 3.22 - LCF results at 900°C/ $R\sigma=0.05/f=0.5$  Hz.

### 3.5 Dwell-fatigue behavior

During service, turbine blades are mechanically loaded with a complex thermo-mechanical history, involving both creep and fatigue loadings. The main aim of the section is to get a better understanding of creep-fatigue interactions, trying to identify which kind of loading path leads to a “creep-dominated” or a “fatigue-dominated” behavior and damage. For this purpose, load-controlled dwell-

fatigue tests have been performed at 900°C, using a trapezoidal waveform, different dwell times  $\Delta t$  at maximum load (1, 10 or 300 seconds), and a stress ratio  $R\sigma=0.05$ . Such a kind of tests can also be qualified as “cyclic creep” tests since, as presented below, they induce a continuous ratcheting. Moreover, pure creep tests and pure LCF tests presented in previous sections of this chapter will be used as references to understand the dwell-fatigue behavior and durability of the alloy.

Figure 3.23 shows a comparison of the plastic strain evolution as a function of the time spent at maximum stress  $\sigma_{max}$  in dwell-fatigue for both DS and  $\sim <001>$  SX specimens. It is observed that the higher the dwell time, the faster the strain rate, whatever the specimen type and maximum applied stress during these tests. The time to failure during these tests does not seem to be significantly affected by dwell time, except for the DS-T specimen with  $\Delta t = 300$  seconds, for which a debit is observed compared to short dwell times of 1 and 10 seconds (see Figure 3.23(d)). The pure creep reference has systematically been added in these plots. Pure creep curve always leads to a shorter time to failure and to a faster strain rate, except for DS-T specimens for which the pure creep and the dwell-fatigue test exhibit the same increase behavior (see Figure 3.23(d)). The higher scatter in mechanical properties of DS-T specimens can partly be at the origin of this almost similar inelastic behavior. This figure also shows the increase of ductility when increasing dwell time, the ductility being almost equal for pure creep and dwell-fatigue tests, whatever the specimen type. For a very short dwell time (i.e.  $\Delta t=1s$ ), the strain rate observed at the end of the tests is greatly reduced compared to experiments with longer dwell times, and the plastic strain at failure is nearly four times smaller than in pure creep or with a 300s dwell time. This dependence of the strain to failure to dwell time strongly suggests a change in damage mechanisms.

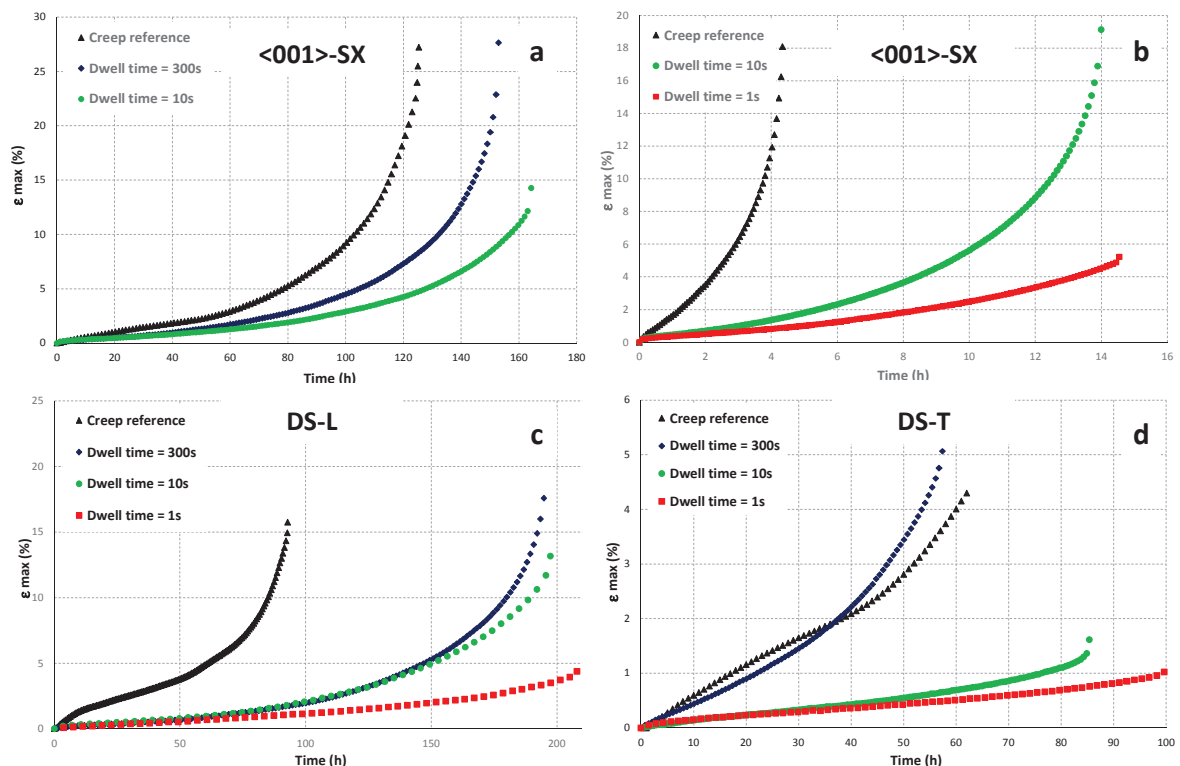


Figure 3.23 – Effect of the dwell time at maximum stress ( $\sigma_{max}$ ) on the inelastic elongation during dwell-fatigue tests at 900°C/ $\sigma_{max}=400$  MPa/ $R\sigma=0.05$  for  $\sim <001>$  SX specimens (a), for DS specimens loaded along longitudinal (c) and transverse (d) directions and at 900°C/ $\sigma_{max}=520$  MPa/ $R\sigma=0.05$  for  $\sim <001>$  SX specimens (b). Results have been compared with the pure creep behavior reference at 900°C/400 MPa for each kind of specimen. Note the X-axis is the time spent at maximum applied stress  $\sigma_{max}$ .

After presenting the effect of the dwell time on the inelastic elongation, Figure 3.24 below summarizes dwell-fatigue results in terms of number of cycles to failure. This figure proposes a comparison of the dwell-fatigue life in air with LCF for each type of specimen (results already presented in the previous section). Dwell-fatigue results in high vacuum have not been added in this figure since the dwell-fatigue life has been observed to be hardly affected by environment (see Appendix 5). As expected from the dwell-fatigue behavior presented in Figure 3.23, Figure 3.24 shows a drop in the number of cycles to failure by introducing a dwell time at maximum load. The decrease in the number of cycles to failure is greater when increasing dwell time, as observed previously. As an example, the number of cycles to failure is divided by a factor of 30 for  $\sim\langle 001 \rangle$  SX specimens when introducing a dwell time  $\Delta t = 10$  s in the cycle at  $\sigma_{\max} = 520$  MPa.

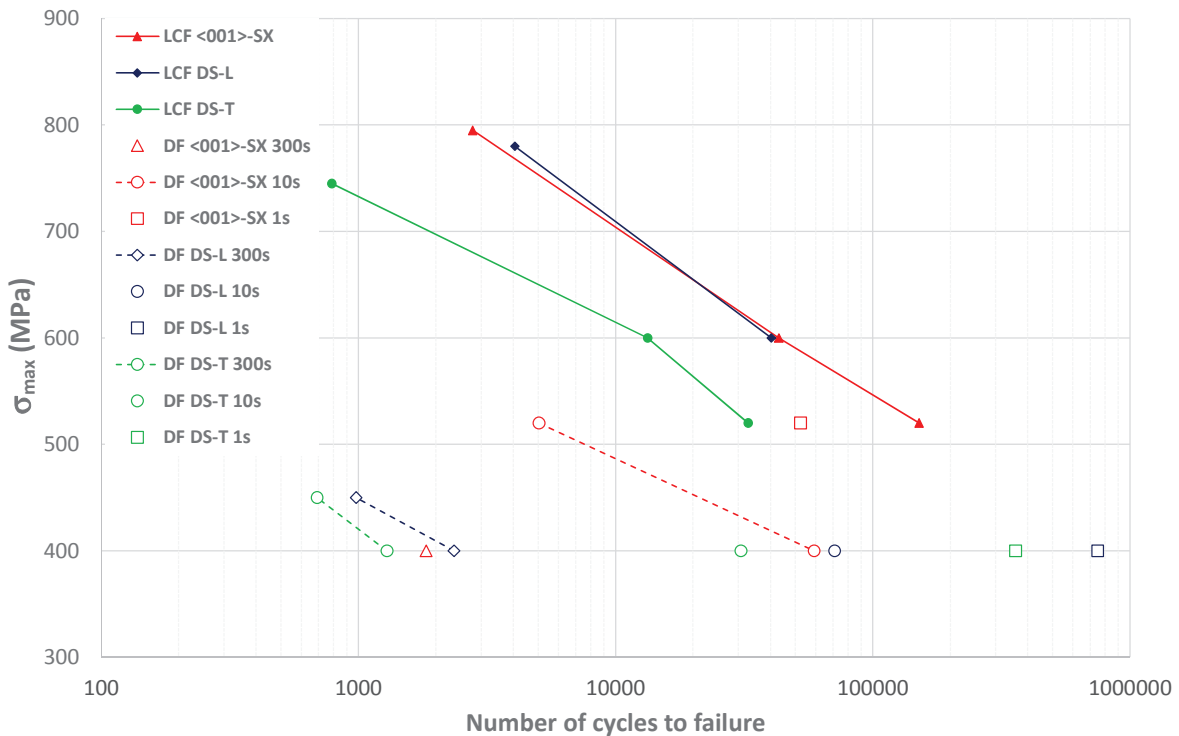


Figure 3.24 - Comparison LCF and dwell-fatigue (DF) results for each type of specimens at  $900^{\circ}\text{C}/R\sigma=0.05$  for different dwell times.

To get a better understanding of the creep-fatigue interactions, all specimens tested in dwell-fatigue at  $\sigma_{\max} = 400$  MPa were observed along longitudinal sections after the tests, 1.5 mm away from the fracture surface. Typical microstructures at the precipitation scale are presented in Figure 3.25 for  $\langle 001 \rangle$  SX specimens (Figure 3.25(a) and (b)), as well as for DS specimens mechanically loaded along longitudinal direction (Figure 3.25(c-e)) or along transverse direction (Figure 3.25(f-h)). Longer  $\gamma$ -rafts are observed for specimens tested with a short dwell time (compare, e.g. Figure 3.25(e) with Figure 3.25(c) for DS-L specimens and Figure 3.25(h) with Figure 3.25(f) for DS-T specimens).

A stereological characterization of the  $\gamma$ '-rafts thickness as well as of the  $\gamma$  channel width has been performed at the end of the dwell-fatigue tests using SX and DS-L specimens, as well as at the end of their respective pure creep references. These characterizations have not been performed for DS-T specimens since the morphological evolution of the  $\gamma/\gamma'$  microstructure is highly sensitive to the local grain orientation (see Figure 3.14). Figure 3.26 presents the typical  $\gamma$ -rafts thickness and  $\gamma$  channel width distributions for DS specimens loaded along longitudinal direction. Increasing the dwell time at maximum load induces an increase of the mean values appear for both  $\gamma$  thickness and  $\gamma$  channel

width (i.e. of the periodicity of the  $\gamma/\gamma'$  lamellar microstructure), in addition to a broadening of these distributions. Indeed, no typical Log-Normal or Gaussian type distribution can be recognized for the  $\gamma'$  thickness distributions after pure creep testing at 900°C/400 MPa or after a dwell-fatigue test with  $\Delta t = 300$  seconds, indicating an already advanced  $\gamma/\gamma'$  microstructure degradation under the form of a topological inversion.

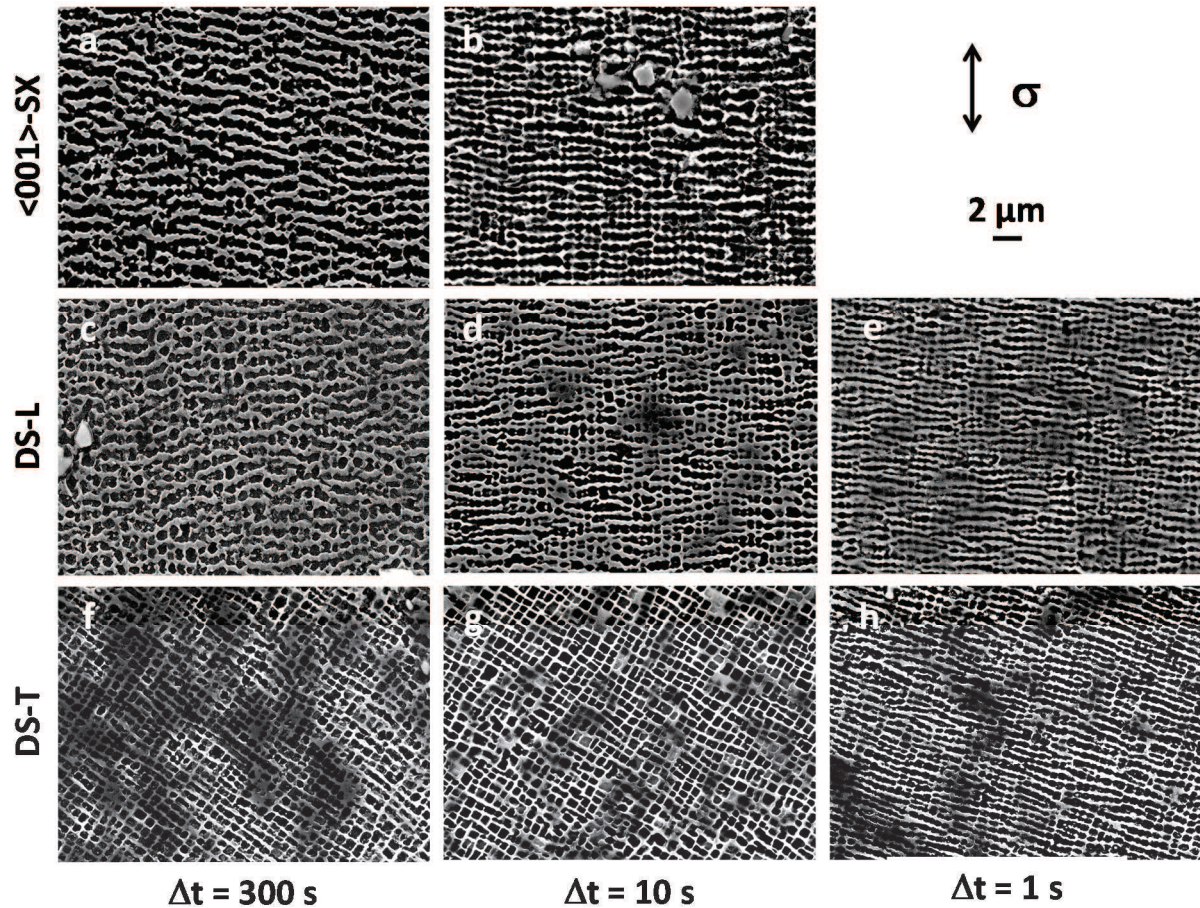


Figure 3.25 - Typical  $\gamma/\gamma'$  microstructure observed at the end of dwell-fatigue tests at 900°C/ $R\sigma=0.05/\sigma_{max}=400$  MPa for a  $\sim <001>$  SX specimen/ $\Delta t = 300$  s/ $N_f = 1,834$  cycles (a); a  $\sim <001>$  SX specimen/ $\Delta t = 10$  s/ $N_f = 59,139$  cycles (b); a DS-L specimen/ $\Delta t = 300$  s/ $N_f = 2,351$  cycles (c); a DS-L specimen/ $\Delta t = 10$  s/ $N_f = 71,038$  cycles (d); a DS-L specimen/ $\Delta t = 1$  s/ $N_f = 748,352$  cycles (e); a DS-T specimen/ $\Delta t = 300$  s/ $N_f = 1,292$  cycles (f); a DS-T specimen/ $\Delta t = 10$  s/ $N_f = 30,728$  cycles (g) and a DS-T specimen/ $\Delta t = 1$  s/ $N_f = 359,020$  cycles (h).

To get an easier understanding of  $\gamma/\gamma'$  microstructure evolutions during dwell-fatigue tests, the mean  $\gamma'$ -rafts thickness and mean  $\gamma$  channel width at the end of the tests have been plotted as a function of the dwell time in Figure 3.27. Both quantities increase monotonically with dwell time for both  $\sim <001>$  SX and DS-L specimens. Having in mind the dwell-fatigue behavior presented in Figure 3.23, this figure suggests that the increase in plastic strain rate with the increase of the dwell-time results from a more pronounced degradation of the  $\gamma/\gamma'$  microstructure. Indeed, wider  $\gamma$  channels are known to ease the dislocation movements within the matrix due to a decrease of the Orowan stress, leading to an overall increase in creep rate [34, 35]. Dislocation by-passing and/or dislocations climb are indeed the typical rate-controlling mechanisms at this temperature [4, 36, 37]. This microstructure degradation is observed both for the  $\gamma$  channels width and for the  $\gamma'$ -rafts thickness (see Figure 3.27), i.e. for the periodicity (the sum of the average  $\gamma$  channel width and  $\gamma'$ -raft thickness) of the  $\gamma/\gamma'$  microstructure

which is also often considered to be a good indicator of the creep strength in Ni-based single crystal superalloys [38].

As a main conclusion from these dwell-fatigue characterizations, it appears that reducing the frequency of the tests (i.e. longer  $\Delta t$  at  $\sigma_{max}$ ) leads to wider  $\gamma$  channels and then, a faster plastic strain rate. One of the surprising results from dwell-fatigue experiments is that despite a decrease of the dwell time at  $\sigma_{max}$  corresponds to an increase of the total time of the tests at 900°C (see Appendix 5),  $\gamma$  channels width is lower for shorter  $\Delta t$  at  $\sigma_{max}$  (Figure 3.27). This trend disagrees with previous results established by Matan et al. [16] in pure creep. Indeed, once a given amount of creep strain introduced at high temperature has been reached ( $\sim 0.10\%$  at 950°C in  $\langle 001 \rangle$  Ni-based SX CMSX-4 alloy [16]),  $\gamma$  rafting can further proceed without any external applied stress. If this observation would apply to our dwell-fatigue experiments, wider  $\gamma$  channels and thicker  $\gamma'$  rafts would have been observed for short  $\Delta t$  (due to a longer total test duration), which is not the case: only longer  $\gamma'$  rafts were qualitatively observed when decreasing the dwell time at  $\sigma_{max}$  (compare, e.g. Figure 3.25(e) with Figure 3.25(c) for DS-L specimens and Figure 3.25(h) with Figure 3.25(f) for DS-T specimens). Creep-fatigue interactions are probably more complex and interrupted tests at same plastic strain and/or same total time would be necessary to better understand  $\gamma/\gamma'$  microstructure evolutions (by SEM and TEM observations) and their consequences on the dwell-fatigue performances.

Finally, one should notice that no direct comparison between pure creep and dwell-fatigue experiments can be done in terms of microstructure evolutions. Indeed, according to Figure 3.27, thinner  $\gamma'$  rafts and narrower  $\gamma$  channels in SX and DS-L specimens tested in pure creep conditions are observed. This directly results from the fact that creep tests have a faster creep damage development, leading to a shorter (total) time to failure in comparison to dwell-fatigue experiments (see Figure 3.23).

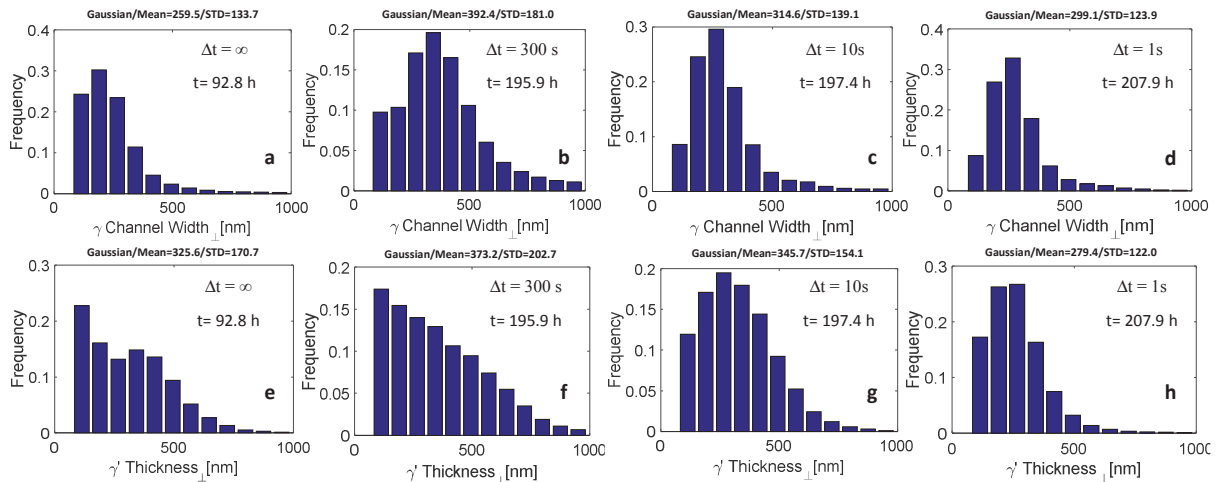


Figure 3.26 – Distributions of  $\gamma$  channel width (a-d) and  $\gamma'$  thickness (e-h) after dwell fatigue tests at 900°C/ $\sigma_{max} = 400$  MPa/ $R\sigma=0.05$  using DS specimens loaded along longitudinal direction. Note that the dwell time ( $\Delta t$ ) and total time at  $\sigma_{max}$  have been added on each plot to ease the reading and that pure creep tests are identified by a dwell time  $\Delta t=\infty$ .

As a summary, dwell-fatigue lifetime is controlled by a coupling between  $\gamma$  channel widening (which increases the creep rate) and the mechanical cycling (which reduces the increase of  $\gamma$  channel width). These creep-fatigue interactions will be further analyzed in the next chapter through fracture surface investigations.

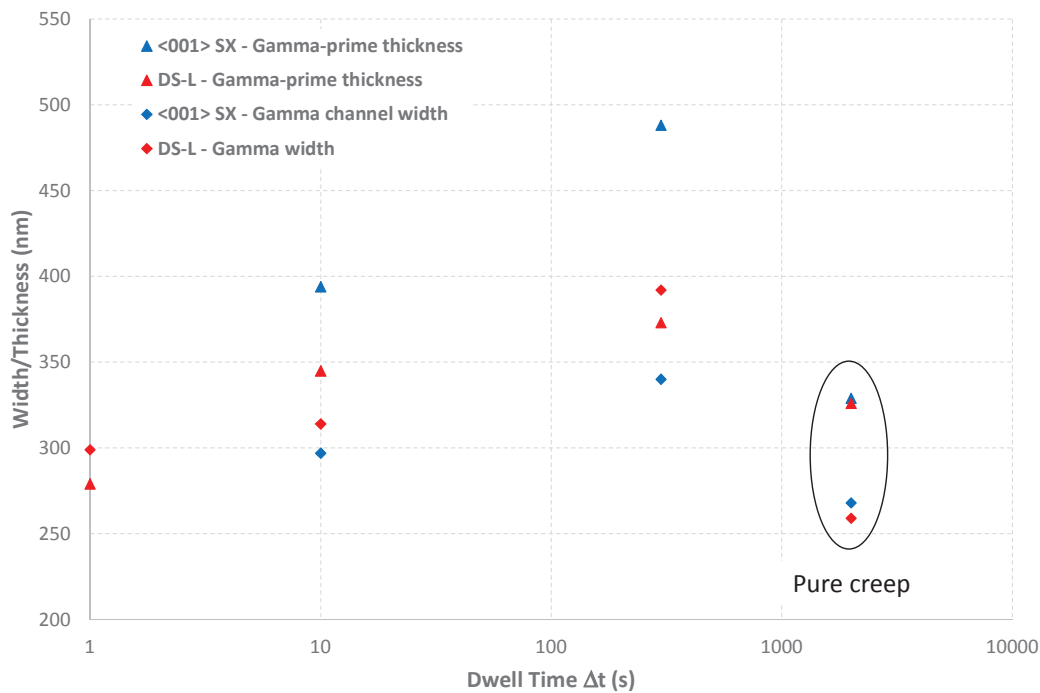


Figure 3.27 - Comparison of mean  $\gamma'$  thickness and mean  $\gamma$  channel width at the end of dwell-fatigue tests at  $900^\circ\text{C}/\bar{\sigma}_{max} = 400 \text{ MPa}/R\sigma=0.05$  using DS specimens loaded along longitudinal direction and  $\sim <001>$  SX specimens and compared to their respective counterparts at the end of creep tests. Note that their creep results have been artificially positioned at a dwell time  $\Delta t = 2000\text{s}$  to ease the comparison.

### 3.6 Conclusions

The dependence of mechanical properties (tensile, creep, low cycle fatigue and dwell-fatigue) on crystal orientation and the durability of DS200+Hf alloy have been presented in this chapter, mainly at  $650^\circ\text{C}$  and  $900^\circ\text{C}$ , with additional creep characterizations at  $750^\circ\text{C}$  and  $1100^\circ\text{C}$ . The mechanical behavior of the alloy along different orientations with respect to the solidification direction has been compared to the mechanical behavior of single crystalline specimens with different crystallographic orientations but exactly the same chemistry.

From these characterizations, the following main conclusions can be established:

- The tensile behavior is highly anisotropic at  $650^\circ\text{C}$  for both DS and SX specimen, especially considering yield stress and ultimate tensile stress. This mainly results from the number of slip systems activated. At  $900^\circ\text{C}$ , the anisotropy is greatly reduced compared to  $650^\circ\text{C}$  but the alloy exhibits a pronounced strain rate sensitivity. A very low tensile ductility for DS specimens along transverse direction.
- The anisotropy in creep properties decreases when increasing testing temperature both for DS and SX specimens. This is correlated to the  $\gamma'$  rafting which is already observed during short creep tests (duration  $< 40\text{h}$ ) at  $900^\circ\text{C}$  and which leads to a more homogeneous creep deformation. The shape of the creep curves observed during these experiments are in good agreement with results from the open literature for Ni-based single crystalline superalloys.
- The creep ductility along transverse direction of DS specimens is very low (typically below 5%). Such a low ductility results in lower creep lives along transverse direction, whatever the creep condition, the debit in creep life being even greater when decreasing the grain size. This low ductility for DS-T specimen induces premature failure within the primary creep stage at low temperature/high applied stress.



- Creep strain evolutions at the grain scale have been characterized at 750°C/700 MPa, 750°C/750 MPa, 750°C/800 MPa and 900°C/400 MPa during transverse creep testing of DS specimens. Contrary to creep tests at 900°C, a huge heterogeneity in creep elongation can be observed at grain scale at 750°C.
- The low cycle fatigue behavior at 650°C/R $\sigma$ =0.05 generates strain ratcheting during the first 5-20 cycles, then a macroscopic elastic behavior for the rest of the LCF life, whatever the specimen type. At 650°C/R $\sigma$ =-1, an elastic behavior has been observed except for very high stress amplitude tests which present ratcheting toward the compression side. At 900°C/R $\sigma$ =0.05, a continuous ratcheting up to failure has been observed for all types of specimens.
- <001> SX specimens present LCF lives equal or better than DS-L specimens in all conditions. They are followed by specimens machined at 45° of the solidification direction and then, by specimens machined along transverse direction.
- At 900°C, the environment (i.e. air vs high vacuum) seems to have no significant effect on LCF life of DS and ~<001> SX specimens.
- A sluggish  $\gamma'$  rafting develops during LCF tests at 900°C/R $\sigma$ =0.05, whatever the specimen type.
- Dwell-fatigue tests performed at 900°C/R $\sigma$ =0.05 with dwell times ranging from 1 second up to 300 seconds present increased time to failure compared to their respective pure creep references. Moreover, the introduction of a dwell time at  $\sigma_{\max}$  induces a decrease in the number of cycles to failure compared to their pure LCF counterparts. It is observed that the higher the dwell time, the lower the number of cycles to failure.
- The increase of the dwell time at  $\sigma_{\max}$  leads to a faster plastic strain rate and to a higher ductility during these dwell-fatigue tests. This results from wider  $\gamma$  channels when increasing the dwell time and hence, easier viscoplastic flow.
- Despite longer time at high temperature, dwell-fatigue tests with short dwell times exhibit a finer  $\gamma/\gamma'$  microstructure. This suggests a complex morphological evolution of the  $\gamma'$  precipitates, their morphology being sensitive to both the dwell time at  $\sigma_{\max}$  and to the loading/unloading sequences.

After this mechanical behavior characterizations complemented by observations at the  $\gamma/\gamma'$  scale, a special focus will be paid in the next chapter to the crack initiation and crack propagation mechanisms during creep, LCF and dwell-fatigue tests. A special attention will be paid to the role of oxidation in the damage nucleation and subsequent development.

### References of Chapter 3

1. R.A. MacKay, R.L. Dreshfield, and R.D. Maier. *Anisotropy of nickel-base superalloy single crystals*. in *Superalloys 1980*. 1980. Seven Springs, Champion, PA, USA: TMS, Warrendale, PA. p. 385-394.
2. F. Coudon, *Comportement mécanique à haute température d'un superalliage à solidification dirigée DS200+Hf*, PhD Thesis. 2017, Mines ParisTech, Centre des Matériaux.
3. R. Desmorat, A. Mattiello, and J. Cormier, *A tensorial thermodynamic framework to account for the  $\gamma'$  rafting in nickel-based single crystal superalloys*. International Journal of Plasticity, 2017.
4. H. Mughrabi, *Microstructural aspects of high temperature deformation of monocrystalline nickel base superalloys: some open problems*. Materials Science and Technology, 2009. **25**(2): p. 191-204.
5. P. Caron, Y. Ohta, Y.G. Nakagawa, and T. Khan. *Creep deformation anisotropy in single crystal superalloys*. in *Superalloys 1988*. 1988. Seven Springs, Champion, PA, USA: TMS. p. 215-224.
6. R.A. Mackay and R.D. Maier, *The Influence of Orientation on the Stress Rupture Properties of Nickel-Base Superalloy Single Crystals*. Metallurgical and Materials Transactions A, 1982. **13A**: p. 1747-1754.
7. V. Sass, U. Glatzel, and M. Feller-Kniepmeier, *Anisotropic creep properties of the nickel-base superalloy CMSX-4*. Acta materialia, 1996. **44**(5): p. 1967-1977.
8. C.M.F. Rae, M.A. Rist, D.C. Cox, R.C. Reed, and N. Matan, *On the primary creep of CMSX-4 superalloy single crystals*. Metallurgical and materials transactions A, 2000. **31**(9): p. 2219-2228.
9. C.M.F. Rae and R.C. Reed, *Primary creep in single crystal superalloys: origins, mechanisms and effects*. Acta Materialia, 2007. **55**(3): p. 1067-1081.
10. J. Svoboda and P. Lukáš, *Model of creep in  $\langle 001 \rangle$ -oriented superalloy single crystals*. Acta Materialia, 1998. **46**(10): p. 3421-3431.
11. X. Wu, P. Wollgramm, C. Somsen, A. Dlouhy, A. Kostka, and G. Eggeler, *Double minimum creep of single crystal Ni-base superalloys*. Acta Materialia, 2016. **112**: p. 242-260.
12. D.N. Duhal and C.P. Sullivan, *Some effects of hafnium additions on the mechanical properties of a columnar-grained nickel-base superalloy*. Journal of Metals, 1971. **23**(7): p. 38-40.
13. V. Sass, U. Glatzel, and M. Feller-Kniepmeier, *Anisotropic creep properties of nickel-base superalloy CMSX-4*. Acta mater, 1996. **44**(5): p. 1967-1977.
14. J.C. Stinville, K. Gallup, and T.M. Pollock, *Transverse Creep of Nickel-Base Superalloy Bicrystals*. Metallurgical and Materials Transactions A, 2015. **46A**: p. 2516-2529.
15. A. Epishin, T. Link, U. Brückner, and P. Portella, *Kinetics of the topological inversion of the  $\gamma/\gamma'$  microstructure during creep of a nickel-based superalloy*. Acta materialia, 2001. **49**(19): p. 4017-4023.
16. N. Matan, D. Cox, C. Rae, and R. Reed, *On the kinetics of rafting in CMSX-4 superalloy single crystals*. Acta materialia, 1999. **47**(7): p. 2031-2045.
17. P. Caron, C. Ramusat, and F. Diologent. *Influence of the  $\gamma'$  fraction on the  $\gamma/\gamma'$  topological inversion during high temperature creep of single crystal superalloys*. in *Superalloys 2008*. 2008. Seven Springs, PA, USA: TMS. p. 159-167.
18. A. Gaubert, M. Jouiad, J. Cormier, Y. Le Bouar, and J. Ghighi, *Three-dimensional imaging and phase-field simulations of the microstructure evolution during creep tests of-oriented Ni-based superalloys*. Acta Materialia, 2015. **84**: p. 237-255.
19. R.C. Reed, N. Matan, D.C. Cox, M.A. Rist, and C.M.F. Rae, *Creep of CMSX-4 superalloy single crystals: effects of rafting at high temperature*. Acta mater, 1999. **47**(12): p. 3367-3381.
20. J. Cormier. *Thermal Cycling Creep Resistance of Ni-Based Single Crystal Superalloys*. in *Superalloys 2016: Proceedings of the 13th International Symposium of Superalloys*. 2016. Seven Springs, PA, USA: Wiley Online Library. p. 383-394.

21. T. Khan, P. Caron, and Y. Nakagawa, *Mechanical behavior and processing of DS and single crystal superalloys*. JOM, 1986. **38**(7): p. 16-19.
22. J. Tien and S. Copley, *The effect of orientation and sense of applied uniaxial stress on the morphology of coherent gamma prime precipitates in stress annealed nickel-base superalloy crystals*. Metallurgical Transactions, 1971. **2**(2): p. 543-553.
23. A. Epishin, T. Link, H. Klingelhöffer, B. Fedelich, and P. Portella, *Creep damage of single-crystal nickel base superalloys: mechanisms and effect on low cycle fatigue*. Materials at high temperatures, 2014.
24. M. Ott and H. Mughrabi, *Dependence of the high-temperature low-cycle fatigue behaviour of the monocrystalline nickel-base superalloys CMSX-4 and CMSX-6 on the  $\gamma/\gamma'$ -morphology*. Materials Science and Engineering: A, 1999. **272**(1): p. 24-30.
25. A. Altincekiç and E. Balıkcı, *Precipitate rafting in a polycrystalline superalloy during compression creep*. Metallurgical and Materials Transactions A, 2014. **45**(13): p. 5923-5936.
26. R. Reed, D. Cox, and C. Rae, *Damage accumulation during creep deformation of a single crystal superalloy at 1150 C*. Materials Science and Engineering: A, 2007. **448**(1): p. 88-96.
27. A. Epishin, T. Link, H. Klingelhoff, P. Portella, and B. Fedelich, *Creep damage of single-crystal superalloys: mechanisms and effect on low cycle fatigue*. Materials At High Temperature, 2010. **23**(1): p. 53-59.
28. R. Chieragatti and L. Remy, *Influence of orientation on the low cycle fatigue of MAR-M 200 single crystals at 650° C: Fatigue life behaviour*. Materials Science and Engineering: A, 1991. **141**(1): p. 1-9.
29. D. Shah and D. Duhl. *The effect of orientation, temperature and gamma prime size on the yield strength of a single crystal nickel base superalloy*. in *Proceedings of the fifth international symposium on superalloys, ASM, Metals Park, Ohio*. 1984
30. H. Frenz, J. Kinder, and P. Portella. *Behavior of single crystal superalloys under cyclic loading at high temperatures*. in *EUROMAT 97: 5 th European Conference on Advanced Materials and Processes and Applications*. 1997. p. 1997.
31. U. Tetzlaff and H. Mughrabi, *Enhancement of the high-temperature tensile creep strength of monocrystalline nickel-base superalloys by pre-rafting in compression*. Pollock, TM, Kissinger, RD, Bowman, RR, Green, KA, McLean, M. et, 2000.
32. H. Mughrabi and U. Tetzlaff, *Microstructure and High-Temperature Strength of Monocrystalline Nickel-Base Superalloys*. Advanced Engineering Materials, 2000. **2**(6): p. 319-326.
33. P.K. Wright and A.F. Anderson. *The influence of orientation on the fatigue of directionally solidified superalloys*. in *Superalloys 1980*. 1980. Seven Springs, Champion, PA, USA: TMS. p. 689-698.
34. J. Cormier and G. Cailletaud, *Constitutive modeling of the creep behavior of single crystal superalloys under non-isothermal conditions inducing phase transformations*. Materials Science and Engineering: A, 2010. **527**(23): p. 6300-6312.
35. M. Benyoucef, A. Coujou, B. Barbker, and N. Clement, *In situ deformation experiments on a  $\gamma/\gamma'$  superalloy Strengthening mechanisms*. Materials Science and Engineering: A, 1997. **234**: p. 692-694.
36. T. Pollock and A. Argon, *Directional coarsening in nickel-base single crystals with high volume fractions of coherent precipitates*. Acta metallurgica et materialia, 1994. **42**(6): p. 1859-1874.
37. T. Pollock and A. Argon, *Creep resistance of CMSX-3 nickel base superalloy single crystals*. Acta Metallurgica et Materialia, 1992. **40**(1): p. 1-30.
38. A. Epishin, T. Link, H. Klingelhöffer, B. Fedelich, U. Brückner, and P.D. Portella, *New technique for characterization of microstructural degradation under creep: Application to the nickel-base superalloy CMSX-4*. Materials Science and Engineering: A, 2009. **510**: p. 262-265.

# Chapter 4 – Damage mechanisms and durability

## Chapitre 4 Mécanismes d'endommagement et durabilité

Ce dernier chapitre constitue le cœur de ces travaux de thèse et celui contenant la plus forte plus-value scientifique. Il aborde les mécanismes d'endommagement observés pour l'alliage DS200+Hf, en focalisant sur la durabilité en fatigue et en fluage et en comparant les résultats expérimentaux à des modèles de prédiction de durée de vie.

Le premier facteur contribuant à l'endommagement de cet alliage est la présence de nombreux défauts métallurgiques dans la microstructure du DS200+Hf. En raison de la haute teneur en Hafnium qui est ajoutée à l'alliage pour faciliter la solidification de composants relativement élancés, ainsi qu'un haut taux de carbone, de nombreux carbures primaires sont observés dans cet alliage (HfC, TiC, NbC), principalement aux joints des grains. En plus de ces carbures, des pores de solidification, des borures ainsi que des eutectiques sont présents dans les espaces interdendritiques. Il convient de noter que la porosité observée dans le DS200+Hf est bien plus faible que dans de nombreux autres alliages monogranulaires de première et deuxième génération solidifiés avec un procédé Bridgman analogue. Dans ce chapitre un focus particulier a été porté au rôle des carbures. En effet, de nombreux amorçages en fatigue oligocyclique à 650°C ont été obtenus en interne sur des amas de carbures HfC et il a été observé qu'en fluage et en fatigue oligocyclique à 900°C, l'amorçage des fissures intervient à la surface, depuis des carbures oxydés. L'un des résultats les plus spectaculaires obtenus dans ce travail a été de montrer que dès 5 minutes d'oxydation pure à 900°C, de nombreux carbures/borures présents à la surface du matériau sont déjà fissurés, probablement en raison des différences de dilatation thermique entre les carbures et la « matrice »  $\gamma/\gamma'$  entourant ces carbures. Ainsi, ces inclusions fissurées servent de sites d'amorçage préférentiels pour le développement de fissures longues en fatigue et fluage. .

L'effet de l'oxydation à 900°C a été creusé plus en détails pour comprendre l'endommagement préférentiel depuis les carbures/borures sous air. Ceci a été possible via la conduite d'essais de fatigue et de fluage sous air et sous vide secondaire. Vu que cet alliage ne forme pas une couche d' $Al_2O_3$  continue, dense et donc protectrice à 900°C, une fois que les carbures sont fissurés, l'oxydation se forme à l'intérieur des lèvres des fissures et assiste la propagation des fissures expliquant ainsi la fissure intergranulaire préférentielle observée en fluage et en fatigue sous air. En outre, il a été montré au travers d'essais ATG que l'augmentation de la densité de joints de grains dans les échantillons accélère l'oxydation, montrant bien le rôle néfaste de l'oxydation sur les propriétés mécaniques en favorisant la fissuration intergranulaire. Ceci a notamment été vérifié clairement via la réalisation d'essais de fluage avec des échantillons à parois minces ( $e = 0.5 \text{ mm}, 0.8 \text{ mm}$  et  $1.5 \text{ mm}$ ) ; il a été observé un bien plus fort abattement de la durée de vie en fluage en sens travers (de par l'oxydation aux joints des grains) et aucun effet paroi mince sur les échantillons monogranulaires.

Les essais de fissuration réalisés sous air et sous vide ont permis de mieux comprendre pourquoi les durées de vie en fatigue oligocyclique sous air et sous vide à 900°C sont les mêmes, quand bien même il a été montré que les carbures sont fissurés dès le début de l'essai. Il a été observé que sous air, la fissure se développe plus rapidement dû aux carbures oxydés mais la propagation est légèrement plus lente dans le domaine de Paris et le seuil de fissuration est plus élevé car l'épaisseur de la couche oxydée en pointe de fissure conduit à son émoussement, réduisant ainsi les contraintes en pointes de fissures. Sous vide, les carbures ne sont plus les sites d'amorçage principaux (amorçage sub-surfacique sur pore). Ainsi, l'amorçage est plus long à intervenir, mais une fois amorcée, la fissure se propage très vite avec aucun émoussement et très peu de fermeture. De plus, le seuil de fissuration est bien plus bas sous vide comparativement à l'air. Ainsi, cette non différence de durée de vie en fatigue à 900°C, quelle que soit la direction de sollicitation, résulte de proportions amorçage/propagation totalement différentes sous air et sous vide. Le mode de fissuration intergranulaire est le seul mode

d'endommagement observé pour le DS200 pour une sollicitation transverse. Cela est expliqué par la grande quantité de carbure présente aux joints de grain. Pour des sollicitations en sens long, une durée de vie supérieure est obtenue en fluage et fatigue car le mode de rupture est principalement transgranulaire, autorisant un plus grand cumul de déformation et donc, plus de cavitation à rupture (à partir des défauts comme les eutectiques, pores de solidification et aussi carbures).

Un focus particulier a été porté dans ces travaux sur la criticité des joints de grains lors de sollicitations en sens travers, en se posant comme question quels sont les configurations cristallines les plus critiques. Ceci a été réalisé via des essais de fluage avec marqueurs de déformations dans les grains, ainsi que par corrélation d'images, couplé à des analyses EBSD. A 900°C, la cristallographie semble avoir peu d'effet sur l'amorçage intergranulaire et l'oxydation des carbures/borures aux joints des grains est le principal mécanisme contrôlant l'amorçage de fissure. A 750°C et sous fortes contraintes appliquées ( $\sigma$  égales ou supérieures à 700 MPa) les fissures se développent de façon préférentielle entre des grains orientés  $\langle 100 \rangle$  et des grains proches à  $\langle 110 \rangle$  suivant l'axe de sollicitation. Une seconde configuration critique a pu être identifiée, avec un amorçage intergranulaire entre un grain  $\langle 100 \rangle$  et un grain  $\langle 102 \rangle$ . Il a été observé que l'amorçage intergranulaire à 750°C pour ces deux configurations correspond à un fort contraste de déformation à l'échelle des grains, les grains orientés proche à  $\langle 110 \rangle$  se déforment relativement peu dans une configuration DS sollicitée en sens travers, quand bien même ils ont été montrés comme très ductiles dans ces conditions de fluage en version monogranulaire, en raison de leur forte aptitude à la rotation cristalline. Ainsi, l'amorçage intergranulaire en fluage à basse température/forte contrainte est principalement contrôlé par la compatibilité à la rotation cristalline de part et d'autre du joint de grain (les grains orientés proche  $\langle 100 \rangle$  sont peu aptes à la rotation cristalline tandis que ceux orientés proche de  $\langle 102 \rangle$  ou  $\langle 110 \rangle$ , étant orientés pour du glissement simple, sont plus aptes à tourner cristallographiquement).

Pour conclure ce chapitre, des travaux de modélisations ont été entrepris. Deux modèles de prévisions de la durée de vie en fatigue et en fluage ont été développés. Le modèle de fatigue est basé sur une loi Onera et il a été employé pour reproduire au mieux la base de données expérimentale de fatigue oligocyclique à 650°C. Il a par la suite été identifié à 900°C, avec un travail particulier sur la prise en compte des interactions fatigue-fluage pour reproduire au mieux les essais de fatigue avec temps de maintien. Ainsi, il a été montré qu'un cumul de dommage linéaire est plus performant qu'un cumul non-linéaire pour reproduire les données expérimentales. Un modèle de fluage basé sur la loi Norton couplée avec la loi Rabotnov-Kachanov et prenant en considération les effets de l'oxydation a également été développé. La principale originalité de ce modèle de fluage est que, de par sa formulation avec une normalisation de la contrainte appliquée par la contrainte ultime en traction, il permet de prendre en compte implicitement l'anisotropie de durée de vie en fluage. Ainsi, l'ensemble des données expérimentales de fluage (essais sous air ou sous vide, échantillons massifs ou à parois minces, échantillons monogranulaires ou DS sollicités en sens long ou travers) a été re-simulé avec ce modèle et il a été montré une excellente prévision à fois de la durée de vie et de la vitesse de fluage minimales à 900°C. Ce modèle couplé comportement-endommagement de fluage, s'il permet de prendre en compte l'oxydation et l'anisotropie, ne considère pas les changements microstructuraux comme la mise en radeaux de précipités. C'est aussi le cas des modèles de fatigue identifiés. Ainsi, prendre en compte la dégradation de la microstructure de précipitation  $\gamma'$  (i.e. mise en radeaux, grossissement de la microstructure) serait nécessaire pour avoir une meilleure prévision du comportement et de la durée de vie, notamment pour des chargements anisothermes.

Les principales conclusions de ce chapitre peuvent être donc résumées de la manière suivante : l'endommagement du DS200 + Hf en fluage et en fatigue résulte de l'amorçage de fissures depuis des défauts métallurgiques que sont les carbures et/ou les pores. Cet amorçage, ainsi que la propagation

ultérieure, sont largement influencés par l'oxydation qui possède à la fois un rôle néfaste sur l'amorçage et plutôt un effet positif sur la propagation des fissures. La cristallographie locale est également un facteur primordial pour comprendre quels joints de grains sont les plus critiques lors de sollicitations de fluage à basse température/fortes charges Enfin, la mise en radeaux de la phase  $\gamma'$ , même si elle ne peut pas être considérée comme endommagement en tant que tel (au sens du mécanicien), contribue néanmoins à accélérer la déformation viscoplastique et donc, à accélérer l'amorçage de fissures, comme cela a pu être observé lors des essais de fatigue avec temps de maintien.





## Table of contents (Chapter 4)

4.	Damage mechanisms and durability .....	122
4.1	Introduction.....	122
4.2	Crack initiation mechanisms from metallurgical defects .....	122
4.2.1	Crack initiation from metallurgical defects in low cycle fatigue .....	122
4.2.2	Crack initiation from metallurgical defects in creep .....	129
4.3	Impact of oxidation on the LCF and creep durability .....	135
4.3.1	TGA experiments .....	135
4.3.2	LCF at 900°C.....	138
4.3.3	Crack propagation tests.....	143
4.3.4	Creep at 900°C.....	147
4.4	Intergranular crack initiation during transverse creep testing .....	157
4.5	Creep, LCF and Dwell-fatigue life modeling .....	168
4.5.1	LCF life modeling at 650°C.....	169
4.5.2	Creep-oxidation-damage modeling at 900°C .....	171
4.5.3	Dwell-fatigue interactions modeling at 900°C .....	178
4.6	Conclusions.....	184

## Figures and tables (Chapter 4)

Figure 4.1 – Crack initiation sites in LCF in air at 650°C/Rσ=0.05 in DS-L (a, b), DS-T (c) and <001>-SX (d, e) specimens.....	124
Figure 4.2 – Typical crack initiation site in LCF at 650°C (a) and associated EDX analyzes showing the high hafnium content (b,c,d). This crack initiation site has already been presented in Figure 4.1(b). The atomic and mass concentrations resulting from a point chemical analysis in the middle of the particle (see green cross in (a)) are provided in (d). .....	125
Figure 4.3 – Grain boundary carbides in the as-received state in DS200+Hf alloy observed in back-scattered imaging mode to reveal chemical composition heterogeneities (see red arrows) (a, b). These heterogeneities are better observed in the APT characterization provided in (c) where a contrast in Hf content is observed and better quantified in (d) along the profile defined in (c). .....	126
Figure 4.4 – S-N diagram showing the LCF performance of GTD-444 bi-crystalline specimens loaded along transverse direction compared to DS200+Hf and <001>-SX MAR-M200+Hf specimens at 650°C/f=0.5 Hz/Rσ=0.05. ....	127
Figure 4.5 – Typical crack initiation in LCF at 650°C/f=0.5 Hz/Rσ=0.05 for GTD-444 bi-crystalline specimens loaded along transverse direction. White arrows are highlighting the pore serving as the crack initiation site and a eutectic.....	127
Figure 4.6 – Fracture surface after creep tests at 900°C/300 MPa for <001>-SX (a, c, e) and DS-L (b, d, f) specimens. ....	130
Figure 4.7 – Fracture surface after creep tests at 900°C/300 MPa along transverse direction in coarse (a, c, e) and fine (b, d, f) grain areas of DS200+Hf plates.....	131
Figure 4.8 – Fracture surface after transverse creep testing at 900°C/350 MPa in high vacuum in the fine grain area of DS200+Hf plates.....	132
Figure 4.9 – Crack initiation (see red arrows) after creep test at 900°C/350 MPa (a, b) and 900°C/400 MPa in DS-L specimens (c) and 900°C/350 MPa in <001>-SX specimen (d). Red dotted curves in (d) highlight at recrystallized areas around carbides. ....	133
Figure 4.10 – Crack initiation (see white arrows) after creep test at 750°C/800 MPa in DS-L (a) and CG DS-T (b) specimens. A magnified on fractured carbides are proposed in (a). ....	134
Figure 4.11 – Specimen gage length observations after interrupted creep tests at 0.8% creep strain at 900°C/400 MPa in FG DS-T (a, d) and CG DS-T (b, e) specimens and after 2% creep strain at 900°C/350 MPa in a FG DS-T specimen (c, f). White and black arrows show surface cracks. ....	134
Figure 4.12 – Crack initiation mechanisms in DS-T specimens after interrupted creep tests at 900°C/400 MPa/0.8% creep strain (a, b) and 900°C/350 MPa/2% creep strain (c, d). Experiments have been performed both for CG (a) and FG (b, c, d) material. Red arrows show internal crack initiation at grain boundaries and in the vicinity of carbides while horizontal white arrows highlight grain boundary crack initiation in (b, c).....	135
Figure 4.13 – TGA results at 900°C showing the evolution of the mass gain as a function of the grain boundary density. Schematic illustrations on how specimens were machined are shown in this figure. ....	137
Figure 4.14 – EDX characterization after transverse creep testing at 900°C/350 MPa for 57 hours..	137
Figure 4.15 – Fractured carbides after 3h of pure thermal exposure at 900°C observed in top view (a, b) and along cross-section (c, d). (d) is a magnification of (c) showing first stages of crack initiation along a grain boundary (see red arrow).....	138
Figure 4.16 – S-N diagram at 900°C/f=0.5 Hz/Rσ=0.05.....	139

Figure 4.17 – Crack initiation sites in LCF in air at 900°C/Rσ=0.05 in DS-L (a), <001>-SX (b) and DS-T (c) specimens. Red circles indicate initiation sites observed at higher magnification while blue arrows show other crack initiation sites. ....	140
Figure 4.18 – Crack initiation sites in LCF in high vacuum at 900°C/Rσ=0.05 in DS-L (a), <001>-SX (b) and DS-T (c) specimens. ....	142
Figure 4.19 – First stages of crack propagation at 900°C/Rσ=0.05/σ <sub>max</sub> =520 MPa in <001>-SX specimens in high vacuum (Nf=114,608 cycles) (a) and in air (Nf=151,320 cycles) (b). The insert in (b) shows numerous secondary cracks (red arrows) along the gage length. ....	142
Figure 4.20 – Schematic illustration of micro-crack propagation in LCF in DS200+Hf/<001>-SX MAR-M200+Hf alloys at 900°C. ....	143
Figure 4.21 – Crack propagation curves at 650°C and 900°C/20Hz/Rσ=0.05 in air and in high vacuum. ....	144
Figure 4.22 – Effective crack propagation curves at 650°C/20Hz/Rσ=0.05 in air and in high vacuum. ....	145
Figure 4.23 – Crack opening during propagation tests at 650°C/20Hz/Rσ=0.05: ΔK=10 MPa.m <sup>0.5</sup> /Vacuum (a), ΔK=10.2 MPa.m <sup>0.5</sup> /Vacuum (b), ΔK=18 MPa.m <sup>0.5</sup> /Air (c), ΔK=19.8 MPa.m <sup>0.5</sup> /Air (d). Delta' is the derivative of the crack opening. ....	145
Figure 4.24 – Top view observations of the crack propagation paths at 650°C/20Hz/Rσ=0.05. ....	146
Figure 4.25 – Top view observations of the crack propagation paths at 900°C/20Hz/Rσ=0.05. ....	147
Figure 4.26 – Comparison of creep properties in air and in high vacuum at 900°C/350 MPa (a) and 900°C/400 MPa (b). ....	148
Figure 4.27 – Intergranular crack propagation during transverse creep testing at 900°C/350 MPa in DS-T-FG specimens in high vacuum (a, c) and in air (b, d). (c) and (d) are magnified areas of (a) and (b) respectively. ....	149
Figure 4.28 – Transverse creep tests at 900°C/350 MPa in DS200+Hf specimens, first started in air up to a ~ 0.8% creep strain and then continued in high vacuum up to failure. ....	150
Figure 4.29 – Fracture surface after transverse creep testing at 900°C/350 MPa in FG DS-T specimen, first started in air up to a ~ 0.8% creep strain and then continued in high vacuum up to failure. ....	150
Figure 4.30 – Thickness effect on the creep properties at 900°C/350 MPa for <001>-SX (a), DS-L (b) and DS-T (c) specimens. ....	151
Figure 4.31 – Thickness debit in creep at 900°C/300 MPa, 900°C/350 MPa and 900°C/400 MPa in <001>-SX and DS200+Hf specimens along longitudinal and transverse directions. ....	152
Figure 4.32 – Evolution of the creep ductility at 900°C/300 MPa, 900°C/350 MPa and 900°C/400 MPa in <001>-SX and DS200+Hf specimens along longitudinal and transverse directions as a function of the P/S parameter. ....	153
Figure 4.33 – Thickness effect in creep at 900°C/300 MPa (a) and effect of pre-oxidation on creep properties at 900°C/350 MPa (b) in DS200+Hf along transverse direction. ....	154
Figure 4.34 – Creep damage mechanisms after 62 hours in creep at 900 °C/350 MPa (Creep strain = 3.8 %) along transverse direction in a ~0.8 mm thick specimen (a, b). (c) and (d) are magnified areas of (a) showing bulk GB cavitation (c) and oxidation assisted GB cracking (d). (b) is another area of the specimen showing oxidation assisted GB cracks. ....	155
Figure 4.35 – Fracture surfaces in dwell-fatigue at 900°C: <001>-SX/Δt=300s/Air (a), DS-L/Δt=300s/Air (b), DS-T/Δt=300s/Air (c), <001>-SX/Δt=10s/Air (d), DS-L/Δt=10s/Air (e), DS-T/Δt=10s/Air (f), <001>-SX/Δt=10s/Vacuum (g), DS-L/Δt=1s/Air (h) and DS-T/Δt=1s/Air (i). Magnification of crack initiation sites is provided as insert for single site crack initiation cases. ....	156

Figure 4.36 – Local creep strain elongation during transverse creep testing at 900°C/400 MPa and associated EBSD map whose color code refers to the applied stress direction. The grains in which creep strain evolutions are presented have been identified in the EBSD map (grains G1, G2, G3 and G4). .....	158
Figure 4.37 – Local creep strain elongation during transverse creep testing at 750°C/800 MPa and associated EBSD map whose color code refers to the applied stress direction. The grains in which creep strain evolutions are presented have been identified in the EBSD map (grains G1, G2, G3 and G4). .....	160
Figure 4.38 – Local creep strain elongation during transverse creep testing at 750°C/700 MPa using a ~0.5 mm thick specimen and associated EBSD map whose color code refers to the applied stress direction. The grains for which creep strain evolution is presented have been identified in the EBSD map (grains G1, G2 and G3). .....	161
Figure 4.39 – EBSD map of the DS-T specimen tested at 750°C/750 MPa whose color code refers to the applied stress direction (a), focusing on a favorable configuration for crack initiation where secondary cracks (see red arrows) have been detected (b). The rotation of the grains referenced in (b) after the creep tests are shown in (c) while the local $\gamma/\gamma'$ microstructure in grain G1 close to a secondary crack is shown in (d). .....	162
Figure 4.40 – Local creep strain elongation during transverse creep testing at 750°C/750 MPa whose grains referenced as “Grain 1”, “Grain 2”, and “Grain 5” corresponds to grains identified in Figure 4.39(b). .....	163
Figure 4.41 – Macroscopic creep elongation during transverse creep testing followed by DIC at 740°C/700 MPa. ....	164
Figure 4.42 – Longitudinal creep strain profile evolution (a) during transverse creep testing at 740°C/700 MPa along one specimen’s generatrix shown in (b). Two areas of creep strain localization are evidenced in (a), corresponding to the development of the grain boundary fatal crack and of a secondary crack, as shown in (c) and (d). .....	164
Figure 4.43 – Longitudinal creep strain profile evolutions during transverse creep testing at 740°C/700 MPa along different specimen’s generatrices. ....	165
Figure 4.44 – Longitudinal creep strain profile evolutions during transverse creep testing at 740°C/700 MPa along the 60° generatrix, as defined in Figure 4.43. ....	166
Figure 4.45 – EBSD map close to the secondary crack shown in Figure 4.42(d). IPF LD = Inverse Pole Figure along Loading Direction. ....	167
Figure 4.46 – EBSD maps on both sides of the fracture surface of the DS-T specimen tested at 740°C/700 MPa. The observations have been performed close to main crack initiation site according to local strain measurements presented in Figure 4.43. ....	168
Figure 4.47 – LCF modeling at 650°C for <001>-SX (a), DS-L (b) and DS-T (c) specimens. The calibration parameters have been provided for each type of specimen. ....	170
Figure 4.48 – Creep life evolution at 900°C using a radiant furnace as a function of the applied stress normalized by UTS (determined from tensile tests at 900°C/10 <sup>-5</sup> s <sup>-1</sup> ). ....	172
Figure 4.49 – Schematic illustration on how oxidation affects at the load bearing section of creep specimens. ....	173
Figure 4.50 – Comparison of the creep life evolution as a function of the applied stress at 900°C using a radiant furnace (FL) or a resistive furnace (FL). ....	175
Figure 4.51 – Schematic illustration of the loss of load bearing section along longitudinal section for <001>-SX specimens. ....	175

Figure 4.52 – Schematic illustration of the loss of load bearing section along longitudinal section for DS-T specimens. Note that “GB” accounts for a grain boundary.....	176
Figure 4.53 – Comparison of experimental and simulated creep curves at 900°C/350 MPa for DS-L specimens.....	177
Figure 4.54 – Comparison of experimental and simulated creep curves at 900°C/350 MPa for DS-T specimens.....	177
Figure 4.55 – Creep-oxidation-damage model performances in terms of minimum creep rate (a) and creep life (b). .....	178
Figure 4.56 – Schematic illustration of linear and non-linear accumulation of creep and fatigue damages, with $N_c$ the number of cycles up to failure in creep and $N_f$ the number of cycles up to failure in fatigue. ....	180
Figure 4.57 – Creep-fatigue model performances at 900°C using a linear accumulation approach for <001>-SX (a), DS-L (b) and DS-T (c).....	182
Figure 4.58 – Creep-fatigue model performances at 900°C using a non-linear accumulation approach for <001>-SX (a), DS-L (b) and DS-T (c). ....	183
Table 4.1 - Chemical composition of the carbides MC1 and MC2 defined in Fig. 4.3(c) (at. %). .....	126
Table 4.2 - Chemical composition GTD-444 alloy (wt. %). .....	126
Table 4.3 – Size and location of the crack initiation sites in LCF at 650°C/ $f=0.5$ Hz/ $R\sigma=0.05$ in air. Note that the crack initiation site size has been quantified measuring the diameter of the circle in which the crack initiation site can be included. ....	128
Table 4.4 – Size and location of the crack initiation sites in LCF at 900°C/ $f=0.5$ Hz/ $R\sigma=0.05$ in air. Note that the crack initiation site size has been quantified measuring the diameter of the circle in which the crack initiation site can be included. (N.M. = Not Measurable). ....	141
Table 4.5 – Size and location of the crack initiation sites in LCF at 900°C/ $f=0.5$ Hz/ $R\sigma=0.05$ in high vacuum. Note that the crack initiation site size has been quantified measuring the diameter of the circle in which the crack initiation site can be included.....	141
Table 4.6 – Summary of crystallographic configurations leading to crack initiation at low temperature/high applied stress and medium temperature/medium applied stress along transverse direction.....	159
Table 4.7 – Nomenclature of the variables/parameters used in Eqs. 4.2, 4.3 and 4.4.....	169
Table 4.8 – Nomenclature of the variables/parameters used in Eq. 4.6 and Eq. 4.7.....	171
Table 4.9 – Identified coefficients of the creep-damage-oxidation model identified at 900°C and used for massive and thin-walled specimens tested using a resistive furnace and experiments under vacuum. *UTS determined from tensile tests at 900°C/ $10^{-5}$ s <sup>-1</sup> . ** $e_0$ (the initial oxide thickness before applying the mechanical load) is 0 $\mu$ m under vacuum, 1 $\mu$ m for <001>-SX specimens and 5 $\mu$ m for all other DS200+Hf specimens.....	174
Table 4.10 – Coefficients of the creep-damage-oxidation model identified at 900°C and used for massive specimens tested using a radiant furnace. *UTS determined from tensile tests at 900°C/ $10^{-5}$ s <sup>-1</sup> . ** $e_0$ (the initial oxide thickness before applying the mechanical load) is 0 $\mu$ m under vacuum, 1 $\mu$ m for <001>-SX specimens and 5 $\mu$ m for all other DS200+Hf specimens.....	174
Table 4.11 – Calibration parameters for linear accumulation approach. ....	181
Table 4.12 – Calibration parameters for non-linear accumulation approach.....	181

## 4. Damage mechanisms and durability

### 4.1 Introduction

After the presentation of the mechanical behavior in monotonic tension, tension creep, LCF and dwell-fatigue in chapter 3, a special attention will be paid in this chapter to the different types of damage mechanisms observed in DS200+Hf alloy in terms of crack initiation and subsequent propagation mechanisms. Special attention will be paid to damage mechanisms in creep and LCF, especially at 900°C, a temperature at which a pronounced contribution of oxidation to the crack initiation and subsequent crack propagation mechanisms has been observed. This chapter will be organized as follow:

- In a first part, crack initiation mechanisms from metallurgical defects (i.e. clusters of carbides, eutectics, pores) will be presented. It will be shown that carbides may act as the main crack initiation sites in LCF at low temperature and that they could also act as crack initiation sites in creep.
- In a second part, the impact of oxidation on the creep and LCF durability will be presented. A careful analysis of the crack initiation and subsequent propagation for both type of mechanical loading will be performed. To gain a better understanding of the contribution of oxidation to the creep life, thin-wall creep tests will be presented, to increase to contribution of oxidation in the damage mechanisms. To better understand the damage mechanisms in LCF, crack propagation tests in air and in high vacuum will also be presented.
- In a third part, the mechanisms of grain boundary crack initiation during transverse creep testing will be investigated, using specific experiments during which in situ monitoring of the local creep strains have been followed using either strain markers or a digital image correlation technique. The main aim of these experiments is to identify which grain boundaries are the most critical in terms of crack initiation.
- Finally, in a last section, two modeling approaches formulated at the macroscopic scale will be presented and detailed. The first modeling is a coupled Norton-Kachanov approach in which an additional oxidation-induced damage evolution has been introduced. As a main originality of this approach, the anisotropy in creep behavior presented in the previous chapter has been taken into account, leading to one unique set of parameters for the creep behavior at 900°C, whatever the loading direction and specimen-type. The second modeling approach is based on the ONERA damage type laws. Its aim is to achieve a good modeling of the LCF life at 650°C varying the stress ratio, but also, to take into account dwell-fatigue interactions at 900°C, as already presented in the previous chapter.

### 4.2 Crack initiation mechanisms from metallurgical defects

#### 4.2.1 Crack initiation from metallurgical defects in low cycle fatigue

During LCF experiments at 650°C, all crack initiation sites have been observed to be internal or at sub-surface, starting from a carbide or a cluster of carbides (Figure 4.1). This type of crack initiation mechanism concerns DS alloys loaded along longitudinal and transverse directions as well as  $\sim <001>SX$ .

According to Figure 4.1, a first stage of crack propagation in mode I around the inclusion (a propagation supposed to be under vacuum) is first observed followed by a ductile fracture almost perpendicular to the loading direction for all specimens. The most remarkable difference on the fracture surfaces is noticed for DS-T specimens (see Figure 4.1(c)): “strips” corresponding to the dendritic structure are observed on the fracture surface, meaning that after a first stage of crack

propagation in mode I, subsequent stages of crack propagation and final failure occur in an intergranular way for this kind of specimen. It will be analyzed deeper in the following. The crack initiation mechanism observed in Figure 4.1 is in good agreement with the one observed by Chieragatti and Rémy [1]. They indeed observed crack initiation from MC carbides in SX MAR-M200 specimens with different orientations tested in LCF at 650°C in the high plastic strain range, despite no hafnium in their alloy. At lower plastic strain ranges, they however observed crack initiation at sub-surface casting pores. Our results are also in good agreement with the ones obtained by Gell and Leverant [2-4]. They indeed observed internal crack initiation from carbides in a high carbon containing version of MAR-M200 SX alloy in the 20°C-800°C temperature range while pore crack initiation was observed for a low carbon containing version of the alloy in the same ranges of temperature and frequency. **Carbides are hence clearly shown to be more detrimental to the LCF life at intermediate temperature than any other defect like pores or borides.**

To get a better understanding of the nature of crack initiation sites, EDX analyzes of the inclusions at the origin of cracks have been performed for several specimens. Figure 4.2 presents a typical example of all the LCF crack initiation sites observed at 650°C. Fatal cracks nucleate from hafnium rich carbides or clusters of carbides. As observed in the chemical analysis provided in Figure 4.2(d), this type of carbide is not a pure primary carbide of HfC type since the atomic concentration in hafnium and carbon are 28.6% and 54.6% respectively (see red circled lines in Figure 4.2(d)).

To confirm the exact nature of carbides serving as potential crack initiation sites in LCF, atom probe tomography (APT) characterizations have been performed at Max Planck Institute in Düsseldorf, Germany, in collaboration with Dr. P. Kontis. In the as-received state (i.e. after solution and aging heat treatments), it is already observed different contrasts in several carbides using a backscattered electron imaging mode in SEM observations, hence indicating probable differences in local chemical compositions (Figure 4.3(a) and (b)). These differences are observed more clearly using a hafnium density map (Figure 4.3(c)) or plotting the evolutions in hafnium, niobium, titanium and tungsten concentrations along the profile defined in Figure 4.3(c) (see Figure 4.3(d)). According to the average chemical compositions provided in Table 4.1 of the two carbides MC1 and MC2 defined in Figure 4.3(c) (the term “sub-carbides” would be better suited in this case), it is clearly seen that they do not correspond to primary MC carbides. They are rich in hafnium, niobium, titanium and also, tungsten to a lesser degree. By summing the hafnium, titanium and niobium contents, one can observed from Table 4.1 that MC1 and MC2 carbides are very close to a (Hf,Nb,Ti)C chemical composition, i.e. a primary carbide composition but not built with only one metallic type element.

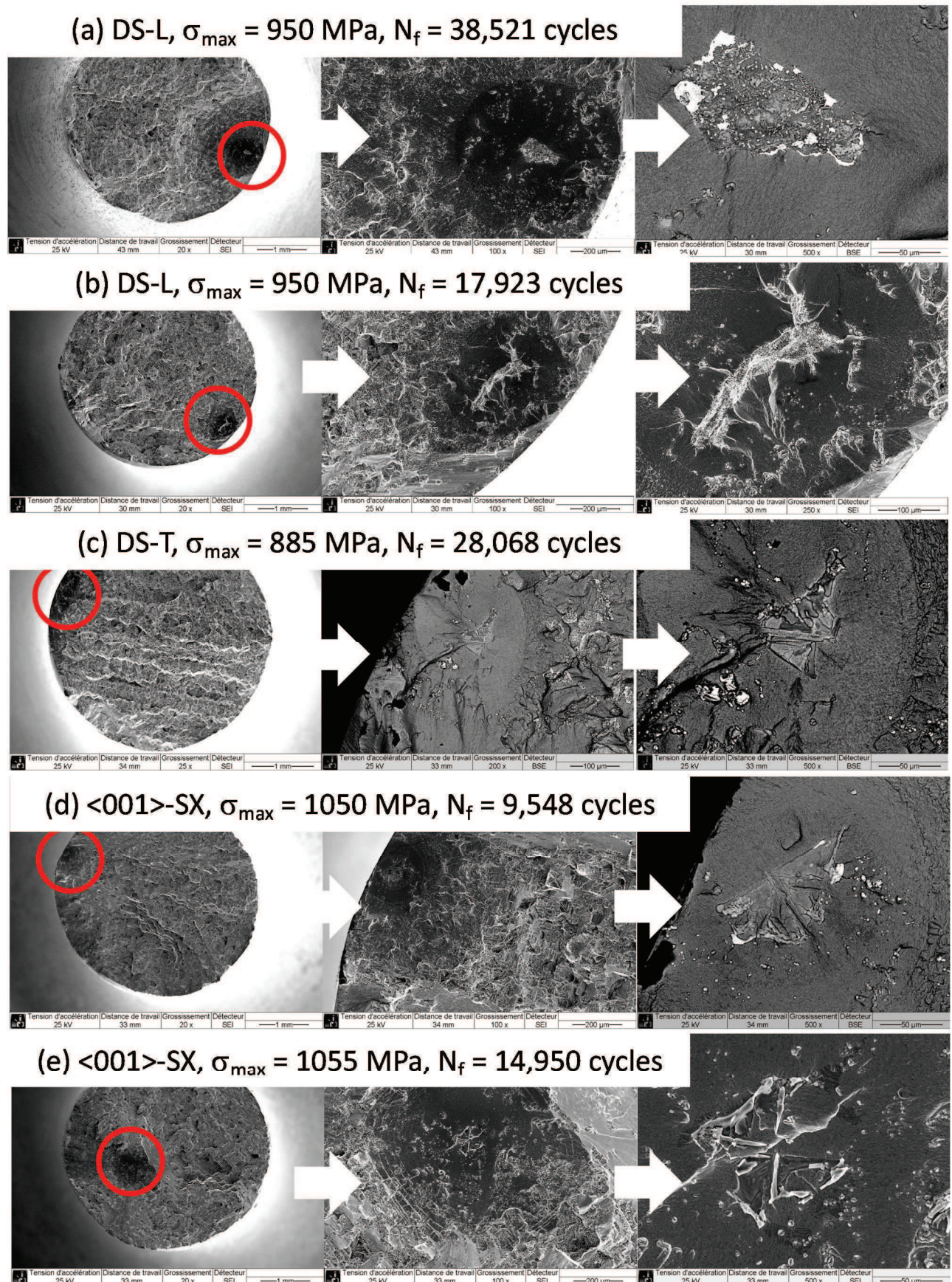


Figure 4.1 – Crack initiation sites in LCF in air at  $650^\circ\text{C}/R=0.05$  in DS-L (a, b), DS-T (c) and <001>-SX (d, e) specimens.



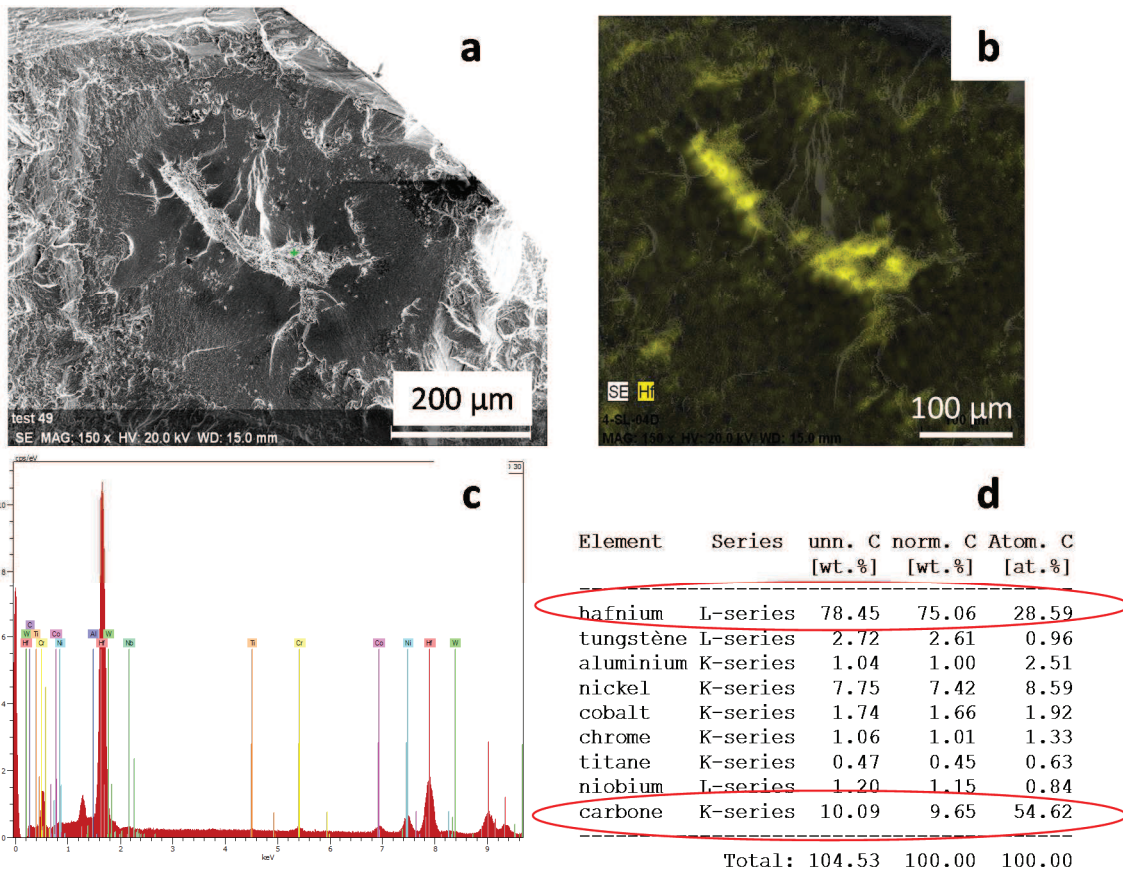


Figure 4.2 – Typical crack initiation site in LCF at 650°C (a) and associated EDX analyzes showing the high hafnium content (b,c,d). This crack initiation site has already been presented in Figure 4.1(b). The atomic and mass concentrations resulting from a point chemical analysis in the middle of the particle (see green cross in (a)) are provided in (d).

According to Figure 4.1(a) and (b), it seems qualitatively that the LCF life in load controlled mode at 650°C is dependent to the defect size at the origin of the total crack. It is indeed observed that for DS-L specimens loaded exactly under the same conditions (i.e.  $\sigma_{\max}=950$  MPa), the LCF life is decreased by a factor of nearly two when increasing the defect maximum diameter from 122  $\mu\text{m}$  to 188  $\mu\text{m}$ . To check this inclusion size dependence of the LCF life at 650°C, several tests have been performed using bi-crystalline GTD-444 specimens machined along transverse direction of a bi-crystalline plate provided by J.C. Stinville and T.M. Pollock from the University of California – Santa Barbara. Additional details about this alloy can be found in reference [5]. Specimens' machining has been done so has to obtain one unique grain boundary in the center of the gage length of the specimen (with a +/- 1 mm tolerance), and perpendicular to the loading axis. The chemical composition of GTD-444 is provided in Table 4.2 and several experimental results can be found in Appendix 6. As a very important information, it is here mentioned that the GTD-444 bi-crystalline plate was solidified using a liquid metal cooling process which is known to reduce the metallurgical defect size, especially the pore size [6, 7]. Compared to DS200+Hf studied during the present PhD thesis, GTD-444 presents a low fraction of primary carbides due to a lower carbon content without any hafnium content. Figure 4.4 shows a better LCF life at 650°C/ $R\sigma=0.05$  of GTD-444 bi-crystalline specimens compared to MAR-M200+Hf DS-T ones, despite both types of specimen have almost the same yield stress at 650°C/ $10^{-3} \text{ s}^{-1}$  (897 MPa for CG DS200+Hf along transverse direction and 885 MPa for GTD-444 bi-crystalline specimens along transverse direction, see appendix 1 and appendix 6

respectively). It is also observed from Figure 4.4 that GTD-444 performs even better than DS-L MAR-M200+Hf and almost similarly to <001>-SX MAR-M200+Hf.

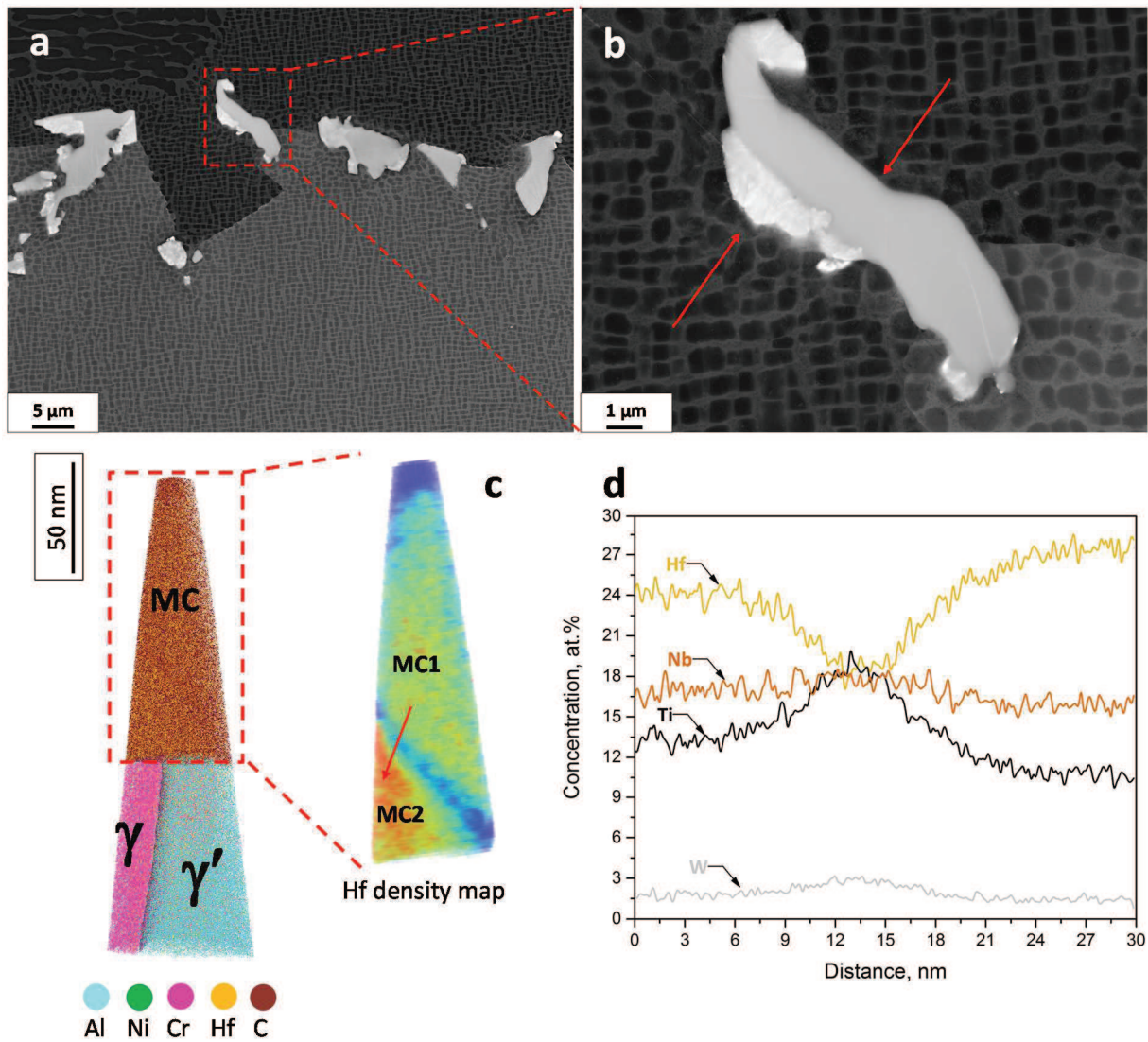


Figure 4.3 – Grain boundary carbides in the as-received state in DS200+Hf alloy observed in back-scattered imaging mode to reveal chemical composition heterogeneities (see red arrows) (a, b). These heterogeneities are better observed in the APT characterization provided in (c) where a contrast in Hf content is observed and better quantified in (d) along the profile defined in (c).

Element	Ni	C	Hf	Nb	Ti	W	Ta	Zr	Si	Cr	Al	Co	B
MC1	0.00	45.31	19.08	15.76	13.85	4.92	0.49	0.39	0.03	0.03	0.00	0.00	0.00
MC2	0.00	45.24	24.27	15.43	11.20	2.06	1.16	0.35	0.03	0.04	0.00	0.00	0.00

Table 4.1 - Chemical composition of the carbides MC1 and MC2 defined in Fig. 4.3(c) (at. %).

Element	Ni	Al	Ti	Ta	Nb	W	Mo	Cr	Co	Hf	C	B
GTD 444	Base	4.2	3.6	4.7	0.5	6.0	1.5	9.6	7.5	0.12	0.09	0.009

Table 4.2 - Chemical composition GTD-444 alloy (wt. %).

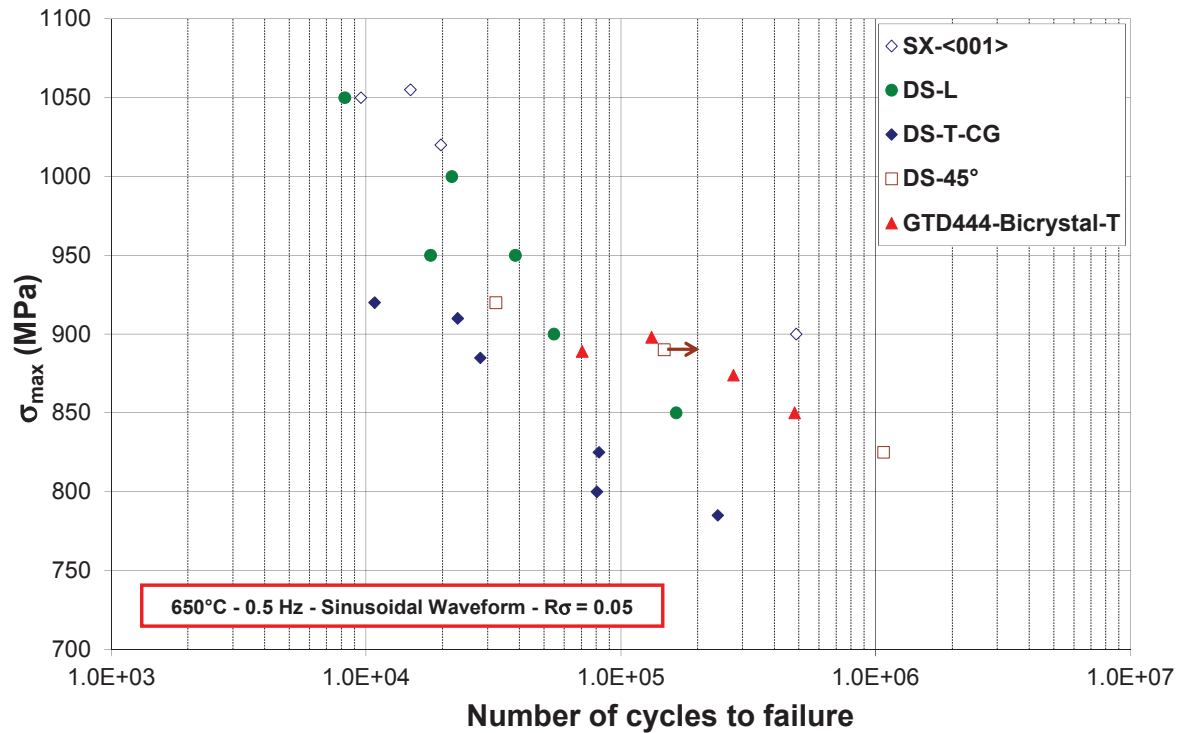


Figure 4.4 – S-N diagram showing the LCF performance of GTD-444 bi-crystalline specimens loaded along transverse direction compared to DS200+Hf and <001>-SX MAR-M200+Hf specimens at 650°C/f=0.5 Hz/Rσ=0.05.

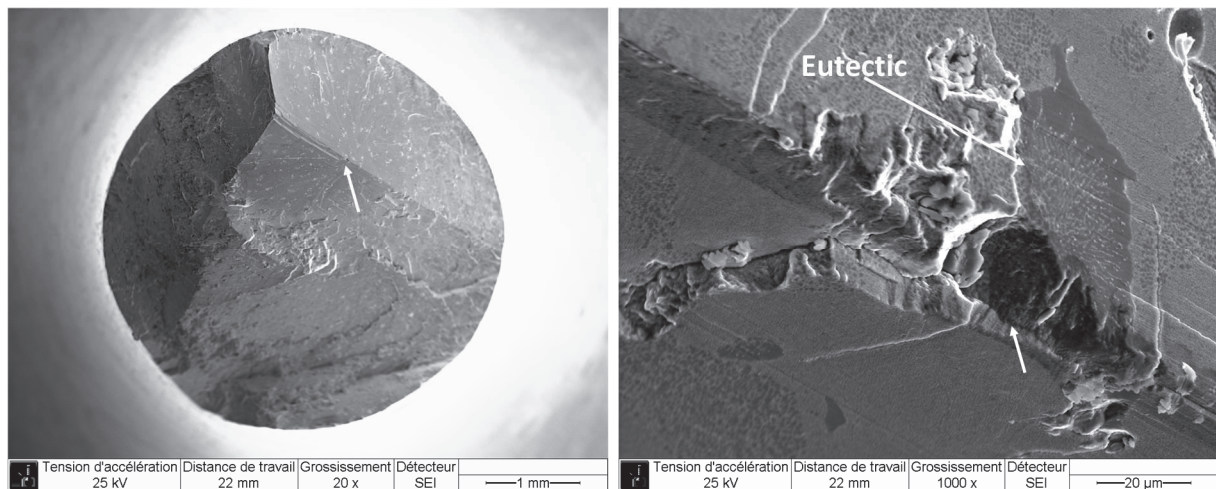


Figure 4.5 – Typical crack initiation in LCF at 650°C/f=0.5 Hz/Rσ=0.05 for GTD-444 bi-crystalline specimens loaded along transverse direction. White arrows are highlighting the pore serving as the crack initiation site and a eutectic.

These improved LCF performances of GTD-444 are better understood when analyzing the crack initiation mechanism. Once again, internal crack initiation is obtained in GTD-444 (Figure 4.5), in good agreement with Figure 4.1 and with the literature for this class of alloys and in this temperature range [7]. In case of GTD-444 specimens, internal crack initiation from pores was observed in LCF at 650°C in three experiments over four (see Table 4.3). Isolated pores or pores in the vicinity of remaining eutectic pools serve as crack initiation sites and only one crack initiation from a carbide/boride was observed. It is also clearly noted that, unlike DS-T MAR-M200+Hf specimens (see Figure 4.1(c)), crack initiation always occurred outside of the grain boundary in GTD-444 specimens

and no evidence of crack propagation along the grain boundary was observed during LCF experiments at 650°C. The maximum size of pores/inclusion serving as crack initiation sites in LCF for GTD-444 is in the [62 μm – 146 μm] range while it is [57 μm – 189 μm] for DS200+Hf/MAR-M200+Hf SX specimens (see Table 4.3). Based on this comparison in LCF performance between both alloys, it seems that (Hf,Ti,Nb)C carbides are more detrimental to the LCF life at 650°C, probably due to their brittleness, but also, due to their larger size in comparison to the pores observed in GTD-444. **LCF life at 650°C/Rσ=0.05/f=0.05Hz is hence clearly inclusion nature and size dependent, and then, chemistry and process dependent.**

Material	Specimen	σ <sub>max</sub> (MPa)	Initiation site maximum diameter (μm)	Type	Location
DS200+Hf/MAR-M200+Hf	DS-L	950	123	Carbide/Cluster	Internal
		950	189	Carbide/Cluster	Sub-surface
		1000	123	Carbide	Internal
		1050	104	Carbide	Internal
		900	123	Carbide	Internal
		850	115	Carbide	Internal
	DS-T	885	75	Carbide	Internal
		910	151	Carbide	Surface
		920	94	Carbide	Surface
		825	113	Pore + Carbides	Internal
		800	57	Carbide	Internal
		785	94	Carbide	Internal
	<001>-SX	1050	85	Carbide	Sub-surface
		1055	113	Carbide	Internal
		1020	104	Carbide	Internal
		900	85	Pore + Carbides	Internal
	DS-45°	920	106	Carbide	Internal
		825	135	Pore + Carbides	Internal
GTD-444	Bircrystal-T	874	128	Pore	Internal
		889	72	Pore	Internal
		850	62	Pore/Eutectic	Internal
		898	146	Carbide/Boride	Internal

Table 4.3 – Size and location of the crack initiation sites in LCF at 650°C/f=0.5 Hz/Rσ=0.05 in air. Note that the crack initiation site size has been quantified measuring the diameter of the circle in which the crack initiation site can be included.

Based on the measurement of the crack initiation sites presented in Table 4.3, an attempt has been made to correlate the total fatigue life to the size of the defect serving as the fatal crack initiation site. For that, a fatigue indicator parameter (FIP) approach has been evaluated, such as the one used successfully recently by Steuer et al. [7] and then, Cervellon et al. [8]. In these two references in which SX alloys were studied, the fatigue life has been correlated to the following FIP ( Eq. 4.1):

$$FIP = \frac{\mu \Delta \sigma}{E} \left[ 1 + k \frac{\Delta K}{\Delta K_{Threshold}} \right] \quad Eq. 4.1$$

where μ is the Schmid factor on the most heavily loaded slip system, E is the Young's modulus, Δσ is the applied stress amplitude, ΔK the stress intensity factor range, ΔK<sub>Threshold</sub> is the crack propagation threshold and k is a material parameter. In this kind of approach, the defect size dependence is hidden in the ΔK value, assuming that the defect serving as the crack initiation site is already a notch. Unfortunately, this kind of approach failed here to reproduce accurately the experimental LCF lives (not shown in this manuscript). This is probably due to the fact that the size of the defects serving as crack initiation sites is already large enough in several cases so that the ΔK value is already larger than the crack propagation threshold, as it will be shown later in this chapter. Indeed, as already observed previously by Chieragatti and Rémy, LCF crack initiation in SX MAR-M200 may occur directly during the first cycle in the high plastic strain range [1]. Several of our experiments have been developed within this domain (see chapter 3, Figs. 3.17 and 3.18), meaning that the LCF life at 650°C

is mainly spent within the crack (micro-)propagation domain, except at very low applied stresses (e.g.  $\sigma_{\max}=850$  MPa for DS-L or  $\sigma_{\max}=900$  MPa for  $\langle 001 \rangle$ -SX specimens).

Finally, as already shown in the previous chapter in Fig. 3.21, the anisotropy in LCF life at 650°C mainly results from the anisotropy in yield stress. No clear difference is observed in Table 4.3 in crack initiation site size as a function of the loading direction. Since the first stage of crack propagation is in mode I, whatever the loading direction, it is suspected that the anisotropy in LCF life mainly results from the extent of the volume affected by plasticity around non-metallic inclusions serving as crack initiation sites.

Crack initiation from carbides in LCF at 900°C in air has also been present in most of the cases, hence indicating that these particles are also detrimental at higher temperatures. However, since these crack initiations are mainly located at the surface of the specimens, the LCF crack initiation mechanisms at 900°C will be reported in section 4.3 of this chapter specifically devoted to the contribution of oxidation to the durability of the alloy.

#### 4.2.2 Crack initiation from metallurgical defects in creep

Typical fracture surfaces obtained in creep are shown in Figure 4.6 for DS-L and  $\langle 001 \rangle$ -SX specimens and in Figure 4.7 for DS-T specimens. These fracture surface observations are really typical of the ones obtained in creep, whatever the testing temperature (i.e. at 750°C, 900°C and 1100°C). The only specimens having a really different fracture mode are SX specimen far away from the perfect [001] crystallographic direction. At 750°C, a flat and inclined fracture surface is observed for [212] oriented specimens, despite a huge creep elongation in excess of 20% (see appendix 2 and Fig. 3.6). Compared to fracture in LCF, no single crack initiation site can be recognized. Ductile fracture is observed for monocrystalline specimen along the  $\langle 001 \rangle$  direction (Figure 4.6(a)) and also after longitudinal creep testing of DS specimens ((Figure 4.6(b)). At a higher magnification in backscattered imaging mode, carbides are present on the fracture surface of both type of specimen (see white spots in Figure 4.6(c), (d), (e) and (f)).

The situation is somewhat different after transverse creep testing. Indeed, like in LCF (see Figure 4.1(c)), an intergranular fracture mode is obtained, whatever the grain size (see Figure 4.7). At a higher magnification, an impressive network of carbides on the fracture surface was observed (see Figure 4.7(c), (d), (e) and (f)) once again indicating the intergranular character of fracture. Carbides are indeed mainly located at grain boundaries in DS200+Hf to strengthen them and increase the high temperature creep ductility [9]. According to Figure 4.8, intergranular fracture is also obtained during transverse creep tests at 900°C in high vacuum. Hence, this type of fracture is really intrinsic to transverse creep testing.

To get a better understanding of the role of metallurgical defects on the creep damage mechanisms, post-mortem longitudinal sections have been prepared and observed using scanning electron microscopy. Figure 4.9 and Figure 4.10 show damage development in the bulk of DS and SX specimens after creep tests at 900°C and 750°C, respectively. These observations have been performed far from the fracture surface (i.e. outside of the necking area of the specimens).

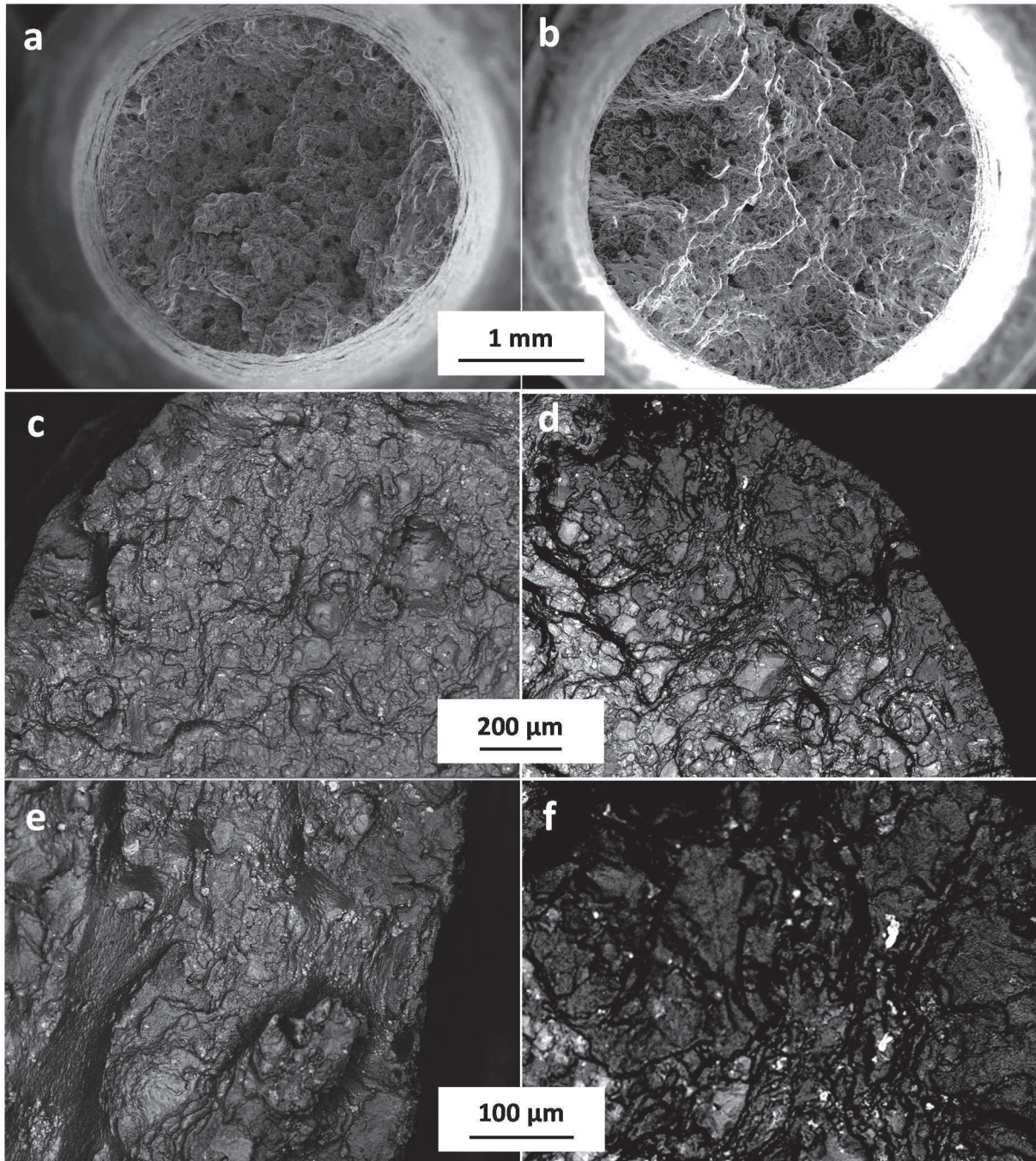


Figure 4.6 – Fracture surface after creep tests at 900°C/300 MPa for  $\langle 001 \rangle\text{-SX}$  (a, c, e) and DS-L (b, d, f) specimens.

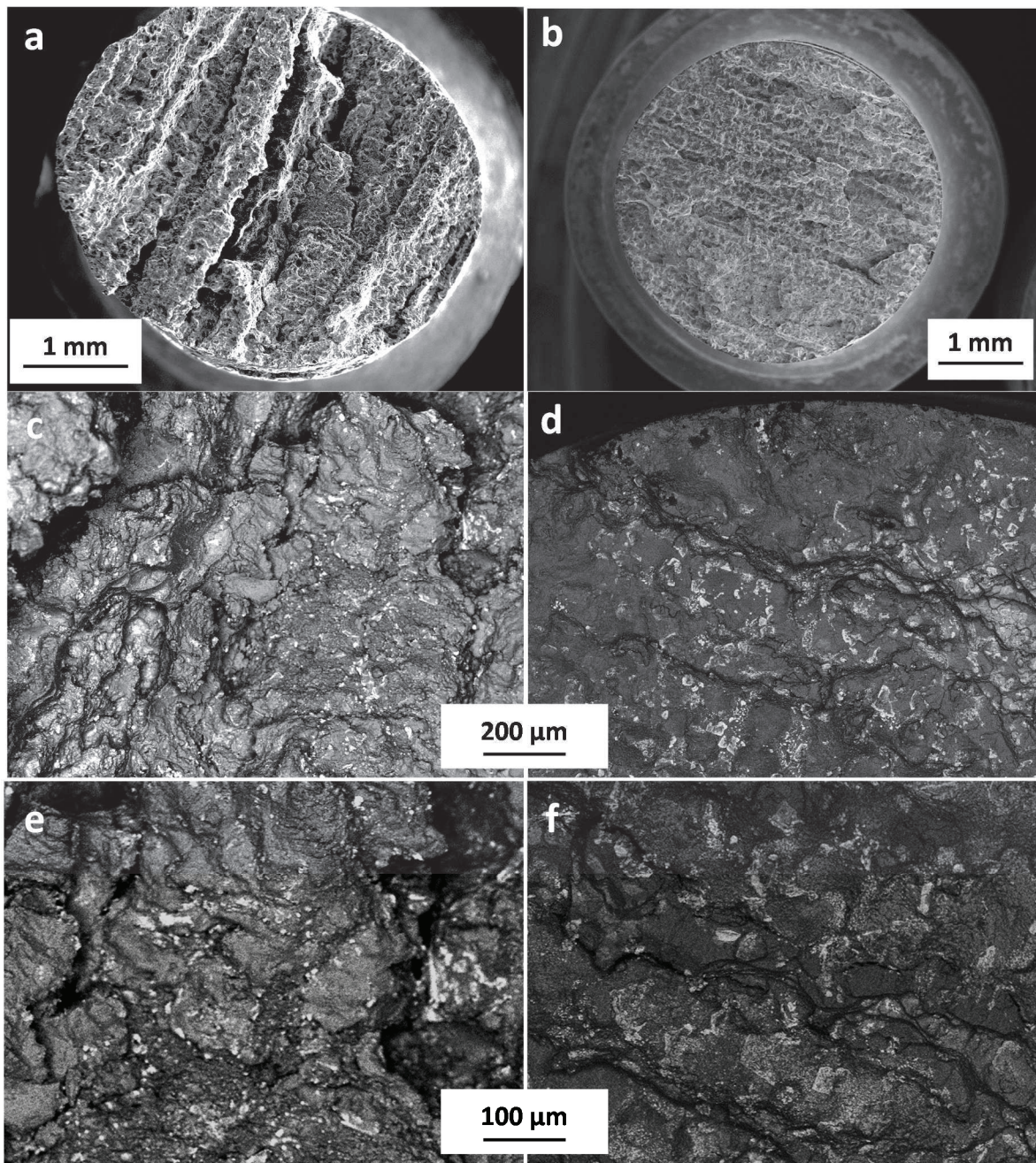


Figure 4.7 – Fracture surface after creep tests at 900°C/300 MPa along transverse direction in coarse (a, c, e) and fine (b, d, f) grain areas of DS200+Hf plates.

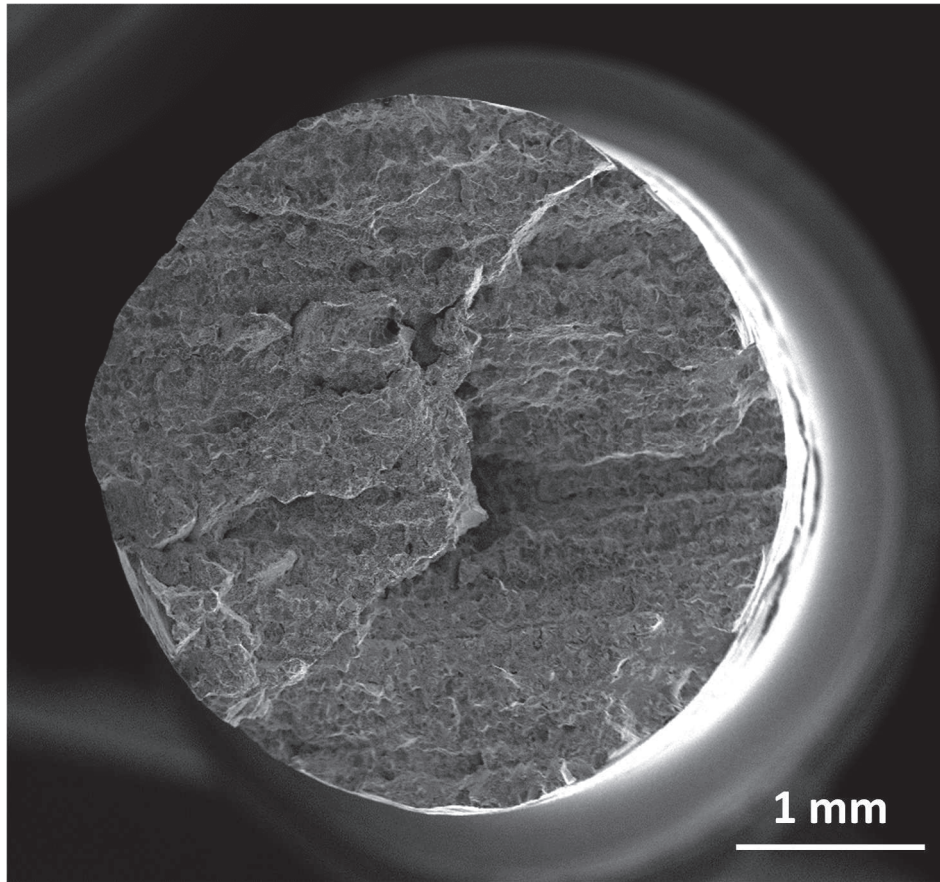


Figure 4.8 – Fracture surface after transverse creep testing at 900°C/350 MPa in high vacuum in the fine grain area of DS200+Hf plates.

Red arrows in Figure 4.9 point out several cracks nucleated in the vicinity of carbides or even, cracked carbides after creep tests at 900°C/350 MPa and 900°C/400 MPa. Similar features are present after longitudinal and transverse creep tests at 750°C/800 MPa in DS specimens (Figure 4.10). It is worth mentioning that there is no crack initiation from pores on these longitudinal sections. Micro-cracks develop along portions of grain boundaries almost perpendicular to the loading direction at 750°C/800 MPa (see especially Figure 4.10(a)), in good agreement with Q. Li et al. [10]. According to these observations, it is obvious that carbides also act as crack initiation sites in tensile creep both at 750°C and 900°C, like in LCF at 650°C. Moreover, according to Figure 4.9(d), localized recrystallized islands in the vicinity of carbides are observed after a creep test at 900°C/350 MPa using a  $\langle 001 \rangle$ -SX specimen (see areas delimited by red dotted curves), in good agreement with recent observations from L.H. Rettberg and T.M. Pollock after creep tests at 982°C using SX René N5 and DS GTD-444 superalloys (i.e. carbides containing Ni-based superalloys) [11]. At 1100°C/70 MPa, there are almost no internal cracks close to carbides and cracks start from the surface, assisted by oxidation. According to these post mortem characterizations, carbides are clearly detrimental to creep properties due to (i) their intrinsic brittleness leading to their cracking, and also, due to (ii) the stress field created around them (they act as stress concentrators [12]), leading to crack initiation between them and the surrounding  $\gamma/\gamma'$  “matrix” and also to possible localized recrystallization in their vicinity.

However, these observations have been performed after creep tests led up to failure, i.e. after quite large amounts of creep strain (in excess of 15-20% for DS-L and  $\langle 001 \rangle$ -SX specimens, see Figs. 3.8 and 3.10 and also, appendix 2) hence this cracking mode would result from the local large amount of



inelastic strain close to these non-metallic inclusions. To check this, interrupted transverse creep tests at 900°C/350 MPa and 900°C/400 MPa have been performed. These experiments have been conducted using cylindrical specimens machined along transverse direction in both FG and CG areas of DS plates. Experiments have been performed up to 0.8% or 2% creep strains. Before performing longitudinal sections, observations of the gage surface have been performed to detect the presence of cracks at the surface. For this, since the specimens are oxidized after such experiments at 900°C, a smooth polishing using 2000 and then 4000 grade SiC papers was applied, followed by a 10 seconds chemical etching in aqua regia to reveal the grain structure. According to Figure 4.11, several intergranular cracks are already observed after a 0.8% creep strain in both FG and CG specimens (see arrows). More cracks have been detected in the FG specimens, due to a higher grain boundaries density. It is here recalled that a 0.8% creep strain corresponds to the minimum creep rate reached during the experiments conducted at 900°C/350 MPa and 900°C/400 MPa (see Fig. 3.8(b)). We will come back on that point in a subsequent section of the chapter. By increasing the creep strain up to 2%, that is to say, in the tertiary creep stage, very long intergranular crack can be observed (see Figure 4.11(c) and (f)), in addition to a huge density of smaller ones not shown in this figure. Then, from these interrupted creep experiments, it is seen that intergranular cracks are developing very early in the creep life at 900°C of DS specimens.

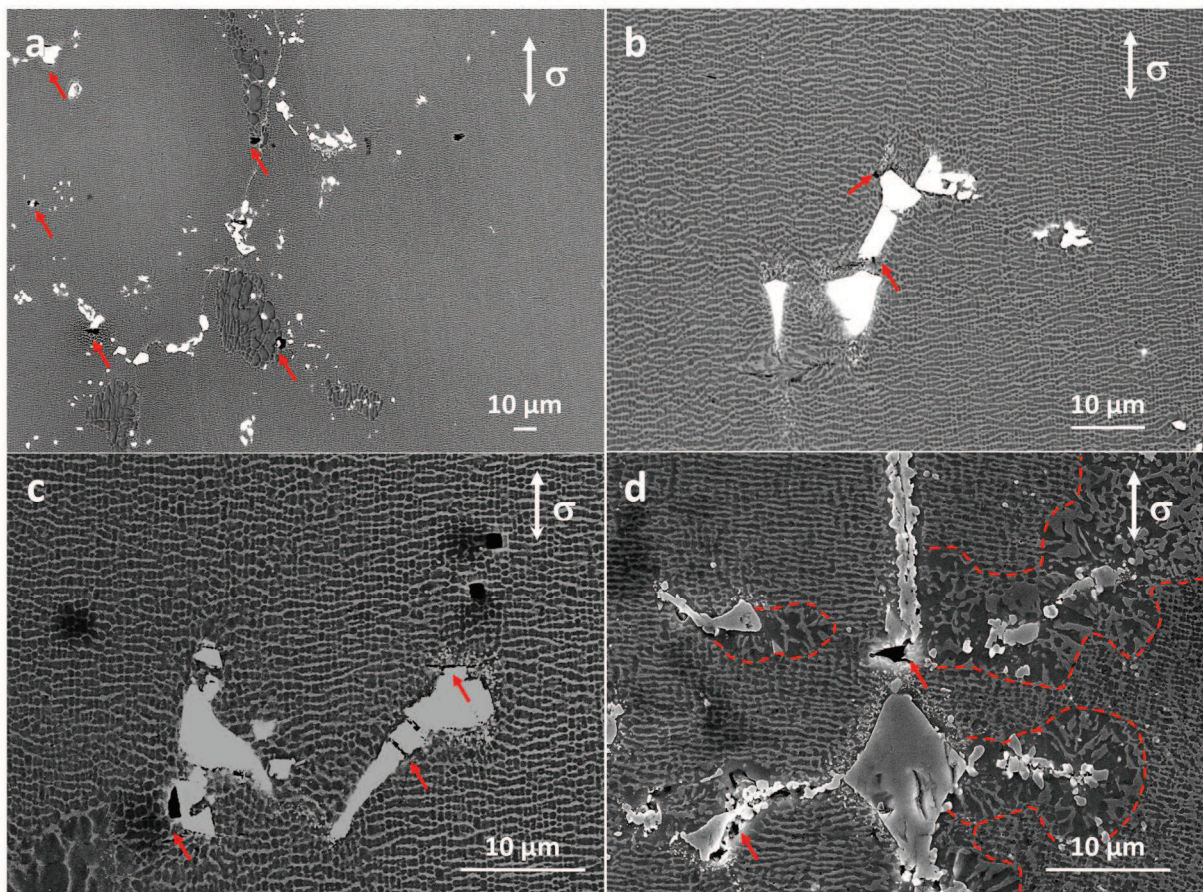


Figure 4.9 – Crack initiation (see red arrows) after creep test at 900°C/350 MPa (a, b) and 900°C/400 MPa in DS-L specimens (c) and 900°C/350 MPa in  $\langle 001 \rangle$ -SX specimen (d). Red dotted curves in (d) highlight at recrystallized areas around carbides.

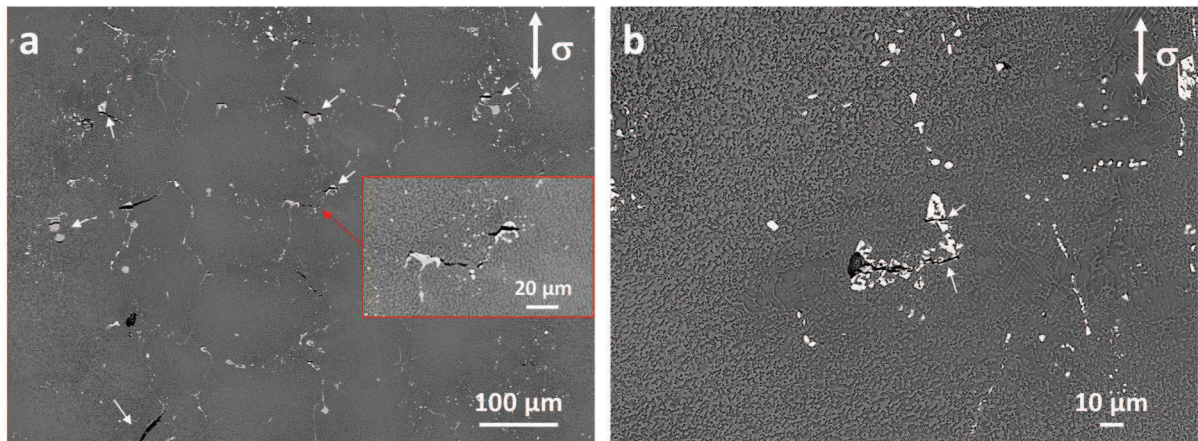


Figure 4.10 – Crack initiation (see white arrows) after creep test at 750°C/800 MPa in DS-L (a) and CG DS-T (b) specimens. A magnified on fractured carbides are proposed in (a).

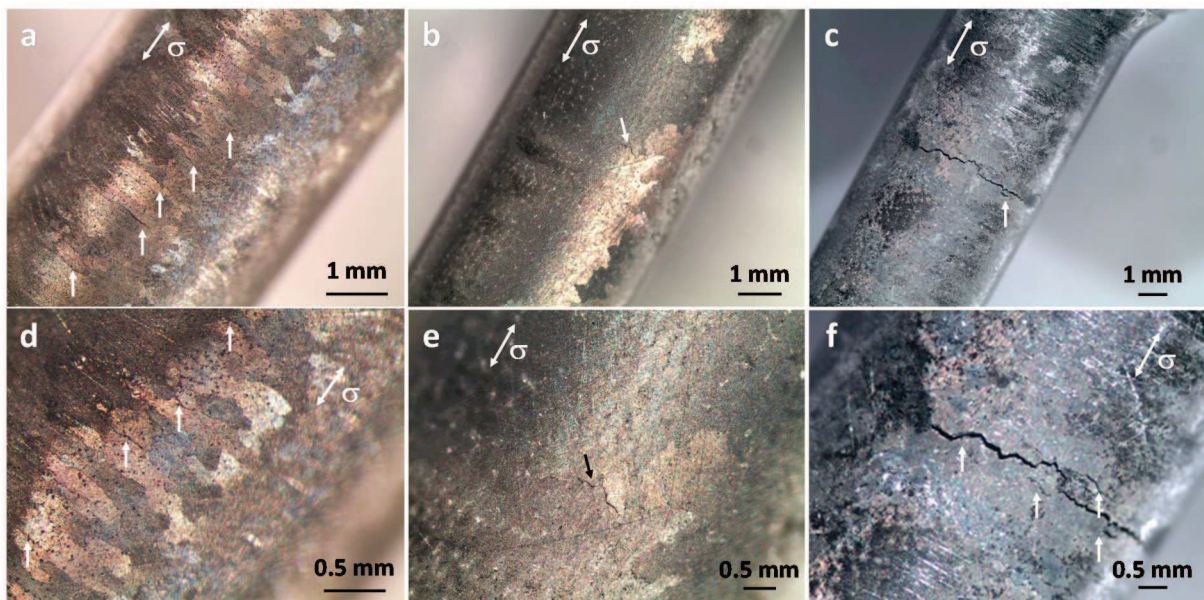


Figure 4.11 – Specimen gage length observations after interrupted creep tests at 0.8% creep strain at 900°C/400 MPa in FG DS-T (a, d) and CG DS-T (b, e) specimens and after 2% creep strain at 900°C/350 MPa in a FG DS-T specimen (c, f). White and black arrows show surface cracks.

After longitudinal sectioning of these specimens, it can be observed in Figure 4.12(b) and (c) that surface cracks observed in Figure 4.11 are oxidized (see white arrows in Figure 4.12). Moreover, several internal micro-cracks starting from carbides or at portions of grain boundaries perpendicular to the applied stress are observed (see red arrows in Figure 4.11(a), (c) and (d)).

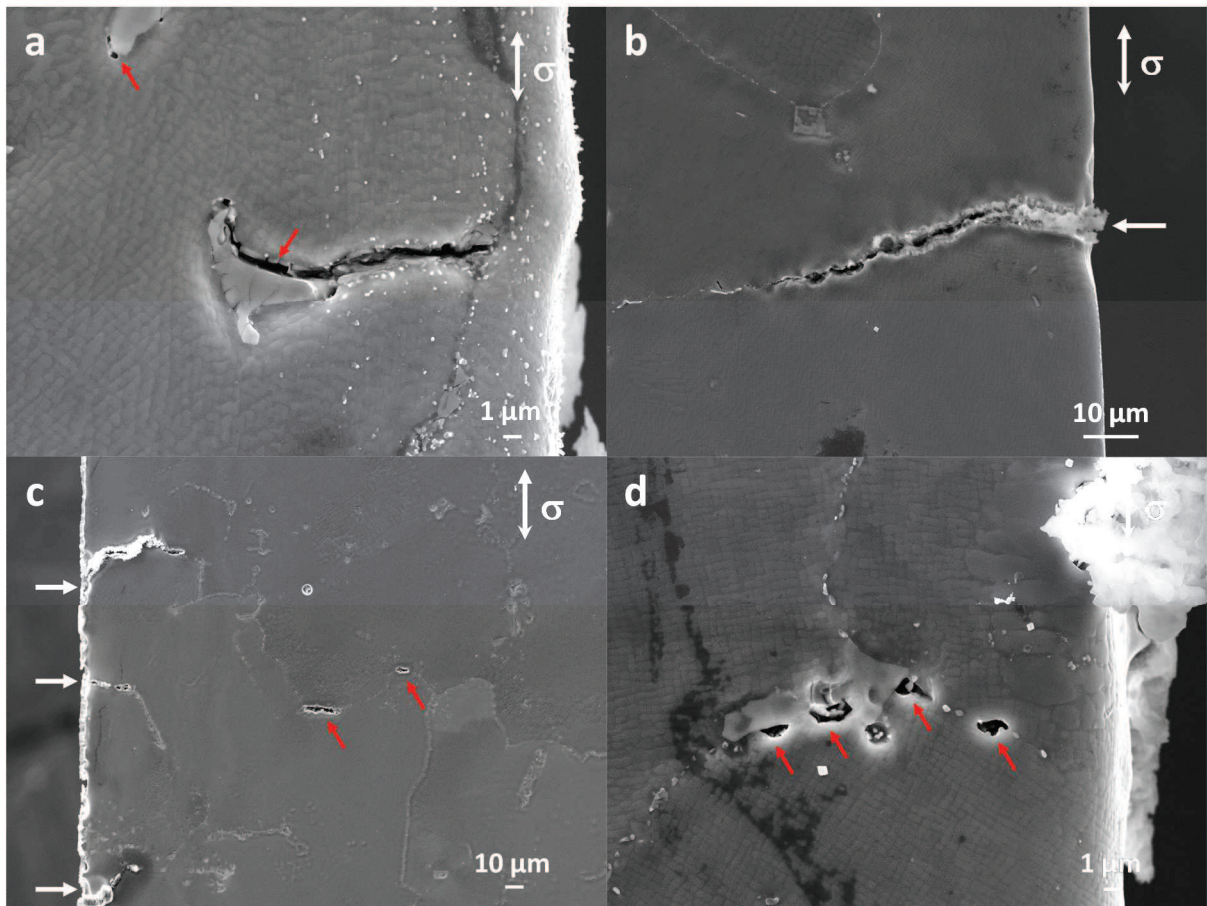


Figure 4.12 – Crack initiation mechanisms in DS-T specimens after interrupted creep tests at 900°C/400 MPa/0.8% creep strain (a, b) and 900°C/350 MPa/2% creep strain (c, d). Experiments have been performed both for CG (a) and FG (b, c, d) material. Red arrows show internal crack initiation at grain boundaries and in the vicinity of carbides while horizontal white arrows highlight grain boundary crack initiation in (b, c).

Finally, according to all of these characterizations, **carbides are clearly demonstrated to be intrinsically detrimental to both LCF and creep properties by favoring crack nucleation in their vicinity**. This is mainly a consequence of both their intrinsic brittleness and their role of stress concentrator, leading to their interfacial debonding with the surrounding  $\gamma/\gamma'$  material or leading to a localized recrystallization.

### 4.3 Impact of oxidation on the LCF and creep durability

This PhD work has shown that the anisotropy in creep and LCF life of DS200+Hf is highly temperature dependent (see Figs. 3.5, 3.20 and 3.22 in the previous chapter). For example, the anisotropy in creep life decreases with a temperature increase. This is in good agreement with the general trend observed in Ni-based single crystalline superalloys [13-15]. However, little works have been done up to now on the factors affecting the anisotropy in creep and LCF properties of DS alloys, and, especially on the contribution of oxidation to the damage mechanisms. This is the main objective of this sub-section.

#### 4.3.1 TGA experiments

As a first characterization, pure isothermal oxidation has been performed at 900°C in synthetic air to investigate the role of grain boundaries on the oxidation kinetics. According to TGA experiments (Figure 4.13), it is observed a higher mass uptake of DS specimens compared to the <001>-SX one.

The specific weight change is indeed ~20% greater in the DS-T-FG specimen compared to the <001>-SX one at the end of the experiments. Moreover, it is observed that this mass gain is slightly higher in the DS-T-FG specimen compared to the DS-T-CG one. This is clear indication that grain boundaries act as easier paths for element diffusion, resulting in faster oxidation.

According to EDX characterizations performed at the end of pure oxidation tests or after a creep test like in Figure 4.14, the oxides formed in the grain boundaries crack are chromium ( $\text{Cr}_2\text{O}_3$ ) and aluminum ( $\text{Al}_2\text{O}_3$ ) rich oxides. According to the literature, additional oxides like  $\text{HfO}_2$ ,  $\text{NbO}_2$ ,  $\text{TiO}_2$ ,  $\text{NiCr}_2\text{O}_4$  and  $\text{NiWO}_4$  are likely to form in this temperature range, but in lower proportions compared to  $\text{Cr}_2\text{O}_3$  and  $\text{Al}_2\text{O}_3$  [16]. Figure 4.14 shows that the oxide looks porous, especially within the grain boundary crack. These oxides are probably not efficient barriers to the further diffusion of oxygen toward the bulk of the material or, along grain boundaries. According to the EDX maps shown in Figure 4.14, it can also be concluded that  $\text{Cr}_2\text{O}_3$  is formed first followed by the formation of an inner layer of  $\text{Al}_2\text{O}_3$ . This can be concluded from Figure 4.14 since a chromium rich oxide is observed up to the crack tip while a lower concentration in aluminum rich oxides is observed close to the crack tip in comparison to the rest of the crack path.

After TGA experiments and short term pure oxidation tests of up to 3 hours at  $900^\circ\text{C}$ , observations of the surface and along cross sections of the specimens have been performed. Several carbides at the surface are found to be fractured (see Figure 4.15(a)). Similar fractured carbides have been observed after 30 minutes of pure thermal exposure at  $900^\circ\text{C}$ . The process of carbide cracking may occur due to the mismatch in thermal expansion between the carbide itself and the neighboring “ $\gamma/\gamma'$ ” matrix [17]. Moreover, an additional volume expansion is expected by the oxidation of the carbide. Figure 4.15(b) and Figure 4.15(c) clearly show fully cracked portions of the carbides and the very first evidence of crack initiation along the grain boundary from the carbide (see red arrow in Figure 4.15(c)). **This is a clear indication that carbides are highly sensitive to oxidation and that they may be already developing cracking along grain boundaries, even in the absence of any applied mechanical loading [18]. Once cracked, these carbides can be considered as “open doors” for further oxygen penetration along grain boundaries.**

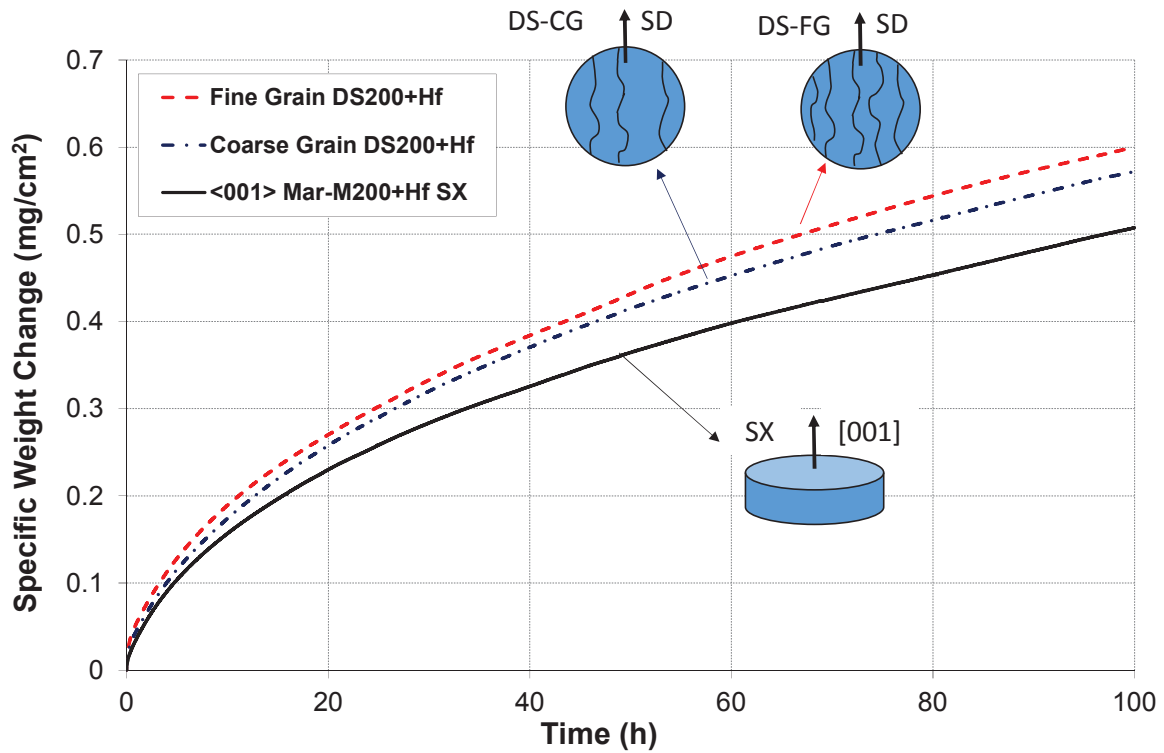


Figure 4.13 – TGA results at 900°C showing the evolution of the mass gain as a function of the grain boundary density. Schematic illustrations on how specimens were machined are shown in this figure.

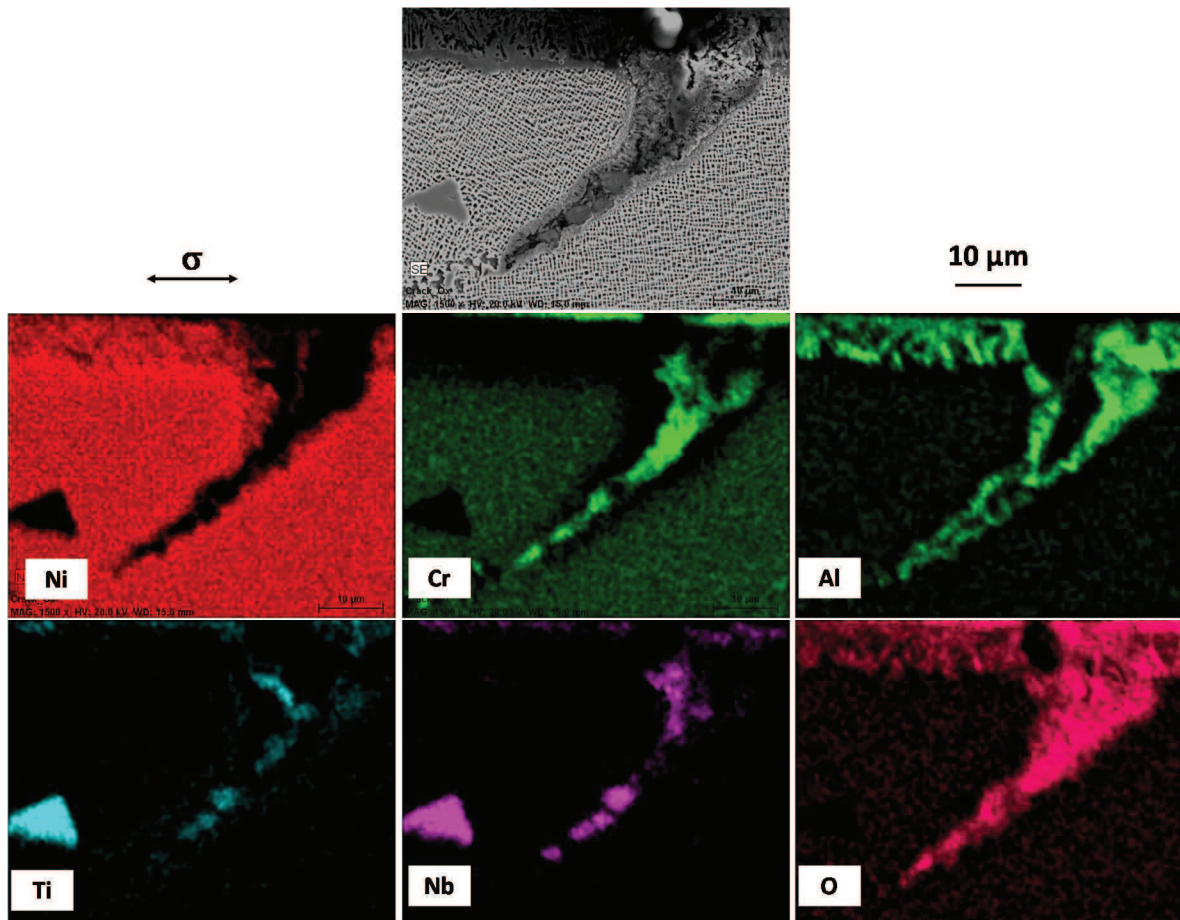


Figure 4.14 – EDX characterization after transverse creep testing at 900°C/350 MPa for 57 hours.

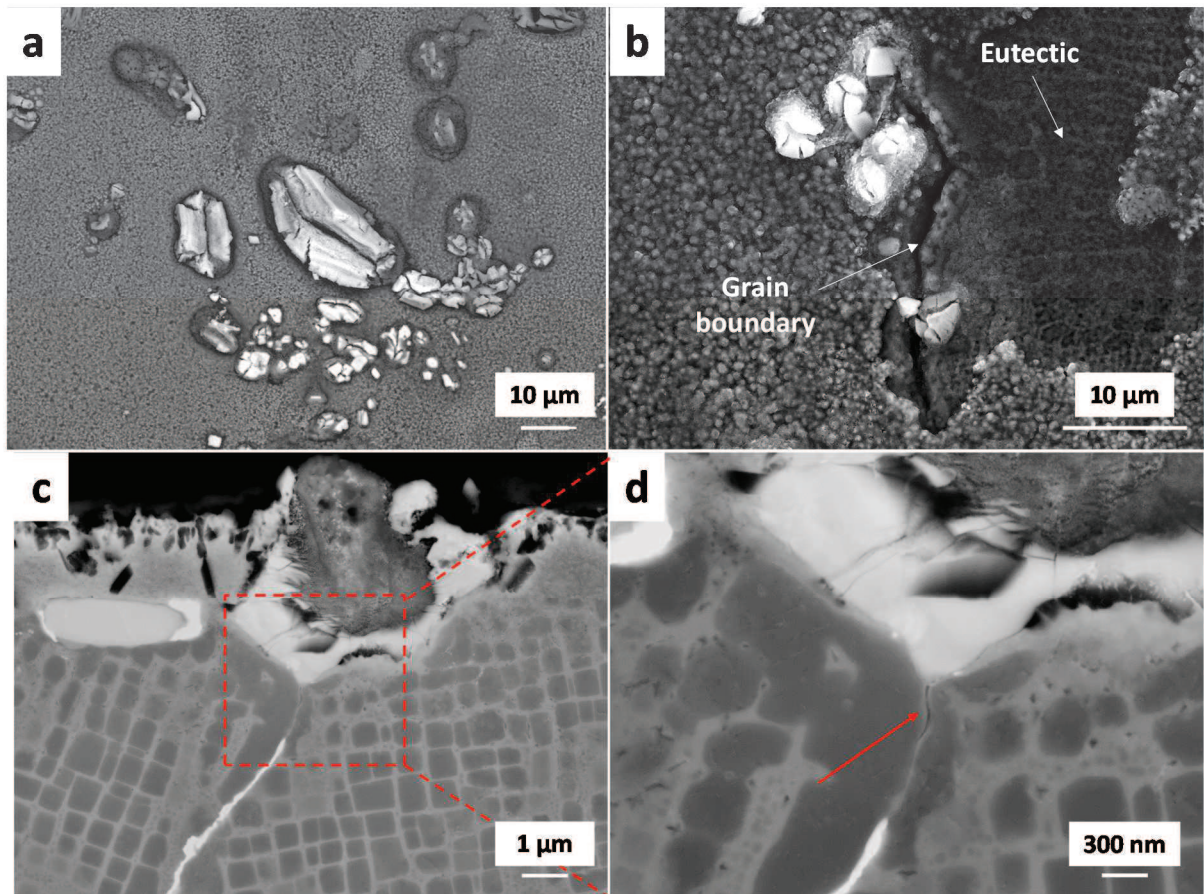


Figure 4.15 – Fractured carbides after 3h of pure thermal exposure at 900°C observed in top view (a, b) and along cross-section (c, d). (d) is a magnification of (c) showing first stages of crack initiation along a grain boundary (see red arrow).

#### 4.3.2 LCF at 900°C

One of the very surprising results presented in chapter 3 and shown again hereafter in Figure 4.16 is the apparent absence of any oxidation impact on the LCF life at 900°C/ $R\sigma=0.05$  in DS200+Hf as well as in <001>-SX MAR-M200+Hf specimens. Indeed, LCF lives in air and in high vacuum are almost the same for both materials. It is really surprising considering most of the results from the open literature showing major contribution of oxidation to the LCF life at temperatures in excess of 850°C-900°C in most of Ni-based single crystalline superalloys [7, 19]. To understand this non obvious result, several characterizations have been performed.

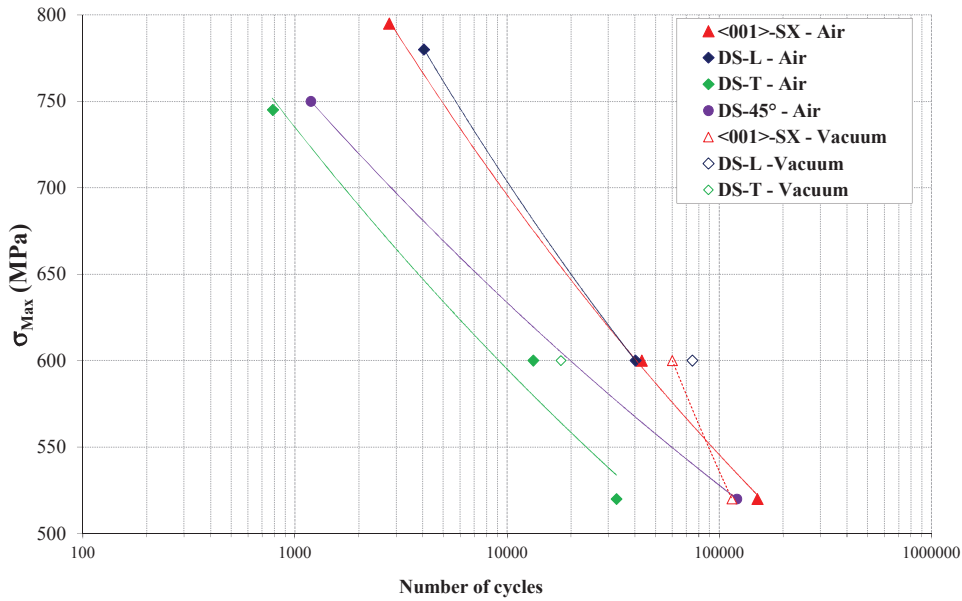


Figure 4.16 – S-N diagram at 900°C/f=0.5 Hz/Rσ=0.05.

Figure 4.17 shows typical fracture surfaces and crack initiation sites in LCF at 900°C in air for <001>-SX, DS-L and DS-T specimens. The type of fracture surface is always the same, whatever the applied stress amplitude. Contrary to LCF at 650°C, crack initiation almost always comes from the surface, from oxidized carbides, from the oxide scale or from a pore filled with carbides (see Table 4.4). The only exception concerns one DS-L specimen in which the main crack initiated from one large internal pore filled with small carbides. Moreover, several secondary cracks starting from the surface are observed in Figure 4.17 (see blue arrows) while only one single internal crack initiation site was detected in LCF at 650°C (see Figure 4.1). According to Table 4.4, crack initiation sites in LCF at 900°C are almost in the same range of size as the ones measured in LCF at 650°C (see Table 4.3), with sometimes a very small initiation site, corresponding to isolated oxidized carbides. It is also worth noticing that both DS-T MAR-M200+Hf and GTD-444 bi-crystalline specimens have a macroscopic intergranular fracture surface (see Figure 4.17(c) and Fig. A5-5, respectively). This was already the case for DS200+Hf in LCF at 650°C along transverse direction while GTD-444 did not exhibit intergranular fracture at 650°C (see Figure 4.5). It is a clear indication that oxidation also affects the crack propagation mode in bi-crystalline GTD-444 alloy. Moreover, contrary to the trend obtained at 650°C (see Figure 4.4), transverse LCF properties at 900°C in GTD-444 and DS200+Hf are almost the same (see Fig. A5-3). This may result from almost similar creep strength along transverse direction for both alloys at 900°C since continuous ratcheting is obtained in these LCF conditions (see Figs. 3.18(c) and 3.18(d)) and also, from the higher oxidation contribution to crack initiation.

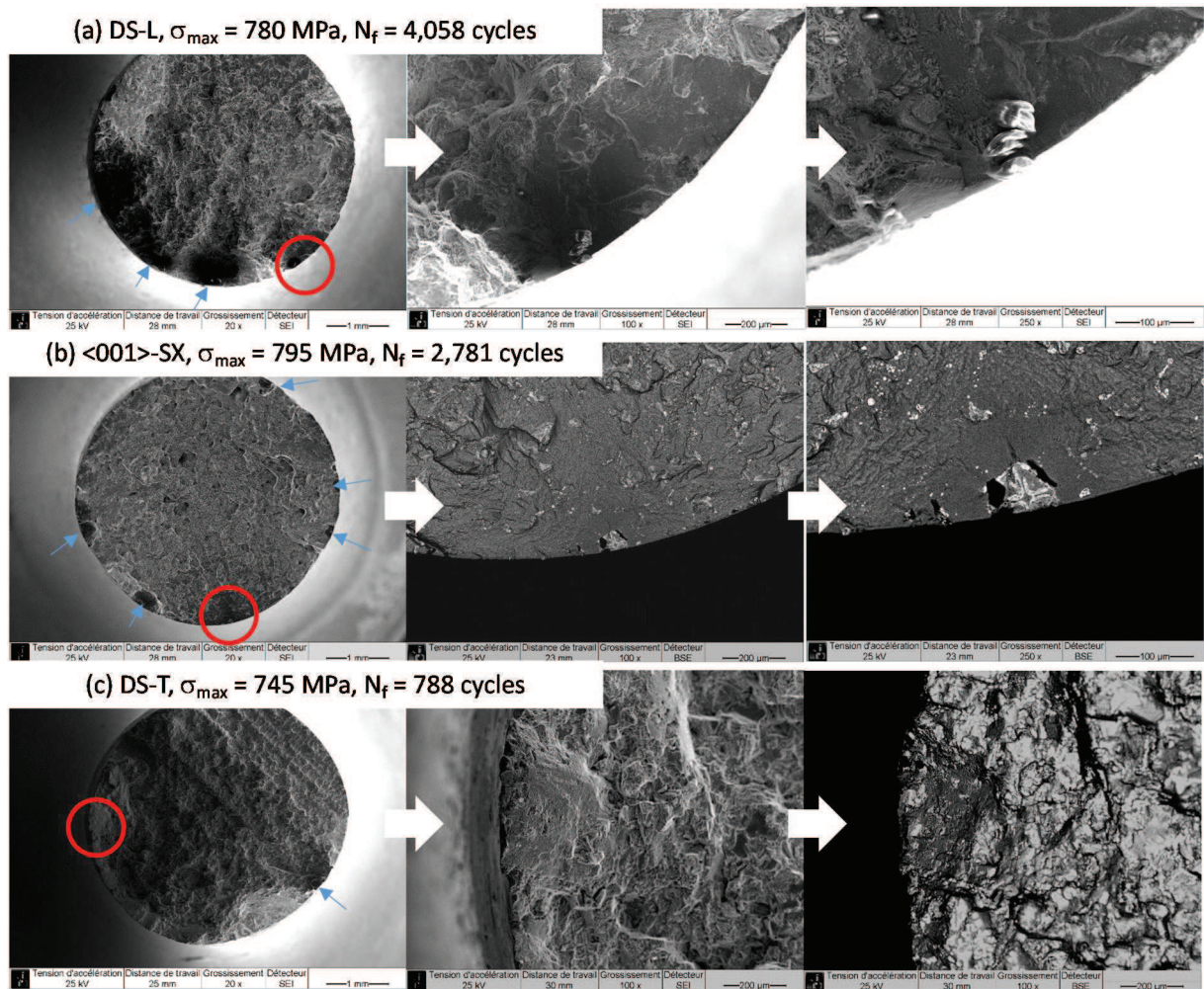


Figure 4.17 – Crack initiation sites in LCF in air at  $900^\circ\text{C}/R\sigma=0.05$  in DS-L (a),  $\langle 001 \rangle$ -SX (b) and DS-T (c) specimens. Red circles indicate initiation sites observed at higher magnification while blue arrows show other crack initiation sites.

Fracture surface after LCF test at  $900^\circ\text{C}$  in high vacuum are presented in Figure 4.18. Even if only 4 tests have been performed (see Table 4.5), a different crack initiation mode is clearly seen. First of all, cracks initiated from internal inclusions for two experiments like in LCF tests at  $650^\circ\text{C}$  (see, e.g. Figure 4.18(a)). Moreover, the two other specimens failed from a large solidification pore, connected to the surface of the specimen, in good agreement with the LCF results at  $950^\circ\text{C}$  in high vacuum obtained by Steuer et al. using AM1 Ni-based SX alloy [7]. Another main difference with LCF experiments at  $900^\circ\text{C}$  in air is that only one single crack initiation site has been detected in high vacuum in every experiment, as in LCF at  $650^\circ\text{C}$ .



Material	Specimen	$\sigma_{max}$ (MPa)	Initiation site maximum diameter ( $\mu\text{m}$ )	Type	Location
DS200+Hf/MAR-M200+Hf	DS-L	780	100	Carbide	Surface
		600	163	Pore + carbides	Internal
	DS-T	745	38	Carbide	Surface
		600	119	Carbide	Surface
		520	154	Oxide scale	Surface
	<001>-SX	795	87	Carbide	Surface
		600	196	Pore + Carbides	Surface
		520	135	Oxide scale	Surface
		520	48	Carbide	Surface
	DS-45°	750	105	Pore/carbide	Surface
520		115	Oxide scale	Surface	
GTD-444	Bircrystal-T	795	N.M.	/	Surface
		520	28/39/79	Pores (3)	Surface
		600	40	Pore	Internal

Table 4.4 – Size and location of the crack initiation sites in LCF at 900°C/f=0.5 Hz/R $\sigma$ =0.05 in air. Note that the crack initiation site size has been quantified measuring the diameter of the circle in which the crack initiation site can be included. (N.M. = Not Measurable).

Material	Specimen	$\sigma_{max}$ (MPa)	Initiation site maximum diameter ( $\mu\text{m}$ )	Type	Location
DS200+Hf/MAR-M200+Hf	DS-L	600	153	Carbide	Internal
	DS-T	600	114	Pore	Sub-surface
	<001>-SX	600	186	Pore cluster	Surface
		520	193	Pore + carbides	Internal

Table 4.5 – Size and location of the crack initiation sites in LCF at 900°C/f=0.5 Hz/R $\sigma$ =0.05 in high vacuum. Note that the crack initiation site size has been quantified measuring the diameter of the circle in which the crack initiation site can be included.

Having in mind these differences in crack initiation mode in LCF at 900°C when changing the environment, and the fact that surface carbides are highly sensitive to oxidation, longitudinal sections of LCF specimens have been performed to observe the morphology of secondary cracks, far from fracture. Figure 4.19 shows the morphology of short secondary cracks (length below 50  $\mu\text{m}$ ) in SX specimens tested in LCF at 900°C in air and high vacuum. According to this figure, several secondary cracks along the gage length in air (see insert in Figure 4.19(b)) are observed while only one secondary crack could have been detected along the gage length of the <001>-SX specimen tested in high vacuum, after three polishing attempts (Figure 4.19(a)). This crack is very sharp (Figure 4.19(a)) and it starts from a fractured carbide. A huge difference in crack morphology appears in air: the crack is full of oxides (mainly Cr<sub>2</sub>O<sub>3</sub> and Al<sub>2</sub>O<sub>3</sub> oxides, like in Figure 4.14 after a creep test at the same temperature). Moreover, crack tip blunting is observed, in addition to a  $\gamma'$ -depleted layer ahead of the crack tip and in the vicinity of the crack path. No such  $\gamma'$ -depleted layer is detected after LCF test in high vacuum in the vicinity of secondary cracks (see Figure 4.19(a)). Schematic illustrations of the crack initiation mechanisms and of the first stages of crack propagation in high vacuum and in air are proposed in Figure 4.20, with local microstructure evolutions.

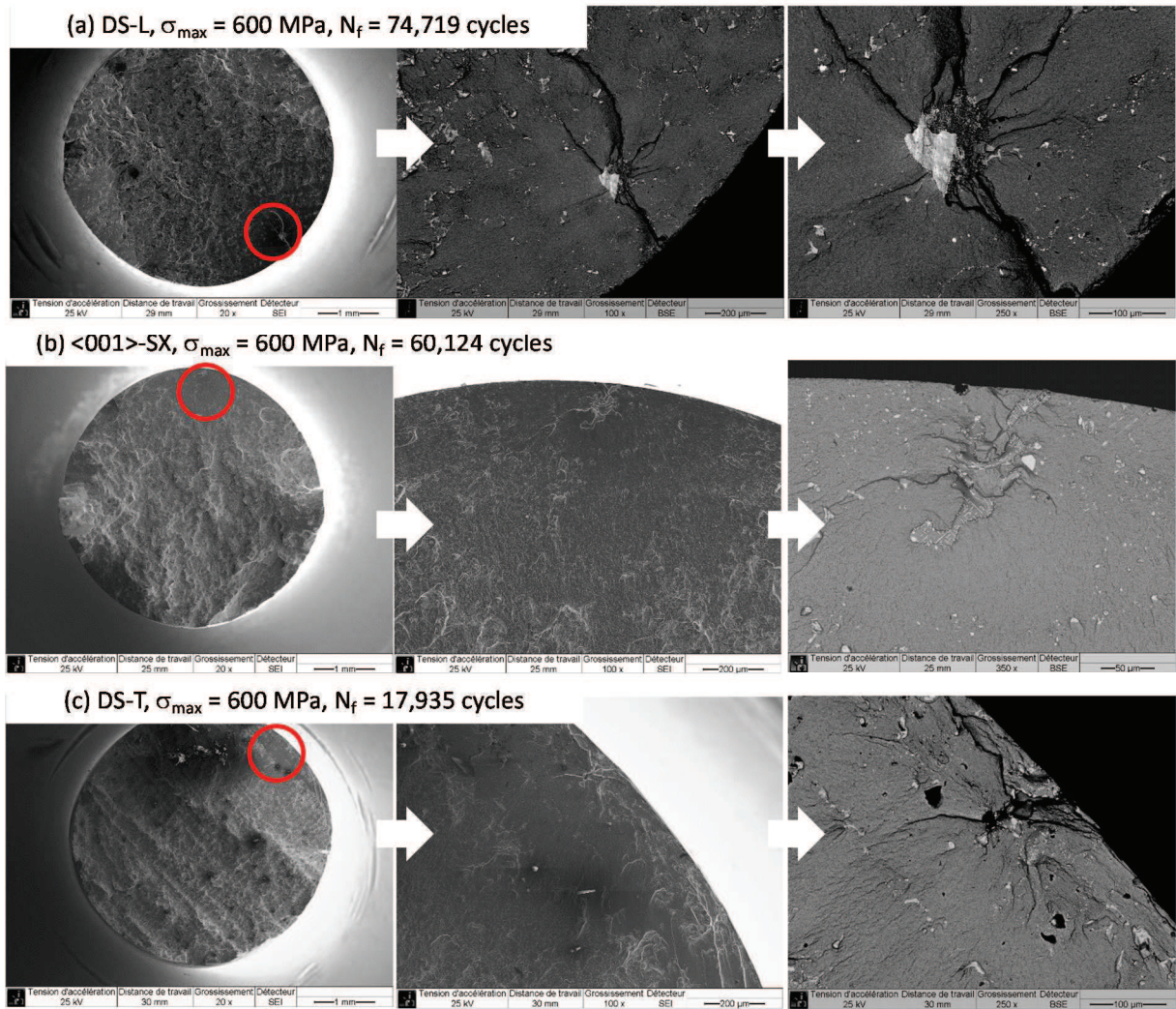


Figure 4.18 – Crack initiation sites in LCF in high vacuum at  $900^\circ\text{C}/R\sigma=0.05$  in DS-L (a), <001>-SX (b) and DS-T (c) specimens.

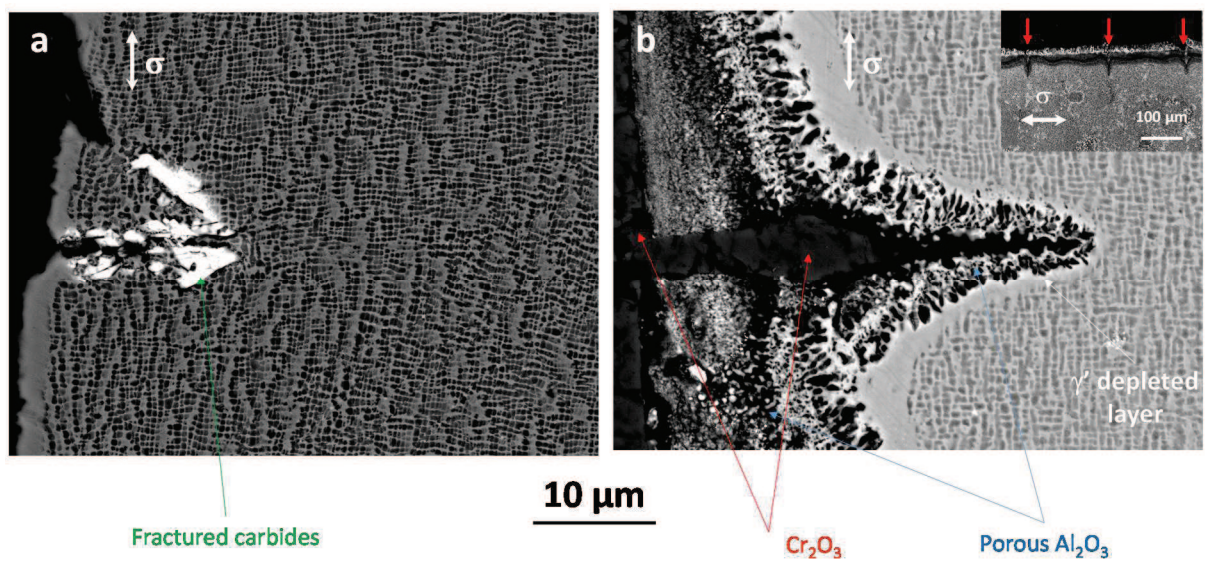


Figure 4.19 – First stages of crack propagation at  $900^\circ\text{C}/R\sigma=0.05/\sigma_{\max}=520$  MPa in <001>-SX specimens in high vacuum ( $N_f=114,608$  cycles) (a) and in air ( $N_f=151,320$  cycles) (b). The insert in (b) shows numerous secondary cracks (red arrows) along the gage length.

From all these observations, crack initiation in high vacuum occurs at a (sub-)surface pore or carbide and then, the crack propagates from this defect following  $\gamma$  matrix channels (Figure 4.20(a)). The crack hence appears very sharp since no crack tip blunting may occur due to oxidation or due to fast creep deformation ahead of the crack tip. In air, several cracks initiate from surface oxidized carbides (see Figure 4.15(a)). Indeed, since a soak time of  $\sim 30$  minutes at  $900^\circ\text{C}$  is applied before each LCF tests at  $900^\circ\text{C}$ , there are already several fractured carbides right from the beginning of the tests. The sequence just after this early stage combines the oxidation of carbides and of the crack tip in addition to the creation of a  $\gamma'$  depleted layer ahead of the crack tip. As a consequence, a spectacular blunting is observed (Figure 4.20(b)). The dependence of the crack tip morphology in LCF to the environment is in good agreement with past observations from E. Aghion et al. using MAR-M200+Hf  $\langle 001 \rangle$ -SX specimens with a (huge) 2.4% hafnium content [16]. In their study, they assumed that “*the presence of 20% oxygen in the surrounding atmosphere involves an increase in the effective service life of the alloy compared with that in an inert atmosphere, is due to a retardation of the effective growth rate of the crack towards failure.*” Although no LCF lives or crack propagation data were provided in their paper, their assumption can be easily understood, considering that the stress magnitude ahead of the crack tip at maximum macroscopic applied stress should be lower in air due to the crack tip blunting, and also due to crack closure effects. This will be investigated in the next section, by performing crack propagation tests.

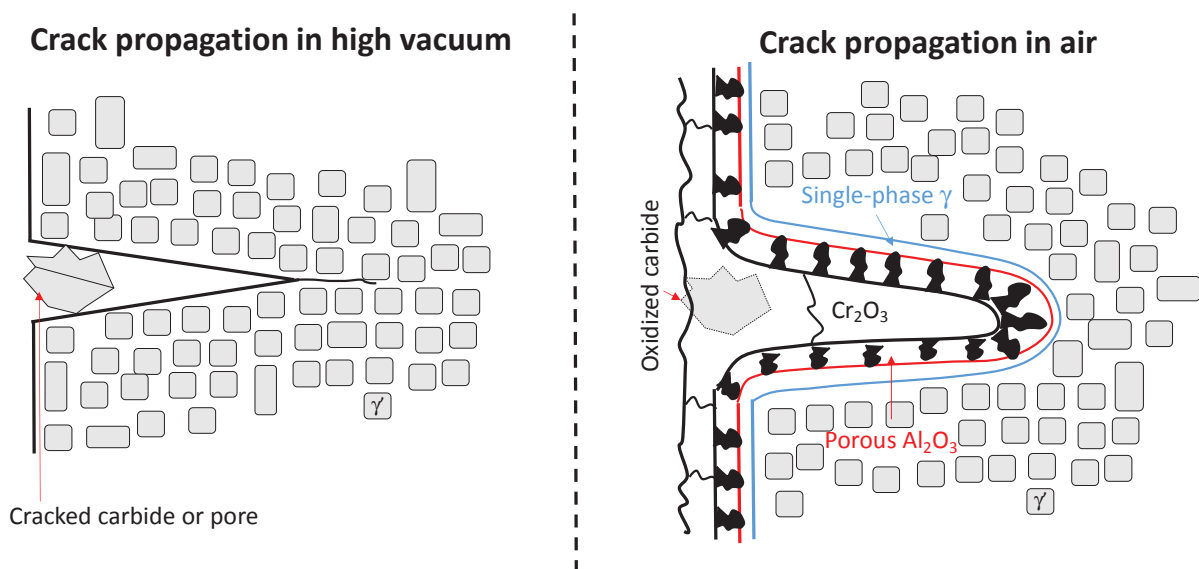


Figure 4.20 – Schematic illustration of micro-crack propagation in LCF in DS200+Hf/ $\langle 001 \rangle$ -SX MAR-M200+Hf alloys at  $900^\circ\text{C}$ .

#### 4.3.3 Crack propagation tests

Crack propagation tests have been performed in air and in high vacuum at  $650^\circ\text{C}$  and  $900^\circ\text{C}$ , at 20 Hz using CT32 specimens. A crack opening measurement was performed periodically (each 20,000 cycles) to characterize crack closure effects. Unfortunately, it was not possible to do such measurements at  $900^\circ\text{C}$  in high vacuum due to technical issues (creep deformation of the screws used for the crack opening measurement set-up). It is recalled that these tests have been performed by increasing progressively the maximum applied load, keeping the stress ratio constant, up to reaching a measurable crack growth rate. Then, the applied maximum and minimum loads were kept constant up to failure. It is also recalled that the frequency of these crack propagation tests is higher than the one used during our LCF experiments (20 Hz versus 0.5 Hz, respectively) to avoid too long tests. So, they are not perfectly representative of our LCF conditions.

Figure 4.21 shows crack propagation curves at 650°C and 900°C in air and in high vacuum. At both temperatures, a huge difference in crack propagation threshold is observed between air and vacuum conditions, while the Paris domain of the curves is not affected deeply. The crack propagation threshold is of  $\sim 9\text{-}10 \text{ MPa}\cdot\text{m}^{0.5}$  at both temperatures in high vacuum while it is of  $\sim 18 \text{ MPa}\cdot\text{m}^{0.5}$  at 650°C and of  $\sim 16 \text{ MPa}\cdot\text{m}^{0.5}$  at 900°C in air. The crack propagation curve in air at 900°C close to the propagation threshold does not contain many points since a grip failure occurred during the beginning of the test, when a measurable crack propagation rate was detected. We hence decided to re-machine the crack by EDM, then do once again pre-cracking at room temperature and start again the test at 900°C at  $16 \text{ MPa}\cdot\text{m}^{0.5}$ , i.e. when a crack propagation was detected before failure. On re-loading the specimen, a crack propagation rate close to the one obtained before grip failure (i.e. of  $\sim 2.0 \cdot 10^{-10} \text{ m/cycle}$ ) was first measured and then, a sharp increase in crack propagation rate, as observed in Figure 4.21.

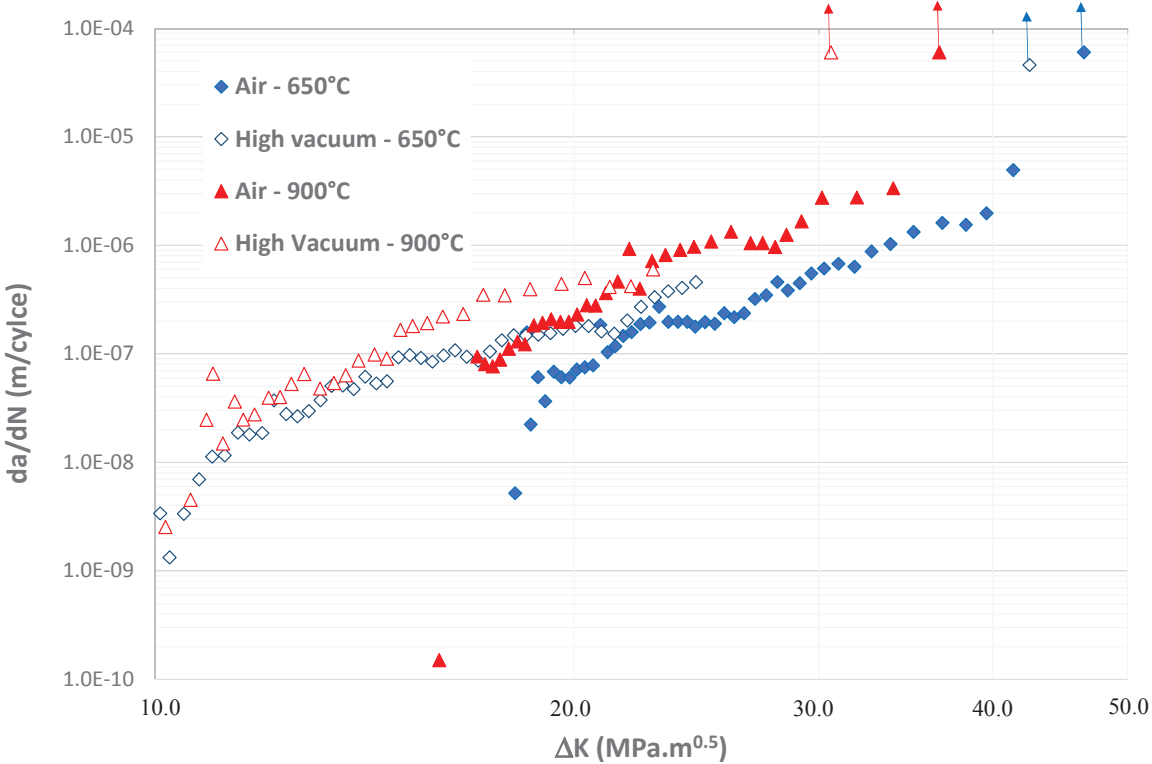


Figure 4.21 – Crack propagation curves at 650°C and 900°C/20Hz/Rσ=0.05 in air and in high vacuum.

To get a better understanding of the intrinsic crack propagation behavior, crack propagation curves at 650°C presented in Figure 4.21 have been replotted using the effective  $\Delta K$  ( $\Delta K_{\text{eff}}$ ) taking into account crack closure effects. As observed in Figure 4.22, crack propagation curves in air and in high vacuum at 650°C are almost superimposed in this  $da/dN$  versus  $\Delta K_{\text{eff}}$  plot, both in the Paris domain and close to the crack propagation threshold. Indeed, as observed in Figure 4.23 where the applied load (or normalized applied load) is plotted as a function of the derivative of the crack opening ( $\Delta\sigma'$ ), no crack closure is observed very rapidly in the test under vacuum (see Figure 4.23(b)). Only during a very brief period at the beginning of the test a crack closure effect is detected, due to the pre-cracking at room temperature (60% of crack closure is observed in Figure 4.23(a) at the very beginning of the propagation in vacuum). This is in good agreement with the sharp crack shape observed in Figure 4.19(a).

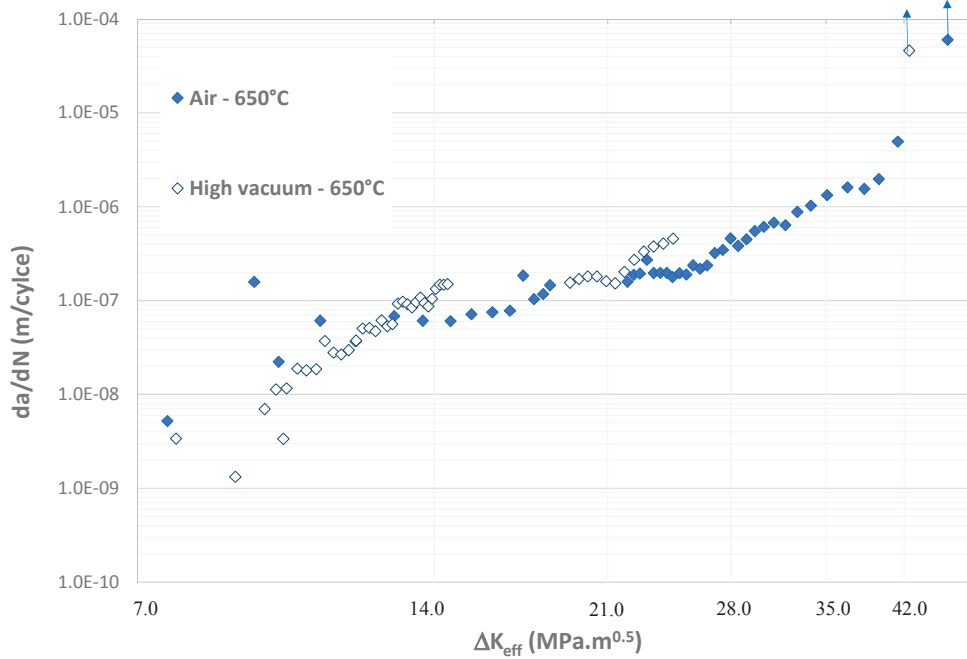


Figure 4.22 – Effective crack propagation curves at 650°C/20Hz/Rσ=0.05 in air and in high vacuum.

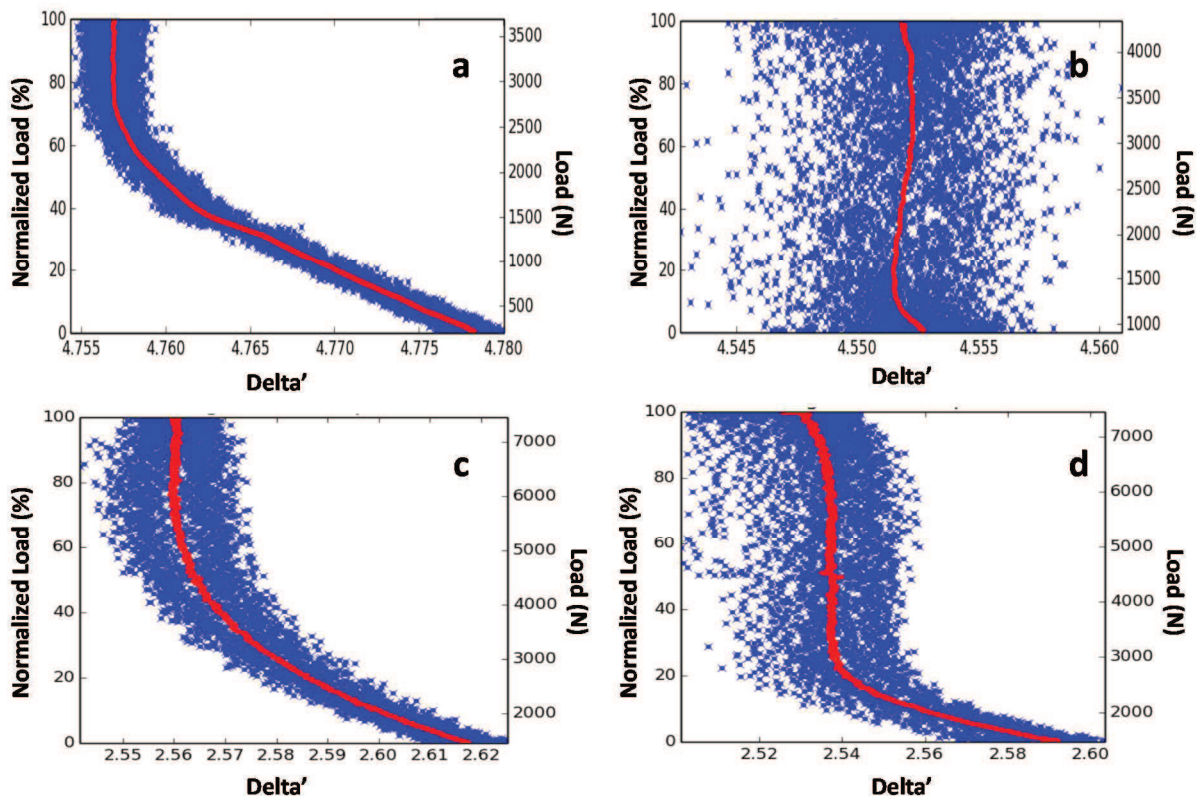


Figure 4.23 – Crack opening during propagation tests at 650°C/20Hz/Rσ=0.05:  $\Delta K=10$  MPa.m<sup>0.5</sup>/Vacuum (a),  $\Delta K=10.2$  MPa.m<sup>0.5</sup>/Vacuum (b),  $\Delta K=18$  MPa.m<sup>0.5</sup>/Air (c),  $\Delta K=19.8$  MPa.m<sup>0.5</sup>/Air (d). Delta' is the derivative of the crack opening.

In air, crack closure is measured in the short crack propagation domain (see Figure 4.23(c) and Figure 4.23(d)) where applying 60% and 20% of the maximum load is necessary to fully open the crack at

$\Delta K=18 \text{ MPa}\cdot\text{m}^{0.5}$  and  $\Delta K=19.8 \text{ MPa}\cdot\text{m}^{0.5}$ , respectively. This crack closure has been detected up to a  $\Delta K$  value of  $\sim 24 \text{ MPa}\cdot\text{m}^{0.5}$  in air. Crack propagation paths have been investigated by optical microscopy (Figure 4.24) and a darker fracture surface in air due to oxidation is clearly observed. Moreover, when comparing the crack propagation surfaces in vacuum and in air at a higher magnification (see Figure 4.24), a greater roughness is observed in air, with crack deviations close to carbides. The dendritic structure appears clearly in Figure 4.24, especially for the specimen tested in vacuum, indicating that the crack propagation follows a (001) plane at the macroscopic scale. This is in good agreement with the fact that the crack tip follows  $\gamma/\gamma'$  interfaces as observed in Figure 4.19(a) and illustrated in Figure 4.20(a). The crack closure effect observed at 650°C in air hence mainly results from the increased roughness of the crack propagation surface, which could itself results from oxidation.

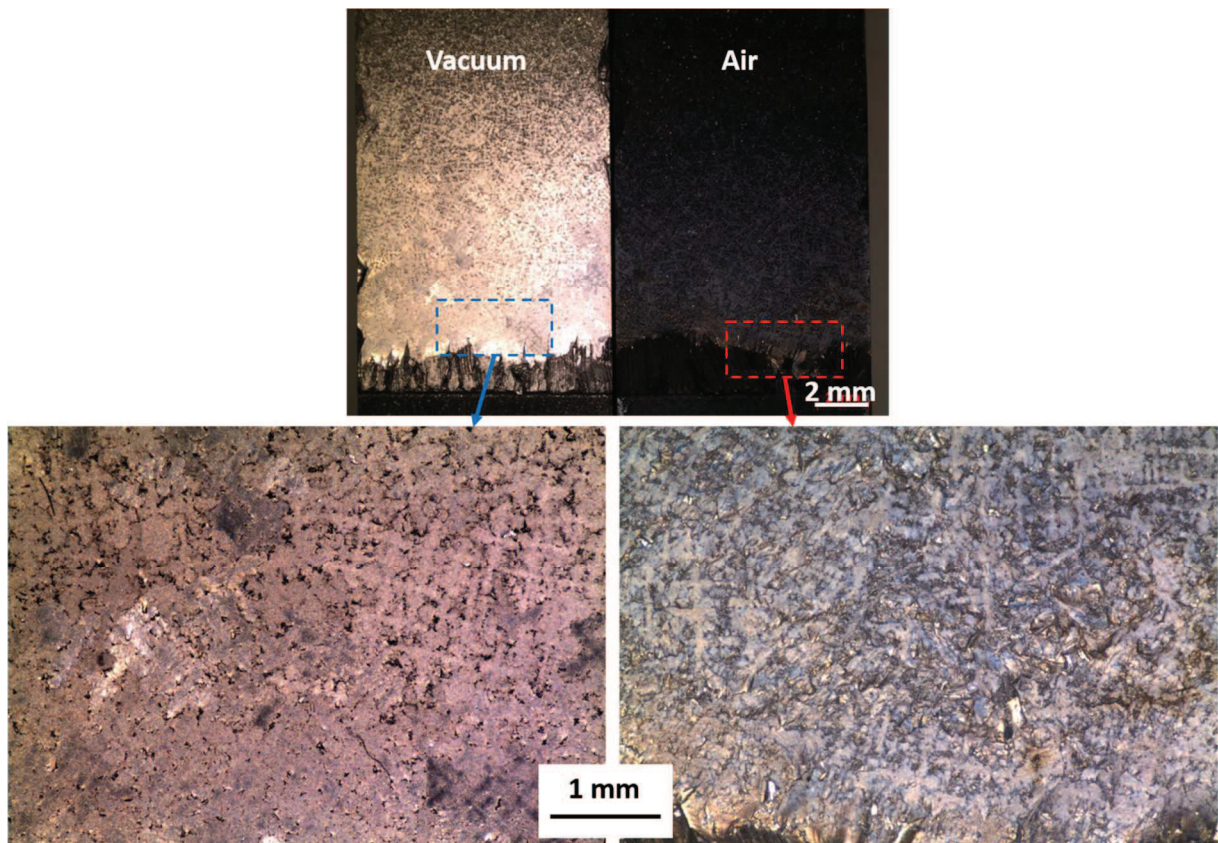


Figure 4.24 – Top view observations of the crack propagation paths at 650°C/20Hz/ $R\sigma=0.05$ .

Similar observations can be done for crack propagation surfaces at 900°C (see Figure 4.25). Hence, even if no crack closure measurements could have been performed at this temperature, it is very likely that the difference in crack propagation threshold observed in Figure 4.21 at this temperature mainly results from oxidation and associated crack tip blunting (Figure 4.19Fig. (a)).

Even if performing crack propagation tests at 0.5Hz instead of 20Hz would have been much more reliable in an attempt to calculate precisely the crack propagation contribution to the fatigue life at both 650°C and 900°C, it is recalled that these tests were aimed at understanding what controls the LCF life at high temperature in DS200+Hf, especially at 900°C. According to these crack propagation experiments, it is clearly shown that the same total LCF life in air and high vacuum at 900°C is really fortuitous. Indeed, in high vacuum, the total LCF life is mainly crack initiation controlled while in air, it is mainly crack propagation controlled since surface oxidized carbides (Figure 4.17) are already fractured at the beginning of the tests (Figure 4.15(a)). The higher crack propagation threshold leads

to longer crack propagation lives in air and lowering the frequency would even increase this trend, allowing more time for oxidation. **In summary, if oxidation can be seen as detrimental in terms of crack initiation at high temperature in DS200+Hf/SX MAR-M200+Hf, it is clearly beneficial from a crack propagation point of view, by increasing the crack propagation threshold and hardly affecting the Paris regime.** This beneficial effect of oxidation to the crack propagation life of this alloy was already pointed out by E. Aghion & al. [16].

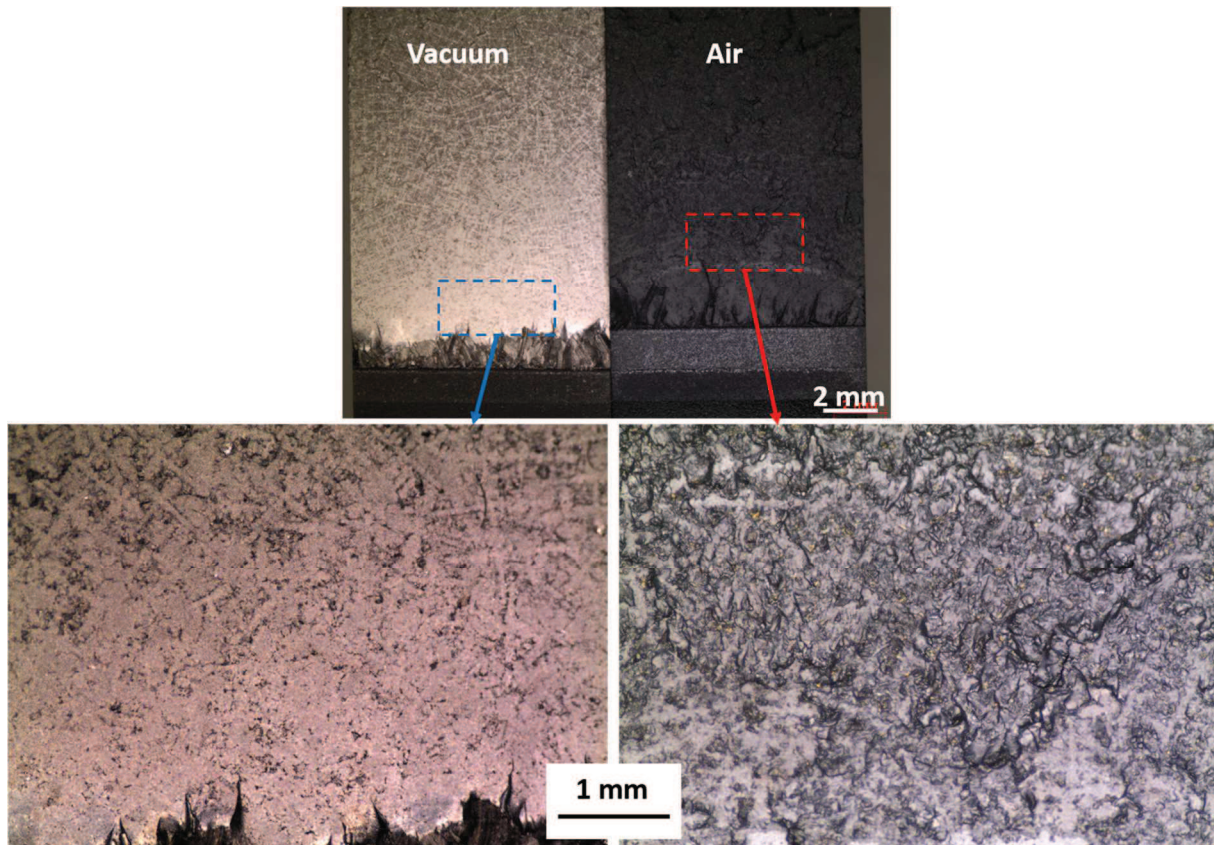


Figure 4.25 – Top view observations of the crack propagation paths at 900°C/20Hz/R $\sigma$ =0.05.

#### 4.3.4 Creep at 900°C

Oxidation has just been observed to affect both crack initiation and crack propagation in LCF. In the following subsection, its effect on the creep behavior and creep life will be analyzed. In a last part of this subsection, the contribution of oxidation to the overall creep life will be investigated by reducing the specimen's thickness.

##### 4.3.4.1 On the role of oxidation

In Figure 4.26, creep curves at 900°C/350 MPa and 900°C/400 MPa established in air and in high vacuum using radiant furnaces are presented. <001>-SX, DS-T and DS-L specimens have been tested. Higher creep lives are reached in vacuum compared to the ones obtained in air in the same conditions. As observed more clearly in Figure 4.26(b), the minimum creep rate is lower in vacuum. The creep life improvement by suppressing oxidation is spectacular during transverse creep testing of DS specimens since it can reach a factor of 6-7 for fine grain material. It is also observed in Figure 4.26(a) that almost no creep life anisotropy is observed in high vacuum while pronounced differences are observed in air, as already presented in chapter 3.

As a very striking result from these experiments, if a difference in transverse creep properties between fine and coarse grain DS materials is observed in air, it almost totally disappears in high

vacuum (see Figure 4.26(a) and Figure 4.26(b)). This is a clear indication that the differences in transverse creep resistance in air with the grain size only results from the contribution of oxidation at grain boundaries, in good agreement with TGA experiments (see Figure 4.13). These macroscopic creep results are also in good agreement with previous observations showing that cracks develop at grain boundaries during transverse creep testing of DS specimens for creep strains as low as 0.8% (see Figure 4.11 and Figure 4.12), and probably at even lower creep strains.

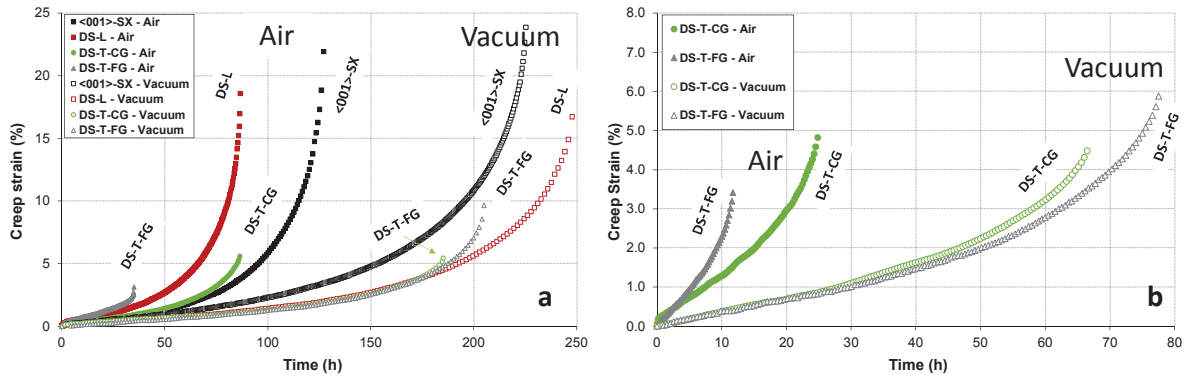


Figure 4.26 – Comparison of creep properties in air and in high vacuum at 900°C/350 MPa (a) and 900°C/400 MPa (b).

Longitudinal cuts after creep tests presented in Figure 4.27 reveal that, as expected, cracks develop along grain boundaries during transverse creep testing of DS200+Hf specimens, whatever the environment. However, no  $\gamma$  depletion is observed along the crack path in high vacuum and cracks propagate following grain boundaries and fractured carbides (see Figure 4.27(a) and (c)). In air, crack propagation along grain boundaries is assisted by oxidation and a  $\gamma$  depleted layer can be observed all along the crack path, up to the crack tip (see Figure 4.27(b) and (d)).

To check how oxidation affects the transverse creep resistance, “combo” creep tests have been performed. They consist in a first sequence of creep deformation in air up to a given creep strain followed by creep up to failure in high vacuum. It has been chosen to switch the environment after a 0.8% creep strain has been reached since grain boundary cracks were already observed after this amount of creep deformation (see Figure 4.11) and since it corresponds to the minimum creep rate at 900°C/350 MPa (see Fig. 3.8). Interruptions were done by switching off the electrical supply of the furnace, keeping the applied load. Figure 4.28 shows the reconstructed creep curves of these combo creep tests. First of all, almost no difference in creep elongation has been observed between CG and FG material during air testing. When switching the environment from air to vacuum, a spectacular decrease of creep strain rate is first observed for both specimens. The reduction in creep rate is much more pronounced for CG material, leading to a longer residual creep life in vacuum for this specimen. Even if the reduction in creep strain rate may result from the change in creep rig and, hence, from differences in temperature homogeneity along the gage length of the specimens, the reduction in creep strain rate when changing the environment is an unambiguous proof that oxidation controls creep properties of DS200+Hf at 900°C, especially along transverse direction.



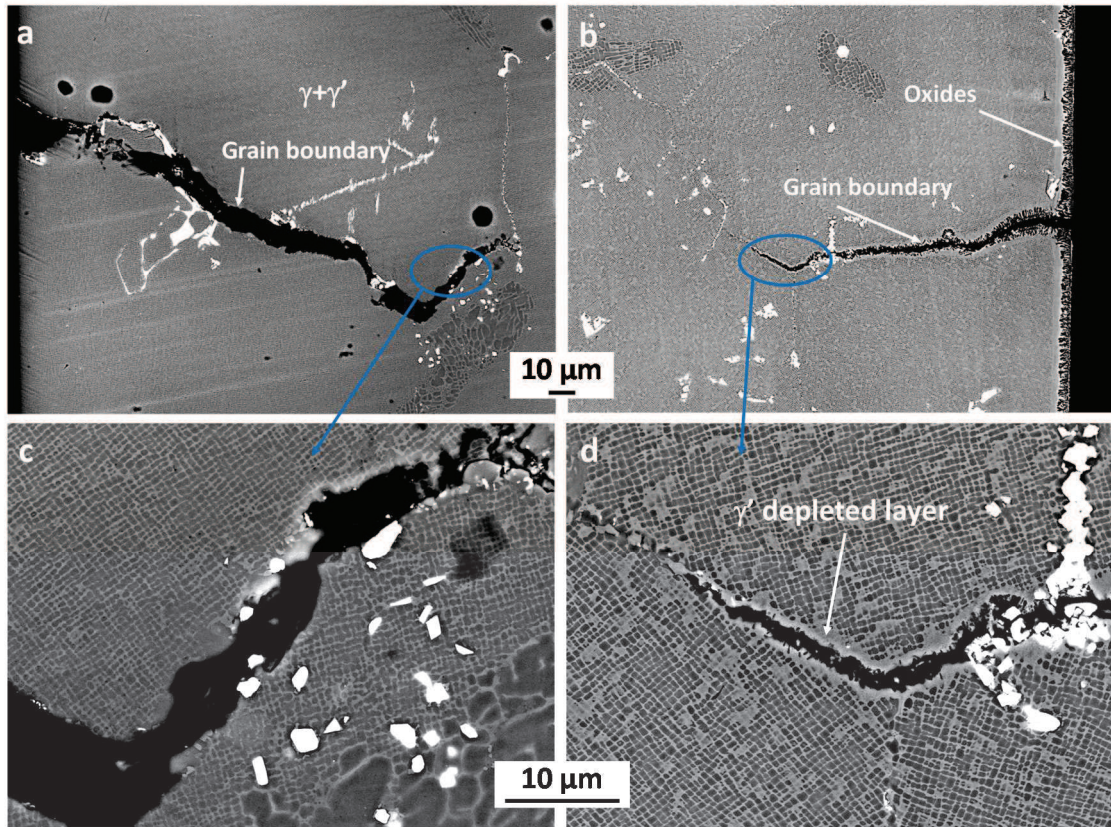


Figure 4.27 – Intergranular crack propagation during transverse creep testing at 900°C/350 MPa in DS-T-FG specimens in high vacuum (a, c) and in air (b, d). (c) and (d) are magnified areas of (a) and (b) respectively.

Fractographic observations after these combo creep tests revealed, as expected, that first stages of grain boundary cracking were already reached before changing the environment, as observed in Figure 4.29. It is indeed observed in the magnified area of the fracture surface a small oxidized crack starting from the surface (see area delimited by a red dotted curve), presumably from an oxidized carbide. It is also observed that the subsequent crack propagation is intergranular, but without the help of oxidation (no trace of oxidation is indeed observed on the rest of the fracture surface). According to this fractographic observation, the difference in residual creep life in vacuum between CG and FG material may result from both the density of cracks initiated during the first stage of creep deformation in air up to a 0.8% creep strain and from their extent from the surface. As a summary of these combo creep experiments, we have demonstrated unambiguously that DS200+Hf alloy is highly oxidation sensitive and that its creep behavior is affected by the environment, even using massive specimens. This results from the development of non-protective oxides at 900°C and from the preferential oxidation of carbides located at grain boundaries. **All in all, the grain size effect on transverse creep resistance of DS200+Hf alloy only results from the preferred oxidation at grain boundaries.**

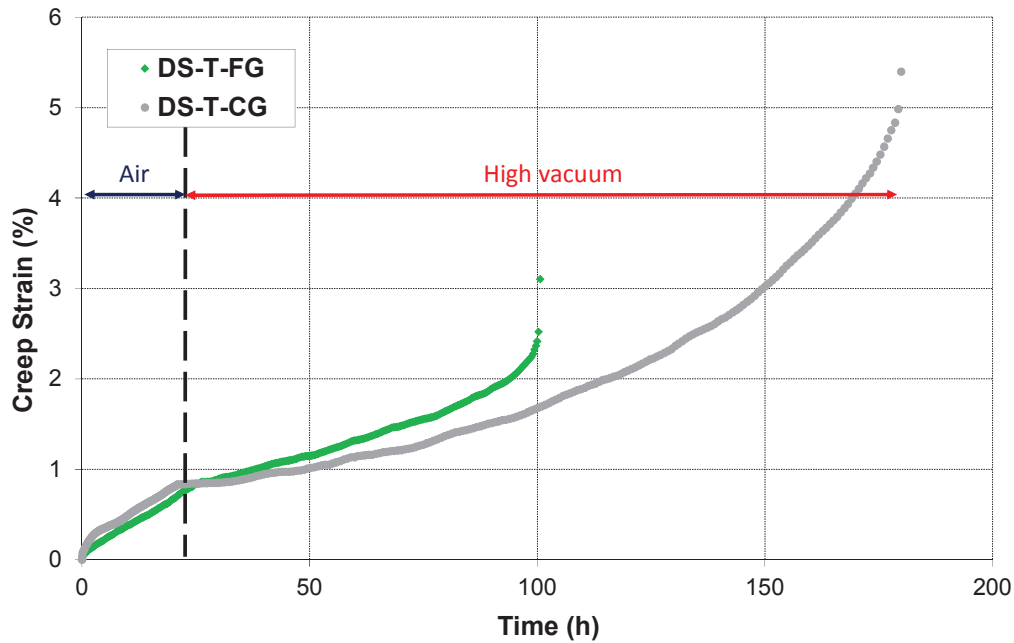


Figure 4.28 – Transverse creep tests at 900°C/350 MPa in DS200+Hf specimens, first started in air up to a ~ 0.8% creep strain and then continued in high vacuum up to failure.

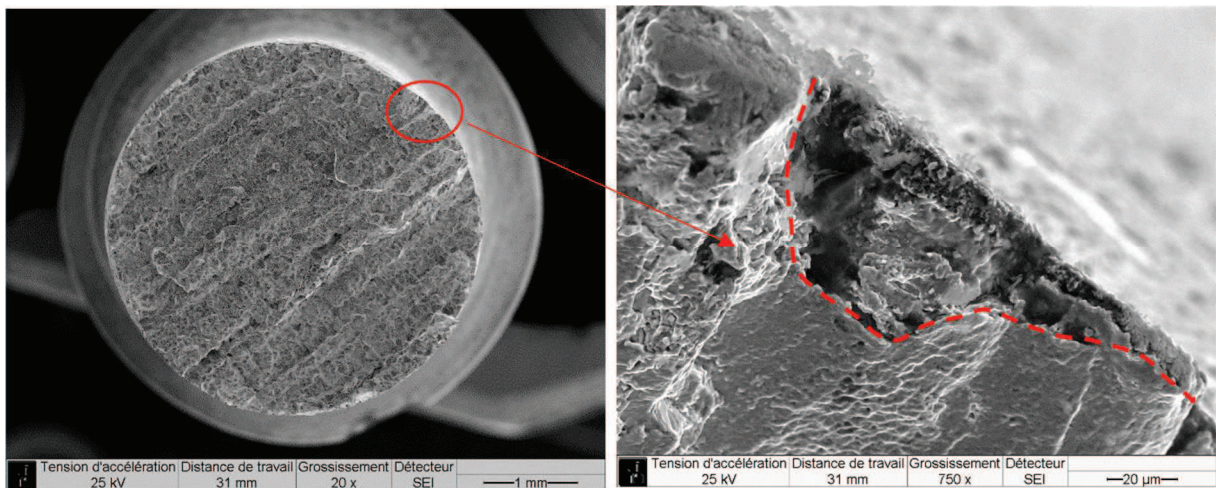


Figure 4.29 – Fracture surface after transverse creep testing at 900°C/350 MPa in FG DS-T specimen, first started in air up to a ~ 0.8% creep strain and then continued in high vacuum up to failure.

#### 4.3.4.2 Thin-wall creep tests

To deepen the understanding of the contribution of oxidation to the creep resistance and to reach more representative thicknesses like the ones encountered in low pressure turbine blades, thin-wall creep testing has been performed at 900°C. A summary of these tests is proposed in Appendix 3. Thin-walled creep specimens with thicknesses of 0.5 mm, 0.8 mm and 1.5 mm were machined out from our DS200+Hf plates as well as from <001>-SX bars by EDM. It is here recalled that the surface and edges of these specimens have been mechanically polished carefully and their final dimensions before testing were also measured with special attention to achieve reliable results (see chapter 2 for additional details). Figure 4.30 presents a comparison of the creep curves with different specimen's thickness for <001>-SX (Figure 4.30(a)), DS-L (Figure 4.30(b)) and DS-T (Figure 4.30(c)) specimens. A comparison with the creep performances using massive specimens (i.e. cylindrical specimens having a 4 mm diameter) tested in air and in high vacuum is also proposed in this figure. It is worth

mentioning that all creep curves in air presented in this figure have been established using a resistive furnace. This type of furnace leads to a very homogeneous temperature along the gage length of the specimens (a +/- 1°C temperature heterogeneity), which is really important when trying to characterize the thin-wall debit in creep, if any.

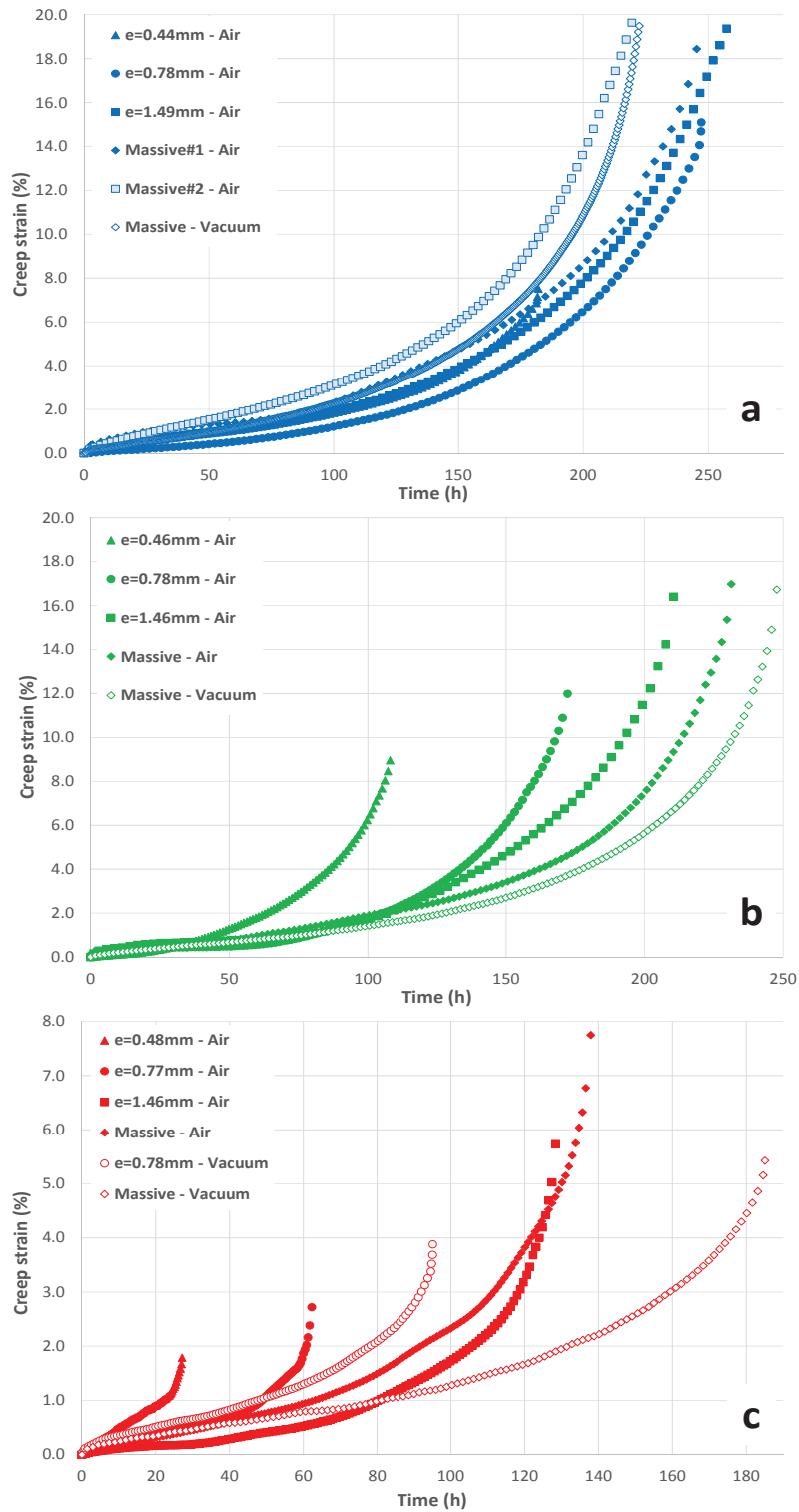


Figure 4.30 – Thickness effect on the creep properties at 900°C/350 MPa for <001>-SX (a), DS-L (b) and DS-T (c) specimens.

According to Figure 4.30(a), almost no thickness effect on the creep life at 900°C/350 MPa is observed for monocrystalline <001>-specimens. Two massive specimens were indeed tested in air to get an idea of the possible scatter and it is seen from this figure that creep lives are all lying within a 210-260 hours range. We may only notice a decrease of the creep ductility for the thinnest SX specimen. Creep life debit is however observed for DS-L (Figure 4.30(b)) and DS-T (Figure 4.30(c)) specimens. The thinner the specimen is, the lower its creep life. Moreover, it is seen that massive creep specimens tested in vacuum always have the higher creep life, followed by massive creep specimens tested in air. The decrease in creep life is more clearly visible in Figure 4.31 where the evolution of the relative creep life is plotted as a function of the P/S ratio (perimeter of the gage section over load bearing section ratio). A P/S ratio of 1.0 in this plot corresponds to the creep life of the massive sample tested in air which is taken as the reference. It has been chosen to use such a P/S parameter to analyze the thin wall debit in creep life since our specimens do not have all the same thickness and since it is a reliable parameter to measure the external surface of specimens exposed to oxidation relatively to their load bearing section. Indeed, a high P/S ratio corresponds to a specimen in which the surface exposed to oxidation is large in comparison to its load bearing section, while a small P/S ratio corresponds to a massive sample in which oxidation is expected to have little influence. Finally, this parameter will be used in the modeling approach proposed in the last section of this chapter.

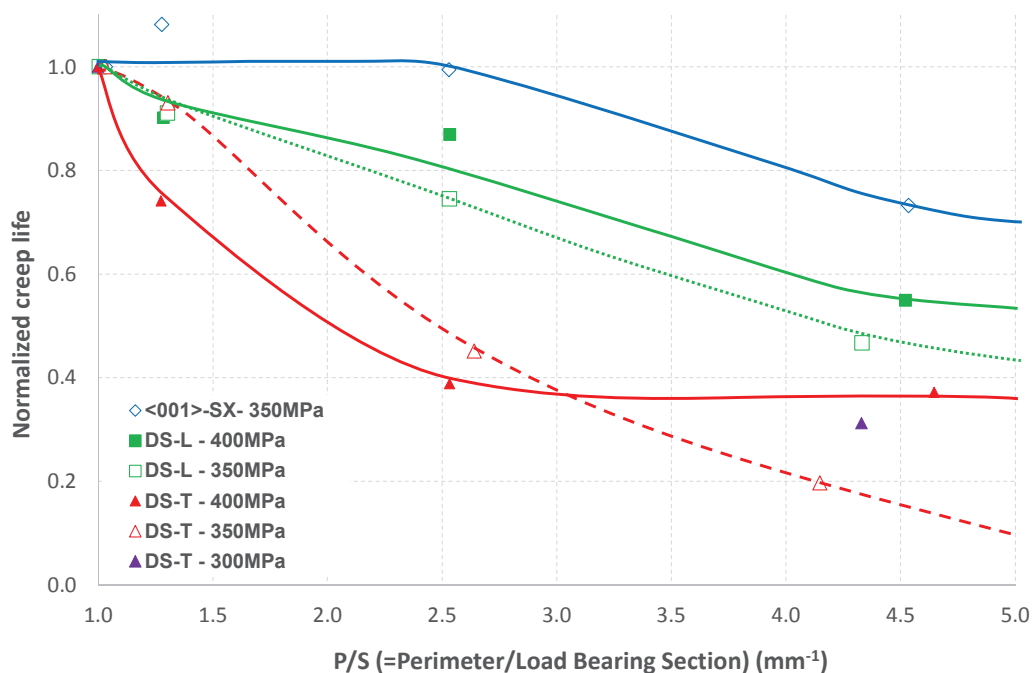


Figure 4.31 – Thickness debit in creep at 900°C/300 MPa, 900°C/350 MPa and 900°C/400 MPa in <001>-SX and DS200+Hf specimens along longitudinal and transverse directions.

According to Figure 4.31, the thin-wall creep debit is more pronounced along transverse direction for DS200+Hf specimen (up to a factor of 5 for transverse loading compared to a factor of ~ 2 for longitudinal loading at 900°C/350 MPa), as expected considering grain boundaries oxidation. The debit is less at 900°C/400 MPa for the thinnest DS-T and DS-L specimens, probably due to a shorter time for oxidation to induce grain boundary damage. A decrease in ductility is also observed for both types of DS specimen decreasing the thickness (see Figure 4.30(b) Figure 4.30(c)). This is more clearly observed in Figure 4.32. This loss of creep ductility which has often been observed for Ni-based SX superalloys [20-24] also contributes to the thickness debit in creep life. In the case of DS200+Hf, this

loss of creep ductility is associated to the size of carbides and, to a lower degree, to the one of the largest pores, which becomes of the same order of magnitude of the specimen thickness for thinnest samples. It is indeed recall here that the largest cluster of carbides and pores may reach sizes of nearly 200  $\mu\text{m}$  (see Table 4.3, Table 4.4 and Table 4.5), i.e. 2 to 2.5 times smaller than the thickness of  $\sim 0.5\text{ mm}$  thick samples. According to Seetharaman & al. [23], this ductility loss is associated to the extent of the stress concentration around carbides/pores [25] which may reach the specimen's thickness for the thinnest ones. However, testing cast-to-size specimens leads to a lower thickness debit in ductility since metallurgical defects such as pores are smaller in size and they are only in very few cases connected to the surface, while it is highly likely to occur in machined specimens [23].

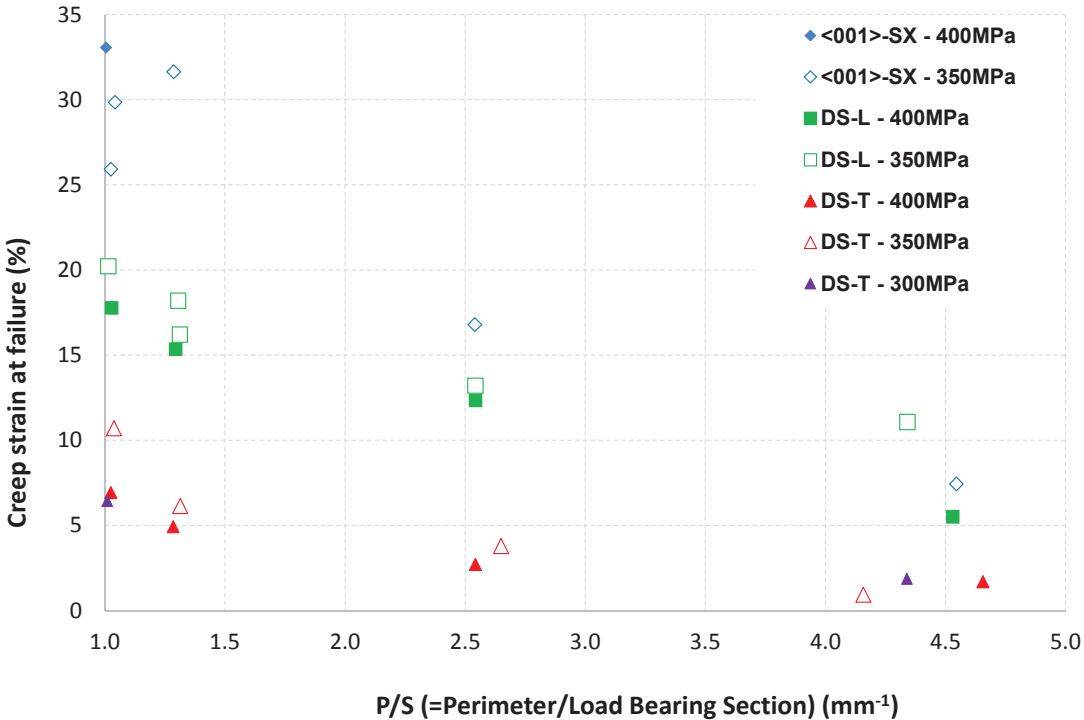


Figure 4.32 – Evolution of the creep ductility at 900°C/300 MPa, 900°C/350 MPa and 900°C/400 MPa in <001>-SX and DS200+Hf specimens along longitudinal and transverse directions as a function of the P/S parameter.

To check our understanding of the thin-wall debit in creep at 900°C, a set of additional transverse creep tests has been performed. First of all, two transverse creep tests at 300 MPa using a massive specimen and a  $\sim 0.5\text{ mm}$  thick one have been performed to increase the duration of the tests, and hence, the oxidation contribution. A clear thickness debit can be seen from Figure 4.33(a). However, when positioning the result using the thinner specimen at 900°C/300 MPa in Figure 4.31, contrary to what one would have expected, a greater thickness debit in creep life is not observed compared to the experiments performed at 900°C/350 MPa. Hence, oxidation may not be the only contribution to the thickness debit in creep. This feeling has been confirmed by performing a thin-wall creep test using a  $\sim 0.8\text{ mm}$  thick specimen in high vacuum. It is seen in Figure 4.30(c) that the  $\sim 0.8\text{ mm}$  thick specimen tested in vacuum performs better than the 0.8 mm one tested in air. However, if oxidation would be the only contributor to the thin-wall debit in creep life, one would have expected a non-sensitive creep strength in high vacuum according to the sample thickness. Finally, a creep test using  $\sim 0.8\text{ mm}$  thick specimens has been performed after a prior 100h pre-oxidation at 900°C. Since it is known that such a prior thermal exposure may lead to a coarsening of the bulk  $\gamma'$  particles and hence, to lower creep resistance [26-28], a 0.8 mm thick specimen pre-oxidized under the same

conditions and then repolished up to a 4000 SiC grade has also been tested. It can be seen in Figure 4.33(b) that the pre-oxidation at 900°C for 100 hours has almost no effect on the creep life compared to the non-pre-oxidized specimens. All these results suggest that the damage development around carbides (see Figure 4.9 and Figure 4.10) may also have a contribution to the thin-wall debit in creep life, as suggested by Baldan [29]. Indeed, from a mechanical point of view, recrystallized areas around carbides and  $\gamma/\gamma'$ -carbides cracks will have a larger contribution for thinner specimen's thickness [29].

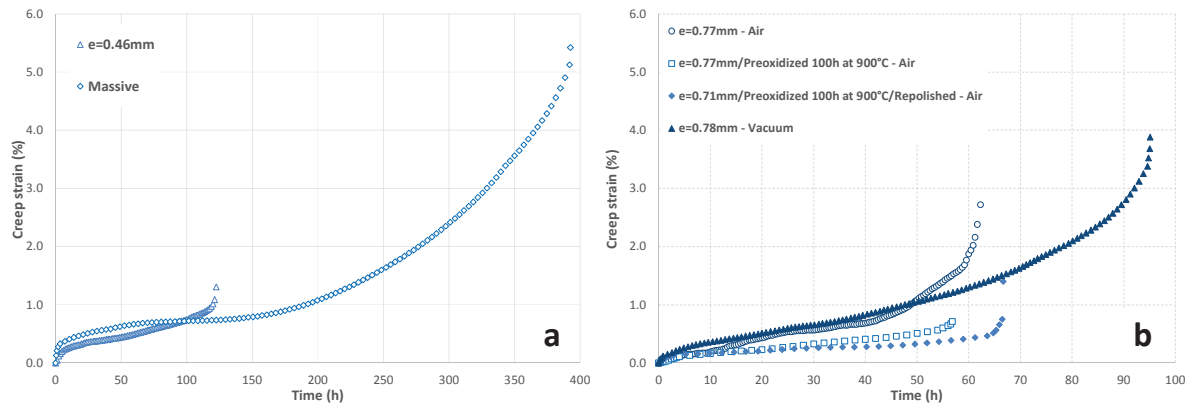


Figure 4.33 – Thickness effect in creep at 900°C/300 MPa (a) and effect of pre-oxidation on creep properties at 900°C/350 MPa (b) in DS200+Hf along transverse direction.

Several observations along longitudinal cuts of thin-walled specimens have been performed. Figure 4.34 shows typical damages that can be detected after transverse creep tests. Both cavitation close to grain boundary carbides (Figure 4.34(a) and (c)) and grain boundary cracking from the surface assisted by oxidation (Figure 4.34(b) and (d)) can be observed. The oxides are very porous, especially along grain boundary cracks (Figure 4.34(d)), in good agreement with LCF experiments performed at the same temperature (Figure 4.19(b)).

As a main conclusion of these experiments, **oxidation contributes to the thin-wall debit in creep since porous oxides are formed both at the surface and within the cracks. However, oxidation by itself is not the only reason for the decrease in creep strength when decreasing the specimen's thickness.** We have then to consider a strong coupling between oxidation and cavitation under applied tensile stress state in DS200+Hf alloy, especially close to grain boundaries. The pronounced decrease in creep ductility when decreasing the thickness also strongly contributes to the creep life debit. All these observations and data will be used in the last section of this chapter to build a coupled creep behavior and creep damage model accounting for the thickness effect. Finally, the author also want to recall that despite a schematic illustration of the thickness debit evolution in creep for columnar grain and conventionally cast superalloys has been proposed by Seetharaman and Cetel [23], it is believed that the data presented in this work are the first ones available for DS superalloys in the open literature.

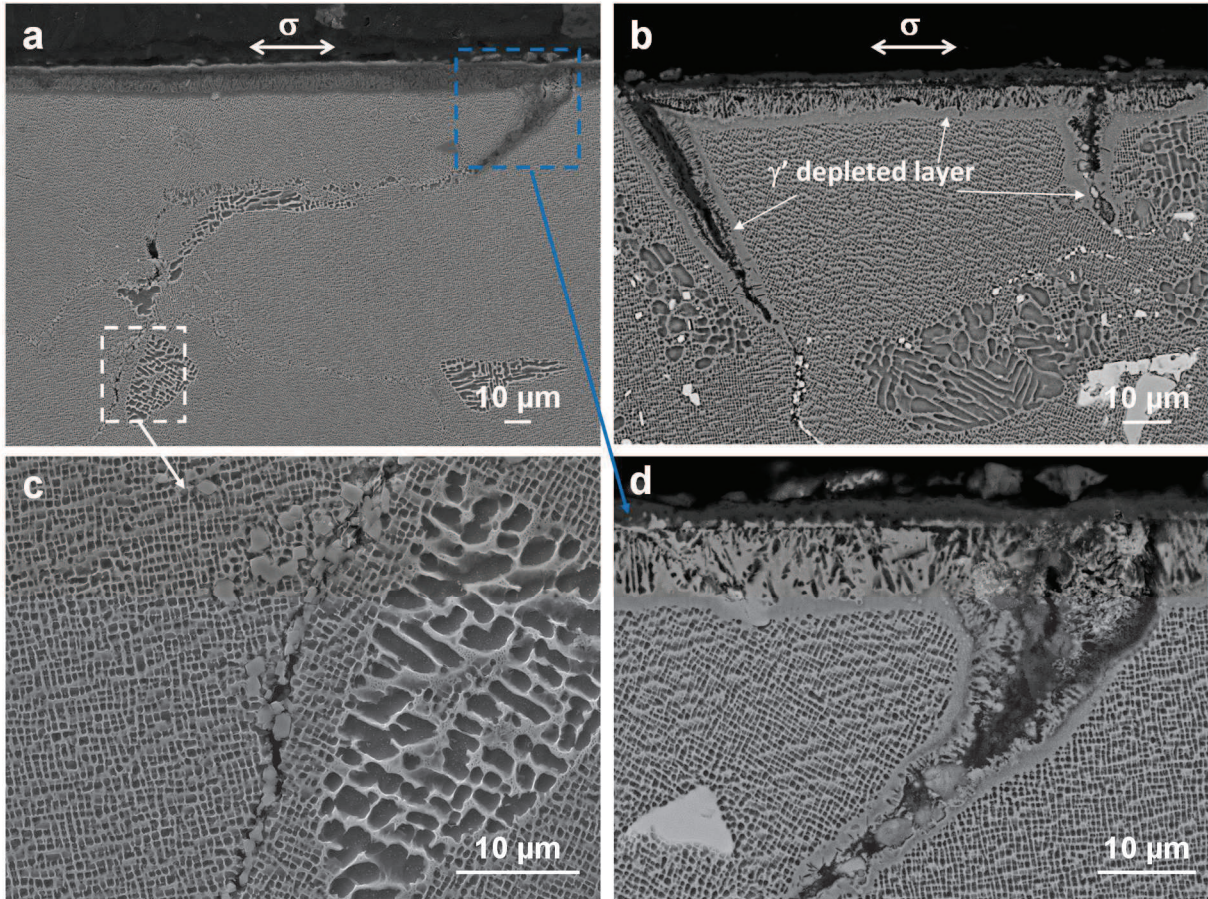


Figure 4.34 – Creep damage mechanisms after 62 hours in creep at 900 °C/350 MPa (Creep strain = 3.8 %) along transverse direction in a ~0.8 mm thick specimen (a, b). (c) and (d) are magnified areas of (a) showing bulk GB cavitation (c) and oxidation assisted GB cracking (d). (b) is another area of the specimen showing oxidation assisted GB cracks.

#### 4.3.4.3 Creep-fatigue at 900°C

The evolution of the dwell-fatigue behavior and of the dwell-fatigue life as a function of the dwell-time  $\Delta t$  at  $\sigma_{\max}$  have already been presented previously in chapter 3, in Figs. 3.23 and 3.24 respectively. Five additional tests were performed in high vacuum (see Appendix 5) and no clear effect of the environment has been noticed on the creep-fatigue life for dwell times of 10s and 300s. Fracture surface after load-controlled dwell-fatigue tests performed either in air or in vacuum are presented in Figure 4.35, for various dwell times. For  $\Delta t = 300$ s, the fracture surface (Figure 4.35(a), (b) and (c)) is really similar to the one observed in creep (Figure 4.6 and Figure 4.7). No clear crack initiation site can be identified, except for DS-T specimen in which the fatal crack came from the surface, from oxidized carbides (Figure 4.35(c)). By decreasing the dwell time to 10s and 1s, a transition toward single crack initiation site appears for SX and DS-L specimens, either internal/at sub-surface (Figure 4.35(e), (g) and (h)) or at the surface from an oxide spike (Figure 4.35(d)). This last crack initiation is quite similar to the one observed in LCF (Figure 4.17(b) and Figure 4.19(b)). Initiation at the surface from oxidized carbide is still observed for DS-T specimen at low  $\Delta t$  (see, e.g., Figure 4.35(i)). In summary, a transition from a creep-dominated to a fatigue-dominated fracture mode when decreasing the dwell time at  $\sigma_{\max}$  appears. The transition corresponds approximately to a dwell-time  $\Delta t = 10$ s. No specific difference in fracture mode has been observed when changing the environment.

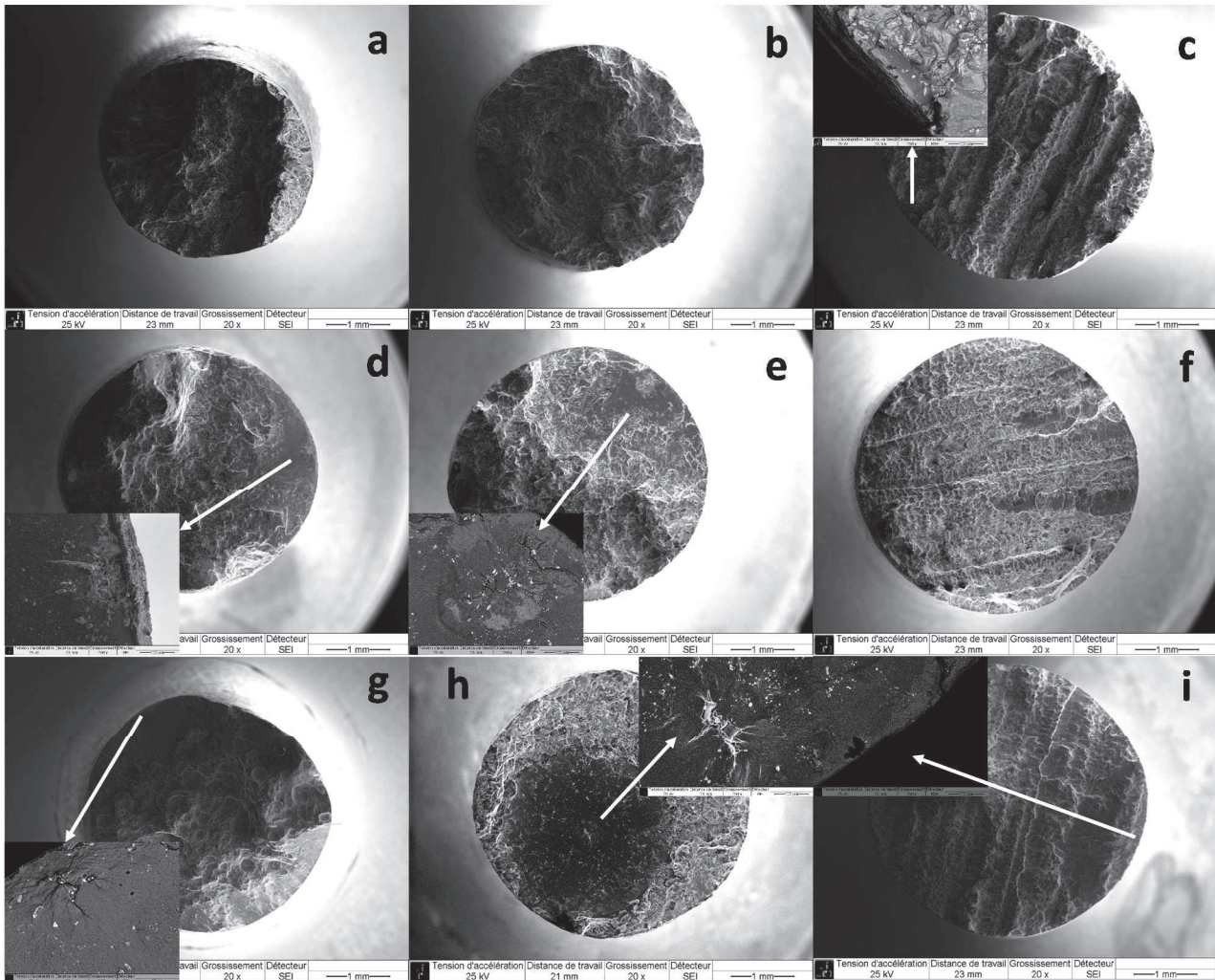


Figure 4.35 – Fracture surfaces in dwell-fatigue at 900°C: <001>-SX/ $\Delta t=300s$ /Air (a), DS-L/ $\Delta t=300s$ /Air (b), DS-T/ $\Delta t=300s$ /Air (c), <001>-SX/ $\Delta t=10s$ /Air (d), DS-L/ $\Delta t=10s$ /Air (e), DS-T/ $\Delta t=10s$ /Air (f), <001>-SX/ $\Delta t=10s$ /Vacuum (g), DS-L/ $\Delta t=1s$ /Air (h) and DS-T/ $\Delta t=1s$ /Air (i). Magnification of crack initiation sites is provided as insert for single site crack initiation cases.

The only really surprising result is the internal crack initiation observed in DS-L specimens tested at  $\Delta t = 1s$  and  $\Delta t = 10s$  (Figure 4.35(e) and (h)). Indeed surface crack initiation was almost always observed at the surface in LCF at 900°C for SX and DS-L specimens (see Table 4.4). It is suspected here that the accumulation of creep damage around internal defects in the form of carbide cracking or localized recrystallization (Table 4.9, Figure 4.9 and Figure 4.10) may be more detrimental than surface oxidized carbides, especially from a dwell-fatigue crack propagation rate point of view. Indeed, according to crack propagation tests presented in Figure 4.21, the threshold for propagation is lower in vacuum. This may also be the case in dwell-fatigue and the Paris regime may also be affected by the environment, all in all leading internal defects to be more detrimental in dwell-fatigue due to a faster crack propagation around them. Crack propagation tests in dwell-fatigue mode or also, in pure creep, would be necessary to check this.



#### 4.4 Intergranular crack initiation during transverse creep testing

It has been observed in the previous sub-sections of this chapter that intergranular failure occurs almost always during transverse creep or fatigue testing of DS200+Hf alloy. Even if a first stage of transgranular short crack propagation in mode I from the crack initiation site may be encountered (see Figs. 4.1(c) or 4.17(c) for fatigue tests), a transition to intergranular crack propagation is then observed. Based on these observations, we may wonder if a (or several) critical grain boundary configuration(s) leading to such intergranular failure exist(s)? And if yes, which one(s)? This question is even more important when considering strict production reject criteria of DS castings such as, e.g., having grain boundaries perpendicular to the main blade profile axis and hence, perpendicular to the centrifugal forces.

To answer these questions, five transverse creep experiments equipped with strain markers have been performed at 750°C/700 MPa, 750°C/750 MPa, 750°C/800 MPa and 900°C/400 MPa (2 experiments for this last condition). Moreover, a last experiment at 740°C/700 MPa followed by digital image correlation (DIC) along 6 different generatrices of the specimen has been performed. Before each experiment, an EBSD map of the whole surface of the specimen equipped with strain markers has been performed to be able to identify the local crystallographic environment where cracks are developing. This EBSD mapping was only done after the experiment for the cylindrical specimen used for the experiment followed by DIC. In the following, a  $[h_1k_1l_1]/[h_2k_2l_2]$  notation will be used to account for the grain orientation on each side of the grain boundary where the crack had developed. Each crystallographic direction  $[h_ik_1l_1]$  will account for the grain orientation with respect to the macroscopic loading direction.

First, such experiments have been performed at 900°C/400 MPa. Figure 4.36, which was already presented in chapter 3, presents the evolution of the creep strain in different grains of the specimen. All grains present almost the same creep curve (i.e. few differences in creep curve shape) which is very similar to the typical macroscopic one obtained at 900°C/350 MPa or 900°C/400 MPa along transverse direction (see, e.g., Figure 4.26). It is indeed recalled here that the anisotropy in creep behavior is reduced at 900°C, compared to 750°C due to the degradation of the  $\gamma'$  microstructure (i.e.  $\gamma'$  coarsening and N-type  $\gamma'$  rafting) as already shown in Figs. 3.13 and 3.14. During the experiment presented in Figure 4.36, the fatal crack developed between a “red grain” and an “orange grain”, i.e. a  $\sim[001]/\sim[103]$  grain boundary crystallographic configuration. Three secondary intergranular cracks have also been observed after failure in this specimen. Their crystallographic configuration is shown in Table 4.6 in which all the crystallographic configurations leading to either failure or initiation of secondary cracks are gathered. According to the two first lines of this table, which correspond to the two experiments at 900°C/400 MPa, no single one crystallographic configuration leads to crack initiation. Moreover, according to Figure 4.36 in which the Schmid factor of the most heavily loaded slip systems in each grain have been added on the EBSD map, crack initiation does not seem to be linked to a large contrast in plastic activity and/or Schmid factor magnitude. **Based on the analysis of eleven fatal and secondary cracks, it appears that no specific crystallographic configuration favors intergranular crack initiation during transverse creep at 900°C.** This is in good agreement with previous results presented in this chapter showing that oxidation has a major role in controlling intergranular crack initiation (see section 4.3). The development of cracks at grain boundaries during transverse creep at 900°C hence probably depends on the size and position of intergranular carbides with respect to the free surface and on their oxidation sensitivity (i.e. their exact chemistry).

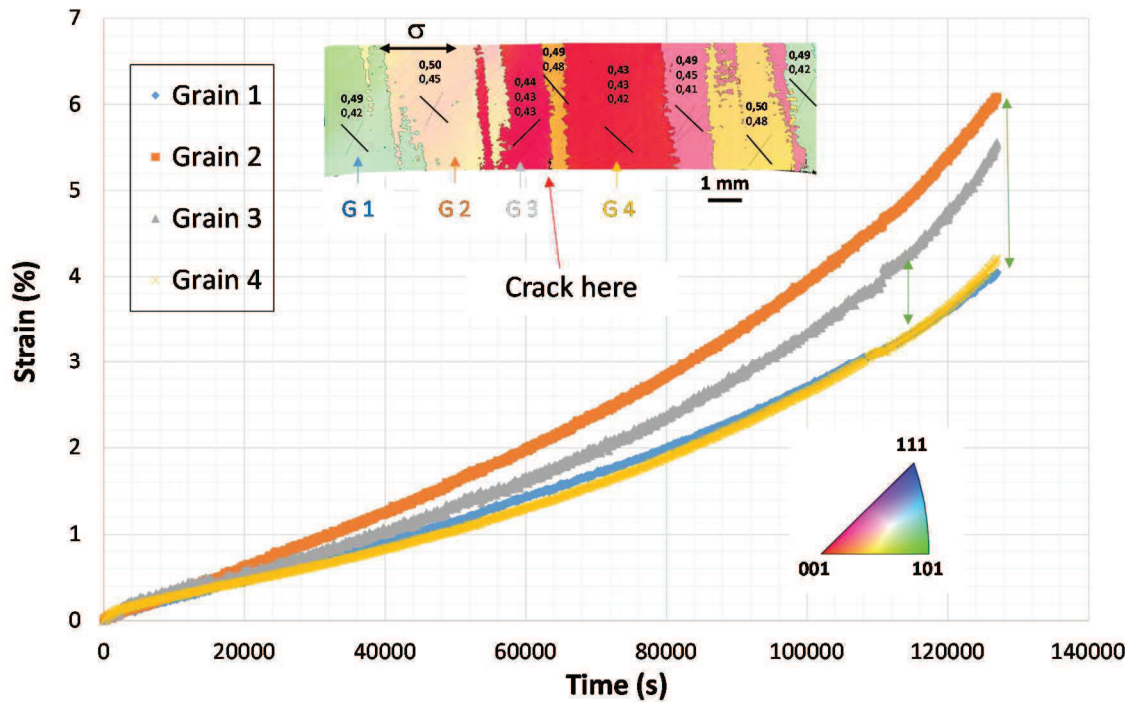
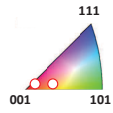
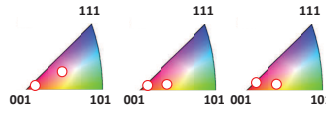
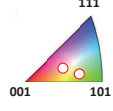
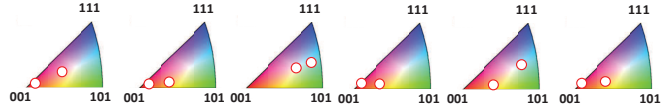
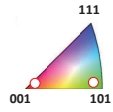
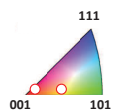
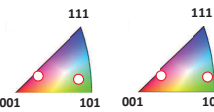
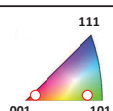
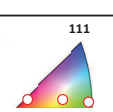
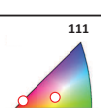


Figure 4.36 – Local creep strain elongation during transverse creep testing at 900°C/400 MPa and associated EBSD map whose color code refers to the applied stress direction. The grains in which creep strain evolutions are presented have been identified in the EBSD map (grains G1, G2, G3 and G4).

A similar investigation has been performed at lower temperature to limit the contribution of oxidation to intergranular crack initiation and to avoid the morphological evolution of  $\gamma'$  particles. At 750°C and high applied stresses (700 MPa to 800 MPa), a large heterogeneity in creep elongation at the grain scale has been observed (Figure 4.37 and Figure 4.38). Cracks have been observed to nucleate systematically at high angle grain boundaries (see grain misorientations in Table 4.6), corresponding to a large mismatch in creep deformation across the grain boundary. This is especially the case for the experiments at 750°C/800 MPa (Figure 4.37) and 750°C/700 MPa (Figure 4.38) where fatal cracks nucleated between two grains whose misorientation is in excess of 30 degrees (see Table 4.6). This “red-green” crystallographic configuration (i.e.  $\sim[001]/\sim[101]$ ) hence seems to favor intergranular crack initiation. This configuration is probably more critical in terms of intergranular crack initiation due to a large contrast in creep strain on both sides of the grain boundary. The heterogeneity in creep behavior observed at the grain scale is in good agreement with the larger creep life anisotropy at low temperature/high applied stress already presented in Fig. 3.5, and more generally, with the open literature on Ni-based SX alloys [13, 14]. The differences in creep elongation at the grain scale is related to the number of activated octahedral slip systems on both sides of the grain boundary (which is 8 for a perfectly [001]-oriented grain and 4 for a perfectly [101]-oriented grain) and also, to the mechanisms of strain hardening under such creep conditions [14, 30, 31]. Moreover, the sensitivity to intergranular crack initiation could also be dependent on the intragranular strain hardening mechanism (linked to the number of active slip systems), the differences in Young’s modulus and the ability for lattice rotation across the grain boundaries. It is also noted from Table 4.6 that no secondary cracks have been detected at the end of these two experiments.

Table 4.6 – Summary of crystallographic configurations leading to crack initiation at low temperature/high applied stress and medium temperature/medium applied stress along transverse direction.

Creep condition	Extensometry	Creep life	Grain boundary misorientation of the fatal crack	Grain boundary crystallographic configuration of the fatal crack	Grain boundary crystallographic configuration of secondary cracks
900°C/400 MPa	Strain markers	17.6 h	20.5°		
900°C/400 MPa	Strain markers	35.3 h	24.0 °		
750°C/800 MPa	Strain markers	2.3 h	35.8°		
750°C/750 MPa	Strain markers	5.0 h	21.5°		
750°C/700 MPa	Strain markers	2.4 h	31.0°		
740°C/700 MPa	DIC	36.2 h	N.M.		

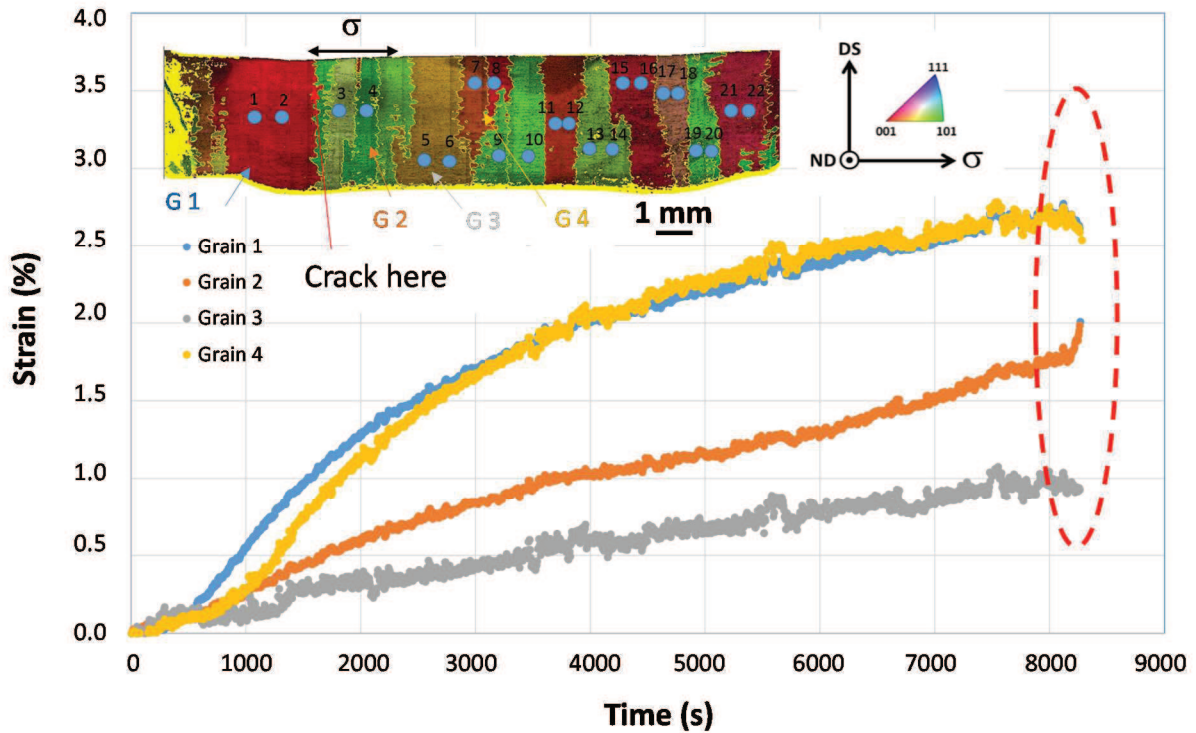


Figure 4.37 – Local creep strain elongation during transverse creep testing at 750°C/800 MPa and associated EBSD map whose color code refers to the applied stress direction. The grains in which creep strain evolutions are presented have been identified in the EBSD map (grains G1, G2, G3 and G4).

A  $\sim[001]/\sim[101]$  configuration is also detrimental in terms of intergranular crack initiation since it induces a large contrast in elastic strain, close to the largest possible for a DS specimen machined like what has been done during these experiments (i.e. with the solidification direction perpendicular to the loading direction and along the width of the specimens). The Young's modulus of a  $\langle 001 \rangle$  oriented grain is  $\sim 101$  GPa while it is  $\sim 185$  GPa for a  $\langle 011 \rangle$  oriented grain at 750°C. A factor close to 2 in elastic strain magnitude is then encountered for such a “red-green” grain boundary configuration, also contributing possibly to crack initiation.

According to Figure 4.37 and Figure 4.38, one also observes that grains close to the  $\langle 101 \rangle$  pole in the stereographic triangle present a creep behavior somehow different from the one observed using a SX specimen with a nearly similar orientation and loaded at 750°C/800 MPa. Indeed,  $\sim\langle 101 \rangle$  SX specimens are known to present a very poor creep resistance at low temperature/high applied stress [13, 14] and it has been shown in the previous chapter in Fig. 3.6 that a  $\sim\langle 212 \rangle$  SX specimen had a very poor creep resistance (creep life of 0.5 hours, see Appendix 2) with almost no strain hardening and a spectacular increase in ellipticity of the specimen, indicating single slip activity and lattice rotation. Even if the creep curves of each grain plotted in Figure 4.37 and Figure 4.38 may be affected by the fact that there may be not only one grain through the thickness of the specimens, pronounced differences are observed in creep elongation between close-to- $\langle 101 \rangle$  grains in these DS specimens and the one obtained using a SX specimen for which a spectacular creep acceleration is observed in less than 0.25h at 750°C/800 MPa. According to this difference in creep behavior, it is highly likely that other grains on each sides of a close-to- $\langle 101 \rangle$  grain, and more generally, the polycrystalline nature of DS alloys, impose boundary conditions preventing it behaving as a single crystal, with possible free lattice rotation, as this is the case in our SX creep experiments.

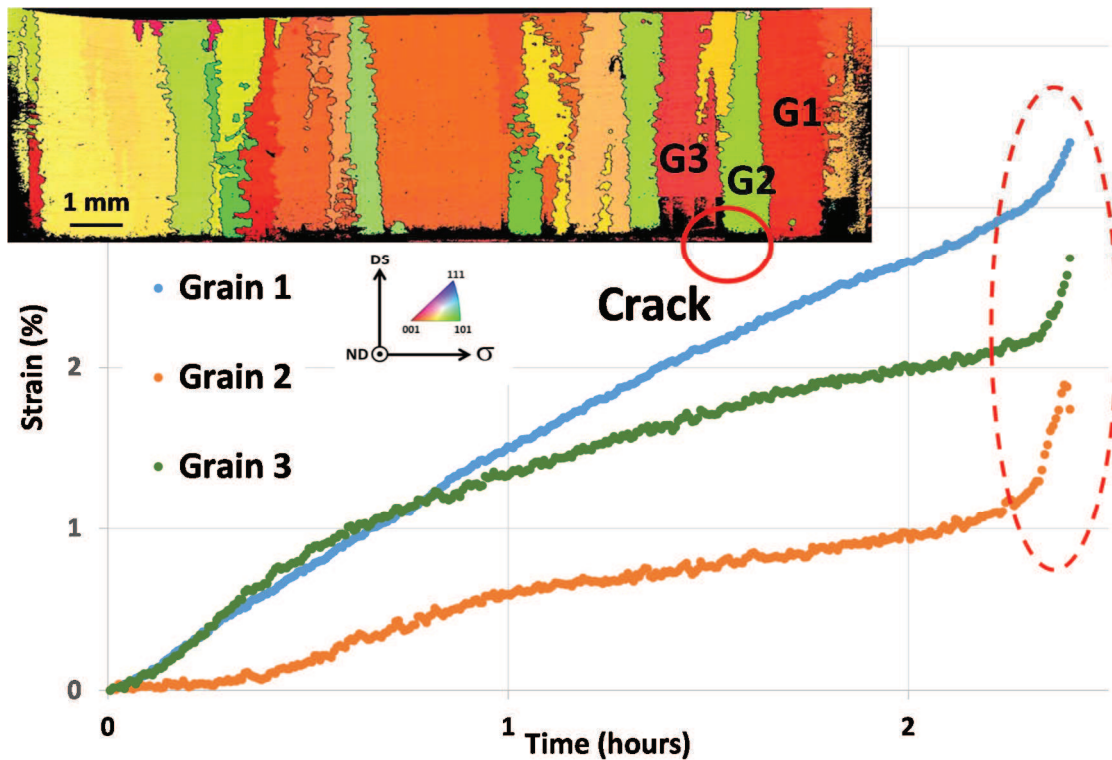


Figure 4.38 – Local creep strain elongation during transverse creep testing at 750°C/700 MPa using a ~0.5 mm thick specimen and associated EBSD map whose color code refers to the applied stress direction. The grains for which creep strain evolution is presented have been identified in the EBSD map (grains G1, G2 and G3).

From Figure 4.37 and Figure 4.38, it is also observed that the initiation of cracks occurs very late in the creep life. The development of damage indeed lasts for 10% of the total creep test duration at maximum. In the experiment at 750°C/700 MPa (Figure 4.38), a strain acceleration has been observed in the three grains close to the fatal crack and no strain acceleration in grains far from failure (not shown). During the experiment at 750°C/800 MPa (Figure 4.37), a decrease in strain has been observed in Grains 1, 3 and 4, and an increase in strain in Grain 2 once the main crack has been opened. Even if these strain evolution may be affected by the exact positions of strain markers with respect to grain boundaries, we believe that the decrease in strain in Grains 1, 3 and 4 results from the elastic unloading upon crack opening and subsequent propagation while the increase in strain for grain 2 may result from its intrinsic possible rotation once a crack is opened.

In Figure 4.39, a last experiment performed at 750°C and 750 MPa is presented. A “red-green” configuration is observed on the right part of the gage length (see Figure 4.39(a) and (b)), with a very wide ~[101] grain. Despite this ~[101] grain (identified as G1) had undergone a very large creep strain (see Figure 4.40), failure did not occur between grain G1 and grain G2 as we would have expected from previous experiments. Failure occurred at the rear face of the specimen, at a ~[001]/~[102] crystallographic configuration (see Table 4.6). After failure, observing the fracture surface, two grains present across the thickness of the specimen were detected, probably all along the specimen’s gauge length. Despite this “unexpected” failure, two secondary cracks have been observed at G1/G2 and G2/G3 grain boundaries (see red arrows in Figure 4.39(b)). These two secondary cracks correspond once again to the configuration we identified at 750°C/700 MPa and 750°C/800 MPa as being the most critical one. Looking carefully at the  $\gamma/\gamma'$  microstructure close to one of these secondary cracks in the G1 grain, spectacular shearing bands were observed (see Figure 4.39(d)), probably resulting from the large amount of local creep strain in grain G1 (see Figure 4.40). These bands were not

identified as micro-twins according to EBSD characterizations (lattice rotation of 45 to 50° when plotting an orientation profile perpendicular to these bands). However, it has clearly been evidenced after this test that each grain close to these secondary cracks had undergone lattice rotation along the normal to the specimen's main face (the normal to Figure 4.39(a) or (b)), as observed in Figure 4.39(c). We highly suspect that intergranular crack initiation during transverse creep testing at 750°C/high applied stress may also result from the differences in lattice rotation across the grain boundary, as already observed by J.C. Stinville & al. during transverse creep tests of bi-crystalline Ni-based specimens at 982°C [5].

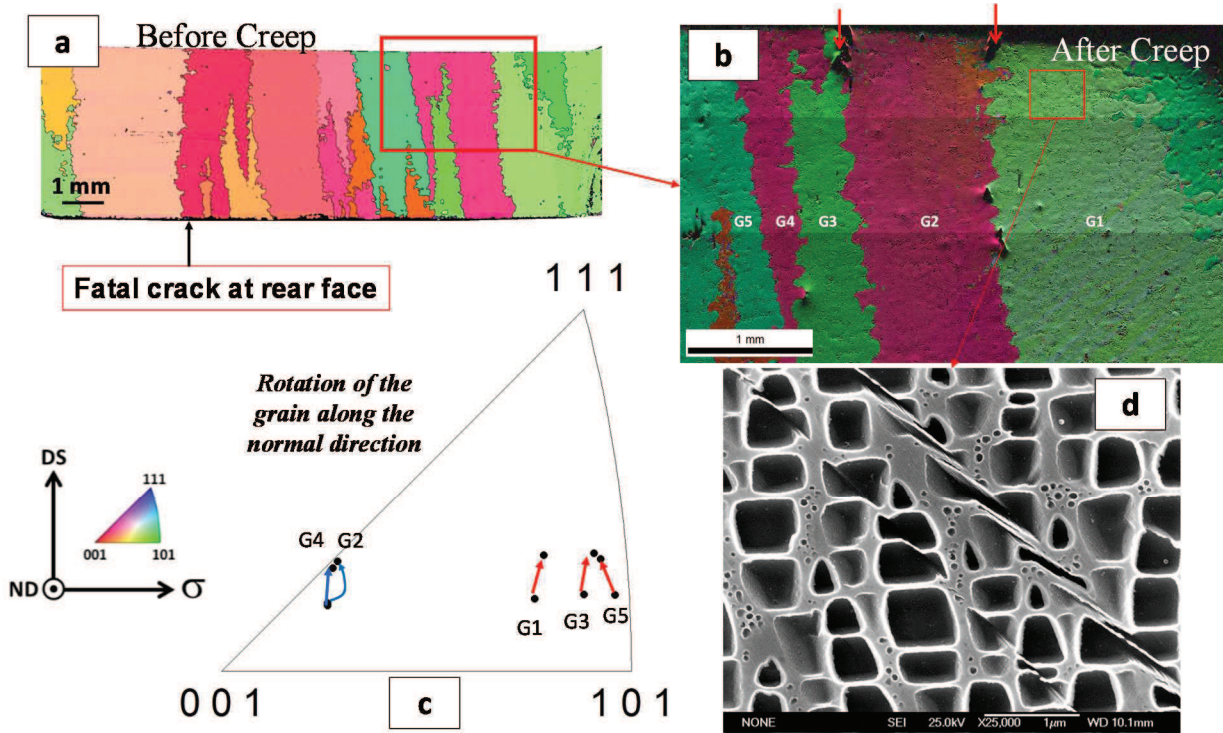


Figure 4.39 – EBSD map of the DS-T specimen tested at 750°C/750 MPa whose color code refers to the applied stress direction (a), focusing on a favorable configuration for crack initiation where secondary cracks (see red arrows) have been detected (b). The rotation of the grains referenced in (b) after the creep tests are shown in (c) while the local  $\gamma/\gamma'$  microstructure in grain G1 close to a secondary crack is shown in (d).

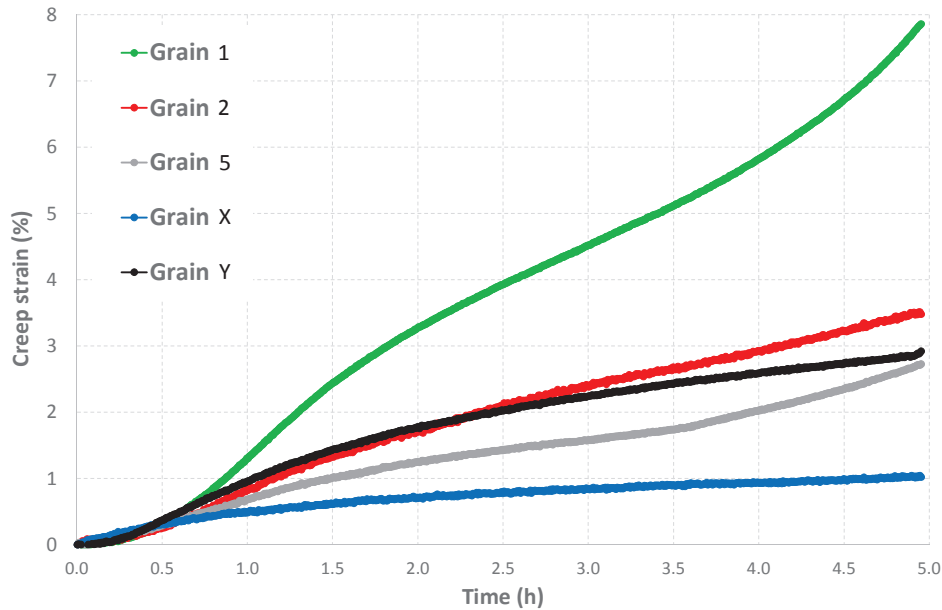


Figure 4.40 – Local creep strain elongation during transverse creep testing at 750°C/750 MPa whose grains referenced as “Grain 1”, “Grain 2”, and “Grain 5” corresponds to grains identified in Figure 4.39(b).

To deepen our understanding of intergranular crack initiation during transverse creep testing of DS200+Hf, a last experiment at 740°C/700 MPa with full field strain measurement has been performed in the Materials Department of the University of California – Santa Barbara. For this, a special set-up has been developed by J.C. Stinville, as already presented in section 2.5 and Fig. 2.11. Strain measurements have been performed along six different generatrices of a CG DS-T cylindrical specimen using a digital image correlation (DIC) technique.

Figure 4.41 presents the macroscopic elongation of the specimen. It is observed as a very steep tertiary creep stage, occurring in the very last hour of the test, and with a very small creep strain at failure. This macroscopic creep behavior is indicative of a highly localized fracture. According to the longitudinal creep strain profile history along the gauge length shown in Figure 4.42(a), the development of only two cracks are indeed observed at axial positions of ~7 mm and ~13 mm. Figure 4.42(b), (c) and (d) show that the secondary crack is intergranular, as expected. Figure 4.43 also shows that the evolution of the longitudinal strain profile is different when changing of generatrix. Both the fatal and the secondary crack developed first close to 0° and 165° generatrices and a plateau in creep strain can be observed on the left hand side of the main peak in the 15° and 150° plots of Figure 4.43, corresponding to crack tip localized plasticity. Figure 4.44 presents more clearly the history of the fatal crack development. One can clearly see a strain localization since 22.5 hours where the fatal crack will subsequently developed. However, it is impossible to observe any intergranular crack or damage with the resolution of the pictures used for the DIC post-processing. The main crack has been detected after 30 hours of creep, with a sharper peak in terms of strain localization (see Figure 4.44).

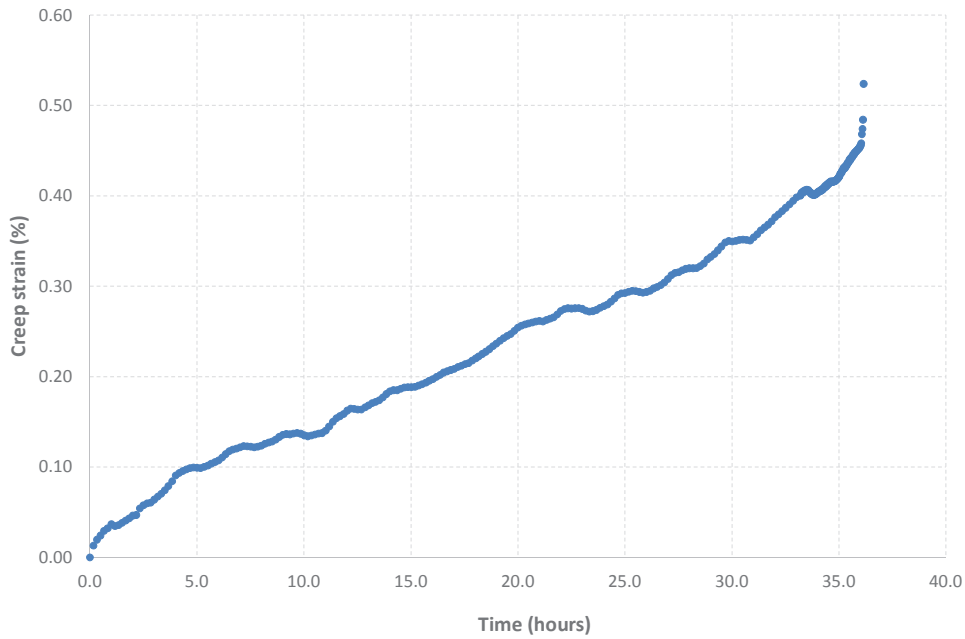


Figure 4.41 – Macroscopic creep elongation during transverse creep testing followed by DIC at 740°C/700 MPa.

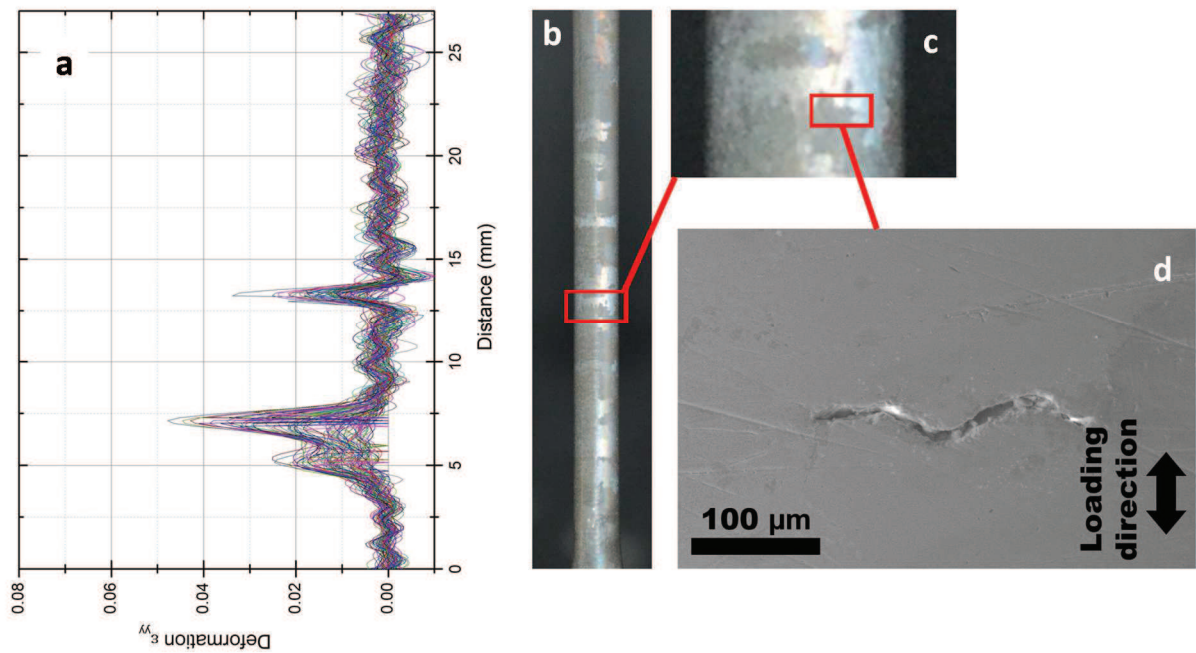


Figure 4.42 – Longitudinal creep strain profile evolution (a) during transverse creep testing at 740°C/700 MPa along one specimen's generatrix shown in (b). Two areas of creep strain localization are evidenced in (a), corresponding to the development of the grain boundary fatal crack and of a secondary crack, as shown in (c) and (d).



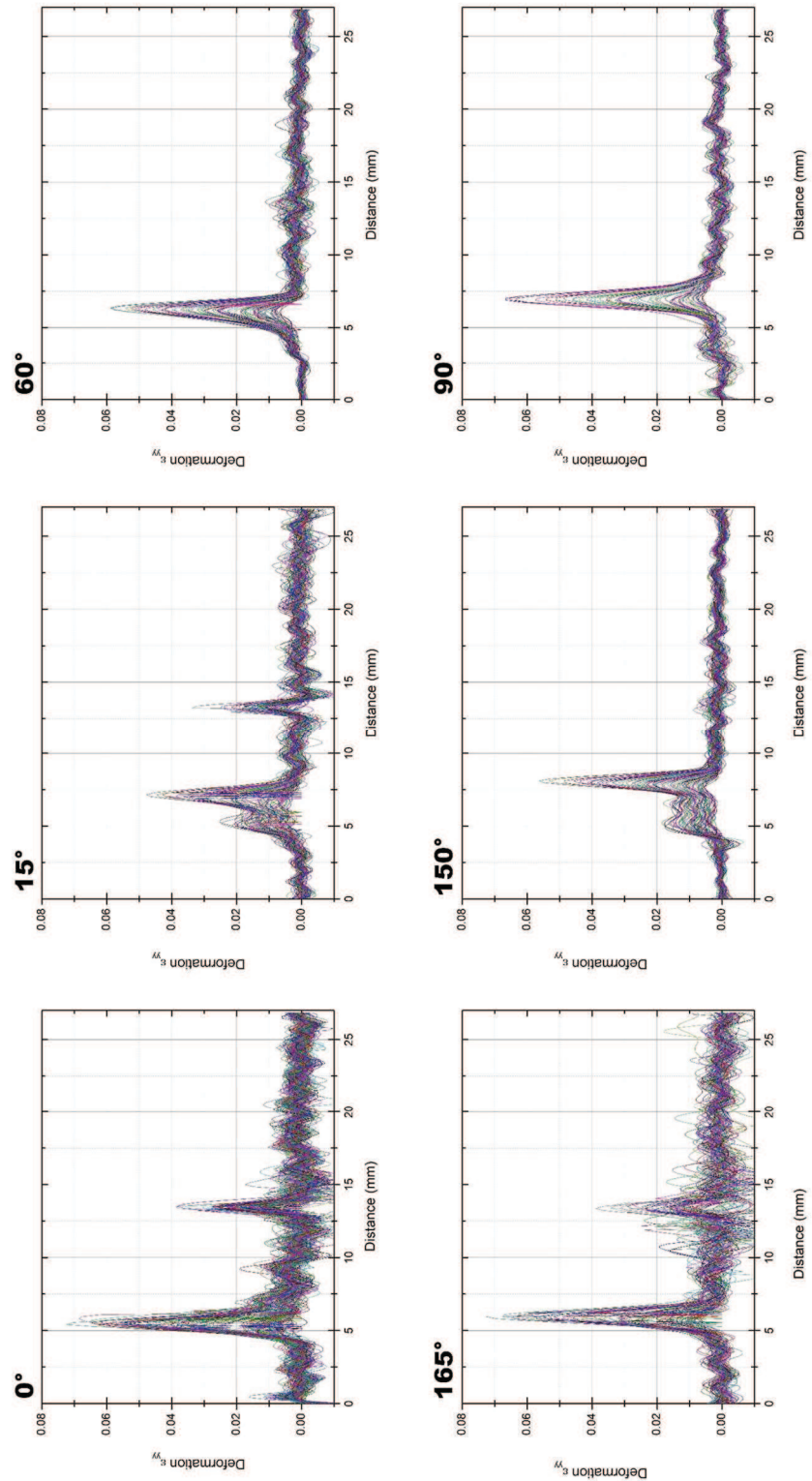


Figure 4.43 – Longitudinal creep strain profile evolutions during transverse creep testing at 740°C/700 MPa along different specimen’s generatrices.

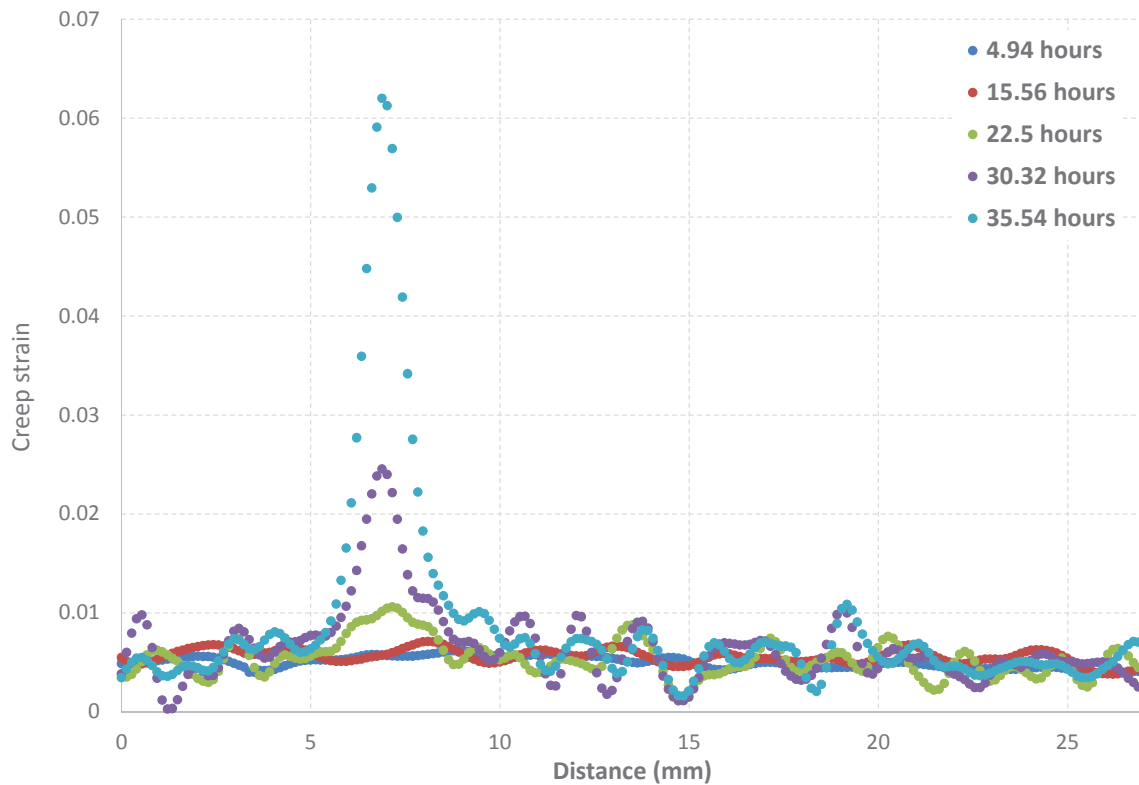


Figure 4.44 – Longitudinal creep strain profile evolutions during transverse creep testing at 740°C/700 MPa along the 60° generatrix, as defined in Figure 4.43.

These full field strain measurements suggest that local grain boundary creep strain localization precede crack initiation and that this strain localization is undetectable on the macroscopic creep curve when it starts to develop (see Figure 4.41). Indeed, according to DIC strain profiles like the one presented in Figure 4.44, when the tertiary creep stage is detected at the macroscopic scale (i.e. after 35.5h in Figure 4.41), it already corresponds to a local longitudinal creep strain in excess of 6%, i.e. to a widely open crack. Based on such an analysis, it is better understood why the transverse creep life of DS200+Hf is scattered at low temperature/high applied stress (see, e.g., Larson Miller plot in Fig. 3.5(a)) and more generally, why creep properties are scattered for coarse grain cast Ni-based alloys.

To go deeper into the analysis of the specimen followed by DIC strain measurement, EBSD characterization has been performed after the test. Unfortunately, due to the specimen's geometry, it was not possible to perform such a characterization before the test and hence, all the orientations presented in the next two figures may have changed due to lattice rotation during the creep test. Figure 4.45 shows that the secondary crack has developed at a  $\sim[001]/\sim[102]$  grain boundary, at a portion of the grain boundary perpendicular to the applied stress. Regarding the main crack, special attention has been paid to performing a longitudinal cut intercepting the crack initiation site, that is not an easy task. It can be observed in Figure 4.46 that there is a quite complex crystallographic configuration close to the initiation site. Once again, a close-to-[001] grain is observed at the surface in the area of the initiation site, in addition to a close-to-[102] and a close-to-[101] grains. Given the very small size of the  $\sim[001]$  grain in Figure 4.46, it is possible that the large  $\sim[101]$  grain may also be connected to the surface below or above the cutting plane. The preparation of the specimen (cutting and subsequent mechanical polishing) may have indeed led to an observation plane slightly shifted with respect to the exact crack initiation site at the surface of the specimen. It is also observed in Figure 4.46 several bands starting from the fracture surface in each "green" grain. These bands may correspond to local shearing, as already observed in Figure 4.39(d) and in a previous paper from

Stinville et al. [5]. Based on the crystallographic configuration observed in Figure 4.46, it is difficult to identify one single grain boundary where the fatal crack may have first initiated. We will hence keep in this case a  $\sim[001]/\sim[102] + \sim[001]/\sim[101]$  main crack initiation site.

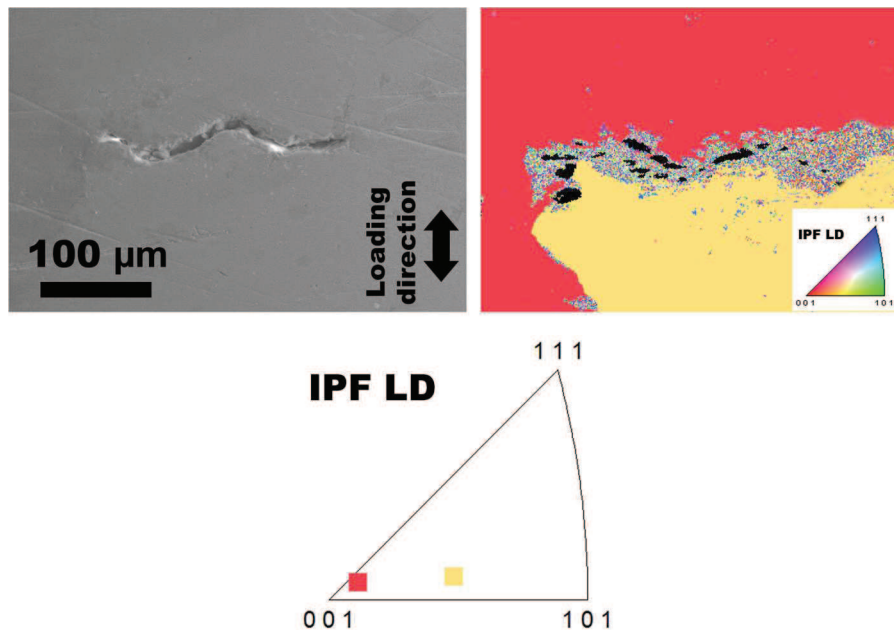


Figure 4.45 – EBSD map close to the secondary crack shown in Figure 4.42(d). IPF LD = Inverse Pole Figure along Loading Direction.

As a summary of these experiments, no specific crystallographic configuration favoring intergranular crack initiation has been observed during transverse creep at 900°C. **At this temperature, crack initiation is hence mainly controlled by grain boundary oxidation, and more specifically, by the oxidation of carbides**, as already presented and discussed before. However, at low temperature ( $\sim 750^\circ\text{C}$ ) and high applied stresses,  $\sim[001]/\sim[102]$  and  $\sim[001]/\sim[101]$  configurations have been identified as the most favorable ones triggering intergranular crack initiation (see Table 4.6). Both configurations correspond to a high angle boundary which was shown previously to be detrimental to the transverse creep ductility at 982°C/207 MPa in René N4 bicrystalline specimens [5]. We have already mentioned before that such crystallographic configurations lead to a large mismatch in creep strain due to the difference in the number of activated slip systems, hence favoring intergranular crack initiation. However, it is believed that the main factor controlling intergranular crack initiation at low temperature/high applied stress is the mismatch in lattice rotation occurring during creep across the grain boundary. Indeed, a  $\sim[001]$  grain has systematically been observed in critical configurations at 750°C (see Table 4.6), i.e., a grain which is stable with respect to lattice rotation. However,  $\sim\langle 102 \rangle$  and  $\sim\langle 101 \rangle$  are grains known to rotate during creep deformation since they are favorably oriented for single slip or even, for (micro-)twinning [5, 32-35]. A perfect  $\langle 101 \rangle$  grain is not oriented by nature for lattice rotation but a slight misorientation of few degrees from the perfect misorientation (like in our DS-T specimens) is enough to trigger single slip activity, especially at low temperature/high applied stress [13, 14]. Differences in lattice rotation across grain boundaries have already been shown by other authors to control intergranular crack initiation in DS or bicrystalline Ni-based alloys during transverse creep testing [5, 36]. The location of the very first stage of crack development was even shown to depend on the kinematics of lattice rotation and relative variation in ellipticity of each grain [5]. Such an ellipticity development was not observed during our experiments, probably since our grains are not large enough to characterize it unambiguously. An

interrupted creep test would be necessary to follow the kinetics of lattice rotation at critical configurations and to detect the degree of rotation necessary to trigger intergranular cracking in DS200+Hf. Moreover, the role of carbides in the development of intergranular cracks under such conditions still remain to be elucidated in addition to the effect of the elastic strain mismatch on the grain boundary stress concentration. **In conclusion, preferential intergranular crack initiation at 750°C/high applied stress occurs at high angle boundaries, with a crystallographic configuration inducing a large mismatch in lattice rotation.**

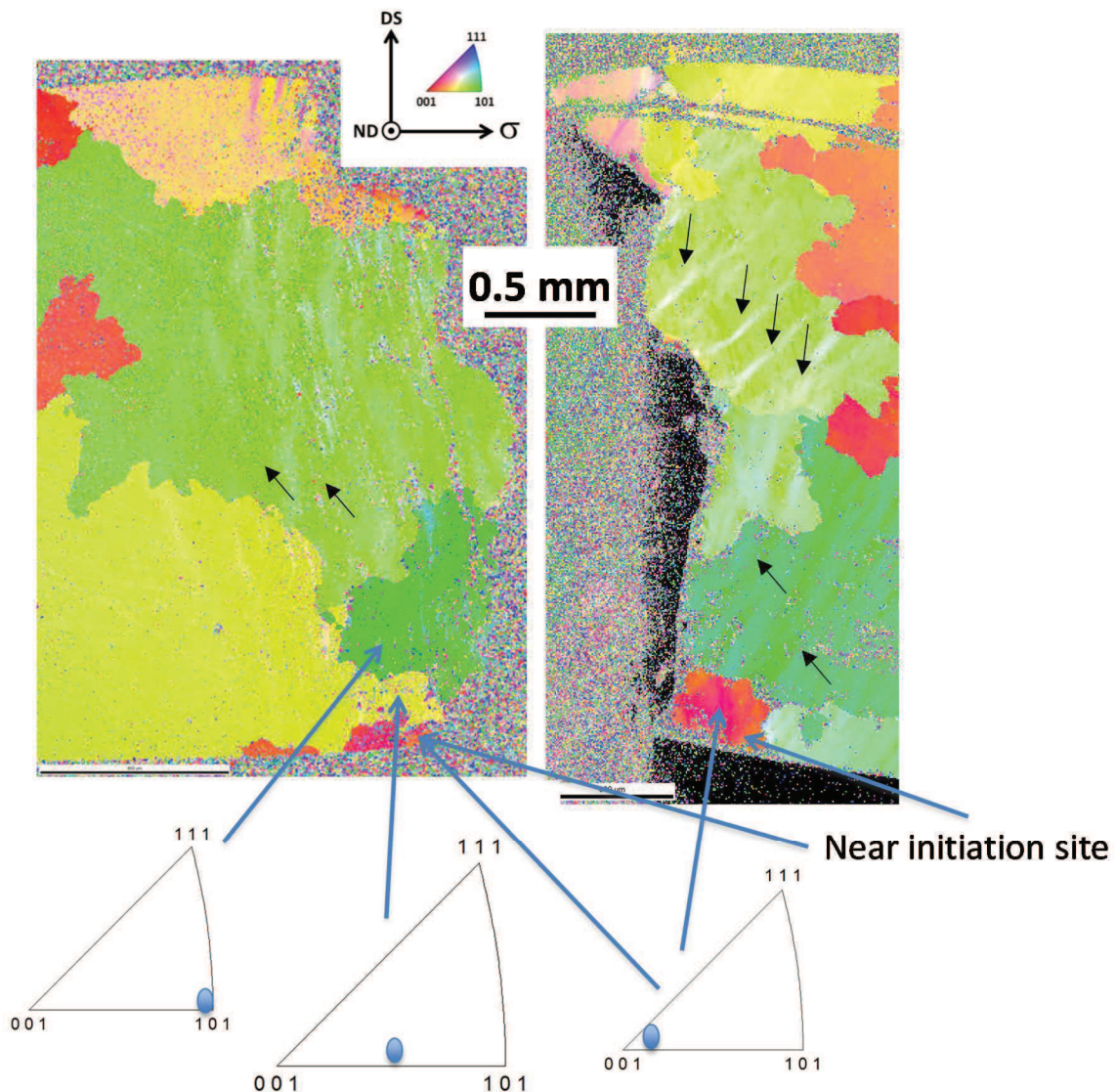


Figure 4.46 – EBSD maps on both sides of the fracture surface of the DS-T specimen tested at 740°C/700 MPa. The observations have been performed close to main crack initiation site according to local strain measurements presented in Figure 4.43.

#### 4.5 Creep, LCF and Dwell-fatigue life modeling

Based on the experimental database generated in this work, phenomenological models have been identified in LCF and dwell-fatigue to compute the number of cycles to failure. Moreover, a simple coupled creep-damage-oxidation taking into account the DS anisotropy has been developed and

identified to compute minimum strain rates and creep lives. This last part of chapter 4 is devoted to the presentation of these models and of their performances.

#### 4.5.1 LCF life modeling at 650°C

An ONERA-type model has been used to calculate LCF lives at 650°C [37]. In this kind of phenomenological approach, the accumulation of the fatigue damage  $D$  at each cycle is described by Eq. 4.2:

$$\frac{\delta D}{\delta N} = \frac{\sigma_{max} - \sigma_l(\sigma_{moy})}{\sigma_u - \sigma_{max}} \left( \frac{\sigma_{max} - \sigma_{moy}}{B(\sigma_{moy})} \right)^\beta \quad Eq. 4.2$$

The variables contained in Eq. 4.2 are defined in Table 4.7, in addition to the parameters required for the identification of this model.

$\sigma_l$	Fatigue limit
$\sigma_{l0}$	Fatigue limit at applied stress ratio $R = -1$
$\sigma_{moy}$	Average applied stress
$\sigma_u$	Ultimate tensile stress
$\sigma_{max}$	Maximum applied stress
$N_f$	Number of cycles up to failure
$\beta, b, B$ and $B_0$	parameters for the calibration of the model

Table 4.7 – Nomenclature of the variables/parameters used in Eqs. 4.2, 4.3 and 4.4.

By integration of Eq. 4.2, assuming a fatigue damage scalar  $D$  of 0 in the initial state and of 1 at failure, one can calculate the number of cycles up to failure according to Eq. 4.3:

$$N_f = \frac{\sigma_u - \sigma_{max}}{\sigma_{max} - \sigma_l(\sigma_{moy})} \left( \frac{\sigma_{max} - \sigma_{moy}}{B(\sigma_{moy})} \right)^{-\beta} \quad Eq. 4.3$$

This model takes into account both the effect of applied stress ratio in S-N diagrams through the presence of the average stress  $\sigma_{moy}$  in Eq. 4.3, but also through the evolution of the fatigue limit  $\sigma_l$  and of the  $B$  parameter (see Eq. 4.4 and Eq. 4.5):

$$\sigma_l = \sigma_{moy} + \sigma_{l0} (1 - b\sigma_{moy}) \quad Eq. 4.4$$

$$B(\sigma_{moy}) = B_0 (1 - b\sigma_{moy}) \quad Eq. 4.5$$

The identification of  $\beta$ ,  $b$  and  $B_0$  parameters has been performed for each type of specimen tested in LCF at 650°C, both at  $R\sigma = -1$  and  $R\sigma = 0.05$ . It is recalled here that all LCF results at 650°C can be found in appendix 4. The ultimate tensile stresses  $\sigma_u$  used for these identification are those obtained during tensile tests performed at 650°C/10<sup>-3</sup> s<sup>-1</sup> (see appendix 1). These identifications have been performed such as to achieve the best fit of our experimental results. Naturally, LCF results up to 10<sup>6</sup>-10<sup>7</sup> cycles would have been necessary to ascertain the fatigue limit value  $\sigma_{l0}$  determined from these parameter identification.

Figure 4.47 hereafter presents the performance of the model for <001>-SX (Figure 4.47(a)), DS-L (Figure 4.47(b)) and DS-T (Figure 4.47(c)) specimens. The set of parameters identified for each type of specimen is also added in this figure. In each case and for both stress ratios  $R$ , good modeling of the experimental fatigue life evolutions is observed. According to the parameters' identification, one can

see that the fatigue limit  $\sigma_{10}$  is lower along transverse direction compared to the two other types of specimens, what seems logical given the lower fatigue strength along this loading direction.

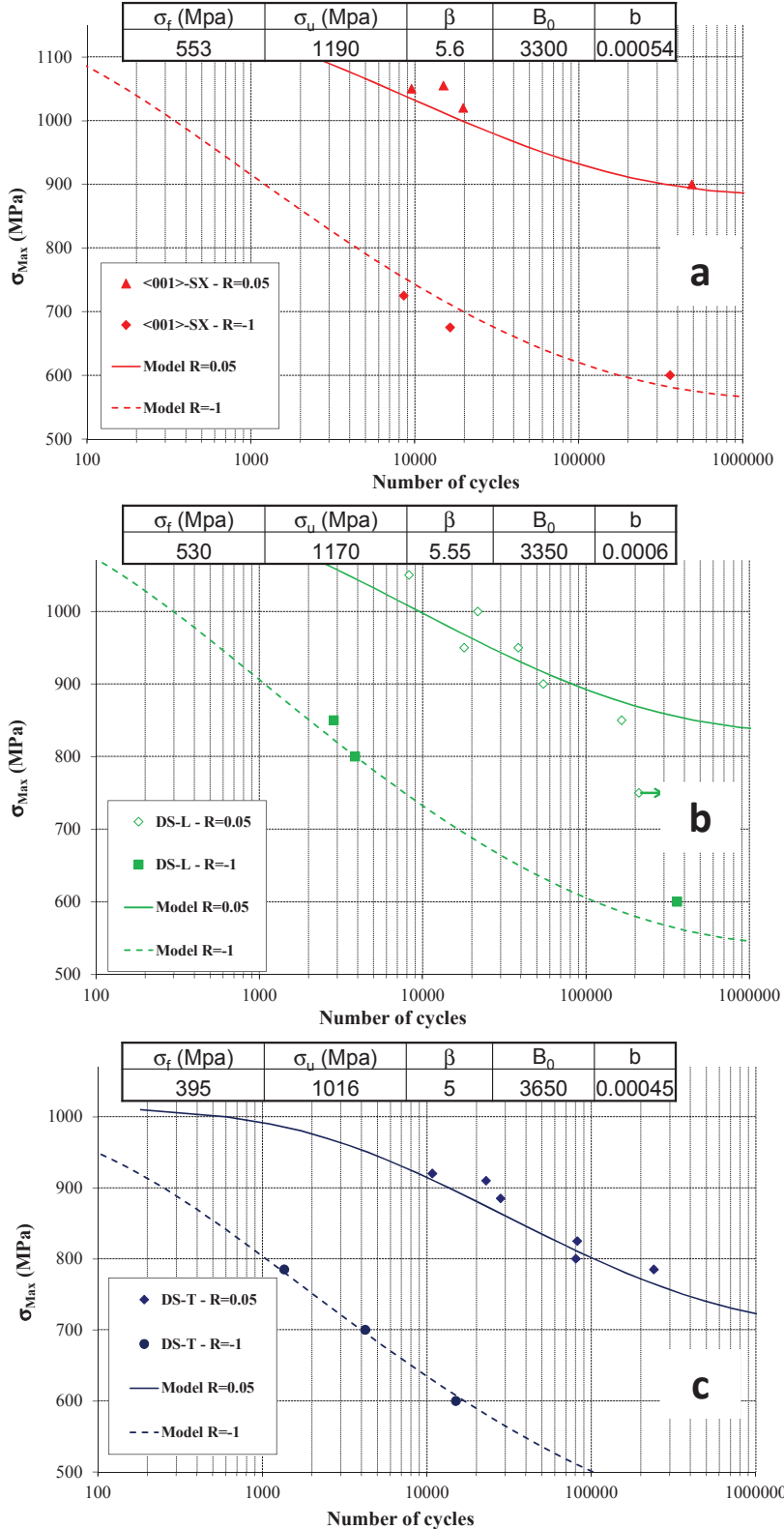


Figure 4.47 – LCF modeling at 650°C for <001>-SX (a), DS-L (b) and DS-T (c) specimens. The calibration parameters have been provided for each type of specimen.

It has to be mentioned that an attempt to identify a unique set of parameters whatever the specimen type has been done, by modifying the formulation of Eq. 4.2. Unfortunately, no satisfactory modification has been found.

#### 4.5.2 Creep-oxidation-damage modeling at 900°C

A coupled oxidation-creep-damage model has been developed to account for creep properties at 900°C. A huge impact of oxidation on the creep properties has been shown in Section 4.3. This model consists in a coupled Norton-Kachanov approach [38-40], taking in account oxidation damage. The Norton law and the evolution of creep damage according to the Rabotnov-Kachanov approach are recalled in Eq. 4.6 and Eq. 4.7 respectively:

$$\dot{\epsilon} = B\sigma_0^n \quad \text{Eq. 4.6}$$

$$\dot{D} = \left(\frac{\sigma}{A_0}\right)^r (1-D)^{-k} \quad \text{Eq. 4.7}$$

Variables and parameters used in Eq. 4.6 and Eq. 4.7 are defined in the Table 4.8.

$\sigma_0$	Initial stress applied
$\epsilon$	Uniaxial creep strain
$D$	Scalar creep damage
$B, n$	Norton's law parameters
$A_0, r, k$	Rabotnov-Kachanov law parameters

Table 4.8 – Nomenclature of the variables/parameters used in Eq. 4.6 and Eq. 4.7.

The coupling between Eq. 4.6 and Eq. 4.7 has been done by using the concept of effective stress  $\sigma_{eff}$ , as defined in Eq. 4.8:

$$\sigma_{eff} = \left(\frac{\sigma_0(1+\epsilon)}{(1-D)}\right) \dots \text{Eq. 4.8}$$

It can be observed that the effective stress we have been using considers both the loss of load bearing section due to the accumulation of creep damage, through the (1-D) term in Eq. 4.8, but also the loss of load bearing section due to the specimen's elongation through the (1+ $\epsilon$ ) term. The creep-damage coupling is subsequently taken into account by introducing the effective stress into Norton's law, leading to Eq. 4.9:

$$\dot{\epsilon} = B\sigma_{eff}^n \quad \text{Eq. 4.9}$$

One of our main aim was to develop a model taking into account the anisotropy in creep properties in a simple way, i.e. to have a unique set of parameters in both the Norton and damage laws per temperature for DS-T, DS-L and <001>-SX specimens. For this, the effective stress defined in Eq. 4.8 has been normalized in Norton's law by the Ultimate Tensile Stress (UTS) as determined from tensile tests at  $10^{-5} \text{ s}^{-1}$ , leading to Eq. 4.10:

$$\dot{\epsilon} = A \left(\frac{\sigma_{eff}}{UTS}\right)^n \quad \text{Eq. 4.10}$$

A similar normalization by the UTS has been adopted recently for modeling of the viscoplastic properties of DS Ni-based superalloys [41], using a Wilshire-type approach [42, 43]. As shown in Figure 4.48, when the creep life at 900°C is plotted as a function of the applied stress normalized by

UTS, it can be observed that creep lives for <001>-SX, DS-L and CG DS-T specimens are almost superimposed. Only FG-DS-T and specimens machined at 45° of the solidification direction are lying outside of this trend (not shown for DS-45° specimens). These last specimens will be re-used at the end of this sub-section for validation of the model performance.

The contribution of oxidation to the overall damage has been considered by introducing a surface loss of load bearing section over a thickness  $e$ . This loss of load bearing section is schematically represented in Figure 4.49 for a sample having a rectangular section. The evolution of this thickness  $e$  has been assumed to be parabolic, in agreement with TGA results presented in Figure 4.13. Eq. 4.11 hence presents the evolution of this affected thickness as a function of time and Eq. 4.12 defines the oxidation kinetics  $K$ , assuming that it follows an Arrhenius-type law, with  $R$  the constant of perfect gases,  $Q$  the activation energy and  $K_0$  a pre-exponential oxidation kinetics. Note that an  $e_0$  factor has been added in Eq. 4.11 since a given oxide thickness may already be present before starting creep deformation (for example, the soak time at maximum temperature before applying the mechanical stress is already enough to develop an oxide scale).

$$e = e_0 + K\sqrt{t} \quad \text{Eq. 4.11}$$

$$K = K_0 e^{\frac{-Q}{RT}} \quad \text{Eq. 4.12}$$

It has to be noted that since our creep and oxidation databases have mainly been generated at 900°C, it will not be possible to identify  $K_0$  and  $Q$  parameters in Eq. 4.12.

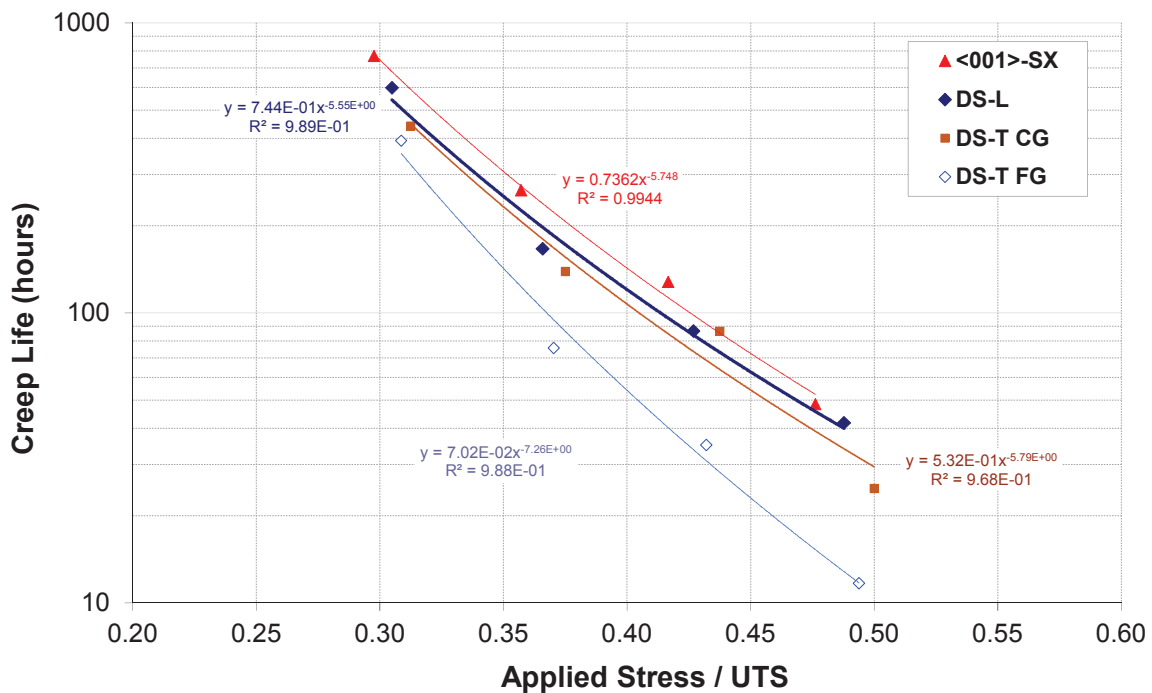


Figure 4.48 – Creep life evolution at 900°C using a radiant furnace as a function of the applied stress normalized by UTS (determined from tensile tests at 900°C/10<sup>-5</sup> s<sup>-1</sup>).



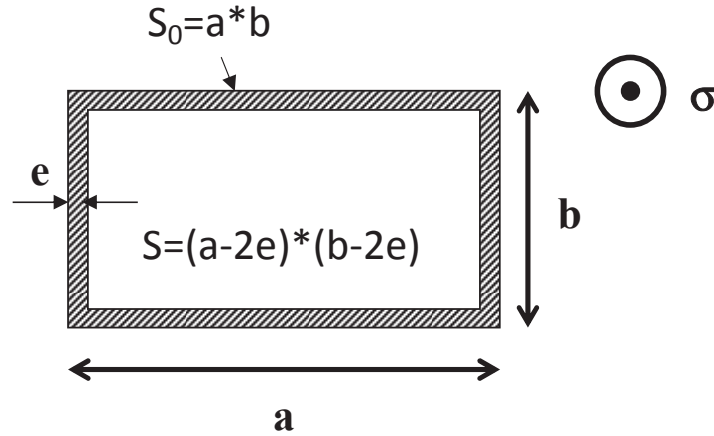


Figure 4.49 – Schematic illustration on how oxidation affects at the load bearing section of creep specimens.

The contribution of oxidation to the creep rate and creep damage evolution has also been taken into account by modifying the effective stress, like the approach developed by Dryepondt and co-workers [44]. Indeed, the oxidation affected layer is considered, like other authors [24, 45], as having no load bearing capacity, overall leading to the final expression of the effective stress:

$$\sigma_{eff} = \left( \frac{\sigma_0(1+\varepsilon)}{(1-D)} \right) * \frac{S_0}{S} \sim \left( \frac{\sigma_0(1+\varepsilon)}{(1-D)} \right) * \frac{1}{\left(1 - \frac{P}{S_0} * e\right)} = \left( \frac{\sigma_0(1+\varepsilon)}{(1-D) * \left(1 - \frac{P}{S_0} * e\right)} \right) \quad Eq. 4.13$$

Note that the initial and actual bearing section  $S_0$  and  $S$  have been defined in Figure 4.49 and that  $P$  is the perimeter of the load bearing section. One can observe in this equation the perimeter over load bearing ( $P/S$ ) parameter that was defined in Section 4.3.4.2 devoted to thin-wall creep tests. Finally, the normalization by UTS has also been introduced in the Kachanov-Rabotnov law (see Eq. 4.7) as already justified from Figure 4.48 and it has been assumed that  $k=r$  to reduce the number of parameters to identify. The final expression of the damage law is:

$$\dot{D} = \left( \frac{\sigma_{eff}}{A' * UTS} \right)^r \quad Eq. 4.14$$

Table 4.9 and Table 4.10 show the set of parameters identified at 900°C for the Norton's and damage laws used (Eq. 4.10 and Eq. 4.14). The oxidation kinetics  $K$  defined in Eq. 4.11 is also given in these tables. The parameters of the Norton's law  $A$  and  $n$  have been determined from the minimum strain rate versus applied stress/UTS plot for massive specimens while the parameters of the damage law  $r$  and  $A'$  were determined from creep life versus applied stress/UTS plot, also using data of massive specimens (note that these plots are not shown here to ease the reading of this sub-section). Upon identification of optimal materials parameters for these two laws, it appeared that two sets of coefficients have to be extracted, depending if creep tests have been performed using a radiant furnace (FL – Furnace with Lamps - in Figure 4.50) or a resistive furnace (FR – Furnace with Resistances - in Figure 4.50). It is here recalled that only massive specimens have been tested using a radiant furnace while both massive and thin-wall specimens have been tested using a resistive one.

	<001>-SX	DS-L	CG DS-T	FG DS-T	DS-45°
Ultimate Tensile Stress* UTS (MPa)	672	678	626	642	580
Oxidation kinetics** K ( $10^{-6}$ m.h <sup>-0.5</sup> )	0.2	2.1	5.0		
Norton law coefficients [MPa,h <sup>-1</sup> ]					
n	8.13				
A	0.0155				
Rabotnov Kachanov law coefficients [MPa,h <sup>-1</sup> ]					
r	6.19				
A'	1.72				

Table 4.9 – Identified coefficients of the creep-damage-oxidation model identified at 900°C and used for massive and thin-walled specimens tested using a resistive furnace and experiments under vacuum. \*UTS determined from tensile tests at 900°C/10<sup>-5</sup> s<sup>-1</sup>. \*\* e<sub>0</sub> (the initial oxide thickness before applying the mechanical load) is 0 μm under vacuum, 1 μm for <001>-SX specimens and 5 μm for all other DS200+Hf specimens.

	<001>-SX	DS-L	CG DS-T	FG DS-T	DS-45°
Ultimate Tensile Stress* UTS (MPa)	672	678	626	642	580
Oxidation kinetics** K ( $10^{-6}$ m.h <sup>-0.5</sup> )	0.2	2.1	5.0		
Norton law coefficients [MPa,h <sup>-1</sup> ]					
n	7.12				
A	0.0228				
Rabotnov Kachanov law coefficients [MPa,h <sup>-1</sup> ]					
r	5.67				
A'	1.63				

Table 4.10 – Coefficients of the creep-damage-oxidation model identified at 900°C and used for massive specimens tested using a radiant furnace. \*UTS determined from tensile tests at 900°C/10<sup>-5</sup> s<sup>-1</sup>. \*\* e<sub>0</sub> (the initial oxide thickness before applying the mechanical load) is 0 μm under vacuum, 1 μm for <001>-SX specimens and 5 μm for all other DS200+Hf specimens.

This “furnace effect” on creep performances has already been observed in previous studies [46, 47]. Despite a very careful attention in performing creep tests with an accurate and reliable temperature control during tests, one-heating-zone radiant furnace are known to favor earlier onset of tertiary creep, by inducing earlier strain localization, what finally leads to shorter creep lives, as observed in Figure 4.50.

According to Table 4.9 and Table 4.10, different oxidation kinetics have been identified for SX, DS-L and DS-T specimens. Indeed, as already observed earlier in this chapter, grain boundaries affect the oxidation kinetics (see TGA results in Figure 4.13 once again). The oxidation kinetics parameters K in Table 4.9 and Table 4.10 have been determined so as to achieve the best modeling of creep life when changing the specimen’s thickness (see Figure 4.55(b)). It can be seen that the oxidation kinetics is 10 times smaller for SX specimens in comparison to DS-L ones and 25 times smaller compared to the DS-T specimens. This huge difference in oxidation kinetics results from the fact that in SX specimens, oxidation only affects a surface without grain boundaries, leading to γ-depleted layer, a γ affected layer (i.e. with a lower fraction of γ particles), as already proposed by other groups [20-22, 48, 49] and also observed in this work. These affected layers may be represented by an overall affected layer

without any load bearing capacity (i.e. a  $\gamma$ -phased layer) having a thickness  $e$  smaller compared to the total extent of the affected layer by oxidation (see schematic illustration in Figure 4.51).

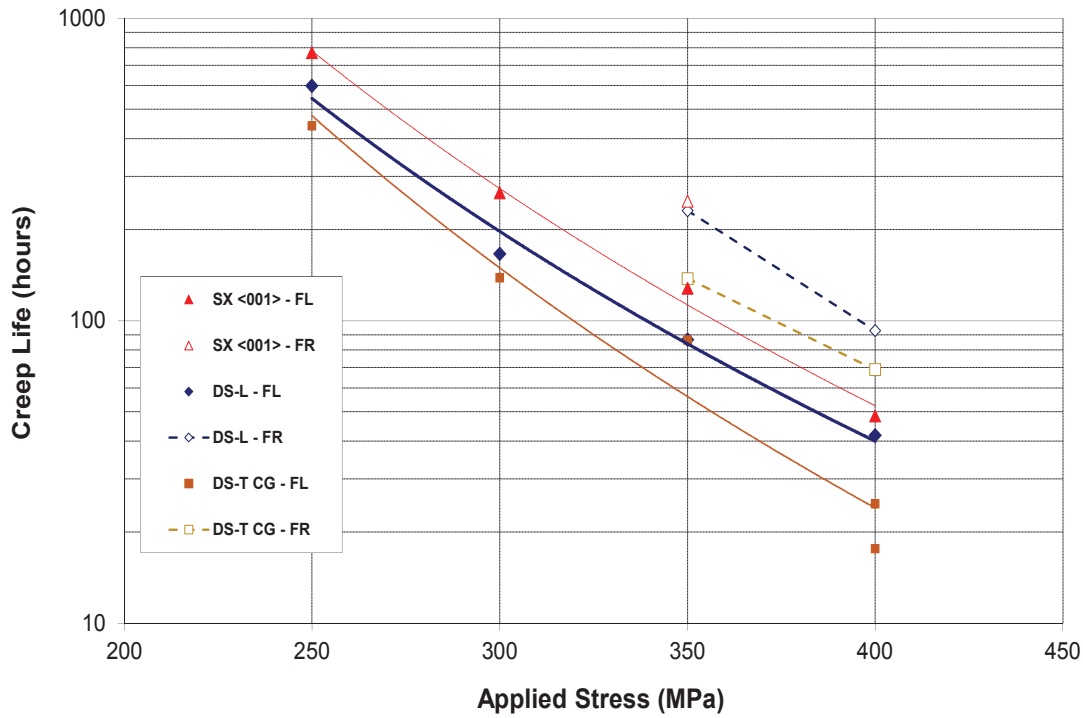


Figure 4.50 – Comparison of the creep life evolution as a function of the applied stress at 900°C using a radiant furnace (FL) or a resistive furnace (FR).

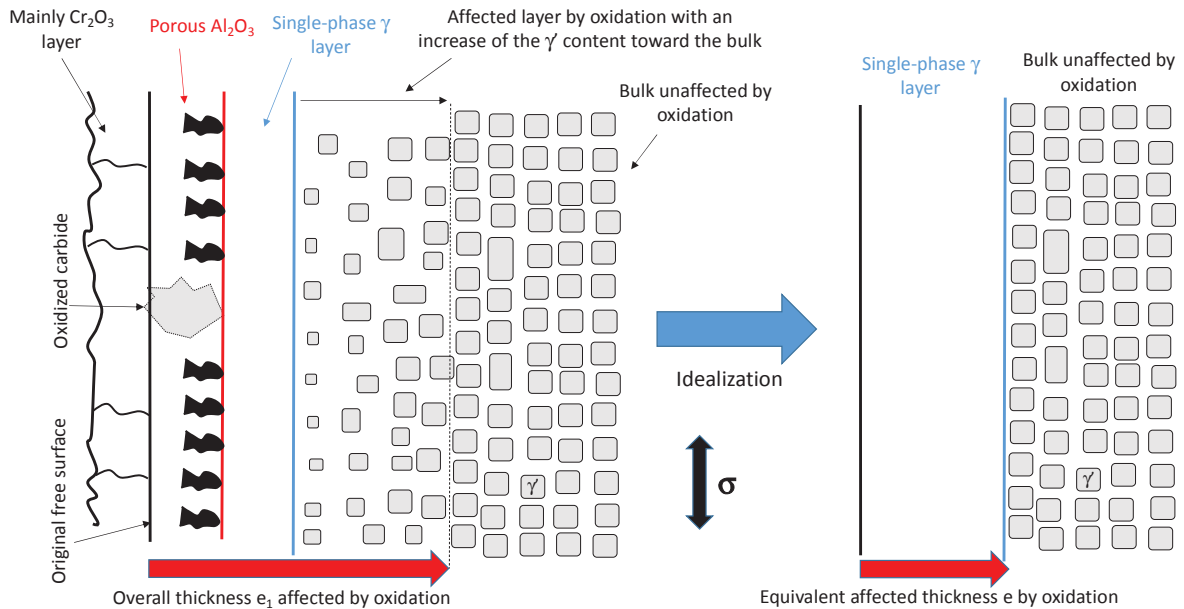


Figure 4.51 – Schematic illustration of the loss of load bearing section along longitudinal section for  $\langle 001 \rangle$ -SX specimens.

In the presence of grain boundaries, the extent of the affected layer is deeper (see Figure 4.52 for a schematic illustration or see Figure 4.34 for an experimental evidence), the reason why the oxidation kinetics  $K$  in Table 4.9 and Table 4.10 is higher for DS-L and DS-T specimens.

By using Eq. 4.10, Eq. 4.11 and Eq. 4.14, in addition to the parameters identified in Table 4.9, it is possible to plot creep curves obtained at 900°C/350 MPa for DS-L specimens (Figure 4.53) and DS-T specimens (Figure 4.54) having different thicknesses, and to compare it with the experimental creep curves. These curves have been plotted using an explicit integration scheme for both Eq. 4.10 and Eq. 4.14. It can be observed in these two figures that the thickness debit in creep life is taken into account for both types of specimens. Moreover, the decrease in strain at failure when decreasing the specimen's thickness is also captured qualitatively. To get a better overview on the model overall performances, Figure 4.55 presents the predicted minimum strain rate as a function of the experimental one (Figure 4.55(a)) and the predicted creep life as a function of the experimental one (Figure 4.55(b)) using all the experimental database generated at 900°C (i.e. massive and thin walled specimens, radiant and resistive furnace results, <001>-SX, DS-L, CG DS-T, FG DS-T and DS-45° specimens). It is observed for both plots good performances of the model we have developed since almost all results fall into a factor 2 scatter band extending on each side of the perfect modeling represented by a solid line (i.e. the bisectrix) in Figure 4.55(a) and (b). Even experimental results obtained for fine grains DS-T and for DS-45° specimens which were not used for the identification of the model are well reproduced.

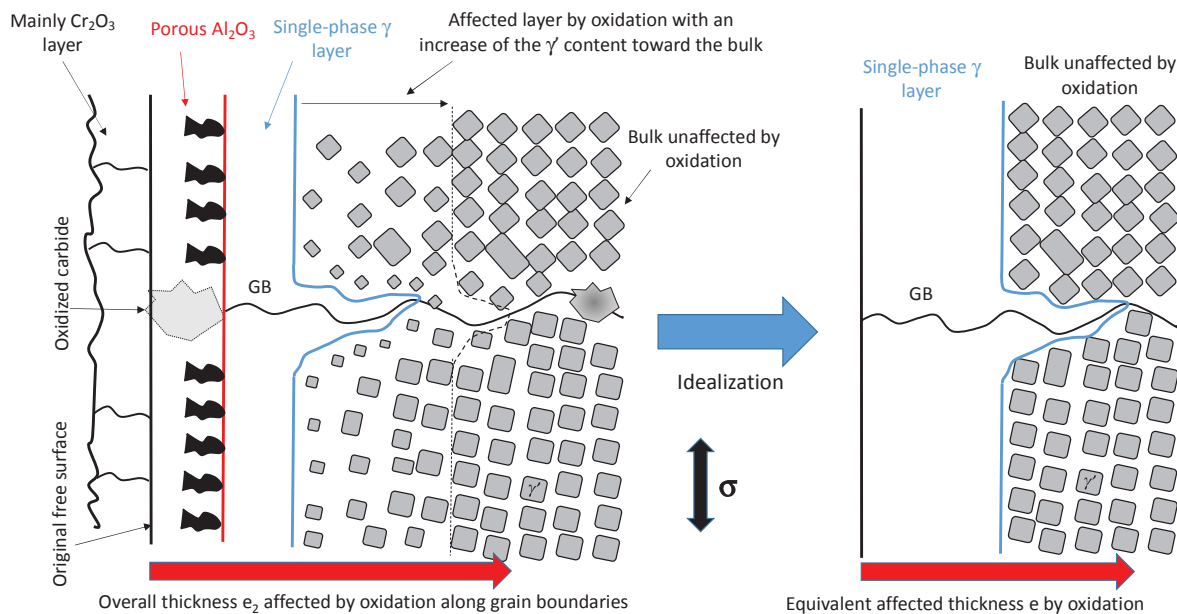


Figure 4.52 – Schematic illustration of the loss of load bearing section along longitudinal section for DS-T specimens. Note that “GB” accounts for a grain boundary.

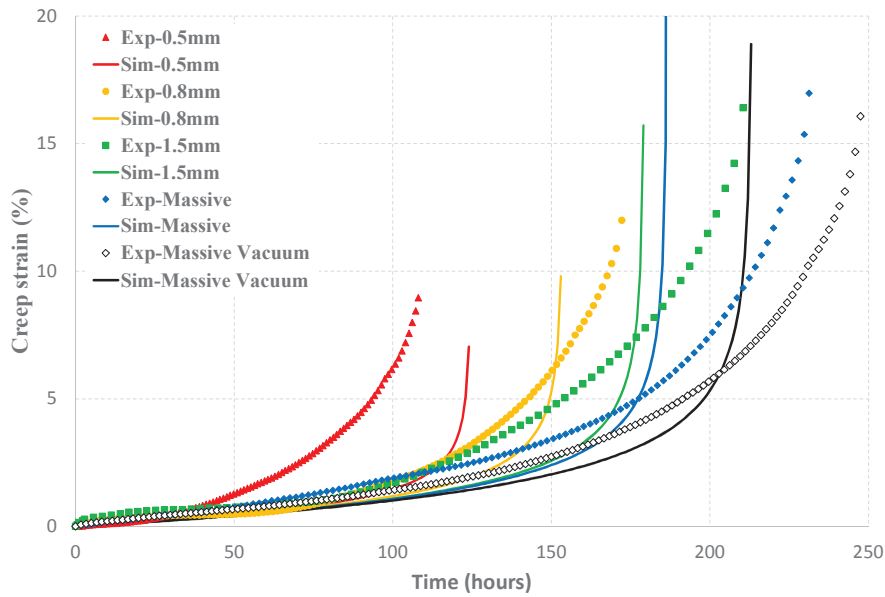


Figure 4.53 – Comparison of experimental and simulated creep curves at 900°C/350 MPa for DS-L specimens.

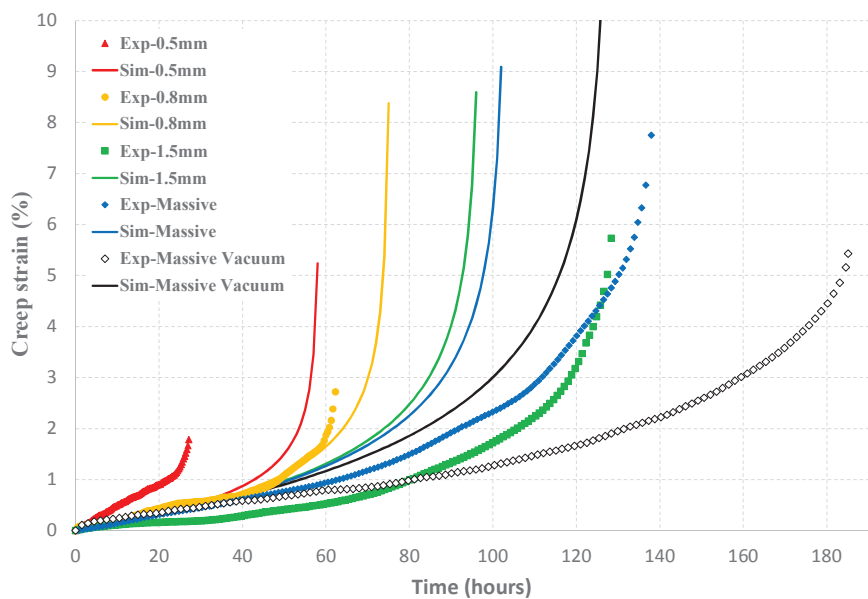


Figure 4.54 – Comparison of experimental and simulated creep curves at 900°C/350 MPa for DS-T specimens.

Even if good overall performances of our model are obtained, paying a more careful attention to Figure 4.55(a), one can observe that more points are lying outside of the factor 2 scatter band compared to Figure 4.55(b). It means that the model's performances are better in terms of creep life compared to minimum strain rate modeling. This was already observed in both Figure 4.53 and Figure 4.54 (see, e.g. the difference in creep rate for the ~ 0.5 mm thick specimen in Figure 4.54). These worse strain rate modeling in terms of strain rate may originate from difficulties in the experimental determination of this quantity since no clear stage II of creep is reached in these conditions (see Fig. 3.8(b)). Moreover, the simulated minimum strain rate is systematically the initial one in the simulations given the flow rule we used, while, during experiments, a primary creep stage

is almost always observed (see Fig. 3.8(b)), what cannot be reproduced with a simple Norton's law as the one used here.

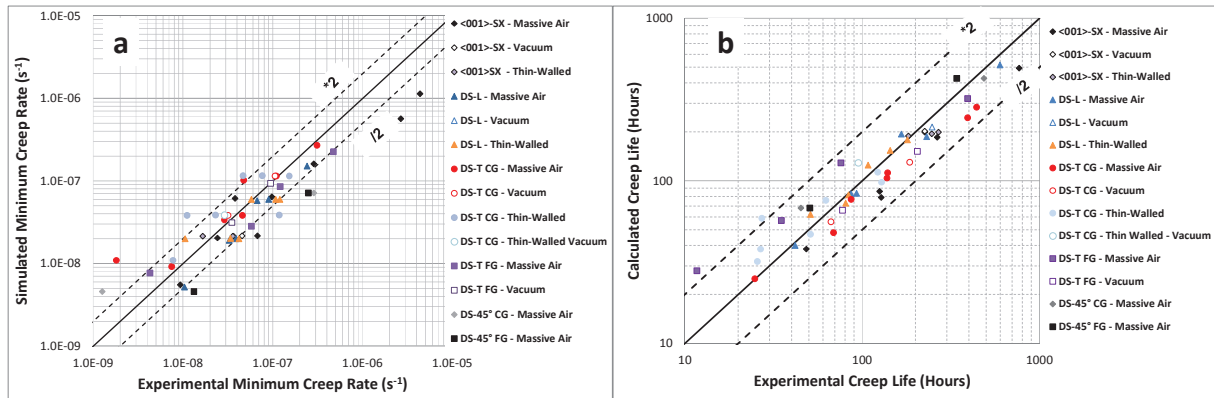


Figure 4.55 – Creep-oxidation-damage model performances in terms of minimum creep rate (a) and creep life (b).

From Figure 4.53 and Figure 4.54, a steeper tertiary creep stage is observed in the simulated curves compared to the experimental ones. One possibility for such a defect is that in our modeling approach, the thin-wall debit in creep properties has been taken into account through the only contribution of oxidation. However, as observed and discussed in sub-section 4.3.4.2, the thickness debit in creep strength does not only result from the contribution of oxidation for DS200+Hf/<001>-SX MAR-M200+Hf alloys as already proposed by Baldan [29]. A possible contribution of carbides to the thickness debit in creep properties is suspected (see analyzes of thin-walled creep results), what has not been taken into account here. Hence, by adjusting the values of the oxidation kinetics K parameters to reproduce experimental results, the contribution of oxidation to the overall damage has been increased probably above its actual one. Indeed, even if the thickening of the affected layer by oxidation is greater along grain boundaries (as shown schematically in Figure 4.52), we feel that having K values of  $\sim 2 \mu\text{m/h}$  and  $\sim 5 \mu\text{m/h}$  for DS-L and DS-T specimens respectively (see Table 4.9) is very high.

Finally, even if FG DS-T and DS-45° creep properties were not used for the identification of the model parameters, one can observe that the model provides good predictions of their creep lives. However, most of the minimum strain rate results for these specimens are lying outside of the factor 2 scatter band around perfect modeling (see Figure 4.55(a)). Experimental minimum strain rates for these specimens are indeed two to three times smaller than the model prevision.

If this simple and original modeling approach is really encouraging, we feel that a more refined one would be required to capture in an even better way all our results. Introducing internal variables in the flow rule, accounting for, e.g., microstructure degradation (the  $\gamma$  rafting and its kinetics as a function of the orientation [50]) and having a more refined description of the damage development could be a solution for this.

#### 4.5.3 Dwell-fatigue interactions modeling at 900°C

Dwell-fatigue interactions have been modeled using a post-processing tool of the ZéBuLoN Z-Set module [51]. For this, one dwell-fatigue cycle has been simulated using a representative volume element (an RVE, i.e. a cube with a homogeneous tension stress state) changing the maximum applied stress  $\sigma_{\text{max}}$  and dwell time  $\Delta t$  at  $\sigma_{\text{max}}$  to cover the investigated experimental conditions. After this, the resulting stress states and loading path have been extracted from the RVE to compute creep and fatigue damage evolutions and then, the number of cycles up to failure  $N_r$  in dwell-fatigue.

The number of cycles  $N_c$  and  $N_f$  leading to failure in pure creep and pure fatigue respectively are defined according to Eq. 4.15 and Eq. 4.16:

$$N_c = \frac{1}{k+1} \left( \int_{cycle} \left( \frac{|\sigma|}{A} \right)^r dt \right)^{-1} \quad Eq. 4.15$$

$$N_f = \frac{1}{a(\beta+1)} \left\langle \frac{1-\sigma_{max}}{\sigma_{max}-\sigma_l} \right\rangle \left( \frac{\frac{\Delta\sigma}{2}}{\frac{B_0}{\sigma_u}} \right)^{-\beta} \quad Eq. 4.16$$

It is recognized in Eq. 4.15 a Rabotnov-Kachanov type law (see Eq. 4.7) while a ONERA-type law (see Eq. 4.2 and Eq. 4.3) is recognized in Eq. 4.16. The variables and parameters in these equations have then been already defined previously.

Two types of creep and fatigue accumulations rules have been used to calculate the number of cycles to failure  $N_r$ . A linear accumulation, as defined in Eq. 4.17 has been used:

$$\frac{N_r}{N_c} + \frac{N_r}{N_f} = 1 \quad Eq. 4.17$$

Moreover, a non-linear creep-fatigue accumulation (defined as NLC-ONERA in the ZéBuLoN code) has been used. It considers that the total damage  $D$  in creep-fatigue interaction affects both the pure creep and pure fatigue damages ( $D_c$  and  $D_f$  respectively) according to Eq. 4.18 and Eq. 4.19:

$$\frac{1}{N_c} = (1 - D_c)^{k+1} - (1 - D)^{k+1} \quad Eq. 4.18$$

$$\frac{1}{N_f} = \left[ 1 - (1 - D_f)^{\beta+1} \right]^{1-\alpha} - \left[ 1 - (1 - D)^{\beta+1} \right]^{1-\alpha} \quad Eq. 4.19$$

The evolution of damage from  $D_c$  to  $D_f$  is then calculated in each cycle. To increase the dwell-fatigue interaction, the  $\alpha$  parameter in Eq. 4.19 has the following evolution, with  $\sigma_l$  being the fatigue limit, already defined in Eq. 4.4:

$$\alpha = 1 - a * \left( \frac{\frac{\Delta\sigma}{2} - \sigma_l}{\sigma_u - \sigma_{max}} \right) \quad Eq. 4.20$$

The dwell-fatigue life using such an accumulation rule generally leads to Eq. 4.21 and the dwell-fatigue interactions using a linear or a non-linear accumulation rule are schematically compared in Figure 4.56:

$$\frac{N_r}{N_c} + \frac{N_r}{N_f} < 1 \quad Eq. 4.21$$

An identification of creep and fatigue damage parameters in Eq. 4.15, Eq. 4.16, Eq. 4.18 and Eq. 4.19 are provided in Table 4.11 and Table 4.12 for the linear and non-linear accumulation rules, respectively. These parameters have been identified after several iterations so as to achieve the best compromise in dwell-fatigue life modeling for both LCF results when fatigue damage dominates and for high dwell times ( $\Delta t=300s$ ) when creep damage dominates.

Figure 4.57 and Figure 4.58 present S-N diagrams comparing experimental and numerical results obtained with linear and non-linear damage accumulation approaches, respectively. With the linear

accumulation approach (see Figure 4.57), it is observed that pure fatigue results are not well modeled, especially for SX and DS-L specimens. Dwell-fatigue results with  $\Delta t=300s$  are however well reproduced and the evolution in dwell-fatigue life when changing the dwell time is also well captured by the model. When using a non-linear accumulation rule (see Figure 4.58), both pure fatigue and dwell-fatigue results with a large  $\Delta t$  are modeled satisfactorily. However, dwell-fatigue curves for  $\Delta t=10s$  and  $\Delta t=1s$  are not reproduced correctly by this non-linear accumulation approach. Indeed, the model underestimates actual dwell-fatigue lives.

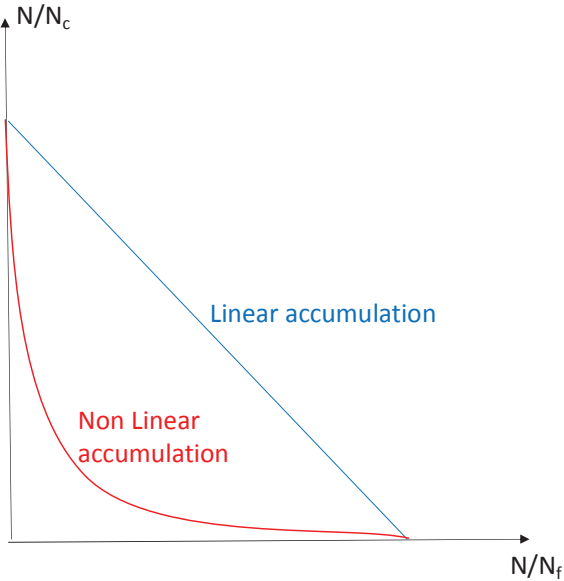


Figure 4.56 – Schematic illustration of linear and non-linear accumulation of creep and fatigue damages, with  $N_c$  the number of cycles up to failure in creep and  $N_f$  the number of cycles up to failure in fatigue.



	DS-L	<001>-SX	DS-T
LCF			
M	4000	2000	2500
$\beta$	3.4	3.4	3.4
$\sigma_l$	200	200	150
$\sigma_u$	911	911	860
b	0.00122	0.00122	0.00122
a	0.006	0.006	0.006
Creep			
A	6000	6000	5000
k=r	5.67	5.67	5.67

Table 4.11 – Calibration parameters for linear accumulation approach.

	DS-L	<001>-SX	DS-T
LCF			
M	4000	3000	1600
$\beta$	3.4	3.4	3.4
$\sigma_l$	200	200	150
$\sigma_u$	911	960	860
$b_1$	0.00122	0.00122	0.00122
a	0.006	0.006	0.006
Creep			
A	6000	6800	8000
k=r	5.67	5.67	5.67

Table 4.12 – Calibration parameters for non-linear accumulation approach.

As a summary, dwell-fatigue life of DS200+Hf and <001>-SX MAR-M200+Hf is better reproduced by a linear damage accumulation rule. This means that fatigue and creep damages are developing independently at each other. This can be understood since, according to experimental observations provided earlier in this chapter, fatigue damage is mainly dominated by single carbide cracking and first stages of crack propagation while creep damage is dominated by carbides debonding and local recrystallization due to creep elongation.

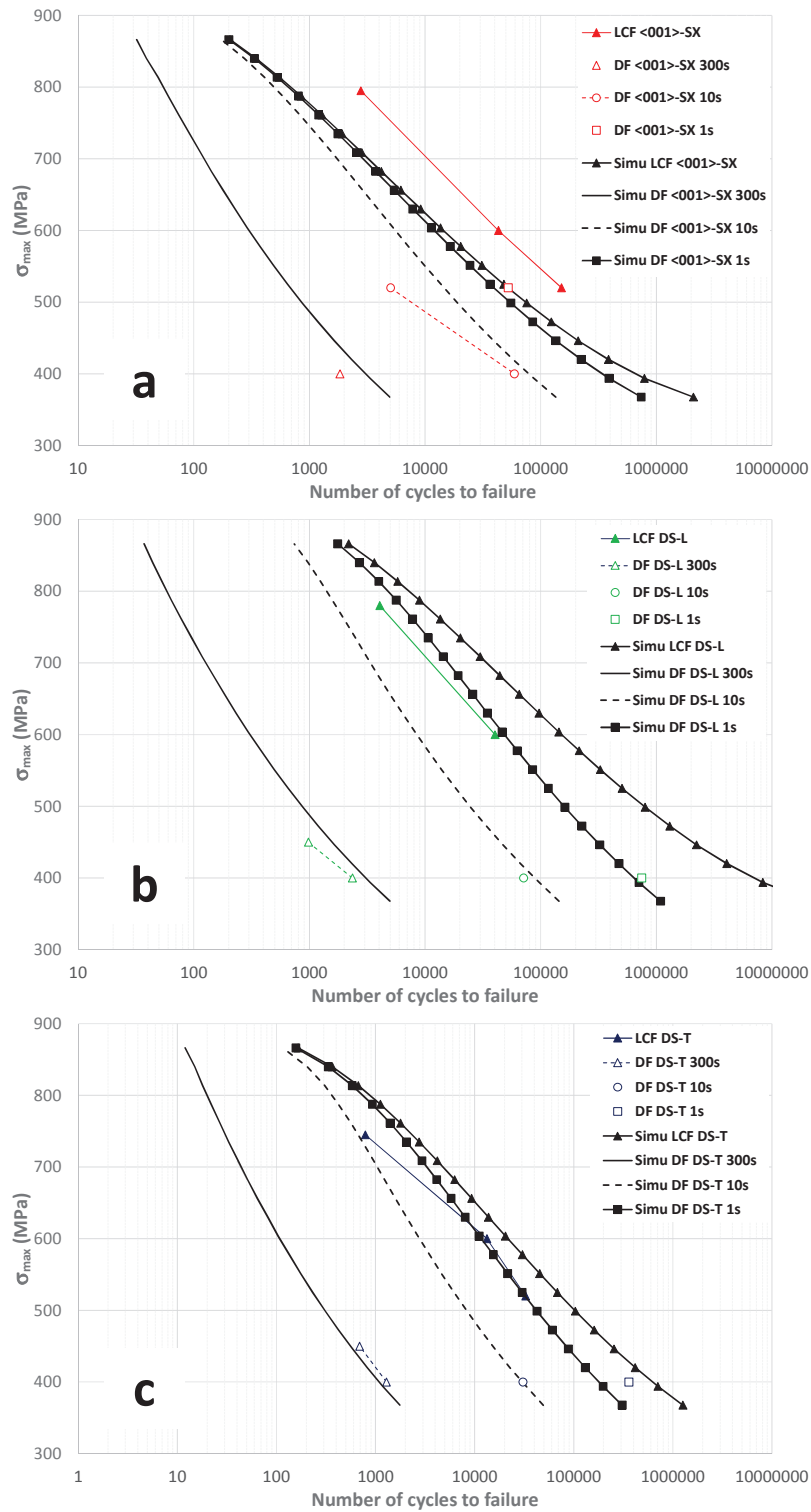


Figure 4.57 – Creep-fatigue model performances at 900°C using a linear accumulation approach for <001>-SX (a), DS-L (b) and DS-T (c).

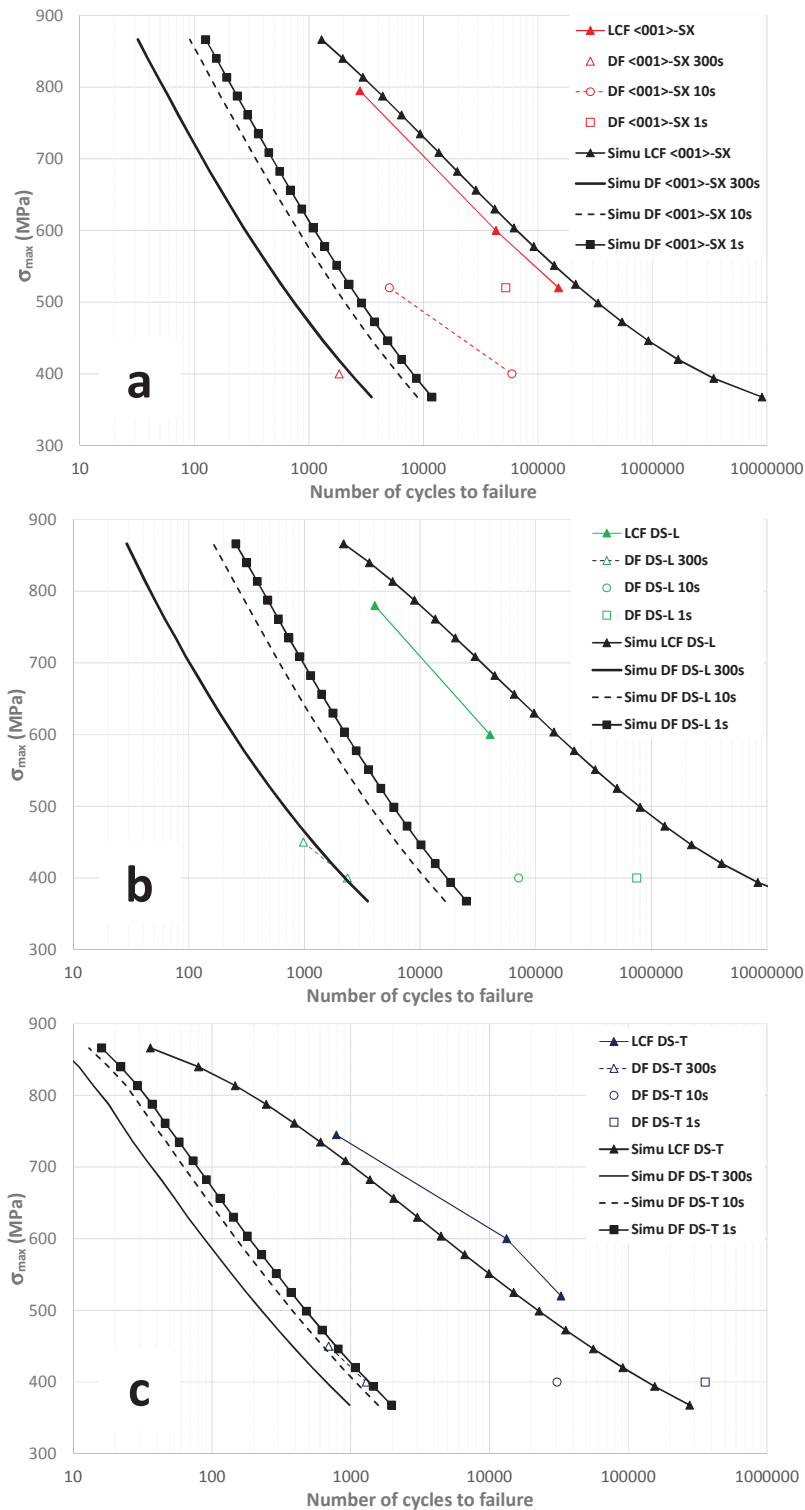


Figure 4.58 – Creep-fatigue model performances at 900°C using a non-linear accumulation approach for <001>-SX (a), DS-L (b) and DS-T (c).

Greater interplays between both types of damage would have been expected from our experimental observations, this does not seem to be the case. One would have especially expected greater difficulties in modeling the effect of the dwell time, since it was shown in chapter 3 (see Section 3.5) to affect the development of  $\gamma'$  rafting. A microstructure-sensitive modeling approach using an adapted flow rule enriched with internal variables [50, 52, 53] would be necessary to capture both

microstructure evolutions, and their effect on the total dwell-fatigue life. This work remains to be done.

#### 4.6 Conclusions

In this chapter, in which most of the original results of this study are gathered, the damage mechanisms in creep, low cycle fatigue and dwell fatigue have been investigated, paying a special attention to the role of inclusions (i.e. carbides), pores and oxidation. Different models have been proposed/identified to account for both LCF and dwell-fatigue life and also, for the effect of oxidation on the creep behavior and life. The following main conclusions can be established:

- Carbides and cluster of carbides control the LCF life at low temperature, whatever the specimen's type. Internal crack initiation has almost always been observed at such particles during LCF at 650°C/f=0.5Hz/R<sub>σ</sub>=-1 or R<sub>σ</sub>=0.05.
- The oxidation of carbides has been shown to control LCF strength in air at 900°C while internal crack initiation at pores has been observed in high vacuum. Several carbides, especially Hf-rich ones, may indeed already been cracked before LCF loading due to their own oxidation and due to the mismatch in thermal expansion between carbides and their neighboring γ-γ' "matrix".
- LCF lives at 900°C in air and in high vacuum are almost the same. It results from very different damage mechanisms. In high vacuum, the LCF life is mainly crack initiation controlled while it is mainly crack propagation controlled in air.
- LCF crack propagation at 650°C and 900°C is highly environment sensitive. Oxidation has been shown to induce crack closure, by inducing crack tip blunting and by increasing the roughness along the crack path. Oxidation is hence beneficial to the crack propagation resistance of DS200+Hf, especially by increasing the crack propagation threshold.
- Creep life is highly anisotropic due to a change in fracture mode from transgranular along longitudinal direction to intergranular along transverse direction of DS200+Hf.
- Strain assisted damage development around carbides has been observed in creep under the form of carbide cracking, cracking at carbide/ γ-γ' interface and local recrystallization around carbides.
- Oxidation controls the creep strength along transverse direction of DS200+Hf specimens at 900°C. Indeed, since intergranular cracks are developing at creep strain as low as 0.8%, further grain boundary crack propagation is assisted by oxidation. The grain size effect on creep properties at 900°C in air along transverse direction totally disappears in high vacuum.
- Thin-wall debit in creep properties has been observed at 900°C for DS-L and DS-T specimens. A decrease in creep life compared to massive specimens up to a factor 2 and up to a factor 5 is obtained when decreasing specimen's thickness to ~0.5 mm for DS-L and DS-T specimens, respectively. The thickness debit in creep properties for SX specimens is only measurable for ~0.5 mm thick specimen, with a decrease in creep life of nearly 20% compared to the massive specimen.
- The thickness debit in creep properties does not only result from oxidation according to experiments performed either using a prior oxidation or performed in high vacuum using a thin-walled specimen.
- <001>/<101> and <001>/<102> grain boundaries are the most critical from a crack initiation point of view during transverse creep testing at 750°C and high applied stresses. It results from large

differences in creep behavior, in elasticity and in lattice rotation across the grain boundary for such crystallographic configurations.

- A change in fatigue-dominated to creep-dominated fracture mode is observed in dwell-fatigue by increasing the dwell time  $\Delta t$  at maximum load. The transition in fracture mode is observed for  $\Delta t=10s$ . As a surprising result, internal crack initiation is observed at low  $\Delta t$ , but was not observed in pure LCF. It is suspected large differences in dwell-fatigue crack growth rates from internal defects or from the surface explain such a result.

- Two phenomenological models have been identified to account for pure LCF results at 650°C and LCF/Dwell-fatigue results at 900°C. A linear accumulation of creep and fatigue damages in dwell-fatigue provides better results.

- A coupled creep-oxidation-damage model has been developed to account for both minimum creep rates and creep lives at 900°C. As a main originality of this model, the anisotropy in creep properties has been taken into account using a simple normalization by the ultimate tensile stress in both the Norton's flow rule and in the Kachanov damage law. This model provides good results in terms of minimum strain rate and creep life, despite the fact that it only considers oxidation as contributing to the thickness effect in creep properties.

## References of Chapter 4

1. R. Chieragatti and L. Rémy, *Influence of orientation on the low cycle fatigue of MAR-M 200 single crystals at 650°C. I: Fatigue life behaviour*. Materials Science and Engineering: A, 1991. **141**(1): p. 1-9.
2. M. Gell and G. Leverant, *The fatigue of the nickel-base superalloy, Mar-M 200, in single-crystal and columnar-grained forms at room temperature (Ni based superalloy cyclic deformation and fracture and high and low cycle fatigue at room temperature, comparing single crystal and columnar grained forms)*. AIME, Transactions, 1968. **242**: p. 1869-1879.
3. G. Leverant and M. Gell, *The elevated temperature fatigue of a Nickel-base superalloy, MAR-M 200, in conventionally cast and directionally solidified forms*. Trans. Met. Soc. AIME, 1969. **245**(6): p. 1167-1173.
4. G. Leverant and M. Gell, *The influence of temperature and cyclic frequency on the fatigue fracture of cube oriented nickel-base superalloy single crystals*. Metallurgical Transactions A, 1975. **6**(2): p. 367-371.
5. J.C. Stinville, K. Gallup, and T.M. Pollock, *Transverse Creep of Nickel-Base Superalloy Bicrystals*. Metallurgical and Materials Transactions A, 2015. **46A**: p. 2516-2529.
6. M. Lamm and R.F. Singer, *The Effect of Casting Conditions on the High-Cycle Fatigue Properties of the Single-Crystal Nickel-Base Superalloy PWA 1483*. Met. Mat. Trans., 2007. **38A**: p. 1177-1183.
7. S. Steuer, P. Villechaise, T. Pollock, and J. Cormier, *Benefits of high gradient solidification for creep and low cycle fatigue of AM1 single crystal superalloy*. Materials Science and Engineering: A, 2015. **645**: p. 109-115.
8. A. Cervellon, J. Cormier, F. Mauget, and Z. Hervier, *VHCF life evolution after microstructure degradation of a Ni-based single crystal superalloy*. International journal of Fatigue, 2017. **104**: p. 251-262.
9. D.N. Duhl and C.P. Sullivan, *Some effects of hafnium additions on the mechanical properties of a columnar-grained nickel-base superalloy*. Journal of Metals, 1971. **23**(7): p. 38-40.
10. Q. Li, S. Tian, H. Yu, N. Tian, Y. Su, and Y. Li, *Effects of carbides and its evolution on creep properties of a directionally solidified nickel-based superalloy*. Materials Science and Engineering A, 2015. **633**: p. 20-27.
11. L. Rettberg and T. Pollock, *Localized recrystallization during creep in nickel-based superalloys GTD444 and René N5*. Acta Materialia, 2014. **73**: p. 287-297.
12. J. Ohe and S. Wakita. *Practical method of thermal history analysis by  $\gamma'$  morphology changes in nickel-base superalloy*. in *Superalloys 1988*. 1988. Seven Springs, PA, USA: TMS. p. 93-102.
13. P. Caron, Y. Ohta, Y.G. Nakagawa, and T. Khan. *Creep deformation anisotropy in single crystal superalloys*. in *Superalloys 1988*. 1988. Seven Springs, Champion, PA, USA: TMS. p. 215-224.
14. R.A. Mackay and R.D. Maier, *The Influence of Orientation on the Stress Rupture Properties of Nickel-Base Superalloy Single Crystals*. Metallurgical and Materials Transactions A, 1982. **13A**: p. 1747-1754.
15. V. Sass, U. Glatzel, and M. Feller-Kniepmeier, *Anisotropic creep properties of the nickel-base superalloy CMSX-4*. Acta materialia, 1996. **44**(5): p. 1967-1977.
16. E. Aghion, M. Bamberger, and A. Berkovits, *High-temperature low-cycle fatigue of a nickel-based MAR-M200+ Hf alloy in AR and AR+ 20% O<sub>2</sub> environment*. Journal of materials science, 1991. **26**(7): p. 1873-1881.
17. F. Alexandre, *Aspects probabilistes et microstructuraux de l'amorçage des fissures de fatigue dans l'alliage Inco 718*, PhD thesis, in *Centre des Matériaux*. 2004, ENSMP: Paris.
18. P. Kontis, D.M. Collins, S. Johansson, A.J. Wilkinson, J.J. Moverare, and R.C. Reed. *Crack Initiation and Propagation During Thermal-Mechanical Fatigue of IN792: Effects of Dwell Time*. in *Superalloys 2016: Proceedings of the 13th International Symposium of Superalloys*. 2016. Seven Springs, PA, USA: Wiley Online Library. p. 763-772.

19. E. Fleury and L. Rémy, *Low cycle fatigue damage in nickel-base superalloy single crystals at elevated temperature*. Materials Science and Engineering A, 1993. **617**: p. 23-30.
20. M. Bensch, E. Fleischmann, C.H. Konrad, M. Fried, C.M. Rae, and U. Glatzel, *Secondary creep of thin-walled specimens affected by oxidation*. Superalloys 2012, 2012: p. 387-94.
21. M. Bensch, C.H. Konrad, E. Fleischmann, C.M.F. Rae, and U. Glatzel, *Influence of oxidation on near-surface  $\gamma'$  fraction and resulting creep behaviour of single crystal Ni-base superalloy M247LC SX*. Materials Science and Engineering: A, 2013. **577**: p. 179-188.
22. M. Brunner, M. Bensch, R. Völkl, E. Affeldt, and U. Glatzel, *Thickness influence on creep properties for Ni-based superalloy M247LC SX*. Materials Science and Engineering: A, 2012. **550**: p. 254-262.
23. V. Seetharaman and A. Cetel. *Thickness debit in creep properties of PWA 1484*. in *Superalloys 2004*. 2004. Seven Springs, PA, USA: TMS. p. 207-214.
24. A. Srivastava, S. Gopagoni, A. Needleman, V. Seetharaman, A. Staroselsky, and R. Banerjee, *Effect of specimen thickness on the creep response of a Ni-based single-crystal superalloy*. Acta Materialia, 2012. **60**(16): p. 5697-5711.
25. J.-B. le Graverend, J. Cormier, S. Kruch, F. Gallerneau, and J. Mendez, *Microstructural parameters controlling high temperature creep life of the nickel base single crystal superalloy MC2*. Metallurgical and Materials Transactions A, 2012. **43A**: p. 3988-3997.
26. P. Caron and T. Khan, *Improvement of creep strength in a nickel-base single crystal superalloy by heat treatment*. Materials Science and Engineering, 1983. **61**: p. 173-194.
27. Z. Shi, J. Li, and S. Liu, *Effect of long term aging on microstructure and stress rupture properties of a nickel based single crystal superalloy*. Progress in Natural Science: Materials International, 2012. **22**(5): p. 426-432.
28. S. Steuer, Z. Hervier, S. Thabart, C. Castaing, T. Pollock, and J. Cormier, *Creep behavior under isothermal and non-isothermal conditions of AM3 single crystal superalloy for different solutioning cooling rates*. Materials Science and Engineering: A, 2014. **601**: p. 145-152.
29. A. Baldan, *On the thin-section size dependent creep strength of a single crystal nickel-base superalloy*. Journal of Materials Science, 1995. **30**: p. 6288-6298.
30. R.A. MacKay, R.L. Dreshfield, and R.D. Maier. *Anisotropy of nickel-base superalloy single crystals*. in *Superalloys 1980*. 1980. Seven Springs, Champion, PA, USA: TMS, Warrendale, PA. p. 385-394.
31. C.M.F. Rae and R.C. Reed, *Primary creep in single crystal superalloys: origins, mechanisms and effects*. Acta Materialia, 2007. **55**(3): p. 1067-1081.
32. M. Ardakani, R. Ghosh, V. Brien, B. Shollock, and M. McLean, *Implications of dislocation micromechanisms for changes in orientation and shape of single crystal superalloys*. Scripta materialia, 1998. **39**(4): p. 465-472.
33. M. Ardakani, M. McLean, and B. Shollock, *Twin formation during creep in single crystals of nickel-based superalloys*. Acta materialia, 1999. **47**(9): p. 2593-2602.
34. D. Barba, E. Alabort, S. Pedrazzini, D. Collins, A. Wilkinson, P. Bagot, M. Moody, C. Atkinson, A. Jérusalem, and R. Reed, *On the microtwinning mechanism in a single crystal superalloy*. Acta Materialia, 2017.
35. A. Staroselsky and B. Cassenti, *Combined rate-independent plasticity and creep model for single crystal*. Mechanics of Materials, 2010. **42**: p. 945-959.
36. D. Kobayashi, M. Miyabe, M. Achiwa, R. Sugiura, and A. Yokobori, *Creep-fatigue crack growth behaviour based on EBSD observations for notched specimen made of directionally solidified Ni-base superalloy*. Materials at High Temperatures, 2014. **31**(4): p. 326-333.
37. J. Lemaitre, J.-L. Chaboche, A. Benallal, and R. Desmorat, *Mécanique des matériaux solides-3eme édition*. 2009: Dunod.
38. L. Kachanov, *Foundations of the theory of plasticity*. North-Holland series in applied mathematics and mechanics (Vol. 12). 1971.
39. F.H. Norton, *The creep of steel at high temperatures*. 1929: McGraw-Hill Book Company, Incorporated.

40. Y.N. Rabotnov, *Creep rupture*, in *Applied mechanics*. 1969, Springer. p. 342-349.
41. J. Huang, D. Shi, and X. Yang, *A modern and robust methodology for modeling anisotropic creep characteristics of Ni-based DS and SC superalloys*. Science China Technological Sciences, 2014. **57**(9): p. 1802-1815.
42. B. Wilshire and P. Scharning, *A new methodology for analysis of creep and creep fracture data for 9–12% chromium steels*. International materials reviews, 2008. **53**(2): p. 91-104.
43. B. Wilshire, P. Scharning, and R. Hurst, *New methodology for long term creep data generation for power plant components*. Energy Materials, 2007. **2**(2): p. 84-88.
44. S. Dryepondt, D. Monceau, F. Crabos, and E. Andrieu, *Static and dynamic aspects of coupling between creep behavior and oxidation on MC2 single crystal superalloy at 1150 C*. Acta materialia, 2005. **53**(15): p. 4199-4209.
45. A. Srivastava and A. Needleman, *Phenomenological modeling of the effect of specimen thickness on the creep response of Ni-based superalloy single crystals*. Acta Materialia, 2013. **61**(17): p. 6506-6516.
46. J. Cormier, *Comportement en fluage anisotherme à haute et très haute température du superalliage monocristallin MC2*, PhD thesis, in *LMPM / ENSMA*. 2006, University of Poitiers: Poitiers.
47. S. Dryepondt, *Comportement et endommagement en fluage à haute température de parois minces en superalliage monocristallin MC2 : effets de l'oxydation et de l'application d'un revêtement MCrAlY*, PhD Thesis, in *ENSIACET / CIRIMAT*. 2004, Institut National Polytechnique: Toulouse - France.
48. M. Bensch, J. Preußner, R. Hüttner, G. Obigodi, S. Virtanen, J. Gabel, and U. Glatzel, *Modelling and analysis of the oxidation influence on creep behaviour of thin-walled structures of the single-crystal nickel-base superalloy René N5 at 980 C*. Acta Materialia, 2010. **58**(5): p. 1607-1617.
49. M. Bensch, A. Sato, N. Warnken, E. Affeldt, R. Reed, and U. Glatzel, *Modelling of high temperature oxidation of alumina-forming single-crystal nickel-base superalloys*. Acta Materialia, 2012. **60**(15): p. 5468-5480.
50. R. Desmorat, A. Mattiello, and J. Cormier, *A tensorial thermodynamic framework to account for the  $\gamma$  rafting in Nickel-based single crystal superalloys*. International Journal of Plasticity, 2017. **95**: p. 43-81.
51. J. Besson, R. Leriche, R. Foerch, and G. Cailletaud, *Object-oriented programming applied to the finite element method part II. application to material behaviors*. Revue européenne des éléments finis, 1998. **7**(5): p. 567-588.
52. J. Cormier and G. Cailletaud, *Constitutive modeling of the creep behavior of single crystal superalloys under non-isothermal conditions inducing phase transformations*. Materials Science and Engineering A, 2010. **527**(23): p. 6300-6312.
53. J.-B. le Graverend, J. Cormier, F. Gallerneau, P. Villechaise, S. Kruch, and J. Mendez, *A microstructure-sensitive constitutive modeling of the inelastic behavior of single crystal nickel based superalloys at very high temperature*. International Journal of Plasticity, 2014. **59**: p. 55-83.



General conclusion and future  
prospects

## General conclusion and future prospects

The damage mechanisms and durability of DS200+Hf alloy at high temperature has been the main focus of this study. This alloy is indeed used for the design of different types of airfoils in aero-engines and, despite being an “old” alloy developed close to 40 years ago, it is still used for the design of blades in the newest gas turbines thanks to its good castability. Mechanical and microstructure characterizations have been performed in this work having in mind the following main questions:

- How does oxidation controls the crack initiation and subsequent crack propagation mechanisms?
- How does the crystallography (i.e. loading direction with respect to the solidification direction, local grain configuration in the vicinity of grain boundaries ...) controls the mechanical behavior and durability of the alloy?
- How does bulk microstructure evolution (e.g.  $\gamma'$  rafting) affect the mechanical behavior of the alloy?
- How does the microstructural defects (carbides) affect damage mechanisms?

To answer these questions, the anisotropy in mechanical properties (tensile, creep, low cycle fatigue and dwell-fatigue properties) and durability of DS200+Hf alloy was studied, mainly at 650°C and 900°C, with additional creep characterization at 750°C and 1100°C. The mechanical behavior of the alloy along different orientations with respect to the solidification direction was compared to the mechanical behavior of single crystalline (SX) specimens oriented mainly along the [001] crystallographic direction, but also along other orientations. It is recalled that SX specimen had exactly the same chemistry as the one of the directionally solidified (DS) version of the alloy.

The tensile behavior is highly anisotropic at 650°C for both DS specimens and SX ones, especially considering yield stress and ultimate tensile stress. This mainly results from the number of slip systems activated. At 900°C, the anisotropy in tensile behavior is greatly reduced compared to 650°C but the alloy exhibits a pronounced strain rate sensitivity: for lower strain rate, when creep-induced microstructure degradation (i.e.  $\gamma'$  coarsening and rafting) is present, ultimate tensile strength and yield stress both drop in a spectacular way. A very low tensile ductility has been observed along transverse direction of DS specimens at 900°C due to an intergranular crack initiation mode.

The anisotropy in creep behavior and life is observed to decrease when increasing the testing temperature for both DS and SX specimens. This is correlated to the  $\gamma'$  coarsening/rafting which is already observed after short (duration < 40h) creep tests at 900°C and which leads to a more homogeneous creep deformation across the grains. The anisotropy in creep properties at lower temperatures (i.e. 750°C) results mainly from the crystallography at the grain scale and the ability to develop single slip or multiple slip activity. Indeed, as observed using SX and DS specimens equipped with strain markers at the grain scale, grains favorably oriented for single slip show very high creep rates at low temperature/high applied stress. A part of the creep life anisotropy results from the very low creep ductility along transverse direction of DS specimens (typically below 5%), due to an intergranular fracture mode. Such a low ductility results in lower creep properties/lives along transverse direction, whatever the creep condition, the debit in creep life being even greater at decreasing grain size. A premature failure within the primary creep stage at low temperature/high applied stress has even been observed along transverse direction of DS specimens. This lower creep ductility originates from carbides concentrated at grain boundaries. They act as crack initiation sites (especially under oxidizing conditions) and favor subsequent propagation along grain boundaries.

Creep strain evolution at the grain scale has been characterized at 750°C and 900°C during transverse creep testing of DS specimens to identify the weakest grain boundaries from a crack initiation point of view. These characterizations have been performed using either strain markers or digital image correlation at high temperature. Contrary to creep tests at 900°C, a huge heterogeneity in creep elongation at the grain scale at 750°C was observed. According to these experiments at 750°C, cracks preferentially developed at grain boundaries separating two grains developing a large contrast in creep strain, i.e. grain boundaries separating one grain favorably oriented for multiple slip and one grain favorably oriented for single slip and/or lattice rotation. In most of the cases, cracks initiated at  $\langle 100 \rangle / \langle 110 \rangle$  or  $\langle 100 \rangle / \langle 120 \rangle$  grain boundaries. These crystallographic configurations are particularly detrimental to the creep life for a coarse grain alloy. At 900°C, grain boundary crack initiation is more random and mainly controlled by oxidation of grain boundary carbides.

The effect of oxidation in creep has been investigated in a deeper way at 900°C by performing thin-wall creep tests using both DS and SX specimens. A progressive decrease of the creep life is obtained by decreasing the specimens' thickness, whatever the loading direction and specimen type. This is accompanied by a decrease of the creep ductility. This thin-wall creep life debit is more pronounced along transverse direction (up to a factor of 5 for transverse loading compared to a factor of  $\sim 2$  for longitudinal loading at 900°C/350 MPa), as expected considering grain boundaries oxidation. The creep life debit is greater decreasing the applied stress because of longer tests and hence, greater oxidation activity. Almost no creep life debit is observed for SX specimens, hence highlighting the key role of oxidation at grain boundaries in the thin-wall debit.

Using all the creep database generated in this work, including thin-wall creep tests and creep tests performed in high vacuum, a unified Norton-Kachanov coupled approach has been developed, taking in account oxidation damage. As a main originality of this work, the anisotropy in creep behavior and creep life has been taken into account by normalizing the initial applied stress by the ultimate tensile stress in both Norton and Kachanov laws. This led to a unique set of Norton and Kachanov laws parameters for all kind of specimens and loading direction. Oxidation is taken into account in this model assuming a parabolic oxide scale growth based on TGA experiments and a sub-surface loss of the load bearing capacity of the alloy, due to the localized  $\gamma'$  dissolution (i.e.  $\gamma'$  depleted layer below the surface). This model has been shown to predict experimental creep lives and minimum creep rates with a good precision (within a factor 2 scatter band) for all orientations/specimens, and even for experimental results not used for its identification (i.e. DS specimens oriented at 45° of the solidification direction and fine grain DS specimens loaded along transverse direction).

$\langle 001 \rangle$  SX specimens have been shown to perform better than DS specimens along longitudinal direction and far better than DS specimens along transverse direction in low cycle fatigue at 650°C. At 900°C, a similar trend is obtained, except that SX specimens and DS ones loaded along longitudinal directions performs almost equally in LCF and dwell-fatigue. The LCF life at 650°C is controlled by the size and position of the largest defects, whatever the specimen type. Hafnium-rich carbides clusters have been identified as very critical crack initiation sites at this temperature. At 900°C in air, oxidation controls the LCF life since crack initiation always occurred at surface oxidized carbides. It has indeed been demonstrated that carbides can already be cracked after only 5 minutes of pure thermal exposure at 900°C, due to both oxidation and the mismatch in thermal expansion between carbides and the surrounding  $\gamma/\gamma'$  "matrix". Crack initiation at 900°C in LCF in high vacuum occurred at internal pores, full of carbides, hence highlighting that the LCF life in air is highly environment dependent.

As a very surprising result, LCF lives at 900°C in air and in high vacuum were found to be almost identical, despite very different crack initiation mechanisms. Crack propagation tests at 650°C and 900°C were performed to better understand the role of oxidation on the crack propagation

mechanisms. The formation of porous chromia and alumina scales in air at 900°C increases the crack propagation threshold by combined crack tip blunting and  $\gamma'$  depletion ahead of the crack tip effects. In high vacuum, due to very sharp small cracks, the crack propagation threshold is by far lower than in air, and almost no crack closure effect is observed.

Finally, creep-fatigue interactions have been studied at 900°C, performing dwell-fatigue tests at 900°C/ $R\sigma=0.05$  with dwell times ranging from 1 second up to 300 seconds. These tests presented longer time to failure compared to their respective pure creep references. Moreover, the introduction of a dwell time at  $\sigma_{\max}$  induces a decrease in the number of cycles to failure compared to their pure LCF counterparts. It is observed that the higher the dwell time, the lower the number of cycles up to failure. The increase of the dwell time at  $\sigma_{\max}$  leads to a faster plastic strain rate and to a higher ductility during these dwell-fatigue tests for all type of specimens (i.e. <001> SX specimens and DS samples loaded along transverse and longitudinal directions). This results from wider  $\gamma$  channels when increasing the dwell time at  $\sigma_{\max}$  and hence, easier viscoplastic flow. Despite longer time at high temperature, dwell-fatigue tests with short dwell times exhibit a finer  $\gamma/\gamma'$  microstructure. This suggests a complex morphological evolution of the  $\gamma'$  precipitates, their morphology being sensitive to both the dwell time at  $\sigma_{\max}$  and to the loading/unloading sequences. The dwell-fatigue life is hence very sensitive to bulk microstructure evolutions at the precipitation scale. Based on LCF and dwell-fatigue results obtained in this study, a coupled creep-fatigue model at the macroscopic scale has been identified for each type of specimen to be able to compute the number of cycles to failure. It has been observed that a linear accumulation of creep and fatigue damage leads to a more reliable prediction of the experimental creep-fatigue lives compared to a non-linear accumulation, suggesting a non-interaction between both processes.

Even if an extensive experimental database has been generated in this work to get a better understanding of the damage mechanisms in creep, fatigue and dwell-fatigue of DS200+Hf alloy, many scientific open questions still remain. Moreover, further characterizations are necessary to be able to fully apply this work to industrial applications. Hereafter, some directions/further characterizations are proposed to deepen the already developed knowledge of the high temperature mechanical properties of this alloy and, more generally, of DS Ni-based superalloys:

- The analysis of the thin walled-debit in creep should be extended to other temperatures, covering all the operating temperatures that could be met during service. It is especially proposed to investigate the thin-wall effect at very high temperatures (e.g. 1100°C) where oxidation is much more active. The contribution of inclusions (i.e. carbides) to the thin-wall debit in creep properties still remain to be elucidated.

- A huge difference between creep tests in air and in high vacuum has been shown, especially along transverse direction in DS specimens. Grain boundary cracking was observed at creep strain as low as 0.8% at 900°C. As a major characterization required in a near future to fully understand the environmental impact, creep-crack propagation tests in air and in high vacuum are mandatory to extract  $da/dt$  versus  $\Delta K$  curves.

- Service operating conditions of airfoils may also induce much more complex loading paths than the experimental conditions investigated in this work. Investigating in-phase and out-of-phase thermo-mechanical fatigue would be even more representative of cooled (or at least, hollow) airfoils. Moreover, characterizing the durability at high to very high loading frequency is now mandatory considering new requirements imposed by the airworthiness authorities (i.e. FAA, EASA). Indeed, during operations, some aero-engines regimes may be close to the frequency of resonance of the

airfoils themselves. First very high cycle results at 1000°C/R=-1/f= 20 kHz using DS200+Hf loaded along longitudinal direction and <001> SX specimens are presented in appendix 7 [1].

- DS200+Hf can also be used with a diffusion coating (NiAl or MCrAlY) to increase the environmental resistance of components. Having a better knowledge of the consequences of the interdiffusion zone between the coating and the substrate on the mechanical properties and of the role of the coating from a fatigue resistance point of view is mandatory.

- The huge oxidation sensitivity of the alloy results from the oxidation of carbides, especially Hf-rich ones. It is highly suspected from this work that the high hafnium content of the alloy studied here (1.6 wt. pct) leads to hafnium segregation at grain boundaries, probably contributing to the environmental sensitivity. Decreasing the hafnium content to a more reasonable level would probably improve the environmental resistance and allow to increase the solution treatment temperature, hence improving the durability of the alloy. This could be another area of research to assess the exact role of the hafnium element, using the present work as a baseline.

-  $\gamma$  rafting is present at 900°C for very short creep tests. Moreover, a sluggish  $\gamma$  rafting has been observed to develop during LCF tests at 900°C/R $\sigma$ =0.05, whatever the specimen type. This  $\gamma$  precipitation degradation controls the dwell-fatigue durability of the alloy. The models developed/identified in this thesis did not take into consideration any microstructural changes such as the  $\gamma$  rafting phenomenon. Taking into account such a progressive microstructure transformation is mandatory if one wants to obtain reliable modeling of the dwell-fatigue inelastic strain rate. This could be done using microstructure sensitive constitutive modeling approaches, like the Polystar [2, 3] or the RaftX models [4] developed recently.

### References of the General Conclusion and Future prospects

1. A. Cervellon, *Durabilité en fatigue HCF d'alliages de fonderie*, PhD thesis, in Institut Pprime. 2018, ISAE-ENSMA.
2. J. Cormier and G. Cailletaud, *Constitutive modeling of the creep behavior of single crystal superalloys under non-isothermal conditions inducing phase transformations*. Materials Science and Engineering A, 2010. **527**(23): p. 6300-6312.
3. J.-B. le Graverend, J. Cormier, F. Gallerneau, P. Villechaise, S. Kruch, and J. Mendez, *A microstructure-sensitive constitutive modeling of the inelastic behavior of single crystal nickel based superalloys at very high temperature*. International Journal of Plasticity, 2014. **59**: p. 55-83.
4. R. Desmorat, A. Mattiello, and J. Cormier, *A tensorial thermodynamic framework to account for the  $\gamma$  rafting in Nickel-based single crystal superalloys*. International Journal of Plasticity, 2017. **95**: p. 43-81.

Appendices

## Appendix 1: Summary of tensile properties

The following tables are summarizing the macroscopic tensile properties obtained both at 650°C and 900°C in terms of Young's modulus (E), yield stress defined at 0.2% plastic elongation (YS 0.2%), ultimate tensile stress (UTS), strain at failure (A%) and reduction in load bearing section (Z%).

### Tensile properties at 650°C

Specimen	Strain rate (s <sup>-1</sup> )	E (GPa)	YS 0.2% (MPa)	UTS (MPa)	A (%)	Z (%)
SX - <001>	1.0E-03	108.0	952	1170	11.0	7.8
SX - <001>	1.0E-03	110.0	990	1089	7.9	12.5
SX - <001>	1.0E-03	117.2	1075	1197	7.2	2.5
SX- <102>	1.0E-03	135.0	815	865	19.4	0.5
SX - <001>	1.0E-05	99.8	1002	1205	11.5	11.7
DS-L	1.0E-03	94.0	929	1173	4.8	8.9
	1.0E-03	99.5	1018	1202	6.5	6.9
DS-T-FG	1.0E-03	120.0	872	1021	8.1	N.M.
DS-T-CG	1.0E-03	130.0	897	1016	8.8	N.M.

### Tensile properties at 900°C

Specimen	Strain rate (s <sup>-1</sup> )	E (GPa)	YS 0.2% (MPa)	UTS (MPa)	A (%)	Z (%)
SX - <001>	1.0E-03	78.0	821	959	19.0	22.0
SX - <001>	1.0E-04	89.9	659	797	24.1	24.6
SX - <001>	1.0E-04	84.6	706	841	27.9	20.9
SX - <001>	1.0E-05	80.0	593	672	23.4	29.2
SX - <102>	1.0E-04	85.0	708	813	19.1	N.M.
DS-L	1.0E-03	82.0	803	911	7.4	18.1
	1.0E-04	78.0	751	823	20.6	23.1
	1.0E-05	81.4	560	678	24.5	25.4
DS-T-FG	1.0E-03	121.5	859	960	4.6	3.1
	1.0E-04	123.3	630	764	2.6	4.0
	1.0E-04	121.6	633	797	3.8	1.5
	1.0E-05	116.3	549	642	4.6	1.5
DS-T-CG	1.0E-03	128.4	752	859	3.4	4.9
	1.0E-04	110.0	651	773	6.6	6.9
	1.0E-05	92.9	551	627	5.9	1.6
DS-45°	1.0E-05	166.9	551	580	20.8	22.8

## Appendix 2: Summary of creep properties using massive specimens

The following tables are summarizing the main creep properties using massive specimens (~ 4 mm in diameter) obtained at 750°C, 900°C and 1100°C obtained in air using a radiant furnace or in high vacuum using a radiant furnace.  $\sigma_0$ ,  $\epsilon_{prim}$ , A% and Z% are the initial applied stress, primary creep strain amplitude, creep strain at failure and reduction in load bearing section, respectively.

### Creep properties at 900°C in air using a radiant furnace

Specimen	$\sigma_0$ (MPa)	T (°C)	Failure ?	Duration (h)	A %	Z %	Minimum strain rate (s <sup>-1</sup> )	$\epsilon_{prim}$ (%)
SX - <001>	520	900	Yes	4.3	22.2	36.3	4.4E-06	0.22
SX - <001>	520	900	Yes	1.8	N.M.	N.M.	N.M.	N.M.
SX - <001>	400	900	Yes	48.5	26.6	43.5	2.9E-07	0.50
SX - <001>	350	900	Yes	127.9	27.6	43.6	3.8E-08	0.27
SX - <001>	300	900	Yes	265.2	30.1	52.5	2.4E-08	0.24
SX - <001>	250	900	Yes	768.6	30.7	53.9	9.4E-09	0.13
SX - <212>	300	900	Yes	104.7	28.9	46.4	1.7E-07	0.11
SX - <102>	300	900	Yes	279.3	21.8	33.4	7.5E-09	0.10
DS-L	520	900	Yes	3.69	18.6	26.3	5.2E-06	0.03
	400	900	Yes	41.8	22.2	34.4	2.4E-07	0.34
	350	900	Yes	86.7	22.5	36.9	6.7E-08	0.34
	300	900	Yes	166.5	23.0	37.1	3.3E-08	0.17
	250	900	Yes	597.8	23.4	36.8	1.0E-08	0.28
DS-T-FG	520	900	Yes	0.6	3.5	1.3	8.9E-06	0.06
	400	900	Yes	11.7	5.9	4.5	5.5E-07	0.09
	400	900	Yes	11.2	4.1	1.5	4.7E-07	0.16
	350	900	Yes	35.0	4.6	2.5	1.2E-07	0.31
	300	900	Yes	75.7	5.5	4.9	5.8E-08	0.19
	250	900	Yes	392.6	6.9	7.8	4.3E-09	0.05
	400	900	No	4.0	0.8	2.5	4.9E-07	0.23
	350	900	No	27.0	2.5	1.5	1.4E-07	0.08
DS-T-CG	400	900	Yes	24.8	6.0	7.8	3.1E-07	0.17
	400	900	Yes	17.6	N.M.	N.M.	N.M.	0.58
	400	900	Yes	35.3	N.M.	N.M.	N.M.	0.35
	350	900	Yes	86.4	6.9	8.6	4.8E-08	0.33
	300	900	Yes	139.0	7.0	7.5	2.9E-08	0.09
	250	900	Yes	441.1	7.3	3.4	7.5E-09	0.04
	400	900	No	14.4	3.5	N.M.	3.3E-07	0.20
	400	900	No	7.1	0.9	2.0	1.9E-07	0.22
	350	900	No	76.1	2.5	1.0	3.2E-08	0.29
DS-45°-FG	350	900	Yes	50.6	11.2	3.2	2.5E-07	0.21
	250	900	Yes	341.6	N.M.	N.M.	1.3E-08	0.21
DS-45°-CG	350	900	Yes	45.2	12.8	13.6	2.9E-07	0.26
	250	900	Yes	485.9	N.M.	N.M.	1.3E-09	0.17



Creep properties at 750°C in air using a radiant furnace

Specimen	$\sigma_0$ (MPa)	T (°C)	Failure ?	Duration (h)	A %	Z %	Minimum strain rate ( $s^{-1}$ )	$\epsilon_{prim}$ (%)
SX - <001>	800	750	Yes	158.1	21.3	9.7	1.4E-07	3.27
SX - <212>	800	750	No	0.5	24.6	N.M.	N.M.	0.00
SX - <102>	800	750	Yes	99.0	6.4	1.5	6.5E-08	0.45
DS-L	800	750	Yes	76.9	13.6	22.4	2.0E-07	4.23
DS-T-FG	800	750	Yes	1.9	5.2	4.5	N.M.	N.M.
	800	750	Yes	2.1	2.8	1.0	N.M.	0.8
DS-T-CG	800	750	Yes	6.1	4.9	4.7	N.M.	1.9
	800	750	Yes	2.3	1.8	N.M.	N.M.	0.22

Creep properties at 1100°C in air using a radiant furnace

Specimen	$\sigma_0$ (MPa)	T (°C)	Failure ?	Duration (h)	A %	Z %	Minimum strain rate ( $s^{-1}$ )	$\epsilon_{prim}$ (%)
SX - <001>	70	1100	Yes	76.0	30.6	75.3	3.1E-08	0.32
DS-L	70	1100	Yes	63.4	27.1	56.0	3.8E-08	0.29
DS-T-FG	70	1100	Yes	41.3	10.2	6.0	4.9E-08	0.11
DS-T-CG	70	1100	Yes	31.8	N.M.	35.5	6.5E-08	0.25

Creep properties at 900°C in high vacuum using a radiant furnace

Specimen	$\sigma_0$ (MPa)	T (°C)	Failure ?	Duration (h)	A %	Z %	Minimum strain rate ( $s^{-1}$ )	$\epsilon_{prim}$ (%)
SX - <001>	350	900	Yes	225.6	35.9	50.6	4.56E-08	0.20
DS-L	350	900	Yes	247.6	21.1	36.4	3.42E-08	0.04
DS-T-FG	350	900	Yes	204.9	13.4	14.6	3.50E-08	0.00
	400	900	Yes	77.5	7.8	6.1	9.44E-08	0.08
DS-T-CG	350	900	Yes	185.1	7.0	13.7	3.17E-08	0.14
	400	900	Yes	66.6	6.5	10.3	1.06E-07	0.00

Creep properties at 900°C/350 MPa for combo creep tests

Specimen	Duration (h)	Sequence	Duration 1 (h)	Minimum strain rate 1 ( $s^{-1}$ )	Duration 2 (h)	Minimum strain rate 2 ( $s^{-1}$ )	A %	Z %
DS-T-FG	100.7	Air up to 0.8% creep strain and then vacuum up to failure	24.0	7.9E-08	76.7	4.1E-08	4.3	1.0
DS-T-CG	174.9	Air up to 0.8% creep strain and then vacuum up to failure	20.4	8.6E-08	154.5	2.2E-08	6.2	6.8
DS-T-FG	127.5	Vacuum up to 0.83% creep strain and then air up to failure	106.9	2.6E-08	20.6	2.8E-07	N.M.	1.9
DS-T-CG	135.4	Vacuum up to 0.8% creep strain and then air up to failure	93.2	2.3E-08	42.2	N.M.	N.M.	N.M.

### Appendix 3: Summary of creep properties using thin-walled specimens

The following table is summarizing the main creep properties using massive specimens (~ 4 mm in diameter) and thin-walled specimens (~ 0.5 mm, ~ 0.8 and 1.5 mm in thickness) specimens creep tested up to failure using a resistive furnace. In this table,  $\sigma_0$ , A% and Z% are the initial applied stress, creep strain at failure and reduction in load bearing section, respectively. The life fraction value correspond to the creep life of a given specimen divided by the creep life of the massive specimen in air.

Specimen	Diameter (mm)	Thickness e (mm)	Width d (mm)	Perimeter P (mm)	Bearing section S (mm <sup>2</sup> )	P/S (mm <sup>-1</sup> )	T (°C)	$\sigma_0$ (MPa)	Creep life (h)	Life fraction	Minimum creep rate (s <sup>-1</sup> )	A%	Z%
SX - <001>	3.94	/	/	12.38	12.19	1.02	900	520	8.7	1.00	2.66E-06	29.2	36.1
	4.02	/	/	12.63	12.69	1.00	900	400	125.3	1.00	9.80E-08	33.1	36.2
	3.94	/	/	12.38	12.19	1.02	900	350	248.6	1.00	2.10E-08	25.9	46.2
	3.88	/	/	12.17	11.79	1.03	900	350	224.9	1.00	6.77E-08	29.9	44.0
	/	1.49	4.02	7.47	5.85	1.28	900	350	268.9	1.08	3.60E-08	31.6	29.7
	/	0.78	4.06	7.97	3.15	2.53	900	350	247.2	0.99	1.66E-08	16.8	27.6
	/	0.44	4.06	8.07	1.78	4.54	900	350	182.0	0.73	3.66E-08	7.4	17.0
DS-L	3.93	/	/	12.35	12.13	1.02	900	400	92.8	1.00	9.00E-08	17.8	33.7
	3.98	/	/	12.50	12.44	1.01	900	350	231.2	1.00	3.91E-08	20.2	33.3
	3.91	/	/	12.28	12.01	1.02	891	332	417.7	1.00	2.06E-08	21.6	32.3
	/	1.48	3.97	7.37	5.74	1.28	900	400	83.7	0.90	1.08E-07	15.4	20.9
	/	1.47	3.98	7.40	5.71	1.30	900	350	163.8	0.71	4.19E-08	18.2	23.3
	/	1.46	3.91	7.26	5.57	1.30	900	350	210.4	0.91	1.80E-08	16.2	18.3
	/	0.78	3.94	7.72	3.05	2.53	900	400	80.7	0.87	5.80E-08	12.3	12.5
	/	0.78	3.94	7.72	3.05	2.53	900	350	172.2	0.74	1.06E-08	13.2	9.8
	/	0.44	3.89	7.73	1.71	4.52	900	400	51.0	0.55	1.20E-07	5.5	18.7
/	0.46	3.99	7.93	1.83	4.33	900	350	108.0	0.47	3.38E-08	11.1	8.7	
DS-T-CG	3.94	/	/	12.38	12.19	1.02	900	400	68.9	1.00	1.10E-07	6.9	6.9
	3.89	/	/	12.22	11.88	1.03	900	350	137.9	1.00	4.60E-08	10.7	10.5
	4.00	/	/	12.57	12.57	1.00	900	300	392.5	1.00	1.81E-09	6.4	6.4
	4.01	/	/	12.60	12.63	1.00	891	368	164.1	1.00	2.83E-08	7.9	8.0
	/	1.49	3.93	7.27	5.71	1.27	900	400	51.1	0.74	1.53E-07	4.9	5.8
	/	1.46	3.98	7.41	5.68	1.30	900	350	128.4	0.93	1.11E-08	6.1	4.2
	/	0.78	3.94	7.72	3.05	2.53	900	400	26.8	0.39	7.67E-08	2.7	1.0
	/	0.75	4.03	7.92	3.00	2.64	900	350	62.3	0.45	2.92E-08	3.8	4.3
	/	0.43	3.88	7.71	1.66	4.65	900	400	25.6	0.37	4.68E-08	1.7	4.2
	/	0.48	3.99	7.92	1.91	4.15	900	350	27.1	0.20	1.18E-07	0.9	4.7
/	0.46	3.88	7.71	1.78	4.33	900	300	122.5	0.31	7.77E-09	1.9	N.M.	

The following table presents the main creep properties using a ~ 0.8 mm thick specimen tested along transverse direction (DS-T-CG) up to failure in a resistive furnace after this specimen had been first exposed to a 100 hours static oxidation at 900°C in air.

Specimen	Diameter (mm)	Thickness e (mm)	Width d (mm)	Perimeter P (mm)	Bearing section S (mm <sup>2</sup> )	P/S (mm <sup>-1</sup> )	T (°C)	$\sigma_0$ (MPa)	Creep life (h)	Life fraction	Minimum creep rate (s <sup>-1</sup> )	A%	Z%
DS-T-CG	/	0.77	3.87	7.59	2.96	2.56	900	350	56.8	0.41	2.30E-08	1.4	6.1

The following table presents the main creep properties using a ~ 0.8 mm thick specimen tested along transverse direction (DS-T-CG) up to failure in a resistive furnace after this specimen had been first exposed to a 100 hours static oxidation at 900°C in air and then repolished before starting the creep test to remove the oxidized and  $\gamma$ -depleted layer.

Specimen	Diameter (mm)	Thickness e (mm)	Width d (mm)	Perimeter P (mm)	Bearing section S (mm <sup>2</sup> )	P/S (mm <sup>-1</sup> )	T (°C)	$\sigma_0$ (MPa)	Creep life (h)	Life fraction	Minimum creep rate (s <sup>-1</sup> )	A%	Z%
DS-T-CG	/	0.71	3.85	7.57	2.72	2.78	900	350	66.8	0.48	1.10E-08	2.1	N.M.

The following table presents the main creep properties using a ~ 0.8 mm thick specimen tested along transverse direction (DS-T-CG) up to failure in high vacuum at 900°C/350 MPa.

Specimen	Diameter (mm)	Thickness e (mm)	Width d (mm)	Perimeter P (mm)	Bearing section S (mm <sup>2</sup> )	P/S (mm <sup>-1</sup> )	T (°C)	$\sigma_0$ (MPa)	Creep life (h)	Life fraction	Minimum creep rate (s <sup>-1</sup> )	A%	Z%
DS-T-CG	/	0.78	3.98	7.81	3.08	2.53	900	350	95.1	/	2.90E-08	5.2	2.3

## Appendix 4: Summary of Low Cycle Fatigue properties

The following tables are summarizing all low cycle fatigue results obtained at 650°C in air ( $R_\sigma = 0.05$  or  $R = -1$ ) and at 900°C in or under high vacuum ( $R_\sigma = 0.05$ ).

Low Cycle Fatigue tests at 650°C in air/ $R_\sigma = 0.05$ /sinusoidal waveform/frequency = 0.5 Hz

Specimen	$\sigma_{\max}$ (MPa)	Nf (cycles)	Total time (h)
SX - <001>	1055	14950	7.2
	1050	9548	5.3
	1020	19680	10.9
	900	488402	271.0
	1050	8253	4.6
	1000	21736	12.1
DS - L	950	38521	21.4
	950	17923	10.0
	900	54679	30.4
	850	164943	91.7
DS-T-CG	920	10796	6.0
	910	22915	12.7
	885	28068	15.6
	825	82038	45.5
	800	80623	44.8
	785	239871	133.3
DS-45°-CG	920	32304	17.9
	890	147821	82.2
	825	1075272	597.4

Low Cycle Fatigue tests at 650°C in air/ $R_\sigma = -1$ /sinusoidal waveform/frequency = 0.5 Hz

Specimen	$\sigma_{\max}$ (MPa)	Nf (cycles)	Total time (h)
SX - <001>	945	16	0.01
	725	8564	4.8
	675	16376	9.1
	600	359945	200.0
DS - L	850	2849	1.6
	800	3855	2.1
	600	360390	200.2
DS-T-CG	785	1356	0.8
	700	4216	2.3
	600	14991	8.3

Low Cycle Fatigue tests at 900°C in air/ $R_\sigma = 0.05$ /sinusoidal waveform/frequency = 0.5 Hz

Specimen	$\sigma_{\max}$ (MPa)	Nf (cycles)	Total time (h)
SX - <001>	795	2781	1.6
	600	43094	23.9
	520	151320	84.0
DS - L	780	4058	2.3
	600	40290	22.4
DS-T-CG	745	788	0.4
	600	13310	7.4
	520	32763	18.2
DS-45°-CG	750	1189	0.7
	520	121010	67.2

Low Cycle Fatigue tests at 900°C under high vacuum/ $R_\sigma = 0.05$ /sinusoidal waveform/frequency = 0.5 Hz

Specimen	$\sigma_{\max}$ (MPa)	Nf (cycles)	Total time (h)
SX - <001>	600	60124	33.4
	520	114608	63.7
DS - L	600	74719	41.5
DS-T-CG	600	17935	10.0

## Appendix 5: Summary of Dwell-Fatigue properties

The two following tables are summarizing the dwell-fatigue results in air and under high vacuum respectively. In these tables,  $\sigma_{max}$ ,  $E_1$ , A% and Z% are the applied stress at maximum load, the Young's modulus upon first loading, the plastic strain at failure and the reduction in load bearing section, respectively.

### Dwell-Fatigue tests at 900°C in air/ $R_\sigma = 0.05$ /trapezoidal waveform/Loading and unloading time of 1s respectively

Specimen	$\sigma_{max}$ (MPa)	Dwell time at $\sigma_{max}$ (s)	Nf (cycles)	Total time (h)	Total time at $\sigma_{max}$ (h)	$E_1$ (GPa)	A%	Z%
SX - <001>	520	10	5036	16.8	14.0	94.1	21.9	30.1
	520	1	52360	43.6	14.5	85.3	7.0	8.4
	400	300	1834	153.9	152.8	87.9	31.0	41.2
	400	10	59139	197.1	164.3	91.5	15.5	18.5
DS - L	450	300	980	82.2	81.7	86.0	29.8	23.5
	400	300	2351	197.2	195.9	87.9	31.0	34.4
	400	10	71068	236.9	197.4	94.4	15.6	15.4
	400	1	748352	623.6	207.9	92.1	8.0	4.9
DS-T-CG	450	300	691	58.0	57.6	104.4	4.8	7.8
	400	300	1292	108.4	107.7	106.0	8.5	5.8
	400	10	30728	102.4	85.4	106.0	3.0	1.5
	400	1	359020	299.2	99.7	125.1	3.5	1.4

### Dwell-Fatigue tests at 900°C under high vacuum/ $R_\sigma = 0.05$ /trapezoidal waveform/Loading and unloading time of 1s respectively

Specimen	$\sigma_{max}$ (MPa)	Dwell time at $\sigma_{max}$ (s)	Nf (cycles)	Total time (h)	Total time at $\sigma_{max}$ (h)	$E_1$ (GPa)	A%	Z%
SX - <001>	400	300	1408	118.1	117.3	N.M.	29.7	43.5
	406	10	65535	218.5	182.0	N.M.	20.9	28.3
DS - L	422	300	1664	139.6	138.7	N.M.	27.0	28.1
DS-T-CG	422	300	1566	131.4	130.5	N.M.	12.2	12.0
	415	10	23475	78.3	65.2	N.M.	6.7	5.6

A dwell-fatigue test with  $R_\sigma = -1$  and a 300 s dwell time at maximum load in tension and under compression has also been performed, to investigate the effect of the compression dwell time on the macroscopic strain rate. The main characteristics of this test are listed hereafter.

### Dwell-Fatigue test at 750°C in air/ $R_\sigma = -1$ /trapezoidal waveform/Half of Loading and unloading time of 1s respectively

Specimen	T (°C)	$\sigma_{max}$ (MPa)	Dwell time at $\sigma_{max}$ (s)	$\sigma_{min}$ (MPa)	Dwell time at $\sigma_{min}$ (s)	Nf (cycles)	Total time (h)
DS-T-CG	750	687	300	-687	300	429	72.0

## Appendix 6: Tensile and LCF properties of bi-crystalline GTD 444 alloy

The following table and figures summarize the tensile and LCF properties of bi-crystalline GTD 444 specimens tested along transverse direction at 650°C and 900°C.

### Tensile properties

T (°C)	Strain rate (s <sup>-1</sup> )	E (GPa)	YS 0.2% (MPa)	UTS (MPa)	A (%)	Z (%)
650	1.0E-03	169.2	885	1099	10.46	NM
900	1.0E-03	164.5	752	787	7.2	NM

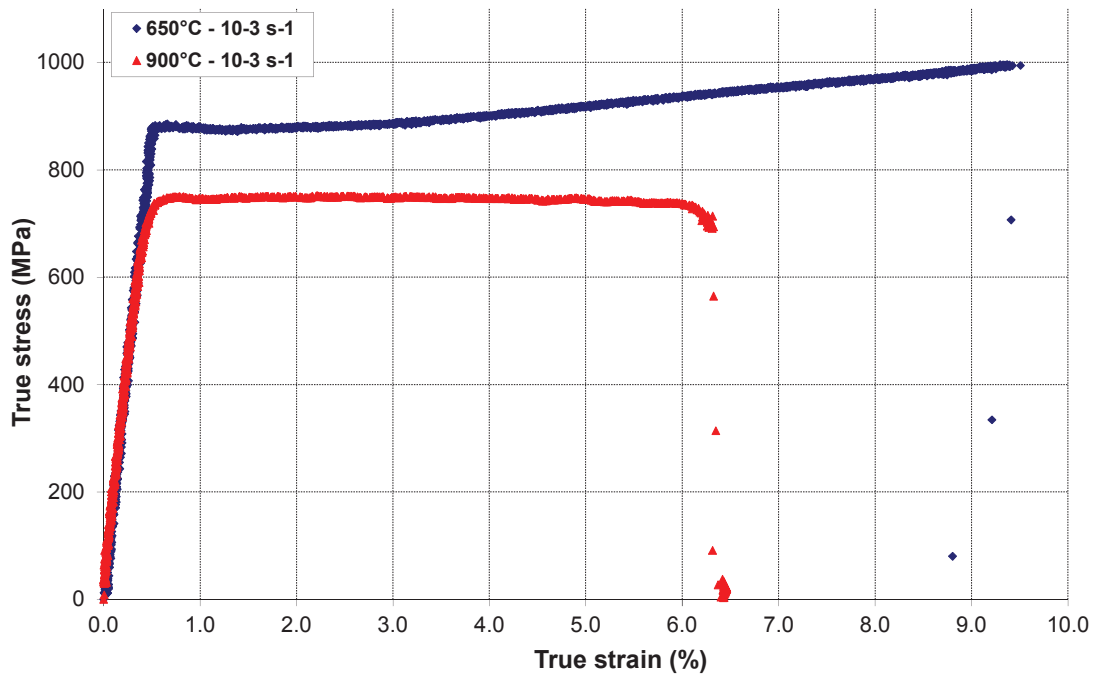


Fig. A5-1 - Tensile behavior at 650°C and 900°C/10<sup>-3</sup> s<sup>-1</sup> of GTD-444 bi-crystalline specimens

### LCF properties

As for DS200+Hf specimens, LCF tests performed using GTD-444 bi-crystalline specimens have been performed under load control mode, using a 0.5 Hz frequency and a sinusoidal waveform. Hereafter are listed the fatigue lives obtained, as well as the strain opening for the first LCF loop ( $\Delta\varepsilon_{t-1}$ )

T (°C)	$\sigma_{\max}$ (MPa)	Nf (cycles)	$\Delta\varepsilon_{t-1}$ (%)
650	874	276679	0.82
650	889	70592	0.58
650	850	480736	0.82
650	898	132100	0.76
900	795	184	0.65
900	520	66293	0.40
900	600	23866	0.58

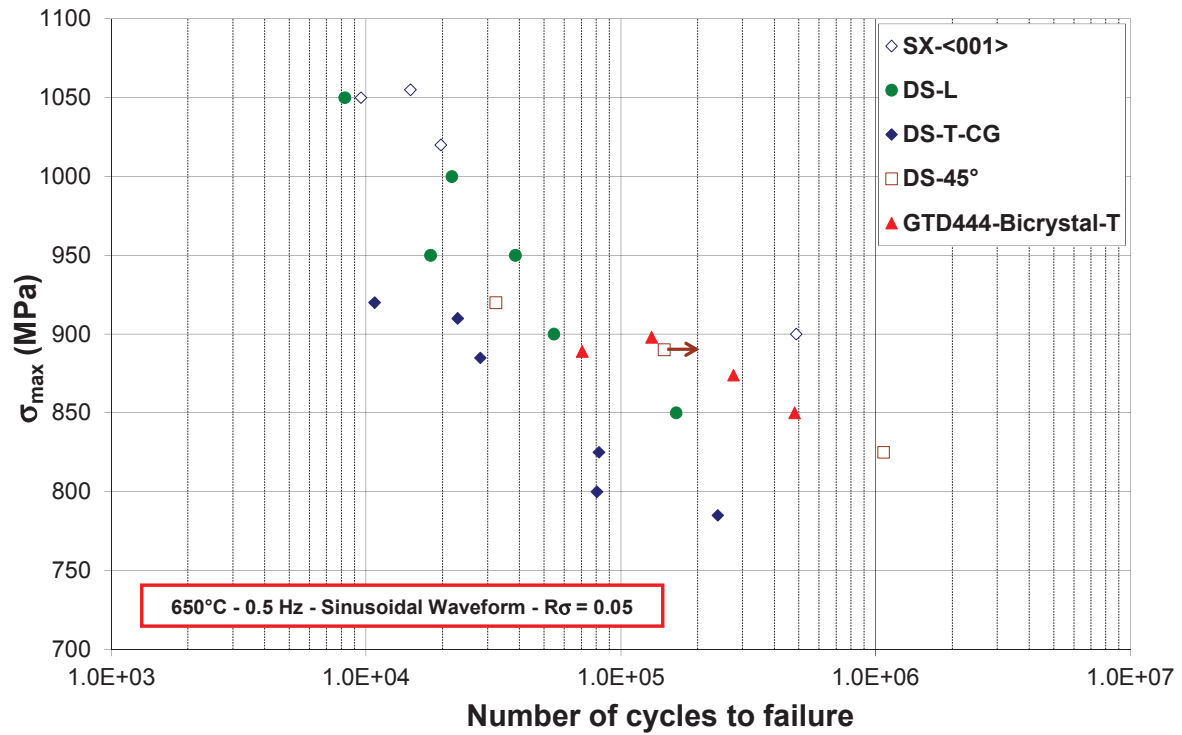


Fig. A5-2 - LCF properties at 650°C of GTD-444 bi-crystalline specimens compared to MAR-M200+Hf specimens (DS or <001>-SX ones)

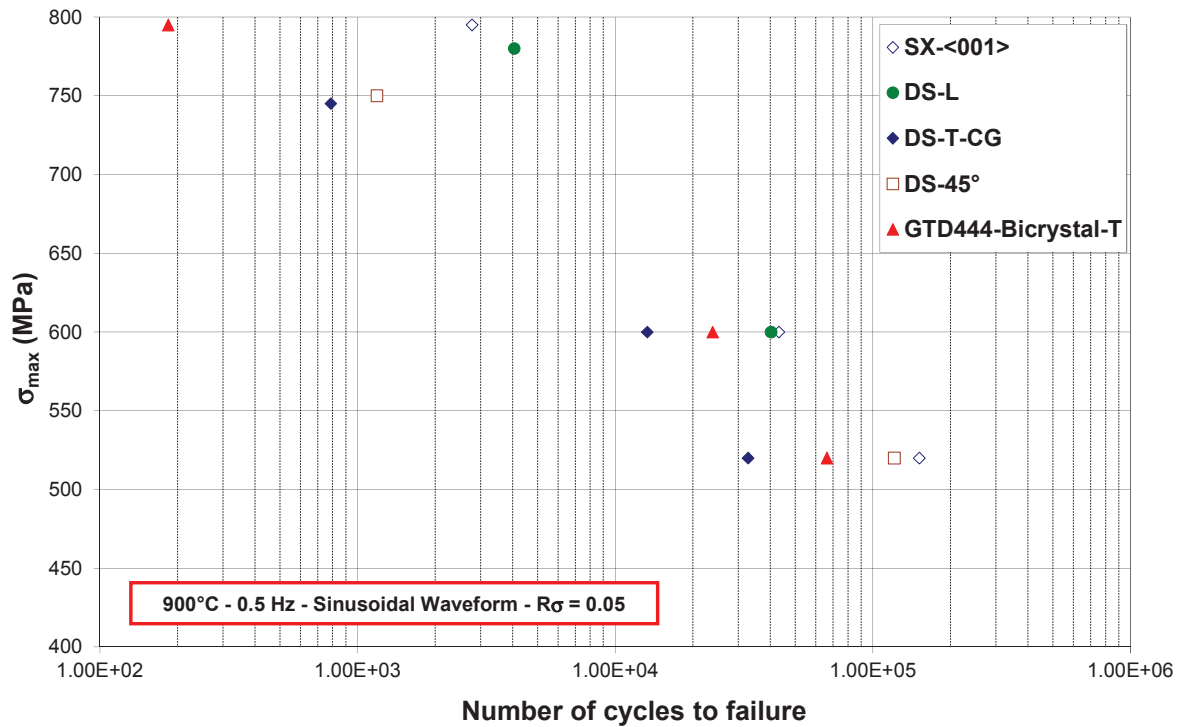


Fig. A5-3 - LCF properties at 900°C of GTD-444 bi-crystalline specimens compared to MAR-M200+Hf specimens (DS or <001>-SX ones)



Compared to DS200+Hf alloy loaded along transverse direction, it is observed better LCF properties of GTD-444 specimens at 650°C, comparable to the ones obtained for DS-L specimens. This mainly result from the smaller crack initiation sites for GTD-444 specimens (see Fig. A5-4), since these specimens have been machined from a plate solidified by the liquid metal cooling technique, a technique known to reduce the size of the metallurgical defects (pores, carbides) and hence, to improve the mechanical properties [1]. At 900°C, LCF properties of GTD-444 specimens are almost comparable to the one obtained for DS-T specimens since they have almost the same creep resistance at this temperature [2]. Indeed, such load controlled LCF tests with a quite high mean stress lead to cyclic ratcheting. The typical fracture surface is shown in Fig. A5-5 where it is observed a typical intergranular creep fracture surface, like for DS200-T specimens tested in LCF at 900°C.

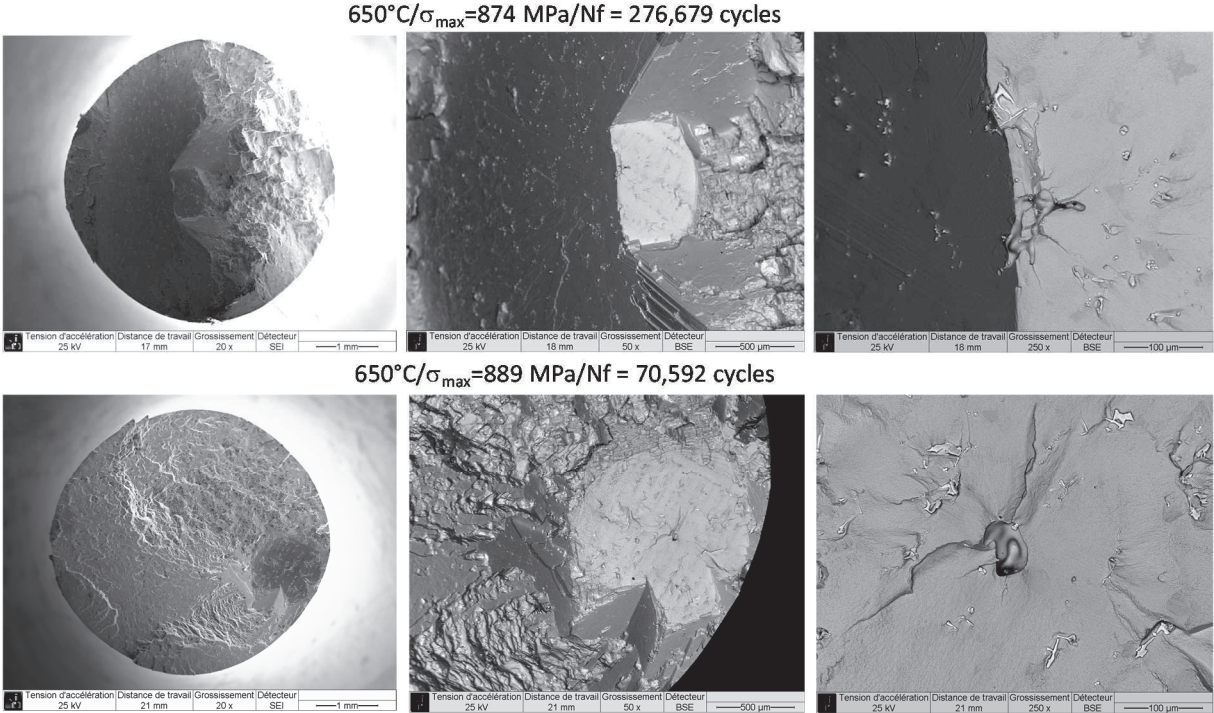


Fig. A5-4 - Typical crack initiation site in LCF at 650°C of GTD-444 bi-crystalline specimens

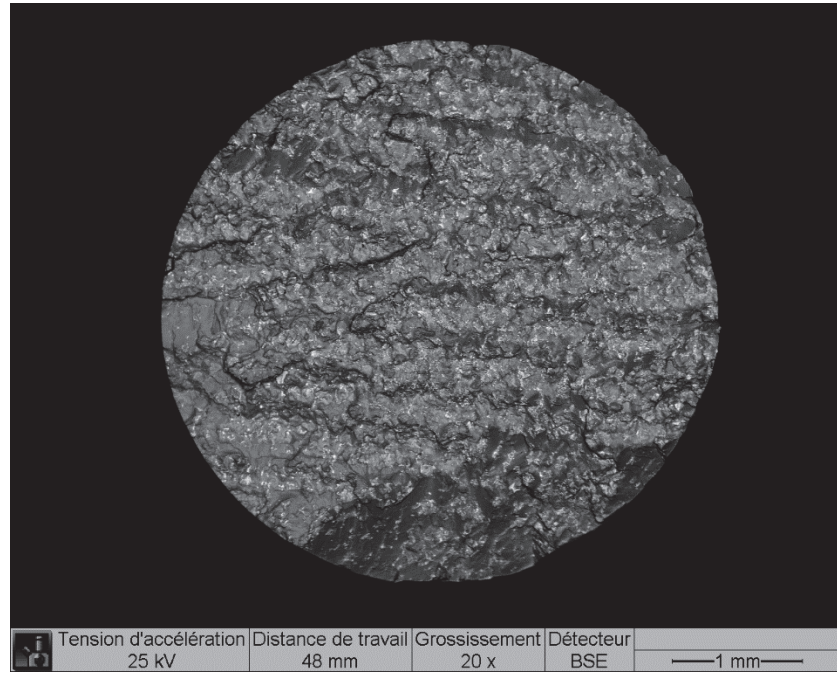


Fig. A5-5 - Typical fracture surface in LCF at 900°C of GTD-444 bi-crystalline specimens ( $\sigma_{\max} = 600$  MPa/Nf = 23,866 cycles)

## Appendix 6: Compression creep of DS200+Hf alloy

A characterization of the compressive creep behavior of DS200+Hf alloy was carried out at Safran Helicopter Engines. Cylindrical specimens of 10 mm in length were machined out from DS bars having a 280 mm of length and a 25 mm diameter. Specimens were machined along transverse direction. Because of greater length of these bars compared to the plates used in this study (which are ~ 150 mm in length), specimens taken in the top of the bar are composed by grains of about 10 mm in size, i.e. very coarse grains in comparison to the largest grains encountered in the plates. These larger grains will be denoted hereafter in this appendix as “Very Coarse Grains Safran Helicopter Engines” (VCG SHE). Specimens machined in the bottom of the bars have similar grain size than the CG of the plates (i.e. around 2.5 mm); they will be hereafter termed “Coarse Grain Safran Helicopter Engines” (CG SHE). Specimens composed of VCG SHE are comparable in terms of granular structure to single crystal specimens used in this PhD thesis, as in one specimen, it can be found only one or two grain(s).

Some creep compression results at 750°C are plotted in Fig. A6-1 and compared to the tension creep behavior obtained during this PhD thesis (see chapter 3). At 750 MPa and 800 MPa creep elongation is faster under tension than under compression if one only considers results using CG materials. VCG SHE material present faster creep deformation compared to CG specimens at 750 MPa and its behavior is almost similar to the one obtained using CG specimens at 800 MPa or <001> SX ones, but tested in tension creep. This lower creep resistance of VCG SHE specimens results from a non-homogeneous creep deformation within the specimen, with potential lattice rotation that may lead to grain boundaries crack development (as shown during tension creep in this work, see chapter 4).

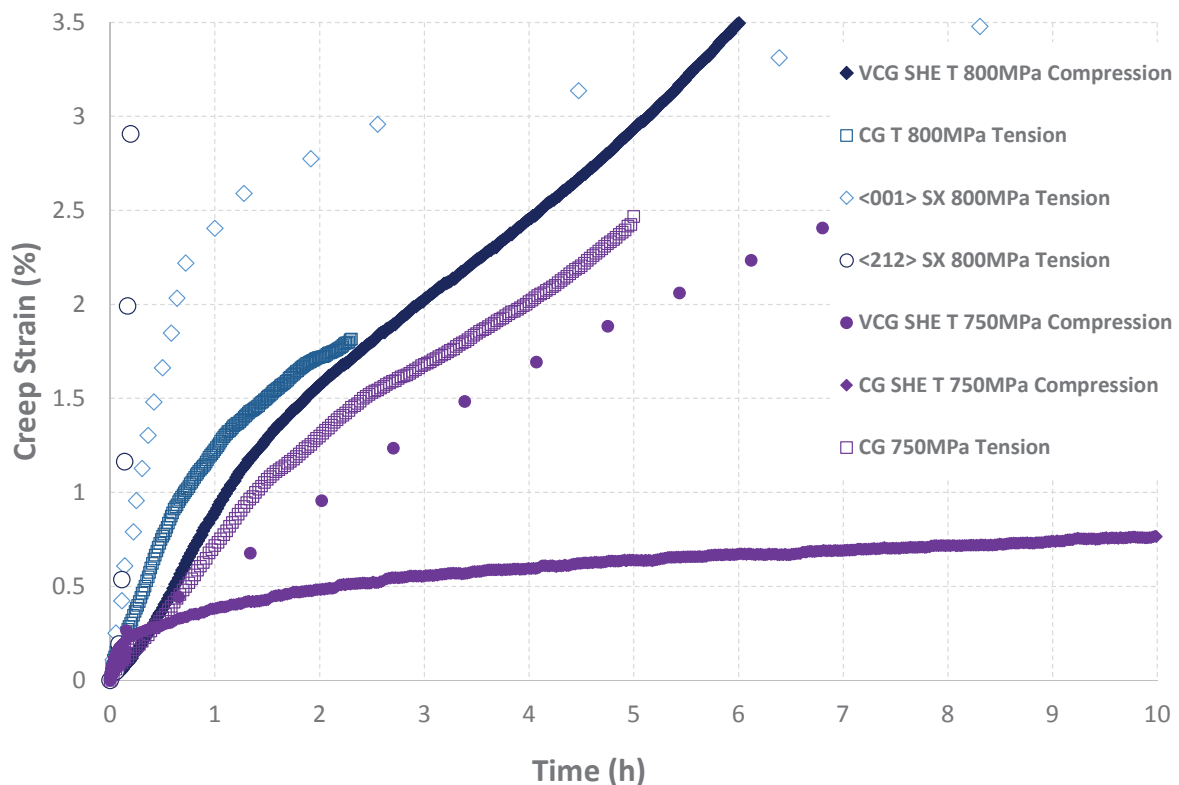


Fig. A6-1 - Compressive creep results along transverse direction at 750°C/750 MPa and 750°C/800 MPa for VCG and CG SHE specimens compared respectively to tensile creep behavior of CG and SX specimens. Note that the opposite of the creep strain is plotted.

This non-homogeneous creep strain is linked to the local grain orientation and led in some specimens to global misalignment and heterogeneous barreling, as observed in Fig. A6-2. It is recalled that at

750°C/800 MPa, the tension creep behavior was already shown in chapter 4 to be highly orientation dependent, as observed again in Fig. A6-1 when comparing the creep curves of SX specimens oriented along the  $\sim \langle 001 \rangle$  or  $\sim \langle 212 \rangle$  directions.



Fig. A6-2 - VCG SHE compression creep specimen tested under 750°C/- 800 MPa

This non-homogeneous creep deformation in the volume can also be observed in the creep strain rate versus time curves under the form of an inflection observed in creep curves for applied stress in excess of 700 MPa (see Fig. A6-3). It is suspected that this inflection point is correlated to the activation of  $\langle 112 \rangle \{111\}$  slip, as already observed during tension creep of CG specimen and shown again more clearly in the insert of Fig. A6-3.

At 850°C, VCG SHE specimens deform faster than CG SHE ones (see Fig. A6-4), as already concluded from compression creep experiments at 750°C. At this temperature, no localized preferred deformation has been observed since the creep deformation mechanisms are known to be mainly restricted to slip within the matrix (see literature review in chapter 1). Examples of microstructure observations at the end of a compression creep tests performed at 750°C/- 750 MPa and 850°C/- 600 MPa using VCG SHE specimens are shown in Fig. A6-5. No  $\gamma'$  directional coarsening could have been observed after these tests. However, it is observed several bands of highly deformed  $\gamma'$  precipitates in both conditions, especially at 750°C/- 750 MPa. These highly deformed bands may correspond to either  $\langle 112 \rangle \{111\}$  type slip or deformation micro-twinning. EBSD and/or TEM observations would be necessary to identify unambiguously the nature of these band of highly deformed precipitates.

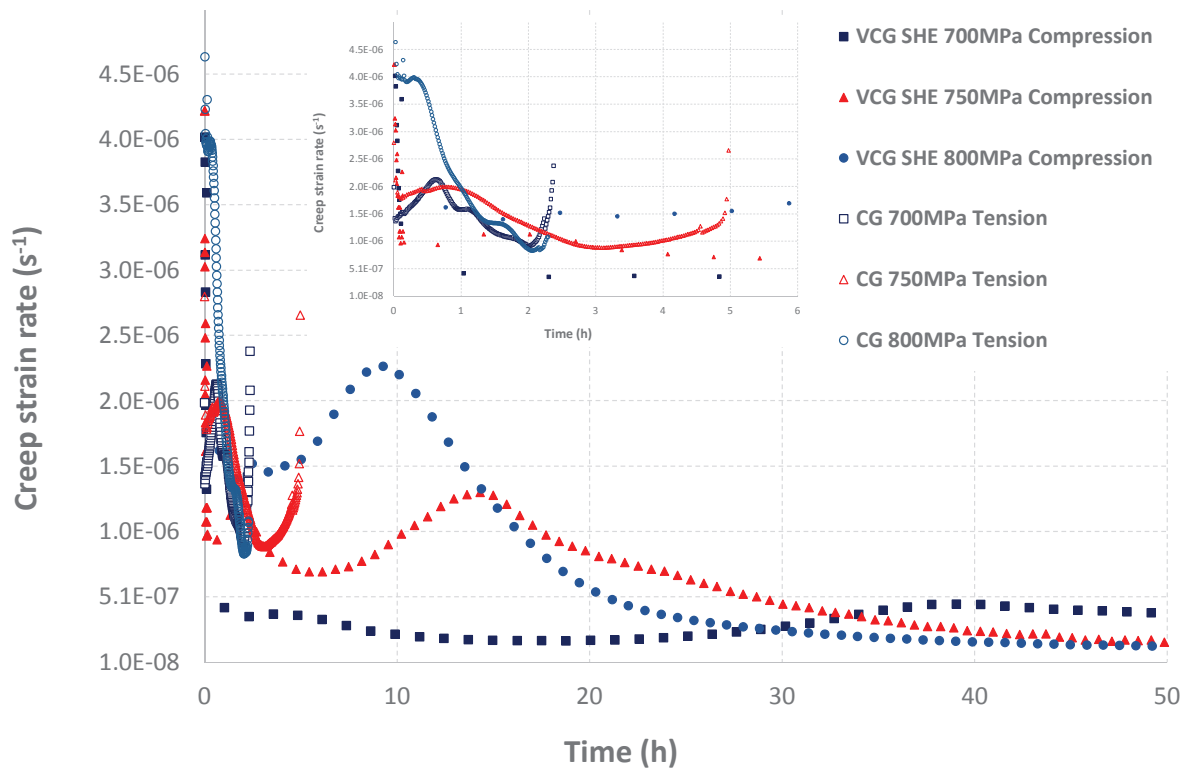


Fig. A6-3 - Compression creep behavior along transverse direction of VCG SHE specimen compared to the tension creep behavior along transverse direction of CG specimen (creep strain rate versus time plot). Note that the opposite of the creep strain rate is plotted for compression creep experiments.

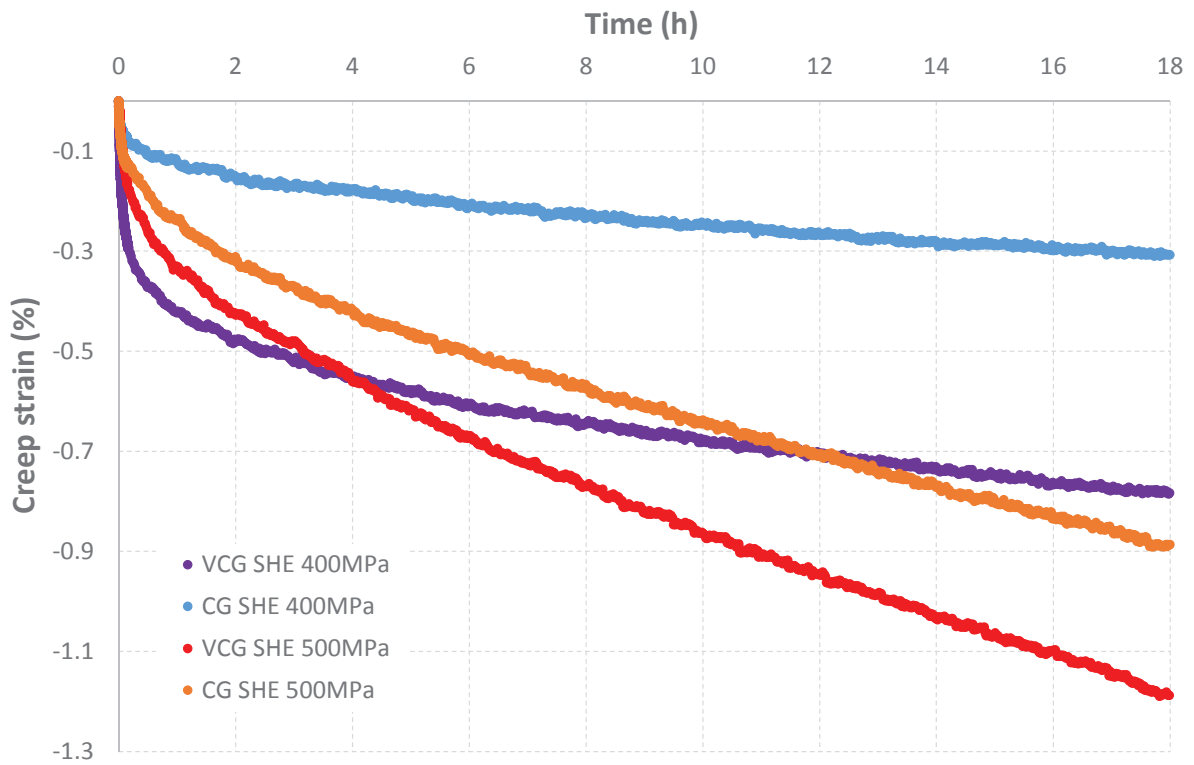


Fig. A6-4 - Compression creep curves along transverse direction at 850°C of CG and VCG SHE specimens.

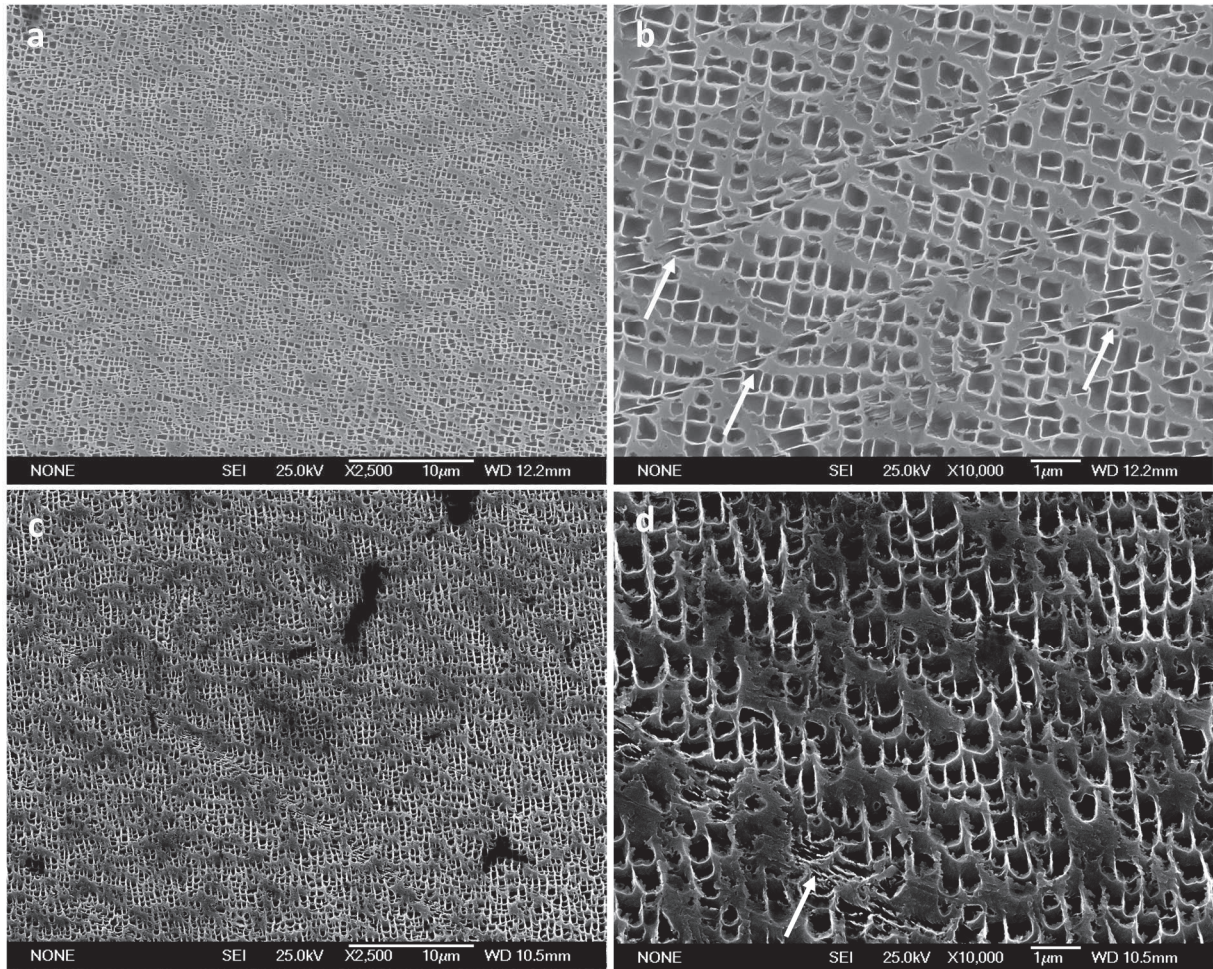


Fig. A6-5 - Microstructure of a VCG SHE specimens after compression creep at 750°C/-750 MPa (a,b) and 850°C/- 600 MPa (c,d). White arrows point out at localized deformation bands.

## Appendix 7: VHCF properties of DS200+Hf and <001> MAR-M200+Hf alloys

Table A7-1 summarizes the Very High Cycle Fatigue (VHCF) properties of DS200+Hf alloy tested along longitudinal direction compared to <001> SX MAR-M200+Hf alloy at 1000°C, R=-1 and 20 KHz. This kind of fatigue testing is especially useful when trying to identify most detrimental metallurgical defects. These results are part of the PhD thesis work of Alice Cervellon at Institut Pprime [3]. Details about experimental procedures, specimens' geometry and other similar tests carried out using CMSX-4 single-crystalline alloy can be found in reference [4]. It is here pointed out that, contrary to most of the VHCF fatigue machine used, a continuous sollicitation has been used in this study.

Material	Alternating stress $\sigma_a$ (MPa)	Nf (cycles)
<001> SX MAR-M200+Hf	144	2,358,344,062
	160	947,935,921
	180	354,011,606
	191	60,526,720
DS200+Hf - L	145	1,877,658,936
	179	79,965,679
	190	31,383,597

Table A7-1 - VHCF results at 1000°C/f=20 kHz/R=-1 using DS200+Hf and <001> SX MAR-M200+Hf alloys.

These results are summarized in the following SN-diagram (Figure A7-1). It is observed that SX specimens perform better in VHCF compared to DS specimens, like in LCF at 650°C.

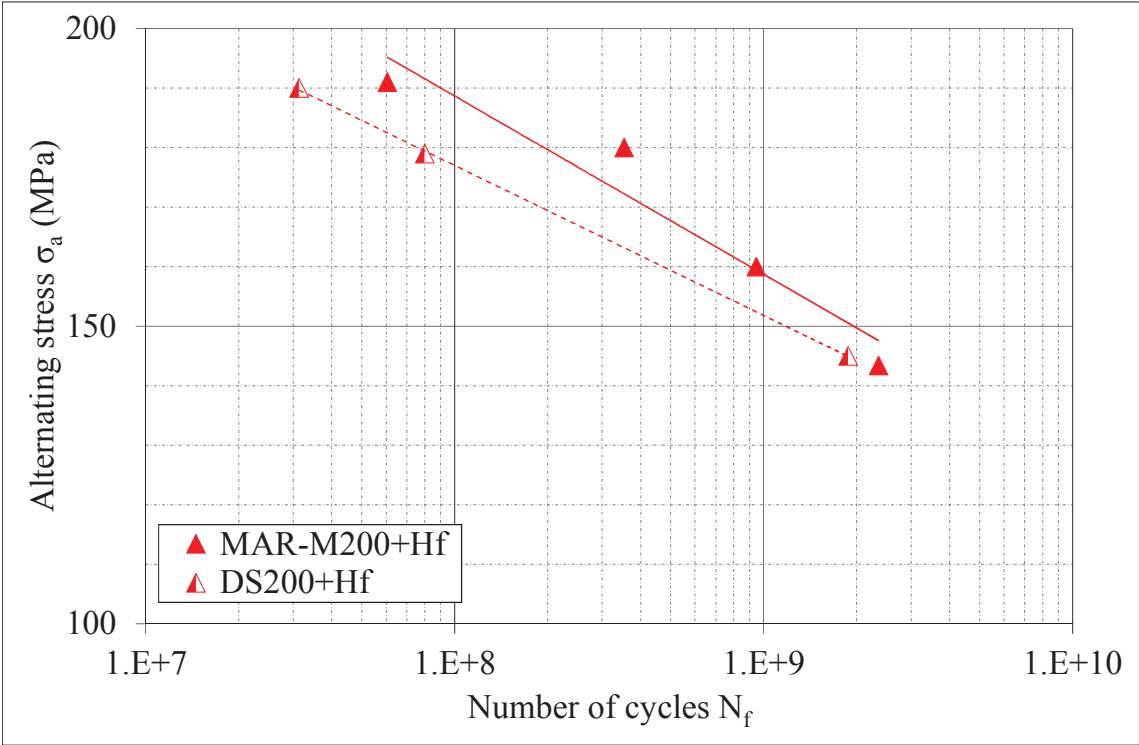


Fig. A7-1 - S-N diagram in the VHCF domain at 1000°C/f=20 kHz/R=-1 of DS200+Hf and <001> SX MAR-M200+Hf alloys.

According to fractographic observations of single crystalline specimens, crack initiation systematically occurs from internal pores with many small carbides inside, as observed in Fig. A7-2. A similar crack initiation mode was observed during LCF experiments at 900°C in high vacuum (see chapter 4). As observed in Fig. A7-2, crack propagation first follows crystallographic plane (as obtained for other Ni-based SX superalloys in this study [3]), and then changes to mode I when the fatal crack reaches the surface and then, crack propagation is assisted by oxidation. Despite crack initiation being internal, from a casting pore, oxidation-assisted crack initiation is also observed in Fig. A7-3. This was already observed on the fracture surface of Fig. A7-2 where many secondary cracks starting from the surface can be seen.

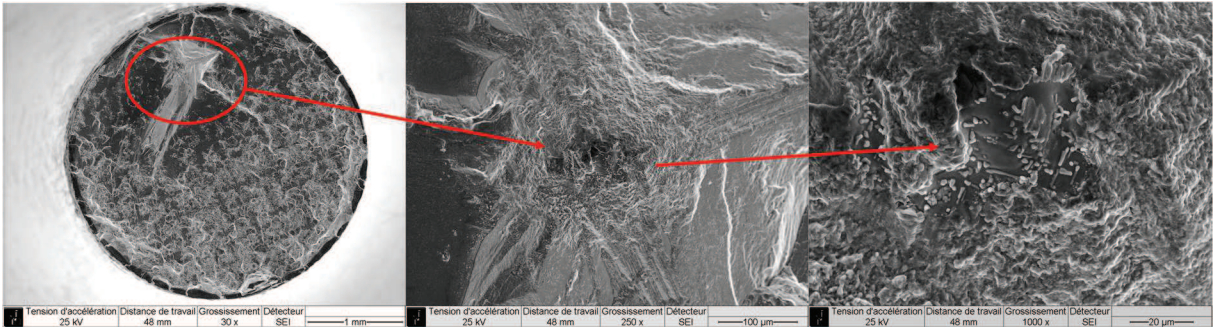


Fig. A7-2 - Crack initiation in <001> SX MAR-M200+Hf at 1000°C/f=20 kHz/R=-1/  $\sigma_a=180\text{MPa}$

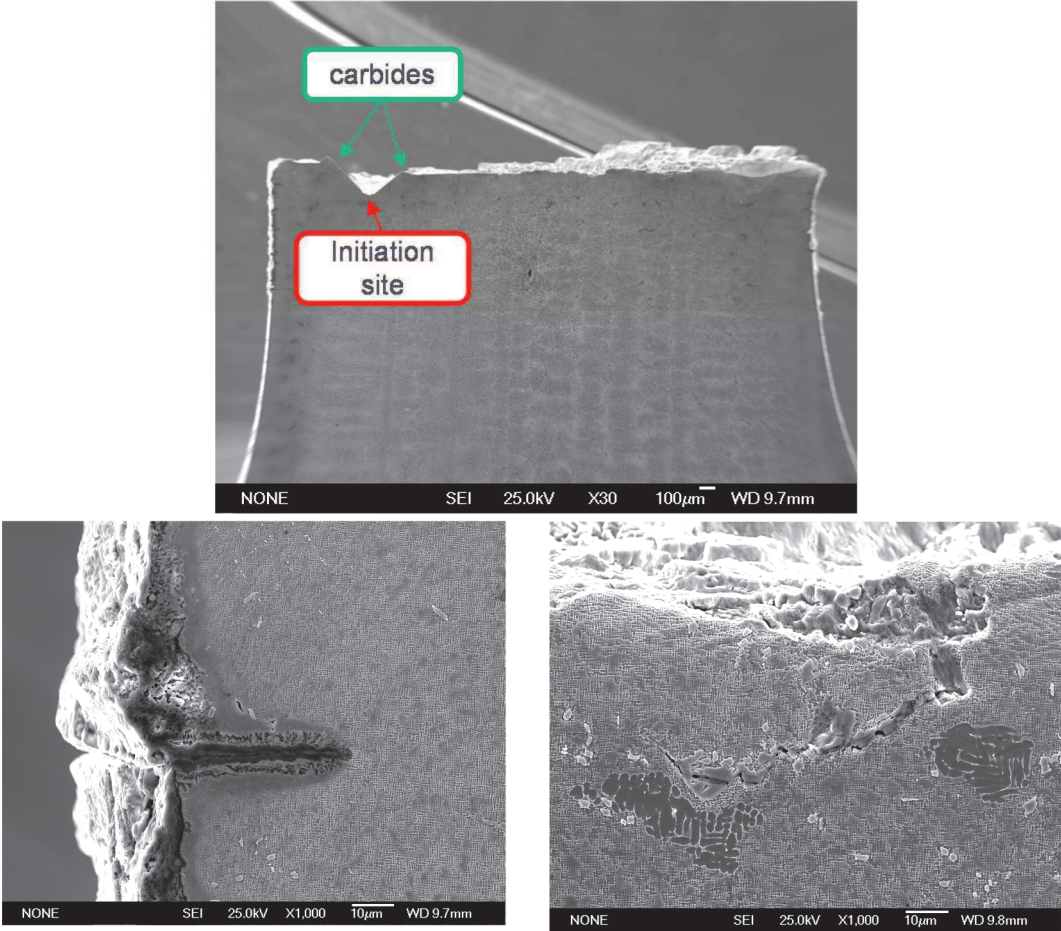


Fig. A7-3 - Crack initiation site along longitudinal cut (upper picture) and oxidation assisted crack initiation and propagation (bottom pictures) in <001> SX MAR-M200+Hf alloy at 1000°C/f=20 kHz/R=-1/  $\sigma_a=180\text{MPa}$



Crack initiation in VHCF in DS200+Hf alloy is influenced by the presence of grain boundaries. Cracks can initiate from pores with Hf rich carbides inside and that are located along or close grain boundaries, or from oxidation spikes, depending on the applied alternating stress (Fig. A7-4). In every cases, a macroscopic mode I crack propagation is observed, with some crack deviations induced by grain boundaries (Figure A7-5). It hence shown in this work then even in ultrasonic fatigue using a continuous solicitation mode, crack initiation may occur from the surface from oxidized carbides if the tests are long enough. It once again shows the poor oxidation resistance of MAR-M200+Hf in the 900-1000°C temperature range.

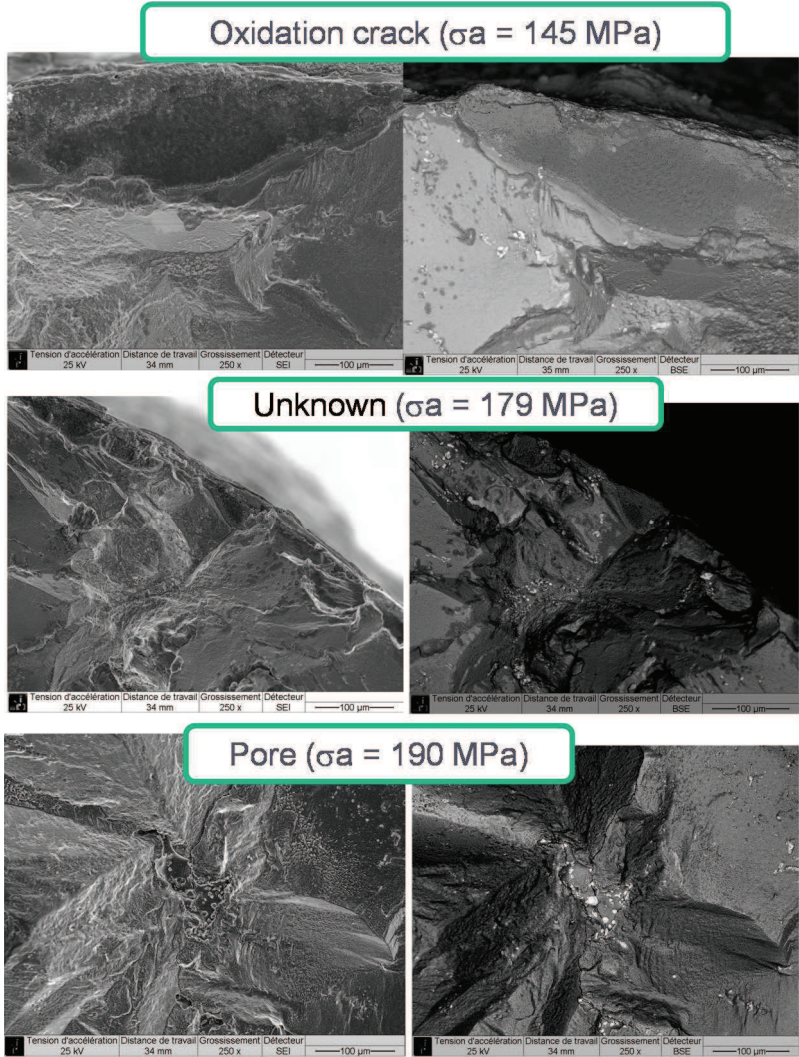


Fig. A7-4 - Crack initiation sites in DS200+Hf alloy tested along longitudinal direction at 1000°C/f=20 kHz/R=-1.

As a perspective for this study in VHCF, tests at R=0.8 are planned to compare the relative VHCF resistances of CMSX4 and MAR-M200+Hf SX alloys under this condition. These two alloys have indeed very different creep resistances that may affect the VHCF life at such a high loading ratio [4]. The final goal is to investigate VHCF crack initiation and propagation mechanisms at high loading ratio (i.e. in the presence of creep damage).

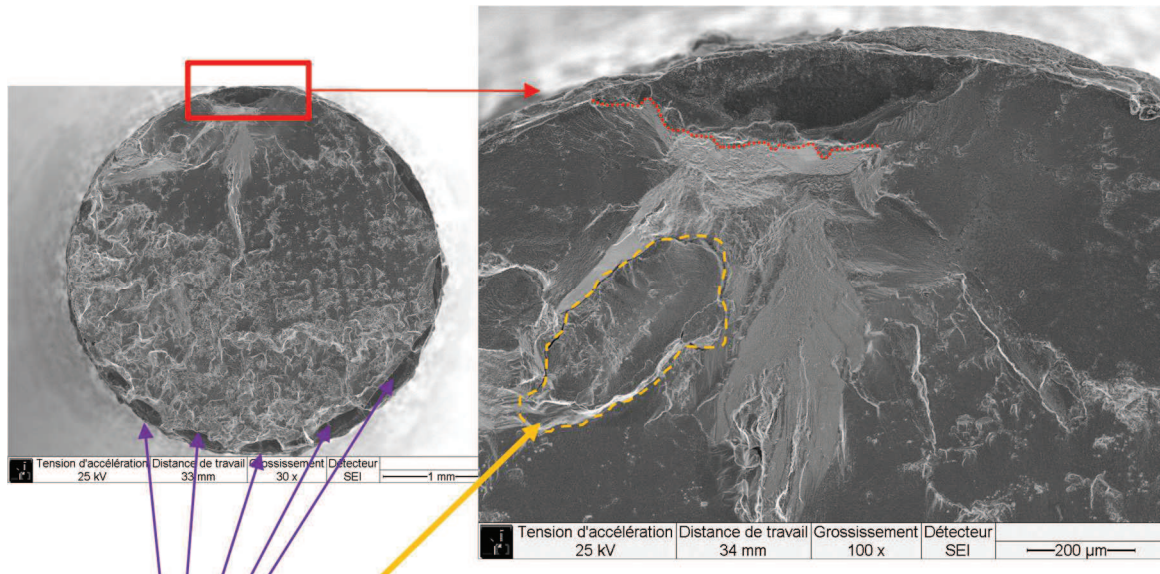


Fig. A7-5 - Mode I crack propagation after crack initiation from the surface from oxidized carbides (red rectangle and purple arrows) in DS200+Hf tested along longitudinal direction at 1000°C/f=20 kHz/R=-1/  $\sigma_a=145\text{MPa}$ . Yellow arrow highlight a carbide cluster located along a grain boundary.

## References of Appendices

1. S. Steuer, P. Villechaise, T. Pollock, and J. Cormier, *Benefits of high gradient solidification for creep and low cycle fatigue of AM1 single crystal superalloy*. Materials Science and Engineering: A, 2015. **645**: p. 109-115.
2. J.C. Stinville, K. Gallup, and T.M. Pollock, *Transverse Creep of Nickel-Base Superalloy Bicrystals*. Metallurgical and Materials Transactions A, 2015. **46A**: p. 2516-2529.
3. A. Cervellon, *Durabilité en fatigue HCF d'alliages de fonderie*, PhD thesis, in Institut Pprime. 2018, ISAE-ENSMA.
4. A. Cervellon, J. Cormier, F. Mauget, and Z. Hervier, *VHCF life evolution after microstructure degradation of a Ni-based single crystal superalloy*. International journal of Fatigue, 2017. **104**: p. 251-262.

## Mécanismes d'endommagement à haute température du superalliage DS200+Hf

L'anisotropie de comportement mécanique du superalliage à solidification dirigée DS200+Hf et les mécanismes d'endommagement ont été étudiés entre 650°C et 1100°C. Des échantillons monogranulaires du même alliage ont été employés afin de mieux comprendre l'anisotropie de propriétés mécaniques et de durabilité. Des essais de traction, fluage, fatigue oligocyclique, fatigue-fluage et de fissuration ont été réalisés, suivis d'observations au MEB afin d'analyser les modes d'endommagement.

A 650°C, une forte anisotropie de durée de vie en fluage (et en fatigue) est observée alors que l'anisotropie est quasi inexistante à 1100°C en fluage. Ceci résulte de la mise en radeaux de la phase  $\gamma$  à haute température qui homogénéise la déformation, dégradation qui conduit à une augmentation de la vitesse de déformation en fatigue avec temps de maintien. Un amorçage intergranulaire a été observé pour tous les essais mécaniques en sens travers, notamment de par la présence de nombreux carbures aux joints des grains. Ces carbures sont les principaux sites d'amorçage de fissure de fatigue à 650°C et 900°C. A haute température (900°C), l'oxydation affecte non seulement l'amorçage en favorisant la fissuration des carbures de surface, mais elle affecte également la phase de propagation, via un processus combiné d'appauvrissement de la phase  $\gamma$  et d'émoussement de la pointe de fissure, le tout conduisant à un seuil de fissuration plus élevé. Sous vide, un tel processus n'est pas observé et les carbures ne sont plus les sites d'amorçage privilégiés. Lors de sollicitation de fluage en sens travers à basse température (750°C), les joints de grains fortement désorientés, avec un grain dans leur voisinage favorablement orienté pour le glissement simple et apte à la rotation cristalline, sont les plus critiques.

Mots-clés : Alliages réfractaires, Fissuration, Fluage, Métaux--Fatigue, Oxydation, Matériaux--Propriétés mécaniques, Carbures, Anisotropie.

## Damage mechanisms at high temperature of DS200+Hf alloy

The anisotropy in mechanical behavior of the directionally solidified DS200+Hf alloy and the damage mechanisms have been investigated between 650°C and 1100°C. Single-crystalline specimens of the same alloy have also been used to get a better understanding of the anisotropy in mechanical properties and durability. Tension, creep, low-cycle fatigue (LCF), dwell-fatigue and crack propagation tests have been performed and analyzed by SEM observations to better understand the damage modes in this alloy.

At 650°C, a considerable creep (and LCF) life anisotropy is observed while almost no anisotropy remains at 1100°C in creep. The  $\gamma$  rafting is mainly responsible for this decrease in creep anisotropy and for the increase in creep rate in dwell-fatigue. An intergranular fracture mode has been observed for all kind of solicitation along transverse direction, mainly due to the presence of grain boundary particles such as carbides. These carbides are also the main crack initiation sites in LCF at 650°C and at 900°C. At high temperature (900°C), oxidation not only controls the crack initiation mechanisms by inducing surface carbides cracking, but it also affects the crack propagation through a combined localized  $\gamma$  depletion and crack tip blunting, leading overall to a higher crack propagation threshold. Such a behavior is not observed in high vacuum and surface carbides are no more the main crack initiation sites. It is shown that at low temperature during transverse creep testing (750°C), highly misoriented grain boundaries, having one grain favorably oriented for single slip and lattice rotation, are the most critical ones.

Keywords: Heat resistant alloys, Cracking, Creep, Metals--Fatigue, Oxidation, Materials—Mechanical properties, Carbides, Anisotropy.